New Bimetallic Catalysts for Dioxygen Activation

(Alternative Format Thesis)

Singer Hobbs, Maya

Award date:
2021

Awarding institution:
University of Bath

New Bimetallic Catalysts for Dioxygen Activation (Alternate Format Thesis)

Singer Hobbs, Maya

Award date:
2021

Awarding institution:
University of Bath

New Bimetallic Catalysts for Dioxygen Activation

Maya Singer Hobbs

Supervisor: Ulrich Hintermair

Co-Supervisor: Karen Edler

A thesis submitted in partial fulfilment for the degree of Doctor of Philosophy

April 2021

Acknowledgments

I would like to thank Uli Hintermair for his supervision and insights throughout the project. I also need to thank the CSCT for the funding and opportunities.

I need to thank a number of staff members/post-docs/friends who helped with specific parts of the project and whose wisdom was invaluable, they include: Frank Marken for his passion and patience about all things electrochemistry, Karen Edler & Julien Schmitt for SAXS help, Gabi Kociok-Köhn for X-Ray expertise, Tom Roseveare for informal crystallography tips and Shaun Reeksting for his help and enthusiasm about mass-spec. I also need to thank Antoine Buchard and Janet Scott for always being on my team. Finally, I need to thank John Lowe and Catherine Lyall, not only for their expertise with NMR, but also for allowing me to adopt them as unofficial mentors.

I feel incredibly lucky to have had some of the most fantastic colleagues/co-conspirators in the Hintermair group & beyond, who provided technical and (much needed) social support throughout. You're all great, but there are a few honourable mentions: Stuart – for never being daunted by a challenging piece of synthesis, Andy – for helping me 'dial in to radio proton', Matt – my thesis writing buddy, Kasia – for much needed discipline (and encouraging words) during write up, and Niko – for his infectious laugh!

Outside of the lab, there are many others who played an important role in getting me to the finish line and without whom this journey would have been considerably less fun. Among these are: Kirsty – you were my anchor to normality (and made sure I was well-fed throughout!) and I couldn't have asked for a better housemate and friend, Emma – for sharing the highs and the lows (research or otherwise!) and for your endless support with the echem (you turned it into something that I even, despite myself, enjoyed!) and Amy – 'soulsista' who's always been steadfast in your love and support.

My parents, Judith and Nigel, who installed in me skills that turned out to be pretty useful whilst doing a PhD: the ability to ask questions, a healthy questioning of authority, and a strong sense of self. Thank you both so much. I also need to thank Cal, for making me belly laugh and pushing me to question the status quo in equal measure.

Finally, Theo. You believed in me when I didn't believe in myself, and for that I am forever grateful. Thank you so much.

Figure 0.2: My principle proof-reader hard at work.

Abstract

The oxygen reduction reaction is a key process for sustainable energy generation, and there is increasing demand for catalysts that perform aerobic oxidations. Although both processes involve oxygen activation, there are limited examples of catalysts that perform both reactions. In this work, a series of six bimetallic cobalt μ-peroxo (μ-OO) and six analogous μ-chloro (μ-Cl) complexes, based on the 3,5-bis-(pyridin-2-yl)pyrazole (Hbpp) ligand, were synthesised and characterised using NMR and UV-vis spectroscopy, X-ray crystallography, mass spectrometry and electrochemistry. The activity of the μ-OO complexes towards the oxygen reduction reaction and oxygen atom transfer was investigated.

Using cyclic voltammetry, the μ-OO complexes were found to undergo a reversible one electron redox event (determined using Randles-Sevcik analysis) at around -0.5 V vs. NHE. Scanning to more negative potentials (-1.5 V vs. NHE) resulted in a second irreversible reduction event (E_{red}). The irreversibility was tentatively ascribed to be due to breaking of the peroxo O–O bond. The E_{red} value for the second reduction was found to negatively correlate to the O–O bond lengths determined using X-ray crystallography, suggesting that complexes that bound O_2 less tightly required less energy to be reduced.

The μ-Cl complexes were found to react with O_2 when in solution to form their corresponding μ-OO complexes. The unsubstituted (Hbpp ligand) parent complex was found to have the fastest rates, whilst the strongly electron-withdrawing nitro substituent effectively stopped any activity. The reactivity of the μ-OO complexes towards the oxygen reduction reaction (ORR) was studied, and the rates were found to correlate to the rates of oxidation, suggesting that O_2-binding is a key step in both processes.

Studies of the reactivity of the μ-OO complexes towards oxygen atom transfer (OAT) revealed that the unsubstituted parent complex and the backbone-bromo substituted complex showed activity towards benzaldehyde. Using NMR spectroscopy and mass spectrometry the main product of the reaction was determined to be a benzoate adduct, indicating nucleophilic reactivity by the peroxo of the metal complex, and an unidentified paramagnetic species. The two reactive μ-OO complexes had E_{red} potentials that were less negative than the other four complexes, suggesting that the ease

with which the oxygen adduct is reduced is important in predicting the reactivity of these complexes.

Attempts to synthesise analogous copper, zinc and palladium complexes to the cobalt species resulted in the formation of dimers (with general formula $M_2(bpp)_2$) or clusters with 4 or 5 metal centres. Dimer formation could be prevented through the use of different ligand architectures, and progress was made towards diversification of the library of ligands.

Finally, in order to investigate the feasibility of the use of operando small angle X-ray scattering (SAXS) for the detection of nanoparticles *in situ*, a study was conducted on a series of iridium water oxidation catalysts. The study confirmed that the catalysts were operationally homogeneous, and proved the viability of SAXS for such studies.

Contents

1 Introduction **3**

1.1 Oxygen as a Reagent/Reactant 5

1.1.1 Oxygen (O_2) Activation 7

1.2 Catalytic Activation of O_2 9

1.2.1 Use of First Row Transition Metals in O_2 Binding and Activation 10

1.2.2 Ligand Effects in O_2 binding 11

1.2.3 Aerobic Oxidations 13

1.2.4 Oxygen Reduction Reaction (ORR) 21

1.3 Oxygen Atom Transfer 27

1.4 Homogeneous vs. Heterogeneous Catalysis 31

1.5 Aims 33

2 Synthesis of Bimetallic Cobalt Complexes **35**

2.1 Introduction 35

2.1.1 Bimetallic Complexes based on the Hbpp Ligand 36

2.2 Ligand Synthesis 40

2.2.1 Ligand Functionalisation 42

2.3 Synthesis of Cobalt Complexes 47

2.3.1 Synthesis of Co(III)-peroxo Complexes: $Co1_{O_2}$ – $Co6_{O_2}$ 47

2.3.2 Synthesis of Co(II) complexes: $Co1_{Cl}$ – $Co6_{Cl}$ 51

2.4 Characterisation and Structural Analysis of Co1 – Co6 52

2.4.1 NMR Spectroscopy Studies of Complexes $Co1_{O_2}$ – $Co6_{O_2}$ 52

2.4.2 NMR Spectroscopy of Paramagnetic Complexes: $Co1_{Cl}$ – $Co6_{Cl}$ 55

2.4.3 Crystallography of Cobalt Complexes 61

2.4.4 UV-vis Spectroscopy of Co1 – Co6 70

2.5 Conclusions 73

2.6 Future Work 75

2.6.1 Additional Characterisation 75

2.7 Experimental 75

2.7.1 Analytical Techniques 75

2.7.2 Ligand Precursor Synthesis 77

2.7.3 Diketone Synthesis . . . 78
2.7.4 Diketone Functionalisation . . . 79
2.7.5 Pyrazole Synthesis . . . 80
2.7.6 Pyrazole Functionalisation . . . 82
2.7.7 Cobalt Complexes . . . 83

3 Reactivity of Cobalt Complexes 91
3.1 Introduction . . . 92
3.1.1 Previous Studies with $\mathbf{Co1_{O2}}$ . . . 92
3.1.2 Oxygen Atom Transfer with Hbpp-based complexes . . . 93
3.2 Analytical Techniques Used in this Chapter . . . 94
3.2.1 Electrochemical Methods . . . 94
3.2.2 Introducing Graphical Rate Analysis . . . 97
3.3 Electrochemical Characterisation and Oxidation Studies of $Co1_{Cl}$ – $Co6_{Cl}$ 98
3.3.1 Electrochemistry of $Co1_{Cl}$ – $Co6_{Cl}$ . . . 98
3.3.2 Oxidation Studies of $Co1_{Cl}$ – $Co6_{Cl}$ . . . 103
3.3.3 Comparisons and Conclusions to studies with $Co1_{Cl}$ – $Co6_{Cl}$ . . 106
3.4 Cyclic Voltammetry Studies on $Co1_{O_2}$ – $Co6_{O_2}$ . . . 109
3.4.1 Determination of E_{mid} Values of $Co1_{O_2}$ – $Co6_{O_2}$ . . . 109
3.4.2 Randles-Sevcik Analysis . . . 110
3.4.3 Wide Scan Width CVs . . . 117
3.4.4 Comparison of Electrochemical Data with Structural Data . . . 124
3.4.5 Electrochemical testing under acidic conditions . . . 125
3.4.6 Conclusion of Cyclic Voltammetry Studies on $Co1_{O2}$ – $Co6_{O2}$ . . 130
3.5 Application of $Co1_{O_2}$ – $Co6_{O_2}$ in the ORR . . . 131
3.5.1 Kinetics of Oxygen Reduction . . . 135
3.5.2 Testing the sequence of reactivity of the complexes under ORR conditions . . . 140
3.5.3 Comparison of ORR results with Electrochemical Properties and Oxidation Reactivity . . . 143
3.5.4 Conclusion to ORR studies . . . 146
3.6 Oxygen Atom Transfer Studies . . . 147
3.6.1 Substrate Screening . . . 147
3.6.2 Identifying the Product(s) of the Reaction with Benzaldehyde . 149

3.6.3 Screening of Complexes for Reactivity towards Oxygen Atom Transfer . . . 156
3.6.4 OAT Conclusions . . . 158
3.7 Conclusions . . . 159
3.8 Future work . . . 162
3.8.1 Investigation of Catalyst Deactivation and Reaction Mechanism 162
3.8.2 Further OAT studies . . . 164
3.9 Experimental . . . 164
3.9.1 General . . . 164
3.9.2 Electrochemical Analysis . . . 165
3.9.3 Interconversion between μ-Cl and μ-OO . . . 165
3.9.4 Oxygen Reduction Reaction . . . 166
3.9.5 Testing the Stability of the Complexes . . . 166
3.9.6 Oxygen Atom Transfer . . . 166
3.9.7 Reagents for Stop-Flow studies . . . 167

4 Further Synthesis of Bimetallic Complexes 169
4.1 Introduction . . . 170
4.1.1 Further Complexes using the Hbpp Ligand . . . 172
4.2 Preliminary Results to Expand the Library of Metal Complexes . . . 175
4.2.1 Copper Complexes using the Hbpp Ligand . . . 175
4.2.2 Zinc Complexes using the Hbpp Ligand . . . 184
4.2.3 Palladium Complexes using the Hbpp Ligand . . . 185
4.2.4 Conclusion to Further Metal Complex Synthesis . . . 187
4.3 A brief discussion of an *ortho*-Bromo Ligand . . . 188
4.4 Further Ligand Functionalisation . . . 189
4.4.1 Addition of a Binding Site: NNX Functionalisation . . . 189
4.4.2 Substitution on the Ligand Backbone . . . 198
4.5 Conclusions and Future Work . . . 201
4.5.1 Towards the Synthesis of Heterobimetallics . . . 202
4.6 Experimental . . . 203
4.6.1 Analytical Techniques . . . 203
4.6.2 Metal Complexes . . . 204
4.6.3 Further Ligand Synthesis: *ortho*-Bromo Substitution . . . 207
4.6.4 Further Ligand Synthesis: Addition of a Binding Site . . . 208

4.6.5 Further Ligand Synthesis: Substitution on the Pyrazole Backbone 210

5 In-situ Monitoring of Nanoparticle Formation during Iridium-catalysed Oxygen Evolution by real-time Small Angle X-ray Scattering 213

5.1 Introduction to Published Work . . . 214
5.2 Small Angle X-ray Scattering (SAXS) . . . 215
5.3 Statement of Authorship . . . 218
5.4 In-situ Monitoring of Nanoparticle Formation during Iridium-catalysed Oxygen Evolution by real-time Small Angle X-ray Scattering . . . 219
5.4.1 Introduction . . . 219
5.4.2 Results and Discussion . . . 222
5.4.3 Data Fitting . . . 224
5.4.4 Cp*Ir(pyalk) precursor complexes . . . 226
5.4.5 Correlation with Catalytic O_2 Evolution . . . 227
5.4.6 Conclusion . . . 230
5.4.7 Acknowledgements . . . 231
5.4.8 Conflict of Interest . . . 231
5.4.9 Experimental . . . 231
5.5 Commentary and Conclusions . . . 233

6 Conclusions and Future Work 235

6.1 Future Work . . . 241
6.1.1 Raman Spectroscopy . . . 241
6.1.2 EPR Spectroscopy . . . 241

Bibliography 241

A Appendix 265

A.1 Appendix to Chapter 2 . . . 265
A.1.1 An Introduction to Paramagnetic NMR Spectroscopy . . . 265
A.1.2 Paramagnetic NMR Assignments . . . 269
A.2 Appendix to Chapter 3 . . . 273
A.2.1 Oxidation Studies Initial Rates . . . 273
A.2.2 Electrochemistry Details . . . 273
A.2.3 Conversion between μ-Cl and μ-OO species . . . 277
A.2.4 Oxygen Reduction Reaction . . . 278

A.2.5 Degradation Studies 281
A.2.6 Oxygen Atom Transfer 284
A.3 Appendix to Chapter 5 291
A.3.1 SAXS Apparatus 291
A.3.2 Particle Size Distribution for IrA 291
A.3.3 SAXS data for complexes Ir2 - Ir7 292
A.3.4 O_2 evolution overlaid with NP formation, [IrA] = 5 mM 293
A.4 Crystallography Data 295
A.4.1 $Co2_{Cl}$ 295
A.4.2 $Co3_{O2}$ 296
A.4.3 $Co4_{O2}$ 297
A.4.4 $Co5_{O2}$ 298
A.4.5 $Co6_{O2}$ 299
A.4.6 Mononuclear Co6 300
A.4.7 Copper Dimer 301
A.4.8 Copper Tetramer 302
A.4.9 Copper Cluster 303
A.4.10 Zinc Cluster 304

Abbreviations

BDD	Boron Doped Diamond
bipy	2,2'-Bipyridine
CE	Counter electrode
COSY	Homonuclear Correlation Spectroscopy
Cp*	1,2,3,4,5-pentamethylcyclopentadiene
CV	Cyclic Voltammetry
DCM	Dichloromethane
DFT	Density Functional Theory
DLS	Dynamic Light Scattering
DMSO	Dimethylsulfoxide
DOSY	Diffusion Ordered Spectroscopy
EC	Reversible electron transfer, followed by irreversible homogeneous chemical reaction
EPR	Electron Paramagnetic Resonance spectroscopy
Hbpp	3,5-bis(pyridin-2-yl)-pyrazole
HOMO	Highest Occupied Molecular Orbital
HMBC	Heteronuclear Multiple Bond Correlation
HSQC	Heteronuclear Single Quantum Coherence
LUMO	Lowest Unoccupied Molecular Orbital
Me_8Fc	Octamethyl ferrocene (1,1',2,2',3,3',4,4'-octamethylferrocene)
NHE	Normal Hydrogen Electrode
NMR	Nuclear Magnetic Resonance
OAT	Oxygen Atom Transfer
ORR	Oxygen Reduction Reaction
PCET	Proton Coupled Electron Transfer
RE	Reference electrode
RDS	Rate Determining Step
SAXS	Small angle X-Ray scattering
TFA	Trifluoracetic acid
THF	Tetrahydrofuran
TLC	Thin-layer chromatography
TMEDA	tetramethylethylenediamene
trpy	2,2':6',2"-Terpyridine
UV-vis	Ultraviolet-visible spectroscopy
WE	Working electrode
XRD	X-ray diffraction
VTNA	Variable Time Normalised Analysis

Chapter 1

Introduction

Although first isolated in the early 1600s by Michael Sendivogius, and then again by Carl Wilhelm Scheele, it was Joseph Priestly who is most commonly remembered as the person who first discovered and isolated oxygen, although he referred to it as "dephlogisticated air".[1] Phlogiston theory was an attempt to explain combustion and had been the dominant principle in combustion theory for the past 100 years. Around the same time as Priestly, Antoine Lavoisier identified oxygen as an element, determined its role in combustion, and was instrumental in overturning phlogiston theory completely.[2] In 1794 Elizabeth Fulhame published "An Essay on Combustion" which built on Lavoisier's findings, and is also thought to be the first time catalysis is described.[3] Unfortunately, as is true of many historical female scientists, her name is little known.[4]

Since the 1700s, both oxygen and catalysis have become better understood. Oxidation reactions are now incredibly important for a whole range of industrial processes, including the production of bulk and fine chemicals.[5] Traditionally, oxidation chemistry has been carried out using commercially available oxidants based on metals such as chromium or manganese, and used in stoichiometric quantities. One of the most famous oxidation reactions is the Swern Oxidation, Figure 1.1, which is an early example of a selective oxidation using mild conditions.[6]

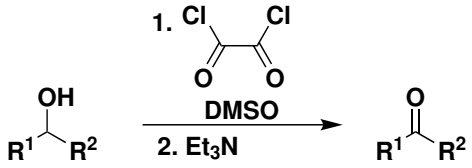

Figure 1.1: The Swern oxidation, which proceeds via reaction of the DMSO with the oxalyl chloride, before the oxidation of the substrate. The byproducts from the reaction include CO, CO_2 and Me_2S.

Industrially, oxidation reactions are a relatively small subsection of the total number of reactions carried out in pharmaceutical synthesis.[7] Historically, limited numbers of

these reactions will have been catalytic, and even fewer used oxygen as the terminal oxidant. Additionally, many of the more benign oxidants, such as m-CPBA (*meta*-chloroperoxybenzoic acid) or NBS (N-bromosuccinimide) are not sufficiently selective for application in fine chemical synthesis.[8]

However, over recent years the field of oxidation chemistry has grown, and there are some notable classes of substrate, oxidation reaction, and catalysts that serve as the basis for further development, including; olefin and alcohol oxidations, epoxidation and oxidation of C–H bonds.[5] Osmium tetroxide is commonly used as a catalyst for olefin oxidations and when used in conjunction with a chiral ligand and a base can produce reasonably good enantioselectivies for the oxidation.[5] Palladium is also widely used to carry out olefin oxidations, *via* a Wacker-style mechanism,[9–11] and more recent studies have investigated the scalability of such processes.[12] Historically, oxidation of alcohols has been carried out using chromium or manganese reagents, which again produce considerable quantities of stoichometric, toxic, waste, or alternatively, the Swern oxidation is used (Figure 1.1). More recent developments in alcohol oxidation have used milder reagents such as TEMPO (2,2',6,6'-tetramethylpoperidine-*N*-oxyl) which is used as a catalyst in the presence of a terminal oxidant, such as sodium hypochlorite (NaOCl). Further developments have focused on the synthesis of metal catalysts to perform such reactions aerobically, often in the presence of TEMPO, as discussed further in Section 1.2.3.

Many of the design criteria for synthetic aerobic oxidation catalysts also apply to the search for oxygen reduction reaction catalysts for use in fuel cells.[13–15] These design criteria include:

- **Oxidatively robust ancilliary ligands:** Ligands are commonly polyaromatic systems with nitrogen donors and no CH_2 groups.
- **Metal centres with multiple accessible oxidation states:** iron and copper are commonly found in naturally occurring systems.
- **Ability to bind and activate O_2:** the species needs to activate O_2 but not form an oxygen adduct that is too stable to perform catalysis.
- **High catalytic performance:** In order for a process to be truly sustainable, the catalyst loading needs to be low, and the cost of producing ancillary ligands needs to be cheap.

1.1 Oxygen as a Reagent/Reactant

The relationship between transition metals and molecular oxygen, particularly for the inorganic chemist, is often characterised by ill-will due to the ready decomposition of many organometallic complexes of the transition metals in the presence of O_2.[16] However, this interaction is as important outside the chemistry department as it is in the laboratory. Without the well-known activation of oxygen by iron found in haem, Figure 1.2, human life on earth would not exist.[17–19]

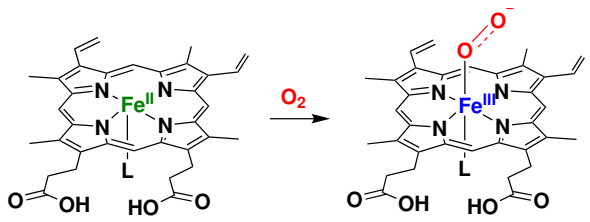

Figure 1.2: The reaction between the iron centre in haem and O_2 (L = histidine, or 4-methylimidazole).[20,21]

Nature performs the effective transformation of abundant substrates, using first-row transition metals such as iron and copper, in aqueous media at ambient pressures and temperatures. As a consequence, oxidation chemistry has traditionally been inspired by nature, where there is ample inspiration for synthetic analogues to perform oxidation catalysis.[18] Iron-based systems are one of a number of oxidising metalloenzymes, which perform aerobic oxidations using O_2 on varied substrates, including the oxidation of steroids, fatty acids and other aromatic substrates.[21,22] One of the most famous of these is cytochrome P450, which contains a haem-cofactor and, among other things, performs epoxidations of C–C double bonds.[18] Metalloenzymes are often used as a starting point when looking more closely at the interaction between transition metals and dioxygen, and can inform rational design of homogeneous catalysts by looking at common moieties found in nature.

However, despite the many attractions of using O_2 as a reagent, including cost, abundance and environmental impact, there are a number of challenges associated with its use, including the synthesis of active catalysts. Additionally, the safe operation of high pressure reactions in the presence of O_2 and flammable solvents is challenging and as such there are still limited examples of its use in industrial oxidations.[7,23–25]

The limiting oxygen concentration (LOC) is the concentration below which a combust-

ible mixture is not supported. According to the combustion triangle, it is not simply enough to remove ignition sources, the presence of sufficient fuel, oxidiser (O_2) and heat, or energy, can cause combustion. LOCs are specific to different solvents at varied temperatures and pressures.[26] Even air is above the limiting oxygen concentration (LOC) for safe operation under some circumstances, and there are examples where the oxygen concentration is diluted through addition of nitrogen.[26]

As a consequence, most oxidations in the context of synthetic chemistry are carried out using stoichiometric oxidising agents such as permanganate or chromium-based reagents.[27] Although effective, the focus on sustainable chemical solutions means such reagents are less favoured due to their poor atom economy and toxic byproducts.[28,29] Aerobic oxidation chemistry has seen a growing interest as the urgency for sustainable synthetic routes to commodity chemicals has increased.[10,30] Therefore, green oxidants, such as O_2 or H_2O_2, are of interest to improve the sustainability of oxidation chemistry.

Dioxygen is paramagnetic with a triplet ground state, 1.3a. Generally, the presence of unpaired electrons leads to highly reactive species which are short-lived, although synthetically such species can be stabilised through the use of bulky substituents.[19] In order to understand oxygen reactivity, it is first necessary to understand why O_2 does not tend to undergo spontaneous reactions with organic substrates. Dioxgyen's σ bond is relatively weak, but recent studies by Thatcher-Borden *et al.* showed that the resonance of the π bond contribute a stabilisation of 418 kJ/mol, 1.3b.[19] It is also of note that in most cases, activation of the O_2 bond is reductive, in order to populate the π^* orbital, although it is possible to use spin inversion to singlet O_2.

The reaction of most molecules with oxygen is strongly thermodynamically favoured. The combustion of methane has an enthalpy of -890 kJ mol^{-1},[31] and the formation of haematite, an iron oxide, has an enthalpy of reaction of -822 kJ mol^{-1}.[32] Despite this, dioxygen comprises 21% of the Earth's atmosphere, and most objects do not spontaneously combust upon contact with O_2. The triplet ground state of dioxygen means that the reaction with most organic substrates, which have closed shell singlet electronic configurations, requires a large activation energy, due to the spin forbidden nature of the reaction. In natural systems, metalloenzymes reduce O_2 (bond order = 2) to peroxide (O_2^{2-}, bond order = 1) or superoxide (O_2^-, bond order = 1.5) forms which are no longer in the tripler state, and therefore considerably more reactive towards organic substrates.

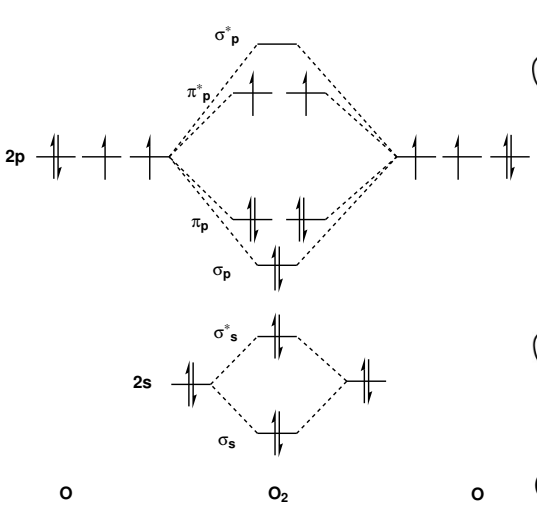

(a) The molecular orbital diagram for triplet dioxygen.

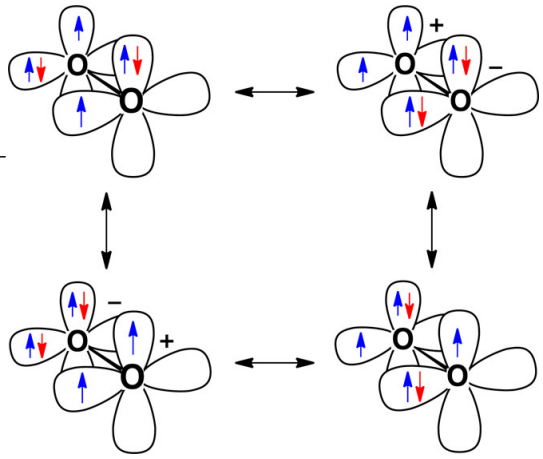

(b) Resonance of the π bond in O_2. Reprinted with permission from *J. Am. Chem. Soc.* 2017, **139**, 9010-9018. Copyright (2017) American Chemical Society.[19])

Figure 1.3: The MO diagram for O_2, showing the two unpaired elections, and the resonance of the O–O bond which contributes to its stability.

Predicting the reactivity between transition metals and O_2 can be challenging, as there are a number of factors that need to be taken into account; the oxidation state of the metal, the coordination environment around the metal centre, the ligands, and of course the thermodynamic drivers and kinetic barriers for the reaction. Extended lattices of metals and oxygen (metal oxides) tend to act as 'thermodynamic sinks' for the catalyst, forming readily under oxidising conditions. As a consequence, within the field of homogeneous catalysis, it is necessary to tune both the metal complex and the reaction conditions to prevent the formation of such species. Developing aerobic oxidation catalysts requires lowering the activation energy required to facilitate reaction of a substrate with O_2, without resulting in uncontrolled total oxidation (combustion), whilst also preventing the formation of thermodynamically favoured metal oxides. This is achieved by ensuring the catalyst can "return" to its reduced state without loss of the ligand, as discussed further in Section 1.2.2.

1.1.1 Oxygen (O_2) Activation

Metalloenzymes activate dioxygen by reducing it to the more reactive peroxide (O_2^{2-}) or superoxide (O^{2-}) species, Figure 1.4.[33] Most of the oxygen binding metalloenzymes are bimetallic copper systems, and are "type-3" proteins, Figure 1.9.[34–36] These are a class of proteins that have a bimetallic core of two copper centres, each of which

is coordinated by three histidine residues. The type-3 oxidising enzymes include catechol oxidase, which is found in some plants and fungi and transforms diphenols into ortho-quinones, and tyrosinase which catalyses the transition of phenols to catechols and quinones.[33] Low temperature studies (−78 °C) of metalloenzyme analogues have helped reveal important characteristics of the reactivity of the bimetallic copper centre, including structural and electronic properties, and potential reactivities.[37]

Although many metalloenzymes are bimetallic, there are some notable mono-metallic examples, such as haemoglobin and other porphyrin complexes. In mono-metallic systems, O_2 is bound to the metal centre via one of two binding modes, η^1 or η^2, shown in Figure 1.4. Note that when bound in the η^1 form the bound dioxygen more closely resembles the superoxide state discussed previously (O_2^-, bond order = 1.5) whereas in the η^2 binding mode, the dioxygen is closer to a peroxo state. These binding modes are observed in natural systems, such as iron porphyrin complexes like haemoglobin, and synthetic analogues.[38]

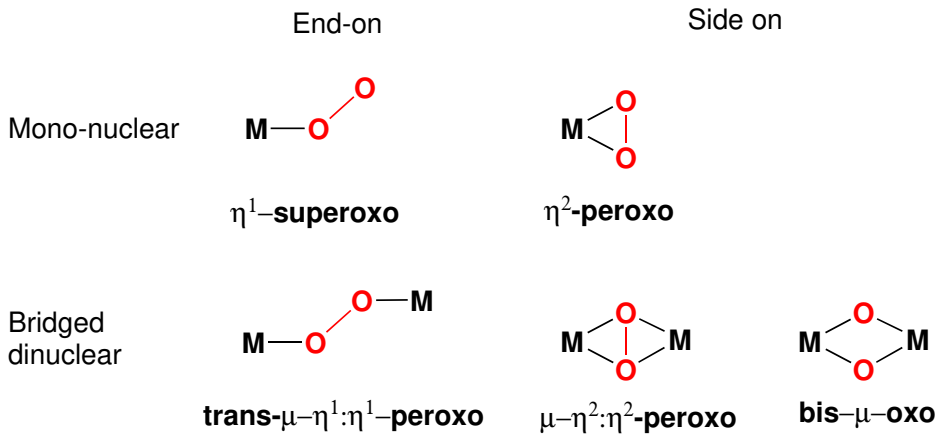

Figure 1.4: The binding modes of O_2 to one or two metal centres. The binding mode gives an indication of the degree to which the complex has activated the O–O bond. The end-on mode is colloquially referred to as the Pauling binding mode, whilst the side-on mode is known as Griffith binding.[39] Examples of each can be found in Figure 1.5. Note that both bridging dinuclear peroxo species are also collectively called bis-μ-peroxo species.

Elwell *et al.* report on series of mono-copper oxygen complexes, stating that upon binding dioxygen, the degree of electron transfer, and therefore the degree of activation of the O–O bond, is dependent on the "electron-donating power and denticity of the supporting ligands".[36] In their reported Cu–O and O–O distances, determined by X-ray crystallography, the O–O distances are consistently greater when the oxygen is bound

in an η^2-binding mode than in an η^1 configuration, suggesting that the O–O bond is weaker when bound in an η^2 configuration. The use of Raman spectroscopy can help distinguish between different binding modes, as the wavenumber associated with the O–O stretch will give an indication of the bond strength, with higher wavenumbers indicating a stronger bond, according to Equation 1.1:

$$\tilde{\nu} \propto \sqrt{\frac{k}{\mu}} \tag{1.1}$$

Raman spectroscopy can also allow investigations into the metal-to-ligand charge transfer (MLCT) transitions of the M–O bond.[36,40] In general, complexes where the bound O_2 is assigned as η^1 have wavenumbers in the region associated with superoxides (ν(O–O) = ≈1100 cm^{-1}) and bond lengths in the region of 1.2 – 1.3 Å, whereas those with η^2 binding modes have wavenumbers under 1000 cm^{-1} which is more similar to those of peroxides, with bond lengths closer to 1.4 Å.[36]

The mechanisms of catalytic aerobic oxidation reactions in naturally occurring systems have been studied in depth, including structural investigations into the active site of the enzyme and the mechanism of oxygen activation.[35] These studies have informed the design of synthetic analogues, and allowed insights into the binding modes of O_2 by first row transition metals, the impact of this on the activation of the O–O bond, the roles of ancillary ligands, and the mechanism of oxygen activation.[13] This is discussed in more detail in Section 1.2.1 of Chapter 2.

1.2 Catalytic Activation of O_2

Building on the activation of O_2 discussed in Section 1.1.1, catalytic activation of O_2 opens the door to a range of different applications. This includes aerobic oxidations, which has synthetic chemistry applications, and oxygen reduction reactions for fuel cell applications.

The two oxidations outlined above, the Swern oxidation and the reaction of O_2 with the iron centre in haem, demonstrate an important distinction in some oxidation reactions. The Swern oxidation is an example of a dehydrogenative oxidation, whereby the alcohol undergoes oxidation to a ketone, *via* the loss of a proton. O_2 can be used as a terminal oxidant in these reactions, but is not itself incorporated into the product. Other oxidation reactions result in the transfer of an oxygen atom to the product (oxy-

gen atom transfer, OAT), which will be discussed in more depth in Section 1.3. In many cases, when O_2 is used as the oxygen source, only one oxygen atom is transferred to the product. The other is released from the catalyst, commonly as H_2O which is often facilitated by the addition of a coreductant. A number of the common types of aerobic oxidation reaction are outlined in Table 1.1.

1.2.1 Use of First Row Transition Metals in O_2 Binding and Activation

There are many examples of the use of first row transition metals being used successfully in O_2-binding an activations, although their use is not without challenges. The formation of oxides can hinder the synthesis of homogeneous catalysts, whilst the many variable coordination geometries can complicate the rational design of catalysts. Additionally, although the use of copper and iron is appealing due to their use in metalloenzymes, both are paramagnetic, which can complicate characterisation and monitoring of catalysis.

However, there are many examples that use other first row transition metals, including cobalt, nickel and manganese, to perform such transformations. One of the key features of many of these catalysts is their bimetallic nature, either through the use of carefully designed ligands, or through a cooperative mechanism during catalysts.[41–45]

There are a variety of modes in which O_2 is bound to the metal centre(s), Figure 1.4, and identifying these is key in predicting activity. The length of the O–O bond can be used to infer the bond strength, and therefore how activated the O–O species is.[46] Characterisation of these oxygen containing complexes can be carried out using X-ray crystallography and various spectroscopic techniques.[18,39,47]

Unsurprisingly, due to their abundance in nature, porphyrins are commonly found in oxidation chemistry, along with synthetic macrocyclic derivatives.[13] A common motif is a sandwich or "Pac-man" style complex, where two metal centres are held in close proximity to each other, facilitating the binding of O_2 between them.[39,48]

Some of the common synthetic derivatives that employ this "Pac-man" style motif are based on Schiff-bases, due to their ease of synthesis and scalability. Work by Love and coworkers demonstrated a dicobalt complex that spontaneously reacted with O_2 to form a Co_2^{III}-μ-OO species, as shown in Figure 1.5c. Using a mixture of electrochemical oxidation and a sacrificial oxidant, the reactivity of these complexes towards the oxygen

reduction reaction was investigated. Although turnover was observed, the rates of reactivity were low, with the catalyst achieving between 7 – 16 turnovers before loss of activity.[49,50]

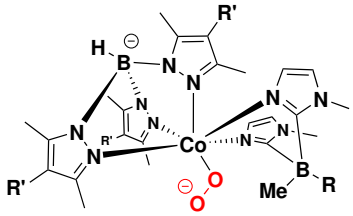

(a) (a) **End-on, mononuclear:** A cobalt η^1-superoxo complex from Nishiura *et al.* Only stable at −80 °C.[51]

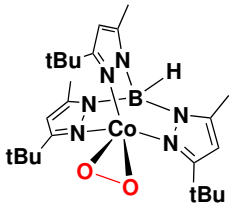

(b)

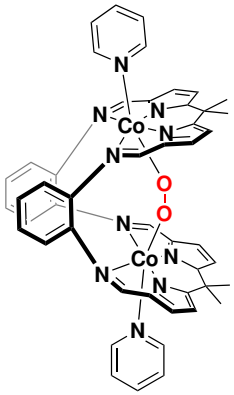

(c)

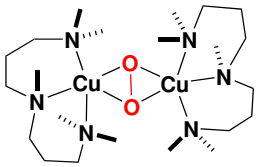

(d)

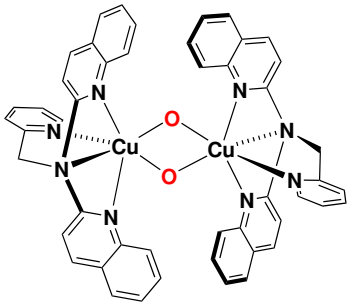

(e)

Figure 1.5: A series of literature examples demonstrating the five potential binding modes shown in Figure 1.4 of first-row transition metal O_2 activation catalysts. (b) **Side-on, mononuclear:** An η^2-peroxo cobalt complex from Cramer *et al.* O–O bond distance: 1.262(8) Å.[46] (c) **End-on, bridged-dinuclear:** A porphyrin-inspired μ-η^1:η^1-peroxo complex reported by Givaja *et al.* O–O bond length: 1.361(3) Å.[49] (d) **Side-on, bridged-dinuclear:** An example of a bimetallic, side-on μ-η^2:η^2-peroxo complex by Park *et al.* O–O bond length 1.540 (5) Å.[52] (e) **Side-on, bridged-dinuclear:** A copper bis-μ-oxo complex reported by Kieber-Emmons *et al.* O–O distance 2.319 Å (from calculations, see reference for further details.)[53]

1.2.2 Ligand Effects in O_2 binding

Not only is tuning the metal centre a challenge in O_2 activation, designing oxidatively robust ligands is also an obstacle to the success of such complexes. The ligands need to withstand the highly oxidising conditions of the reaction, but also variations in the oxidation state of the metal centre, without themselves undergoing redox events. In the 90s, early attempts to design oxidatively robust ligand architectures led to the de-

velopment of "design rules" to apply to ligand architectures.[54] Most of these apply to the position of heteroatoms or substituents around the chelate ring and are designed to prevent common degradation pathways observed in oxidation catalysts.[54] Different metal centres require different ligand frameworks,[55] and some frameworks have proven particularly well suited to different types of catalysis. The pyridine alkoxide ligand, Figure 1.6, has proven able to withstand the harsh conditions required for water oxidation catalysis, including high oxidation states of the metal, without degradation.[56]

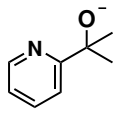

Figure 1.6: The pyridine alkoxide ligand. The pyridine ring provides a rigid N-donor, the alkoxide is a strong donor, the methyl groups are resistant to oxidation, and also provide scope for functionalisation and the ligand has a broad range of solubilities.[56]

The binding environment around the metal centre has a significant effect on reactivity. This is not a recent observation, the phenomenon was demonstrated in a 1975 paper on the impact of the basicity of the ligand on the O_2-adduct stability.[57] Figure 1.5 shows five complexes, representing the different possible binding modes of O_2 to a metal centre. In all cases the ligands are nitrogen-based chelate ligands. The three bridged-dinuclear complexes show bimetallic systems with the two metal centres held in close proximity to each other in order to activate the O–O bond.

A 2018 study by Nishiura *et al.* examined the role of changing ligand substituents on a mono-cobalt complex on the binding affinity of the cobalt(II) centre to O_2, shown in Figure 1.5a. They found that depending on where the substituent was located on the complex had an impact on its effect. Although changing the boron substituent (**R**) had an effect on the oxidation potential of the complex, they found that this did not correlate to the affinity of the Co(II) centre to O_2. Instead, they deduced that steric effect of the substituent in the coordination sphere of the complex had a more pronounced effect.[51] Conversely, by changing the substituent on the pyrazole ring (**R'**), both O_2 affinity and the electrochemical properties of the complex are affected in a similar manner.[51] This led the authors to the conclusion that ligand effects in the secondary coordination sphere have both a steric and inductive effect on the O_2 binding affinity.

The bis-μ-oxo complex shown in Figure 1.5e is formed *via* an end-on μ-η^1:η^1-peroxo complex, as shown in Figure 1.4. The subsequent breakage of the O–O bond to form the

oxo species shows that the complex is able to activate the bond.[53] In subsequent studies by the same group, it was found that changing both the primary and the secondary coordination sphere around the metal centre could promote or limit the conversion from the peroxo- to the oxo- species. These changes were either due to the introduction of Lewis acids which coordinated to the ligand, or substrates, which bound directly to the metal centre. The authors concluded that the impact of the Lewis acids has a steroelectronic effect on the reactivity at the metal centres.[58]

This observation is further supported by a series of examples from Elwell *et al.*, whose review demonstrated the significance of the binding environment around bimetallic copper (I) centres on the reactivity with O_2, Figure 1.7.[36] They deduced that the steric effect of the methyl and quinoyl groups reduced the electron donating ability of the ligand to the copper centres, resulting in μ-η^2:η^2-peroxo dicopper complexes, rather than the bis(μ-oxo) complex seen for the unsubstituted ligand.

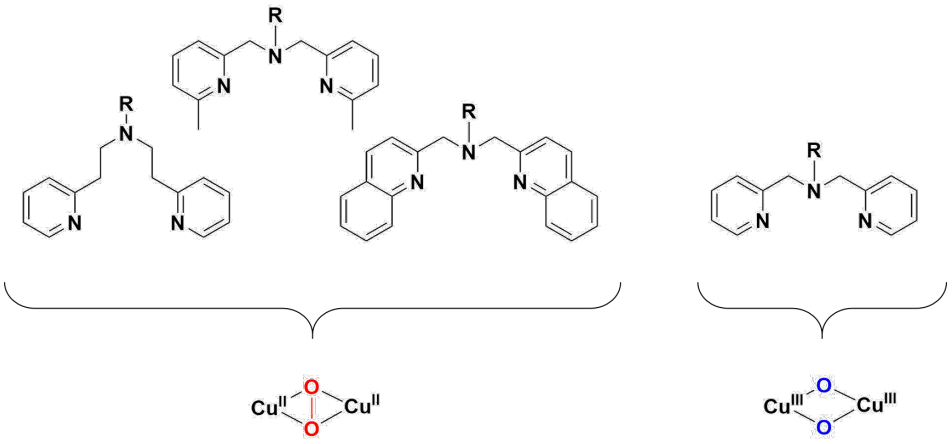

Figure 1.7: The impact on ligand functionalisation on the binding of O_2 by bimetallic copper complexes. The systems on the left resulted in μ-η^2:η^2-peroxo dicopper complexes, whilst the ligand on the right resulted in the formation of a bis(μ-oxo) complex. Reprinted (adapted) with permission from *Chem. Rev.* 2017, **117**, 2059–2107. Copyright (2017) American Chemical Society.[36]

1.2.3 Aerobic Oxidations

Although stoichiometric oxidations of alcohols by palladium (II) and dioxygen were reported as early as 1828 by Berzelius,[59] it took until the 1950s before the techniques were applied catalytically at scale.[9] The Amoco process is used to produce almost 70% of all terephthalic acid used worldwide,[60] using a cobalt–manganese–bromide catalyst and oxygen from air as the oxidant, 1.8b.[61] Many aerobic oxidation catalysts draw

inspiration from biological systems,[62,63] or from Wacker chemistry which uses a palladium/copper system to perform oxidations.[13,64] In Wacker chemistry the copper salts act as a cocatalyst, and are themselves oxidised by O_2 meaning they can regenerate the active Pd(II) species, which does not react with O_2, 1.8a. The Wacker process is an early example of homogeneous organopalladium chemistry used at industrial scale.[23,65]

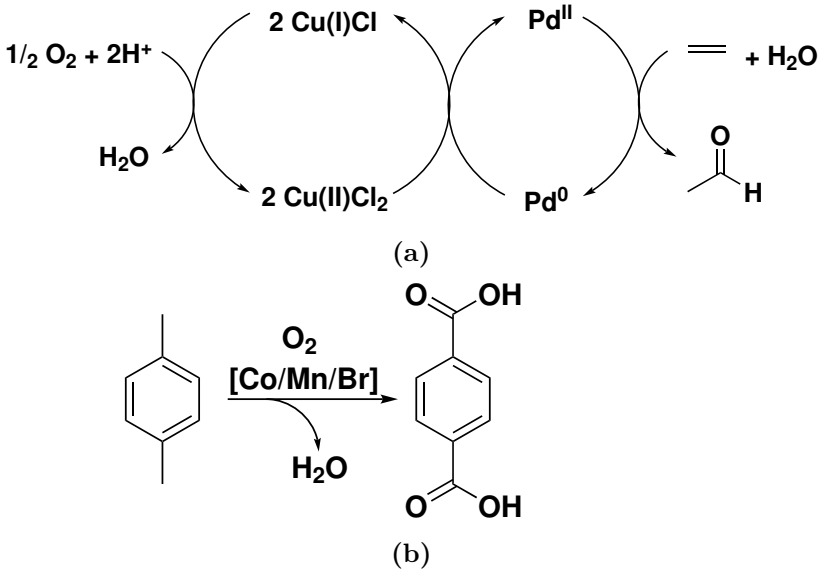

Figure 1.8: (a) The Wacker process, showing the oxidation of the copper cocatalyst by O_2, which oxidises the palladium which can then react with the substrate. (b) The Amoco process, which produces terephthalic acid *via* the catalytic oxidation of p-xylene through an autoxidation process and a cobalt-manganese-bromide catalyst.

Biocatalysis is often used for aerobic oxidations, and there are a range of examples using different oxygenases to perform aerobic oxidations on a diverse range of substrates, including alcohols, alkenes, sulphides and Baeyer-Villiger oxidations on ketones.[66] Additionally, using biological inspiration, there are numerous examples of porphyrin-based catalysis for aerobic oxidations.[67]

Of the oxidising enzymes; bimetallic copper systems emerge as some of the most well understood and characterised. These include catechol oxidase, which is found in some plants and fungi and transforms diphenols into ortho-quinones, and tyrosinase which catalyses the transition of phenols to catechols and quinones.[33] Both catechol oxidase and tyrosinase activate oxygen via the μ-η^2-η^2-peroxo state shown in Figure 1.9.[18] Structural investigations into the active site of the enzyme and the mechanism of oxygen activation have determined that most type-3 copper centres contain antiferromag-

netically coupled copper centres, each coordinated by three histidine residues.[35] These studies have informed the design of synthetic analogues, due to their insights into the way in which the oxygen binds to the metal centres, Figure 1.9, and the mechanism of oxygen activation through different mind modes, Figure 1.12. Many of the studies report that the active species is a copper(I) centre, which upon reaction with dioxygen forms an active species that further oxidises the substrate.[35]

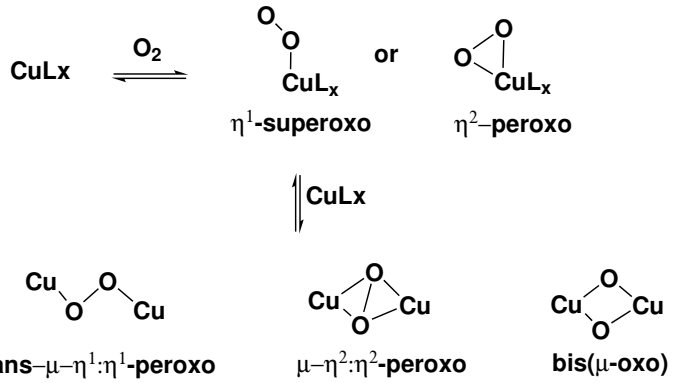

Figure 1.9: Binding modes to copper centres in synthetic aerobic oxidation catalysts. Adapted with permission from *Chem. Rev.* 2004, **104**, 1047–1076. Copyright (2004) American Chemical Society.[68]

As discussed in Section 1.2.2, one of the significant factors in the reactivity of metalloenzymes is the environment around the active site.[34] This is demonstrated again by the examples shown in Figure 1.10 which show the significant differences in O–O bond length by changing the ligand environment. However, the authors found during their studies of dicopper complexes that in addition to the ligand, the use of additives had a pronounced impact on the reactivity of the complex.

Using a different N-donor ligand, (*N*-methyl-*N,N*-bis[3-(dimethylamino)propyl]amine (MeAN), shown in 1.11a), they found that their complex bound O_2 in a μ-η^2-η^2-peroxo configuration, but did not activate it further, meaning the complexes were inactive for oxidation catalysis. Addition of additives such as sodium phenolates or Lewis acids activated the complex, resulting in the cleavage of the O–O bond and consequently oxidative activity, including C–H oxidation, Figure 1.11.[58]

The authors identified that the combination of weak "backbonding" from the metal centre into the σ* orbital of the peroxo, with reduced electron donation from the π^* orbital of the O_2^{2-} to the copper centre (LMCT), resulted in a weaker O–O bond, but no O–O bond cleavage, Figure 1.12. In addition to X-ray crystallography, the different

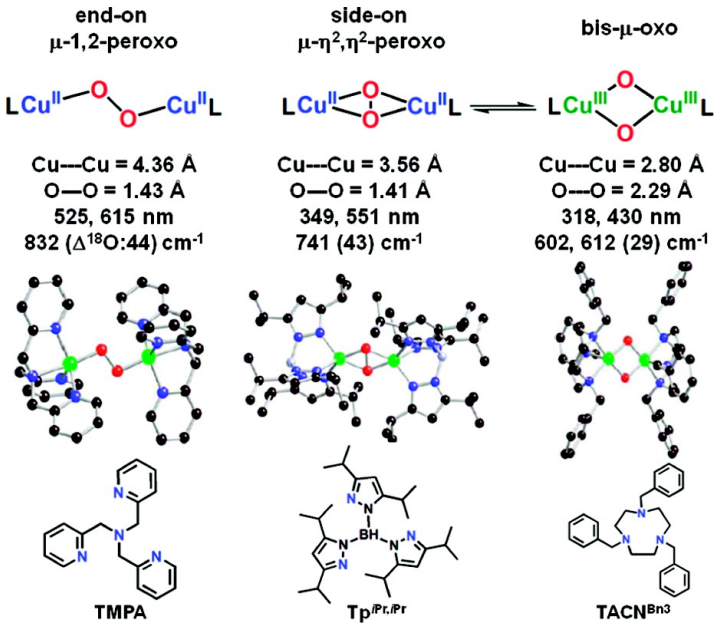

Figure 1.10: The impact of three different N-donor ligands on O–O bond activation, represented through bond length, highlighting the impact of ligand variation. Reproduced with permission from *J. Am. Chem. Soc* 2012, **134**, 8513-8524. Copyright (2012) American Chemical Society.[52]

binding modes can be distinguished by the use of Raman spectroscopy. In Resonance Raman spectroscopy, the use of selective excitation allows vibrations that are strongly affected by the electronic transition to be probed.[69]

The use of phenolates or Lewis acids also illustrated two different activation mechanisms, namely primary coordination sphere activation, by the phenolates, or secondary coordination sphere control by the Lewis acids. The proposed mechanism of activation by phenolates is shown in 1.11b, whereby the phenolate coordinates directly to the copper centre, resulting in a change in oxidation state of the copper centres and breakage of the O–O bond.[58] The phenolate subsequently undergoes C–H activation through electrophilic aromatic substitution, determined through Hammett studies, suggesting electrophilic reactivity of the oxygen in this complex. They propose that Lewis acids coordinate to the axial nitrogen donors of the MeAN ligand, resulting in greater ligand donation from the equatorial ligands, resulting in O–O bond cleavage.[58] This is an example of cooperative catalysis, whereby the environment around an active site or metal centre in a catalytic system "facilitates" a catalytic process. This could be a ligand effect or a neighbouring metal.

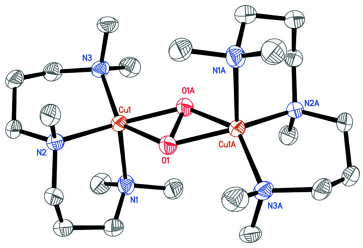

(a) X-Ray crystal structure of $[Cu(MeAN)_2(O_2^{2-})](SbF_6)_2$. Reproduced with permission from *J. Am. Chem. Soc* 2012, **134**, 8513-8524. Copyright (2012) American Chemical Society.[52]

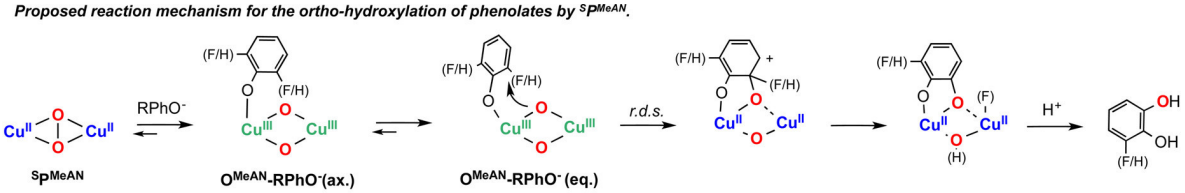

(b) Proposed mechanism of activation of the O–O bond by addition of sodium phenolate. Adapted with permission from *J. Am. Chem. Soc* 2017, **139**, 3186-3195. Copyright (2017) American Chemical Society.[58]

Figure 1.11: The "in-active" copper dimer, and the proposed mechanism of activation with the addition of sodium phenolate.

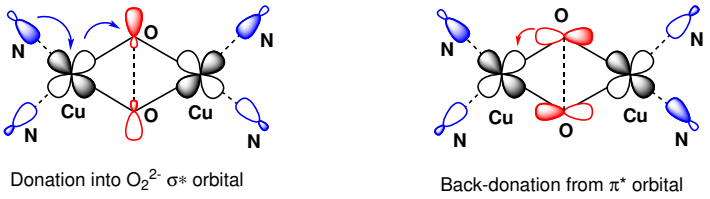

Figure 1.12: Postulated modes of weakening the O–O bond in bimetallic copper complexes with N-donor ligands, Adapted from a diagram by Garcia-Bosch *et al.*[58]

Due to their prevalence in natural systems, copper catalysts have seen widespread use in the field of synthetic aerobic oxidation catalysis.[62] However, most of the examples of copper complexes use simple copper salts with high numbers of additives, or high catalyst loadings. A review by Gulzar *et al.* included some examples with catalyst loadings of $CuCl_2$ of up to 20 mol%, coupled with the use of additives, such as TEMPO, in loadings of up to 50 mol%.[70]

The aerobic oxidation of alcohols using a copper/TEMPO systems shows wide applicability,[71] and the proposed mechanism for such reactions is similar to the mechanism proposed for that of galactose oxidase, which proceeds via a radical mechanism.[18] A mechanistic study by Stahl and coworkers on a Cu/TEMPO catalyst system is shown in Figure 1.13. Their study revealed a two part process: the oxidation of the catalyst and TEMPO-

H by dioxygen, followed by oxidation of the substrate coupled with reduction of the copper centre.[71] They postulate that the oxidation of the substrate and reduction of dioxygen is a bimetallic process, the mechanism of which is shown in Figure 1.13. They propose that dioxygen is initially bound by one Cu(I) centre, forming a mono-metallic superoxo species. This species reacts with another Cu(I) centre, reducing the superoxo species to form a Cu_2O_2 intermediate, the exact structure of which is not known. The authors suggest it could be any of the bimetallic structures shown in Figure 1.4. This species reacts with TEMPO-H in Step 3 (Figure 1.13).

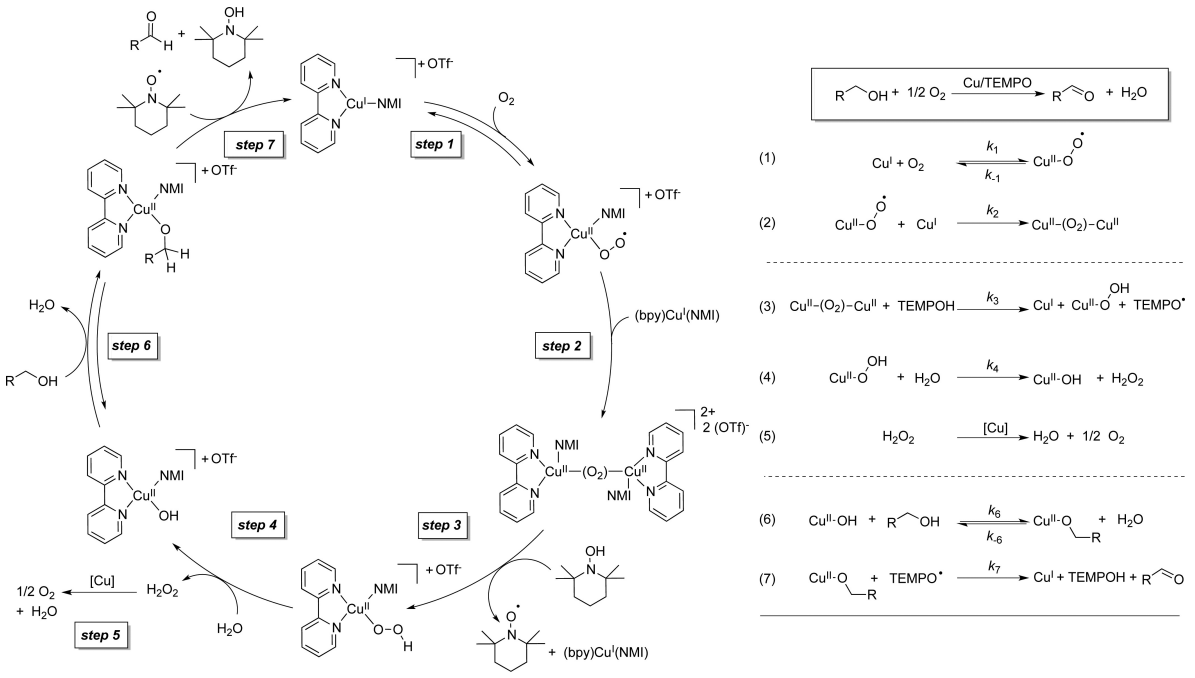

Figure 1.13: Proposed catalytic cycle for the aerobic oxidation of alcohols with a copper catalyst and TEMPO. Reprinted with permission from *J. Am. Chem. Soc* 2013,**135**, 2357-2367. Copyright (2013) American Chemical Society.[71]

This study also highlights the use of stable radicals (TEMPO) as a means of catalysing and promoting the reaction. Unlike the example above, where phenolates or Lewis acids bound directly to the complex (either *via* the metal centre, or the ligand) to activate the O_2, the TEMPO in this example interacts directly with the copper-substrate species (Cu-alkoxide) to break the C–H bond of the primary alcohol and form the aldehyde product. The use of stable radicals in aerobic oxidation catalysis is the focus of a review by Muldoon and coworkers.[72] Many of the reported catalytic systems are based on a Cu^{I}(bipy) system. Indeed, they even report that in some cases, the copper equivalent to a palladium or ruthenium catalyst has a greater substrate scope, which is promising

from a sustainable chemistry perspective.

In contrast to the copper complexes, cobalt oxidation catalysts are often based on salen and salen derivatives. These ligands are commonly used in aerobic oxidations due to their oxidatively robust structure, similarity to some porphyrins, and scope for functionalisation. A study by Stahl and coworkers using a cobalt (II) salophen complex to perform aerobic oxidations on *p*-hydroquinone revealed that the reaction proceeds via a Co^{III}-superoxide adduct, Figure 1.14.

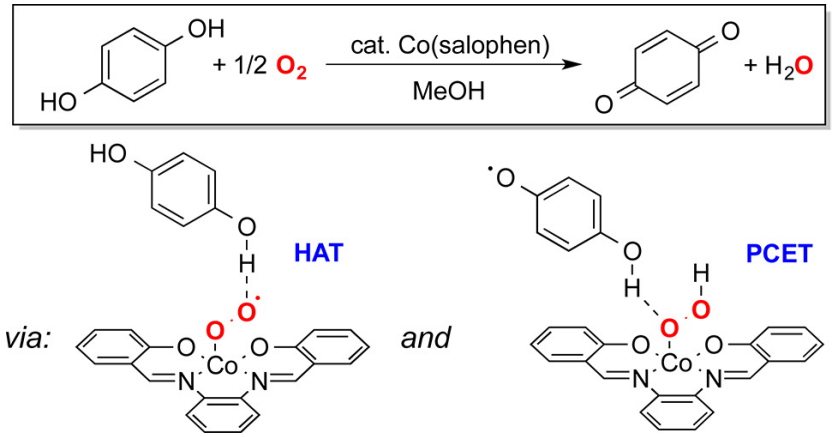

Figure 1.14: Aerobic oxidation of *p*-hydroquinone to *p*-benzoquinone by a cobalt salophen system, with two key intermediates shown. Reprinted with permission from *J. Am. Chem. Soc.* 2016, **138**, 4186–4193. Copyright (2016) American Chemical Society.[73]

Their studies also revealed that the mechanism included hydrogen atom transfer (HAT) and proton coupled electron transfer (PCET), with the latter being the turnover-limiting step. They found that the rate was strongly solvent dependent, with a significant rate enhancement when using methanol, but that mass transfer of O_2 into solution limits the rate.[73] The use of EPR studies helped determine key intermediates (shown in Figure 1.14) during the catalytic cycle in conjunction with UV-vis spectroscopy and density functional theory (DFT) calculations.

The cobalt salophen complex performs the oxidation of the *p*-hydroquinone substrate occurred with the full, 4-electron reduction of O_2 to H_2O. Other mononuclear Co^{II} species with an ONNO ligand framework have also demonstrated C–H bond activation in conjunction with O_2 reduction, suggesting that although historically copper has dominated the field of aerobic oxidation, there is scope for other first-row transition metals to perform such reactions.[74]

Table 1.1: A summary of different types of aerobic oxidation reactions, some common catalysts used, and the role of the O_2 in the process.

Type	Examples	Typical Catalysts	Comments
Autoxidation	Amoco process[61]	Co/Mn/Br[61]	Radical reaction.[75] Air is used.
Wacker-type	Wacker oxidations, olefin oxidations	Pd/Cu co-catalysts[23]	O_2 is not able to directly reoxidise Pd(0) due to its closed shell configuration. Instead, the O_2 oxidises the Cu co-catalyst which is able to reoxidise Pd(0) to Pd(II) and complete the catalytic cycle.[23,76]
Dehydrogenative	Oxidation of alcohols to aldehydes, ketones or esters. Amines to amides. C–H activation[64]	Cu,[77] Ir,[78] Pd,[79] Mn[80,81]	O_2 reoxidises the catalyst.[10] H_2O or H_2O_2 are common products. An example of C–H activation can be seen in 1.11b, which is also an example of O-atom incorporation. Oxidation of alcohols to aldehydes can be seen in Figure 1.13 and in Figure 1.14. Note that Wacker-type reactions are a form of dehydrogenative oxidations.[5]
Oxidative coupling	C–C bond formation, amination, homocoupling of alkynes, amindation. Heck-type reactions.	Cu,[70] Pd,[70] Ni[10]	Proceeds via reductive elimination, followed by regeneration of the catalyst by O_2.[10,70,77,82] H_2O as product.
O-atom incorporation	Hydoxylation, oxygenation	Cu,[83,84] TEMPO,[83] Mn,[84] Fe[84]	The oxygen is incorporated into the product,[66] and in some cases serves to also reoxidise the catalyst. Oxygen atom transfer reactions (discussed further in Section 1.3) are usually non-catalytic O-atom incorporation reactions.
Photoredox	C–H functionalisation, amines to nitriles[85]	Ru,[86] Ir[87]	The light either excites the O_2 so it is no longer in the triplet state and available to react with organic substrates, or excites a photosensitiser that is able to excite the substrate.[86–89]

It is worth noting that although solvent effects can have a pronounced impact on the reactivity of some catalyst systems,[90] for example salen systems,[91] there are no clear rules that can be applied across oxidation catalyst systems. It is therefore recommended that solvent effects are investigated during reactivity screening processes of new O_2-activation catalysts.

1.2.4 Oxygen Reduction Reaction (ORR)

The oxygen reduction reaction is used in fuel cells, which are used for sustainable energy generation. The reduction of O_2 is coupled with the oxidation of a sustainable fuels, such as H_2 generated from water oxidation, in order to generate electrical energy. Electricity is generated *via* the controlled electrochemical oxidation of a fuel, for example H_2, at the anode, and the reduction of an oxidant, O_2, at the cathode. Many of the existing ORR catalysts are based on platinum, which although efficient, has seen a decrease in popularity due to sustainability concerns.[92] As a consequence, there has been a focus on the use of abundant and cheap first row transition metals for catalysis.

In the context of electrocatalysis, efficiency can be described by a range of different parameters. The include the overpotential, which is the difference between the standard potential for a reaction to occur and the applied potential required to obtain a target current density.[93] The Faradaic efficiency describes the ratio between the number of electrons passed as current, and the number of electrons detected in the product. Additionally, for fuel cell applications, the selectivity of the catalyst is significant. It is important that the catalyst performs the four electron reduction to H_2O, rather than the two electron reduction to H_2O_2, since the formation of H_2O provides more eneregy and is therefore more effective for energy production.[13] Additionally, generation of H_2O_2 is of concern due to its corrosive nature as a result of the facile generation of highly reactive radical species ($HO^{\bullet}$). The selectivity of the ORR can be confirmed using iodometric titrations[94,95] or a rotating ring disk electrode.[96]

$$O_2 + 4\,H^+ + 4\,e^- \longrightarrow 2\,H_2O \qquad \text{Potential: } 1.229 \text{ V}^{97}$$

$$O_2 + 2\,H^+ + 2\,e^- \longrightarrow 2\,H_2O_2 \qquad \text{Potential: } 0.695 \text{ V}^{13}$$

Similarly to aerobic oxidations, there are a number of metaloenzymes which perform the desired oxygen reduction reaction (the four electron reduction of $O_2 \longrightarrow H_2O$) and can be used for inspiration for synthetic analogues.[98] Cytochrome *c* oxidase is a transmembrane protein that performs the reduction of oxygen to water, and also acts

as a proton shuttle, it contains two haem units and two copper centres, supported by histidine units. Although there is still some uncertainty in the full catalytic cycle, there are a number of steps that can be confidently assigned, the activation of O_2 in the active site. The active site contains an iron haem and a copper centre, and the mode of O_2 activation is thought to be breakage of the O–O bond, rather than sequential reduction steps, Figure 1.15.[98,99] The iron and copper activate the O_2 cooperatively,[98] an example of heterodinuclear O_2 activation, and a number of model complexes have been synthesised to further study the mechanism of O_2 activation.[100] Such cooperative mechanisms are observed in the oxidases that perform aerobic oxidations, as discussed previously, and the bimetallic copper complexes discussed in Section 1.2.3 which perform aerobic oxidations.

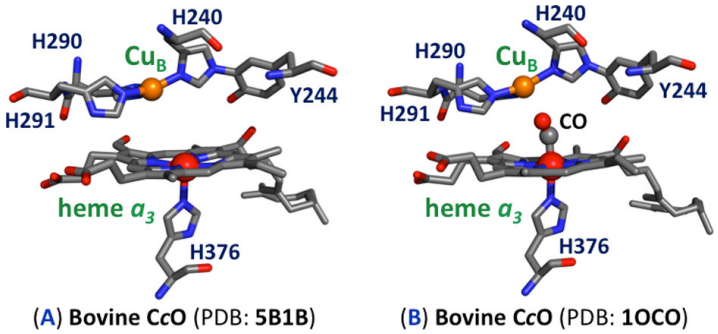

Figure 1.15: The active site of cytochrome *c* oxidase showing the iron porphyrin and copper centre. Image B shows the system with bound carbon monoxide. Reprinted with permission from *Chem. Rev.* 2018, **118**, 10840–11022. Copyright (2018) American Chemical Society.[38]

Although there are many examples of efficient heterogenous ORR catalysts,[92,101] homogeneous systems are often used to probe the reaction mechanism due to the comparative ease of characterising the active site. Homogeneously catalysed ORR can be driven electrochemically or chemically using a range of different reductants.[13] The choice of reductant will be determined by the onset and overpotential of the catalyst and the standard reduction potential of the reductant. Iron, cobalt, manganese and copper are most commonly used for both heterogeneous and homogeneous ORR catalysts, although there are examples of vanadium, zirconium, chromium and molybdenum ORR catalysts.[13]

Many synthetic ORR catalysts are based on porphyrins, since they are easily functionalised and oxidatively robust.[48,102,103] Additionally, many of the systems draw inspiration from cytochrome *c* oxidase and the cooperative nature of the bimetallic system, with

two metal centres held in close proximity to each other, *via* "pacman" style arrangements. First developed in the 80s and 90s, cofacial porphyrin architectures developed, the so-called "pacman" style systems. Since then, they have been developed further, with differing angles between the porphyrin rings, varying substitution patterns and a wide range of different metal centres.[104–106] Some of the more iconic ligand architectures in this field are shown in 1.16a, including Nocera's "hangman" porphyrin (right).

Studies probed the impact of "proton relay" functionality on the porphyrin rings, determining that proton coupled electron transfer plays an important role in O–O bond cleavage, and as such, the introduction of a "proton shuttle" can promote O_2 activation.[102] The proposed mechanism of ORR by the cobalt pacman complexes shown in 1.16b is shown in Figure 1.17. The first protonation of the cobalt-superoxide species is significant in the selectivity of the reaction to the $4e^-$ reduction to H_2O.

A recent study into mono-nuclear cobalt porphyrin ORR electrocatalysts found that changing the substitution on the porphyrin backbone had a pronounced effect on the reactivity of the complex.[108] By changing the pH and overpotential, the authors found that substituents that helped stabilise the O_2-bound intermediates in the reaction mechanism. They found that the inclusion of a cationic quaternary amine resulted in a more pH robust catalyst, as shown in Figure 1.18, which they ascribe to stabilisation of the proposed cobalt peroxide intermediate. The authors compare this reactivity to comparable iron-based porphyrins, where the ORR selectivity can be improved by addition of hydrogen-bonding substituents which can stabilise higher valent intermediates than the cobalt complexes.[108,109]

An alternative approach to functionalisation of a mono-nuclear porphyrin, as shown above, is to use an asymmetric pacman complex. A recent study by Liu *et al.* studied the impact on the rate of ORR activity using the two complexes shown in Figure 1.19. They found a pronounced acceleration in rate and selectivity with the asymmetric species, which suggested a change in mechanism when compared to symmetrical pacman complexes. They attributed this activity to one of the porphyrin moieties functioning as a Lewis acid, stabilising the O_2-adduct.[48]

The systems shown in Figure 1.18 and Figure 1.19 serve to illustrate the impact of electrostatic effects of distal ligand functionalisation, in some cases changing the products of reaction and significantly changing the electrochemical behaviour of the complexes.[48,108] The introduction of an amine group on the complexes shown in Figure 1.18 meant the

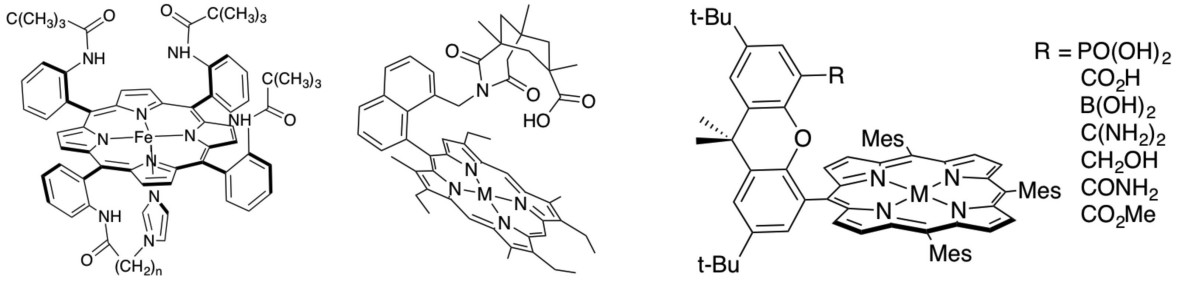

(a) A series of three macrocycle-based ORR catalysts. From left to right; Collman's "picket-fence" porphyrin, Chang's Kemp's "triacid" porphyrin and Nocera's "hangman" porphyrin. Reprinted with permission from *Chem. Rev.* 2018, **118**, 2340-2391. Copyright (2018) American Chemical Society.[13]

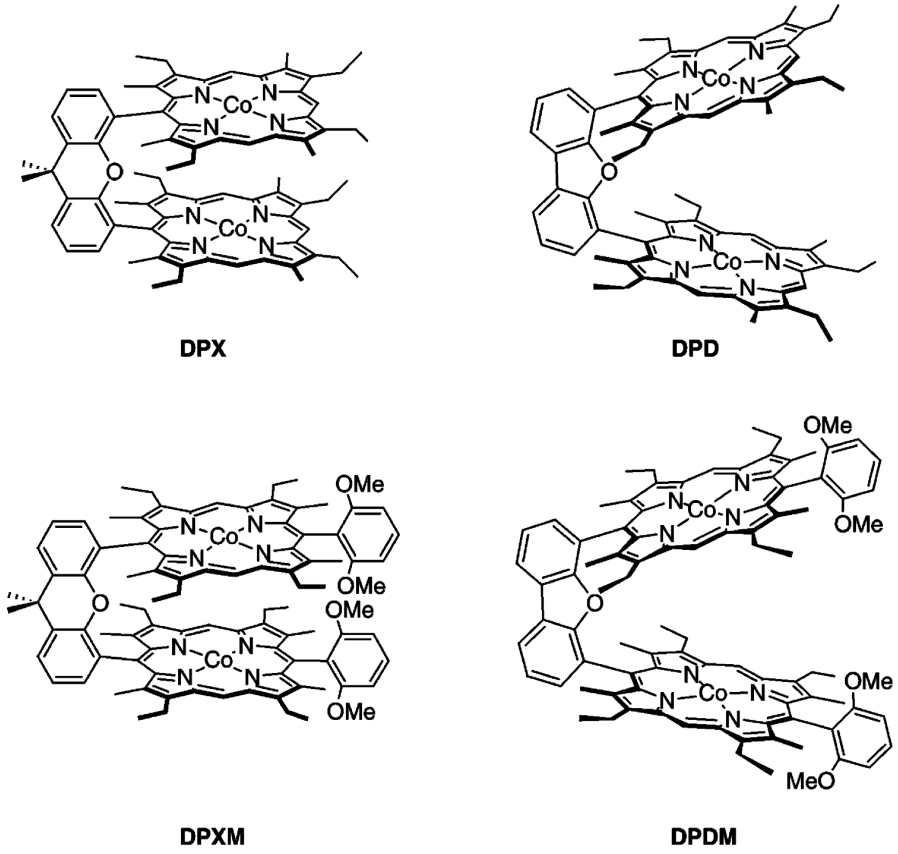

(b) A series of cobalt pacman oxygen reduction catalysts. Reprinted with permission from *J. Am. Chem. Soc* 2004, **126**, 10013-10020. Copyright (2004) American Chemical Society.[107]

Figure 1.16: Architypal porphyrin-based oxygen reduction catalysts.

impact of protonation of the ligand due to changing pH on the mechanism could be studied. This is of specific relevance when the proposed reaction mechanism includes a proton coupled electron transfer (PCET) step. Both systems are electrochemically driven oxygen reduction.

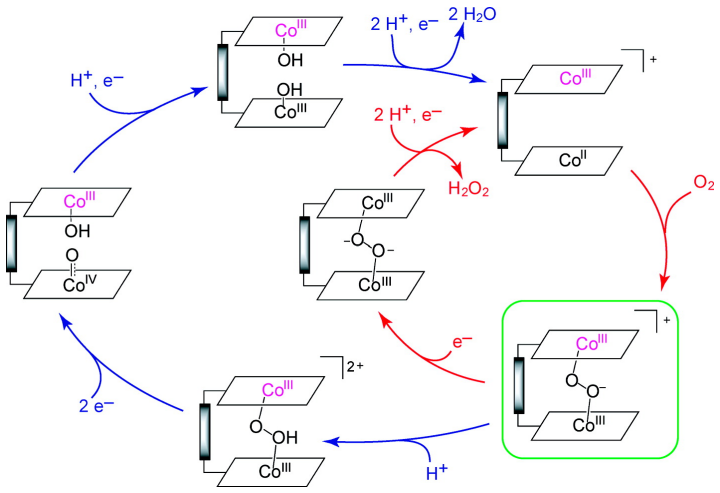

Figure 1.17: The proposed mechanism of oxygen reduction by Nocera's cobalt pacman complex. The first protonation of the superoxo intermediate (green box) is important in promoting the full 4e$^-$ reduction to H_2O, rather than the 2e$^-$ reduction to H_2O_2, illustrated with red arrows. Reprinted with permission from *Acc. Chem. Res.* 2007, **40**, 543-553. Copyright (2007) American Chemical Society.[102]

Proton coupled electron transfer (PCET) is a process commonly found in both synthetic and natural systems, and describes the simultaneous transfer of a proton and an electron.[110] By coupling the transfer into a simultaneous process, the high energy intermediates that would result from just H^+ or e^- transfer are avoided, making the reaction more favourable.[110,111]

As electrochemically driven ORR catalysts, the catalytic performance of the porphyrin systems described above are compared using the overpotential. However, many ORR catalysts are chemically driven, often using terminal reductants such as ferrocene derivatives.[95,112–114] In both electrochemically-driven and chemically driven reactions, the proton source can also have a pronounced effect on the reaction, dictating whether it is a 2-electron reduction to H_2O_2 or the full 4-electron reduction to H_2O. A study by Nocera and coworkers studied two bimetallic cobalt complexes for their reactivity towards O_2 reduction in the presence of different acids. Due to the competing proton reduction to H_2 by some electrode surfaces, it is necessary to choose conditions carefully.[115] They found that the Faradaic efficiency scales with the overpotential, meaning that in the presence of strong acids, the high overpotential favours the ORR pathway that leads to O–O bond cleavage and the production of H_2O. In the presence of weaker acids the formation of H_2O_2 is favoured.[116]

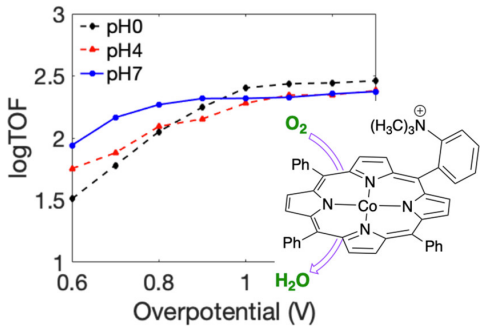

Figure 1.18: Turnover frequencies (TOF) and overpotential at different pH values for the cobalt porphyrin complex shown, reported by Zhang *et al.* Reprinted with permission from *J. Am. Chem. Soc.* 2020, **142**, 13426–13434. Copyright (2020) American Chemical Society.[108]

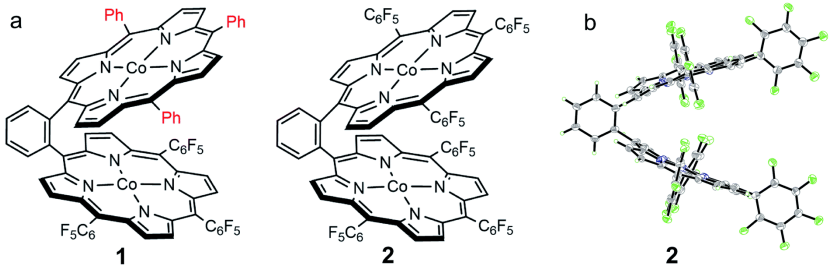

Figure 1.19: Cobalt pacman complexes reported by Liu *et al.* with the unsymmetrical system shown on the left. Reprinted with permission from *Chem. Sci.*, 2020, *11*, 87 - 96. Published by the Royal Society of Chemistry.[48]

As mentioned previously, cobalt salen complexes are often used in oxidation chemistry. Although the partial 2e$^-$ reduction of O_2 to H_2O_2 is not desirable for the ORR, there are still lessons that can be learned from systems that perform such reductions. A recent study into a different series of cobalt salen complexes for the selective reduction of oxygen to hydrogen peroxide ($O_2 + 2\,e^- \longrightarrow H_2O_2$) by decamethylferrocene (Fc*) found that substitution on the ligand backbone had a pronounced effect on the electrochemical properties of the complexes, as shown in Figure 1.20.[95] They found that the $Co^{III/II}$ redox potential corresponded to the chemically driven rates for ORR, where complexes with lower oxidation potentials exhibited higher ORR rates for the formation of H_2O_2.

The correlation between the oxidation potential and chemically driven reactivity suggest that the electrochemical properties of the complex can be used as a method of probing the potential reactivity of the complex. Additionally, the shift in electrochemical properties suggests that changes on the ligand backbone that are multiple bonds away from the metal centre can have a pronounced effect on the electrochemistry of the

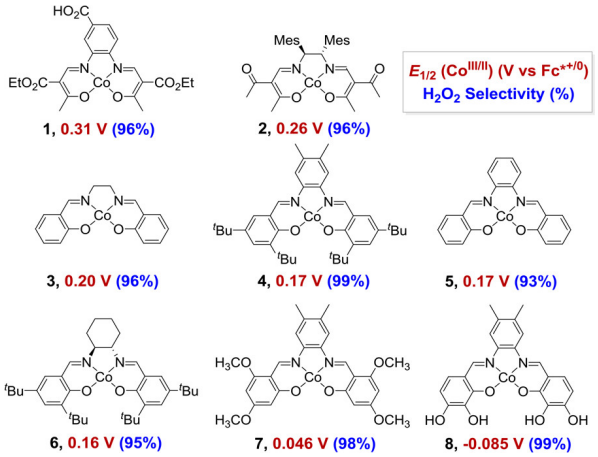

Figure 1.20: The oxidation potentials (red) and selectivities of a series of cobalt complexes for reduction to H_2O_2 (blue) reported by Wang *et al.* Reprinted with permission from *J. Am. Chem. Soc.* 2017, **139**, 16458–16461. Copyright (2017) American Chemical Society.[95]

complex, which can correspond to catalytic activity or potential changes in mechanism.

Although there are examples of water oxidation catalysts that also perform C–H activation,[117,118] and a limited number of aerobic oxidation catalysts that perform oxygen reduction,[30] there are fewer examples of oxygen reduction catalysts that also perform oxidation reactions. The limited examples that exist are heterogeneous electrocatalytic oxygen reduction catalysts that perform oxidation reactions.[119]

1.3 Oxygen Atom Transfer

An interesting feature of metal-oxygen complexes is the potential amphoteric reactivity of the resultant complex.[120,121] Although O_2 itself only behaves as an electrophile, or is reduced as an electron acceptor, metal-oxygen species can react as electrophiles, nucleophiles or in radical reactions, Figure 1.21. Such behaviour can be tuned through reaction conditions, the electronic environment around the metal centre, and the presence of additives.[120]

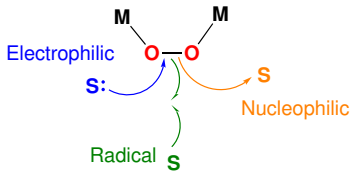

Figure 1.21: Amphoteric reactivity of an M–O peroxo species, where S = substrate.

Oxygen atom transfer is often one part of the mechanism of catalytic aerobic oxida-

tions. In both systems the metal complex needs to bind O_2, and oxidise a substrate. Figure 1.22 shows a simplified reaction mechanism, highlighting some key steps in the process. The first two steps are the same for both, binding O_2, and then binding a substrate, note that the substrate-bound adduct can be bound in a number of different configurations. In many oxygen atom transfer reactions, the oxidised substrate is released from the complex, leaving a metal-oxo species. In order to make the process catalytic and close the cycle, the second oxygen atom needs to be removed from the metal centre. This can be done through a variety of ways, including addition of further substrate,[73] or the formation of water through reductive removal of the oxygen.[78,122]

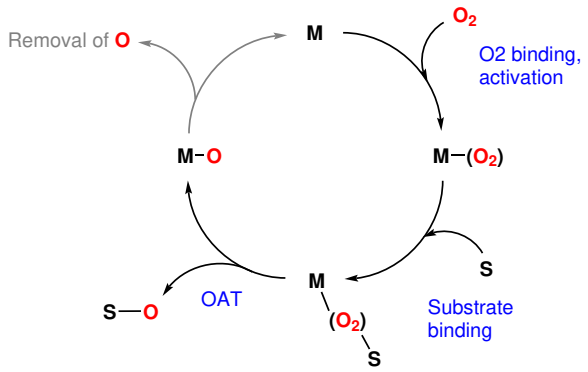

Figure 1.22: A schematic mechanism showing some key steps in oxygen atom transfer reactions and aerobic oxidations. In order for the reaction to be catalytic, the reductive oxo removal step is key, returning the complex to its initial state so that it may bind and activate O_2 again. It is worth noting that substrate binding is shown here as an inner-sphere process, but there are examples of concerted outer-sphere processes.

An example of this is a cobalt-oxo species, reported by Wang *et al.* that performs oxygen atom transfer, C–H activation, and epoxidations, Figure 1.23.[123] Using the correlation between reaction rate and the oxidation potentials of a range of different substrates, they determined that the cobalt-oxo species displayed electrophilic character.

The binding mode, spin and redox state of the metal-oxygen bond can play a significant role in its reactivity. This is illustrated by an example reported by Shin *et al.* from 2016.[124] They found they could activate a side-on η-2 peroxo species (Figure 1.24, top) with perchloric acid to yield an end-on hydroperoxo complex (Figure 1.24, bottom). The O_2 is sourced from H_2O_2, rather than O_2. They found that only the hydroperoxo complex performed oxygen atom transfer on PPh_3 and a series of thioanizoles, Figure 1.24. Addition of 10 equivalents of phosphine revealed quantitative formation of $OPPh_3$, suggesting catalytic OAT. Reaction with 25 equivalents of thioanisole proceeded with 75%

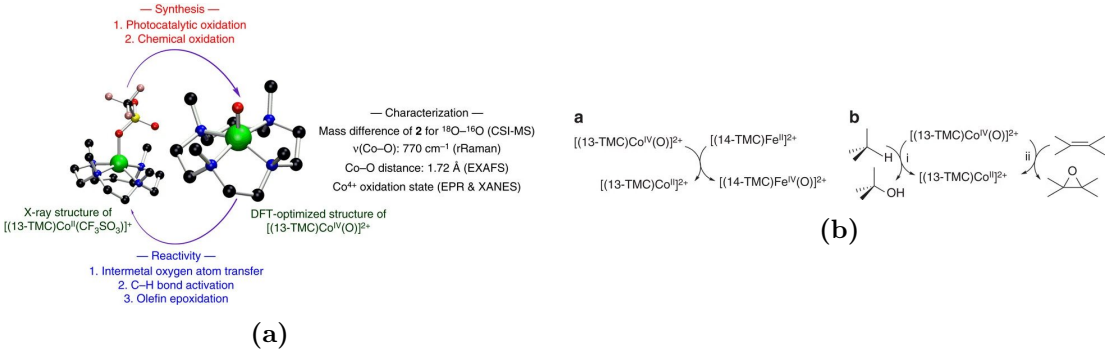

Figure 1.23: The cobalt-oxo species synthesised by Wang *et al.*. (a) Oxygen atom transfer, (b) C–H activation and epoxidation by the cobalt-oxo complex. Figure reproduced from *Nat. Commun.* 2017, **8**, 14839. Licensed under Creative Commons (2017).[123]

yield. A cobalt-hydroxo species was identified in solution by mass spectrometry, which was proposed as a decomposition product of the complex, suggesting some catalytic turnover before deactivation. Through the use of *para*-substituents on the thioanizoles it was possible to construct a Hammett plot, revealing electrophilic reactivity of the cobalt complex in the oxygen atom transfer reactions.[124] Beyond construction of the Hammett plot, mechanistic studies were not carried out, but in both cases the product of the reaction is the result of a transfer of one oxygen from the hydroperoxo complex to the substrate.

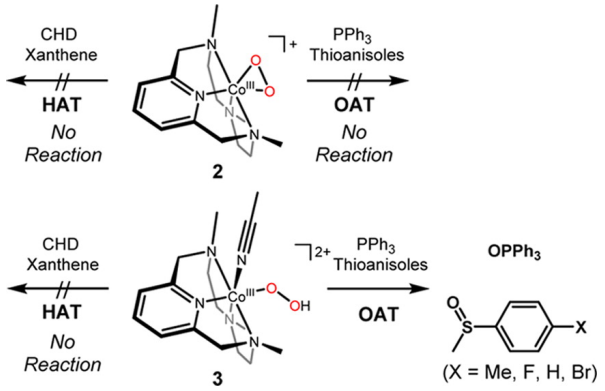

Figure 1.24: The monometallic cobalt complexes reported by Shin *et al.* showing the difference in reactivity between the η-2 peroxo complex and the end-on hydroperoxo species. Reprinted with permission from *Inorg. Chem.* 2016, **55**, 12391–12399. Copyright (2016) American Chemical Society.[124]

This observation was also mirrored in a series of manganese complexes, where the η-2 peroxo complex was not active for either oxygen atom transfer (OAT) or hydrogen atom transfer (HAT), but after the formation of the end-on hydroperoxo species, activity was

observed for both OAT and HAT. Changing substituent X allowed the mechanism of reactivity to be determined.[125]

A mono-nuclear cobalt peroxo species $[Co(13\text{-}TMC)(O_2)]^+$, Figure 1.25, was found to show nucleophilic reactivity towards organic substrates. Reactions with para-substituted benzaldehyde (X = OMe, Me, F, H) allowed the construction of a Hammett plot, which revealed nucleophilic reactivity of the cobalt peroxo towards the substrate.[126] However, upon changing the size of the macrocycle from 13-TMC to 12-TMC, the reactivity of the complex decreased to be almost undetectable.

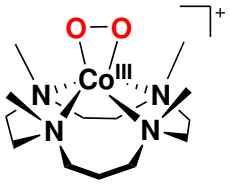

Figure 1.25: $[Co(13\text{-}TMC)(O_2)]^+$ (where 13-TMC = 1,4,7,10-tetramethyl-1,4,7,10-tetraazacyclodecane) which showed nucleophilic reactivity towards benzaldehydes.[126]

Further studies on the use of varying sizes of macrocycles with different metal centres, as a means of tuning the reactivity of the resultant complexes, has been carried out. Such monometallic complexes have been observed to display both electrophilic and nucleophilic reactivity (stoichiometric) depending on the metal used and the resultant metal-oxygen bond, Figure 1.26.[121,127–129]

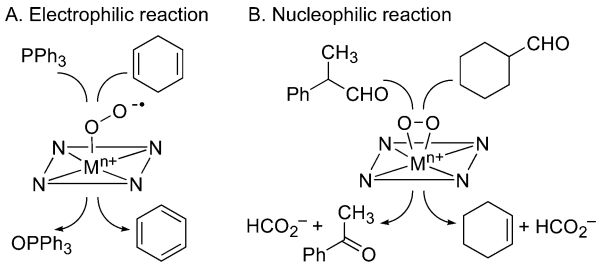

Figure 1.26: Examples of electrophilic and nucleophilic reactivity by a metal-oxygen complex. Reprinted with permission from *Acc. Chem. Res.* 2012, **45**, 1321–1330. Copyright (2012) American Chemical Society.[127]

There are examples of using an aldehyde as a sacrificial reductant, so-called "Mukaiyama's Conditions", for the aerobic oxidation of alcohols to their corresponding ketones with a ruthenium/cobalt catalyst system.[130,131] Studies by Mastrorilli *et al.* into the mechanism of reaction suggested that the cobalt first binds the O_2 to form a superoxo species

which is in equilibrium with a μ-peroxo species. They propose that it is the cobalt superoxo species that reacts with the sacrificial aldehyde, rather than the peroxo species, forming the reactive species which activates the substrate. The reactive species is speculated to be one of a number of possible products, including a hydroperoxo cobalt complex, a coordinated peracyl radical, or a peroxo species. The products of the reaction with the aldehyde are not identified, but are postulated to be an acylperoxo species.[131]

It is clear that the ligand and metal environment have a large influence on the ability of the complex to bind O_2, and the subsequent reactivity of the O_2-bound complex. There are some tentative trends that can be drawn out from the examples shown. The formation of peroxo-bound complexes tends to result in nucleophilic activity by the complex, as observed in Figure 1.25 and Figure 1.26. Conversely, end-on O_2-bound species, such as superoxo or hydroperoxo complexes result in electophilic reactivity, Figure 1.24 and Figure 1.26.

1.4 Homogeneous vs. Heterogeneous Catalysis

The distinction between heterogeneous and homogeneous catalysis was first made in 1902 by Ostwald.[132] Since that time, new chemistry has been developed that blurs they line between the two. This includes nanoparticles (1 – 100 nm), metal clusters (3 + metal atoms) and single-site heterogeneous catalysis.[133]

Understanding the speciation of the catalyst is important in order to gain mechanistic understanding, which can help catalyst optimisation through tuning of the selectivity, lifetime, activity and recovery of the catalyst.[133] Additionally when scaling up a process there are important considerations with reproducibility, scalability, cost, leaching and modelling if the speciation of the catalyst is not known.[134]

These considerations are of particular importance when the potential degradation products of a homogeneous catalyst are active for catalysis themselves, such as palladium nanoparticles in C–C coupling reactions,[134] or iridium oxide in water oxidation.[135] There are even examples of catalysis being due to contamination of reagents, for example the "homeopathic" Suzuki cross couplings, catalysed by palladium contamination in ppb levels in the $NaCO_3$ used,[136] or cross-coupling reactions caused by contamination of the iron species with Cu_2O.[137] Some homogeneous systems are further complicated by the use of sacrificial placeholder ligands, the most famous of which are the loss of

cyclooctadiene (COD) or norbornadiene (NBD) in olefin hydrogenation catalysis with Schrock-Osborn type rhodium catalysts.[138] This also includes the loss of the Cp* in some iridium-based water oxidation catalysts,[139–143] or molybdenum epoxidation systems,[144] which is lost during catalyst activation.

The highly oxidising conditions required for oxidation reactions, or those where oxygen is a reagent, increases the risk of nanoparticle formation.[145] The need for oxidatively robust ligands, as discussed in previously, is of particular importance in these reactions. This is a risk for both chemically driven systems and electochemically driven processes.[146] There are a number of examples where catalysts that were thought to be homogeneous were found to be nanoparticles upon further studies.[134]

There are a number of examples with copper and manganese systems of active catalysts for oxygen activation or water oxidation that further studies have shown to be nanoparticles, rather than homogeneous molecular catalysis.[147–149] The potentially active nature of the nanoparticles, and the increased risk of nanoparticle formation due to the highly oxidising conditions of many oxidation reactions, means determination of catalyst speciation is important.

Methods of probing catalyst speciation include chemical methods, such as the mercury drop test and other poisoning experiments, or scattering methods to determine the presence of nanoparticles. Poisoning experiments work through addition of a selective poison during catalysis. Hg(0) binds selectively to active sites of some heterogeneous catalysis, but will not inhibit true homogeneous species. However, it is less effective for some metals, including iridium, ruthenium and iron, and not effective at all for metal oxides.[145,146]

Poisoning experiments can be effective, but since the poison is added to the active catalyst, it can be hard to extract information about when in the catalytic cycle nanoparticle formation occurs. Scattering experiments are non-invasive, allowing the speciation of catalyst to be studied without disturbing the sample. Light or X-rays are shone through a sample onto a detector, and the resultant scattering pattern is used to extract information about the scatterer in the sample, including the size and quantity of nanoparticles formed. The two commonly used scattering methods are Dynamic Light Scattering (DLS) and Small Angle X-ray Scattering (SAXS).

Although SAXS has higher resolution than DLS, and can detect nanoparticles down to 0.1 nm,[150] DLS is commonly used since high quality measurements can be collected

faster. Although SAXS does not necessarily require collection at a synchrotron, higher flux and better detectors mean synchrotron collection is preferred to obtain high quality resolution. However, DLS is a diffusional technique, meaning the observed solution must be static, and therefore it is not possible to collect data under true reaction conditions which often involve active mixing. In all cases, careful control experiments are necessary to ensure the observed results are not caused by the static conditions required for the DLS, or the potential of radiation damage caused by the X-Rays needed for SAXS.

1.5 Aims

In order to better understand the impact of O_2 binding and activation across two metal centres, a series of bimetallic complexes will be synthesised. These will be complementary to the cytochrome C and pacman complexes. Cobalt and copper will be used due to their relevance for oxygen reduction and activation. The impact of varying ligand substituents on the reactivity of the complex will be studied by synthesising a series of ligands varying electronic and steric properties.

Complexes will be synthesised and structurally characterised, before investigating their electronic properties through the use of cyclic voltammetry. These studies will give insight into the impact of ligand substitution on the oxidation or reduction potentials of the complexes, allowing the electronic impact of the substituents to be probed. The impact of ligand substitution on the activity of the complexes towards the oxygen reduction reaction will be studied. Using the 3,5-bis(2-pyridyl)pyrazole (Hbpp) ligand as the framwork, the following substitutions will be investigated, Figure 1.27

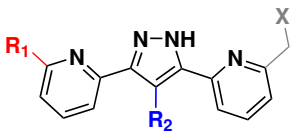

Figure 1.27: The different potential functionalisations of the Hbpp ligand. R_1 is referred to as *ortho*-functionalisation throughout, and R_2 as pyrazole functionalisation. X is discussed further in Chapter 4.

An analogue to a proposed reaction intermediate will be synthesised, allowing further investigation of the mechanism of reaction. The analogue will also be studied by cyclic voltammetry, and the "oxophilicity" of these complexes studied in order to ascertain whether binding of O_2 is rate determining.

As an initial study into the potential reactivity of the complexes for aerobic oxida-

tions, oxygen atom transfer reactions will be studied. A number of substrates will be screened, chosen to represent the different potential reactivities of metal-peroxo complexes. This will include benzaldehyde, triphenyl phosphine and 1,3-cyclohexadiene to probe nucleophilic, electrophilic and radical behaviour by the complexes, respectively.

The use of Small Angle X-ray Scattering (SAXS) to detect the formation of nanoparticles under catalytic conditions will be investigated. In order to do this a well characterised iridium water oxidation catalyst that is known to form nanoparticles will be used. A series of further iridium water oxidation catalysts will be investigated to investigate whether they are truly homogeneous under catalytic conditions.

Chapter 2

Synthesis of Bimetallic Cobalt Complexes

A homologous series of new, bimetallic Co_2^{III}-μ-OO complexes have been synthesised using a series of previously reported ligands, and characterised using NMR spectroscopy, crystallography and UV-vis spectroscopy. The impact of varying ligand substituents on the binding environment around the metal centres was investigated.

Substituents in the *ortho* position were found to result in steric constraints around the binding site between the two cobalt centres, meaning the formation of the bis-peroxo complex was less favourable than in complexes with substituents in other positions on the ligand. The presence of electron donating groups in the 4-position of the pyrazole backbone were found to result in a slightly longer O–O bond length, suggesting a weakening of the O_2 bond. The impact of this on reactivity will be further investigated in Chapter 3.

The corresponding μ-chloro cobalt (II) paramagnetic species have also been synthesised and characterised by wide-spectral width ^{1}H NMR spectroscopy and UV-vis spectroscopy. Although it is not possible to fully assign paramagnetic NMR spectra without the help of computational results, some tentative assignments have been made using results from ^{1}H and COSY spectra.

2.1 Introduction

In the strive for sustainable solutions for oxygen activation, attention has turned to the use of the abundant first row transition metals as replacements for the more rare platinum group metals. The natural world provides ample inspiration, with many metalloenzymes performing oxygen activation reactions using abundant first row transition metals, such as iron and copper, and under mild conditions.[13,36,68,151,152] These naturally occurring systems have offered guidance to synthetic chemists into key steps

in the activation process, the importance of the environment around the active metal centre, and the role of additives or transfer agents.[18]

Design of aerobic oxidation catalysts or oxygen reduction catalysts requires a species that is capable of binding, reducing and cleaving the O–O bond of O_2. The reduced form of the catalyst needs to react with O_2 to activate it, either *via* partial reduction or spin inversion, or both. This species needs to react with the substrate, resulting in O–O cleavage. However, the second step is often challenging and can prevent catalytic turnover, particularly if the O_2-catalyst adduct is too stable, or forms an inactive mono-oxo compound after one turn-over or oxygen atom transfer event. Additionally, the catalyst also needs to be oxidatively robust enough to withstand the conditions used in the catalysis.

2.1.1 Bimetallic Complexes based on the Hbpp Ligand

The tetradentate ligand, 3,5-bis-(pyrdidin-2-yl)pyrazole (Hbpp), Figure 2.1, was first reported in 1969 by Ball and Blake in a nickel (II) complex.[153] The next report of the ligand was not until 1989 by Casabo *et al.* who reported a series of bimetallic first row transition metal complexes based on cobalt, nickel, copper, zinc and cadmium.[154] Since the late 80s, the Hbpp ligand has seen application in a range of different fields, including water oxidation catalysis, single molecular magnets and self-assembly studies.[155–160]

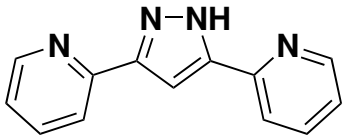

Figure 2.1: 3,5-bis-(pyridin-2-yl)pyrazole (Hbpp)

The dinuclear nature of the complexes obtained through the use of this ligand lends them to investigations into the impact of intramolecular magnetic interactions, resulting in a high number of studies into the magnetic properties of these complexes.[161–163] The ligand has also seen extensive use in the study of spin-crossover phenomena in bis-iron complexes.[164] There are also a wide range of reported metal complexes based on Hbpp or derivatives that show catalytic activity, including ruthenium, cobalt, copper, manganese, nickel and iron.[155,160,165–168] The use of the Hbpp ligand in water oxidation catalysis confirms that it is oxidatively robust under the harsh driving conditions necessary for such reactions.[157,166,169] The ligand supports a wide range of different coordination architectures, some of which are shown in Figure 2.2.

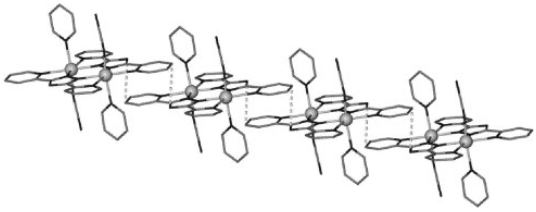

(a) Iron spin-crossover complex. Reprinted with permission from *Polyhedron* 2007, **26**, 1764-1772. Copyright (2007) Elsevier Ltd.[163]

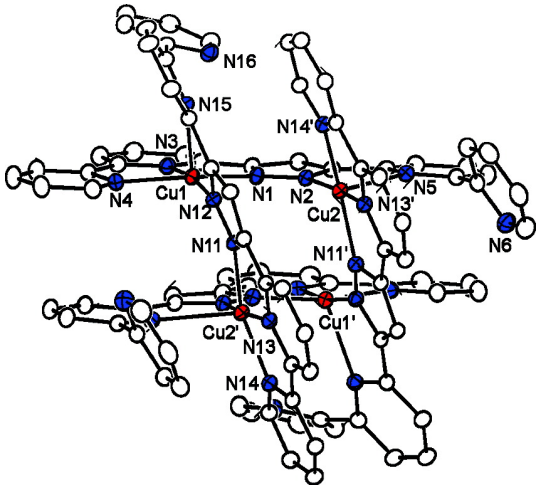

(b) A tetranuclear copper cluster based on a derivative of the Hbpp ligand. Reproduced with permission from *Inorg. Chem.* 2008, **47**, 1576-1585. Copyright (2008) American Chemical Society.[170]

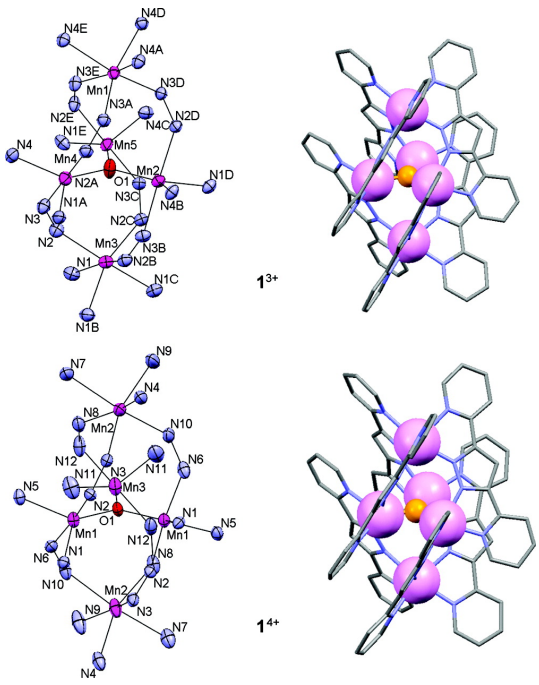

(c) Pentanuclear manganese cluster. Reprinted with permission from *Inorg. Chem.* 2011, **50**, 8427-8436. Copyright (2011) American Chemical Society.[160]

Figure 2.2: Examples of different coordination architectures supported with the Hbpp ligand, or derivatives.

Although there is rotation around the C–C axes between the rings, the polyaromatic structure results in reasonably well-defined distance between the two metal centres when bound in the NN binding sites of around 4 Å. This is similar to the distance between the copper centres in catechol oxidase, a metalloenzyme that performs aerobic oxidations by activating O_2, the Cu–Cu distances varies during catalysis from 2.9 Å to 3.8 Å.[34] The Hbpp ligand also offers scope for tuning the reactivity of the resultant metal complexes through varying the functionalisation around the ligand. Through functionalisation at different positions around the pyridines, or on the pyrazole backbone, it should be possible to investigate the impact of steric or electronic changes to the metal centre.

Indeed, studies of a penta-iron water oxidation catalyst using the Hbpp ligand revealed kinetic effects on the reactivity of the complex when exchanging the proton-substituted pyrazole backbone for a bromo or methyl substituent, these studies helped elucidate a change in mechanism of water oxidation.[171]

Perhaps the most widely investigated bpp-containing complex is $[Ru_2(\mu\text{-Cl})(bpp)(trpy)_2]^{2+}$, synthesised by Llobet *et al.* in 2004 which is active for water oxidation, Figure 2.3.[155] Since 2004, the complex has been the subject of many further mechanistic investigations using a range of techniques including electrochemistry, UV-vis, EPR, isotopic labelling experiments and computational investigations.[157,172–174]

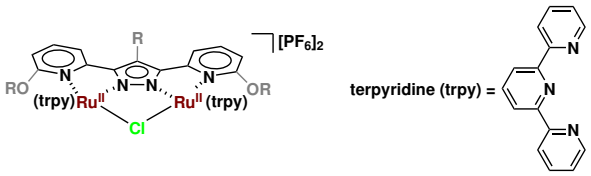

Figure 2.3: The ruthenium water oxidation catalyst, $[Ru_2(\mu\text{-Cl})(bpp)(trpy)_2][PF_6]_2$ with points of functionalisation shown in grey. R = H, Me, NO_2, or tethering *via* a –CH–Ph–CH- linkage. OR = COO-

The impact of varying the ligand substituents has also been investigated, including functionalisation on the pyrazole backbone, addition of oxygen-based substituents in the *ortho*-position of the pyridine rings on the bpp ligand, and the tethering of multiple ligand systems together.[165,175–178] It was found that the addition of an NO_2 substituent on the pyrazole backbone had a pronounced effect on the electochemistry of the complexes, shifting the CVs almost 0.5 V to higher potentials. It was also found that electron-donating groups promoting the electronic coupling between the ruthenium centres.[175] The group found that electron donating groups reduced oxidation potentials, although only by 50 mV relative to the unsubstituted species. Electron withdrawing groups had a more pronounced effect of almost 200 mV.[175] They also investigated the rate of substitution from an aqua complex to an MeCN-bound species, finding that whilst electron donating groups (such as Me) enhanced the substitution kinetics of the complex, the presence of electron donating groups (NO_2) "drastically reduced" the rates.[178]

More recent work by the same group investigated an analogous cobalt complex which exists in the μ-peroxo state, rather than the μ-Cl form of the ruthenium complex. The cobalt complex was initially shown to be active for water oxidation catalysis,[166]

and subsequently for the oxygen reduction reaction,[113] and hydrogen production *via* protonation of a hydride species.[179]

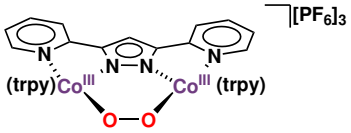

Figure 2.4: The cobalt catalyst synthesised by Llobet and coworkers (referred to as $\mathbf{Co1_{O_2}}$ throughout).

Although there have been subsequent investigations into the mechanism of water oxidation by the cobalt complex, the impact of functionalisation on the Hbpp ligand has not been investigated. In the initial study of the catalyst for water oxidation, the impact of changing the terpyridine ligand for a more electron-donating, tri-chelating, nitrogen-based ligand ($(Me)_2$bimpy, Figure 2.5) was investigated and found to result in lower oxidation potentials. This is consistent with a more electron-rich ligand, and resulted in higher currents when controlled potential electrolysis studies at 2 V of the two complexes was carried out.[166] The group also synthesised the Co(II) μ-Cl complex to offer a structural comparison to the ruthenium complex.[113] By reacting the Co(II) μ-Cl complex with cerium(IV) ammonium nitrate, the Co(III) bis-aqua complex was obtained.

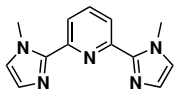

Figure 2.5: Bis-(N-methylimidazoyl)-pyridine ($(Me)_2$bimpy)

The results from the ruthenium complexes suggest that ligand functionalisation might have a pronounced effect on reactivity. Additionally, the studies reported previously in Section 1.2.2 suggest that functionalisation on the Hbpp ligand might have an impact on the binding of O_2 by the cobalt complex.

The impact of ligand functionalisation in the ruthenium studies is supported by a study of a tetranuclear copper water oxidation catalyst.[167] In this complex, the Hbpp ligand had hydroxy groups in the *ortho* position of the pyridine rings. Through pH studies, it was shown that the hydroxy group acts as a proton shuffle during catalysis.

The Hbpp cobalt complex has been shown to be active towards O_2. However, the effect of substitution on the Hbpp ligand on the reactivity of the complex had not

been studied. The Hbpp ligand has multiple sites of functionalisation, the impact of substitution on two of these sites was investigated through the synthesis of a number of different Hbpp ligands. The substituents span a range of electronic and steric properties, meaning the impact of both steric and electronics on the resultant bimetallic cobalt complex was studied.

2.2 Ligand Synthesis

A series of six ligand precursors were synthesised based on 3,5-bis(2-pyridyl)pyrazole (Hbpp), 2.6a and a number previously reported variants, Figure 2.6.[153,175,180–182] The series represents a range of different functionalisations, including sterically bulky (2.6b), electron donating (2.6c and 2.6d), and electron withdrawing (2.6e and 2.6f) groups.

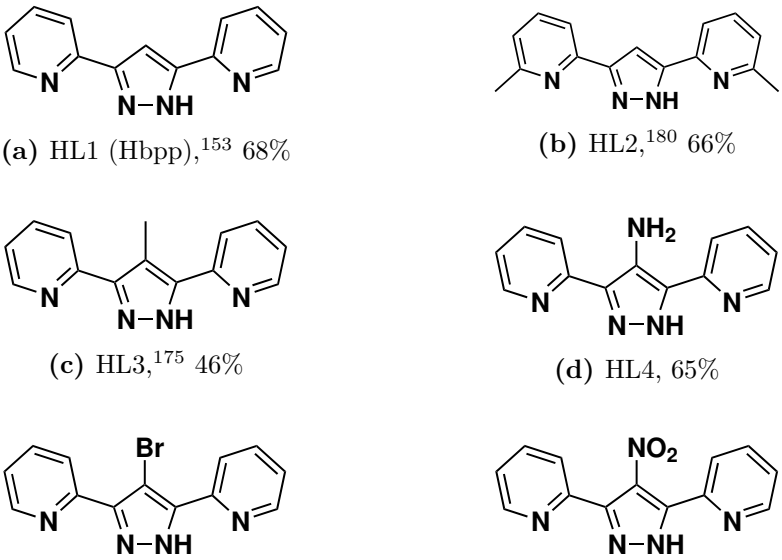

(a) HL1 (Hbpp),[153] 68%

(b) HL2,[180] 66%

(c) HL3,[175] 46%

(d) HL4, 65%

(e) HL5,[182] 57%

(f) HL6,[182] 45%

Figure 2.6: HL1 – HL6 synthesised as ligand precursors for bimetallic cobalt complexes. Isolated yields included.

The different functionalisations of the six ligands represent a range of steric and electronic factors. The *ortho*-methyl groups on HL2 are expected to have a steric effect on the binding pocket of the resultant metal complex. Conversely, the backbone pyrazole substituents are less likely to result in a steric effect, but have varying electronic properties. Using Hammett parameters of the various substituents, Table 2.1,[183] it is possible to see that the four different substituents represent a range of both strong and weak electron-donating and -withdrawing functionalisations.

Table 2.1: Hammett constants for the substituents used in HL1 – HL6. Values are the σ(para) constants reported by Taft and coworkers.[183] Positive is electron-withdrawing, negative is electron-donating.

Substituent	Hammett Parameter, σ(para)
H	0
Me	-0.17
NH_2	-0.66
Br	0.23
NO_2	0.78

The synthesis of the parent Hbpp ligand (2.6a) proceeds *via* a Claisen condensation between an ester and a ketone to form a diketone, followed by a Knorr-pyrazole reaction to form the pyrazole dipyridine product. Although reported a number of times in the literature,[153,154] some optimisation of the procedure was necessary, as discussed below. The optimised procedure is shown in Scheme 2.1.

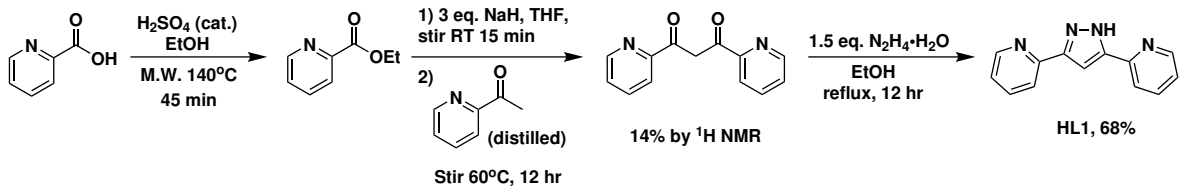

Scheme 2.1: Optimised synthetic route to HL1 ligand (Hbpp). M.W. = microwave reactor.

The esterification of picolinic acid was carried out in the presence of an alcohol with an acid catalyst. Adapting the synthesis to perform the esterification using a microwave reactor dramatically reduced reaction times from 12 hours to 45 minutes. Synthesis of the diketone resulted in consistently low spectroscopic yields, despite variation of solvents (toluene, ethanol, tetrahydrofuran (THF)), bases (sodium ethoxide (NaOEt), sodium hydride (NaH)) and reaction conditions. Despite attempting extensive purification of the diketone product by repeated recrystalisations, it was found that such methods lowered yields, without any impact on purity of the diketone product.

Rather than isolating the diketone, it was used directly in the pyrazole synthesis, without further purification. Removal of the solvent, followed by quenching by addition of water and acetic acid caused the crude diketone product to precipitate, which was filtered. Dissolving the diketone product in ethanol and refluxing in the presence of hydrazine hydrate yielded the pyrazole product. The best results were obtained using

an excess of a hydride base (NaH) in distilled THF, followed by heating at 60 °C for 12 hours. The use of distilled acetyl pyridine and tetrahydrofuran (THF) also had a notable improvement on the yield. The Hbpp ligand product was recrystallised from ethanol and diethyl ether to yield a light brown powder.

Ligand HL2 was synthesised using functionalised starting materials, whilst introduction of substituents on HL3 and HL4 occurred *via* a modified HL1 synthesis, and both HL5 and HL6 were synthesised though post-synthesis functionalisation of HL1, as described in the following Sections.

2.2.1 Ligand Functionalisation

Synthesis of HL2: *Ortho-* Substituents

Addition of methyl groups to the 2-position of the pyridine ring is predicted to have both a steric and inductive effect on the binding of the ligand to a metal centre, due to the proximity to the binding site.[183] Functionalisation in this position may also facilitate the synthesis of another binding site to yield an NNX-type ligand, as illustrated in Figure 1.27. Introduction of a methyl substituent in the ortho position was first reported by Pons *et al.* in 1990,[180] and has since seen minor application in first-row transition metal complex synthesis.[170,184,185]

The synthesis of 3,5-bis-2-(6-methyl)pyridyl-3,5-pyrazole) (HL2) uses methyl substituted acetyl pyridine and picolinic acid starting materials, Scheme 2.2. The synthesis is slightly modified from the synthesis of the unsubstituted ligand (Hbpp), with a lower excess of base used in the Claisen condensation. The final product (HL2) was purified by recrystallisation, yielding a light brown powder, with overall yield of 66%. The product was confirmed by NMR spectroscopy and mass spectrometry.

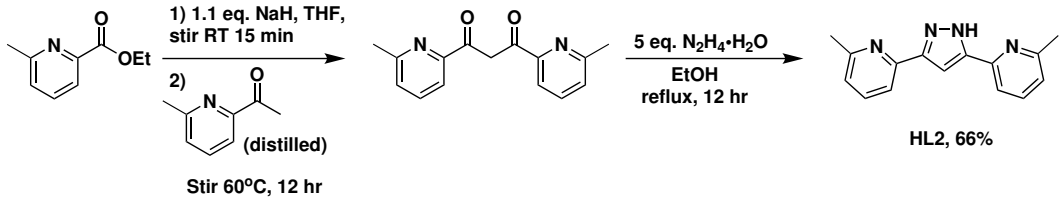

Scheme 2.2: Synthesis of the *ortho*-methyl substituted Hbpp ligand, HL2. Esterification of the 6-methyl picolinic acid to form the ester shown, was carried out using a microwave reactor under the conditions shown in Scheme 2.1.

Functionalisation on the pyrazole backbone

Functionalisation of the pyrazole backbone (Position R_2, Figure 1.27) offers a way of tuning the electronic properties of the ligand, whilst reducing potential steric effects of such a functionalisation on the resultant metal complex. There are three main synthetic routes to install functionality on the pyrazole backbone of the Hbpp ligand; incorporation of the functionality to the precursors (Route 1), addition of a substituent to the diketone intermediate through the nucleophilic substitution of the corresponding enolate (Route 2), or post synthesis functionalisation *via* electrophilic substitution on the pyrazole (Route 3), Scheme 2.3.

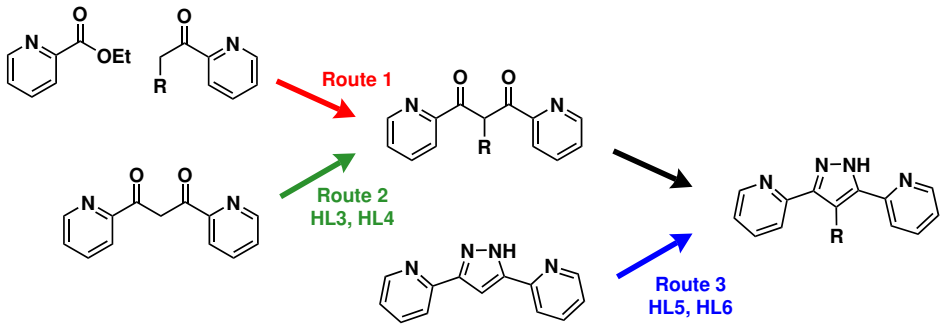

Scheme 2.3: Three generic synthetic routes to functionalisation on the pyrazole backbone, with the route taken for each ligand shown.

Route 1 required the synthesis of suitable functionalised ketones, which were deprotonated to perform the Claisen condensation with the corresponding ester. Both Route 2 and Route 3 required the substituent to be an electrophile, such as methyl iodide or bromine, which limits the substituents available *via* these routes.

Synthesis of HL3: Addition of a methyl substituent

There is literature precedent for the addition of a methyl group *via* Route 1 with a similar ligand system.[186] Therefore, this was investigated for the Hbpp ligand because it would open up scope for the introduction of a range of further substituents, as discussed in more depth in Chapter 4. Although a range of different bases and solvents were investigated for the addition of MeI to acetyl pyridine, Scheme 2.4, none proved successful, Table 2.2. In every case the product of the reaction was an intractable mixture, presumably a mixture self-condensation products of the reaction, which was not prevented by varying order of addition, or keeping the temperature at 0 °C. Due to the lack of any indication that the desired product had formed this synthetic route was not investigated further.

Scheme 2.4: Attempted addition of a methyl group to 2-acetylpyridine, by addition of base to form the enolate, before the use of methyl iodide to form the desired product. Bases and order of addition are outlined in Table 2.2

Table 2.2: Various bases and solvents tried for the addition of a methyl group to 2-acetylpyridine. The 2-acetylpyrdine (2-AP) was distilled prior to use. Base (1.1 eq.) was dissolved in solvent, 2-AP was added and stirred at 0 °C for 30 minutes. Addition of enolate and MeI (1.5 eq.) was done dropwise at 0 °C, solution stirred for 12 hrs at room temperature.

Base	Solvent	Order of addition	Product
1.1 eq. KO^{t}Bu	THF	MeI to enolate	inconclusive
1.1 eq. LiHMDS	THF	MeI to enolate	inconclusive
1.1 eq. KHMDS	THF	Enolate to MeI	inconclusive
1.1 eq. KHMDS	Toluene	Enolate to MeI	inconclusive

As an alternative to Route 1, there was literature precedent for the addition of a methyl group *via* Route 2 for Hbpp,[175] and for a bis-bipy variant.[186] These routes used a mixture of conditions; in the first MeI was added to a solution of the diketone and NaOH in acetonitrile before refluxing overnight. The second route used KHMDS in 1,4-dioxane before addition of MeI.

Using a modified procedure, the methyl-substituted diketone (shown in Scheme 2.5), was synthesised using a different potassium base, KO^{t}Bu, and THF as the solvent. KO^{t}Bu is, like KHMDS, a non-nucleophilic base, but has a lower pKa than the methyl-silyl amine base (KO^{t}Bu = 17, KHMDS = 26) and is considerably cheaper. The product was isolated by quenching the reaction with water before extraction with diethyl ether and drying over $MgSO_4$. The resultant methyl-substituted diketone was then refluxed with hydrazine hydrate in ethanol to yield the methyl-substituted product, Scheme 2.5.

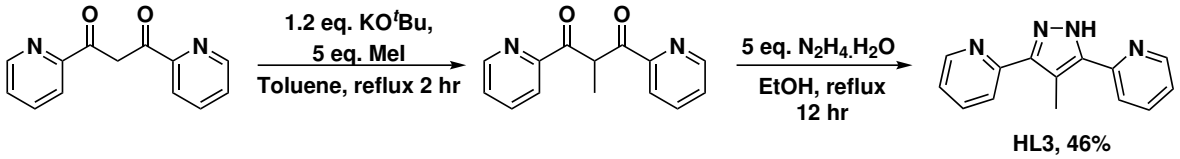

Scheme 2.5: Synthesis of HL3: Addition of a methyl group to the diketone intermediate *via* deprotonation by potassium *tert*-butoxide, followed by addition of methyl iodide and the formation of the pyrazole. Reported yield is for final transformation.

Synthesis of HL4: NH_2 addition

Synthesis of the 4-amino pyrazole was reported in 2011 by Stockmann *et al.* as a by-product of the reaction between isonitriles and tetrazines in a study of biocompatible ligation reactions.[181] In 2018, Franzini *et al.* also reported on the use of the reaction between tetrazines and isonitrile groups for their utility in the controlled release of drugs *in-vivo*, with the 4-amino pyrazole as the byproduct of the reaction, Scheme 2.6.[187]

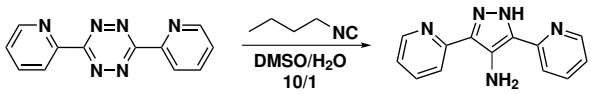

Scheme 2.6: Synthesis of HL4 *via* reaction between isonitriles and tetrazines.[181,187]

Although both literature procedures report the synthesis of HL4 (3,5-di(pyridine-2-yl)-1H-pyrazol-4-amine) in good yields ($> 80\%$), the reactions were performed on small scales (< 100 mg) with poor atom economy. Additionally, both the tetrazine and isocyanide starting materials are expensive reagents, with a multi-step synthesis, so an alternative synthetic route to the ligand was sought.

In order to add amine functionality, N-Bromosuccinimide (NBS) was first used to install a bromine at the alpha-postition of the diketone, Scheme 2.7. The reaction proceeded cleanly *via* the radical reaction of NBS with the diketone in diethyl ether after irradiation by UV-light for 20 minutes. The solvent was evaporated and the resultant oil recrystallised from $EtOH/Et_2O$ to remove unreacted NBS, yielding the bromo-substituted diketone in 56% yield. Refluxing the bromo-diketone product with an excess of hydrazine hydrate resulted in amination in the alpha position and pyrazole formation, to yield the amine-substituted Hbpp ligand, HL4, in 44% yield for this step, as a bright yellow powder. The NMR spectroscopic data was in agreement with reported literature values[181,187] and confirmed with mass spectrometry.

Post-Synthesis Functionalisation of Hbpp: Synthesis of HL5 and HL6

In order to add introduce bromine functionality on the pyrazole backbone, the bromine must be installed *via* Route 3 (Scheme 2.3) in order to prevent amination occurring during the formation of the pyrazole ring, Section 2.2.1. A 2006 report by Sun *et al.* detailed the post-synthesis functionalisation of Hbpp (Route 3, Scheme 2.3) *via* electrophilic substitution with a range of halogens and nitro substituents in good yields.[182]

The synthesis of bromo-substituted HL5 was performed according to the procedure

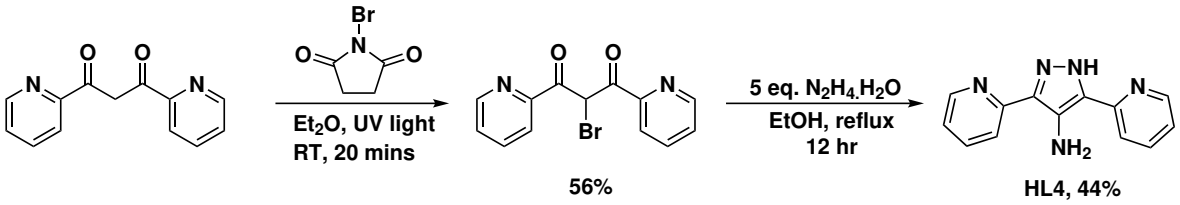

Scheme 2.7: Synthesis of HL4: Addition of a primary amine to the backbone of the Hbpp ligand, *via* a radical addition of bromine, followed by amination with excess hydrazine. The radical addition of bromine using N-Bromosuccinimide followed a previously reported synthetic route by Wu *et al.*[188]

reported by Sun *et al.* and involved stirring the Hbpp ligand in DCM with an excess of bromine in Na_2CO_3 (sat.) at 0 °C before quenching with sodium thiosulphate, Scheme 2.8. The bromo-substituted ligand was obtained in 57% yield after recrystallisation from ethanol and diethyl ether, and was confirmed by NMR spectroscopy and mass spectrometry.

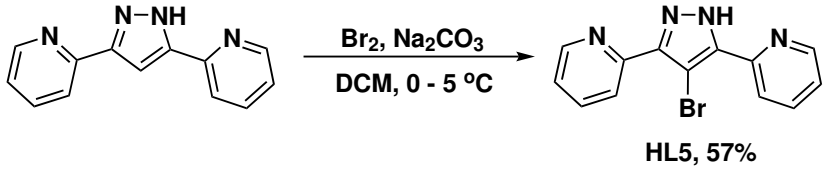

Scheme 2.8: Synthesis of HL5: Addition of a bromine to the pyrazole backbone of the Hbpp ligand.[182]

Sun *et al.* also provided a synthetic route to the nitro-functionalised HL6.[182] Introduction of the nitro group to form HL6 proceeded *via* the synthetic route shown in Scheme 2.9 by dissolving Hbpp in concentrated sulphuric acid at 0 °C, before the careful addition of a nitric / sulphuric acid solution and refluxing at 100 °C for 6 hours. Quenching of the reaction with Na_2CO_3 followed by a biphasic work-up and subsequent recrystallisation from ethanol and diethyl ether yielded HL6 in 45% yield. The product was confirmed by NMR spectroscopy and mass spectrometry and was in agreement with reported literature values.

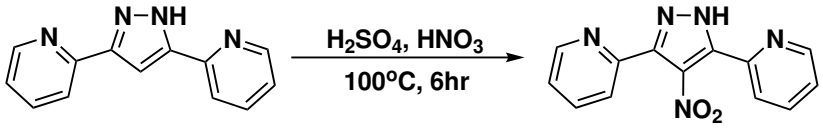

HL6, 45%

Scheme 2.9: Synthesis of HL6: Addition of a nitro group to the pyrazole backbone of the Hbpp ligand.[182]

2.3 Synthesis of Cobalt Complexes

2.3.1 Synthesis of Co(III)-peroxo Complexes: $\mathbf{Co1_{O_2}}$ – $\mathbf{Co6_{O_2}}$

Following a reported literature procedure for $\mathbf{Co1_{O_2}}$, synthesis of the cobalt complexes was carried out by deprotonation of the appropriate ligand with a weak base (NaOH) before addition of two equivalents of cobalt(II) chloride and terpyridine before refluxing in methanol in air. At elevated temperatures the solution was an orange colour, but upon cooling became dark purple, suggesting a chemical change, this is disucssed further in 2.4.4

After cooling, addition of sodium hexafluorophosphate resulted in the cobalt complexes precipitating out of solution, allowing separation by filtration and washing by diethyl ether, Scheme 2.10. The product was further purified by recrystallisation from acetonitrile and methanol with 1M $NaPF_6$.[113,166] The cobalt (III) μ-OO complexes $\mathbf{Co1_{O_2}}$ – $\mathbf{Co5_{O_2}}$ were isolated as deep purple solids, with yields between 45% and 85% after recrystallisation, Figure 2.7. $\mathbf{Co6_{O_2}}$ had a lower overall yield of 28% due to requiring a more extensive purification process. The synthesis of all six complexes was confirmed by mass spectrometry and NMR spectroscopy, Section 2.4.1. Additionally, complexes $\mathbf{Co3_{O_2}}$ – $\mathbf{Co6_{O_2}}$ were characterised by X-ray crystallography, the structures of which can be found in Section 2.4.3. The complexes were further investigated by electrochemical methods, in Chapter 3. Variation of the terpyridine ligand has been seen to be advantageous to the reactivity of the complex, 2.1.1. However, in these studies it was not varied in order to assign any changes in reactivity to variations in the Hbpp ligand.

It is worth noting that the hexafluorophosphate anion undergoes hydrolysis in aqueous solutions,[189] so future work might investigate the use of alternative counterions such as tetrafluoroborate or triflate, which are more robust in aqueous solutions.

$\mathbf{Co1_{O_2}}$ – $\mathbf{Co6_{O_2}}$ are diamagnetic Co^{III} complexes. Using wide spectral width NMR

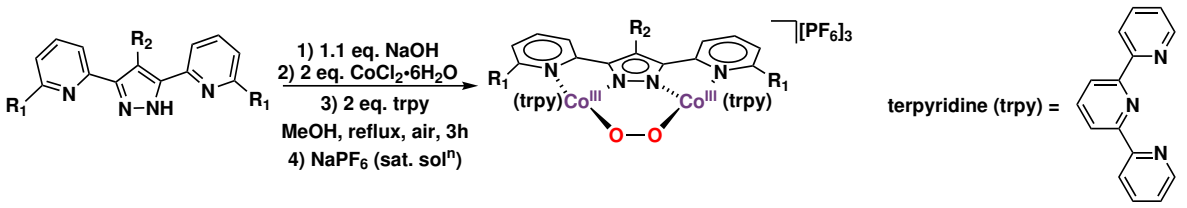

Scheme 2.10: Synthesis of μ-OO cobalt (III) complexes. $R_1 = R_2 = H =$ **Co1$_{O_2}$**, $R_1 =$ $Me, R_2 = H =$ **Co2$_{O_2}$**, $R_1 = H, R_2 = Me =$ **Co3$_{O_2}$**, $R_1 = H, R_2 = NH_2 =$ **Co4$_{O_2}$**, $R_1 =$ $H, R_2 = Br =$ **Co5$_{O_2}$**, $R_1 = H, R_2 = NO_2 =$ **Co6$_{O_2}$**

spectroscopy, it was possible to identify contamination of some of the complexes with their corresponding paramagnetic Co^{II} μ-Cl complexes. In most cases, these species were removed by stirring in MeCN/MeOH in air with $NaPF_6$, reducing the quantity of solvent, and filtering.

Unfortunately, stirring with $NaPF_6$ in air did not work for **Co2$_{O_2}$**, and due to the similarity in mass and polarity, it was not possible to effectively remove all of the μ-Cl species by any usual methods.[i] Therefore, an alternative approach was investigated

[i] Although there are reports of purifying similar complexes using alumina columns, attempts at this were not successful.

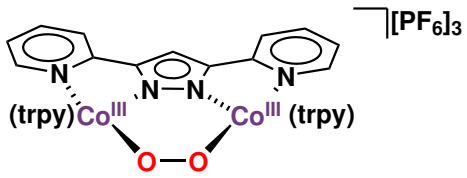

(a) **Co1$_{O_2}$**, 61%

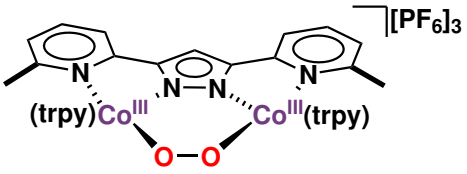

(b) **Co2$_{O_2}$**, 85%

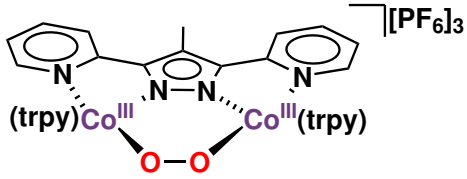

(c) **Co3$_{O_2}$**, 45%

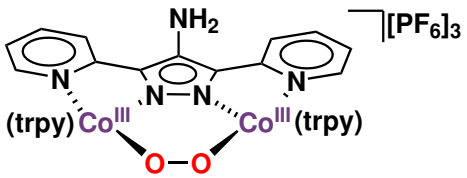

(d) **Co4$_{O_2}$**, 65%

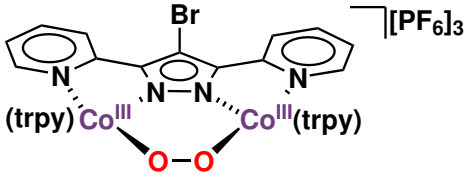

(e) **Co5$_{O_2}$**, 49%

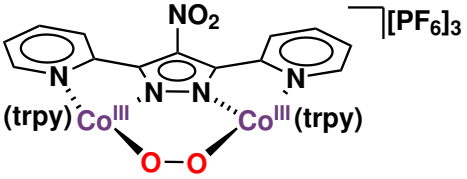

(f) **Co6$_{O_2}$**, 28%

Figure 2.7: **Co1$_{O_2}$** – **Co6$_{O_2}$** with their isolated yields.

to remove the μ-Cl species. In an attempt to drive the paramagnetic impurities in $\mathbf{Co2_{O_2}}$ to the μ-OO form, the complex was refluxed in methanol with sodium peroxide, Na_2O_2. However, this yielded a complex mixture of products unidentifiable by ^{1}H NMR spectroscopy, accompanied by the loss of some of the diagnostic $\mathbf{Co2_{O_2}}$ peaks, suggesting decomposition of the product. The failure of this synthetic route suggests that the binding of O_2 is not merely a substitution reaction, but that the O_2 is reduced and the metal centres oxidised. The O_2^{2-} of Na_2O_2 is already reduced and therefore not able to form the desired product. The difficulties associated with converting $\mathbf{Co2_{Cl}}$ into $\mathbf{Co2_{O_2}}$ suggests that the oxophilicity of the complex is reduced compared to the other substitution patterns. This results in preferential formation of the μ-Cl form of the complex, with a mixture of μ-OO and μ-Cl species of up to 50%. In further work, $\mathbf{Co2_{O_2}}$ was used in its unpurified form. These initial results for $\mathbf{Co2_{O_2}}$ suggest that this complex does not readily form the peroxo species. Despite issues with isolation, it will be studied alongside the other complexes in further studies.

$\mathbf{Co6_{O_2}}$ also required additional purification, as analysis of the ^{1}H NMR suggested the presence of paramagnetic species, similar to $\mathbf{Co2_{O_2}}$, but also a diamagnetic species. Although some impurities were removed by dissolving the complex in MeCN and stirring in air, as discussed above, low concentrations of the impurities persisted. Thin film chromatography suggested the presence of two species in solution which showed good separation on alumina, with R_f values of 0.24 and 0.92 for the product and impurity, respectively. The two species were separated using a short alumina plug and a 10% MeOH in MeCN eluant, yielding a pure sample of $\mathbf{Co6_{O_2}}$. The analysis of the impurities by NMR spectroscopy showed a mixture of unidentified diamagnetic peaks, and paramagnetic peaks that were identified as a small amount of $[Co(trpy)Cl_2]$. The impurities were further analysed by X-ray crystallography after growth of crystals by slow diffusion of diethyl ether into an acetonitrile solution of the impurities and confirmed to be a mono-metallated complex.

Mono-metallated Co6

As discussed previously (Section 2.3.1), a Co^{II} species was formed during the synthesis of $\mathbf{Co6_{O_2}}$. Using X-ray crystallography, this was confirmed to be the mono-metallated form of the complex shown in Figure 2.8. The short Co–Co distance in $\mathbf{Co6_{O_2}}$ possibly suggests that the NO_2 group imposes some steric constraints on the ligand, resulting in a smaller binding pocket. These constraints might help explain the formation of the mono-metallated form of the complex, Figure 2.8.

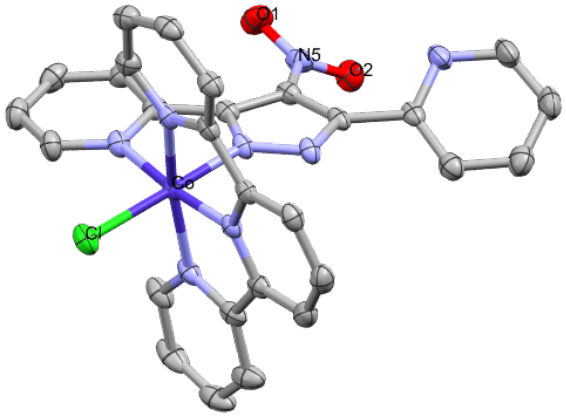

Figure 2.8: Crystal structure of the monometallated NO_2-pyrazole complex. Hydrogen atoms, solvent molecules and counter ions omitted for clarity. Ellipsoids shown at 50% probability. Bond lengths: N(py)–Co = 1.9638(18) Å, N(pz)–Co = 1.8926(17) Å, Co–Cl = 2.2279(6) Å.

The complex has an overall charge of +1, with just one [PF_6] counter-ion in the unit cell. However, the diamagnetic peaks suggest that the complex is Co^{III}, which means the bridging pyrazole ligand must be deprotonated, to the bpp^- form, rather than protonated as Hbpp. Therefore, the formula of the complex is derived as [Co(bpp)(trpy)(Cl)][PF_6].

Figure 2.8 shows the non-binding pyridine ring rotated away from the cobalt centre, and the terpyridine ligand in the opposite conformation to the bimetallic complexes, with the chloro pointing away from the second binding pocket. This conformation is also favoured in the known ruthenium complex with the unsubstituted Hbpp ligand, where this arrangement is referred to as Ru-Cl *out*.[190] The authors ascribe the preference for the *out* isomer to a mixture of steric and electronic effects, suggesting a weak hydrogen bond between the chloro and the hydrogen in the *ortho* postition of the Hbpp-pyridine, and a steric interaction between the terpyridine and the Hbpp ligand in the *in* conformation.

Although initially it might be thought that the formation of the monometallated species opens the door to heterobimetallic complexes, there are a series of problems that need to be overcome before the successful synthesis of heterobimetallic species. The *out* conformation of the complex shown in Figure 2.8 might cause problems, it would be necessary to develop a synthetic route that consistently resulted in the formation of the *in* complex, since separating a mixture would be challenging. Additionally, the deprotonation of the ligand in the course of the reaction means that using the proton to "block"

reactivity in the second binding site is unlikely to be a feasible route. There is some evidence of using the formation of a monometalled bpp species to synthesise a mixed-metal complexes, including a chromium/lanthanide complexes[191] and a ruthenium/zinc species.[192] The potential for heterobimetallic systems is discussed further in Chapter 4.

2.3.2 Synthesis of Co(II) complexes: $\mathbf{Co1_{Cl}}$ – $\mathbf{Co6_{Cl}}$

In order to offer a comparison to the μ-OO complexes, the chloro-bridged equivalents to $\mathbf{Co1_{O_2}}$ – $\mathbf{Co6_{O_2}}$ were synthesised according to a previously reported procedure for $\mathbf{Co1_{Cl}}$.[113] The synthetic route is shown in Scheme 2.11, and is similar to the synthesis of the μ-OO complexes, except that it is conducted in the absence of O_2. The appropriate ligand was deprotonated and the solutions of the ligand and cobalt precursor ($Co(trpy)Cl_2$) were degassed by bubbling argon through the solutions for 10 minutes, before addition of the cobalt to the ligand solution. After addition the solution was stirred at room temperature for 3 hours, before a saturated solution of $NaPF_6$ was added and the solids isolated through cannula filtration. The complexes were obtained as brown/red solids in yields of 45% – 82%, and characterised by paramagnetic NMR (Section 2.4.2) and mass spectrometry (see Experimental, Section 2.7). The complexes were also investigated by UV-vis spectroscopy (Section 2.4.4) and by cyclic voltammetry (Section 3.3.1).

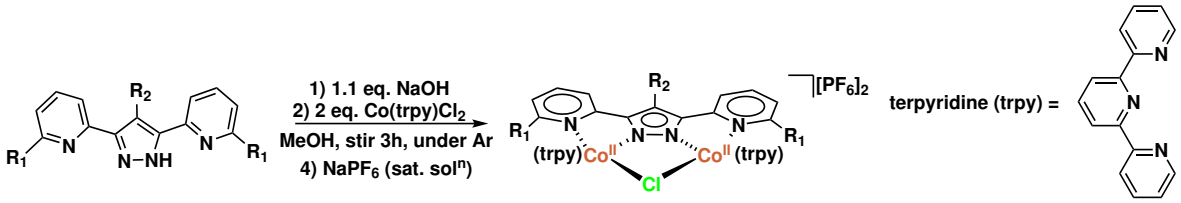

Scheme 2.11: Synthesis of μ-Cl cobalt (II) complexes. In all cases the solid starting materials were predried under high vacuum, and the methanol solutions were degassed by bubbling argon through the solutions for 10 minutes before the solutions were combined.

Despite being stable to oxidation in the solid state over prolonged periods of time, the complexes undergo oxidation to form the $Co^{(III)}$μ-OO complexes in solution in air. As a consequence, during the synthesis of $\mathbf{Co1_{Cl}}$ – $\mathbf{Co6_{Cl}}$, a small amount of the μ-OO complex was formed, most likely due to insufficient deoxygenation of the starting materials, or introduction of oxygen during the purification of the complexes by cannula filtration. The ratio between the two complexes was determined by quantitative ^{1}H NMR spectroscopy using an internal standard to quantify the concentration of Co(III)

complex in solution. In most cases this was less than 5% contamination, with the exception of $\mathbf{Co4_{Cl}}$ which had 8% $\mathbf{Co4_{O_2}}$ present.

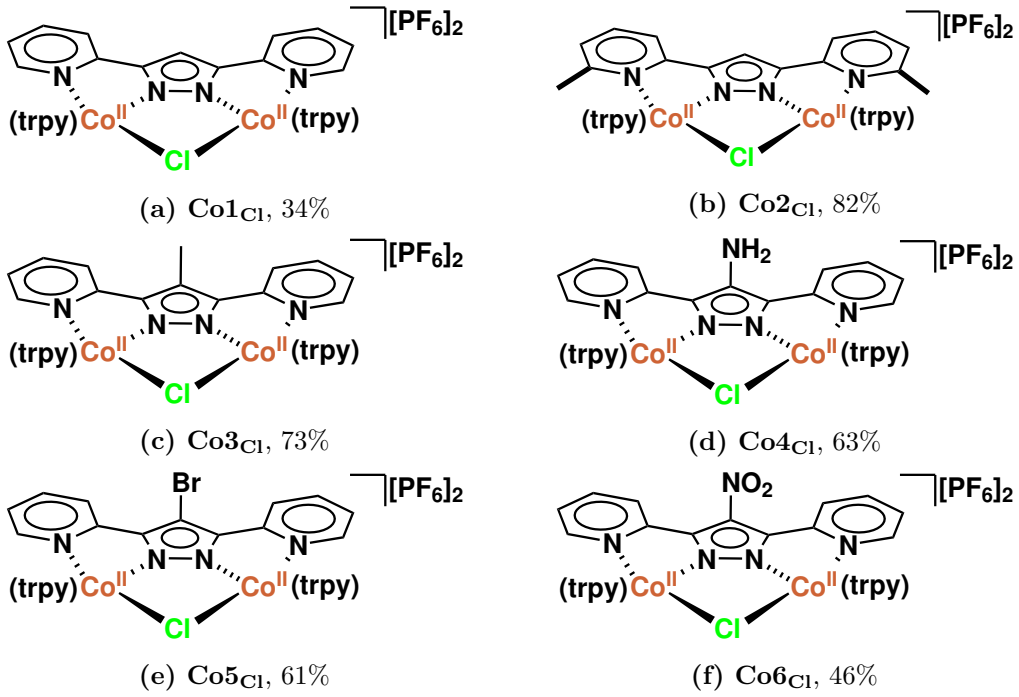

(a) $\mathbf{Co1_{Cl}}$, 34%

(b) $\mathbf{Co2_{Cl}}$, 82%

(c) $\mathbf{Co3_{Cl}}$, 73%

(d) $\mathbf{Co4_{Cl}}$, 63%

(e) $\mathbf{Co5_{Cl}}$, 61%

(f) $\mathbf{Co6_{Cl}}$, 46%

Figure 2.9: $\mathbf{Co1_{Cl}}$ – $\mathbf{Co6_{Cl}}$ structures and isolated yields.

2.4 Characterisation and Structural Analysis of Co1 – Co6

2.4.1 NMR Spectroscopy Studies of Complexes $\mathbf{Co1_{O_2}}$ – $\mathbf{Co6_{O_2}}$

Most of the diagnostic ^{1}H NMR peaks for $\mathbf{Co1_{O_2}}$ – $\mathbf{Co6_{O_2}}$ were found in the aromatic region, between 6.5 and 9 ppm, Figure 2.10. In all cases, the bpp ligand was symmetrical, showing 3 or 4 peaks representative of the pyridine protons and a singlet that corresponded to the pyrazole proton (dependent on functionalisation). The spectra are labelled according to the scheme shown in Figure 2.11.

Whilst the complexes are not strictly C_2 symmetric, due to the position of the terpyridine ligands, they are near C_2 symmetric with an axis running from the backbone of the pyrazole through the O-O bond, Figure 2.12. This is confirmed by the terpyridine ^{1}H NMR peaks, which integrate to two, corresponding to protons diagonally opposite each other on the molecule. The C_2 axis and lack of mirror plane in the solid state are

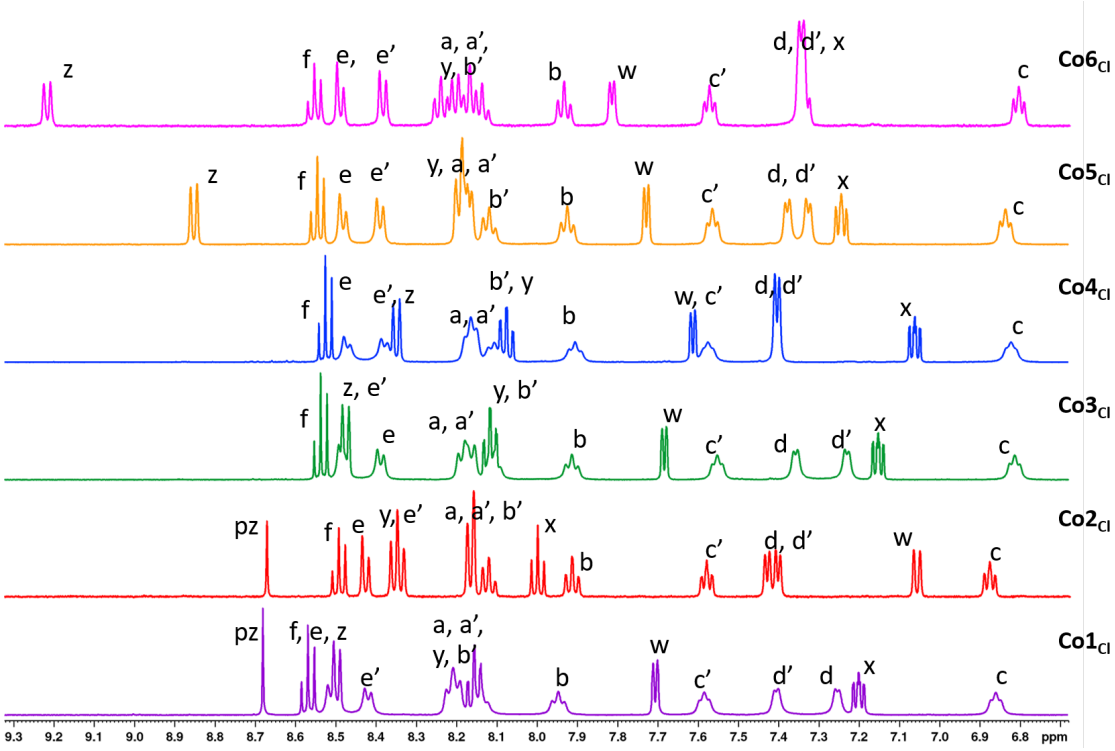

Figure 2.10: Aromatic region of the ^{1}H NMR spectra for $\mathbf{Co1_{O_2}}$ – $\mathbf{Co6_{O_2}}$. Peaks are labelled according to the scheme shown in Figure 2.11

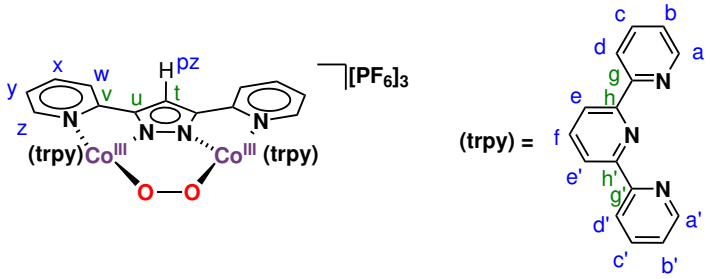

Figure 2.11: Labelled scheme for NMR assignments shown in Figure 2.10. Blue labels correspond to both proton and carbon labels (with the exception of *pz*, green labels correspond to quaternary carbons, with the exception of *t*, which is not quaternary in $\mathbf{Co1_{O_2}}$ and $\mathbf{Co2_{O_2}}$.)

confirmed by X-ray crystallography, Section 2.4.3. The terpyridine peaks show less well defined splitting patterns than the peaks associated with the bpp ligand, Figure 2.10, which suggests these ligands are more dynamic/flexible than the bpp ligand in solution.

Most of the proton signals are found within a 0.1 ppm range from each other across the different functionalisation patterns for $\mathbf{Co1_{O_2}}$ – $\mathbf{Co6_{O_2}}$. However, the presence of electron withdrawing substituents on the bpp ligand results in a pronounced shift to

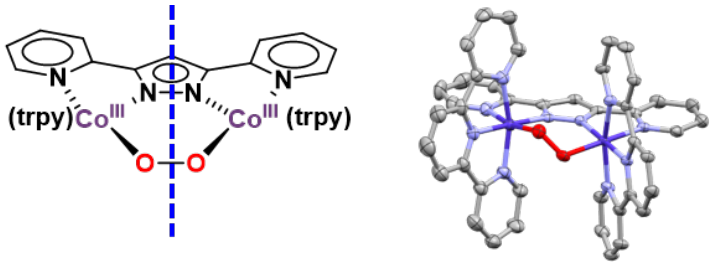

Figure 2.12: $\mathbf{Co1_{O_2}}$ with the C_2 rotational axis shown in blue. The X-ray crystal structure is included to show that the bridging peroxo does not sit in the plane of the bpp ligand. As a consequence there are no mirror planes in the molecule.

proton *z*, which is found between 8.4 – 8.5 ppm for the other four complexes. In both $\mathbf{Co5_{O_2}}$ and $\mathbf{Co6_{O_2}}$ the peak corresponding to proton *z* is significantly more deshielded, $\mathbf{Co5_{O_2}}$ it can be found at just below 9 ppm, whilst the presence of the NO_2 group in $\mathbf{Co6_{O_2}}$ shifts the peak to 9.2 ppm. Figure 2.13 shows the correlation between the Hammett parameter of the pyrazole substituent and the position of proton *z*. This suggests that the pyrazole backbone substituent results in a change in electronic environment across the bpp ligand. The impact of such changes to the electronic environment on the O–O bond length will be further explored through the solid state structures of the complexes, Section 2.4.3.

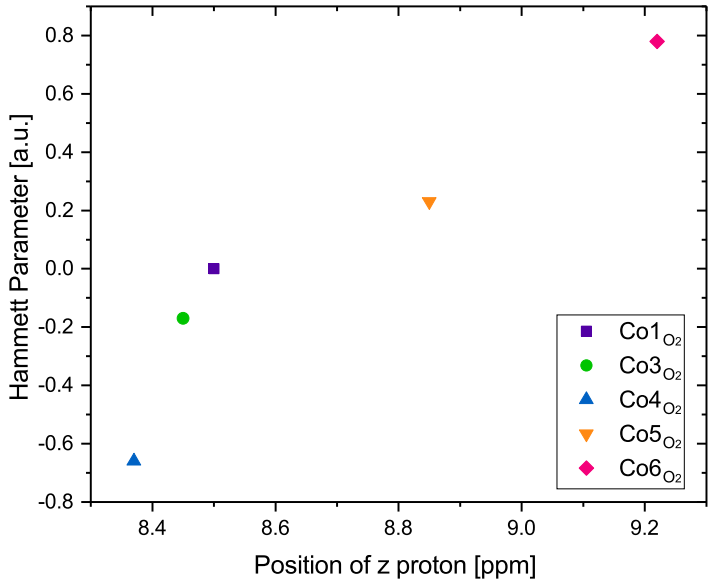

Figure 2.13: Hammett parameter, σ(para), plotted against the position of proton *z* (see Figure 2.11 for labels), showing a clear correlation.

2.4.2 NMR Spectroscopy of Paramagnetic Complexes: $\mathbf{Co1_{Cl}}$ – $\mathbf{Co6_{Cl}}$

Characterisation of paramagnetic complexes is challenging, and in many cases relies solely on mass spectrometry, crystallography or elemental analysis. This is due to the presence of one or more unpaired electrons, which complicate the NMR spectra due to the powerful local magnetic field from the electron, resulting in very short T_1 and T_2 values. This can result in high isotopic shifts of the peaks (resulting in very wide spectral widths), broad peaks (some of which span multiple ppm values) or peaks that are not identifiable at all.[193,194]

Similarly to NMR spectroscopy for diamagnetic complexes, it is possible to extract valuable information from a paramagnetic NMR spectrum. However, unlike diamagnetic NMR spectroscopy, in order to collect good quality data and fully assign spectra, the chemist needs technical knowledge in both NMR spectroscopy, in order to change the relevant parameters to fully optimise the data collection, and also in computational techniques, which are necessary to fully assign most paramagnetic spectra.[194] A more detailed discussion of these effects can be found in the Appendix, Section A.1.1.

NMR samples of $\mathbf{Co1_{Cl}}$ – $\mathbf{Co6_{Cl}}$ were prepared in thoroughly dried and degassed non-deuterated acetonitrile. The use of a solvent suppression pulse programme would routinely be used when employing a non-deuterated solvent to minimise the solvent peak to ensure the peaks of interest are identifiable. However, the use of a solvent suppression programme over the wide spectral width required for paramagnetic species ($\approx$ 200 ppm) resulted in a number of artefacts in the NMR spectra, including an inversion of the peaks, and a distortion of the baseline around the solvent peak, see Appendix, Figure A.2. This is likely due to the use of a different pulse shape for the solvent suppression program. As a consequence, wide spectral window spectra were run without the solvent suppression programme. The peaks of interest were at a sufficient distance from the solvent peak to not undergo distortion. For a full list of parameters changed, see Experimental, Section 2.7.

Using $\mathbf{Co2_{Cl}}$ as an example, Figure 2.14 shows that the ^{1}H peaks observed span an almost 300 ppm range. This results in a distortion to the spectrum, observed by the poor phasing around the solvent peaks (baseline roll[195]), and the "wavy" effect in the baseline. These wiggles are called sinc wiggles and are due to "clipping" or truncation of the FID, due to short acquisition times. Additionally, there is inaccuracy in the

integrals, for example peak **a** is expected to have an integral of 4. Although it is possible to perform some post-data-collection processing by performing linear forward prediction on the data to improve the baseline and definition of the peaks, this can prove problematic if the signal to noise ratio is not good. This is challenging when the peaks are already broad or ill-defined.[196]

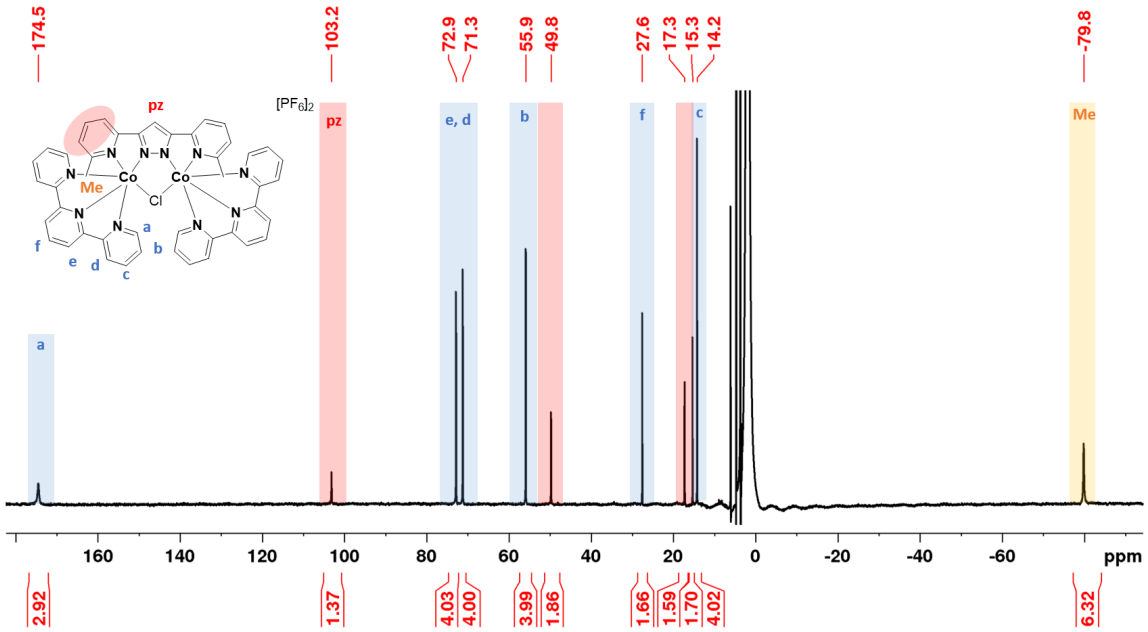

Figure 2.14: ^{1}H NMR spectrum of $\mathbf{Co2_{Cl}}$ in MeCN (non-deuterated), acquired with a spectral wridth of 300 ppm, tentative assignments are highlighted according to the image. Note that the poor phasing and bumps in the baseline are due to the presence of non-detuerated solvent and the wide spectral window, respectively.

As post-data-collection processing was not feasible on such a large spectral width, the data was collected with a narrower spectral width in order to improve the quality of the spectra. Figure 2.15 clearly demonstrates a much smoother baseline and more accurate integral values for the same NMR sample, after data collection on a narrower spectral width. Due to the increased accuracy of integral data and almost 100 ppm difference between peak **a** and the nearest peak, all samples were collected with both a narrow and wide spectral width. The assigned spectra in the Appendix for $\mathbf{Co1_{Cl}}$ and $\mathbf{Co3_{Cl}}$ – $\mathbf{Co6_{Cl}}$ (Section A.1.2) are from data collection on a narrower spectral width to ensure accurate integrals to help with assignment of the peaks.

The reduced number of peaks associated with the terpyridine ligands in the μ-Cl complexes, and the integrals of four, suggest that the μ-Cl complexes have a higher degree

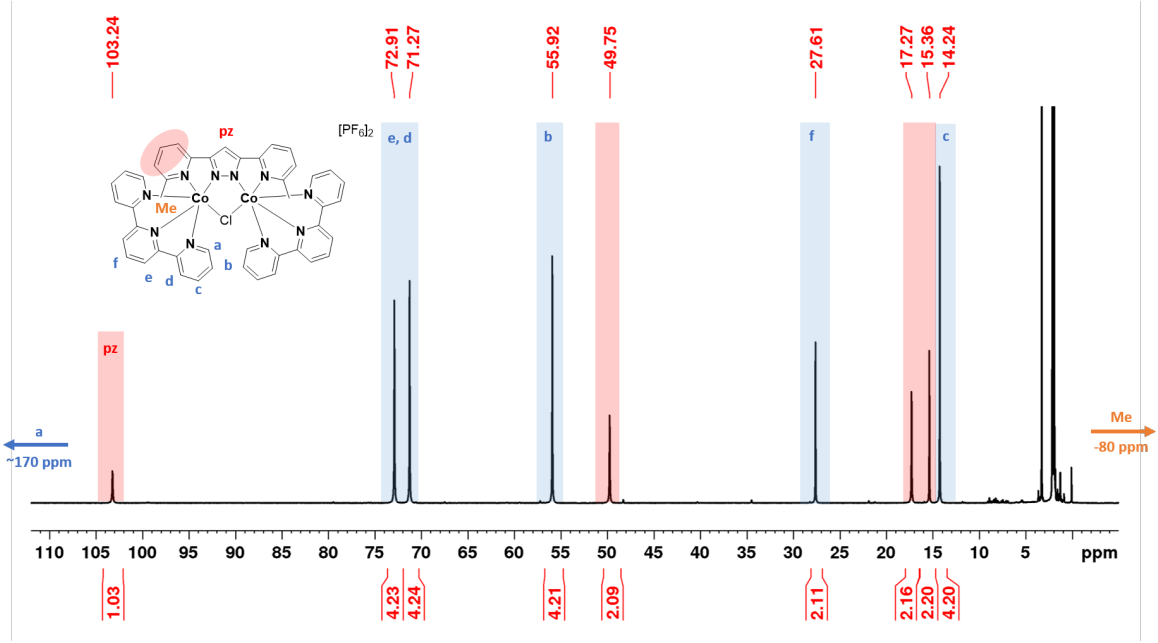

Figure 2.15: ^{1}H NMR spectrum for $\mathbf{Co2_{Cl}}$ acquired with a spectral width of 150 ppm, showing a much clearer baseline and more accurate integrals than Figure 2.14.

of symmetry when compared to their μ-OO counterparts. The complexes have two mirror planes, Figure 2.16, one running along the axis between the bridging chloro and through the pyrazole backbone, and the second in the plane of the bpp^{-} ligand, meaning the symmetry of the complexes is C_{2v}.

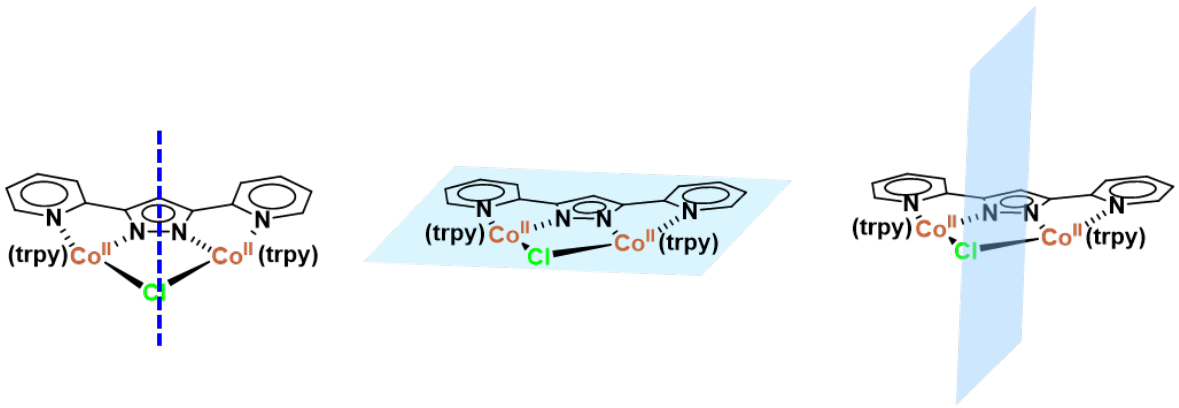

Figure 2.16: $\mathbf{Co1_{Cl}}$ showing its three symmetry elements, the C_2 axis and its two mirror planes. These three symmetry elements and the identity element (E) mean that it belongs to the C_{2v} point group.

Although it might be tempting to made deductions about the environment of the proton from its NMR signature, in order to complete a full assignment of the paramagnetic

spectra it would be necessary to use advanced computational techniques. The contributions of the contact shift terms and the two psuedo-contact shift (PCS) terms would need to be calculated, as both can have significant impacts on the position of the peaks in the spectrum.[194] Pell and collaborators illustrate this using examples of another Co(II) complex from experimental results from Długopolska *et al.* and computational studies by Rouf *et al.* in which the isotropic shift does not depend solely on the number of bonds between the Co(II) centre and proton, but also on the coordination geometry.[197,198]

Using a standard COSY pulse sequence across a wide spectral width can result in intense diagonal peaks which can dominate cross-peak multiplets. Additionally, due to phasing artifacts, the diagonal peaks can mask the presence of nearby cross-peaks.[194] A wide-spectral width COSY was collected for $\mathbf{Co2_{Cl}}$, Figure 2.17, where these artifacts are clearly visible, including symmetrical peaks roughly 20 ppm above and below the cross-peaks. Despite this, it was possible to identify a number of correlations, and in conjunction with the integral data in Figure 2.15 tentative peak assignments have been made.

The COSY spectrum helps identify a correlation between the peak at 27 ppm, with an integral of 2 and the peak at 73 ppm, with an integral of 4, confirming that these are **f** and **e**, respectively. This correlation between **f** and **e** is observed for all six complexes. The peak at 14 ppm is correlated to both the peak at 55 ppm and at 71 ppm, all of which have integrals of 4, which narrows the peak at 14 ppm down to either **b** or **c**, since it's correlated to two other peaks on the terpyrdine backbone.

The most significantly shifted peak is the one at 175 ppm, which has an integral of 3. However, as this peak is at the very edge of the spectrum, this integral is likely to be larger than is displayed here.[ii] The contact terms scale with $\frac{1}{r^3}$, where r is distance from the unpaired electron (for more details see A.1.1). Therefore, the protons that experience the effect of the unpaired electron most will be most significantly shifted, which suggests that the proton that correlates to the peak at 175 ppm is closest to the unpaired electron. Cobalt(II) is d^7, and has a distorted octahedral geometry, which means the unpaired electron should lie in either a $d_{x^2-y^2}$ orbital, or a d_{z^2}, Figure 2.18. It is worth noting that it is clear there is little or no coupling between two low spin d^7

[ii] This spectrum was recorded with a 400 ppm spectral width, centred around 0 ppm, but is displayed here with empty space minimised in order to ensure the key peaks are distinguishable.

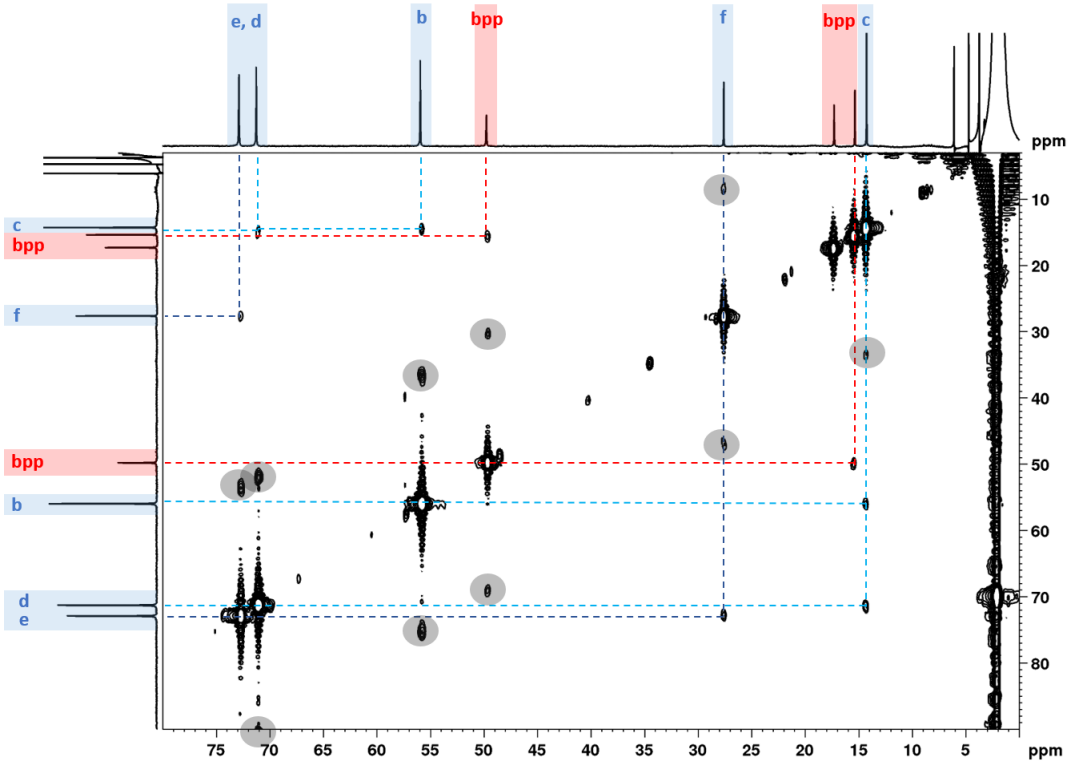

Figure 2.17: Assigned COSY spectrum for $\mathbf{Co2_{Cl}}$. The symmetrical peaks ≈ 20 ppm above and below the cross peaks are phasing artefacts (circled in grey).[194] Assignments for all labelled peaks are consistent with those shown in Figure 2.15.

centres, since this would result in a lower paramagnetic moment.

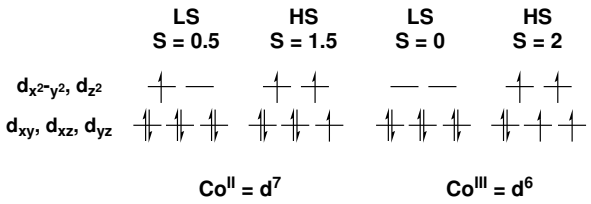

Figure 2.18: The Octahedral Ligand Field Splitting diagram for the four possible d-orbital configurations for octahedral cobalt (II) and cobalt (III).

If the electron were in a $d_{x^2-y^2}$ orbital the protons that would be most shifted would be those closest to the Co in the plane of the Co-bpp ligand - the **pz** proton and the para proton on the central pyridine of the terpyridine (**f**). This is not what is observed, as both the **pz** and **f** are within the range of the other paramagnetic peaks. Therefore, the unpaired electron is likely to lie in the d_{z^2} orbital which sits above/below

the plane, meaning the *ortho*-protons on the terminal pyridine of the terpyridine will experience the effect most significantly. This assignment could be confirmed through electronic structure calculations using computational techniques. Therefore, the peak at 175 ppm can be assigned as **a**, allowing the assignment of the other protons as seen in Figure 2.15. This assignment is further supported by comparison to the literature compound $[Co(trpy)_2[PF_6]_2]$ which uses COSY spectroscopy and the analagous diamagnetic Co(III) complex to help assign proton **a** as the peak most shifted and at the highest ppm values in the spectrum.[199]

In order to assign the bpp protons, it is necessary to compare the spectra of more than one complex. As $\mathbf{Co2_{Cl}}$ does not have a proton in the *ortho*-position of the bpp pyridines (**z**), it should be possible to identify this proton on the other complexes by identifying a similar peak in $\mathbf{Co1_{Cl}}$ and $\mathbf{Co3_{Cl}}$ – $\mathbf{Co6_{Cl}}$. All 5 complexes have a broad peak between 25 and 35 ppm which is not present in $\mathbf{Co2_{Cl}}$, and can therefore be confidently assigned as **z**. The broadness of the peak could suggest that this proton has a T_2 value that is shorter than the other protons on the bpp ligand. The reason behind the short T_2 value is similar to the explanation for **a**, discussed above: the influence of the unpaired electron in the d_{z^2} orbital results in a highly inhomogeneous magnetic field, shortening the T_2 value.

It can be seen from the COSY spectrum (Figure 2.17) that the peak at 15 ppm (integral of 2) is correlated to the peak at 50 ppm, which also has an integral of two. Of the remaining bpp protons, there are two found at low ppm values, between 10 and 20 ppm, which do not vary considerably between complexes. The peak found at lowest ppm values of these two is correlated to the the third bpp peak found close to 60 ppm in every complex. Of the three, it is this third proton which sees the most significant differences in shift according to ligand functionalisation, spanning a 20 ppm range, from 50 ppm in $\mathbf{Co2_{Cl}}$ to over 70 ppm in $\mathbf{Co6_{Cl}}$. Unfortunately peak **z** which is clearly identifiable in $\mathbf{Co1_{Cl}}$ and $\mathbf{Co3_{Cl}}$ – $\mathbf{Co6_{Cl}}$ does not have any visible cross-peaks in the COSY spectra, which makes distinguishing the bpp protons challenging.

Since full assignment was not possible with ^{1}H NMR spectroscopy alone, attention was turned to ^{13}C NMR spectroscopy. There are examples of collecting ^{13}C NMR data on paramagnetic complexes, although this often relies on the use of variable temperature NMR spectroscopy, or the use of a cryogenically cooled detection probe. In 2011, Kruck *et al.* demonstrated the collection of ^{13}C NMR data on a cobalt (II) complex,

with frequencies ranging from 1000 ppm to -220 ppm.[200] Although the collection of ^{13}C NMR data on **Co1$_{Cl}$** – **Co6$_{Cl}$** was attempted, it was not possible to detect peaks. This could be due to the peaks being too broad, or that they were outside of the spectral window used. It might have been possible to optimise the pulse sequences used for ^{13}C nuclei, and future work on these complexes would investigate this possibility.

Using ^{1}H NMR spectroscopy, it was possible to identify most of the peaks in the spectra. However, without the ^{13}C NMR data, it was not possible to fully assign the spectra. This reinforces the need for computational studies to complete the assignment of the spectra for **Co1$_{Cl}$** – **Co6$_{Cl}$**.

In some of the complexes there are a number of peaks identified as unreacted Co(trpy)Cl$_2$ starting material in the spectra, through correlation of the peaks to recorded literature peaks for [Co(trpy)$_2$][PF$_6$]$_2$.[201] These impurities proved challenging to remove due to the air-sensitive nature of the μ-Cl complexes, and in many cases attempts to remove unreacted Co(trpy)Cl$_2$ resulted in higher levels of the μ-OO species present in the sample. In all cases the starting material is present in levels lower than 20%.

2.4.3 Crystallography of Cobalt Complexes

Crystals of **Co3$_{O_2}$** – **Co6$_{O_2}$** suitable for X-ray diffraction analysis were grown by diffusion of diethyl ether into a saturated solution of the cobalt complex in acetonitrile and were characterised by single crystal X-ray diffraction, Figure 2.19. Despite repeated attempts, it was not possible to fully remove all traces of **Co2$_{Cl}$** from the sample of **Co2$_{O_2}$**, and the μ-Cl species preferentially formed crystals, Figure 2.20.

In all cases, the complexes show distorted octahedral geometries around both cobalt centres. **Co1$_{O_2}$** has been previously assigned as two Co(III) centres, which would correspond to a low-spin complex.[166] This is supported by the high field character of both terpyridine and bpp$^-$, due to their π-accepting nature. The MLXZ classification of the bridging ligands is μ-Cl$^-$ = LX and μ-OO^{2-} = XX.[202] The assignment of two Co(III) centres is further supported by NMR spectroscopy of the complex, which shows a diamagnetic complex, as described previously in Section 2.4.1.

The crystal structure of **Co2$_{Cl}$** can be found in Figure 2.20, where the crystal structure of **Co1$_{Cl}$** reported by Mandal *et al.* is included for comparison.[179] The geometry of **Co1$_{Cl}$** and **Co2$_{Cl}$** is similar to the μ-OO complexes with distorted octahedral geometries around the metal centres. However, the cobalt centres in this complex are Co(II)

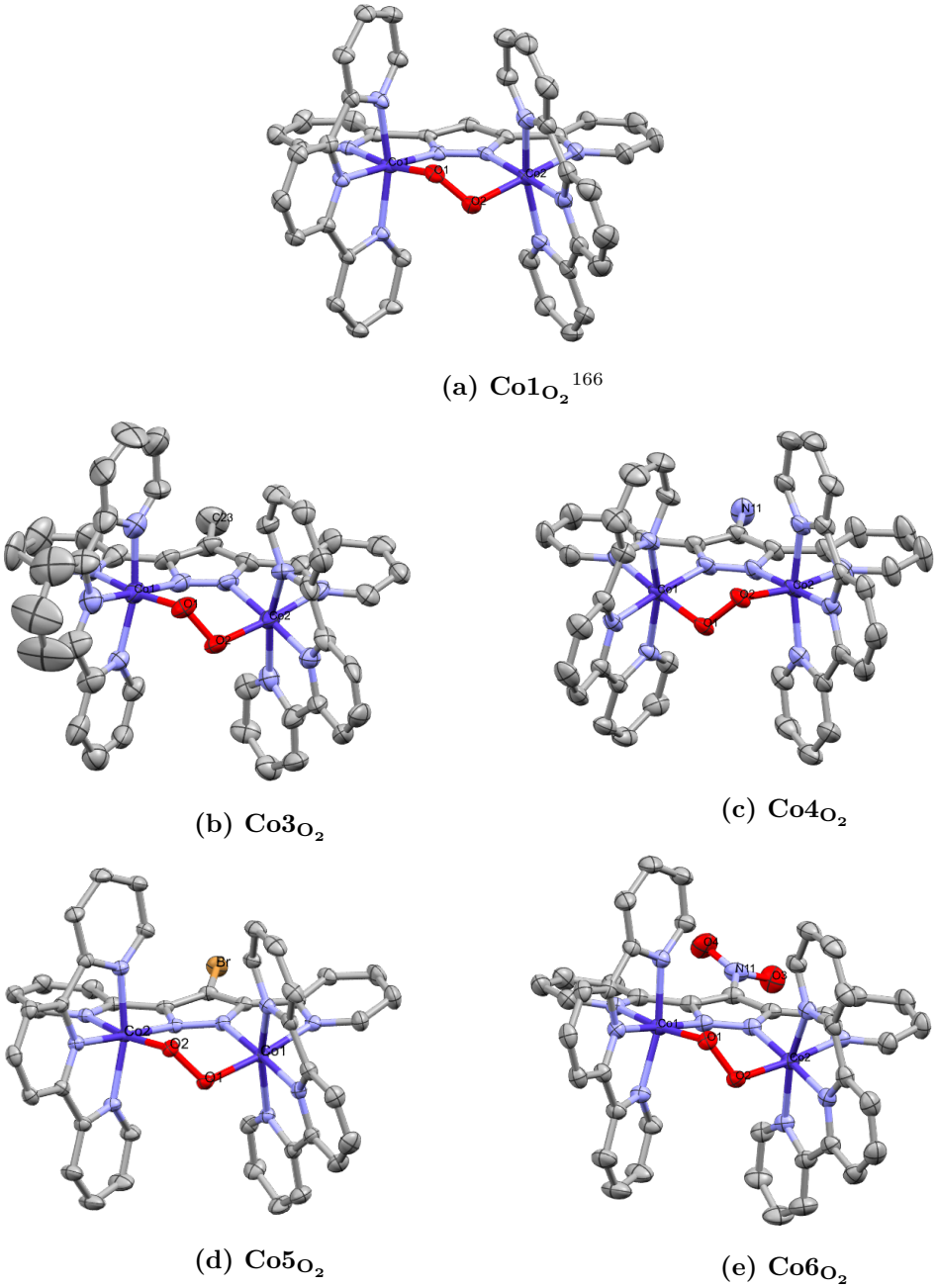

(a) $\mathbf{Co1_{O_2}}$[166]

(b) $\mathbf{Co3_{O_2}}$

(c) $\mathbf{Co4_{O_2}}$

(d) $\mathbf{Co5_{O_2}}$

(e) $\mathbf{Co6_{O_2}}$

Figure 2.19: X-ray crystal structures for $\mathbf{Co1_{O_2}}$ and $\mathbf{Co3_{O_2}}$ – $\mathbf{Co6_{O_2}}$ cobalt complexes. PF_6 counter ions, hydrogen atoms and solvent molecules omitted for clarity, shown with 50% probability ellipsoids. $\mathbf{Co1_{O_2}}$ reproduced from Llobet *et al.*[166]

d^7 low spin complexes, as shown in Figure 2.18. The paramagnetic NMR spectra of the μ-Cl species shows that the complexes have two mirror planes. This agrees with previous studies on a ruthenium complex similar to $\mathbf{Co1_{O_2}}$, which revealed that in the

μ-Cl form the terpyridine ligands sit "facing one another", in the plane of the metal centres and the bpp ligand. This is in contrast to the μ-acetato bridged system, where the terpyrdine ligands are pushed above and below the plane.[165] The μ-peroxo bridging system sits between chloro and acetate in terms of steric bulk, so it would be expected that the terpyridine ligands are slightly distorted out of the plane, as is observed in Figure 2.19.

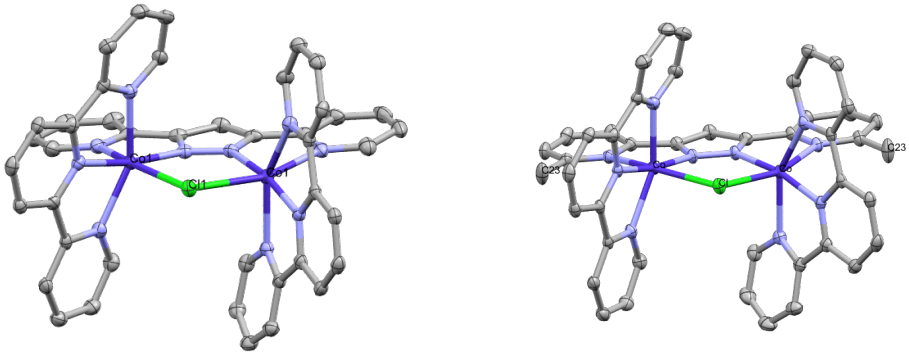

(a) $\mathbf{Co1_{Cl}}$[179] **(b) $\mathbf{Co2_{Cl}}$**

Figure 2.20: X-ray crystal structures for $\mathbf{Co1_{Cl}}$ and $\mathbf{Co2_{Cl}}$. PF_6 counter ions, hydrogen atoms and solvent molecules omitted for clarity, shown with 50% probability ellipsoids. $\mathbf{Co1_{Cl}}$ reproduced from Mandal *et al.*[179]

The bond lengths and angles measured in the complexes are shown in Figure 2.21, the bond lengths are highlighted in blue, and the angles in red. The distortion between the pyridine rings of the bpp^- ligand is obtained by measuring the dihedral angle between the planes of the rings. Bonds angles and lengths were measured using Olex2 software.[203]

It is plausible that functionalisation on the Hbpp ligand will have a steric effect on the binding pocket between the cobalt centres. This could either be through reducing the size of the bite angle, or through limited flexibility of the torsion of the pyridine rings. However, quantification of steric bulk is challenging, with one of the earliest attempts to quantify steric effects in chemical reactions conducted by Taft in the 1950s.[204] In the 1970s, Tolman's extensive studies into the impact of steric bulk on phosphine ligands in homogeneous catalysis resulted in the wildly used "Tolman cone angle" as a measure of steric bulk.[205] Another popularly used measure is the A-value, which is determined from the energy difference between the equatorial or axial configuration of cyclohexane with various substituents.[206] In 1997 the concept of the Accessible Molecular Surface

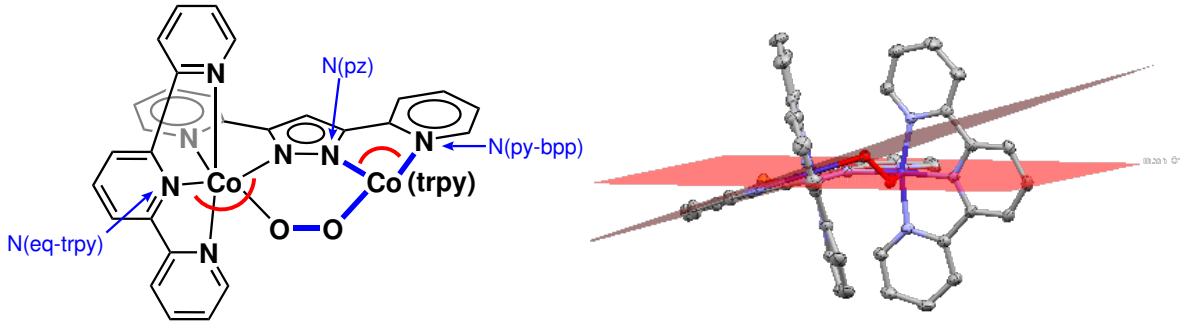

(a) **(b)**

Figure 2.21: (a) Schematic highlighting the bonds angles and lengths reported in Table 2.3 and Table 2.4 for $\mathbf{Co1_{O_2}}$ – $\mathbf{Co6_{O_2}}$. (b) Angle measured between the planes of the pyridine rings of the bpp ligand, shown here for $\mathbf{Co5_{O_2}}$.

(AMS) was described, calculated using molecular modeling and experimental results. The results of CO_2 hydrogenation with a series of rhodium phosphine complexes were used to probe the impact of changing steric bulk on the ligand backbone, revealing a pronounced effect on the rates of catalysis.[207] However, the many attempts to quantify the impact of steric effects highlights the non-universal nature of all of these methods. In order to accurately quantify the steric effects, computational methods will need to be used.

The selected bond angles shown in Table 2.3 confirm that functionalisation on the pyrazole backbone does not significantly change the bonding environment around the cobalt centres. The N(pz)-Co-N(py-bpp) angles are around 80° and the N(py-bpp)-Co-N(eq-trpy) angles are 102° for $\mathbf{Co1_{O_2}}$, $\mathbf{Co3_{O_2}}$ – $\mathbf{Co6_{O_2}}$.

Interestingly, there are some notable differences in the distortion of the bpp ligand, determined by measuring the angle between the two planes of the pyridine rings. $\mathbf{Co1_{O_2}}$ and $\mathbf{Co4_{O_2}}$ show angles of less than 5°, showing little distortion to the bpp ligand, whilst the greatest distortion is observed for $\mathbf{Co5_{O_2}}$. Both $\mathbf{Co1_{Cl}}$ and $\mathbf{Co2_{Cl}}$ have minimal distortion between the planes of the pyridine rings, confirming the symmetrical nature of the μ-Cl complexes.

The presence of the *ortho*-methyl groups on $\mathbf{Co2_{Cl}}$ would be expected to result in a constricted binding pocket. However, the angles reported in Table 2.3 show that there

Table 2.3: Selected bond angles and bpp distortion from $\mathbf{Co1_{O_2}}$ – $\mathbf{Co6_{O_2}}$, as shown in Figure 2.21.

Complex	N(pz)-Co-N(py-bpp)	N(py-bpp)-Co-N(eq-trpy)	bpp distortion[i]
$\mathbf{Co1_{O_2}}$[ii]	79.11(14), 80.45(13)	101.49(13), 103.46(16)	3.90(17)
$\mathbf{Co3_{O_2}}$[iii]	79.9(4), 81.2(4)	102.2(5), 101.0(4)	16.6(4)
	80.9(4), 80.1(4)	101.5(5), 101.6(4)	12.6(4)
$\mathbf{Co4_{O_2}}$	80.12(13), 80.32(15)	103.95(14), 101.17(16)	4.29(16)
$\mathbf{Co5_{O_2}}$	79.84(10), 79.68(10)	101.92(10), 100.68(10)	18.66(10)
$\mathbf{Co6_{O_2}}$	79.89(9), 79.25(9)	103.53(9), 100.59(9)	17.63(9)
$\mathbf{Co1_{Cl}}$[iv, v]	75.93(8)	108.38(8)	5.03(14)
$\mathbf{Co2_{Cl}}$[v]	76.11(6)	109.06(6)	2.95(9)

[i] Measured between the planes of the pyridine rings of the bpp ligand.
[ii] Values taken from structure reported by Rigsby *et al.*[166]
[iii] The crystal structure of $\mathbf{Co3_{O_2}}$ included two molecules in the unit cell, one $\mathbf{Co3_{O_2}}$ molecule, and one mixed $Co^{II}Co^{III}$ species. Mixed valence species is shown in grey. [iv] Values taken from structure reported by Mandal *et al.*[179]
[v] Both $\mathbf{Co1_{Cl}}$ and $\mathbf{Co2_{Cl}}$ had a perfectly symmetrical unit cell, so angles were the same for both cobalt centres.

is not a significant difference between $\mathbf{Co1_{Cl}}$ and $\mathbf{Co2_{Cl}}$. The challenge associated with isolating pure $\mathbf{Co2_{O_2}}$ suggests that perhaps the formation of the μ-OO species is less favourable for this complex. This may be due to steric constraints on the binding pocket caused by the presence of the methyl groups. Since formation of crystals was not possible, computational analysis might offer an alternative route to investigate the environment around the cobalt centres. However, this was beyond the scope of the project.

A comparison of key bond lengths, Table 2.4, reveals some further trends. Free O_2 has a bond length of 1.208 Å,[46] whilst H_2O_2 has a bond length of 1.49 Å.[208] In transition metal chemistry, most O–O bond lengths fall somewhere between these values, suggesting some residual double-bond character. The bond length has been shown to correlate to both bond strength (represented by vibrational frequencies for the bond) and the bond order.[46,127,209] $\mathbf{Co1_{O_2}}$ and $\mathbf{Co3_{O_2}}$ – $\mathbf{Co6_{O_2}}$ have O–O bond lengths in the range 1.32 Å – 1.41 Å.

The O–O bond lengths shown in Table 2.4 do not correlate to the Hammett parameter of the substituent on the pyrazole backbone, Figure 2.22. However, it is possible to draw some tentative correlations to ligand functionalisation. $\mathbf{Co4_{O_2}}$ shows an O–O bond

Table 2.4: Selected bond lengths and distances, as shown in Figure 2.21

Complex	Co–O	Co–N(pz) [Å]	Co–N(bpp-py) [Å]	O–O [Å]	Co–Co [Å]
$\mathbf{Co1_{O_2}}$ [i]	1.918(3), 1.905(3)	1.876(3), 1.900(4)	2.042(4), 2.017(3)	1.363(4)	3.832(7)
$\mathbf{Co3_{O_2}}$ [ii]	1.895(7), 1.893 (7)	1.880(7), 1.859(9)	2.01(1), 2.011(8)	1.408(8)	3.796 (3)
	1.89(1), 1.882(8)	1.885(11), 1.872(7)	2.042(7), 1.98(1)	1.32(1)	3.810(3)
$\mathbf{Co4_{O_2}}$	1.895 (2), 1.884 (2)	1.879 (3), 1.877 (3)	2.012(3), 2.017(4)	1.400(3)	3.804(1)
$\mathbf{Co5_{O_2}}$	1.904(2), 1.900(2)	1.890(2), 1.888(2)	2.043(3), 2.026(2)	1.379(3)	3.8224(5)
$\mathbf{Co6_{O_2}}$	1.888(2), 1.885(2)	1.895(2), 1.884(2)	1.998(2), 2.023(3)	1.384(2)	3.7867(5)

[i] Values taken from structure reported by Rigsby *et al.*[166] [ii] The crystal structure of $\mathbf{Co3_{O_2}}$ included two molecules in the unit cell, one $\mathbf{Co3_{O_2}}$ molecule, and one mixed $Co^{II}Co^{III}$ species. Mixed valence species is shown in grey and is omitted from most further comparisons.

length of 1.400 Å, potentially due to the electron-donating substituent (NH_2) increasing the electron density on the bpp ligand resulting in back donation into antibonding orbitals of the O–O bond, either π^* or σ^* orbitals. This is further supported by the shorter bond length between the cobalt and oxygen for $\mathbf{Co4_{O_2}}$. The longer bond length suggests a weaker O–O bond, with more peroxo character than O_2 double-bond character.

Due to the trans effect, it is possible that substitution in the *para*-position of the pyridine of the Hbpp ligand, rather than on the pyrazole backbone, might have a more pronounced effect on the O–O bond. Substitution in this position would also reduce the steric contribution of the substitution on the pyrazole backbone (illustrated by the bpp distorition in Table Table 2.3) meaning it would be possible to isolate steric from electronic effects. Density functional theory (DFT) could be used to determine the frontier orbitals involved.

$\mathbf{Co3_{O_2}}$ has two complexes in the unit cell, one of which has a long O–O bond, supporting the observations from $\mathbf{Co4_{O_2}}$ that electron-donating substituents results in a longer O–O bond. However, the other structure in the unit cell has the shortest O–O bond length of the five complexes. Interestingly, in both cases the Co–O bond length is relatively short, supporting the proposal of back donation from bpp into the Co–O π^* orbitals.

The unit cell in $\mathbf{Co3_{O_2}}$ contains two cobalt complexes and five counter ions, which could suggest the presence of a mixed valence species, $Co^{III}Co^{II}$, with a Co_2^{III} species. If the extra electron from the Co^{II} is localised on the O–O bond, it would be expected to populate a σ^* antibonding orbital (as shown in 1.3a). This would result in a longer O–

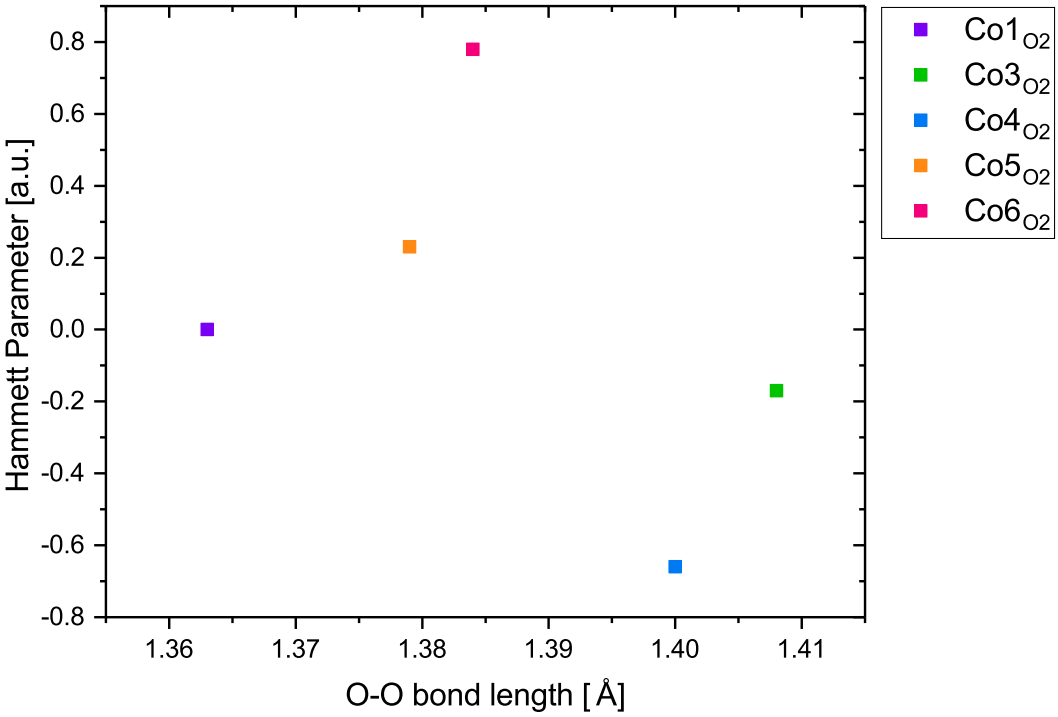

Figure 2.22: O–O bond length plotted against the Hammett parameter, σ(para), showing a lack of correlation between them. *(*Note that the mixed valence **Co3** species is omitted in this figure.)

O bond length, since an increase in electron density in the O–O anti-bonding orbitals would result in a weakening and lengthening the bond. However, without quantum chemical calculations, it is not possible to predict what the lowest unoccupied molecular orbital (LUMO) of the complex is, meaning that although the σ^* orbital of the O–O bond could be the LUMO, the electron could also be centred on one of the cobalt centres, or in a π^* orbital of one of the ligands on the molecule, or a combination of these. Due to the anomalous length of the O–O bond for $\mathbf{Co3_{O_2}}$ reported in Table 2.4, this is assigned as due to the mixed valence species, and is therefore not included in structure/activity relationships discussed in Chapter 3.

A change in oxidation state in the metal centre should be visible by UV-vis spectroscopy, as is discussed in Section 2.4.4. This is not observed for $\mathbf{Co3_{O_2}}$ *via* UV-vis spectrscopy, and additionally, there is no evidence in the NMR spectroscopy of mixed valence species in solution. This suggests that during the crystallisation process, the complex became partially reduced. Fully characterising a mixed valence species e.g. using the Robin-Day classification system,[210] is beyond the scope of this work.

The differences in the peroxo bond lengths suggest that the effect is not purely inductive, as both $\mathbf{Co3_{O_2}}$ and $\mathbf{Co4_{O_2}}$, with electron donating substituents, and $\mathbf{Co5_{O_2}}$ and $\mathbf{Co6_{O_2}}$, with electron withdrawing substituents, have longer O–O bond lengths than the unsubstituted $\mathbf{Co1_{O_2}}$. This suggests that the effect is stereoelectronic, rather than just due to one effect.

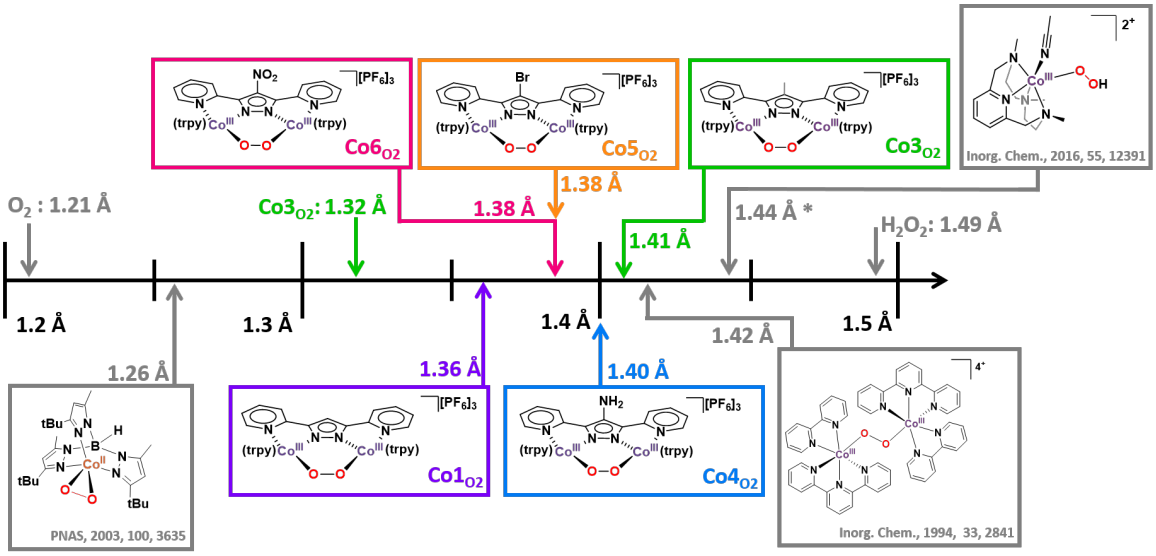

Figure 2.23: The O–O bond lengths of $\mathbf{Co1_{O_2}}$ and $\mathbf{Co3_{O_2}}$ – $\mathbf{Co6_{O_2}}$ with the bond lengths of both O_2[46] and H_2O_2[208] shown. Note that due to the two molecules in the unit cell for $\mathbf{Co3_{O_2}}$ both O–O bond lengths are shown. There are also three literature examples included, from left to right, a superoxo[46,211], a bridging peroxo[212] and a hydroperoxo species (**The hydroperoxo bond-length is a calculated length, rather than determined by spectroscopy*).[124]

Figure 2.23 shows the O–O bond lengths of $\mathbf{Co1_{O_2}}$ and $\mathbf{Co3_{O_2}}$ – $\mathbf{Co6_{O_2}}$ with some other cobalt-oxygen complexes, and both O_2 and H_2O_2 for reference. The series of complexes shows how the O–O bond length varies with different binding modes, illustrating the significance of the binding environment.

The side-on species shown, with an O–O bond length of 1.26 Å is a Co^{II} side-on superoxo species.[46,211] Since the superoxo species has one fewer electrons in the *pi** antibonding orbitals, has a shorter O–O bond length than that of the peroxo species reported in this work. Conversely, the long length of the bridged peroxo dimer (1.42 Å) suggests a weaker O–O bond.[212] The binding arrangement shown in the bridged peroxo complex is very similar to those of $\mathbf{Co1_{O_2}}$ – $\mathbf{Co6_{O_2}}$, with polyaromatic nitrogen-based chelate ligands. However, the notable difference is the lack of bridging ligand between the two cobalt centres. This suggests that the bridging nature of the bpp^- ligand imposes a

slight steric constraint on the binding of O_2.

Finally, the O–O bond length in the cobalt-hydroperoxo complex (1.44 Å), shown in Figure 2.23, is closest to H_2O_2 in length and has the least double-bond character. It is important to note that this bond-length is calculated using DFT calculations, rather than measured using X-ray crystallography.[124] The longer length of the hydroperoxo species suggests that the O–O bond is more activated in this complex than in $\mathbf{Co1_{O_2}}$ and $\mathbf{Co3_{O_2}}$ – $\mathbf{Co6_{O_2}}$, which are shown to have O–O bond lengths that are consistent with other bis-μ-peroxo species in the literature.

Bond length can sometimes be used as a proxy for bond order,[213] giving an indication of how reduced the O_2 is by the complex. The differences in bond length between $\mathbf{Co1_{O_2}}$ and $\mathbf{Co3_{O_2}}$ – $\mathbf{Co6_{O_2}}$ fall between the superoxo and peroxo bond lengths predicted by Vaska in a 1976 paper.[213] This suggests a degree of double-bond character remains, despite a formal charge on the peroxo ligand of O_2^{2-}. Predicting the behaviour of the complex can be challenging, since although a longer bond length suggests a greater degree of activation of the O_2 by the metal complex, if this is a highly stable species, the reactivity of the complex will be low.

The Co-Co distance can be used as a proxy for the size of the binding pocket. Additionally, it gives an indication of whether substitution on the pyrazole backbone has a steric impact on the binding pocket. The Co-Co distance in $\mathbf{Co6_{O_2}}$ is the shortest of all six complexes. The reduced distance could result in steric constraints when binding O_2, which might help explain why the synthesis of this complex was more challenging than the other complexes, Section 2.3.1.

Table 2.5: Selected bond lengths and distances, as shown in Figure 2.21

Complex	Co-Cl	Co-N(pz) [Å]	Co-N(bpp-py) [Å]	Co-Co [Å]
$\mathbf{Co1_{Cl}}$[i]	2.5152(6)	2.0009(19)	2.179(2)	3.9530(7)
$\mathbf{Co2_{Cl}}$	2.5399(5)	2.003(2)	2.280(2)	4.0010(7)

[i] Values taken from structure reported by Mandal *et al.*[179]

A comparison between the μ-Cl and μ-OO complexes reveals that the ligand to cobalt bond distances are longer for the μ-Cl complexes than for the μ-OO complexes, Table 2.4 and Table 2.5. The increase in N–Co bond distances in the Co_2^{II} complexes results in a longer Co–Co distances, which are longer in the μ-Cl complexes, with values closer to 4 Å, than the μ-OO complexes, where the distance is nearer 3.8 Å.

It is interesting to note that the Co–N bond distances reported for $\mathbf{Co1_{Cl}}$ and $\mathbf{Co2_{Cl}}$ are longer than those reported for the mono-cobalt NO_2-substituted complex shown previously in Figure 2.8. This is possibly due to reduced electron density on the cobalt due to the inductive effect of the NO_2 group trans to the Co–Cl bond. This effect might be more pronounced in the mono-metallated complex due to the configuration with the terpyridine in the "in" position.

2.4.4 UV-vis Spectroscopy of Co1 – Co6

The strong colour difference between the Co_{O_2} and Co_{Cl} complexes, as shown in Figure 2.24, suggested that there would be clear differences in the UV-vis spectra of the complexes. Collection of UV-vis spectra of all twelve complexes, Figure 2.25, allowed insight into solution speciation.

Figure 2.24: The pronounced difference in solution colour between the μ-OO complexes (left: $\mathbf{Co1_{O_2}}$, 0.25 mM, centre: $\mathbf{Co2_{O_2}}$, 0.25 mM) and the μ-Cl complexes (right: $\mathbf{Co1_{Cl}}$, 0.25 mM. All in MeCN). These colours are similar across all six complexes. *Note that* $\boldsymbol{Co2_{O_2}}$ *is less intensely coloured due to the presence of* $\boldsymbol{Co2_{Cl}}$ *species in solution, as discussed previously.*

Using previously reported data, the λ_{max} (the wavelength of maximum absorbance, in a given region of the spectrum) of terpyridine is found at 285 nm,[214] which supports assignment of the large UV-vis band at around 300 nm being $\pi \rightarrow \pi^*$ transitions on the terpyridine and Hbpp ligands. The μ-OO complexes all show a distinct feature at around 550 nm, Figure 2.25 while the μ-Cl speces show a lower intensity shoulder peak between 350 and 400 nm. The λ_{max} and molar extinction coefficient (ε) values can be found in Table 2.6.

Due to the intensity of the molar extinction coefficients (ε, Table 2.6) of the peak at around 550 nm for the μ-OO species, and the location in the spectrum, it is likely that this transition is due to a charge transfer process (either metal-to-ligand charge transfer (MLCT) or ligand-to-metal charge transfer (LMCT)). It is notable that the λ_{max} value between 400 and 700 nm for $\mathbf{Co1_{O_2}}$ – $\mathbf{Co6_{O_2}}$ shows only a blue-shift to higher energies with respect to $\mathbf{Co1_{O_2}}$. This is surprising because it would be expected

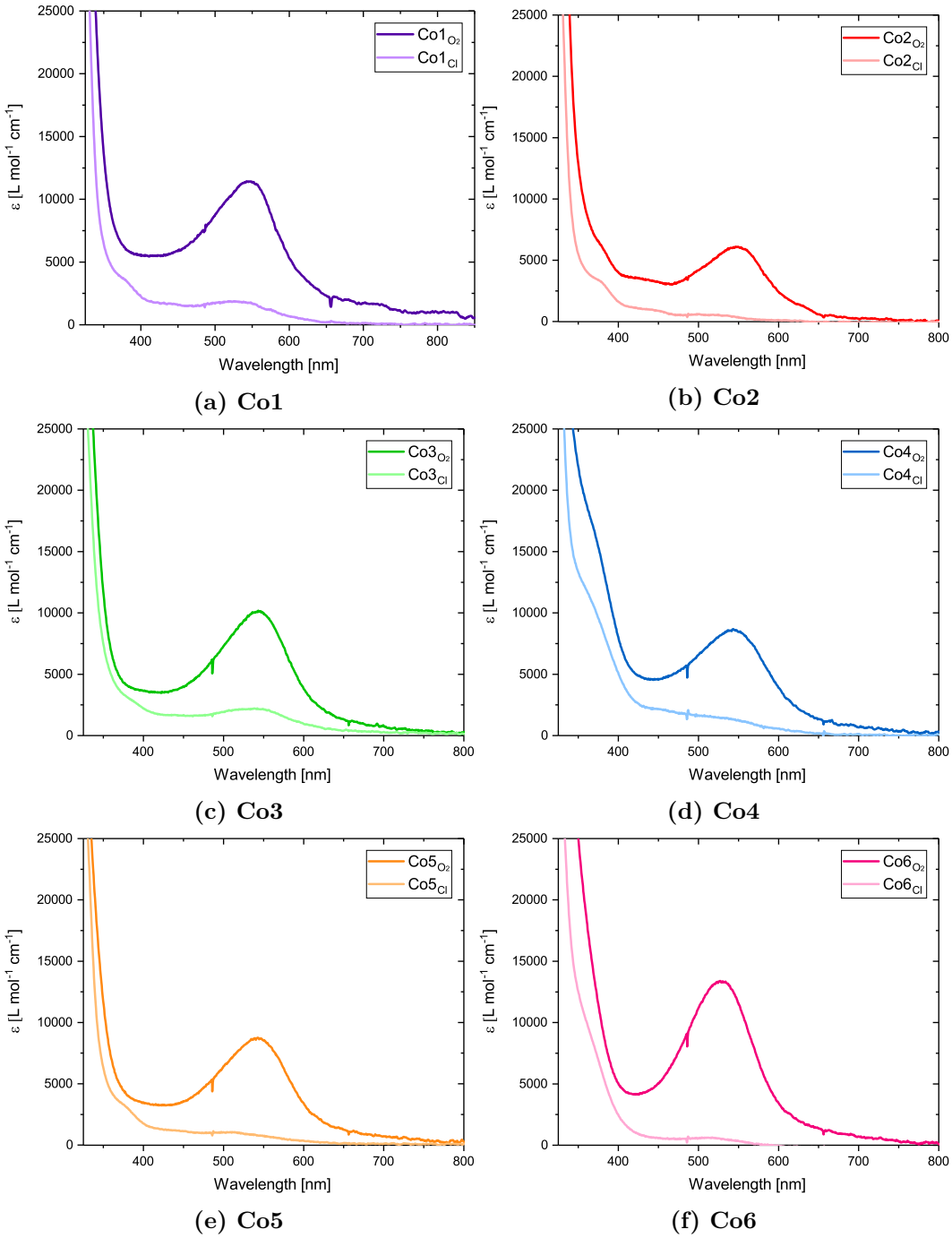

(a) Co1 **(b) Co2**

(c) Co3 **(d) Co4**

(e) Co5 **(f) Co6**

Figure 2.25: UV-vis spectra of $\mathbf{Co1_{O_2}}$ – $\mathbf{Co6_{O_2}}$ and $\mathbf{Co1_{Cl}}$ – $\mathbf{Co6_{Cl}}$ showing the predominant peak for the μ-OO species at around 550 nm, and the distinctive shoulder peak of the μ-Cl complexes between 350 and 400 nm. Solvent = MeCN

Table 2.6: λ_{max} and εvalues for $\mathbf{Co1_{O_2}}$ –$\mathbf{Co6_{O_2}}$ in MeCN.

Complex	λ_{max} [nm] (μ-OO)	$\varepsilon(\lambda_{max})$ [M^{-1} cm^{-1}]
$\mathbf{Co1_{O_2}}$	550	11406
$\mathbf{Co2_{O_2}}$	549	6107
$\mathbf{Co3_{O_2}}$	543	10193
$\mathbf{Co4_{O_2}}$	543	8683
$\mathbf{Co5_{O_2}}$	543	8772
$\mathbf{Co6_{O_2}}$	527	13402

that electron withdrawing and electron donating substituents would results in shifts of the λ_{max} in opposite directions. Given the complexes have two metal centres and three ligand systems, it is likely there are multiple charge transfer events that contribute to what appears to be a single peak in the spectra, Figure 2.25. However, in order to confidently assign these peaks to specific transitions, temperature and solvent-polarity dependence studies would need to be carried out alongside emission studies,[215,216] and complimented by computational techniques, unfortunately such studies were beyond the scope of this work.

There is a pronounced difference in the intensity of the peaks in the UV-vis spectra between the μ-Cl and μ-OO species. This suggests that the transitions in the μ-OO complexes are more allowed by the UV-vis selection rules than the μ-Cl complexes. The spin selection rule states that an electron cannot change spin state during a transition.[217] By looking at the d-orbital configuration for Co^{III} and Co^{II} (Figure 2.18) it can be seen that all d-d spin transitions are allowed for a low-spin Co^{III} complex, whereas there are fewer allowed transitions for a Co^{II} low-spin complex. However, the spin selection rule alone does not explain the significant differences in intensity. The symmetry selection rule states that in order for a transition to be allowed, there must be a change in parity. In simple atoms and centrosymmetric molecules this is explained by the Laporte rule which states that in order for a transition to be allowed it must be gerade $\rightarrow$ ungerade, or ungerade $\rightarrow$ gerade.[217] The orbital selection rule states that for a transition to be allowed the total angular momentum must change by ± 1. In more complex molecules, such as $\mathbf{Co1_{O_2}}$ – $\mathbf{Co6_{O_2}}$, it becomes necessary to use group theory to determine the allowed transitions, although, in general, molecules with higher degrees of symmetry are more likely to have symmetry forbidden transitions.

It is clear from the ^{1}H NMR spectra (Section 2.4.2) and the solid-state structures (Fig-

ure 2.20) that the μ-Cl complexes have higher symmetry than their μ-OO counterparts. Due to the similarity in the spacial arrangement of the ligands in the μ-Cl and μ-OO complexes, it is unlikely that the transitions in the μ-Cl complexes are forbidden by the spacial selection rule. It is therefore likely that the pronounced difference between the two sets of complexes is due to the μ-Cl complexes having fewer allowed transitions due to both the spin and symmetry selection rules not being fulfilled.

When comparing the UV-vis spectra of the μ-OO and μ-Cl series there are a number of shared features between the families, most notably the strong $\pi \rightarrow \pi^*$ transition at around 300 nm. However, the most notable difference between them is the lack of any key features in the μ-Cl spectra in the region between 500 – 600 nm, whereas the μ-OO complexes have a pronounced peak in this region. This suggests that the peroxo ligand may be involved in MLCT or LMCT transition(s) in this region.

2.5 Conclusions

A number of previously reported ligands based on the Hbpp moiety were synthesised, incorporating methyl functionalisation in the *ortho-* position of the ligand and a range of substituents on the pyrazole backbone (Me, NH_2, Br, NO_2). The atom economy of the synthetic route to the amine-subtituted HL4 was improved upon, using NBS, followed by nucleophilic substitution of the bromine substituent by hydrazine.

These ligands were used to make a series of six Co_2^{III}μ-peroxo complexes based on the reported literature complex $\mathbf{Co1_{O_2}}$. Their six Co^{II} chloro equivalents were also synthesised. The twelve complexes were characterised by a combination of NMR spectroscopy, mass spectrometry, crystallography and UV-vis spectroscopy. The ^{1}H NMR spectra of the six diamagnetic Co^{III} complexes did not show significant differences, with the exception of the location of the protons in the *ortho* position on the pyrdines on the bpp^- ligand, which was significantly shifted by the presence of electron withdrawing substituents on the pyrazole backbone. The ^{1}H NMR spectra of the paramagnetic Co^{II} complexes were tentatively assigned using wide-spectral width COSY spectra, showing that most peaks were found in the 10 – 80 ppm region.

The results from the ^{1}H NMR spectroscopy and X-ray crystallography confirm that the μ-OO complexes have close to C_2 symmetry. The complexes have an axis running through the pyrazole backbone and O–O bond, as illustrated in Figure 2.12. It was not possible to crystallise $\mathbf{Co2_{O_2}}$, but $\mathbf{Co2_{Cl}}$ was characterised by X-Ray crystallo-

graphy. The μ-Cl complexes are close to C_{2v} symmetric, and also have an axis running through the pyrazole backbone and bridging chloro. They have two mirror planes, one of which is in the plane of the bpp^- ligand, and the second vertically along the axis that runs through the chloro and pyrazole backbone, as illustrated in Figure 2.16. This is confirmed through ^1H NMR spectroscopy, which showed that each terpyridine peak corresponded to four protons.

The crystal structures of the complexes showed a degree of distortion in the bpp^- backbone and the terpyridine ligands, with the most pronounced distortion in $\mathbf{Co5_{O_2}}$, the bromo-substituted complex. This suggests that substitution on the pyrazole backbone does impart some steric constraints to the complex. All five μ-OO crystal structures show a degree of variation in the Co – Co distance, and the O–O bond in the bridging peroxo ligand. The O–O bond lengths are within the expected range for a bridging peroxo species, and suggest a degree of double-bond character remains. The O–O bond lengths do not correlate to the electron donating or withdrawing ability of the pyrazole substituent, suggesting this is a steroelectronic effect. This suggests that the structure activity relationship between the complexes might not follow the expected trends based purely on electronic factors. This will be investigated further in Section 3.

The structure of $\mathbf{Co2_{Cl}}$ offers some insight into the μ-Cl complexes, confirming the observations from NMR spectroscopy that these species have a higher degree of symmetry. It is also clear that the inclusion of methyl groups in the *ortho*-position of the Hbpp pyridine rings resulted in a level of steric congestion around the binding pocket. The bond angle between the cobalt and the two binding sites on the Hbpp ligand was 4° smaller than for the other complexes, and this was also mirrored in the angle between the Hbpp and terpyridine ligands. The impact of this steric congestion is further studied in Chapter 3.

There are clear differences between the Co^{II}-μ-Cl complexes and the Co^{III}-μ-OO complexes in the UV-vis spectra, which showed a strong peak at around 550 nm for all peroxo complexes, that was not present for the μ-Cl complexes. This peak is likely due to a charge transfer event and was in a similar position for all six peroxo complexes. The chloro complexes showed a peak in the shoulder of the $\pi \rightarrow \pi^*$ transition at around 300 nm, which was much lower intensity than the peak in the peroxo species.

Having carried out structural characterisation of the complexes, they will be investigated to determine whether any of the structural trends correlate with activity. Their

electrochemical properties will be studied and their reactivity towards both oxygen reduction and oxygen atom transfer, in Chapter 3.

2.6 Future Work

There is significant scope for further ligand functionalisation as a way of studying the impact on the cobalt centres. Additionally, such ligand modifications might enable the synthesis of heterobimetallic complexes. This is discussed further in Chapter 4.

2.6.1 Additional Characterisation

Although tentative assignments were made for $\mathbf{Co1_{Cl}}$ – $\mathbf{Co6_{Cl}}$, for complete assignment of the ^{1}H NMR spectra, computation techniques such as density functional theory (DFT) could be used.

X-ray crystal structures of all 12 complexes would allow a more thorough structural comparison, and would help determine the full impact of functionalisation at different locations around the Hbpp ligand backbone. Although the O-O bond will not be active in infrared (IR) spectroscopy, the Co-Cl and Co-O bonds should be active, and might give some insight into the relative strengths of the bonds.

2.7 Experimental

2.7.1 Analytical Techniques

All reactions and workups were carried out in air unless specified otherwise. Reactions under argon were performed using standard Schlenk techniques or an MBraun Unilab Plus glovebox.

NMR spectra were recorded using a Bruker Avance III NMR spectrometer operating either at 500.13 MHz or 400.04 MHz for ^{1}H experiments or a 500 MHz Agilent ProPulse. Unless otherwise specified organic samples were analysed in $CDCl_3$ and metal complexes analysed in MeCN – at 25 °C using standard Bruker pulse sequences (Topspin 2.1). Chemical shifts (δ) are reported in ppm. Typically ^{1}H spectra were acquired with a spectral width (SW) of 20 ppm, and 16 transients. $^{13}C\{^{1}H\}$ spectra were obtained with a SW of 220 ppm and with 1024 transients. Spectra were referenced using the residual solvent signal, at 7.26 or 1.95 ppm for ^{1}H (in $CDCl_3$ or MeCN respectively) and 77.0 or 1.32 ppm for ^{13}C (in $CDCl_3$ or CD_3CN respectively). Where diamagnetic samples were prepared in protonated solvents ^{1}H spectra were acquired with (pre-saturation)

solvent suppression pulse sequences. Unless stated otherwise, paramagnetic samples were acquired using a wide spectral width (SW = 200 ppm) with the spectrum origin = 50 ppm, acquisition times were set to 0.5 s, and relaxation delay reduced to 1 s. Note that the paramagnetic spectra did not show any discernible coupling patterns, so only the ppm values and integrals are reported.

Mass Spectrometry of ligands were conducted on an Agilent Electrospray Quadrupole Time-of-Flight (QTOF) mass spectrometer. Mass spectrometry of $\mathbf{Co1_{O_2}}$ and $\mathbf{Co2_{Cl}}$ were performed at the EPSRC National Mass Spectrometry Facility in Swansea. Analysis of all other cobalt complexes were conducted using a MaXis HD quadrupole electrospray time-of-flight (ESI-QTOF) mass spectrometer (Bruker Daltonik GmbH, Bremen, Germany), using a glass syringe (Hamilton) and syringe pump (KD Scientific, Model 781100) for infusions at a flow rate of 3 µl/min. Analyses were performed in ESI positive mode with the capillary voltage was set to 4500 V, nebulizing gas at 1 bar, drying gas at 6 L/min at 180 °C in each case. The TOF scan range was from 50 – 1000 mass-to-charge ratio (m/z). The MS instrument was calibrated using an infusion of sodium formate calibrant solution. The calibrant solution consisted of 3 parts of 1 M NaOH to 97 parts of 50:50 water:isopropanol with 2% formic acid. Data processing was performed using the Compass Data Analysis software version 4.3 (Bruker Daltonik GmbH, Bremen, Germany).

UV/Vis spectroscopy was conducted using an Avantes AvaLight-DH-S-BAL light source and an Avantes AvaSpec-2048L spectrometer.

Single crystal X-ray diffraction analysis was carried out by Dr Gabriele Kociok-Köhn at the University of Bath using a RIGAKU SuperNova Dual. Crystallography images were rendered using Mercury 4.3.1 software. Angles between atoms, bond distances and angles between planes were calculated using Olex2 software.[203]

Commercially available materials were obtained from Sigma Aldrich, Fisher or Acros and used as recieved unless otherwise stated. Methanol was dried by distillation from magnesium. Toluene was dried by distillation from sodium. THF, Et_2O and hexane were dried by distillation from potassium. Acetonitrile was dried by distillation from calcium hydride and stored over 4 Å molecular sieves.

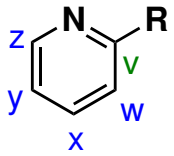

Figure 2.26: Ligand precursor labelling convention used for NMR assignments. Blue are used for carbon and proton assignments, where appropriate, green are carbon assignments.

2.7.2 Ligand Precursor Synthesis

Picolinate Derivatives

Picolinic acid (4 g, 32 mmol) (or equivalent substituted variant (6-methylpicolinic acid, 200 mg, 0.15 mmol)) was dissolved in methanol or ethanol (5 – 10 mL) in a microwave vial and excess hydrochloric acid (0.1 mL) was added. The reaction mixture was placed in the microwave reactor and heated at 150 °C for 45 minutes. The solvent was removed and the acid quenched by addition of saturated sodium bicarbonate solution (10 mL). The product was extracted with dichloromethane (3 x 10 mL), washed with water, dried over $MgSO_4$ and the solvent removed, yielding an oil in all cases.

R = H, Ethyl Picolinate

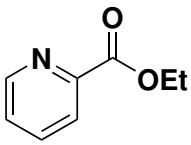

[151.16 g mol^{-1}]

Ethyl picolinate was further purified by distillation under vacuum. (2.9 g, 0.019 mol, 60%)

^{1}H NMR (400 MHz, $CDCl_3$) δ (ppm): 8.75 (*z*, 1H, m), 8.12 (*w*, 1H, dt, $^3J_{w,x}$ = 7.80, $^4J_{w,y}$ 2.12 Hz), 7.83 (*x*, 1H, td, $^3J_{x,w}$ = $^3J_{x,y}$ = 7.75, $^3J_{,zx}$ 1.77 Hz), 7.45 (*y*, 1H, dd, $^3J_{y,z}$ = $^3J_{y,x}$ = 7.75, $^4J_{y,w}$ = 4.74 Hz), 4.47 (CH_2, 2H, q, $^3J_{CH_2,CH_3}$ = 7.12 Hz), 1.44 (CH_3, 3H, t, $^3J_{CH_3,CH_2}$ = 7.14 Hz) $^{13}C\{^1H\}$ NMR (100 MHz, $CDCl_3$) δ (ppm): 156.1 (*C*=*O*), 149.9 (*v*), 148.3 (*z*), 137.0 (*x*), 126.9 (*y*), 125.1 (*w*), 61.8 (CH_2), 14.3 (CH_3). *In agreement with reported literature values.*[218]

R = Me (Methyl-6-methylpicolinate)

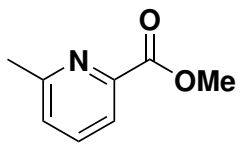

[151.16 g mol^{-1}]

(0.69 g, 4.58 mmol, 77%)

^{1}H NMR (400 MHz, $CDCl_3$) δ (ppm): 7.88 (*w*, 1H, d, $^{3}J_{w,x}$ = 7.81 Hz), 7.66 (*x*, 1H, t, $^{3}J_{x,y}$ = $^{3}J_{x,w}$ = 7.81 Hz), 7.27 (*y*, 1H, d, $^{3}J_{y,x}$ = 7.55 Hz), 3.93 (*CH_3-ester*, 3H, s), 2.59 (CH_3, 3H, s). $^{13}C\{^{1}H\}$ NMR (400 MHz, $CDCl_3$) δ (ppm): 165.93 (*C=O*), 158.95 (*z*), 147.42 (*v*), 137.10 (*y*), 126.84 (*x*), 122.39 (*w*), 52.87 (*OCH_3*), 24.63 (*CH_3*). *In agreement with reported literature values.*[219]

2.7.3 Diketone Synthesis

The picolinate derivative (R = H 5mL, 36 mmol, R = Me 0.69 g, 4.5 mmol) was dissolved in tetrahydrofuran (THF) (R = H, 120 mL, R = Me, 40 mL). Sodium hydride (60% dispersion in paraffin oil) (R = H, 5 g, 120 mmol, R = Me 0.2 g, 5 mmol) was added and the solution stirred for 30 minutes before adding 2-acetylpyrdine or substituted derivative (R = H 4.6 mL, 36.0 mmol, R = Me 0.62 g, 4.5 mmol). THF was added as the mixture thickened (total 100 mL). The solution was stirred at 60 °C for 12 hours. The solvent was removed under vacuum, before carefully adding water (50 mL) whilst stirring vigorously. Upon addition of acetic acid (5 – 10 mL) a yellow/white solid formed which was separated by filtration and washed with ice-cold water.

1,3-dipyridin-2-ylpropane-1,3-dione

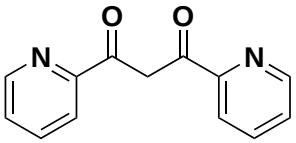

[226.235 g mol^{-1}]

(8.65 g, 38 mmol, 92%) A crude ^{1}H NMR was recorded, but the product was used directly without further purification, as described in the literature.[220] ^{1}H NMR (400 MHz, $CDCl_3$) δ (ppm): 8.74 (*z*, 2H, m), 8.15 (*w*, 2H, d, $^{3}J_{w,x}$ = 7.88 Hz), 7.86 (*x*, 2H, dt, $^{3}J_{x,w}$ = $^{3}J_{x,y}$ = 7.73, $^{3}J_{x,z}$ = 1.74 Hz), 7.44 (*y*, 2H, m), 4.93 (*CH_2*, 2H, s). *In agreement with literature values.*[221]

2-pyridyl-2-(6-methyl)pyridyl-1,3-propandione

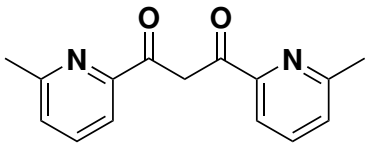

[254.289 g mol^{-1}]

(0.95 g, 3.73 mmol, 82%) A crude ^{1}H NMR was recorded, but the product was used directly without further purification. ^{1}H NMR (400 MHz, $CDCl_3$) δ (ppm): 16.11 (*OH*,

1H, s), 7.95 (*w*, 2H, d, $^3J_{w,x}$ = 7.68 Hz), 7.73 (*x*, 2H, t, $^3J_{x,w}$ = $^3J_{x,y}$ = 8.06 Hz), 7.29 (*y*, 2H, d, $^3J_{y,x}$ = 7.60 Hz), 4.83 (*HC(C=O)$_2$*, 1H, s), 2.67 (*CH$_3$*, 6H, s). *In agreement with literature values.*[180]

2.7.4 Diketone Functionalisation

2-methyl-1,3-di(pyridin-2-yl)propane-1,3-dione

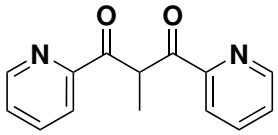

[240.26g mol^{-1}]

Potassium *tert*-butoxide (KO^{t}Bu) (63 mg, 0.56 mmol) was dissolved in THF. 1,3-dipyridin-2-ylpropane-1,3-dione (100 mg, 0.38 mmol) in THF was added to the KO^{t}Bu at 0 °C and the solution allowed to warm to room temperature. After heating at 50 °C for 2 hours the mixture was allowed to cool to room temperature. Methyl iodide (MeI) (70 µl, 1.1 mmol) was added to the solution before stirring at room temperature for 12 hours. The reaction was quenched with addition of water and the aqueous layer extracted with diethyl either (Et_2O) (3 x 10 ml). The organic fractions were combined and dried over $MgSO_4$ before removal of solvent *in vacuo* to yield an orange oil. (0.0712 g, 0.30 mmol, 78.9 %) ^{1}H NMR (400 MHz, $CDCl_3$) δ (ppm): 8.50 – 8.48 (*z*, 2H, m), 8.08 (*w*, 2H, dt, $^3J_{w,x}$ = 7.03, $^4J_{w,y}$ = 1.07 Hz) 7.81 (*x*, 2H, td, $^3J_{x,y}$ = $^3J_{x,w}$ = 7.63, $^4J_{x,z}$ = 1.73 Hz), 7.38 (*y*, 2H, dd, $^3J_{y,z}$ = $^3J_{y,x}$ = 7.70, $^4J_{y,w}$ = 4.27 Hz), 5.72 (*CH*, 1H, q, $^3J_{CH,CH_3}$ = 7.03 Hz), 1.55 (*CH$_3$*, 3H, d, $^3J_{CH_3,CH}$ = 7.04 Hz) ^{13}C{^{1}H} NMR (100 MHz, $CDCl_3$) δ (ppm): 199.17 (*C=O*), 152.36 (*v*), 148.70 (*z*), 137.03 (*x*), 126.90 (*y*), 122.40 (*e*), 50.10 ((*CH*)), 13.08 (*CH$_3$*). *In agreement with literature values.*[222]

2-bromo-1,3-di(pyridin-2-yl)propane-1,3-dione

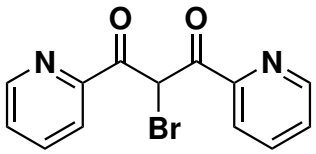

[305.131g mol^{-1}]

1,3-dipyridin-2-ylpropane-1,3-dione (500 mg, 1.8 mmol) and *N*-Bromosuccinimide (NBS) (368 mg, 2.1 mmol) were placed in a flask and degassed thoroughly for 1 hr, after which Et_2O was added (80 mL). The resultant solution was stirred and irradiated with UV light for 20 minutes resulting in a yellow/brown solution. The solvent was removed and the product recrystallised from EtOH and Et_2O yielding the product as a yellow/brown solid. (323 mg, 1.1 mmol, 56%) ^{1}H NMR (400 MHz, $CDCl_3$) δ (ppm): 8.51 (*z*, 2H, d, $^3J_{z,y}$ = 4.3 Hz), 8.15 (*w*, 2H, d, $^3J_{w,x}$ = 7.8 Hz), 7.86 (*x*, 2H, t, $^3J_{x,w}$ = $^3J_{x,y}$ = 7.3

Hz), 7.49 – 7.38 (*y*, 2H, m), 7.33 (*CH*, 1H, s). $^{13}C\{^1H\}$ NMR (100 MHz, $CDCl_3$) δ (ppm): 189.9 (*C=O*), 150.6 (*v*), 148.7 (*z*), 137.1 (*x*), 127.3 (*y*), 122.9 (*w*), 53.7 (*CH*). MS (ESI+), Calculated m/z [M] = 303.9851, Found [M] = 303.9847

2.7.5 Pyrazole Synthesis

The appropriately substituted diketone (R = H, (9 g, 41 mmol), R = *ortho*-Me (0.95 g, 3.7 mmol), R = Me (0.86 g, 3.6 mmol), R = Br *(For synthesis of HL4, where R = NH_2)* (0.42 g, 1.1 mmol)) was dissolved in ethanol (varied). An excess of hydrazine hydrate ($N_2H_4 \cdot H_2O$) (5 eq) was added and the solution heated at reflux for 12 hours. After cooling to room temperature the total volume was reduced until solids formed, which was separated by filtration and washed with ice-cold ethanol. The resultant solids were purified by recrystallization from boiling ethanol and diethyl ether.

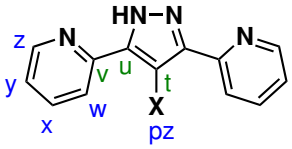

Figure 2.27: Labelling convention used for NMR assignments of pyrazoles. Blue are used for carbon and proton assignments, where appropriate, green are carbon assignments.

HL1: R = H, 3,5-bis(pyridin-2-yl)-pyrazole (Hbpp)

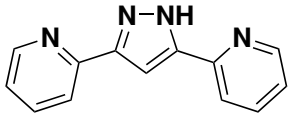

[222.25g mol^{-1}]

(3.03 g, 0.014 mol, 68 %)

^1H NMR (400 MHz, $CDCl_3$) δ (ppm): 11.27 (*N–H*, 1H, s), 8.64 (*w*, 2H, m), 7.89 (*z*, 2H, d, $^3J_{z,y}$ = 7.80 Hz), 7.77 (*y*, 2H, dt, $^3J_{y,z}$ = $^3J_{y,x}$ = 7.72, $^4J_{y,w}$ = 1.76 Hz), 7.39 (*pz–H*, 1H, s), 7.26 (*x*, 2H, m). $^{13}C\{^1H\}$ NMR (100 MHz, $CDCl_3$) δ (ppm): 149.9 (*v*), 149.32 (*w*), 136.89 (*y*), 128.2 (*u*), 122.86 (*x*), 120.03 (*z*), 101.41 (*t*).*In agreement with literature values.*[221] MS (ESI+), Calculated m/z $[M+H]^+$ = 223.0978, Found $[M+H]^+$ = 223.0977

HL2, R = *ortho*-Me: 2,2'-(1H-Pyrazole-3,5-diyl)bis(6-methylpyridine)

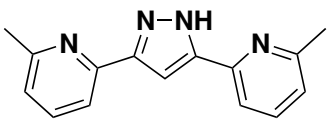

[251.13g mol^{-1}]

(0.62 g, 2.5 mmol, 66.0 %)

^{1}H NMR (400 MHz, $CDCl_3$) δ (ppm): 11.81 (*N–H*, 1H), 7.68 (*w*, 2H, d, $^3J_{w,x}$ = 7.72 Hz), 7.61 (*x*, 2H, t, $^3J_{x,w}$ = $^3J_{x,y}$ = 7.66 Hz), 7.37 (*pz–H*, 1H, s), 7.07 (*y*, 2H, d, $^3J_{y,x}$ = 7.64 Hz), 2.61 (CH_3, 6H, s) $^{13}C\{^1H\}$ NMR (100 MHz, $CDCl_3$) δ (ppm): 158.25 (*z*), 149.29 (*u*), 148.34 (*v*), 137.02 (*x*), 122.41 (*y*), 117.08 (*w*), 101.31 (*t*), 24.56 (*CH_3*). *In agreement with literature values.*[180] MS (ESI+), Calculated m/z $[M+H]^+$ = 251.1291, Found $[M+H]^+$ = 251.1292

HL3, R = Me: 2,2'-(4-methyl-1H-pyrazole-3,5-diyl)dipyridine

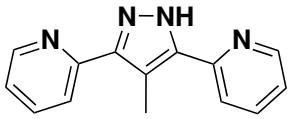

[236.28g mol^{-1}]

(0.3914 g, 1.66 mmol, 46%)

^{1}H NMR (400 MHz, $CDCl_3$) δ (ppm): 11.27 (N–H, 1H, br), 8.66 (*z*, 2H, dt, $^3J_{z,y}$ = 4.94, $^4J_{z,y}$ = 1.39 Hz), 7.84 – 7.82 (*w*, 2H, m), 7.77 (*y*, 2H, td, $^3J_{y,x}$ = 7.81, $^4J_{y,z}$ 2.00 Hz), 7.25 – 7.22 (*x*, 2H, m), 2.73 (CH_3–pz, 3H, s). $^{13}C\{^1H\}$ NMR (100 MHz, $CDCl_3$) δ (ppm): 151.49 (*v*), 149.26 (*z*), 145.44 (*u*), 137.02 (*y*), 122.23 (*w*), 121.50 (*x*), 113.53 (*t*), 11.00 (CH_3–pz). MS (ESI+), Calculated m/z $[M+H]^+$ = [237.1136], Found $[M+H]^+$ = [237.1135]

HL4, R = NH_2: 3,5-di(pyridin-2-yl)-1H-pyrazol-4-amine

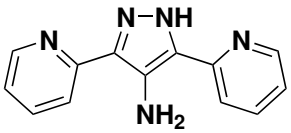

[237.266g mol^{-1}]

(0.11 g, 0.46 mmol, 44%)

^{1}H NMR (500 MHz, DMSO-d6), δ (ppm): 13.16 (*N–H*, 1H, s), 8.59 – 8.57 (*z*, 2H, m), 7.98 – 7.77 (*x, y*, 4H, m), 7.22 – 7.19 (*w*, 2H, m), 6.03 (*NH_2*, 2H, s) *In agreement with reported literature values.*[181] $^{13}C\{^1H\}$ NMR (125 MHz, DMSO-d6) δ (ppm): 149.6 (*v*), 149.2 (*z*), 138.2 (*y*), 124.6 (*u*), 123.0 *t*, 121.3 (*w*), 119.8 (*x*). MS (ESI+), Calculated m/z [M] = [237.1019], Found $[M+H]^+$ = 238.1092.

2.7.6 Pyrazole Functionalisation

HL5, R = Br: 4-Bromo-3,5-bis(2-pyridyl)-1H-pyrazole

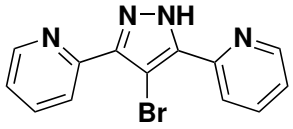

[301.147g mol^{-1}]

Hbpp (222 mg, 1 mmol) was dissolved in DCM and cooled to 0 °C. Bromine (0.3 mL in 10 mL saturated aqueous Na_2CO_2) was added dropwise and stirred at 0 °C for 1 hour. The solution was quenched with $Na_2S_2O_3$ until decolourised and extracted with DCM (3 x 10 mL) before being dried over $MgSO_4$ and the solvent removed *in vacuo*. The product was recrystallised from ethanol and diethyl ether. (0.170 g, 0.57 mmol, 57%) ^{1}H NMR (400 MHz, $CDCl_3$) δ (ppm): 8.73 (pyridyl-*z*, 2H, d, $^3J_{z,y}$ = 4.73 Hz), 8.24 (pyridyl-*w*, 2H, d, $^3J_{w,x}$ = 7.40 Hz), 7.83 (pyridyl-*x*, 2H, td, $^3J_{x,w}$ = 7.80, $^3J_{x,y}$ 1.55 Hz), 7.34 – 7.31 (pyridyl-*y*, 2H, m) ^{13}C{^{1}H} NMR (125 MHz, $CDCl_3$) δ (ppm): 149.6 (*z*), 148.9 (*v*), 144.6 (*u*), 137.1 (*x*), 123.3 (*y*), 121.9 (*w*), 91.4 (*t*) *In agreement with reported literature values.*[182] MS (ESI+), Calculated m/z $[M+H]^+$ = 300.0011 Found $[M+H]^+$ = 303.0069

HL6, R = NO_2: 4-Nitro-3,5-bis(2-pyridyl)-1H-pyrazole

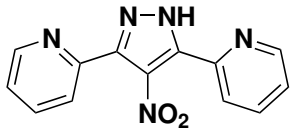

[267.248g mol^{-1}]

Hbpp (222 mg, 1 mmol) was dissolved in H_2SO_4 (80%, 6 mL) at 0 °C. A solution of HNO_3 (65%, 3 mL) and H_2SO_4 (80%, 3 mL) was added dropwise over 20 min at 0 °C. The solution was heated at reflux for 6 hours then cooled to room temperature before the addition of ice (100 g) and carefully neutralised with Na_2CO_3. The product was extracted with DCM (3 x 30 mL), dried over $MgSO_4$ and the solvent removed *in vacuo*. The solids were purified by recrystalisation from 1:1 EtOH/Et_2O.

(120 mg, 0.45 mmol, 45%) ^{1}H NMR (500 MHz, $CDCl_3$, δ (ppm): 8.68 (*z*, 2H, d, $^3J_{z,y}$ = 4.79 Hz), 7.94 (*w*, 2H, d, $^3J_{w,x}$ = 7.80 Hz), 7.84 (*x*, 2H, td, $^3J_{x,y}$ = $^3J_{x,w}$ = 7.80, $^4J_{x,z}$ = 1.52 Hz), 7.38 (*y*, 2H, dd, $^3J_{y,x}$ = $^3J_{y,z}$ = 7.94, $^4J_{y,w}$ 5.03 Hz). *In agreement with reported literature values.*[182] ^{13}C{^{1}H} NMR (125 MHz, $CDCl_3$) δ (ppm): 149.6 (*z*), 146.9 (*v*), 137.2 (*y*), 130.3 (*u*), 124.5 (*x*), 122.8 (*w*). MS (ESI+), Calculated m/z $[M+H]^+$ = 267.0756 Found $[M+H]^+$ = 267.0754

2.7.7 Cobalt Complexes

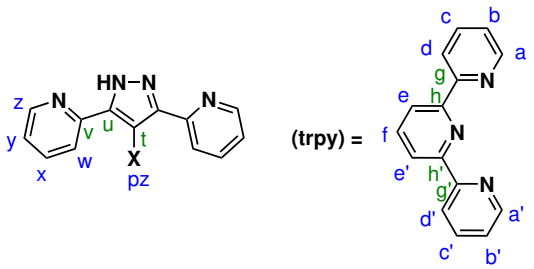

Figure 2.28: Labelling convention used for NMR assignments. Blue are used for carbon and proton assignments, where appropriate, green are carbon assignments.

Cobalt mono-terpyridine: $Co(trpy)Cl_2$ [363.107]

$CoCl_2 \cdot 6\,H_2O$ (300 mg, 1.3 mmol) was dissolved in ethanol (25 mL). Terpyridine (295 mg, 1.3 mmol) dissolved in ethanol (25 mL) was added. The solution was heated at reflux for 10 – 30 minutes during which time the solution changed from brown to green. Upon cooling to room temperature a green precipitate formed which was separated by filtration and washed with ethanol (10 mL) and diethyl ether (2 x 10 mL). (0.42 g, 1.2 mmol, 92%) ^{1}H NMR (500 MHz, MeCN) δ (ppm): 98.9, 57.0, 48.0, 34.3, 21.8, 8.9 *In agreement with reported literature values.*[199] MS (ESI+), Calculated m/z [M-Cl] = 326.9973 Found [M-Cl] = 326.9972

$Co1_{O_2}$: $[Co_2(bpp)(\mu\text{-}O{-}O)(trpy)_2][PF_6]_3$

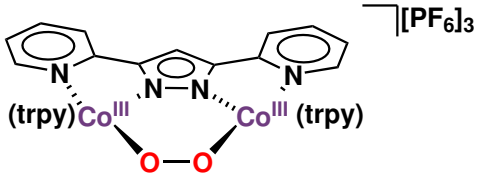

[1272.02g mol^{-1}]

To a suspension of Hbpp (140.68 mg, 0.63 mmol) in methanol (20 mL), NaOH (25.3 mg, 0.63 mmol) was added and stirred at room temperature for 10 minutes. $CoCl_2 \cdot 6\,H_2O$ (300 mg, 1.27 mmol) was added and the solution stirred for a further 30 minutes at R.T. terpyridine (295.3 mg, 1.27 mmol) was added and the reaction was refluxed under air for 3 hours and 70°. After cooling to R.T. a solution of $NaPF_6$ in methanol (5 mL) was added and stirred. The solution was filtered and washed with ice cold methanol (10 mL) and diethyl ether (2 x 10 mL) before recrystallizing from acetonitrile and a further solution of $NaPF_6$ in methanol. (0.489 g, 0.38 mmol, 61 %) ^{1}H NMR (500 MHz, MeCN) δ (ppm): 8.68 (*H-pz*, 1H, s), 8.55 (*f*, 2H, q, $^3J_{f,e'}$ = 11.20 Hz), 8.50 (*e, z*, 4H, m), 8.42 (*e'*, 2H, d, $^3J_{e,f}$ = 7.75 Hz), 8.12 – 8.23 (*a, a', y, b*, 8H, m), 7.95 (*b*, 2H, t, $^3J_{b,c}$

= 7.48 Hz), 7.71 (*w*, 2H, d, $^3J_{w,x}$ = 5.35 Hz), 7.58 (*c'*, 2H, t, $^3J_{c',d'}$ = 6.00 Hz), 7.40 (*d*, 2H, d, $^3J_{d,c}$ = 4.50 Hz), 7.25 (*d'*, 2H, d, $^3J_{c',d'}$ = 4.60 Hz), 7.20 (*x*, 2H, m), 6.86 (*c*, 2H, t, $^3J_{c,d}$ = 6.00 Hz). *In agreement with literature values.*[166] $^{13}C\{^1H\}$ NMR (125 MHz, MeCN) δ (ppm): 160.1 (*h*), 157.5 (*h'*), 156.0 (*g'*), 155.8 (*g*), 152.8 (*v*), 151.7 (*d*), 151.5 (*w*), 150.0 (*d'*), 142.9 (*z*), 142.0 (*f*), 141.5 (*b'*), 141.4 (*b*), 128.9 (*c'*), 127.6 (*c*), 127.2 (*u*), 125.9 (*x*), 124.8 (*a*), 124.7 (*a'*), 124.1 (*e'*), 122.3 (*e*), 107.7 (*t*).

MS (FTMS + pNSI), Calculated m/z $[M - 3\,PF_6]^{+++}$ = 279.1433, Found m/z $[M - 3\,PF_6]^{+++}$ = 279.0426

$Co1_{Cl}$: $[Co_2(bpp)(\mu\text{-}Cl)(trpy)_2][PF_6]_2$

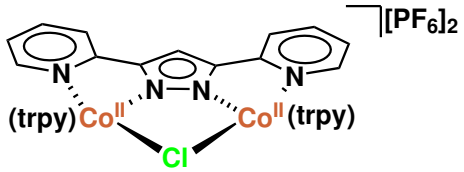

[1131.04g mol^{-1}]

$Co(trpy)Cl_2$ (200 mg, 0.55 mmol) was dissolved in MeOH (25 mL) and degassed by bubbling argon through the solution for 15 min. In a separate vessel NaOH (16.8 mg, 0.3 mmol) was added to a solution of Hbpp (60 mg, 0.27 mmol) in methanol (25 mL), and was degassed by bubbling argon through the solution for 15 min. The two solutions were combined and stirred at room temperature under argon for 3 hours. A saturated solution of $NaPF_6$ (3 mL) in methanol was added and the mixture stirred before separation by cannula filtration.

(213 mg, 0.19 mmol, 34%) ^1H NMR (500 MHz, MeCN) δ (ppm): 177.62 (4H), 106.22 (1H), 71.33 (4H), 70.51 (4H), 55.89 (4H), 54.99 (2H), 29.20 (2H), 26.61 (2H), 18.82 (2H), 15.55 (4H), 13.30 (2H)

MS (FTMS + pNSI), Calculated m/z $[M - 2\,PF_6]^{++}$ = 420.0537, Found m/z $[M - 2\,PF_6]^{++}$ = 420.0550

$Co2_{O_2}$: $[Co_2(Me_2bpp)(\mu\text{-}OO)(trpy)_2][PF_6]_3$

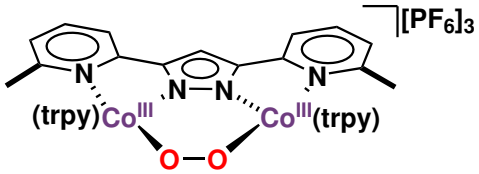

[1300.60g mol^{-1}]

(0.63 g, 0.54 mmol, 85.5%)

Synthetic procedure as detailed for **$Co1_{O_2}$**.

HL2 (158.4 mg, 0.63 mmol), $CoCl_2 \cdot 6\,H_2O$ (300 mg, 1.27 mmol), trpy (295.3 mg, 1.27 mmol), NaOH (25.3 mg, 0.63 mmol), $NaPF_6$ (320 mg, 1.9 mmol).

^{1}H NMR (500 MHz, MeCN), δ (ppm): 8.72 ((*H-pz*), 1H, s), 8.45 – 8.38 ((*f, e, e', y'*), 8H, m), 8.22 – 8.15 ((*a, a', b'*), 6H, m), 8.03 ((*x*), 2H, t, $^3J_{x,w} = 7.70$ Hz), 7.95 ((*b*), 2H, t, $^3J_{b,c} = 7.70$ Hz), 7.63 ((*c'*), 2H, t, $^3J_{c',d'} = 6.16$ Hz), 7.48 – 7.46 ((*d, d'*), 4H, m), 7.09 ((*w*), 2H, d, $^3J_{w,x} = 7.51$ Hz), 6.93 ((*c*), 2H, t, $^3J_{c,b} = 6.15$ Hz), 1.56 (6H, s)

^{13}C{^{1}H}NMR (125 MHz, MeCN), δ (ppm): 164.17 (*z*), 160.77 (*v*), 158.55 (*h*), 158.24 (*h'*), 157.02(*g*), 156.89 (*g'*), 153.97 (*d'*), 152.89 (*d*), 150.24 (*u*), 143.62 (*f*), 142.86 (*b'*), 142.56 (*b*), 141.74 (*x*), 130.01 (*c'*), 129.02 (*c*), 127.84 (*w*), 125.97 (*e*), 125.65 (*e'*), 125.51 (*a'*), 125.06 (*a*), 120.81 (*y*), 108.67 (*t*), 24.07 (CH_3).

MS (FTMS + pNSI), Calculated m/z $[M - 3\,PF_6]^{+++} = 288.387$, Found m/z $[M - 3\,PF_6]^{+++} = 288.385$

Attempts to convert residual μ-Cl to μ-OO species in $\mathbf{Co2_{O_2}}$

A sample of $\mathbf{Co2_{O_2}}$ with $\mathbf{Co2_{Cl}}$ contaminants (10 mg, 0.008 mmol) was dissolved in MeCN (10 mL). $AgBF_4$ (2.5 mg, 0.01 mmol) was added and the solution stirred in the dark for 15 minutes at room temperature. A solution of Na_2O_2 (1 mg, 0.01 mmol) in MeOH (3 mL) was added and the solution refluxed for 3 hrs. Upon cooling the solution was filtered to remove silver salts, and the solvent removed *in vacuo*. ^{1}H NMR spectroscopy revealed degradation of the complex.

$\mathbf{Co2_{Cl}}$: $\mathbf{[Co_2(Mebpp)(\mu\text{-}Cl)(trpy)_2][PF_6]_2}$

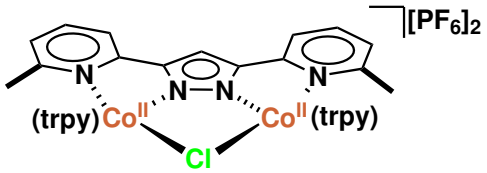

[1158.07g mol^{-1}]

(0.13 g, 0.11 mmol, 82%)

Synthetic procedure as detailed for $\mathbf{Co1_{Cl}}$. X-ray crystallography standard crystals were grown by the layering method from acetonitrile, with diethyl either as the anti-solvent.

^{1}H NMR (500 MHz, MeCN), δ (ppm): 174.54 (4H), 103.24 (1H), 72.91 (4H), 71.27 (4H), 55.92 (4H), 49.75 (2H), 27.61 (2H), 17.27 (2H), 15.36 (2H), 14.24 (4H), -79.82 (6H)

MS (FTMS + pNSI), Calculated m/z $[M - 2\,PF_6]^{++}$ = 434.0694. 434.5709, Found m/z $[M - 2\,PF_6]^{++}$ = 434.0687, 434.5701

$Co3_{O_2}$: $[Co_2((Me-pz)bpp)(\mu\text{-}O-O)(trpy)_2][PF_6]_3$

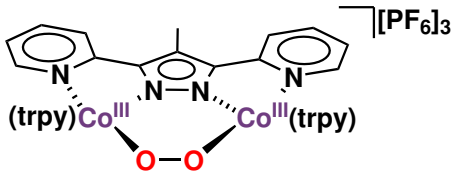

[1227.6g mol^{-1}]

(0.058 g, 0.05 mmol, 45%)

Synthetic procedure as detailed for $\mathbf{Co1_{O_2}}$. X-ray crystallography standard crystals were grown by the layering method from acetonitrile, with diethyl either as the anti-solvent.

^{1}H NMR (500 MHz, MeCN), δ (ppm): 8.57 (*f*, 2H, t, $^3J_{f,e}$ = 8.04 Hz), 8.51 – 8.49 (*z, e'*, 4H, m), 8.39 (*e*, 2H, d, $^3J_{e,f}$ = 7.70 Hz) 8.22 – 8.17 (*a, a'*, 4H, m), 8.13 – 8.09 (*y, b'*, 4H, m), 7.93 (*b*, 2H, t, $^3J_{b,c}$ = 7.54 Hz), 7.70 (*w*, 2H, d, $^3J_{w,x}$ = 5.04 Hz), 7.57 (*c'*, 2H, t, $^3J_{fc',d'}$ = 6.21 Hz), 7.38 (*d*, 2H, d, $^3J_{d,c}$ = 4.95 Hz), 7.25 (*d'*, 2H, d, $^3J_{d',c'}$ = 4.83 Hz), 7.19 – 7.15 (*x*, 2H, m), 6.83 (*c*, 2H, t, $^3J_{c,d}$ = 5.95 Hz), 3.35 (*CH_3-pz*, 3H, s)

^{13}C{^{1}H} NMR (125 MHz, MeCN), δ (ppm): 158.32 (*h*), 157.99 (*h'*), 157.53 (*t*), 156.80 (*g, g'*), 156.59(*u*), 153.59 (*d*), 152.77 (*w*), 152.59 (*d'*), 151.08 (*v*), 143.61 (*f*), 142.82 (*b*), 142.40 (*b'*), 142.01 (*y*), 129.75 (*c'*), 128.46 (*c*), 126.30 (*x*), 125.68 (*e*), 125.49 (*a'*), 124.93 (*a*), 123.59(*e'*), 123.43 (*z*), 11.58 (*CH_3-pz*)

MS (FTMS + pNSI), Calculated m/z $[M - 3\,PF_6]^{+++}$ = 283.7145, Found m/z $[M - 3\,PF_6]^{+++}$ = 283.7150

$Co3_{Cl}$: $[Co_2((Me-pz)bpp)(\mu\text{-}Cl)(trpy)_2][PF_6]_2$

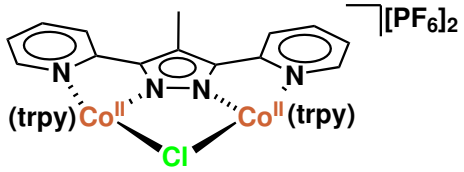

[1145.1g mol^{-1}]

(0.114 g, 0.10 mmol, 72.3%)

Synthetic procedure as detailed for $\mathbf{Co1_{Cl}}$.

^{1}H NMR (500 MHz, MeCN), δ (ppm): 176.72 (4H), 73.02 (4H), 72.52 (4H) 60.30 (2H), 57.12 (4H), 41.57 (3H), 34.45 (2H), 27.76 (2H), 18.91 (2H), 16.57 (4H), 14.71 (2H)

MS (FTMS + pNSI), Calculated m/z $[M - 2\,PF_6]^{++}$ = 427.0616, Found m/z $[M - 2\,PF_6]^{++}$ = 427.0629

$Co4_{O_2}$: $[Co_2((NH_2)bpp)(\mu\text{-}O{-}O)(trpy)_2][PF_6]_3$

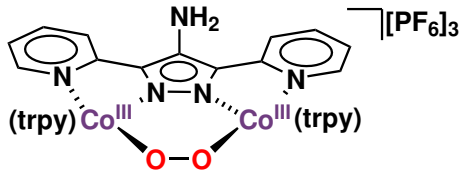

[1287.6g mol^{-1}]

(0.117 g, 0.10 mmol, 65%)

Synthetic procedure as detailed for **$Co1_{O_2}$**. X-ray crystallography standard crystals were grown by the layering method from acetonitrile, with diethyl either as the anti-solvent.

^{1}H NMR (500 MHz, MeCN), δ (ppm): 8.54 – 8.46 (*f, e*, 4H, m), 8.39 – 8.35 (*e', z*, 4H, m), 8.18 – 8.15 (*a, a'*, 4H, m), 8.12 – 8.06 (*b', y*, 4H, m), 7.91 (*b*, 2H, t, $^3J_{b,a}$ = 7.12 Hz), 7.61 (*w*, 2H, d, $^3J_{w,x}$ = 5.54 Hz), 7.58 (*c'*, 2H, t, $^3J_{c',d'}$ = 5.93 Hz), 7.41 (*d, d'*, 4H, d, $^3J_{(d,d'),c,c'}$ = 5.14 Hz), 7.06 (*x*, 2H, t, $^3J_{x,y}$ = 6.33 Hz), 6.82 (*c*, 2H, t, $^3J_{c,d}$ = 5.93 Hz), 5.43 (*CH_3-pz*, 3H, s)/

^{13}C{^{1}H} NMR (125 MHz, MeCN), δ (ppm): 157.08 (*h, h'*), 156.13 (*g'*), 155.36 (*g*), 152.25 (*d'*), 151.69 (*d*), 151.56 (*z*), 150.3 (*v*), 146.6 (*t*), 142.65 (*f*), 141.72 (*b'*), 141.55 (*b*), 140.88 (*x*), 128.94 (*c'*), 127.67 (*c*), 124.51 (*y*), 124.37 (*a, a'*), 124.54 (*e*), 124.26 (*e'*), 123.85 (*u*), 120.98 (*w*).

MS (FTMS + pNSI), Calculated m/z $[M - 3\,PF_6 - H]^{++}$ = 425.5658, Found m/z $[M - 3\,PF_6 - H]^{++}$ = 425.5649

$Co4_{Cl}$: $[Co_2((NH_2)bpp)(\mu\text{-}Cl)(trpy)_2s][PF_6]_2$

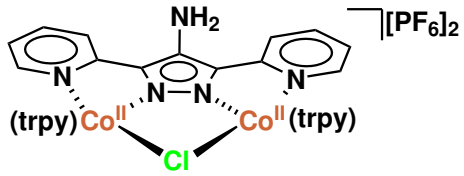

[1146.1g mol^{-1}]

(0.1 g, 0.09 mmol, 63%)

Synthetic procedure as detailed for **$Co1_{Cl}$**.

^{1}H NMR (500 MHz, MeCN), δ (ppm): 180.62 (4H), 72.36 (4H), 71.94 (4H), 56.81 (4H), 56.04 (2H), 38.86 (2H), 33.68 (2H), 27.02 (2H), 16.84 (2H), 16.03 (4H), 13.30 (2H)

MS (FTMS + pNSI), Calculated m/z [M – $2\,PF_6$]$^{++}$ = 427.5592, Found m/z [M – $2\,PF_6$]$^{++}$ = 427.4486

$Co5_{O_2}$: $[Co_2((Br-pz)bpp)(\mu\text{-}OO)(trpy)_2][PF_6]_3$

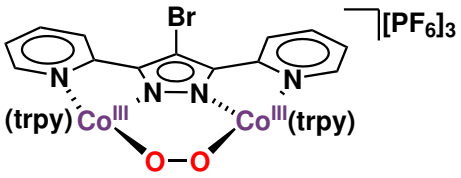

[1292.5g mol^{-1}]

(0.20 g, 0.15 mmol, 49%)

Synthetic procedure as detailed for $\mathbf{Co1_{O_2}}$. X-ray crystallography standard crystals were grown by the layering method from acetonitrile, with diethyl either as the anti-solvent.

^{1}H NMR (500 MHz, MeCN), δ (ppm): 8.85 (*z*, 2H, d, J = 8.07 Hz), 8.54 (*f*, 2H, t, J = 8.08 Hz), 8.48 (*e*, 2H, d, J = 7.49 Hz), 8.39 (*e'*, 2H, d, J = 7.49 Hz), 8.20 – 8.10 (*y, a, a', b'*, 8H, m), 7.92 (*b*, 2H, t, J = 7.82 Hz), 7.72 (*w*, 2H, d, J = 5.62 Hz), 7.56 (*c'*, 2H, t, J = 6.35 Hz), 7.35 (*d, d'*, 4H, dd, J = 26.08, 5.11 Hz), 7.24 (*x*, 2H, t, J = 6.43 Hz), 6.83 (*c*, 2H, t, J = 6.26 Hz)

^{13}C{^{1}H} NMR (125 MHz, MeCN), δ (ppm): 158.39 (*z*), 158.13 (*h, h'*), 156.80 (*g'*), 156.58 (*g*), 153.68 (*d*), 153.15 (*d'*), 152.53 (*w*), 149.39 (*v*), 143.79 (*u*), 142.97 (*f*), 142.56 (*b, b'*), 142.31 (*y*), 129.87 (*c'*), 128.60 (*c*), 127.42 (*x*), 125.82 (*e'*), 125.62 (*a', e*), 125.07 (*a*), 123.47 (*t*)

MS (FTMS + pNSI), Calculated m/z [M – $3\,PF_6$]$^{+++}$ = 305.0128, Found m/z [M – $3\,PF_6$]$^{+++}$ = 305.0139

$Co5_{Cl}$: $[Co_2((Br-pz)bpp)(\mu\text{-}Cl)(trpy)_2][PF_6]_2$

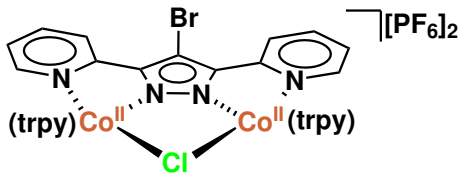

[1209.9g mol^{-1}]

(0.101 g, 0.08 mmol, 61.5%)

Synthetic procedure as detailed for $\mathbf{Co1_{Cl}}$.

^{1}H NMR (500 MHz, MeCN), δ (ppm): 176.24 (4H), 71.58 (4H), 71.27 (4H), 62.11 (2H), 56.21 (4H), 29.43 (2H), 25.37 (2H), 18.09 (2H), 14.88 (4H), 13.91 (2H)

MS (FTMS + pNSI), Calculated m/z $[M - 2\,PF_6]^{++}$ = 459.0090, Found m/z $[M - 2\,PF_6]^{++}$ = 459.0100

Co6$_{O_2}$: [Co$_2$((NO$_2$)bpp)(μ-O−O)(trpy)$_2$][PF$_6$]$_3$

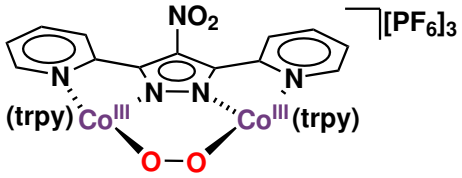

[1317.5g mol^{-1}]

(0.068 g, 0.05 mmol, 28%)

Synthetic procedure as detailed for **Co1$_{O_2}$**. After collection of the solid, the product was purified by alumina column chromatography using 10% MeOH in MeCN as the eluant. X-ray crystallography standard crystals were grown by the layering method from acetonitrile, with diethyl either as the anti-solvent.

^{1}H NMR (500 MHz, MeCN), δ (ppm): 9.22 (*z*, 2H, d, J = 8.17 Hz), 8.55 (*f*, 2H, t, J = 8.01 Hz), 8.49 (*e*, 2H, d, J = 8.08 Hz), 8.38 (*e'*, 2H, d, J = 8.12 Hz), 8.26 – 8.14 (*y, a, a', b'*, 8H, m), 7.93 (*b*, 2H, t, 7.62 Hz), 7.82 (*w*, 2H, d, J = 5.50 Hz), 7.57 (*c'*, 2H, t, 6.94 Hz), 7.35 – 7.33 (*d, d', x*, 6H, m), 6.81 (*c*, 2H, t, J = 6.66 Hz)

^{13}C{^{1}H} NMR (125 MHz, MeCN), δ (ppm): 157.38 (*h, h'*), 157.04 (*g*), 156.31 (*u, u'*), 154.68 (*g'*), 152.53 (*d*), 152.16 (*d'*), 151.38 (*v, v'*), 143.44 (*f*), 142.60 (*b'*), 142.14 (*b*), 142.05 (*y*), 131.10 (*w*), 129.12 (*c'*), 128.28 (*x*), 128.02 (*c*), 127.45 (*t, t'*), 127.12 (*z*), 125.37 (*a, e, e'*), 124.5 (*a'*).

MS (FTMS + pNSI), Calculated m/z $[M - 3\,PF_6 + H]^{++}$ = 441.5607, Found m/z $[M - 3\,PF_6 + H]^{++}$ = 441.5576

Co6$_{Cl}$: [Co$_2$((NO$_2$−pz)bpp)(μ-Cl)(trpy)$_2$][PF$_6$]$_2$

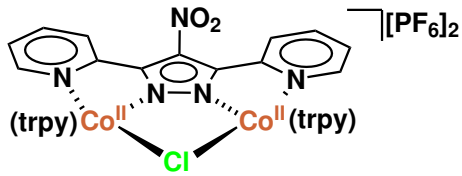

[1176.0g mol^{-1}]

(0.10 g, 0.085 mmol, 46%)

Synthetic procedure as detailed for **Co1$_{Cl}$**.

^{1}H NMR (500 MHz, MeCN), δ (ppm): 168.33 (4H), 71.56 (4H), 71.47 (4H), 70.71 (2H), 55.62 (4H), 28.33 (2H), 23.22 (2H), 19.88 (2H), 14.36 (2H), 13.07 (4H)

MS (FTMS + pNSI), Calculated m/z [M – $2\,PF_6$]$^{++}$ = 442.5463, Found m/z [M – $2\,PF_6$]$^{++}$ = 442.5472

Chapter 3

Reactivity of Cobalt Complexes

The properties and reactivity of the novel cobalt complexes synthesised in Chapter 2 were investigated. Electrochemical methods were used to probe the Co^{III}/Co^{II} reduction potentials of the μ-OO complexes, and Randles-Sevcik analysis was used to determine the number of electrons involved in the redox event. The activity of the complexes towards catalytic oxygen reduction and in stoichiometic oxygen atom transfer was studied.

The oxidation potentials of the μ-Cl species were also studied. Additionally, the conversion of the Co_2^{II} μ-Cl complexes to their corresponding Co_2^{III} μ-OO species is also analysed using UV-vis spectroscopy. The interconversion between the μ-Cl and μ-OO complexes were studied as an approximation for the oxophilicity of the complexes, revealing that the unsubstituted complex, $\mathbf{Co1_{Cl}}$ showed the fastest oxidation to $\mathbf{Co1_{O_2}}$, whilst $\mathbf{Co2_{Cl}}$ and $\mathbf{Co6_{Cl}}$ showed extremely slow rates. These observations correlate to the rates of oxygen reduction calculated for the six complexes, where $\mathbf{Co1_{O_2}}$ and $\mathbf{Co4_{O_2}}$ showed reasonably fast rates, whilst $\mathbf{Co2_{Cl}}$ and $\mathbf{Co6_{Cl}}$ again showed very sluggish activity for the oxygen reduction reaction (ORR). This suggests that different substituents on the ligand backbone have an impact on the ability of the complex to bind O_2 might be significant for catalysis.

Finally, a preliminary study into the reactivity of $\mathbf{Co1_{O_2}}$ – $\mathbf{Co6_{O_2}}$ towards oxygen atom transfer (OAT) reactions was carried out with a range of substrates. Metal-peroxo complexes can behave as both electrophiles and nucleophiles, so the substrates were chosen to represent a range of activities and included benzaldehyde, styrene, 1,3-cyclohexane and triphenylphospine. $\mathbf{Co1_{O_2}}$ and $\mathbf{Co5_{O_2}}$ underwent reaction with benzaldehyde, yielding a benzoate adduct, suggesting the complexes are capable of performing oxygen atom transfer. The other four complexes did not show any oxygen atom transfer activity.

3.1 Introduction

3.1.1 Previous Studies with $\mathbf{Co1_{O2}}$

$\mathbf{Co1_{O_2}}$ has been demonstrated to perform both water oxidation and oxygen reduction by employing different conditions.[113,166,223] The mechanisms involved in the water oxidation reaction have been studied in more depth than those in the ORR. A key cobalt-hydroxo-superoxo intermediate in the water oxidation mechanism has been identified through the use of Electron Paramagnetic Resonance (EPR) spectroscopy, resonance Raman, isotopic labelling, various X-ray techniques (including X-ray Absorption Near Edge Structure (XANES) and X-ray Absorption Fine Structure (EXAFS)) and density functional theory (DFT) calculations.[223,224] In addition to $\mathbf{Co1_{O_2}}$, Llobet and coworkers have identified and isolated one other shared species between the water oxidation and the oxygen reduction reaction, the **Co1-aqua-hydroxo** species shown in Figure 3.1.

The reactivity of $\mathbf{Co1_{O_2}}$ towards the oxygen reduction reaction has not been studied in as much depth as its reactivity towards water oxidation. However, Llobet and coworkers proposed the reaction mechanism shown in Figure 3.1, suggesting proton coupled electron transfer (PCET) as the rate determining step (RDS). Confusingly, the RDS is illustrated as two steps, an equilibrium step followed by protonation. The PCET step results in the breakage of the O–O bond.[113]

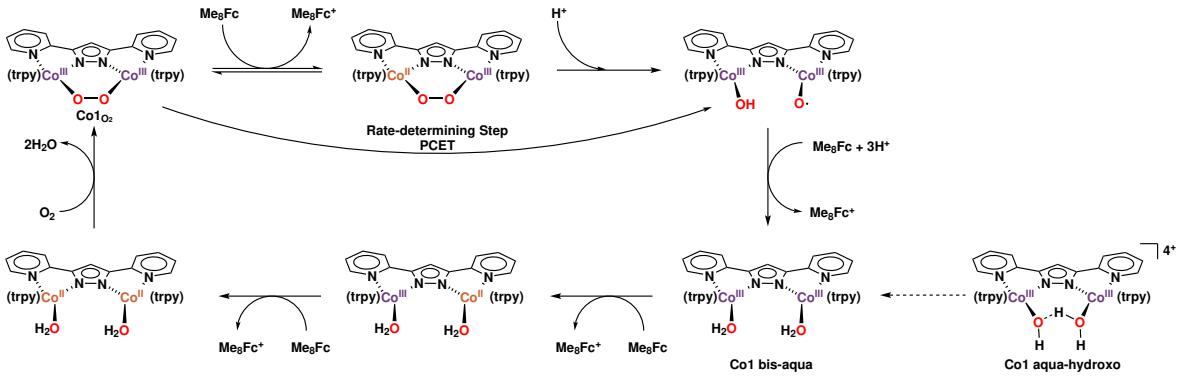

Figure 3.1: Proposed catalytic cycle for the reduction of O_2 by octamethyl ferrocene (Me_8Fc), catalysed by $\mathbf{Co1_{O_2}}$ in the presence of trifluoroacetic acid (TFA).[113] **Co1-aqua-hydroxo** species synthesised as an intermediate in the ORR,[113] and used for proton reduction.[179] Reprinted (adapted) with permission from Journal of the American Chemical Society, 134(24), 9906–9909. Copyright (2012) American Chemical Society.

Using iodometric titrations it was confirmed that no H_2O_2 was formed in the reaction, verifying the selective 4 electron reduction of O_2 to H_2O. The RDS was confirmed to

be proton coupled electron transfer (PCET) by measuring the electron transfer from the terminal reductant (octamethyl ferrocene, Me_8Fc) to $\mathbf{Co1_{O_2}}$ in the presence trifluoracetic acid under an inert atmosphere to prevent catalytic turnover (of oxygen reduction). The reaction was monitored by UV-vis spectroscopy by tracking the decrease in intensity of the peak corresponding to $\mathbf{Co1_{O_2}}$. It was found that the rate of decay of $\mathbf{Co1_{O_2}}$ correlated to the formation of 4 equivalents of Me_8Fc^+, and that the formation of Me_8Fc^+ obeyed first-order kinetics.[113] The authors found that rate increased linearly with increasing concentration of $\mathbf{Co1_{O_2}}$, but was independent of the concentration of O_2. This allowed them to produce the proposed kinetic equation:

$$\frac{d[Me_8Fc^+]}{dt} = k_{cat}[Me_8Fc][\mathbf{Co1_{O_2}}] \tag{3.1}$$

where k_{cat} is the second-order catalytic rate constant for the reaction.

The Co_2^{III}-bis-aqua species shown in Figure 3.1 is also proposed to be a key intermediate in the water oxidation mechanism. The off-cycle Co_2^{III}-aqua-hydroxo species was synthesised by Llobet and coworkers in order to study the reaction further.[113] After reducing the aqua-hydroxo species with two equivalents of Me_8Fc, the rate of conversion of this species to $\mathbf{Co1_{O_2}}$ was studied. As the rate of conversion of the aqua-hydroxo complex to $\mathbf{Co1_{O_2}}$ was much faster than the measured PCET step, they deduced that the conversion between the **Co1-bis-aqua** species and $\mathbf{Co1_{O_2}}$ was not rate limiting, and the RDS must be prior to the formation of the bis-aqua species in the cycle. The proposed cycle in shown in Figure 3.1, with the RDS labelled.

As outlined in Section 1.2.2, the ligand can have a significant impact on the reactivity of the complex. This has been observed for the water oxidation activity of $\mathbf{Co1_{O_2}}$ by changing the terpyridine ligands to the more electron rich Me_2bimpy ligand, which resulted in lower oxidation potentials and correspondingly faster rates of reactivity, as discussed previously in Section 2.1.1.

3.1.2 Oxygen Atom Transfer with Hbpp-based complexes

In order to perform effective aerobic oxidation, a complex must be able to both bind and activate O_2, a criterion clearly fulfilled by the $\mathbf{Co1_{O_2}}$ – $\mathbf{Co6_{O_2}}$ series, but also transfer the oxygen to the desired substrate. Oxygen atom transfer is a precursor to catalytic aerobic oxidations, and can be used to investigate the mode of reactivity of the complex towards the substrate, e.g. nucleophilic vs electrophilic vs radical,[120] as

discussed in more detail in Section 1.3.

Oxygen atom transfer has been demonstrated in the ruthenium-hydroxo analogue of $\mathbf{Co1_{O_2}}$.[155,190] A report of the hydroxo bridged ruthenium bpp complex reacting with two equivalents of benzaldehyde is reported, forming a benzoate bridged species. However, the reaction is refluxed under a nitrogen atmosphere for over 24 hr before this conversion is observed, Scheme 3.1.[225] They proposed that the μ-benzoate forms via a Cannizzaro-type reaction, whereby an excess of aldehyde forms an alcohol and a carboxylate anion.[226]

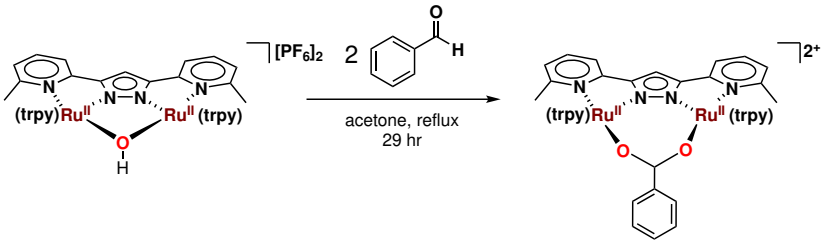

Scheme 3.1: An example of the formation of a benzoate bridged ruthenium analogue to **Co2**, reported by Catalano *et al.*[225]

3.2 Analytical Techniques Used in this Chapter

3.2.1 Electrochemical Methods

Electrochemistry as a discipline has many uses, but for the synthetic chemist it is a tool that allows them to probe the redox activity of a given species. Cyclic voltammetry (CV) is the most commonly used technique, as careful analysis of CV data can allow the determination of redox potentials, the reversibility of the redox process, and various other kinetic and thermodynamic properties of the system.[115,227,228] It also helps determine whether there is catalytic activity occurring, information about intermediates and more detailed information such as the number of electrons in the process.[93,229,230]

CV is conducted by scanning the potential linearly with time in one direction, before reversing the direction and scanning back to the original potential, whilst measuring the current response, Figure 3.2. In a truly reversible system, the current response produces the "classic CV duck", 3.2b, where positive currents represent oxidation events, and negative currents reduction events.[115] The relative concentrations of the oxidised and reduced species of the redox couple are related to each other and to the electrode

potential, by the Nernst equation:

$$E = E^{0'} + \frac{RT}{nF} ln \frac{[ox]}{[red]} \tag{3.2}$$

Where E = electrode potential (V), $E^{0'}$ = formal reduction potential (V), R = gas constant (J K^{-1} mol^{-1}), T = temperature (K), F = Faraday's constant (C mol^{-1}), n = number of electrons transferred in the redox event, and [ox] and [red] are the concentrations of the oxidised and reduced species.[96] The Nernst equation states that at the mid-point potential, E_{mid} (sometimes referred to as $E_{1/2}$), the concentrations of the reduced and oxidised species are equal: $[red] = [ox], E_{1/2} \approx E^{0'}$.

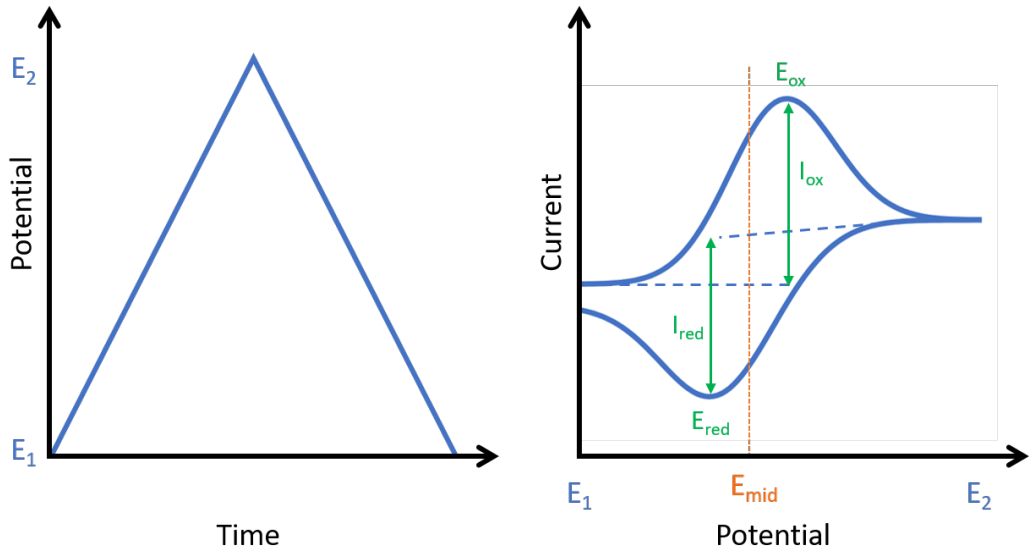

Figure 3.2: (a) Change in potential with time in linear sweep cyclic voltammetry, (b) A typical current response upon changing potential for a fully reversible redox event, with key parameters labelled. Note that I_{ox} and I_{red} are measured from the maximum current of the peak to the baseline of the CV prior to the onset of the redox event, potentially leading to non-zero gradients in the dashed lines shown.

In a fully reversible system, the difference between the oxidation and reduction peak potentials (E_{ox} and E_{red}, respectively), denoted as ΔE_p will be 57 mV at 25 °C for 1 electron redox events, as determined by the Nernst equation. However, it is important to note that even for reactions that are expected to be fully reversible, for example with ferrocene which is often used as a reference standard, the ΔE_p is often larger

than 57 mV due to resistance in the system, most commonly from the electrolyte. An electrochemically irreversible, or quasi-reversible, system refers to the electron transfer kinetics, rather than the reversibility of the redox reaction. Slow electron transfer can lead to very large ΔE_p values, therefore another measure of reversibility is the ratio of the peak oxidation and reduction currents, I_{ox} and I_{red}, respectively. In a perfectly reversible system, I_{ox} and I_{red} are equal, so the ratio of the two peak currents should be close to one. In cases where this value is not true, the use of variable scan rate data can be used to help deduce the cause of the lack of reversibility.[96]

The area in close proximity to the electrode surface is known as the "diffusion layer". In this region, the concentration of redox species varies as the potential is changed and the analyte is oxidised or reduced. Changing the scan rate of a CV changes the size of the diffusion layer, with lower scan rates resulting in larger diffusion layers and correspondingly smaller currents. In a perfectly reversible system the peak potentials will not change with increasing scan rate (E_p = ν-independent), whereas in an irreversible (or quasi-reversible) system, the E_{ox} and E_{red} values will shift further apart with higher scan rates ($E_p \neq \nu$-independent). However, in all cases, the E_{mid} value is expected to remain constant.

Further information about the reversibility of a redox event can be obtained through the collection of variable scan rate data using the Randles-Sevcik equation (Equation 3.3), which describes the relationship between peak current (I_p, measured in amps (A)) and the square root of the scan rate (ν, V s^{-1}) for a freely diffusing, fully reversible redox process.

$$I_p = 0.446nFAC^0 \left(\frac{nF\nu D_o}{RT}\right)^{1/2} \tag{3.3}$$

Where n = number of transferred electrons, F = Faraday constant (C mol^{-1}), A = surface area of electrode (cm^2), ν = scan rate (V s^{-1}), D_o = diffusion coefficient (cm^2 s^{-1}), C^0 = concentration of bulk analyte, R = ideal gas constant (J K^{-1} mol^{-1}), T = temperature (K).

A Randles-Sevcik plot shows the current vs the square root of scan rate. A linear plot suggests that the analyte is freely diffusing in solution. Variations from linearity suggest adsorption onto the surface of the electrode or quasi-reversibility. In a system where surface adsorption has occurred, there is expected to be no peak-to-peak separation of the E_{ox} and E_{red} peaks, i.e. $E_{ox} = E_{red} = E_{mid}$.[115,228] It is also possible to use the Randles-Sevcik equation to calculate the number of electrons in the process, a crucial

piece of information in mechanistic analysis of a redox process.

3.2.2 Introducing Graphical Rate Analysis

Unlike initial rates analysis, graphical rate analysis allows the whole reaction profile to be investigated. This can illuminate changes which might occur after the initial data collection, such as changes in order as the reaction proceeds or identify catalyst deactivation. Additionally, as the whole reaction profile is used, fewer experiments need to be conducted, in comparison to initial rates analysis where many experiments are required in order to perform kinetic analysis.

Variable Time Normalised Analysis (VTNA) is a variation on Reaction Progress Kinetic Analysis (RPKA), first described by Blackmond, which uses visual comparison of the entire reaction profile to deduce the reaction order.[231,232] Unlike RPKA, which requires rate data, VTNA requires concentration data. The concentration data is plotted against a normalised time scale, multiplying against the catalyst loading raised to the order in catalyst (n) ($t[cat]^n_T$).[233–235] The kinetic profiles of the different catalyst loadings are plotted on the same graph, and the order in catalyst is varied until the concentration profiles overlay, allowing easy determination of the order, Figure 3.3.

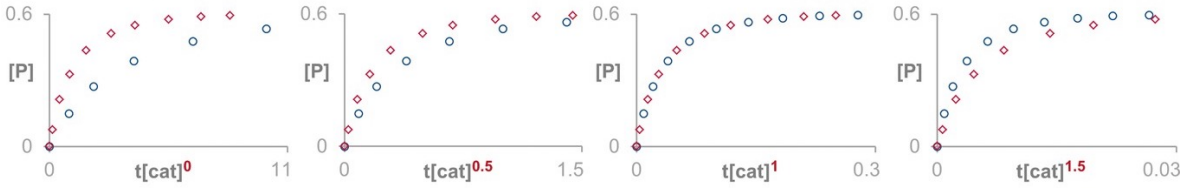

Figure 3.3: Using VTNA to determine order in catalyst through the visual overlay of two catalyst loadings and the variation in catalyst order (n). It is clear in this example the order is 1 in catalyst. Adapted with permission from Angew. Chem. Int. Ed. 2016, 55,16084–16087. Copyright (2016) 2016 Wiley-VCH Verlag GmbH & Co. KGaA, Weinheim.[234]

The use of concentration data, rather than rate data, means that VTNA can be performed on data collected using a range of different reaction monitoring techniques. Indeed, there are a growing number of examples of its use with different methods, including NMR data[236] and electrochemical measurements.[118]

3.3 Electrochemical Characterisation and Oxidation Studies of $\mathbf{Co1_{Cl}}$ – $\mathbf{Co6_{Cl}}$

3.3.1 Electrochemistry of $\mathbf{Co1_{Cl}}$ – $\mathbf{Co6_{Cl}}$

The final step of the catalytic cycle proposed in Figure 3.1 is the re-oxidation of a $Co^{II}{}_2$-bis-aqua species to a Co^{III}_2μ-OO species, coupled by a formal two electron reduction of O_2 to form the bridging peroxo species. This was determined not to be the rate determining step, as discussed previously in Section 3.1.1. The Co^{II}_2μ-Cl species is analogous to the bis-aqua complex shown in Figure 3.1, but more easily synthesised and characterised, and should provide insight into how functionalisation of the ligand backbone has an impact on the oxidation potentials of the complexes. The O_2/H_2O_2 redox couple is 0.0695 V (vs SHE), and the O_2/H_2O couple is 1.229 V (vs SHE),[97,101] and the position of the oxidation potential of the μ-Cl complexes should give an indication of how thermodynamically favourable the reaction of the complexes with O_2 is.

The mechanism of reaction of the μ-Cl complexes with O_2 has not been determined, but likely proceeds as shown in Figure 3.4. The first step is dissociation of the chloride, forming the tricationic Co^{II}-solvent/Co^{II}-solvent intermediate, which subsequently binds O_2. The formation of the M–O bonds are the result of a formal biradical coupling, yielding the low-spin Co^{III} complex, and corresponding to a reduction in the O–O bond order, as illustrated in 1.3a.

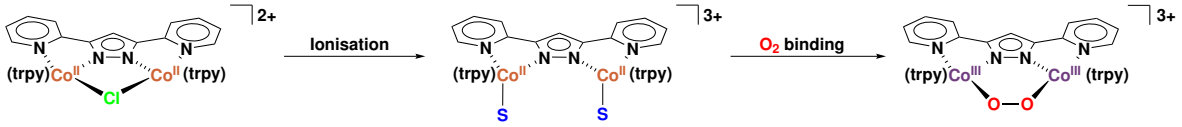

Figure 3.4: Postulated mechanism for the reaction between the Co^{II}, $\mathbf{Co1_{Cl}}$ and O_2. The reaction proceeds *via* a Co^{II}-solvent/Co^{II}-solvent species (where solvent = MeCN or H_2O), which reacts further with O_2 *via* biradical coupling, yielding $\mathbf{Co1_{O_2}}$ (Co^{III}, low spin).

Additionally, changing the ligand can result in changes in reaction mechanism, as discussed previously in Section 4.1.1. For example, in the penta-iron water oxidation catalysts, functionalisation on the bpp^- backbone resulted in a difference in reaction mechanism *via* oxidation of different metal centres and concerted reaction with water. Although the two cobalt environments are equivalent in $\mathbf{Co1_{Cl}}$ – $\mathbf{Co6_{Cl}}$, different substituents might affect those environments in different ways, potentially leading to differences in reactivity as observed in the iron clusters, such as concerted rather than

step-wise reactivity. It is therefore not implausible that the re-oxidation of the $Co^{II}{}_2$ species back to the $Co^{III}{}_2$-peroxo in the ORR could become rate limiting with differently functionalised ligands.

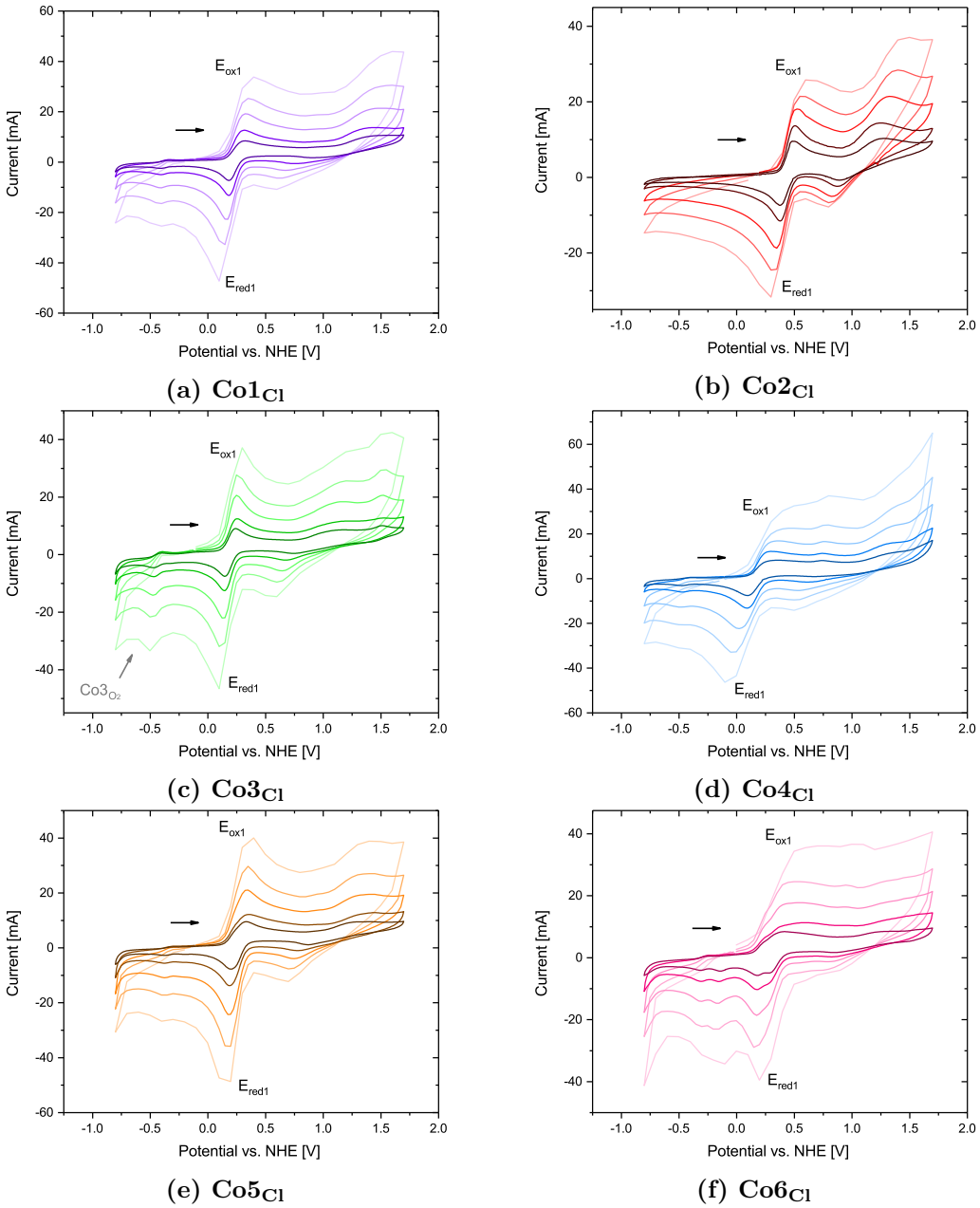

(a) $\mathbf{Co1_{Cl}}$ (b) $\mathbf{Co2_{Cl}}$

(c) $\mathbf{Co3_{Cl}}$ (d) $\mathbf{Co4_{Cl}}$

(e) $\mathbf{Co5_{Cl}}$ (f) $\mathbf{Co6_{Cl}}$

Figure 3.5: Cyclic voltammograms of $\mathbf{Co1_{Cl}}$ – $\mathbf{Co6_{Cl}}$ complexes at different scan rates (dark to light: 50, 100, 250, 500, 1000 mVs^{-1}), WE: GC, RE: $Ag/AgNO_3$, CE: Pt wire, electrolyte: TBAF, (0.1 M), solvent: MeCN (dried, degassed), T = 20 °C, air-free, direction of scan illustrated by arrow.

Non-aqueous cyclic voltammograms were collected for all six complexes using a standard three electrode cell (working electrode (WE): glassy carbon (GC), reference electrode (RE): $Ag/AgNO_3$, counter electrode (CE): Pt wire) by scanning between –0.8 – 1.7 V vs NHE. Acetonitrile and tetrabutylammonium hexafluorophosphate (TBAF) were used as the electrolyte which allowed for a wide potential window to be scanned.[115] In all initial studies, data was collected at five different scan rates (50, 100, 250, 500, 1000 $mV\,s^{-1}$), Figure 3.17. In all cases the working electrode was rinsed after data collection and a blank solution of electrolyte tested to ensure there was no deposition of the complex onto the electrode surface. This is particularly important when using glassy carbon electrodes due to the precedent for deposition of an active mono-layer onto the surface.[237] Due to the previously reported water oxidation activity of $\mathbf{Co1_{O_2}}$,[166] the acetonitrile was dried over molecular sieves prior to use. Additionally, CVs were collected under air-free conditions to prevent reduction of O_2 dissolved in solution by the glassy carbon electrode.[238]

Figure 3.5 shows that all complexes, with the exception of $\mathbf{Co6_{Cl}}$, showed a well defined quasi-reversible redox peak at ≈ 0 V vs NHE. This is likely a 1 electron redox event, corresponding to the $Co^{II}{}_2 \rightarrow Co^{II}Co^{III}$ oxidation. The electrochemical reversibility of this peak indicates that the oxidised state is still a μ-chloro species, since dissociation of the chloride would result in an irreversible electrochemical process, and that this intermediate is stable on electrochemical timescales.

There are some minor peaks observed at ≈ –0.5 V, which correspond to contamination by μ-OO species.[i] A second oxidation, to a $Co^{III}{}_2$ species, was not observed in the scan window recorded (–0.8 to 1.7 V). The CV of $\mathbf{Co6_{Cl}}$ is very poorly defined, with multiple redox peaks which are particularly clear at lower scan rates, this suggests there are multiple redox active species in solution.

We begin by comparing the complexes bearing substituents on the bpp^- backbone. The pattern observed in the oxidation potentials of the six complexes (Figure 3.6) suggests that the electron donating nature of the substituents on $\mathbf{Co3_{Cl}}$ and $\mathbf{Co4_{Cl}}$ (Me and NH_2, respectively) stabilise the higher oxidation state, resulting in lower oxidation potentials for these complexes of around 0.2 V. Conversely, the electron withdrawing

[i]The experiments were conducted on the bench under an argon atmosphere, rather than in a glovebox, so small amounts of the μ-OO species is to be expected. Also note that although the ^{1}H NMR spectroscopy showed the presence of some unreacted $Co(trpy)Cl_2$ precursor in the μ-Cl complexes, the redox potentials are outside of the potential window scanned in these experiments.

Table 3.1: Peak oxidation and reduction potentials for the $Co_2^{II} \rightarrow Co^{II}Co^{III}$ transition for $\mathbf{Co1_{Cl}}$ – $\mathbf{Co6_{Cl}}$ with the $E_{mid}(ox)$ values and peak-to-peak separation (ΔE) noted. All potentials taken from 100 mVs^{-1} data.

Complex	E_{ox1} vs NHE / V	E_{red1} vs NHE / V	$E_{mid}(ox)$ / V	ΔE / V
$\mathbf{Co1_{Cl}}$	0.32	0.18	0.25	0.14
$\mathbf{Co2_{Cl}}$	0.48	0.38	0.44	0.13
$\mathbf{Co3_{Cl}}$	0.26	0.15	0.20	0.11
$\mathbf{Co4_{Cl}}$	0.09	0.30	0.19	0.21
$\mathbf{Co5_{Cl}}$	0.19	0.36	0.27	0.17
$\mathbf{Co6_{Cl}}$	0.22 – 0.37	0.18 – 0.29	0.21 – 0.33	N/A

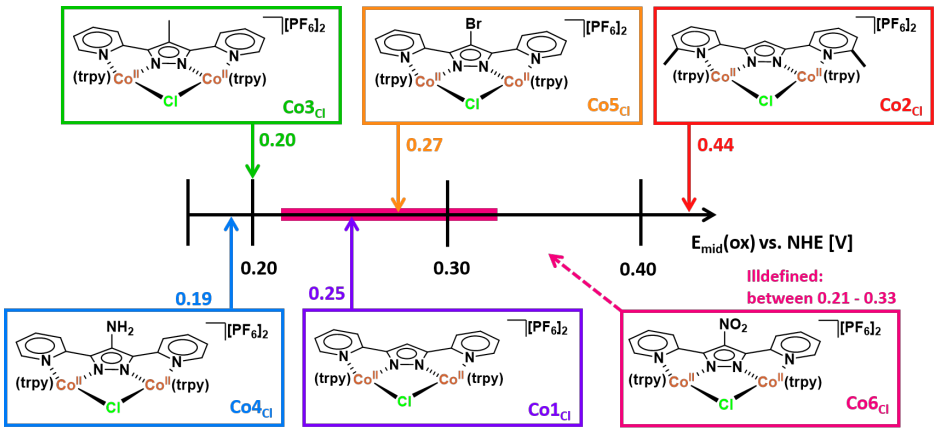

Figure 3.6: $E_{mid}(ox)$ values for μ-Cl complexes, from the 100 mVs^{-1} scan rate in Figure 3.5. *Note: value for* ***Co6$_{Cl}$*** *is highlighted with pink bar over scale. Calculated as the range between the two sets of peaks visible.*

nature of the substituents on $\mathbf{Co5_{Cl}}$ and $\mathbf{Co6_{Cl}}$ result in higher oxidation potentials (despite the poorly defined E_{mid} range for $\mathbf{Co6_{Cl}}$). The unsubstituted parent complex, $\mathbf{Co1_{Cl}}$, has an oxidation potential of 0.25 V vs NHE, between those of the complexes bearing electron-donating and electron-withdrawing substituents. The surprising position of $\mathbf{Co2_{Cl}}$, which has the highest oxidation potential of all six complexes, is discussed in more detail below.

These trends might be explained by looking at the Hammett parameters of the various substituents, see Table 2.1. Methyl groups and primary amines have Hammett parameters of -0.17 and -0.66, respectively, indicating that the NH_2 is more electron donating than the methyl group. Conversely, the Hammett parameters of the bromo and nitro group reflect that they are electron withdrawing substituents (Br = 0.23,

$NO_2 = 0.78$).[204] These values are reflected in Figure 3.6, where **Co4$_{Cl}$** (NH_2 functionalised) has the lowest oxidation potential, whilst **Co5$_{Cl}$** and **Co6$_{Cl}$** have correspondingly higher values. Figure 3.7 shows a weak correlation between the complexes, with the exception of **Co2$_{Cl}$**.

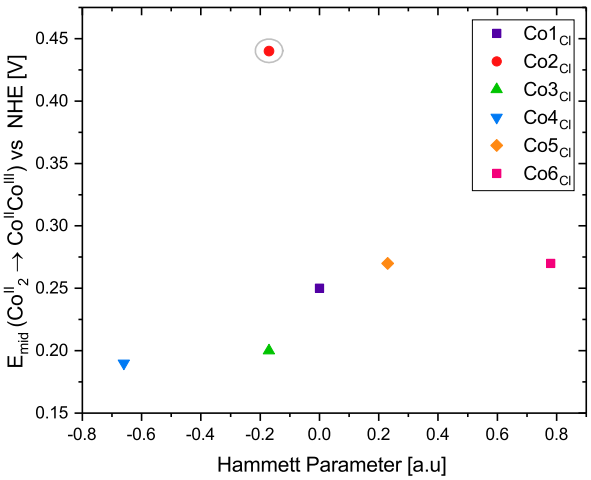

Figure 3.7: E_{mid} values for **Co1$_{Cl}$** – **Co6$_{Cl}$** plotted against the Hammett Parameters for the ligand substituent. **Co2$_{Cl}$** is an outlier due to the different location of ligand substitution, and is circled in grey.

Co2$_{Cl}$ has a different substitution pattern to the other five complexes, with methyl groups in the *ortho* position on the ligand backbone. This changes the sterics of the complex, as discussed in Section 2.4.3, and clearly has a pronounced impact on the electochemistry of the complex. However, the difference in the position of the substituents means comparisons to the other complexes is challenging. Excluding **Co2$_{Cl}$** reveals an electronic trend that scales with the Hammett parameters.

In summary, the ligand variations resulted in a range of redox potentials between 0.19 V and 0.44 V. The highest shift in redox potential was observed in **Co2$_{Cl}$**, when the ligand was functionalised with *ortho*-methyl groups, which had an oxidation potential of 0.44 V, a shift of 0.19 V relative to the unsubstituted **Co1$_{Cl}$** (0.25 V). There was a large variation in the E_{mid}(ox) values for the μ-Cl complexes, although they broadly followed the expected trends. Electron donating substituents have lower oxidation potentials, followed by the unsubstituted **Co1$_{Cl}$**, and the electron withdrawing substituents resulting in higher E_{mid}(ox) values. The exception was **Co2$_{Cl}$** that showed an E_{mid}(ox) value that was considerably higher than the others, suggesting that both steric and inductive effects have an impact on the electrochemical properties of the complexes.

Upon reaction with O_2 the cobalt centres undergo oxidation from Co^{II} to Co^{III}. Therefore, it is possible that the position of the oxidation potential of the μ-Cl complexes might give some indication of the potential reactivity of the complexes towards O_2. According to Figure 3.6, it would be expected that the complexes with electron donating substituents, $\mathbf{Co3_{Cl}}$ and $\mathbf{Co4_{Cl}}$ would react more readily with O_2 due to their lower oxidation potentials. This is also supported by the proposed mechanism in Figure 3.4, where more electron-rich complexes would result in easier ionisation, and more favourble binding of O_2. $\mathbf{Co2_{Cl}}$, which has a very high E_{mid}, is not expected to show high levels of reactivity towards O_2.

3.3.2 Oxidation Studies of $\mathbf{Co1_{Cl}}$ – $\mathbf{Co6_{Cl}}$

Although stable to oxidation whilst in the solid form, it was observed that the red/brown μ-Cl complexes readily oxidised to the deep purple μ-OO cobalt(III) form when in solution and exposed to air, Scheme 3.2. The clear difference in the UV-vis spectra between the μ-Cl and μ-OO complexes (see Section 2.4.4 in Chapter 2) allowed the rate of interconversion between the μ-Cl → μ-OO forms to be monitored by UV-vis spectroscopy. The relative rates of oxidation of $\mathbf{Co1_{Cl}}$ – $\mathbf{Co6_{Cl}}$ were investigated, representing the reactivity of the complexes towards O_2. These results were compared to the oxidation potentials recorded previously (Section 3.3.1), and should offer insight into the potential of these complexes towards aerobic oxidation activity.

The oxidation from Co^{II} to Co^{III}, coupled with binding of O_2 to form the μ-OO complex, is the final step of the catalytic cycle proposed by Llobet *et al.*, Figure 3.1. This step is not suggested to be rate determining in their proposal;[113] however, the electrochemical results (Section 3.3.1) show that ligand functionalisation has an effect on the oxidation potentials of the complexes.

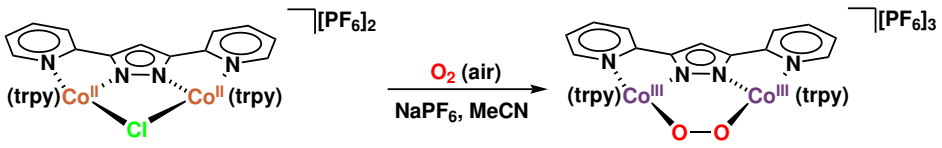

Scheme 3.2: The redox reaction between $\mathbf{Co1_{Cl}}$ (a cobalt (II) complex) and O_2 to form the corresponding $\mathbf{Co1_{O_2}}$-μ-OO cobalt (III) complex. Reaction carried out in the presence of O_2 and $NaPF_6$ in MeCN at room temperature.

An initial UV-vis spectrum of the stirred μ-Cl complex in acetonitrile and under an argon atmosphere was recorded. Continuous data collection was started before the

removal of the seal, introduction of air as the source of O_2, and the addition of one equivalent of $NaPF_6$ as a counterion to facilitate the ionisation required for oxidation (as outlined in Figure 3.4) to the Co^{III}μ-OO state. The absorbance corresponding to the purple $\mathbf{Co1_{O_2}}$ – $\mathbf{Co6_{O_2}}$ complexes at approximately 550 nm (as detailed in Section 2.4.4) was used to plot kinetic data. After one hour of continuous data collection, time points were collected at 24 hr and 1 week. A representative series of UV-vis spectra is shown in Figure 3.8 for the oxidation of $\mathbf{Co1_{Cl}}$ to $\mathbf{Co1_{O_2}}$, with λ_{max} clearly identifiable at 550 nm. Spectra for the oxidation of $\mathbf{Co2_{Cl}}$ – $\mathbf{Co6_{Cl}}$ can be found in the Appendix, Figure A.12.

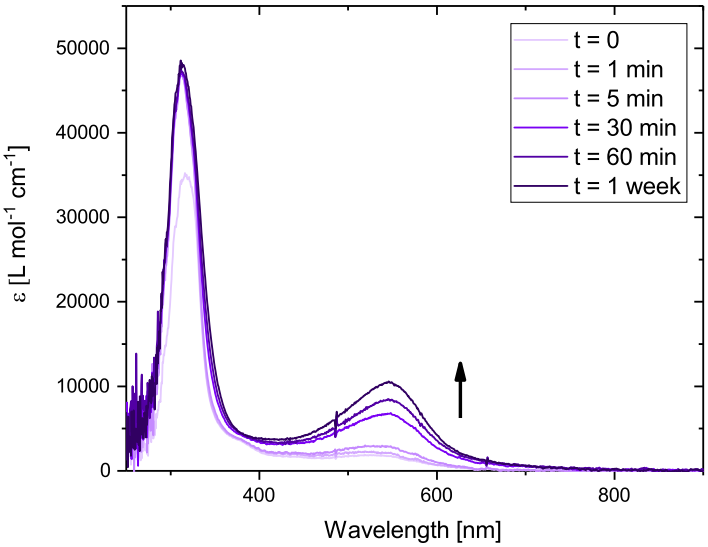

Figure 3.8: Overlaid spectra of $\mathbf{Co1_{Cl}}$ after addition of $NaPF_6$ and exposure to air showing the growth of the peak at 550 nm indicating the formation of $\mathbf{Co1_{O_2}}$. $[\mathbf{Co1_{Cl}}] = 25\,\mu M$, $[NaPF_6] = 25\,\mu M$, solvent = MeCN, temperature = 20 °C, stir rate = 400 RPM, direction of growth indicated by arrow.

All μ-Cl complexes had some contamination from their corresponding μ-OO species, due to unavoidable introduction of O_2 during synthesis and isolation, as discussed previously in Section 2.3.2. This can be seen from the starting point of the traces shown in Figure 3.9. The concentration of air saturated acetonitrile is 2.5 mM[239], which exceeds the concentration of cobalt complexes in solution, so O_2 was not a limiting reagent in these reactions. Additionally, the solution was stirred to ensure good mass transport during the reaction.

There are significant differences in the rate of oxidation, as shown clearly in Figure 3.9 and tabulated in Table 3.2. Unsubstituted $\mathbf{Co1_{Cl}}$ had the fastest rates of O_2 binding,

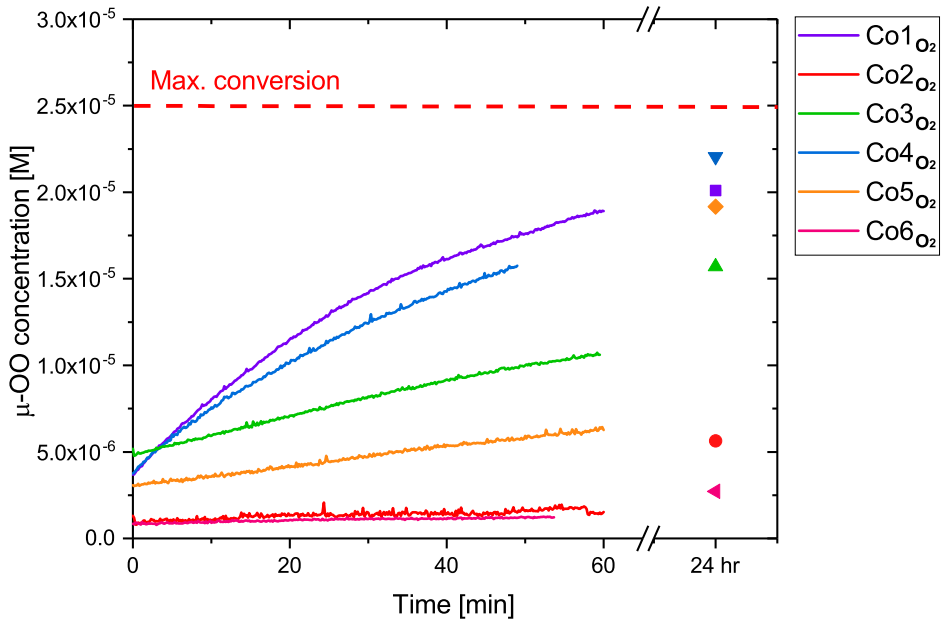

Figure 3.9: Oxidation of Co^{II} μ-Cl complexes to their corresponding Co^{III} μ-OO complexes. [Co] = 25 μM, [$NaPF_6$] = 25 μM, 3 mL MeCN total volume. Maximum theoretical conversion shown. *Note that all complexes have some contamination with μ-OO species, therefore the concentration at t=0 corresponds to the initial concentration of μ-OO species present, calculated by quantitative NMR spectroscopy.*

closely followed by **Co4$_{Cl}$** and **Co3$_{Cl}$**, suggesting that the electron donating nature of these substituents might stabilise the higher oxidation state on the cobalt centres, or solvent-bound intermediates, as discussed previously.

Co2$_{Cl}$ shows the slowest rates of all six complexes, which demonstrates that the presence of methyl substituents in the *ortho* position on the ligand backbone has a pronounced effect on the reactivity of the complex. It is expected that ionisation of the complex (Figure 3.4) is favoured by the electron donating effect of the methyl groups. However, in **Co2$_{Cl}$** O_2 binding might be less favourable due to the steric constraints on the Co – Co binding pocket.

Interestingly, there was a divergence in the behaviour of the complexes with electron withdrawing substituents, **Co5$_{Cl}$** and **Co6$_{Cl}$**. **Co5$_{Cl}$** reached almost full conversion within 24 hours, whereas **Co6$_{Cl}$** showed very little oxidation, reaching only 11% conversion after 24 hours. The CV of **Co6$_{Cl}$** also showed poorly defined peaks, perhaps suggesting a mixture of species in solution, or more complicated reactivity. It is possible that the mixed valence species, or the presence of the nitro group, renders **Co6**

unreactive.

Due to solvent evaporation over extended periods of time, the exact concentration is not known, resulting in uncertainty when following the reaction using UV-vis spectroscopy. Therefore, additional ^{1}H NMR analysis was conducted after one week using an internal standard to determine the final conversion between the μ-Cl and μ-OO species, and also to observe the stability of $\mathbf{Co1_{O_2}}$ – $\mathbf{Co6_{O_2}}$ in solution over time. It is worth noting that the oxidation results in a change from a paramagnetic Co^{II} complexes into a diamagnetic Co^{III} complex. Addition of an NMR standard meant the concentration of the diamagnetic peaks could be calculated and used to calculate the final conversion, and a wide spectral width spectrum helped determine whether there was any residual paramagnetic peaks correlating to the μ-Cl species. Additionally, the spectra were used to check whether there was any degradation of the complex in solution over time.

After one week, ^{1}H NMR spectra collected of $\mathbf{Co1_{O_2}}$ and $\mathbf{Co3_{O_2}}$ – $\mathbf{Co5_{O_2}}$ showed peaks corresponding to the expected μ-OO species (as reported in Section 2.4.1). A lack of paramagnetic peaks suggested that the complexes had undergone complete conversion to the bridging peroxo species, and any deviations from 100% conversion were either due to uncertainty in the concentration or minor degradation of the complex over the course of a week in solution. Both **Co2** and **Co6**, in comparison, did not show peaks in the aromatic region of the ^{1}H NMR spectra that correlated to their μ-OO species, suggesting deactivation of the complexes had occurred. Additionally, the absence of the diagnostic paramagnetic peaks for the μ-Cl species further supports the proposal that degradation of the complexes had occurred, along with the low levels of the μ-OO species that formed initially.

3.3.3 Comparisons and Conclusions to studies with $\mathbf{Co1_{Cl}}$ – $\mathbf{Co6_{Cl}}$

The E_{mid}(ox) values for the oxidation of $\mathbf{Co1_{Cl}}$ – $\mathbf{Co6_{Cl}}$ correspond to the Co_2^{II} / $Co^{II}Co^{III}$ redox couple. This state is not likely to involve the breaking of Co–Cl bonds, as previously discussed, due to the reversibility of the CV. The proposed mechanism for the oxidation of the μ-Cl complexes to their μ-OO counterparts has not been determined, but it is proposed to go *via* halide dissociation, followed by O_2 binding, as shown in Figure 3.4. Therefore, the E_{mid}(ox) values are not representative of the intermediates in the oxidation reaction. However, the binding of O_2 is a two-electron oxidation to the Co_2^{III} state, so comparing the E_{mid}(ox) values for the first oxidation to the $Co^{II}Co^{III}$ state

Table 3.2: Initial rates for the oxidation of μ-Cl to μ-OO species determined by absorbance at λ_{max}, the molar extinction coefficient of the fully oxidised μ-OO species, and the conversion after 24 hr. *Note that graph with initial rates can be found in Appendix, Figure A.9*

Complex	Initial rate $[10^{-3} \cdot min^{-1}]$	λ_{max} [nm] (μ-OO)	$\varepsilon(\lambda_{max})$ $[M^{-1}\ cm^{-1}]$ (μ-OO)	Conversion at 24 hr[i]	Conversion at 1 week[ii]
Co1	4.4	550	11406	80 %	91%
Co2	0.12	549	6107	12 %	17% (degradation observed)
Co3	1.1	543	10193	62 %	70%
Co4	3.7	543	8683	93 %	95%
Co5	0.52	543	8772	78 %	94%
Co6	0.11	527	13402	11 %	16% (degradation observed)

[i] Determined by UV-vis spectroscopy. [ii] Determined by ^{1}H NMR spectroscopy with addition of trimethoxybenzene (TMB) as standard.

to the rates of oxidation will give an indication of the significance of the accessibility of the $Co^{II}Co^{III}$ state to the O_2 binding ability of the complexes.

The comparison between the initial rates reported in Table 3.2 and the E_{mid}(ox) values for the oxidation of the Co^{II}μ-Cl complexes (Figure 3.6) reveals a lack of correlation, Figure 3.10. The E_{mid} values are a thermodynamic property of the complexes, so will not necessarily correlate to the kinetic rates of reaction. This suggests that the oxidation of the cobalt centres is not the rate determining step in the binding of O_2. Unfortunately, due to limitations of the glassy carbon working electrode, it was not possible to scan to high enough potentials to observe the second $Co^{II}Co^{III} \longrightarrow Co_2^{III}$ oxidation in order to compare this to the oxidation rates.

$\mathbf{Co1_{Cl}}$ and $\mathbf{Co4_{Cl}}$ show markedly faster rates of oxidation than the other complexes, which are broadly correlated to less positive E_{mid}(ox) values. Conversely, $\mathbf{Co2_{Cl}}$ has a much slower rate of oxidation, and a correspondingly high oxidation potential. $\mathbf{Co3_{Cl}}$ and $\mathbf{Co5_{Cl}}$ have rates that lie between the the fast conversion of $\mathbf{Co1_{Cl}}$ and $\mathbf{Co4_{Cl}}$ and the exceptionally slow turnover of the *ortho*-methyl and nitro substituted $\mathbf{Co2_{Cl}}$ and $\mathbf{Co6_{Cl}}$.

Although the E_{mid}(ox) values appear to correlate to the electronic impact of the substituent, as measured through Hammett parameters (Section 3.3.1), this effect is not

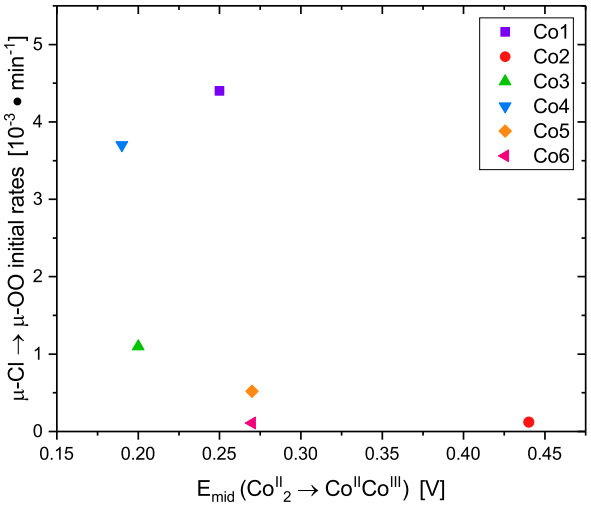

Figure 3.10: Rates of conversion between the μ-Cl and μ-OO species (plotted from data in Table 3.2) against the E_{mid}(ox) values for the oxidation of $Co^{II}{}_2$ complexes shown in Figure 3.6. *Note: No value for E_{mid}(ox) for* ***Co6$_{Cl}$****, so median value plotted.*

observed in the initial rates for the oxidation of the μ-Cl complexes to their μ-OO counterparts. This can be partially explained by both the E_{mid} and Hammett parameters being thermodynamic measures, but reaction rates are due to the kinetics of the system. The difference in activity between $\mathbf{Co4_{Cl}}$ and $\mathbf{Co6_{Cl}}$, with intermediate activity from $\mathbf{Co3_{Cl}}$ and $\mathbf{Co5_{Cl}}$, could be rationalised by deducing that electron-donating substituents result in higher rates. However, if the effect were purely inductive through the bpp ligand, $\mathbf{Co1_{Cl}}$ would be expected to also fall in the middle between $\mathbf{Co3_{Cl}}$ and $\mathbf{Co5_{Cl}}$. This is not observed, further confirming the proposal that the effect is stereoelectronic.

Interestingly, the very slow oxidation rate of the nitro-substituted $\mathbf{Co6_{Cl}}$ is mirrored by a previous study on a ruthenium analogue for water oxidation catalysis by Roeser *et al.*, Figure 3.11.[178] In their study, the substitution kinetics of a ruthenium aqua complex to the corresponding ruthenium-acetonitrile species was investigated by UV-vis spectroscopy. They found that although the addition of an electron donating substituent on the backbone of the terpyridine ligand did not have a pronounced effect on the substitution rates, the addition of a nitro group reduced the rate of substitution by an order of magnitude. They found that this effect corresponded to very low rates of water oxidation catalysis which the authors ascribed to inductive effects through the bpp ligand.[178] Rather than inductive effects, this is likely to be a conjugative effect of the nitro group, and might also help explain the unusual electrochemical behaviour of $\mathbf{Co6_{Cl}}$ and the low rates of O_2-adduct formation.

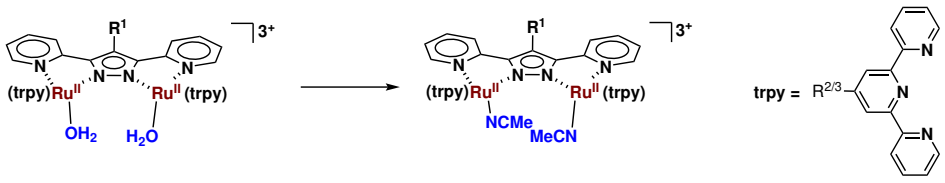

Figure 3.11: The substitution reaction studied by Roeser *et al.* on ruthenium analogues to the cobalt complexes studied in this work.[178] Complexes studied: (a) $R^{1,\,2,\,3}$ = H

Functionalisation of the bpp ligand in the *ortho*-position on $\mathbf{Co2_{Cl}}$ has a significant impact on both the E_{mid}(ox) value, resulting in a very high oxidation potential when compared to the other five complexes, and very low oxidation rates. This effect, particularly when compared to the activity of $\mathbf{Co3_{Cl}}$ which is also methyl substituted, suggests that the environment around the cobalt centre is significant to the reactivity of the complex, and the steric hinderance of functionalisation in the *ortho* position outweighs the inductive effect of two methyl groups. The potential steric effect of functionalisation in the *ortho*-position, and lack of inductive effect, is significant when designing further ligand functionalisation patterns to improve catalysis.

Before studying the effect of ligand functionalisation on the oxygen reduction reaction (ORR) activity of the complexes, the electrochemical properties of the μ-OO complexes were studied, since the position of the reduction potentials of the μ-OO complexes would give insight into the accessibility of the reduction state of the complexes. The impact of ligand functionalisation on the reduction potentials was also examined.

3.4 Cyclic Voltammetry Studies on $\mathbf{Co1_{O_2}}$ – $\mathbf{Co6_{O_2}}$

3.4.1 Determination of $\mathbf{E_{mid}}$ Values of $\mathbf{Co1_{O_2}}$ – $\mathbf{Co6_{O_2}}$

The proposed rate-determining-step of the $\mathbf{Co1_{O_2}}$ catalysed reduction of O_2 to water by octamethyl ferrocene in the presence of acid is proton-coupled electron transfer (PCET), as previously described in the literature (Figure 3.1).[113]

In order to probe the first reduction step further and examine the impact of ligand functionalisation on the reduction potentials, non-aqueous cyclic voltammograms were recorded for all six complexes. Cyclic voltammograms were collected using a standard three electrode cell (working electrode (WE): glassy carbon (GC), reference electrode (RE): $Ag/AgNO_3$, counter electrode (CE): Pt wire) by scanning between –0.8 – 1.7 V vs NHE. Acetonitrile and tetrabutylammonium hexafluorophosphate (TBAF) were

used as the electrolyte which allowed for a wide potential window to be scanned.[115] In all initial studies, data was collected at five different scan rates (50, 100, 250, 500, 1000 $mV\,s^{-1}$), Figure 3.12. In all cases the working electrode was rinsed after data collection and a blank solution of electrolyte tested to ensure there was no deposition of the complex onto the electrode surface. This is particularly important when using glassy carbon electrodes due to the precedent for deposition of an active mono-layer onto the surface.[237] Due to the previously reported water oxidation activity of $\mathbf{Co1_{O_2}}$,[166] the acetonitrile was dried over molecular sieves prior to use. Additionally, CVs were collected under air-free conditions to prevent reduction of O_2 dissolved in solution by the glassy carbon electrode.[238]

In all cases, the CVs showed a quasi-reversible peak at around -0.5 V vs NHE, with a possible onset of a second reduction event at around -0.8 V vs NHE. The reversible peak is ascribed to a 1 electron reduction to the $Co^{II}Co^{III}$ state from the Co_2^{III} state. It is worth noting that this is the same mixed oxidation state as the oxidation CVs of the Co_2^{II}-μ-Cl, but with a different bridging ligand. The complexes also showed a peak at high potentials, with the onset at around 1.5 V vs NHE. This peak is irreversible and is likely due to the oxidation of the complex to a $Co^{III}Co^{IV}$ state. This peak is promising for water oxidation activity, and further work might investigate these complexes for their activity under water oxidation conditions. The CV for $\mathbf{Co2_{O_2}}$ shows some contamination by $\mathbf{Co2_{Cl}}$, which is highlighted on the CV in grey.

The E_{mid}(red) values are listed in Table 3.3 with the ΔE values. All six complexes show a peak-to-peak separation of over 60 mV, which might suggest irreversibility. However, lack of variation with increasing scan rate suggests that these larger ΔE values are likely due to inherent ohmic drop, or resistance in the system (as explained in Section 3.2.1), rather than irreversibility.

3.4.2 Randles-Sevcik Analysis

As peak current analysis revealed that the redox events were not fully reversible for all six complexes, the reversibility was investigated further using Randles-Sevcik (RS) analysis. The Randles-Sevcik equation, Equation 3.3, states that for a freely diffusing, fully reversible system, the current is proportional to the square root of the scan rate.[240] Plotting this relationship can help determine the reversibility of the electron transfer process. Furthermore, deviations from linearity, and a difference in gradient between the reduction and oxidation peak currents, are indicative of adsorption of the analyte

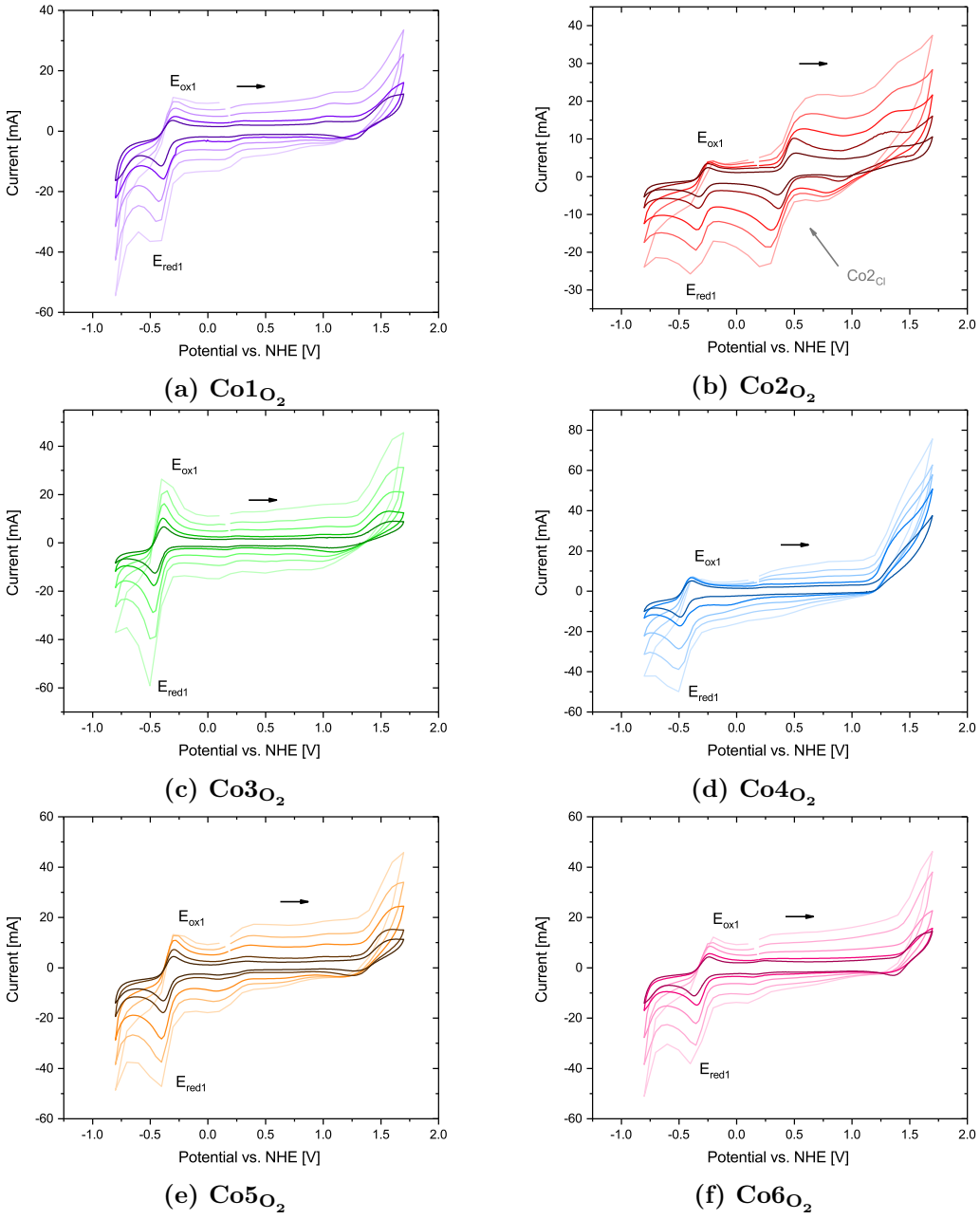

Figure 3.12: Cyclic voltammograms of complexes $\mathbf{Co1_{O_2}}$ – $\mathbf{Co6_{O_2}}$ (1 mM) at different scan rates (dark to light: 50, 100, 250, 500, 1000 mVs^{-1}), WE: GC, RE: $Ag/AgNO_3$, CE: Pt wire, electrolyte: TBAF (0.1 M), solvent: MeCN (dried, degassed), T = 20 °C, air-free, direction of scan illustrated by arrow. The presence of $\mathbf{Co2_{Cl}}$ impurity in 3.12b is highlighted in grey.

to the electrode surface, or a chemical reaction.[115] The results of RS analysis are also useful in explaining the variation in the values of the current ratios for the oxidation and reduction, reported in Table 3.5.

Table 3.3: Peak oxidation and reduction potentials for the $Co_2^{III} \rightarrow Co^{III}Co^{II}$ transition for $\mathbf{Co1_{O_2}}$ – $\mathbf{Co6_{O_2}}$ with the E_{mid}(red) values and peak-to-peak separation (ΔE) noted. All potentials taken from 100 mVs^{-1} data.

Complex	E_{ox1} vs NHE / V	E_{red1} vs NHE / V	E_{mid}(red) / V	ΔE / V
$\mathbf{Co1_{O_2}}$	-0.28	-0.41	-0.35	0.13
$\mathbf{Co2_{O_2}}$	-0.25	-0.33	-0.29	0.08
$\mathbf{Co3_{O_2}}$	-0.39	-0.47	-0.43	0.08
$\mathbf{Co4_{O_2}}$	-0.40	-0.49	-0.45	0.09
$\mathbf{Co5_{O_2}}$	-0.29	-0.39	-0.34	0.10
$\mathbf{Co6_{O_2}}$	-0.24	-0.34	-0.29	0.10

Collection of CV data at 50, 100, 250, 500 and 1000 mV s^{-1} allowed detailed RS analysis to be performed on the reversible peak shown previously in Figure 3.12. RS plots of the redox peaks are shown in Figure 3.13, displaying varying degrees of linearity. All complexes show differences in the gradient of the oxidation and reduction event, supporting the suggestion that the redox event is not perfectly reversible, potentially due to adsorption onto the electrode surface. $\mathbf{Co1_{O_2}}$ – $\mathbf{Co6_{O_2}}$ show varying degrees of deviation from linearity for their oxidation plots, as shown by the R^2 values, indicating absorption to the electrode surface or a lack of reversibility. The reduction plots are more linear which suggests that the complexes are freely diffusing in solution, with the exception of $\mathbf{Co4_{O_2}}$ which shows some deviation at lower scan rates.

Traditionally, Randles-Sevcik analysis is used to determine the diffusion coefficient of the species of interest, or simply to confirm that the analyte is freely diffusing in solution.[115,241] However, by using an approximation of the diffusion coefficient it is possible to calculate the number of electrons in the redox process (for details see Appendix A.2.2. Diffusion coefficient calculated using Equation A.3, reported by Wilke and Chang.[242]). As $\mathbf{Co1_{O_2}}$ – $\mathbf{Co6_{O_2}}$ are bimetallic complexes, it is particularly important to determine whether the redox peaks in the CV are due to one or two electron transfer processes.

The rearranged Randles-Sevcik equation and determination of the diffusion coefficient can be found in the Appendix A.2.2. The values for the diffusion coefficient were used to calculate the number of electrons in the redox process of the reversible peak. The values in Table 3.4 are calculated at 100 mVs^{-1}.

An electron transfer process cannot correspond to a non-integer number of electrons.

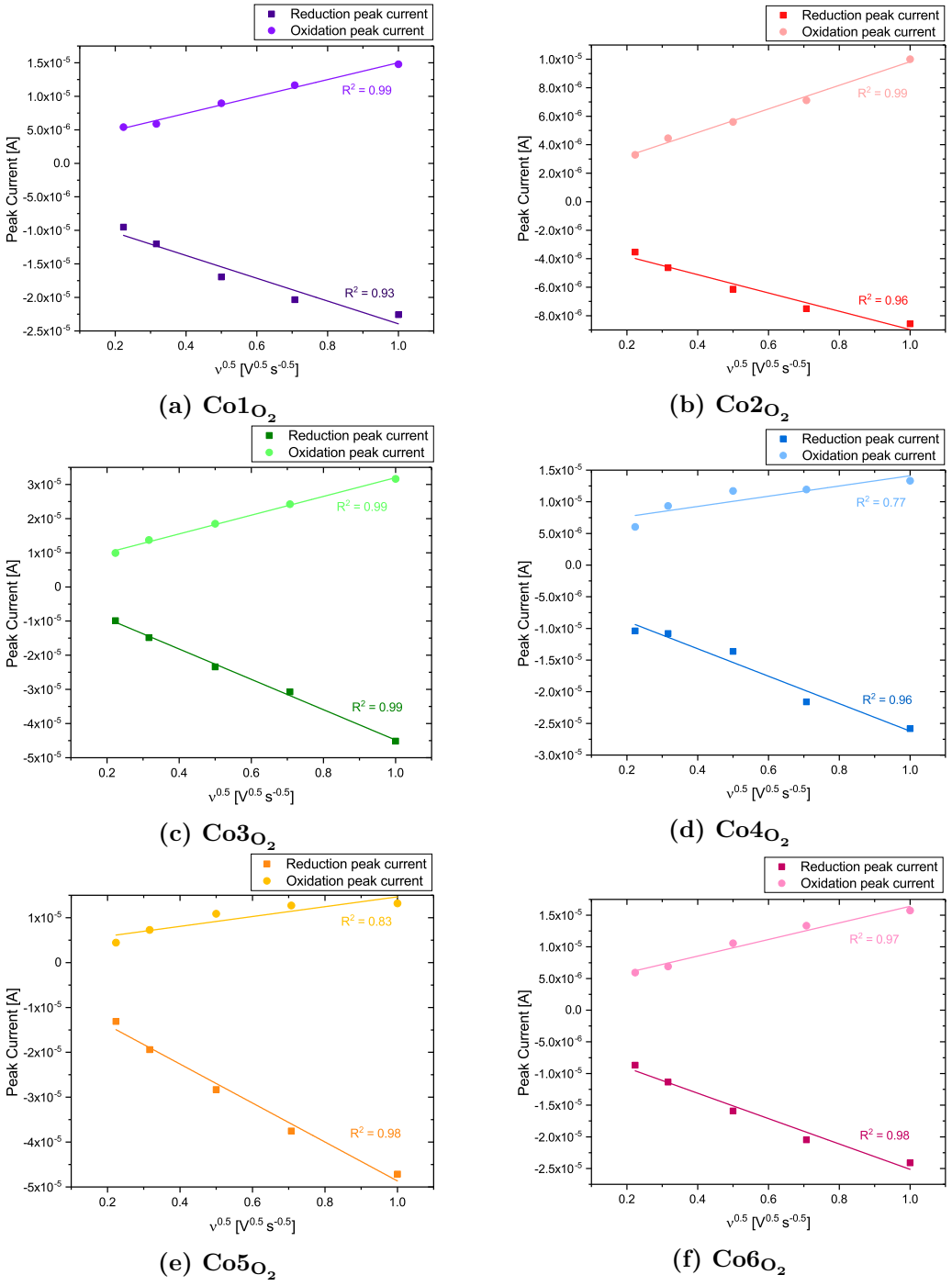

(a) $\mathbf{Co1_{O_2}}$ (b) $\mathbf{Co2_{O_2}}$

(c) $\mathbf{Co3_{O_2}}$ (d) $\mathbf{Co4_{O_2}}$

(e) $\mathbf{Co5_{O_2}}$ (f) $\mathbf{Co6_{O_2}}$

Figure 3.13: Randles-Sevcik plots of $\mathbf{Co1_{O_2}}$ – $\mathbf{Co6_{O_2}}$ with peak current plotted against the square root of the scan rate. The reduction peak currents are shown in dark, the corresponding oxidation peaks in light. Conditions: [Co]: 1 mm, WE: GC, RE: $Ag/AgNO_3$, CE: Pt-wire, electrolyte: TBAF (O.1M), solvent: MeCN (dried, degassed), T: 20 °C, air-free. The fit is shown with the R^2 value.

Table 3.4: Number of electrons in the redox processes of the reversible peak shown in Figure 3.12. Calculated at 100 mVs^{-1}.

Complex	No. electrons, reduction peak	No. electrons, ox. peak
$\mathbf{Co1_{O_2}}$	0.8	0.5
$\mathbf{Co2_{O_2}}$	0.4	0.4
$\mathbf{Co3_{O_2}}$	0.9	0.8
$\mathbf{Co4_{O_2}}$	0.7	0.7
$\mathbf{Co5_{O_2}}$	1.1	0.5
$\mathbf{Co6_{O_2}}$	0.8	0.5

Therefore the values reported in Table 3.4 show that the redox peaks are 1 electron processes, so the assignment of a 1 electron reduction of the cobalt complex ($Co^{III}{}_2$ $\rightarrow$ $Co^{III}Co^{II}$) is confirmed. However, the values of less than one suggest that there is another reason for lower electron transfer, either deposition onto the electrode surface, or subsequent chemical steps. For most complexes, the return peak (E_{ox}, Table 3.4) has a lower value for the number of electrons, which supports the hypothesis that either reaction occurs after the first reduction, or deposition to the electrode occurs from the $Co^{II}Co^{III}$ state. $\mathbf{Co2_{O_2}}$, $\mathbf{Co3_{O_2}}$ and $\mathbf{Co4_{O_2}}$ have values for the oxidation peak that are very close to that of the corresponding reduction, suggesting a highly reversible process.

Although no indication of deposition was observed between experiments (through collection of a CV in fresh electrolyte), some surface interactions cannot be ruled out. It is possible that very weak adsorption of the species to the electrode surface occurs, and is released as the scan sweeps to higher potentials. Further investigation of surface adsorption was performed using the information extracted from peak-to-peak separation (ΔE). In Table A.2, ΔE values at different scan rates are reported for all complexes ($\mathbf{Co1_{O_2}}$ – $\mathbf{Co6_{O_2}}$).

A freely diffusing, quasi-reversible, species will result in values of ΔE shifting to higher values as scan rate increases, whilst for surface-adsorbed species the ΔE remains constant. All six complexes show an increase in ΔE values which indicates that no irreversible deposition had occurred. Although the ΔE changes are less pronounced for $\mathbf{Co5_{O_2}}$ and $\mathbf{Co3_{O_2}}$ there is not enough evidence to support surface adsorption.

In a similar manner to the μ-Cl complexes discussed previously, Section 3.3.1, the E_{mid}(red) values broadly follow the expected trend, Figure 3.14. Electron withdrawing substituents result in less negative reduction potentials, followed by the unsubstituted

Co1$_{O_2}$, and the electron donating substituents with the most negative potentials. The electron withdrawing effect of a nitro group is stronger than that of bromine, and this is reflected in the relative positions of **Co6$_{O_2}$** and **Co5$_{O_2}$**, respectively.[183] Unlike **Co6$_{Cl}$**, the CV of **Co6$_{O_2}$** is well-defined, with no evidence of other activity in the potential window scanned in the CV.

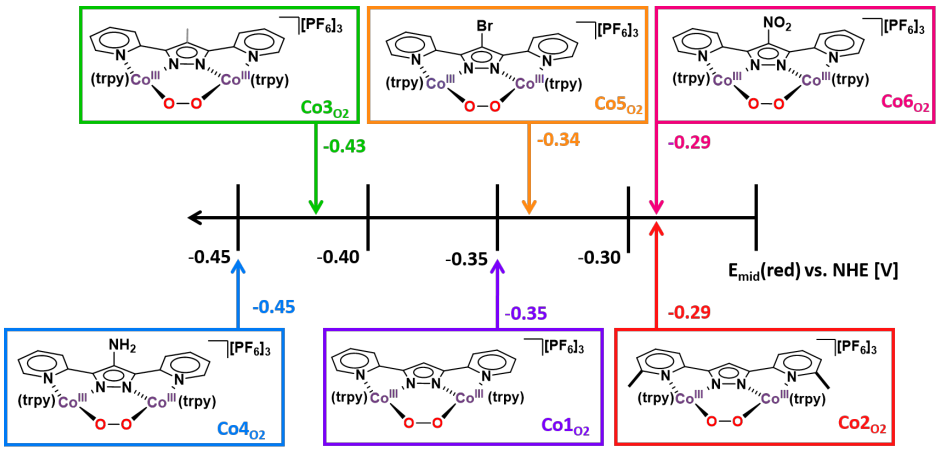

Figure 3.14: E_{mid}(red) values for **Co1$_{O_2}$** – **Co6$_{O_2}$**, determined from the 100 mVs^{-1} scan rate trace in Figure 3.12.

The E_{mid} values correlate to the Hammett parameters of the substituents, Figure 3.15. Both the E_{mid} values and the Hammett parameters are thermodynamic properties of the complexes, and such a correlation was also observed for the E_{mid} values for the oxidation of the Co_2^{II} μ-Cl complexes, as discussed previously.

As discussed previously, **Co2$_{O_2}$** is an outlier. The *ortho*-methyl substitution results in behaviour that does not follow the trends observed in the rest of the series. It shows one of the least negative reduction potentials, suggesting that the inductive impact of substituents in the *ortho* position of the pyridine ring of the bpp^- ligand is considerably reduced when compared to functionalisation on the pyrazole backbone. This is further supported by the findings with **Co2$_{Cl}$**, Section 3.3.1, which has a significantly higher oxidation potential than the other five complexes. Because the E_{mid}(red) value for **Co2$_{O_2}$** does not follow the trend seen with the other substituents, it also seems likely that *ortho* substituents have a stronger stereoelectronic influence on the metal centre than substituents on the pyrazole backbone.

Although the larger ΔE values could be ascribed to resistance in the system, the ratio of the peak currents shown in Table 3.5 also suggested that the process is not fully

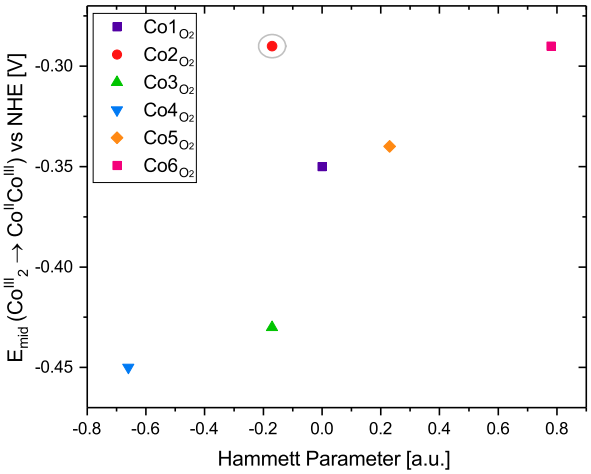

Figure 3.15: A comparison between the Hammett parameters of the substituents and the E_{mid1} values. $\mathbf{Co2_{O_2}}$ is circled in grey as an outlier due to its substitution pattern, as discussed previously.

Table 3.5: Peak current for $\mathbf{Co1_{O_2}}$ – $\mathbf{Co6_{O_2}}$ for CVs collected at 100 mVs^{-1}

Complex	peak i_{ox1} / µA	peak i_{red1} / µA	peak i_{ox1} / peak i_{red1}
$\mathbf{Co1_{O_2}}$	6.78	12.02	0.56
$\mathbf{Co2_{O_2}}$	4.46	4.64	0.96
$\mathbf{Co3_{O_2}}$	14.85	13.72	1.08
$\mathbf{Co4_{O_2}}$	10.78	9.36	1.15
$\mathbf{Co5_{O_2}}$	9.81	15.29	0.64
$\mathbf{Co6_{O_2}}$	6.90	11.35	0.61

reversible for all six complexes. The ratio of the peak currents for $\mathbf{Co2_{O_2}}$, $\mathbf{Co3_{O_2}}$ and $\mathbf{Co4_{O_2}}$ are close to 1, indicating reversibility. However, the other three complexes have ratios of less than one, suggesting a degree of irreversibility of the redox event. Although various CVs of $\mathbf{Co1_{O_2}}$ had been collected previously,[113] multiple scan rate analysis had not been conducted, so the lack of full reversibility had not been previously reported.

The current ratio should be independent of scan rate for a chemically reversible species.[96] All six complexes show some variation in the ratio with changing scan rates, Table A.1; however, measuring the baseline of the return scan (the E_{ox} peak) can be challenging and result in slight variations. Singe the magnitude in variations is small, they are likely due to errors in the baseline.

The results shown are in agreement to the oxidation studies conducted on the µ-Cl

complexes in Section 3.3.1, whereby most of the complexes show the expected trends. The exception is the *ortho*-methyl substituted $\mathbf{Co2_{O_2}}$, which shows unexpectedly low reduction potentials relative to the other five complexes. This was seen for $\mathbf{Co2_{Cl}}$, which shows unexpectedly high oxidation potentials.

The impact of ligand functionalisation on the E_{mid}(red) values are supported by studies on ruthenium water oxidation complexes based on the unsubstituted, methyl- and nitro- pyrazole functionalised ligands.[175] In the ruthenium complexes, the impact of ligand functionalisation on oxidation, rather than reduction, potentials was investigated. Methyl functionalisation reduced the oxidation potentials by a small amount relative to the unsubstituted complex. Conversely, the nitro substituent had a very pronounced impact on the oxidation potential, with a shift of nearly 0.2 V to more positive potentials when compared to the unsubstituted complex.

3.4.3 Wide Scan Width CVs

The use of Randles-Sevcik analysis allowed the confident assignment of the one electron reduction of Co_2^{III} to $Co^{II}Co^{III}$, Figure 3.12. By scanning to more reducing potentials, the two electron conversion between Co_2^{III} and Co_2^{II} will be measured.

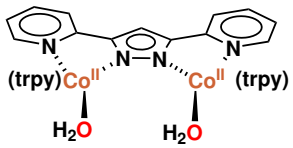

Figure 3.16: The $Co^{II}{}_2$ bis-aqua species proposed by Llobet and coworkers as an intermediate in the ORR.[113]

Since the CVs reported in Section 3.4.1 scan a potential window with just one reduction event, CVs were collected on a wider potential scan window, to investigate further redox events at more negative potentials. Previous studies on $\mathbf{Co1_{O_2}}$ revealed the presence of a second irreversible redox event at lower potentials,[113] so CVs were collected by scanning between 1.3 – 1.7 V vs NHE. The results are shown in Figure 3.17.

All six complexes showed two non-reversible reduction peaks in the region –1.0 – 0 V. The first can confidently be assigned as the $Co^{III}{}_2 \rightarrow Co^{III}Co^{II}$ transition (E_{red1}), which corresponds to the reversible event observed previously. This is followed by a further reduction, which likely corresponds to the $Co^{II}{}_2$ (E_{red2}) oxidation state. This supports the previously reported CV data for $\mathbf{Co1_{O_2}}$.[113] For all six complexes, increasing scan

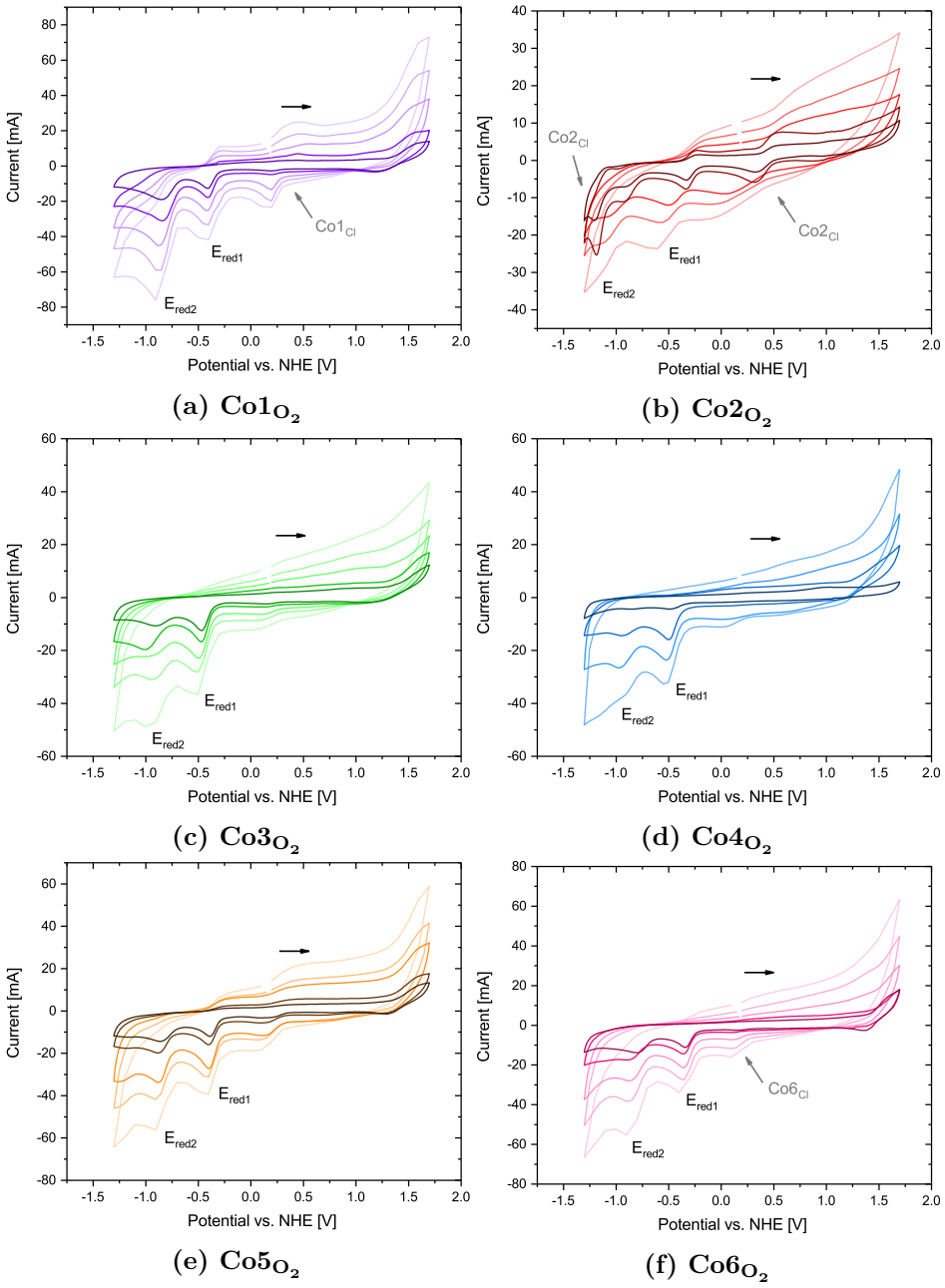

(a) $\mathbf{Co1_{O_2}}$ (b) $\mathbf{Co2_{O_2}}$

(c) $\mathbf{Co3_{O_2}}$ (d) $\mathbf{Co4_{O_2}}$

(e) $\mathbf{Co5_{O_2}}$ (f) $\mathbf{Co6_{O_2}}$

Figure 3.17: Cyclic voltammograms of complexes $\mathbf{Co1_{O_2}}$ – $\mathbf{Co6_{O_2}}$ (1 mM) at different scan rates (dark to light: 50, 100, 250, 500, 1000 mVs^{-1}), WE: GC, RE: $Ag/AgNO_3$, CE: Pt wire, electrolyte: TBAF, (0.1 M), solvent: MeCN (dried, degassed), T = 20 °C, air-free, direction of scan illustrated by arrow.

rate increased the current response, with a very slight drift of the E_{red} values to more negative potentials, as expected for freely diffusing species in solution.

$\mathbf{Co1_{O_2}}$, $\mathbf{Co2_{O_2}}$ and $\mathbf{Co6_{O_2}}$ display another quasi-reversible peak in the region 0 –

0.5 V, Figure 3.17, although the intensity of this peak is lower than that of the two irreversible reduction peaks. This peak is assigned to a small degree of contamination in the sample from the $\mathbf{Co_{Cl}}$ species, as discussed in Section 3.3.1, and can be seen clearly in the overlay shown in Figure 3.18. $\mathbf{Co2_{O_2}}$ also has a large irreversible peak in the -1 – -1.5 V region, which can be confidently assigned as contamination by $\mathbf{Co2_{Cl}}$ in the sample. This is supported by the NMR spectroscopy studies reported in Chapter 2 where $\mathbf{Co2_{O_2}}$ proved challenging to isolate without $\mathbf{Co2_{Cl}}$ contamination.

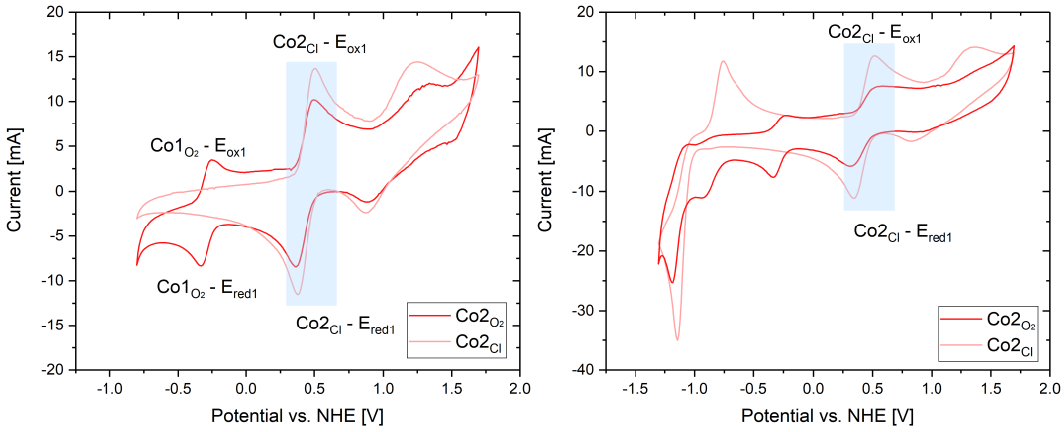

(a) Narrow scan window. **(b)** Wide scan window.

Figure 3.18: Cyclic voltammograms of $\mathbf{Co2_{O_2}}$ and $\mathbf{Co2_{Cl}}$ showing contamination of $\mathbf{Co2_{O_2}}$ with the chloro-bridged $\mathbf{Co2_{Cl}}$. ([Co2] = 1 mM, 100 mVs^{-1}), WE: GC, RE: $Ag/AgNO_3$, CE: Pt wire, electrolyte: TBAF, (0.1 M), solvent: MeCN (dried, degassed), T = 20 °C, air-free, direction of scan illustrated by arrow.

An important detail in these CVs is that both redox events shown in Figure 3.17 are irreversible, whilst E_{red1} is reversible when the the reduction sweep is reversed before the onset of the second reduction, Figure 3.12. In CVs that show a degree of irreversibility, it is possible to use features of the CV to determine the cause. In order to distinguish between chemical steps and electron transfer processes the terms C and E are used, respectively. An EC mechanism is a reversible electron transfer process, followed by an irreversible chemical step. The impact on the voltammogram is dependent on the respective rate constants of the two processes.[115,228] Generally, for an EC mechanism, increasing scan rate improves reversibility, although this depends on the rate of the electron transfer process being greater than the subsequent chemical step.[115]

The lack of reversibility of the two reduction peaks for all six complexes (E_{red1} and E_{red2}) shown in Figure 3.17 at a range of scan rates, (including 1000 mVs^{-1}) suggests the two redox events are followed by a rapid irreversible chemical process, Figure 3.19.[115] This

is likely the cleavage of the O–O bond, an irreversible chemical change, resulting in a lack of oxidation peaks on the reverse sweep in the CV. This was also proposed by Llobet and coworkers in their previous studies on $\mathbf{Co1_{O_2}}$.[113] The process is therefore an EC mechanism, as discussed previously, whereby a redox event is followed by a rapid chemical process.[115]

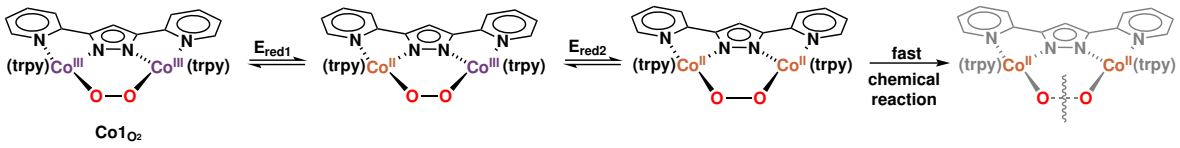

Figure 3.19: The sequence of reduction steps and subsequent electrochemical intermediates in the proposed EC mechansim. The proposed product of the chemical step after E_{red2} has not been confirmed. It is likely that it involves the cleavage of the O–O bond, as shown, but could also involve protonation, rearrangement, or some combination of the three.

Without further evidence it is not possible to deduce the mechanism of bond breakage that occurs, although it can confidently be assigned to the active site (the cobalt/peroxo unit) because the other bonds in the complexes are likely to need higher potentials to activate the bonds. It was not possible to identify the species that formed after the irreversible EC, resulting in the O–O cleavage, although it can be assumed to be an OH, H_2O or MeCN adduct of $Co^{II}{}_2$, although this species is not electrochemically observable in the scan window collected. Due to the absence of O_2 in the electrochemical cell, repeat scans will have been probing fresh $Co^{III}{}_2$-μ-OO.

The two irreversible electron transfer steps are the only redox events occurring in this scan window, which suggests that the products of the chemical transformation must have redox potentials outside of the scan window shown, Figure 3.20, and are expected to be reactive and therefore very short-lived. The reversibility of the redox peaks is not restored upon faster scan rates, suggesting that the chemical step is very rapid.

In some cases it is possible to use the distance between two redox peaks in a CV to determine whether the redox events are a concerted electron transfer mechanism, or in a bimetallic system can give an indication of the degree to which the two metal centres can "communicate". However, this analysis relies on reversible redox events.[243] Therefore, due to the irreversible nature of the two reduction peaks observed for $\mathbf{Co1_{O_2}}$ – $\mathbf{Co6_{O_2}}$ (E_{red1} and E_{red2}) it is not possible to investigate their dependence on each other. However, the fact that the two reductions are stepwise, rather than concerted, in the CVs suggests that catalytic oxygen reduction with these complexes will also

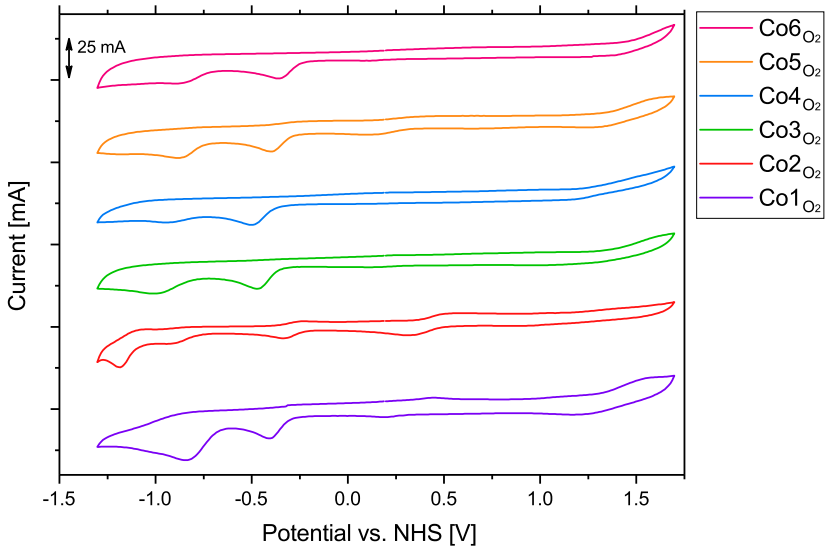

Figure 3.20: Cyclic voltammograms of complexes $\mathbf{Co1_{O_2}}$ – $\mathbf{Co6_{O_2}}$ with 1 mM [Co], 0.1 M TBAF electrolyte in dry MeCN under argon at room temperature (WE: GC, RE: $Ag/AgNO_3$, CE: Pt wire, SR: 100 mVs-1)

proceed through mixed-valent $Co^{II}Co^{III}$ intermediates.

Further investigation of the irreversible chemical step is challenging. Although these complexes are known to undergo PCET (Figure 3.1), under the conditions in which the CVs were collected (dry, degassed acetonitrile) it is unlikely that the chemical step in this process is PCET, due to the absence of available protons. Furthermore, although low concentrations of water in the solution could provide protons, any significant amount of H^+ would be observable in the CV as it would undergo proton-reduction by the glassy carbon electrode.[238,244]

Unlike E_{mid} values, which are a thermodynamic property of the redox event and should be unchanged at different scan rates and under differing conditions, E_{red} values are a kinetic property. This helps explain the lack of correlation observed between the E_{red2} values and the Hammett parameters of the complexes, as shown in Figure 3.22.

However, the E_{red2} can still be used as a useful means of comparing the six complexes to each other when measured under comparable conditions. In $\mathbf{Co1_{O_2}}$ and $\mathbf{Co3_{O_2}}$ – $\mathbf{Co6_{O_2}}$, the E_{red2} peaks shown in Figure 3.17 do not shift significantly with increasing scan rate, so the E_{red} values can be used as an approximation of the E_{mid}(red) value. Additionally, it can be seen in Table 3.6 that the E_{mid1} and E_{red1} values follow the same trend relative to each other, so E_{red1} can be used as a direct comparison to

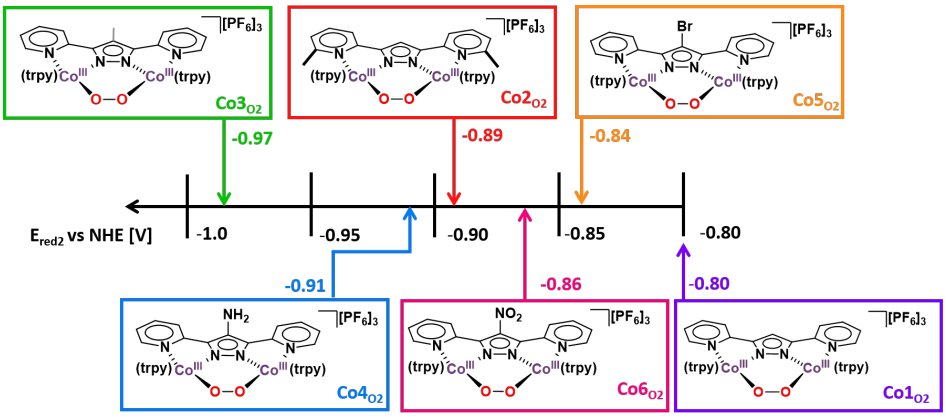

Figure 3.21: E_{red2} values for $\mathbf{Co1_{O_2}}$ – $\mathbf{Co6_{O_2}}$, from the 100 mVs^{-1} scan rate trace in Figure 3.17.

the E_{red2} values obtained for the second reduction. By plotting the E_{red2} values it is possible to investigate the kinetic properties of the complexes and the impact of ligand functionalisation, Figure 3.21.

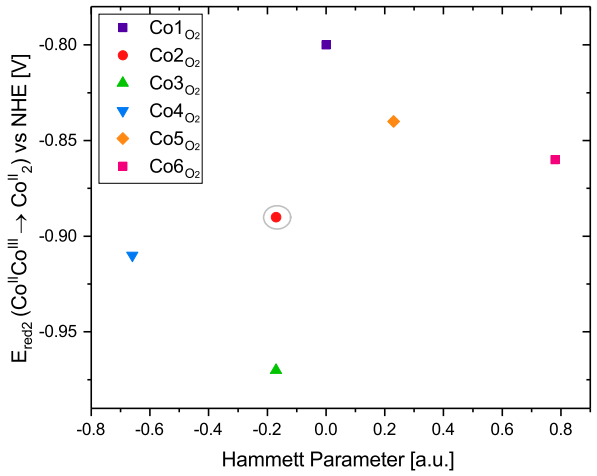

Figure 3.22: A comparison between the Hammett parameters of the substituents and the E_{red2} values. $\mathbf{Co2_{O_2}}$ is circled in grey as an outlier due to its substitution pattern, as discussed previously.

The more negative reduction potentials observed in Figure 3.21 in complexes bearing electron donating substituents ($\mathbf{Co2_{O_2}}$, $\mathbf{Co3_{O_2}}$, $\mathbf{Co4_{O_2}}$) are consistent with a higher electron density on the metal centres, requiring a higher potential to be further reduced. It is surprising that $\mathbf{Co3_{O_2}}$ has the most negative E_{red2} value, since the inductive effect of a methyl group is less than that of a primary amine,[183] so would be expected that $\mathbf{Co4_{O_2}}$ would have the most negative E_{red2} value. The difference in value between $\mathbf{Co2_{O_2}}$ and

Table 3.6: E_{mid}(red), E_{red1} and E_{red2} values for $\mathbf{Co1_{O_2}}$ – $\mathbf{Co6_{O_2}}$ (from CVs collected at 100 mVs^{-1})

Complex	E_{mid1}	E_{red1}	E_{red2}
$\mathbf{Co1_{O_2}}$	-0.35	-0.42	-0.80
$\mathbf{Co2_{O_2}}$	-0.29	-0.33	-0.89
$\mathbf{Co3_{O_2}}$	-0.43	-0.47	-0.97
$\mathbf{Co4_{O_2}}$	-0.45	-0.50	-0.91
$\mathbf{Co5_{O_2}}$	-0.34	-0.39	-0.84
$\mathbf{Co6_{O_2}}$	-0.29	-0.34	-0.86

$\mathbf{Co3_{O_2}}$, which are both methyl functionalised, further supports the suggestion that functionalisation on the pyrazole backbone has a stronger inductive effect than the presence of methyl groups in the *ortho* position of the pyridine rings, indicated by the considerably less negative E_{red2} value for $\mathbf{Co2_{O_2}}$. This is also supported by Figure 3.22 where $\mathbf{Co2_{O_2}}$ and $\mathbf{Co3_{O_2}}$ have the same Hammett parameter, but notably different E_{red2} values.

One might expect the more electron withdrawing substituents on $\mathbf{Co5_{O_2}}$ and $\mathbf{Co6_{O_2}}$ to result in E_{red2} values that are less negative than those of $\mathbf{Co1_{O_2}}$. However, this was not what was observed. Although both have E_{red2} values in the region of -0.9 V, which is less negative than the electron-donating substituents, $\mathbf{Co1_{O_2}}$ has an E_{red2} value of -0.8 V, which was the least negative value reported for the six complexes. The reasons for this are unclear, although they could give an indication into the strength of the O–O bond, which is discussed further in Section 3.4.4.

The EC mechanism displayed by all six complexes suggests that upon reduction to the $Co^{II}{}_2$ state, O–O bond breakage occurs. Unfortunately, identification of the product of this reaction was not possible, although could be achieved through bulk electrolysis of the solution. The electrochemical results suggest that this step is concerted and rapid, which has implications for the reactivity or potential catalytic activity of the complexes.

Reduction to the Co^{II}_2 species of the second redox event (E_{red2}) is not the RDS in the proposed ORR catalytic cycle with chemical reductant Me_8Fc and in the presence of trifluoroacetic acid as the proton source (Figure 3.1). However, the accessibility of this redox state and subsequent O–O bond breakage might be relevant for oxygen atom transfer reactions, or aerobic oxidations, due to the activation of the O–O bond. The more easily the O_2 adduct is reduced means it is potentially more likely to oxidise a

moderately reducing organic substrate. It might therefore be expected that the complexes with the least negative E_{red2} values, $\mathbf{Co1_{O_2}}$ followed by $\mathbf{Co5_{O_2}}$ and $\mathbf{Co6_{O_2}}$, would be most active for these forms of reactivity. This is discussed further in Section 3.6.

3.4.4 Comparison of Electrochemical Data with Structural Data

As complexes for oxygen activation, an investigation into whether there are correlations between the electronic properties of the complexes and the structural information obtained through X-ray crystallography (as discussed in Section 2.4.3) may offer insight into potential reactivity. In order to investigate these correlations, the E_{red} values for the two redox events are plotted against the O–O bond length, Figure 3.23. As the reversible first redox peak does not lead to O–O activation, there is no correlation with O–O bond distance, 3.23a, since this is purely a metal-based redox event. However, it is clear in 3.23b that there is a negative correlation between the E_{red2} values and the O–O bond length, consistent with the assumption of O–O bond breakage in an EC mechanism.

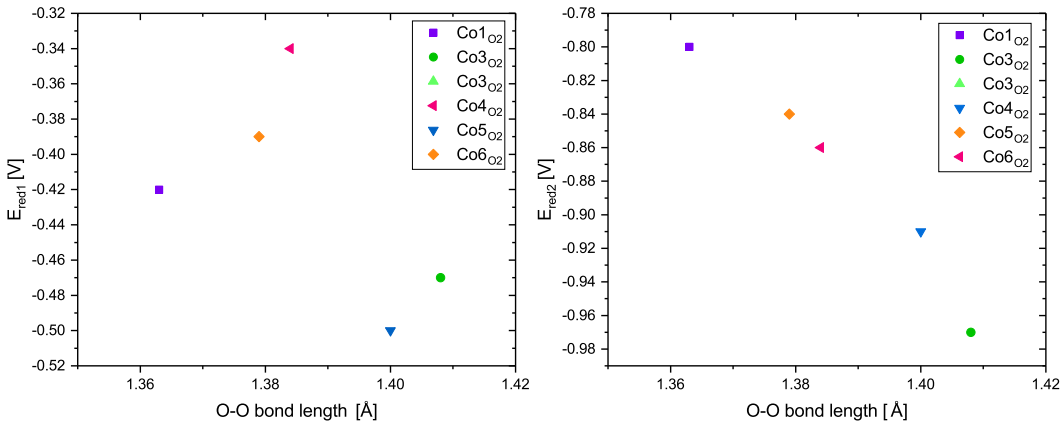

(a) $Co^{III}{}_2 \rightarrow Co^{II}Co^{III}$ **(b)** $Co^{II}Co^{III} \rightarrow Co^{II}{}_2$

Figure 3.23: A comparison between O–O bond length (as reported in Table 2.4) and (a) the E_{red1} values for the reversible redox peak, as shown in Figure 3.12 or (b) the E_{red2} values for the second reduction for each complex. *Note: The mixed valence* $\boldsymbol{Co3_{O_2}}$ *is omitted.*

The surprising observation that $\mathbf{Co1_{O_2}}$ has the least negative E_{red2} value of all six complexes (Figure 3.17) is further complicated by the observation in Figure 3.23, which shows a negative correlation between the O–O bond length and the E_{red2} values for $\mathbf{Co1_{O_2}}$ and $\mathbf{Co3_{O_2}}$ – $\mathbf{Co6_{O_2}}$.[ii] This initially seems counterintuitive as the irreversibility

[ii] $\mathbf{Co2_{O_2}}$ is not included since it was not possible to obtain an X-ray structure.

of the reduction peak is suggested to be due to the breaking of the O–O bond. It was postulated in Section 2.4.3 that the longer bond lengths in $\mathbf{Co3_{O_2}}$ and $\mathbf{Co4_{O_2}}$ were due to increased donation from the cobalt into the π^* orbitals, lengthening, and therefore weakening, the bond. It would therefore be reasonable to expect that there would be a positive correlation between the E_{red2} potential and the O–O bond length, since a weaker bond would require less energy to break.

However, 3.23b shows that complexes which bind O_2 more strongly, leading to longer O–O bond distance, require more energy (more negative reduction potentials) to cleave the O–O bond. The lengthening of the O–O bond upon binding to the two cobalt(II) centres is due to population of the HOMO, which is a π^* orbital. In the μ-OO complexes, the HOMO is fully occupied, hence the diamagnetic character of the complexes. The electrochemistry probes the further reduction of this species, most likely populating the LUMO of the O_2 (the σ^* orbital), resulting in O–O bond cleavage after the second reduction. The results shown in 3.23b show that complexes which bind O_2 more strongly, resulting in longer O–O bond lengths, require more energy (more negative potentials) to break the O–O bond.

3.4.5 Electrochemical testing under acidic conditions

CVs recorded under catalytic conditions can reveal important information about the active species for catalysis, meaning mechanistic information can be extracted from the onset potential. During oxygen reduction reaction (ORR) catalysis, the reaction takes place in the presence of excess oxygen and acid. Unfortunately, latent O_2 and H^+ reduction by the glassy carbon working electrode takes place at potentials close to those recorded for the second reduction peak, Figure A.10.[238,244] The relationship between pH and the redox potential can be described with a Pourbaix diagram,[229] which changes the potential at which different electrochemical processes become favourable.

However, the proposed RDS of ORR is proton coupled electron transfer (PCET), so finding a method of studying the electrochemistry in the presence of acid might offer insight into the catalytic activity of the complexes. As a consequence, an alternative working electrode material was investigated. Due to its low reactivity and wide solvent window, boron-doped-diamond (BDD) is often used for the investigation of redox species which either bind to glassy carbon surfaces or react with the surface.[237,245]

Although literature reports suggested that BDD would be an appropriate electrode material with which to collect CV data under acidic conditions on complexes $\mathbf{Co1_{O_2}}$

– $\mathbf{Co6_{O_2}}$, it was necessary to check whether the data was consistent between different electrode surfaces, so a comparison between GC and BDD was run with $\mathbf{Co3_{O_2}}$, Figure 3.24.[237] Additionally, it was important to check whether latent oxygen reduction would interfere with the reduction peaks of interest. Blank BDD tests can be found in the Appendix, Figure A.11.

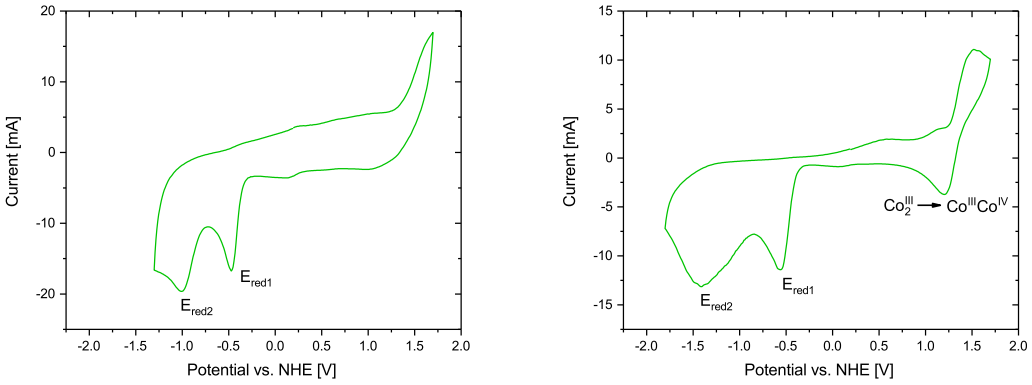

(a) $\mathbf{Co3_{O_2}}$ on GC WE **(b)** $\mathbf{Co3_{O_2}}$ on BDD WE

Figure 3.24: CVs of the $\mathbf{Co3_{O_2}}$ using (a) glassy carbon and (b) boron doped diamond working electrodes, respectively. The broadness of the reduction peak at -1.5 V and the uneven curve on the BDD suggests the complex is interacting with the electrode surface. ([$\mathbf{Co3_{O_2}}$] = 1 mM, [TBAF] = 0.1 M, RE: $Ag/AgNO_3$, CE: Pt wire, Scan rate = 100 mVs^{-1}, solvent: MeCN (dried, degassed), air-free, T = 20 °C)

Although both reduction peaks are irreversible, and the first reduction peak occurs at the same potential on both electrodes, it is clear from Figure 3.24 that the complex used as a test ($\mathbf{Co3_{O_2}}$) behaved differently on the BDD electrode surface. The broadness of the second reduction peak, coupled with the unevenness observable between -1 and -1.5 volts, suggests that the complex is interacting with the electrode surface.

Interestingly, the $Co^{III}{}_2$ to $Co^{III}Co^{IV}$ oxidation peak is identifiable when using the BDD working electrode, with an E_{mid} value of 1.34 V vs NHE. This is in contrast to the GC working electrode, where it is not possible to identify the oxidation redox event.

Due to the apparent reaction of the reduced complex with the BDD electrode, studies in the presence of acid were carried out using glassy carbon electrodes. As a result of the background reduction of protons by glassy carbon occurring at ≈ -1.3 V, Figure A.10, it was not possible to investigate the impact of acid on the second reduction peak. However, it was possible to investigate the impact of the addition of acid on the position of the first, reversible, reduction peak.

The proposed RDS of the oxygen reduction reaction discussed previously, Figure 3.1, involves the reduction of the $Co^{III}{}_2$ species to a mixed $Co^{III}Co^{II}$ species, before oxidation back to the Co^{III}_2 species. Therefore, as the RDS, the thermodynamic accessibility of the first reduction would be expected to correlate to the reactivity of the complex towards Me_8Fc. The position of the first reduction of the cobalt complex must be sufficiently close to the oxidation potential of Me_8Fc (-0.13 V vs. NHE) in order to make the reaction energetically favourable.

The addition of 2mM TFA[iii] changes the CVs by shifting the $E_{red1'}$ to more positive potentials, whilst also reducing the reversibility of the peak, Figure 3.25.

Although addition of acid could conceivably result in protonation of the complex, the UV-vis spectra of $\mathbf{Co1_{O_2}}$ – $\mathbf{Co6_{O_2}}$ in the presence of TFA did not show any change over a 15 minute period (Figure A.17). Bridging oxo and peroxo species are not typically very basic, and since the Co^{III} peroxo species are tricationic, protonation is unlikely. Therefore, these results suggest that the complexes are not protonated in the presence of TFA. However, the more reduced, electron rich, states are more likely to undergo protonation.

There is a large variation in the degree to which the reduction peak was shifted between the different complexes upon the addition of acid, Figure 3.26. Complexes with electron withdrawing substituents saw the most pronounced shift, whilst $\mathbf{Co2_{O_2}}$ was shifted by an almost negligible amount. Reducing the pH reduces the reduction potentials as the addition of a positive charge means the molecule more readily accepts electrons. Both $\mathbf{Co5_{O_2}}$ and $\mathbf{Co6_{O_2}}$ already have E_{mid}(red) values in the absence of TFA that are lower than $\mathbf{Co1_{O_2}}$ and the complexes with electron donating substituents, $\mathbf{Co3_{O_2}}$ and $\mathbf{Co4_{O_2}}$.

Llobet and coworkers claim that *"electron transfer from Me_8Fc to $\boldsymbol{Co1_{O_2}}$ is thermodynamically unfavourable but becomes energetically feasible in the presence of TFA."*[113] This suggests that if the reduction of the $Co^{III}{}_2$ species by Me_8Fc is the RDS of the ORR reaction, $\mathbf{Co5_{O_2}}$ and $\mathbf{Co6_{O_2}}$ should be more active for catalysis. This is discussed further in Section 3.5. It is important to note that although the $E_{red1'}$ of $\mathbf{Co1_{O_2}}$ – $\mathbf{Co6_{O_2}}$ in the presence of TFA are shifted to less negative potentials, and $\mathbf{Co6_{O_2}}$ specifically is significantly closer to Me_8Fc, they do not overlap with the oxidation potential of

[iii] Trifluoroacetic acid is a strong acid ($pK_a = 12.7$[244]), but as it is used in the ORR catalysis (Section 3.5) it was used in these studies to allow comparison with catalytic results.

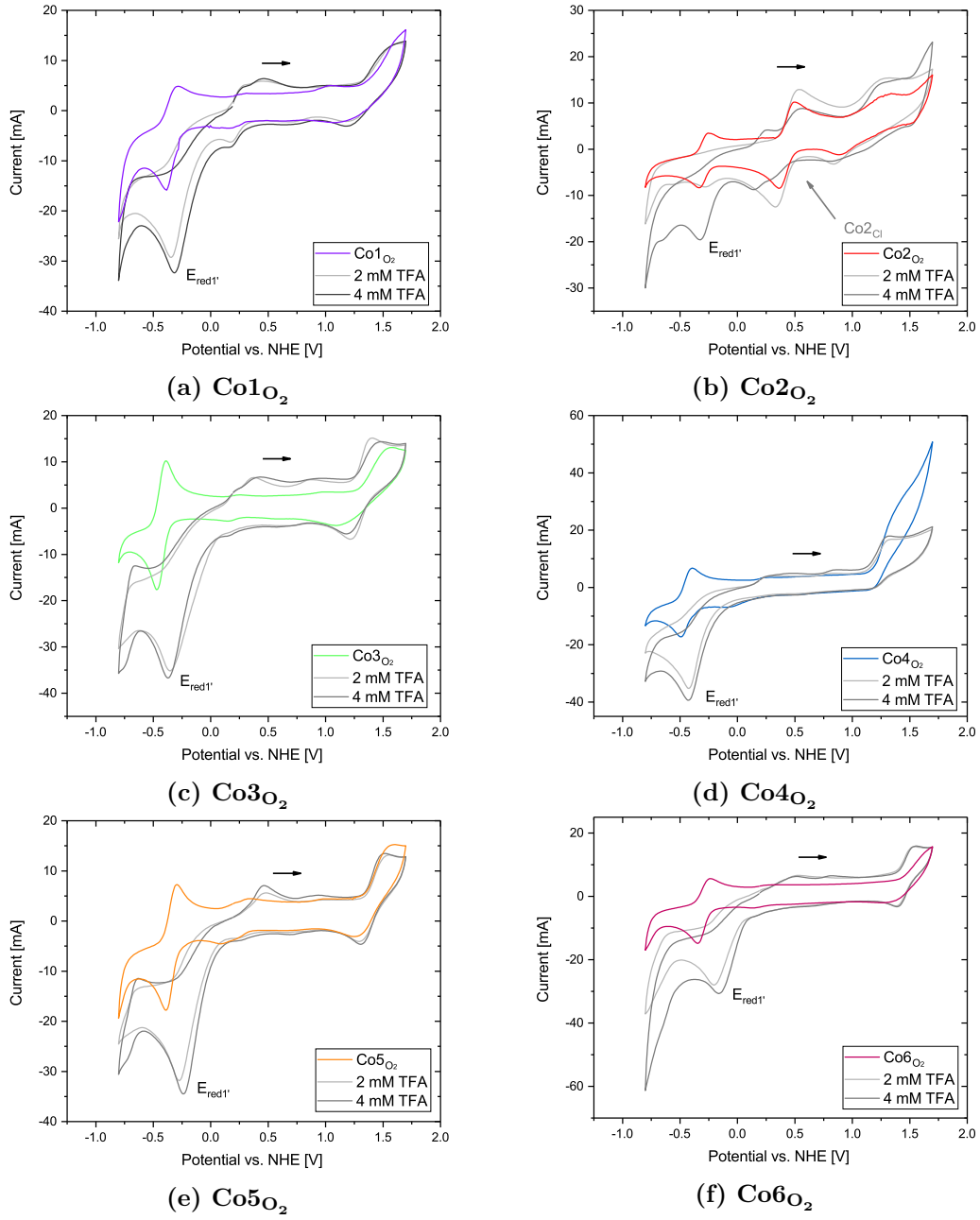

(a) $\mathbf{Co1_{O_2}}$ (b) $\mathbf{Co2_{O_2}}$

(c) $\mathbf{Co3_{O_2}}$ (d) $\mathbf{Co4_{O_2}}$

(e) $\mathbf{Co5_{O_2}}$ (f) $\mathbf{Co6_{O_2}}$

Figure 3.25: Cyclic voltammetry data of $\mathbf{Co1_{O_2}}$ – $\mathbf{Co6_{O_2}}$, with overlaid CVs of the complex in the presence of two different concentrations of trifluoroacetic acid (TFA). Collected under an atmosphere of argon, [Co] = 1 mM, WE: GC, RE: $Ag/AgNO_3$, CE: Pt wire, scan rate: 100 mVs^{-1}, T = rt. Direction of scan illustrated by arrow.

Me_8Fc. However, under catalytic conditions, TFA is used in concentrations of 50 mM. Figure 3.25 illustrates that $E_{red1'}$ shifts to less negative potentials when increasing TFA concentration from 2 mM to 4 mM, so addition of 50 mM will likely shift the potential

further, resulting in an overlap in potentials with Me_8Fc.

$Co1_{O_2}$ and **$Co3_{O_2}$** show multiple oxidation peaks between 0 and 0.5 V. The reversible peak is likely due to low levels of contamination by the μ-Cl complex. However, the irreversible peak could be representative of very slow electron transfer kinetics of the redox event.

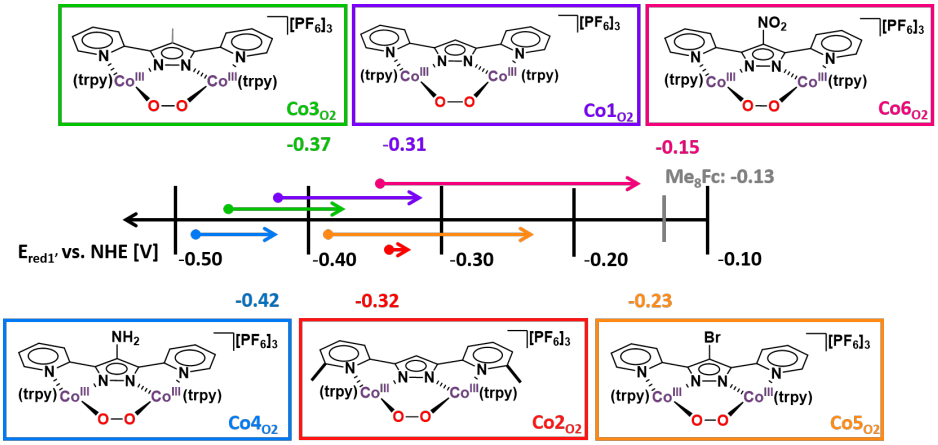

Figure 3.26: $E_{red1'}$ values for **$Co1_{O_2}$** – **$Co6_{O_2}$** in the presence of 4 mM TFA. The shift from the E_{red1} values without TFA present are shown by arrows showing the difference in shift.

Table 3.7: Peak reduction potentials in the absence and presence of TFA for **$Co1_{O_2}$** – **$Co6_{O_2}$** and the difference between these values (ΔE) noted. All potentials taken from 100 mVs^{-1} data. (Note that E_{red1} values are used for the reduction potential in the absence of TFA, rather than E_{mid}(red) values, to offer a direct comparison.)

Complex	E_{red1} vs NHE / V[1]	$E_{red1'}$ + TFA vs NHE / V	ΔE_{red} / V
$Co1_{O_2}$	-0.42	-0.31	0.11
$Co2_{O_2}$	-0.33	-0.32	0.01
$Co3_{O_2}$	-0.47	-0.37	0.10
$Co4_{O_2}$	-0.49	-0.42	0.07
$Co5_{O_2}$	-0.39	-0.23	0.16
$Co6_{O_2}$	-0.34	-0.15	0.19

[1] E_{red1} values reported in Table 3.3.

It is likely that the proton coordinates to one of the oxygen atoms of the bridging peroxo. The lack of reversibility of the redox event suggests a chemical step follows the reduction, which is likely to be the breakage of the O–O bond, facilitated by the binding of H^+ to one (or both) of the oxygen atoms. It has previously been suggested that the RDS of the reaction is PCET.[113] If this hypothesis is correct, it might be expected that

the position of the $E_{red1'}$ peak in the presence of TFA for the six cobalt complexes will correspond to their reactivity in the ORR. This is further discussed in Section 3.5.

3.4.6 Conclusion of Cyclic Voltammetry Studies on $\mathbf{Co1_{O2}}$ – $\mathbf{Co6_{O2}}$

Electrochemical studies on $\mathbf{Co1_{O_2}}$ – $\mathbf{Co6_{O_2}}$ reveal that the complexes undergo two irreversible reduction events when scanning to negative potentials. If the scan is stopped before the second reduction event, the reversibility of the first redox event is restored. Using Randles-Sevcik (RS) analysis, the reversible redox event is confirmed to be a one electron process, corresponding to the $Co_2^{III} \longrightarrow Co^{III}Co^{II}$ reduction, followed by the irreversible $Co^{III}Co^{II} \longrightarrow Co_2^{II}$ reduction event. The irreversiblity of the second reduction is due to a chemical step, most likely the breakage of the O–O bond, although further studies are needed to confirm this.

The fully irreversible nature of the redox event supports the assignment of O–O bond breakage, since Co–O bond breakage would be likely to be partially reversible due to the bridging nature of the peroxo ligand. In order to determine which bonds are breaking (Co–O or O–O) spectroelectrochemistry could be employed. Alternatively, bulk electrolysis might allow analysis of the products.

The RS analysis reveals that the electrochemically reversible redox event is not completely reversible in all six complexes, due to variation in the gradient of the RS plots between the oxidaton and reduction event. This is more pronounced in some of the complexes, both $\mathbf{Co2_{O_2}}$ and $\mathbf{Co4_{O_2}}$ appear to be fully reversible, whereas the other complexes show varying degrees of irreversibilty.

The E_{mid1} values follow the expected trend in terms of the electronic properties of the substituents on the pyrazole backbone, as illustrated in Figure 3.15. The E_{red2} values did not show such a clear correlation, but they do give an indication of the potential reactivity of the complexes due to the ease with which the peroxo is reduced. As previously discussed, $\mathbf{Co2_{O_2}}$ is the exception to all of the trends observed, again confirming that substitution in the *ortho*-position of the bpp^- ligand has a significant impact on the electrochemical properties of the complex.

Upon addition of acid the $E_{red1'}$ values shift to less negative potentials, depending on the concentration of acid, suggesting that under catalytic conditions, when high concentrations of acid are used, the $E_{red1'}$ values would be sufficiently shifted to overlap

with that of Me_8Fc.

3.5 Application of $\mathbf{Co1_{O_2}}$ – $\mathbf{Co6_{O_2}}$ in the ORR

The oxygen reduction reaction (ORR) activity of $\mathbf{Co1_{O_2}}$ has been previously studied.[113] However, the impact of functionalisation on the bpp$^-$ ligand on the activity of the complexes towards the ORR has not been investigated. The rate of reaction of the ORR with $\mathbf{Co1_{O_2}}$ – $\mathbf{Co6_{O_2}}$ will be compared to each other in order to investigate the impact on ligand substitution on catalytic oxygen reduction. These results will be compared to the electrochemical and oxidation results reported in previous sections of this chapter. This will help examine any correlations, which can be used to determine whether changes in ligand substituents have an impact on the mechanism, specifically O_2 binding.

In order to study the ORR, a stop-flow set-up was used. NMR spectroscopy is not feasible due to the relatively fast reaction rates and single electron redox chemistry, the products are not suitable for gas chromatography, so UV-vis spectroscopy in stopped-flow mode was used. Stop-flow reactors allow the measurement of very fast kinetics through the rapid mixing of reagents coordinated with the initiation of data collection.[246] Using the set-up shown in Figure 3.27, the reagents are mixed immediately prior to entering the UV-cell, and the ejection of solution into the stop syringe initiates data collection. The use of the stop-flow equipment allows rapid collection of initial rate data, and also enables collection of multiple repeats.

The reduction of oxygen by octamethyl ferrocene (Me_8Fc) catalysed by the cobalt complexes was investigated using the stop-flow apparatus by taking advantage of the pronounced colour change between Me_8Fc (orange) and the oxidised form, Me_8Fc^+ (green/blue), Figure 3.28. The reaction was monitored by UV-vis spectroscopy, by following the formation of Me_8Fc^+ using the absorbance at 750 nm ($\varepsilon = 410$ M^{-1} cm^{-1})[113].

Literature studies of $\mathbf{Co1_{O_2}}$ confirmed that the 4e$^-$ reduction of O_2 to H_2O proceeds cleanly with no H_2O_2 formed, meaning the stoichiometry of the reaction is 4 equivalents of Me_8Fc to 1 O_2, Scheme 3.3.[113]

$$4\,Me_8Fc + O_2 + 4\,H^+ \xrightarrow{[Co]} 4\,Me_8Fc^+ + 2\,H_2O$$

Scheme 3.3: Oxygen reduction by octamethyl ferrocene, catalysed by a cobalt catalyst and in the presence of acid.

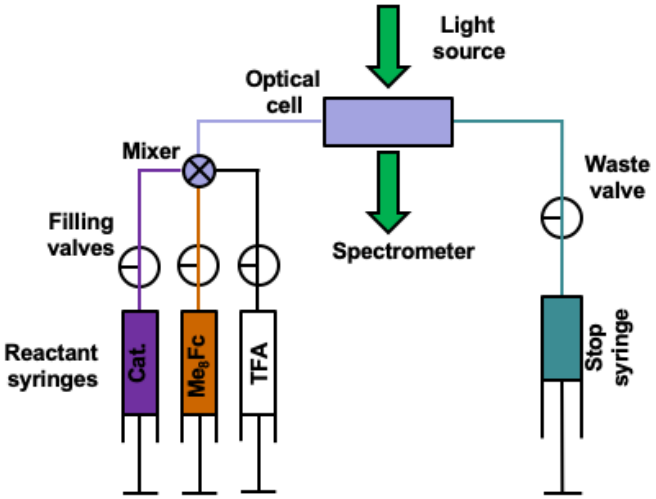

Figure 3.27: UV-vis stop-flow set-up for measuring the formation of Me_8Fc^+ during the ORR. Optical path length = 10 mm, cell volume = 90 µl, deadtime (between mixing and injection) = 8 ms, tubing is jacketed to provide temperature control. Note that the micromixer sits immediately before the optical cell.

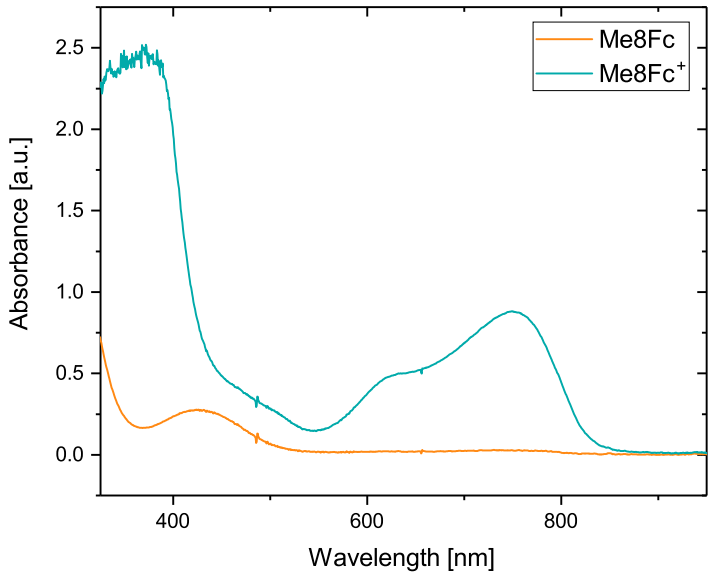

Figure 3.28: The oxidation of Me_8Fc (2 mM) in MeCN to Me_8Fc^+ by addition of $NaIO_4$ (excess) over the course of 1 min.

All complexes showed activity for oxygen reduction under the conditions tested, Fig-

ure 3.29, although there were markedly different rates between the different complexes. $\mathbf{Co1_{O_2}}$, the unsubstituted complex, showed the fastest rates of oxygen reduction, which were in agreement with reported literature values.[113] This was followed by $\mathbf{Co4_{O_2}}$, the amine substituted complex, with both of them reaching over 75% conversion within 20 s. The initial rates for all six complexes are included in Table 3.8, see Figure A.13 for determination of initial rates.

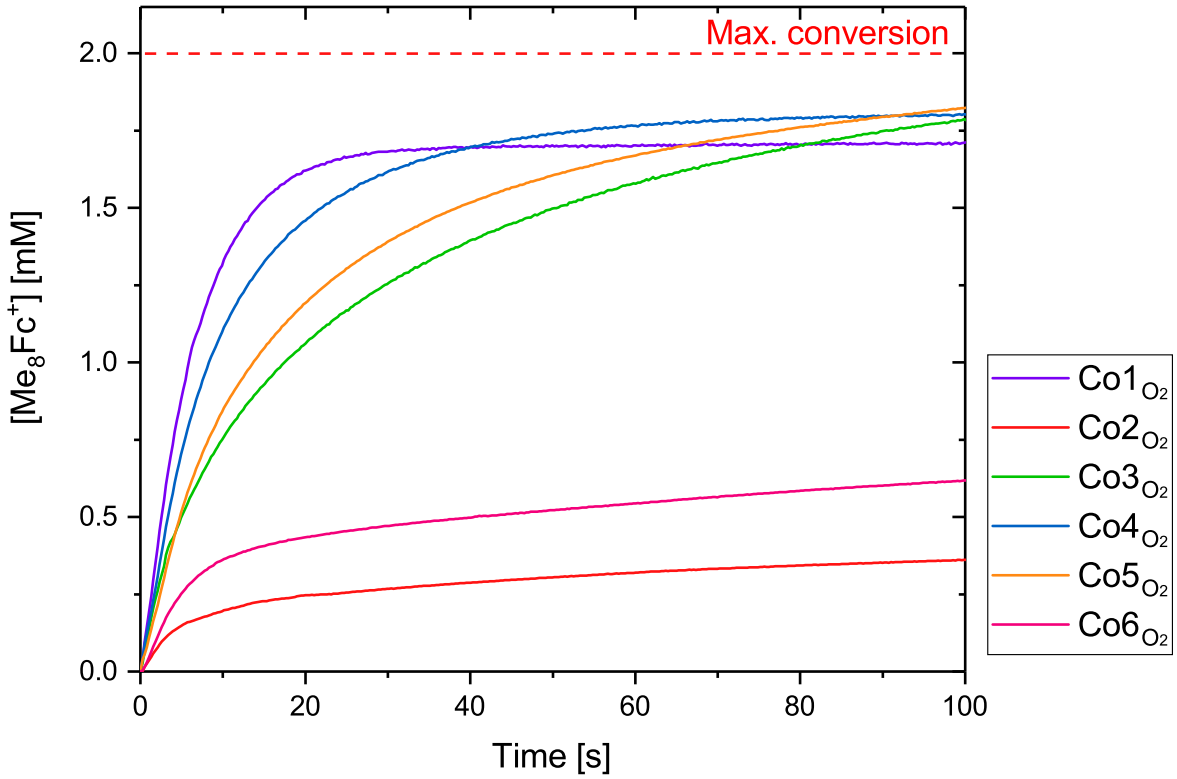

Figure 3.29: Reaction profiles for the oxygen reduction reaction catalysed by $\mathbf{Co1_{O_2}}$ – $\mathbf{Co6_{O_2}}$ monitored by the formation of $[Me_8Fc^+]$ by UV-vis spectroscopy. [Co] = 25 µM, $[Me_8Fc]$ = 2 mM, [TFA] = 50 mM. Solvent = aerated MeCN, 25 °C. *Note that solubility of O_2 in MeCN: 8.1 mM, 25 °C, 1 atm.*[238,247] *Concentration of air saturated MeCN is 2.5 mM,*[239] *which exceeds the concentration of Me_8Fc.*

Whilst complexes $\mathbf{Co1_{O_2}}$ and $\mathbf{Co3_{O_2}}$ – $\mathbf{Co5_{O_2}}$ display clear monoexponential growth, suggesting first order kinetics, in Figure 3.29, both $\mathbf{Co2_{O_2}}$ and $\mathbf{Co6_{O_2}}$ show very slow rates with two kinetic stages, with a fast, initial burst, followed by a slow increase after approximately 10 s. According to the reaction scheme proposed by Llobet *et al.* in Scheme 3.3, the reduction of the catalyst requires four equivalents of Me_8Fc. Therefore, if catalyst turnover is limiting the reactivity, leading to a stoichiometric reaction, it would be expected that only 4 equivalents (100 µM, 0.1 mM) Me_8Fc^+ would

Table 3.8: Initial rates for the formation of Me_8Fc^+. The initial rates are determined in Figure A.13.

Complex	Initial rate [mM s^{-1}]
$\mathbf{Co1_{O_2}}$	0.18
$\mathbf{Co2_{O_2}}$	0.027
$\mathbf{Co3_{O_2}}$	0.89
$\mathbf{Co4_{O_2}}$	0.13
$\mathbf{Co5_{O_2}}$	0.1
$\mathbf{Co6_{O_2}}$	0.049

be formed. The initial burst activity of $\mathbf{Co6_{O_2}}$ plateaued at around 0.5 mM, which corresponds to between 4 and 5 turnoverover. This suggests that some catalyst turnover was occurring, before either deactivation of the catalyst, or that these catalysts required a higher concentration of acid in order to drive the reaction.

Fitting monoexponential and biexponential curves to the kinetic traces of $\mathbf{Co2_{O_2}}$ and $\mathbf{Co6_{O_2}}$, Figure 3.30, reveals biexponential growth for both complexes. This shows there are two competing mechanisms for the formation of Me_8Fc^+ in the presence of $\mathbf{Co2_{O_2}}$ and $\mathbf{Co6_{O_2}}$. It is likely that the initial, fast, component mirrors that observed in the other complexes, corresponding to the complete reduction of O_2 to water. The second, slower, component might be due to the incomplete reduction of O_2 to H_2O_2 (which would still produce Me_8Fc^+), which modifies or deactivates the catalyst resulting in slower rates of Me_8Fc^+ formation.

The electrochemical properties of $\mathbf{Co2_{O_2}}$ and $\mathbf{Co6_{O_2}}$ broadly follow the expected trends. However, the oxidation of $\mathbf{Co2_{Cl}}$ and $\mathbf{Co6_{Cl}}$ to their corresponding μ-OO complexes is very slow, as discussed in Section 3.3.2. Since O_2 binding is a key step in both the ORR and the oxidation of the μ-Cl complexes, this suggests that the slow rate of $\mathbf{Co2_{O_2}}$ and $\mathbf{Co6_{O_2}}$ in the ORR could be due to their poor ability to bind O_2.

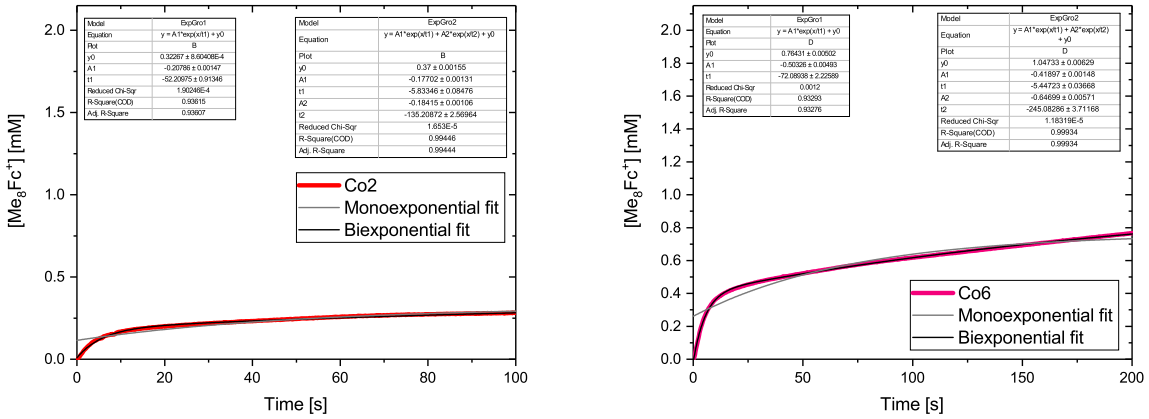

Figure 3.30: Mono- and biexponential fitting performed on the kinetic trace of the ORR of $\mathbf{Co2_{O_2}}$ and $\mathbf{Co6_{O_2}}$ using the exponential fitting tool in the Origin2017 software package. Conditions: [Co] = 25 µM, [Me_8Fc] = 2 mM, [TFA] = 50 mM. Solvent = aerated MeCN, 25 °C.

3.5.1 Kinetics of Oxygen Reduction

Llobet and coworkers carried out some mechanistic investigations into the activity of $\mathbf{Co1_{O_2}}$, as discussed in Section 3.1.1.[113] Their studies lead them to deduce that the reaction is first order in catalyst, and that the rate determining step is PCET, Figure 3.1. In order determine whether the order in catalyst is consistent for all six complexes, and to try and further elucidate the mechanism, Variable Time Normalised Analysis (VTNA), a form of graphical rate analysis, was undertaken for $\mathbf{Co1_{O_2}}$ – $\mathbf{Co6_{O_2}}$. The principles behind graphic rate analysis are discussed in Section 3.2.2.

The results shown in Figure 3.29 suggest that for $\mathbf{Co2_{O_2}}$ and $\mathbf{Co6_{O_2}}$ there may be more than one reaction mechanism taking place, as indicated by the two different kinetic regimes.

VTNA studies of $\mathbf{Co1_{O_2}}$ – $\mathbf{Co6_{O_2}}$

In order to perform VTNA analysis on the complexes, to help determine the order in catalyst and any other changes in mechanism throughout the reaction, ORR data was collected at three catalyst loadings, Figure 3.31, before VTNA normalisation was applied, Figure 3.32

All six complexes show some variation in their final conversion plateau points, with some complexes plateauing well below the maximum conversion of 2 mM Me_8Fc^+. The trends in plateau point do not appear to follow the rates observed, with $\mathbf{Co1_{O_2}}$ showing the

fastest rates, but plateauing at a point nearer 85% conversion. Conversely, $\mathbf{Co3_{O_2}}$ and $\mathbf{Co5_{O_2}}$, which are slower than both $\mathbf{Co1_{O_2}}$ and $\mathbf{Co4_{O_2}}$, reach almost 100% conversion, but at slower rates.

With the exception of $\mathbf{Co1_{O_2}}$, the lowest catalyst loading, 12.5 µM, fails to reach the same level of conversion that the other two catalyst loadings reach, even after 200 s. This suggests that there is some catalyst degradation or deactivation occurring, as changing catalyst concentration should only result in a change in rate, rather than conversion. The stability of the complexes under reaction conditions is briefly investigated in Section 3.5.2.

$\mathbf{Co2_{O_2}}$ shows exceptionally low rates and conversions, suggesting that functionalisation on the ligand backbone in the *ortho* position strongly inhibits catalysis. Indeed, $\mathbf{Co2_{Cl}}$ also exhibited a very slow conversion from the µ-Cl complex to the µ-OO peroxo complex in Section 3.3.2, and did not reach full conversion. It also proved challenging to isolate $\mathbf{Co2_{O_2}}$ in the pure µ-OO form, both for crystallographic characterisation and NMR spectroscopic analysis. This suggests that oxidation of $\mathbf{Co2_{O_2}}$ to form the Co_2^{III} µ-OO complex ($\mathbf{Co2_{O_2}}$) is less thermodynamically favourable than the other five complexes. As a consequence of the low activity and lack of variation in catalyst activity with changing concentration, kinetic analysis was not carried out on $\mathbf{Co2_{O_2}}$.

Using an iterative process, VTNA was applied to $\mathbf{Co1_{O_2}}$ and $\mathbf{Co3_{O_2}}$ – $\mathbf{Co6_{O_2}}$, Figure 3.32. This is complicated by the low conversion with the lowest catalyst loading, meaning this trace does not overlay with the other two concentration profiles. Applying VTNA to the results for $\mathbf{Co1_{O_2}}$ revealed an order of 1 in catalyst, in agreement with previously reported results.[113] Although there was good agreement up to around 50% conversion, there was some deviation as the traces reach the plateau point, indicative of catalyst deactivation.[248]

The apparent deactivation of the catalyst, and subsequent plateauing at a lower conversion, means conducting VTNA analysis on the reaction profiles traces is challenging. With the exception of $\mathbf{Co1_{O_2}}$, the VTNA fits of the data are not good enough to take full advantage of VTNA and draw any firm conclusions about the order in catalyst. In the early stages of the reaction, all complexes show a reasonable agreement with an order 1, after accounting for catalyst deactivation. $\mathbf{Co5_{O_2}}$ shows a possible agreement with a catalyst order of 1, with clear degradation visible in a similar manner to that of $\mathbf{Co1_{O_2}}$.

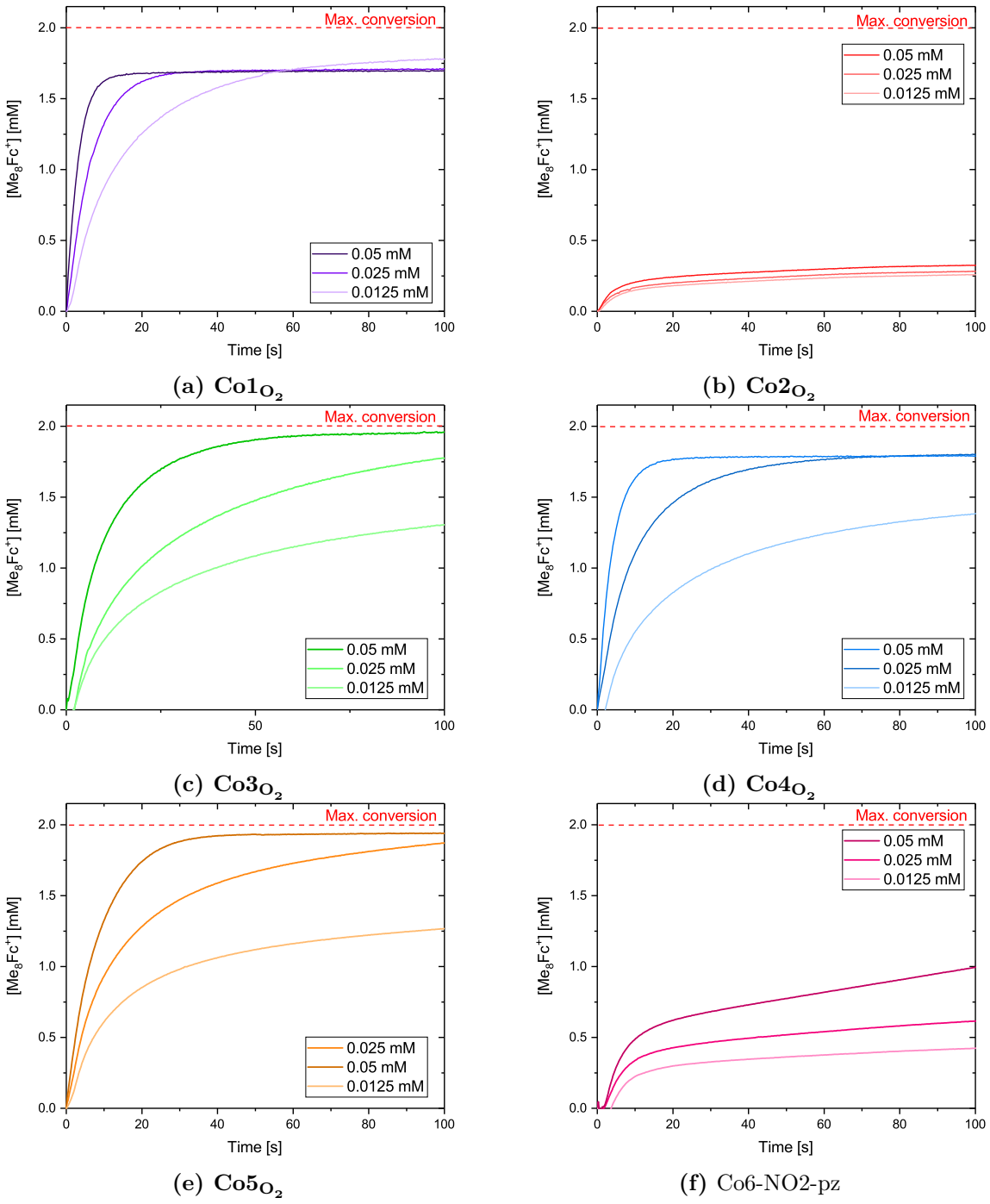

Figure 3.31: Oxygen reduction activity of $\mathbf{Co1_{O_2}}$ – $\mathbf{Co6_{O_2}}$ measured by the formation of Me_8Fc^+ at three different catalyst loadings over 100 s. [Me_8Fc] = 2 mM, [TFA] = 50 mM. *Note: dips at beginning of graph due to resistance in the stop-flow system.*

In order to complement the VTNA analysis, initial rates analysis and log/log plots were made, Figure A.15. These results suggest that the order in catalyst for $\mathbf{Co4_{O_2}}$

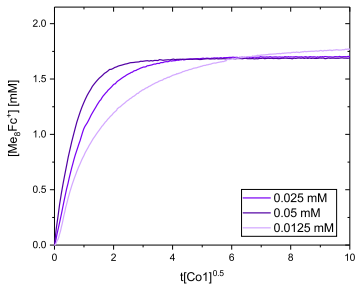

(a) $\mathbf{Co1_{O_2}}$ VTNA factor: 0.5

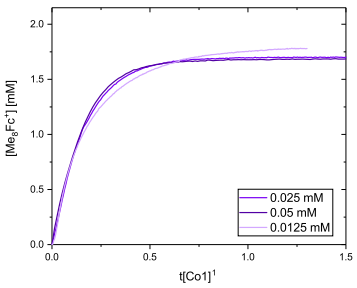

(b) $\mathbf{Co1_{O_2}}$ VTNA factor: 1

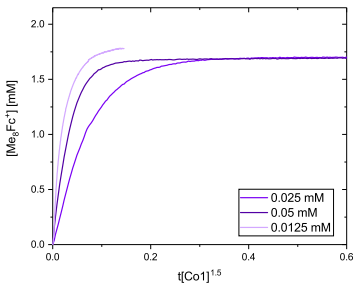

(c) $\mathbf{Co1_{O_2}}$ VTNA factor: 1.5

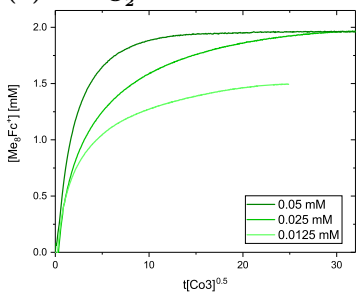

(d) $\mathbf{Co3_{O_2}}$ VTNA factor: 0.5

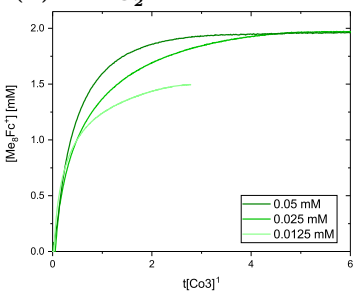

(e) $\mathbf{Co3_{O_2}}$ VTNA factor: 1

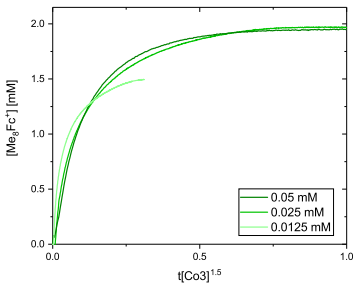

(f) $\mathbf{Co3_{O_2}}$ VTNA factor: 1.5

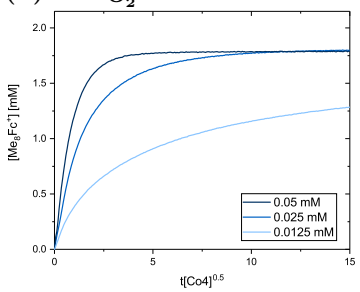

(g) $\mathbf{Co4_{O_2}}$ VTNA factor: 0.5

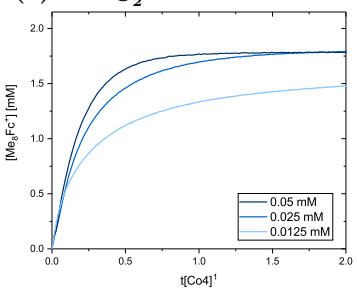

(h) $\mathbf{Co4_{O_2}}$ VTNA factor: 1

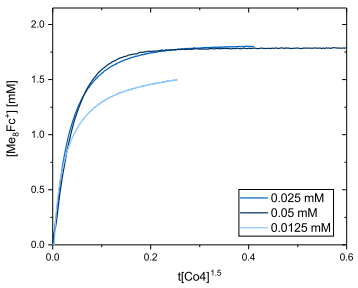

(i) $\mathbf{Co4_{O_2}}$ VTNA factor: 1.5

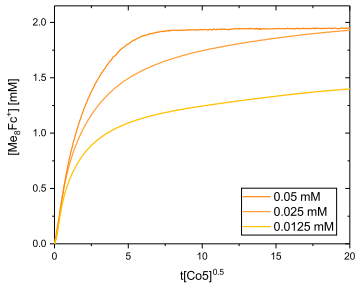

(j) $\mathbf{Co5_{O_2}}$ VTNA factor: 0.5

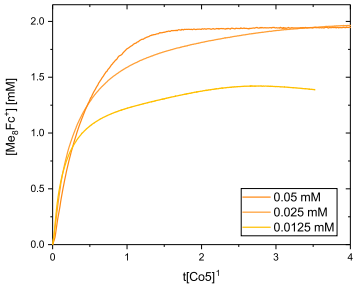

(k) $\mathbf{Co5_{O_2}}$ VTNA factor: 1

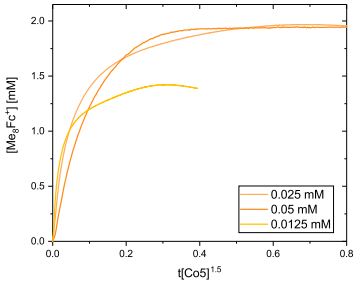

(l) $\mathbf{Co5_{O_2}}$ VTNA factor: 1.5

is first order. This suggests that although $\mathbf{Co4_{O_2}}$ has lower rates than $\mathbf{Co1_{O_2}}$, the mechanism of reactivity towards O_2 is similar. The inclusion of an amine substituent on the pyrazole backbone results in a reduced rate of O_2 reduction activity, although the reaction likely proceeds via the same mechanistic pathway. In the oxidation from the μ-Cl to the μ-OO species, $\mathbf{Co4_{Cl}}$ shows the second fastest rate after $\mathbf{Co1_{O_2}}$, again suggesting that the inclusion of the amine group on the ligand backbone reduces the

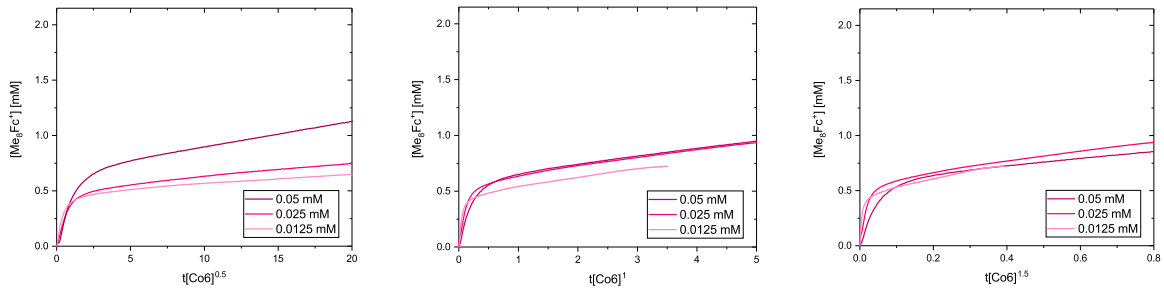

(m) $\mathbf{Co6_{O_2}}$ VTNA factor: 0.5 **(n)** $\mathbf{Co6_{O_2}}$ VTNA factor: 1 **(o)** $\mathbf{Co6_{O_2}}$ VTNA factor: 1.5

Figure 3.32: VTNA studies for $\mathbf{Co1_{O_2}}$ – $\mathbf{Co6_{O_2}}$ (excluding $\mathbf{Co2_{O_2}}$ due to low conversion). Each complex is plotted with three different VTNA factors, detailed underneath each graph. (0.5, 1, 1.5, 2). [Me_8Fc] = 2 mM, [TFA] = 50 mM.

rate of reaction towards O_2. However, the similarity in rate and reaction order suggests that this is not due to a change in reaction mechanism.

Unlike $\mathbf{Co1_{O_2}}$ and $\mathbf{Co4_{O_2}}$, the VTNA results and initial rates analysis (Figure A.15) do not suggest a clear order in catalyst for $\mathbf{Co3_{O_2}}$, $\mathbf{Co5_{O_2}}$ and $\mathbf{Co6_{O_2}}$. Therefore, it is not possible to confirm that the functionalised complexes share the mechanism for ORR with $\mathbf{Co1_{O_2}}$.

Due to the unusual activity displayed by $\mathbf{Co6_{O_2}}$ interpretation of the VTNA results is more challenging. In the earlier stages of the reaction an order of 0.5 was observed. However, after the initial burst the reaction slows to a steady increase where a VTNA factor of 1 results in a better overlap between the concentration profiles. Although Bures shows that VTNA can be used to determine the order in examples where the order in catalyst varies with changing catalyst concentration,[233] the fits for $\mathbf{Co6_{O_2}}$ are not adequate to claim an order in catalyst, and are further complicated by the clear deactivation of catalyst at low concentrations.

The biexponential fits also reveal that there are multiple mechanisms involved in the production of Me_8Fc^+ in the presence of $\mathbf{Co6_{O_2}}$. This suggests that there could be a competing mechanism, and the catalyst deactivation only effects the species that shows fast activity. Alternatively, the slow component could be activity from the deactivation product, which is less clear in the other complexes since initial turn-over and conversion is higher.

As discussed in Section 4.1.1, the introduction of a nitro group on the pyrazole backbone of the bpp ligand has previously been shown to result in a significant reduction in the

rate of water oxidation in ruthenium catalysts, which is attributed to inductive effects through the bpp ligand.[178] A similar process could be the cause of the notably different behaviour of $\mathbf{Co6_{O_2}}$. The resonance effect of the nitro group draws electron density away from the cobalt centres, making oxidation of the cobalt centres less favourable. The slow rate of ORR with $\mathbf{Co6_{O_2}}$ is consistent with oxidation of the cobalt centres as part of the rate determining step, which could correlate to the O_2-binding step and concurrent oxidation of the two Co^{II} centres to Co^{III}, Figure 3.1.

It is also possible that water, which is a product of the reaction, is causing product inhibition, reducing the rate of reaction and preventing high catalyst turnover. Alternatively, H_2O_2 is sometimes formed in incomplete O_2 reduction reactions, and could act as an inhibitor, potentially explaining the lower rates of reactivity for $\mathbf{Co2_{O_2}}$ – $\mathbf{Co6_{O_2}}$. Although it is possible to include potential catalyst deactivation or product inhibition into the VTNA normalisation factor, the poor quality of the VTNA results means this is unlikely to provide clarity to the results. It would be possible to investigate product inhibition or catalyst deactivation through spiking the reaction with water, or reintroducing Me_8Fc after turnover plateaus, respectively, and determining the impact, if any, on the rate. If there is competition between catalyst turnover and deactivation, low catalyst loadings may result in a rate of turnover that is too slow to prevent degradation. If catalyst deactivation is occurring, there should be turnover, but at a reduced rate. Strategies to investigate this further are discussed in Section 3.8.1.

3.5.2 Testing the sequence of reactivity of the complexes under ORR conditions

Some of the results reported in Section 3.5.1 suggested that there was catalyst degradation occurring under reaction conditions. Therefore, in order to confirm the stability of the complexes under catalytic conditions, the complexes were mixed with TFA and Me_8Fc separately and monitored using UV-vis spectroscopy. Additionally, these studies will help determine whether the proposed rate determining step (RDS) is PCET (middle route, Scheme 3.4), or whether electron or proton transfer occur independently of each other, Scheme 3.4. As drawn in Figure 3.1, the proposed RDS suggests that electron transfer occurs between the Me_8Fc and the cobalt complex under a reversible process, followed by protonation. If the LUMO of the complex is on the cobalt centres, it should be possible to observe the electron transfer, due to the change in oxidation state of the cobalt centre and oxidation of the Me_8Fc, and protonation of the com-

plex, by UV-vis spectroscopy. This allows the investigation of the RDS and potential degradation pathways by the same set of experiments.

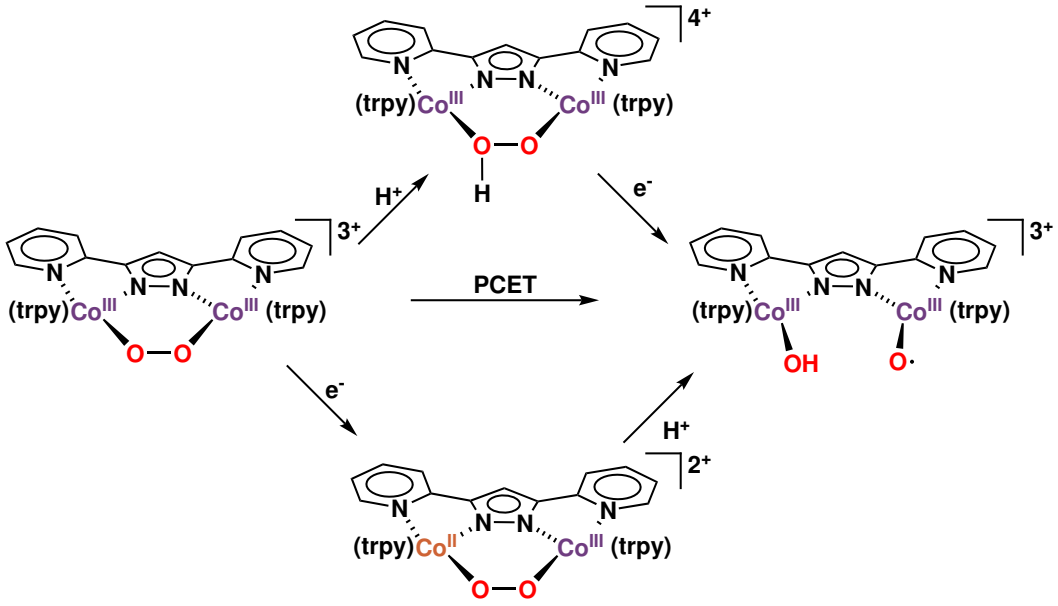

Scheme 3.4: The rate-determining step (RDS) proposed by Llobet and coworkers for the ORR catalysed by $\mathbf{Co1_{O_2}}$ is proton-coupled electron transfer. However, in the full cycle, shown in Figure 3.1, the authors propose that the PCET proceeds *via* the reduction, followed by protonation route.

The studies were conducted in a stirred cuvette containing the cobalt complex, data collection was started before addition of Me_8Fc or TFA (final concentrations: [Co] = 0.025 mM, Me_8Fc = 2 mM, TFA = 50 mM). The solution was then removed from the cuvette and stored in a sealed vial for 15 minutes, before transfer back into the cuvette to collect a second data point.

Although there were slight shifts in the location of the peak associated with the Co complexes of $\approx$ 5 – 10 nm for $\mathbf{Co1_{O_2}}$ – $\mathbf{Co5_{O_2}}$ the peaks were stable over 15 minutes in the presence of both TFA and Me_8Fc, which is almost 10 times longer than the ORR reaction times above. The spectra can be found in the Appendix (Figure A.16 and Figure A.17). Since there is catalytic turnover for all complexes, it is clear that deactivation is occuring later in the catalysts, but the lack of change for $\mathbf{Co1_{O_2}}$ – $\mathbf{Co5_{O_2}}$ suggests that neither Me_8Fc or TFA alone results in significant changes to the complexes.

$\mathbf{Co6_{O_2}}$ showed a pronounced difference in the presence of Me_8Fc over a 15 minute

timescale, Figure 3.33, with a clear decrease in the intensity of the $\mathbf{Co6_{O_2}}$ peak at around 550 nm and the Me_8Fc peak at around 425 nm. There is a very minor increase at 750 nm, possibly suggesting some minor electron transfer from Me_8Fc to $\mathbf{Co6_{O_2}}$ (since Me_8Fc^+ is observed at 750 nm). The change in spectrum shown in Figure 3.33 might therefore indicate that Me_8Fc is thermodynamically capable of reducing $\mathbf{Co6_{O_2}}$ without the addition of acid, and the change in UV-vis spectrum is due to electron transfer occurring, rather than deactivation of the complex in the presence of Me_8Fc.

$\mathbf{Co6_{O_2}}$ has an E_{mid}(red) value for the first reduction of the complex to a mixed $Co^{III}Co^{II}$ state of -0.29 V which is the lowest reduction potential reported for any of the six complexes ($\mathbf{Co2_{O_2}}$ also has a value of -0.29 V), as shown in Figure 3.14. The oxidation potential of Me_8Fc is -0.13 V vs NHE, which is a potential gap of 0.16 V. This gap suggests that electron transfer from Me_8Fc to $\mathbf{Co6_{O_2}}$ is not thermodynamically favourable, which is supported by the lack of change observed for $\mathbf{Co2_{O_2}}$, which also has an E_{mid}(red) value of -0.29 V. Note that the conditions in the reaction vessel are not identical to those of the CVs, which were run using rigorously dried and degassed acetonitrile, which may have shifted the potentials. However, in the presence of TFA, $\mathbf{Co6_{O_2}}$ did not show any change by UV-vis, Figure A.17. It would be expected that if the Me_8Fc is capable of reducing the complex without the presence of TFA, the observed catalytic activity would be greater for this complex, but this is not what is observed. Finally, although there is a very minor increase at 750 nm at 15 minutes in Figure 3.33, which is indicative of the formation of Me_8Fc^+, it is within the margin of error.

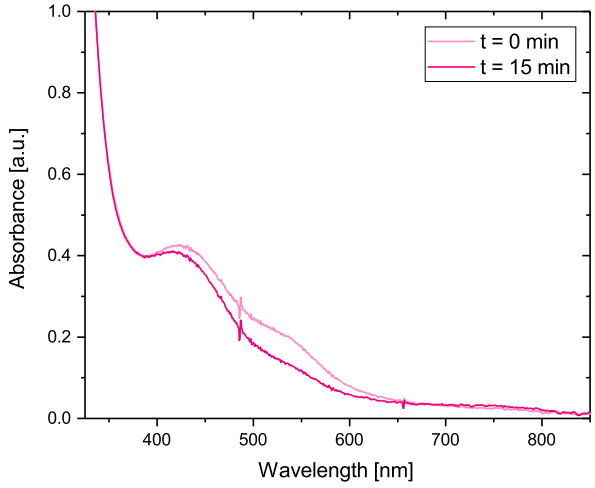

Figure 3.33: $\mathbf{Co6_{O_2}}$ in the presence of Me_8Fc. [Co] = 0.025 mM, [Me_8Fc] = 2 mM, T = 20 °C.

With the exception of $\mathbf{Co6_{O_2}}$ it is clear that neither electron transfer or protonation occur independently of each other, confirming that the first step in the reaction process is PCET. Proton coupled electron transfer allows high energy intermediates, such as the reduced or protonated species, to be circumvented which allows the direct formation of the thermodynamically favourable product of PCET (Scheme 3.4).[111]

However, these findings alone do not reveal whether this first PCET step is rate-determining. It would be possible to investigate this further by carrying out a reaction of the cobalt complex in the presence of Me_8Fc and acid, but without the inclusion of O_2 to prevent catalytic turnover, which should allow the rate of electron transfer to be monitored. Comparison of this rate to the rate of ORR should help determine whether the initial PCET is part of the rate determining step. This is discussed further in the Future Work, Section 3.8.1.

3.5.3 Comparison of ORR results with Electrochemical Properties and Oxidation Reactivity

A comparison of the ORR initial rates with the initial rate data for the oxidation of the complexes from the μ-Cl to the μ-OO species, as discussed in Section 3.3.2, reveals a weak correlation, Figure 3.34. The six complexes can be broadly categorised into two groups, with $\mathbf{Co1_{O_2}}$ and $\mathbf{Co4_{O_2}}$ showing high rates for ORR and also displaying fast rates for the oxidation studies. Conversely, the other four complexes show low activity for ORR also show slow oxidation rates.

Both **Co1** and **Co4** showed fast rates for both reactions, with $\mathbf{Co1_{O_2}}$ considerably faster at both ORR and the oxidation studies than the other five complexes. These two complexes also showed first order kinetics for the ORR reaction (Figure A.15) suggesting that although substitution on the ligand backbone reduces the rate, the mechanism of reactivity towards O_2 is the same for both complexes.

Co3 and **Co5** showed similar rates to each other, which is interesting given the different inductive properties of the functionalisation on the bpp^- pyrazole (methyl and bromo, respectively). Although both methyl- and bromo- groups have relatively weak inductive effects,[204] the impact of these substituents is clearly observed in the electrochemical properties of the complexes, as discussed in Section 3.4. It is of note that that difference in electrochemical properties did not have a pronounced effect on their reactivity in the ORR, as can be seen in the similarty of their rates.

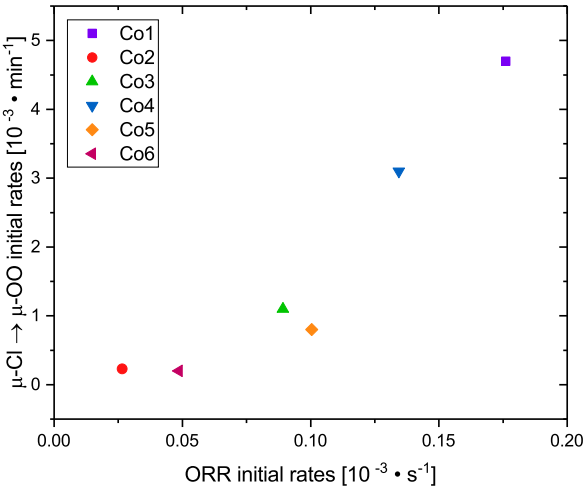

Figure 3.34: Initial rates of ORR plotted against initial rates of oxidation from the Co^{II}_2 μ-Cl species to the Co^{III}_2 μ-OO species, using the initial rates shown in Table 3.2. Linear fit of the data points shows a weak correlation between the two sets of data ($R^2 = 0.88$).

The correlation of the oxidation rates of the μ-Cl complexes with the ORR activity is interesting, as it potentially suggests that the reoxidation and O_2 binding from the Co^{II}_2 species in the ORR catalytic cycle is significant. Previous studies by Llobet and coworkers into the reactivity of $\mathbf{Co1_{O_2}}$ looked at the rate of catalysis when starting the reaction from the aqua-hydroxo species shown in Figure 3.1. Their study suggested that the re-oxidation of the Co^{II}_2 species and binding of O_2 were not rate limiting for $\mathbf{Co1_{O_2}}$. Llobet and coworkers also investigated whether the ORR with $\mathbf{Co1_{O_2}}$ was O_2 limited, finding that it was not.[113] The correlation illustrated in Figure 3.34 could simply indicate that complexes that are active for ORR are also more oxophilic, resulting in higher rate of oxidation, rather than a causal relationship.

Co2 and **Co6** showed very low rates of oxygen reduction activity. As previously discussed in Section 3.3.2, these two complexes also show low rates of oxidation from the μ-Cl → μ-OO species, as can be seen in Figure 3.34. It is proposed that the oxidation reaction proceeds *via* displacement of the μ-chloro before binding of O_2, as outlined in Figure 3.4. Since both reactions share a common step, the binding of O_2, it is therefore plausible that this step is rate limiting for these two complexes. Although the reaction of $\mathbf{Co1_{O_2}}$ with O_2 was not found to be limiting, the pronounced difference in reactivity for **Co2** and **Co6** suggests that the ORR might proceed *via* a different reaction mechanism, where reaction with O_2 does become limiting. Further, in a comparison of the rates of ORR with the reduction potentials of the complexes, Figure 3.35, a lack of

correlation is observed. This suggests that the redox potentials of these two complexes do not affect the rate of reaction.

Llobet and coworkers proposed that the RDS for the ORR with $\mathbf{Co1_{O_2}}$ (Scheme 3.4) is PCET. They state that addition of acid is necessary for catalysis by shifting the reduction potential of the cobalt catalyst such that Me_8Fc is capable of reducing the complex.[113] If PCET were rate determining for all six complexes, there should be a correlation between the ORR rates and the $E_{red1'}$ values, since $E_{red1'}$ simulates PCET under electrochemical conditions. However, the clear lack of correlation between the initial rates and the $E_{red1'}$ results, Figure 3.35 suggest that there is another factor in play in terms of the reaction mechanism, which is likely to be O_2-binding. The lack of correlation across the series of six complexes does not mean that PCET is not rate determining for all complexes, rather that different mechanisms might be at play for different complexes.

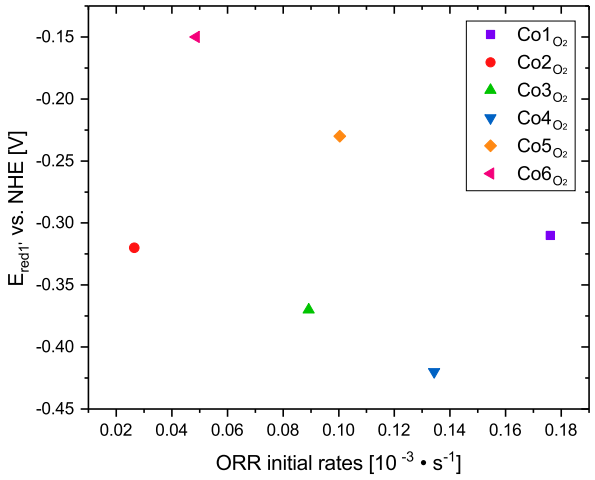

Figure 3.35: Initial rates of ORR plotted against the $E_{red1'}$ values for the six complexes in the presence of 4 mM TFA, Figure 3.26.

Although there is a correlation between the O–O bond lengths and E_{red2} (3.23b), attributed to what is assumed to be the breakage of the O–O, there was no correlation observed between the ORR initial rates and O–O bond length, (Appendix, Figure A.19). PCET is part of the reaction mechanism, as demonstrated in Section 3.5.2, but unlike the literature studies on $\mathbf{Co1_{O_2}}$, the rate of catalysis is also correlated to O_2 binding, Figure 3.34, suggesting this is an important step in the reaction mechanism.

3.5.4 Conclusion to ORR studies

All six μ-OO complexes show activity for the oxygen reduction reaction. However, the rates of activity vary markedly between the complexes, and all six complexes show deactivation during catalysis, which is more pronounced at low loadings. The unsubstituted $\mathbf{Co1_{O_2}}$ shows the fastest rates, and using VTNA, initial rates and log/log plots the order in catalyst is confirmed to be 1, supporting previous studies on this complex.[113] However, VTNA revealed low levels of catalyst deactivation for $\mathbf{Co1_{O_2}}$, indicated by a slight deviation in the VTNA profiles at low loadings, which has not been observed for $\mathbf{Co1_{O_2}}$ before.

Both $\mathbf{Co2_{O_2}}$ and $\mathbf{Co6_{O_2}}$ showed very slow rates with biexponetial behaviour and clear indications of catalyst degradation under catalytic conditions. Interestingly, $\mathbf{Co6_{O_2}}$ was shown to be reducible by Me_8Fc in the absence of protons, unlike the other complexes, although this did not result in higher activity in the ORR.

$\mathbf{Co3_{O_2}}$, $\mathbf{Co4_{O_2}}$ and $\mathbf{Co5_{O_2}}$ show similar rates to each other and show a clear improvement on the overall yield when compared to $\mathbf{Co1_{O_2}}$. However, all three complexes have clear catalyst deactivation at low catalyst loadings. The VTNA data was not good enough for these three complexes to draw conclusions on the order of reaction in catalyst. The inclusion of an amine on the pyrazole backbone in $\mathbf{Co4_{O_2}}$ resulted in reduced rates, potentially due to the notably higher E_{mid}(red) value of the first reduction of the complex to the mixed Co^{II}/Co^{III} state relative to $\mathbf{Co1_{O_2}}$, Figure 3.14. The initial rates and log/log plots for $\mathbf{Co3_{O_2}}$ and $\mathbf{Co5_{O_2}}$ suggest an order of 0.5 in catalyst. This suggests the mechanism of ORR is different to that of $\mathbf{Co1_{O_2}}$ and $\mathbf{Co4_{O_2}}$. However, non-integer orders in catalyst can be complex to assign, and further experiments would be necessary to determine the mechanism, as discussed further in Section 3.8.1.

The proposed mechanism by Llobet and coworkers suggests that the initial PCET is the rate limiting step.[113] However, the lack of correlation between the ORR rates and the electrochemical results in the presence of acid suggest that the accessibility of the first reduction of the complex to the $Co^{III}Co^{II}$ state is not rate limiting, although this might be due to the relatively low concentration of acid added in the electrochemical studies. The studies with $\mathbf{Co1_{O_2}}$ – $\mathbf{Co6_{O_2}}$ in the presence of just Me_8Fc or TFA support the hypothesis that the complexes undergo PCET, since with the exception of $\mathbf{Co6_{O_2}}$ there is no electron or proton transfer observed in the absence of the other. However, in order to determine whether the first PCET step is rate limiting will require further studies,

as discussed in Section 3.8.1.

The strong correlation shown in Figure 3.34 between the ORR rates and the oxidation from the μ-Cl species to the μ-OO species (Section 3.3.2) suggests that the latent oxophilicity of the complex is a reasonable indicator of its reactivity. This also indicates that the reoxidation step could be rate limiting for some complexes. According to the proposed catalytic cycle (Figure 3.1) the final step is an elimination of water, followed by the binding of O_2, and corresponding oxidation of the metal centres. The liberation of water, which is produced in the reaction, and the corresponding reoxidation to the Co_2^{III} state could be the rate determining step. Potential experiments to further explore this are discussed in Section 3.8.1.

The finding that both $\mathbf{Co2_{O_2}}$ and $\mathbf{Co6_{O_2}}$ display biexponential behaviour in the ORR suggests that there are two mechansims at play in the formation of Me_8Fc. One of these is very slow, and it is possible that such a mechanism is also present in the other complexes, but due to the high rates of the main component is not observable.

3.6 Oxygen Atom Transfer Studies

Although $\mathbf{Co1_{O_2}}$ has been studied for ORR and water oxidation, its reactivity towards substrates or for oxidation chemistry has not been studied. The reactivity of $\mathbf{Co1_{Cl}}$ – $\mathbf{Co6_{Cl}}$ towards O_2 has been investigated in Section 3.3.2, where $\mathbf{Co1_{Cl}}$ was found to be the most active, followed by the amine substituted $\mathbf{Co4_{Cl}}$. However, in oxygen atom transfer (OAT) studies, it is the ability of the complex to transfer the oxygen to a substrate that will be investigated. For a complex to be active for catalytic aerobic oxidation, it must both activate O_2, and transfer it to a substrate, in order to complete the catalytic cycle. $\mathbf{Co1_{O_2}}$ – $\mathbf{Co6_{O_2}}$ will be studied for their OAT reactivity towards a range of substrates.

3.6.1 Substrate Screening

A series of potential substrates were chosen that should represent the full range of activity discussed previously in Section 1.3, the reactivity of the substrate is included in Table 3.9. As oxygen atom transfer generally results in the transfer of one oxygen atom to a substrate, the presence of two oxygen atoms in the cobalt complexes suggests that it might be possible for the transfer to occur twice, Scheme 3.5. In order to investigate this possibility, in the initial screening tests, two equivalents of substrate were included, relative to the cobalt complex. Substrate screening was carried out using

$\mathbf{Co1_{O_2}}$ as a benchmark complex, before all six complexes being screened for reactivity towards promising substrates. Reactions were carried out under an inert atmosphere in order to rule out aerobic oxidation of the substrate, and heated to 50 °C in order to promote the reaction but not boil the solvent.

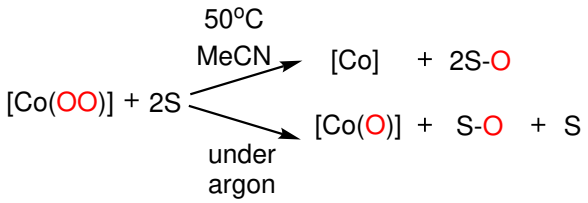

Scheme 3.5: Two potential outcomes from an oxygen atom transfer from $\mathbf{Co1_{O_2}}$ – $\mathbf{Co6_{O_2}}$ to two equivalents of a substrate (S).

The results of the initial screening tests are shown in Table 3.9. The reactions were monitored by ^{1}H NMR spectroscopy with spectra collected periodically and the NMR tubes heated at 50 °C in between measurements. No reaction was observed for any of the electrophilic substrates, or for the epoxidation with styrene. There were very low levels of benzene observed in the reaction with 1,4-cyclohexadiene, which suggests that the reaction could be a radical process, since 1,4-cyclohexadiene is reported to have radical activity.[249] The low levels of benzene formation can be seen in the ^{1}H NMR spectra shown in Figure 3.37. However, after 5 days of heating at 50 °C, conversion remained below 10%. The reaction with $\mathbf{Co1_{O_2}}$ did not result in the formation of any paramagnetic species, nor any change to $\mathbf{Co1_{O_2}}$, as determined by ^{1}H NMR spectroscopy. This suggests that the reaction did not result in a change in oxidation state of $\mathbf{Co1_{O_2}}$ in levels detectable by ^{1}H NMR spectroscopy. Due to the low levels of conversion, the reaction was not investigated further.

Upon addition of $\mathbf{Co1_{O_2}}$ to the benzaldehyde solution, however, a colour change from purple to orange/brown occurred almost immediately, Figure 3.36. The orange/brown colour is similar to the colour observed when the μ-Cl complexes were dissolved in solution (as seen in Chapter 2, Figure 2.24), which suggests that the reaction between the benzaldehyde and $\mathbf{Co1_{O_2}}$ resulted in a change in the oxidation state of the cobalt complex. This was accompanied by the appearance of new peaks in the ^{1}H NMR spectra in both the para- and diamagnetic regions, supporting the proposal that the reaction results in a change in oxidation state. The characterisation of these peaks is discussed further in Section 3.6.2.

Table 3.9: Oxidation test reactions carried out with $\mathbf{Co1_{O_2}}$ on an NMR scale. Reaction volume = 0.5 mL, [$\mathbf{Co1_{O_2}}$] = 20 mM, [substrate] = 40 mM, solvent = MeCN (dried, degassed), heat at 50 °C

Substrate	Expected product	Reactivity by Complex	Outcome
PPh_3	$O{=}PPh_3$	Electrophilic[120]	No reaction
Styrene	Styrene oxide	Electrophilic[123]	No reaction
Diphenyl sulphide	Diphenyl sulfoxide	Electrophilic[120]	No reaction
1,3-cyclohexadiene	Benzene	Radical Reaction	No reaction
1,4-cyclohexadiene	Benzene	Nucleophilic[120]	Low levels benzene (< 10%)
Benzaldehyde	Benzoic acid	Nucleophilic[120]	Appearance of new peaks by ^{1}H NMR, colour change observed (purple to orange, Figure 3.36)

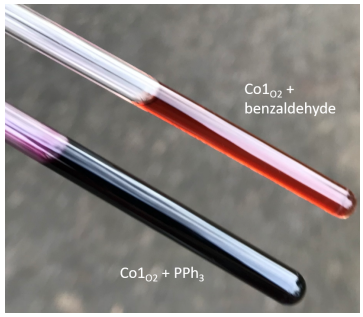

Figure 3.36: A solution of $\mathbf{Co1_{O_2}}$ with benzaldehyde in comparison with $\mathbf{Co1_{O_2}}$ with PPh_3, showing the difference in colour after 10 minutes.

3.6.2 Identifying the Product(s) of the Reaction with Benzaldehyde

Wide spectral width ^{1}H NMR spectroscopy showed that there was a mixture of both dia- and paramagnetic products in solution, which suggested than not all Co^{III} species were reduced to Co^{II} species. The ^{1}H NMR spectra shown in Figure 3.38 show that upon the initial addition of benzaldehyde to a solution of $\mathbf{Co1_{O_2}}$ there were a large mixture of species in solution, (orange spectra), that gradually, over the course of a week, formed one main product with a small number of unidentified peaks (120 hr, blue spectra). It is clear in Figure 3.38 that there is no unreacted $\mathbf{Co1_{O_2}}$ left in solution. It is also worth

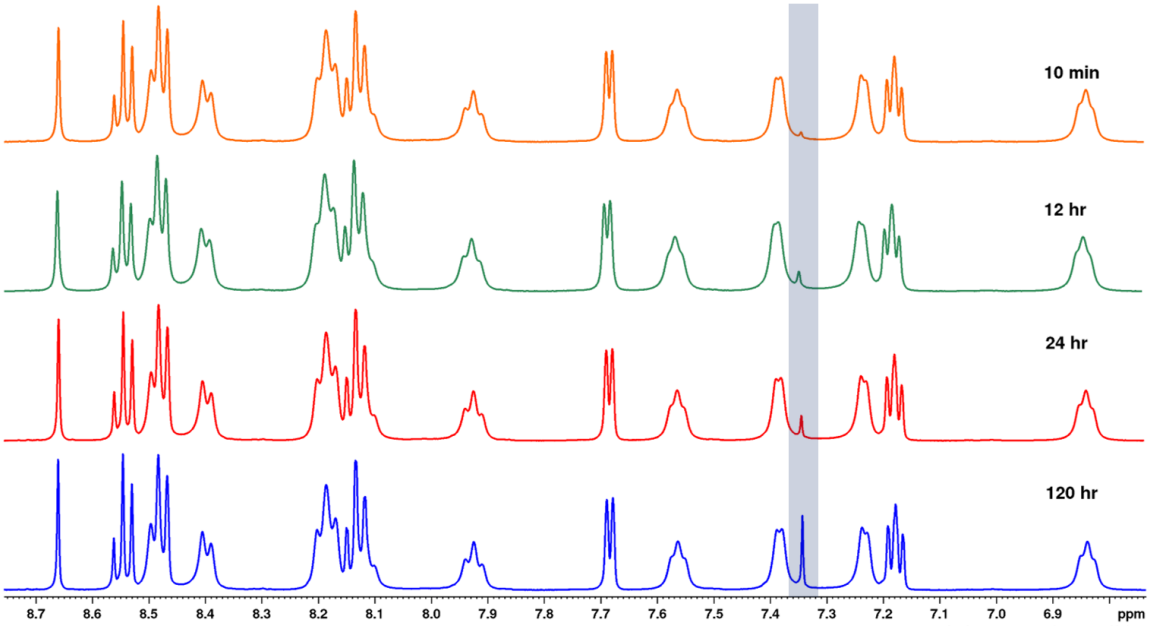

Figure 3.37: ^{1}H NMR spectra of a solution of $\mathbf{Co1_{O_2}}$ (20 mM) with 1,4-cyclohexadiene (40 mM) over time, showing the lack of change to the $\mathbf{Co1_{O_2}}$ peaks and the increase in the peak attributed to benzene highlighted in blue. *Note: This is a dehydrogenative oxidation (with water as the byproduct) by the complex, rather than OAT.*[120]

noting that these reactions were conducted on an NMR scale (0.5 ml) in air-free NMR tubes, so although they were heated at 50 °C the mass transfer and mixing in an NMR tube is sub-optimal.

The doublet at 5.4 ppm which grows in over time (Figure 3.38) appears to be a diagnostic peak, corresponding to a new species in solution. In order to confirm that the peak at 5.4 ppm is coordinated to the cobalt complex, diffusion ordered spectroscopy (DOSY) spectroscopy was employed. Using a sample that had been spiked with excess benzaldehyde, it can be seen clearly in Figure 3.39 that the aromatic peaks and peak at 5.4 ppm diffuse at the same rate, confirming that they are all part of the same species.

Having confirmed that the doublet was part of the complex, a series of 2D spectra were employed to attempt to assign the rest of the peaks. In the ruthenium benzoate analogue which was discussed in the introduction (Section 3.1.2), the authors identified the benzoate peaks as being present between 6 and 7 ppm. They identified a doublet at 5.7 ppm, slightly further upfield than in the cobalt analogue, which they assigned to a proton on the bpp or terpyridine backbone.[225] However, the authors did not provide any 2D spectra as evidence of this, and this assignment does not seem consistent with

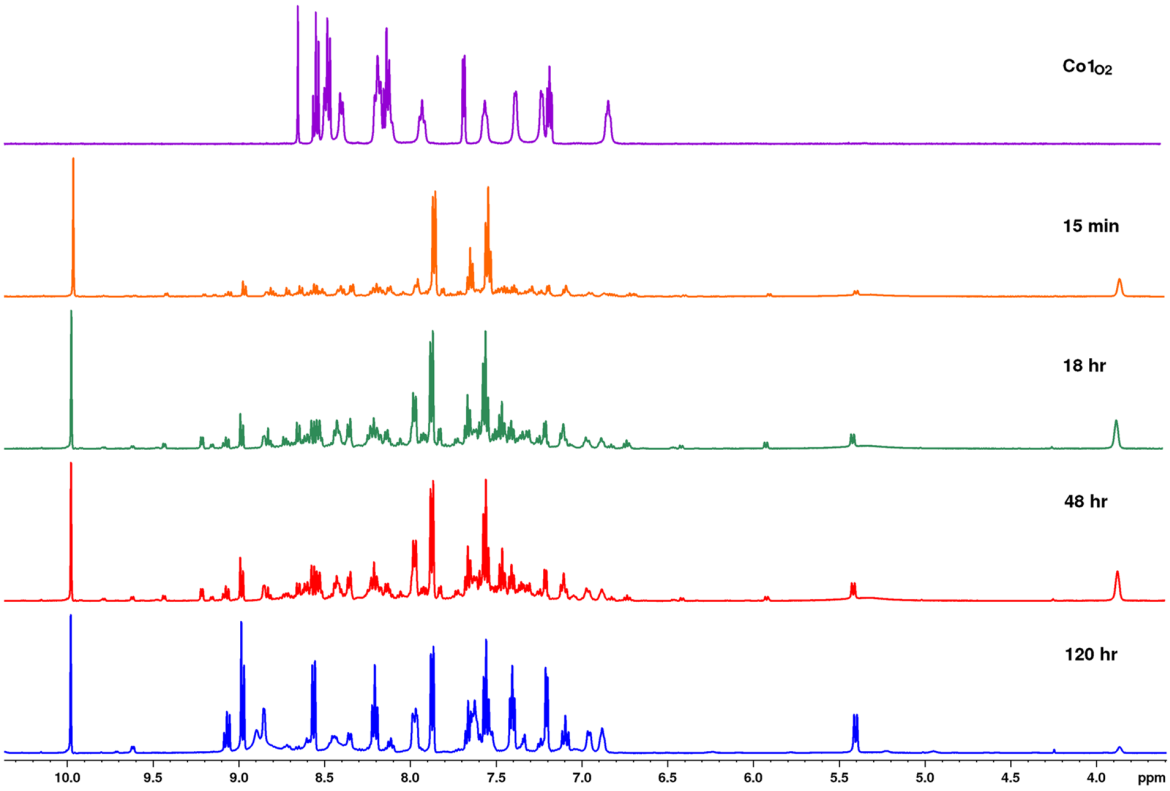

Figure 3.38: An overlay of $\mathbf{Co1_{O_2}}$ (purple) and the aromatic region of the spectrum at various time points after the addition of benzaldehyde. (Conditions: $[\mathbf{Co1_{O_2}}] = 20\,\text{mM}$, [benzaldehyde] = 40 mM, T = 50 °C), solvent = MeCN (0.5 mL))

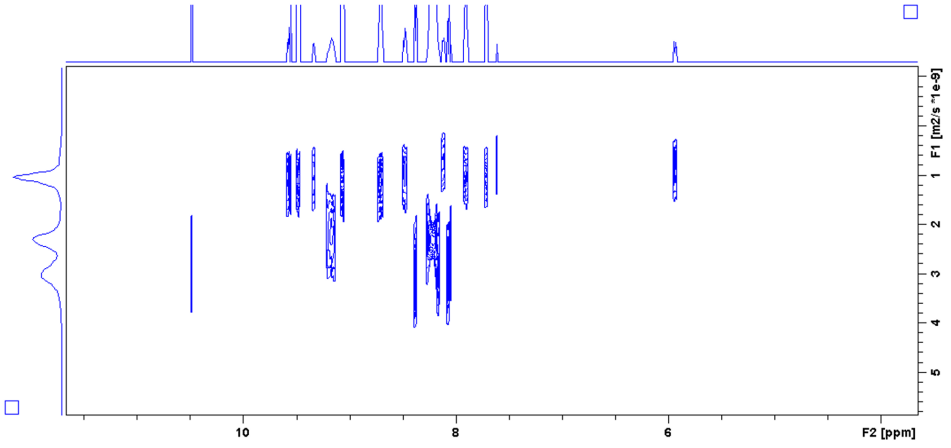

Figure 3.39: DOSY spectrum showing clearly that the peak at 5.5 pm diffuses at the same rate as the other aromatic peaks, whilst the benzaldehyde diffuses faster, with a potential impurtity at 9 ppm.

the results for the cobalt complex presented below.

Using a combination of 2D spectra, including COSY, HSQC, HMBC and H2BC, the spectra of $\mathbf{Co1_{O_2}}$ with two equivalents of benzaldehyde has been tentatively assigned as a benzoate adduct (see Appendix, Section A.2.6 for 2D spectra). Due to overlaps between the peaks, unreacted benzaldehyde, the presence of paramagnetic species and low levels of side products in the aromatic region of the ^{1}H NMR, it was not possible to fully assign the spectra. However, there are some conclusions that can be drawn to help postulate about the structure of the diamagnetic complex.

The spectrum shown in Figure 3.40 shows the tentative assignments for the product of the reaction. The peaks corresponding to the terpyridine ligands have been confidently assigned, as shown in blue, using 2D correlation spectra. Most peaks are shifted to higher ppm values than in $\mathbf{Co1_{O_2}}$ and the peaks are relatively well-defined. Using a COSY spectrum, the three proton peaks associated with the benzoate adduct have also been assigned (shown in green). The peak at 5.4 ppm is identified as the ortho protons on the benzoate adduct, and are correlated to the meta protons, which are correlated to the single para proton. The para proton overlaps with a peak that is thought to be part of the bpp ligand.

Unfortunately, assignment of the five bpp protons was more challenging. This is particularly true of the singlet associated with the pyrazole backbone, which, in $\mathbf{Co1_{O_2}}$ is found more downfield than the peaks associated with the terpyridine ligands, but cannot be identified in the spectra shown in Figure 3.40. The position of the four protons on the pyridine ring are tentatively identified using cross-peaks in the COSY and ^{13}C correlation spectra, although not specifically assigned, Figure 3.40. 2D spectra can be found in the Appendix, Section A.2.6.

Having tentatively assigned the diamagnetic peaks to a benzoate adduct, attention was turned to the paramagnetic species. As discussed in Section 2.4.2 in order to fully characterise paramagnetic species, computational chemistry techniques must be employed. However, by comparing the paramagnetic spectra of the product to $\mathbf{Co1_{Cl}}$, Figure 3.41, it is possible to identify some peaks which correlate to each other. Most notably, the two singlets at $\approx$ 65 ppm are clearly visible and can be confidently assigned as being part of the terpyridine ligand. Using the integral of these peaks to compare to the diamagnetic region of the spectrum it was possible to calculate the ratio between the two, revealing a roughly 2:1 ratio between diamagnetic : paramagnetic species in

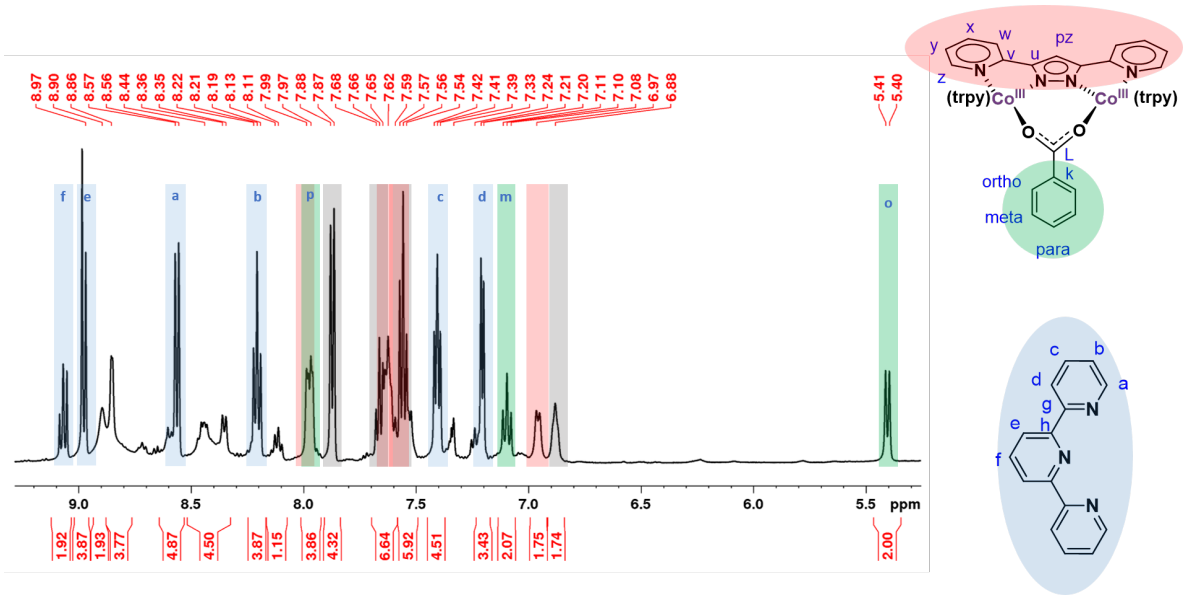

Figure 3.40: Tentatively assigned spectrum of the product from the reaction between $\mathbf{Co1_{O_2}}$ and 2 equivalents of benzaldehyde after 120 hr. Unreacted benzaldehyde or peaks identifed as paramagnetic species highlighted in grey. Other assignments as shown. (Conditions: [$\mathbf{Co1_{O_2}}$] = 20 mM, [benzaldehyde] = 40 mM, T = 50 °C), solvent = MeCN (0.5 mL)

solution.

In a recent report a benzoate-bridged bimetallic cobalt species, with a mixed $Co^{III/II}$ state, was reported to be active for oxidation chemistry.[250] A mixed $Co^{III/II}$ complex would be paramagnetic, but the similarity between some of the peaks observed in the paramagnetic spectra shown in Figure 3.41 of the product of the benzaldehyde reaction (bottom) and $\mathbf{Co1_{Cl}}$ (top) suggests that the oxidation state and electronic environment of the metal centres is similar. This is most notable with the two singlets between 65 – 75 ppm, corresponding to peaks *d* and *e* on the terpyridine ligands. It is therefore unlikely that the paramagnetic product of the reaction between $\mathbf{Co1_{O_2}}$ and benzaldehyde is a mixed $Co^{III/II}$ complex, since it is expected that this would result in a significant shift in the peaks.

However, there are two peaks between -10 and -20 ppm in the bottom spectrum (blue) of Figure 3.41. These are considerably different to those observed in the $\mathbf{Co1_{Cl}}$ spectrum (red), which are likely a new resonance, rather than a shift of an existing signal. Unfortunately, without the use of computational techniques, and in the absence of mass spectrometry or X-ray crystallography data it is not possible to assign the paramagnetic peaks. Additionally, since the spectra are run without solvent suppression, the

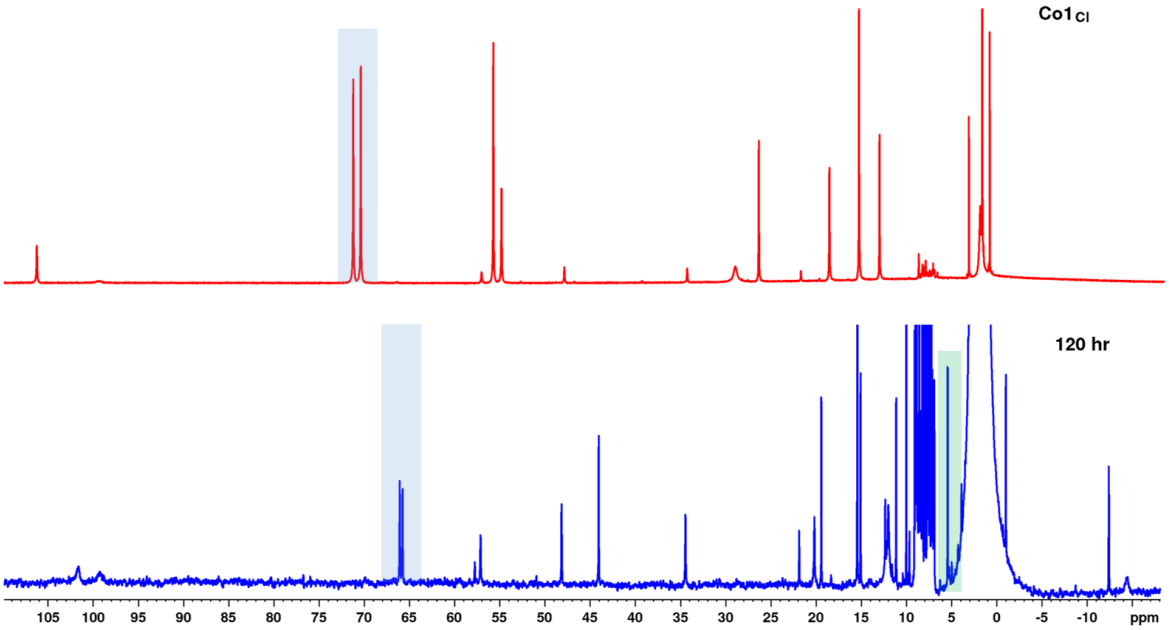

Figure 3.41: ^{1}H NMR spectra showing $\mathbf{Co1_{Cl}}$ (top) and the paramagnetic species after the reaction of $\mathbf{Co1_{O_2}}$ with benzaldehyde, shown at 120 hr (bottom). The diagnostic peaks are highlighted, with the two peaks between 65 and 70 ppm correlating to 8 protons (see Section 2.4.2) and the doublet around 5.5 ppm. The integrals can be found in Appendix, Figure A.21. *Note: the complex is contaminated by some Co(trpy)Cl_2, present in that batch of catalyst.*

integrals of some peaks will be distorted, and a number of the peaks lie in the aromatic region of the diamagnetic species, again complicating assignment. The wide-spectral width spectrum can be found in the Appendix, Figure A.21.

Using the diagnostic peaks at 5.5 ppm allowed the ratio of cobalt complex to unreacted benzaldehyde to be calculated, revealing that there is twice as much benzaldehde in the solution as resultant cobalt complex. This suggests the ratios as shown in Figure 3.42.

The use of mass spectrometry confirmed the presence of the Co_2^{III}-benzoate adduct proposed in Figure 3.40 and Figure 3.42 (see Figure A.27 for mass spectrometry data). However, characterisation of the paramagnetic species was not possible, meaning it was not possible to determine the mechanism of reaction. It was proposed by the authors that the ruthenium-benzote complex reported in Section 3.1.2, was synthesised *via* a Cannizzaro-style mechanism, Scheme 3.6, from the ruthenium-hydroxo species.[225] The mechanism, Scheme 3.6, shows the formation of the carboxylate product occurs with the formation of one equivalent of benzyl alcohol. The use of ^{13}C NMR spectroscopy confirmed that there is no benzoic acid liberated in the reaction.

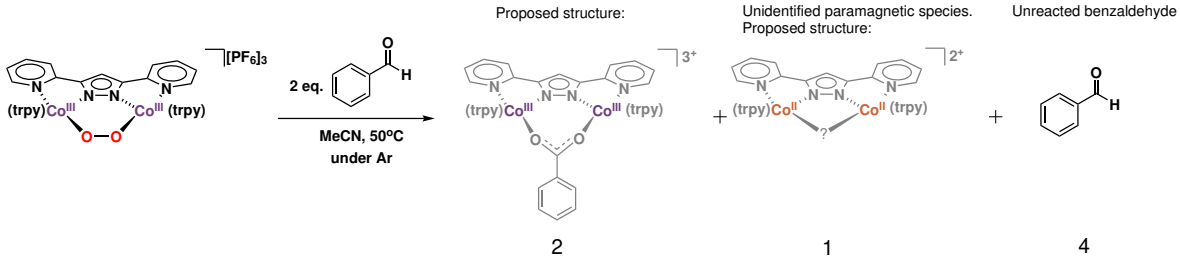

Figure 3.42: Relative ratios of each of the proposed products (diamagnetic and paramagnetic species, and unreacted benzeldehyde) calculated using integral data, as discussed in the text. *Note that the structure of each product is postulated, and more structural data is necessary to fully identify the complexes.*

If the mechanism were proceeding through a Cannizzaro-style mechanism, there should be one equivalent of benzyl alcohol formed for every equivalent of benzoate adduct. The absence of peaks corresponding to benzyl alcohol in the spectra (Figure 3.40), most notably the absence of a CH_2 peak in the 4 – 5 ppm region, suggest that this is not the mechanism of reactivity for $\mathbf{Co1_{O_2}}$. Additionally, there was no exogenous base added to the reaction mixture, which it can be seen in Scheme 3.6 is necessary for the reaction to proceed.

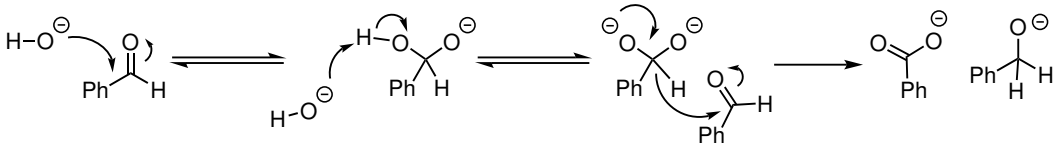

Scheme 3.6: The Cannizzaro reaction proposed by Catalano *et al.* as the mechanism for benzoate formation. Mechanism adapted from Organic Chemistry, 2001, Oxford University Press.[226]

Although the reaction does not appear to be a Cannizzaro-style mechanism, it is likely that the first step is similar, with the peroxo behaving as a nucleophile. Nucleophilic reactivity of metal peroxo species towards benzaldehyde is well documented,[120] and is observed in other cobalt-peroxo species, as discussed in Section 1.3.

In order to investigate whether the complex-adduct underwent reoxidation in air to yield $\mathbf{Co1_{O_2}}$ and the oxidised substrate (which was assumed to be benzoic acid), the solution was opened to air and monitored by ^{1}H NMR spectroscopy. Although there was a slight increase in benzoic acid peaks, over the course of 48 hr the peaks identified in Figure 3.40 decreased and the aromatic region showed the presence of many species, suggesting decomposition had occurred. The reformation of $\mathbf{Co1_{O_2}}$ was also not observed by

NMR spectroscopy. In order for the complex to perform aerobic oxidation catalysis, the benzoate adduct will need to be released from the complex and the cobalt species able to bind O_2 in order to complete catalytic turnover. Further studies would investigate different reaction conditions or additives in order to promote turnover.

3.6.3 Screening of Complexes for Reactivity towards Oxygen Atom Transfer

As benzaldehyde yielded the most promising results with $\mathbf{Co1_{O_2}}$, the same conditions were employed to test the reactivity of $\mathbf{Co2_{O_2}}$ – $\mathbf{Co6_{O_2}}$. The results from these experiments are summarised in Table 3.10 showing that there was no reaction for any of the complexes except the bromo-substituted $\mathbf{Co5_{O_2}}$, which showed similar activity to $\mathbf{Co1_{O_2}}$, although with lower conversions.

Table 3.10: Testing the reactivity of $\mathbf{Co2_{O_2}}$ – $\mathbf{Co6_{O_2}}$, on an NMR scale. Reaction volume = 0.5 mL, [Co] = 10 mM, [benzaldehyde] = 20 mM, solvent = MeCN (dried, degassed), heat at 50 °C

Complex	Result	Comments
$\mathbf{Co2_{O_2}}$	No reaction	–
$\mathbf{Co3_{O_2}}$	No reaction	–
$\mathbf{Co4_{O_2}}$	No reaction	–
$\mathbf{Co5_{O_2}}$	Reaction	Immediate colour change, as seen for $\mathbf{Co1_{O_2}}$.
$\mathbf{Co6_{O_2}}$	No reaction	–

$\mathbf{Co5_{O_2}}$ also underwent reaction with benzaldehyde, with a visible colour change to an orange/brown similar to that of the reaction with $\mathbf{Co1_{O_2}}$, (Figure 3.36). However, although both complexes underwent a similar visible change, the ^{1}H NMR spectroscopy suggested that the products of the reaction with $\mathbf{Co5_{O_2}}$ differs to the benzoate adduct discussed previously. In a similar manner to $\mathbf{Co1_{O_2}}$ there were a large number of species present in the initial stages of the reaction, Figure 3.43. However, unlike $\mathbf{Co1_{O_2}}$, after one week there were still a large number of species in solution, suggesting that the rate of reaction with $\mathbf{Co5_{O_2}}$ is considerably slower than with $\mathbf{Co1_{O_2}}$. Alternatively, this might suggest that there are a number of species in equilibrium with each other. The 2D spectra can be found in the Appendix, Section A.2.6.

After many months stored in an argon filled glovebox there were still a number of species present *via* ^{1}H NMR spectroscopy, suggesting multiple products in equilibrium, or that

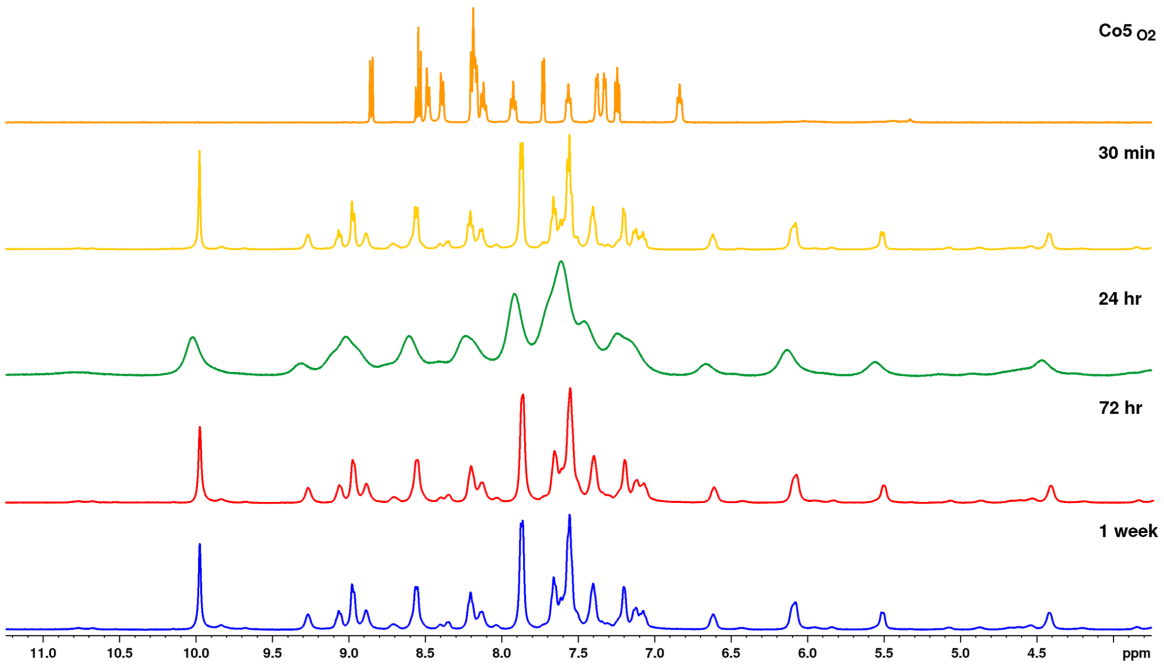

Figure 3.43: An overlay of ^{1}H NMR spectra of $\mathbf{Co5_{O_2}}$ (orange, top) and the aromatic region of the spectra at various time points after the addition of benzaldehyde. (Conditions: [$\mathbf{Co5_{O_2}}$] = 20 mM, [benzaldehyde] = 40 mM, T = 50°, solvent = MeCN (0.5 mL))

there are multiple reaction pathways, resulting in a mixture of products. Preliminary mass spectrometry experiments did not detect the presence of a benzoate adduct in solution, although detection of adducts using mass spectrometry is challenging. This could be due to the instability of such a species under mass spectrometry conditions, or could suggest that it was not formed. If there are multiple species in equilibrium, or if there are competing reaction pathways, changing the reaction conditions might help alter the balance of products.

Similarly to the diamagnetic spectra, the wide-spectral width spectrum revealed a large number of species in solution. In addition, the paramagnetic spectrum does not have the easily identifiable pair of peaks between 65 and 75 ppm that are present in the μ-Cl species. A lack of identifiable peaks means determining the ratio of diamagnetic to paramagnetic species in solution is also challenging. However, there are some similarities, most notably the two peaks at -9 and -17 ppm, which are similar to those observed for the reaction with $\mathbf{Co1_{O_2}}$. Although it is not possible to assign these, it can be deduced that at least one of the paramagnetic species in solution is similar between the two cobalt complexes.

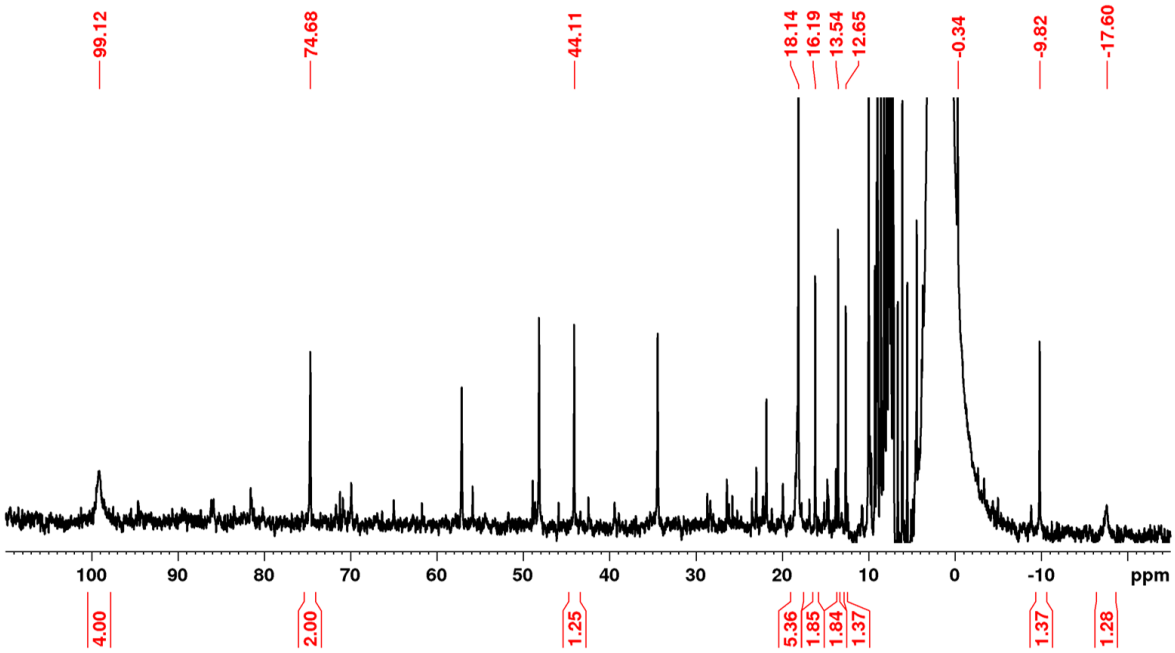

Figure 3.44: Wide spectral width ^{1}H NMR spectrum of the reaction between $\mathbf{Co5_{O_2}}$ and benzaldehyde after 1 week. Smaller peaks are not labelled to improve readability. Also note that some unlabelled peaks are contamination of Co(trpy)Cl_2 in the $\mathbf{Co5_{O_2}}$ sample.

The activity of $\mathbf{Co1_{O_2}}$ and $\mathbf{Co5_{O_2}}$ for oxygen atom transfer activity is surprising since although $\mathbf{Co1_{O_2}}$ consistently shows high activity for oxidation or ORR studies, $\mathbf{Co5_{O_2}}$ did not. Additionally, benzaldehyde suggests that the reactivity of the metal-oxygen complex is nucleophilic.[120] The electron withdrawing bromo-substituent on $\mathbf{Co5_{O_2}}$ should mean there is less electron-density on the metal centres, resulting in a less nucleophilic metal-oxygen species. However, another look at the electrochemical results sheds light on the reactivity. As discussed in Section 3.4.3, complexes with a less negative values for E_{red2} suggest that the O_2-adduct is more likely to oxidise organic substrates. $\mathbf{Co1_{O_2}}$ has the least negative reduction potential (-0.80 V vs NHE), followed by $\mathbf{Co5_{O_2}}$ (-0.84 V vs NHE), supporting the suggestion that the "reducability" of the μ-OO complexes is an indicator of reactivity towards substrates.

3.6.4 OAT Conclusions

Preliminary oxygen atom transfer studies suggest that $\mathbf{Co1_{O_2}}$ and $\mathbf{Co5_{O_2}}$ show promising nucleophilic oxygen atom transfer activity towards benzaldehyde. Although the products of the reaction were not conclusively determined, they have been tentatively assigned as a benzoate adduct, suggesting that oxygen atom transfer has taken place

from the cobalt μ-peroxo species to the benzaldehyde. Further studies are required to determine the products of the reaction, and further investigate the mechanism of reactivity. The activity of $\mathbf{Co1_{O_2}}$ and $\mathbf{Co5_{O_2}}$ towards benzaldehyde suggest that the electrochemical properties of the complexes are significant in predicting their reactivity in OAT reactions.

Since only $\mathbf{Co1_{O_2}}$ was tested for reactivity towards other substrates, it might be that although the other complexes did not show any reactivity towards benzaldehyde, they might react in an electrophilic manner towards a different class of substrates. This mode of reactivity might also help shine a light on the different reactivities of the complexes.

3.7 Conclusions

The electrochemical studies of the one electron oxidation of $\mathbf{Co1_{Cl}}$ – $\mathbf{Co6_{Cl}}$ from $Co^{II}_2 \longrightarrow Co^{II}Co^{III}$ revealed E_{mid}(ox) values that broadly follow the expected trends. The complexes with electron-donating substitutents have lower oxidation potentials than those with electron withdrawing substitutents. However, $\mathbf{Co6_{Cl}}$ had very poorly defined CVs, suggesting contamination by another redox active species, possibly suggesting high activity of this complex. Additionally, the *ortho*-methyl substituted $\mathbf{Co2_{Cl}}$ had an oxidation potential that was significantly higher than the other five complexes, showing that functionalisation in this location of the ligand backbone has a pronounced effect on the electrochemical properties of the complex. As a consequence, **Co2** is not included in the correlations of the rest of the series.

Oxidation studies of the six μ-Cl complexes were used as a proxy for measuring the oxophilicity of the complexes, by observing the rate at which the μ-Cl complexes coordinated O_2 to form their corresponding μ-OO complexes. The unsubstituted $\mathbf{Co1_{Cl}}$ showed the fastest rates of O_2 binding, followed by $\mathbf{Co4_{Cl}}$, which is amine substituted. Both $\mathbf{Co2_{Cl}}$ and $\mathbf{Co6_{Cl}}$ are slow, with rates an order of magnitude slower than $\mathbf{Co1_{Cl}}$, showing almost no reactivity with oxygen over the course of the study. $\mathbf{Co3_{Cl}}$ (methyl) and $\mathbf{Co5_{Cl}}$ (bromo) have rates in the middle. The rates of oxidation were compared to the E_{mid}(ox) values for the complexes, revealing a lack of correlation.

Electrochemical studies of the μ-OO complexes showed that they undergo a reversible redox event at around -0.35 V vs NHE. The reduction potentials broadly followed the expected trends in terms of the electron donating and withdrawing ability of the substituents on the bpp backbone, with $\mathbf{Co3_{O_2}}$ and $\mathbf{Co4_{O_2}}$ having the most negative

redox potentials, followed by $\mathbf{Co1_{O_2}}$ and then $\mathbf{Co5_{O_2}}$ and $\mathbf{Co6_{O_2}}$. As observed previously, the exception is the *ortho*-methyl substituted $\mathbf{Co2_{O_2}}$, which showed considerably lower redox potentials than the other complexes containing electron donating substituents. Randles-Sevcik analysis revealed that this redox event is a one electron process, confirming that it is a $Co_2^{III} \longrightarrow Co^{III}Co^{II}$ reduction.

When scanning to lower potentials, the complexes undergo a second, irreversible, redox event, that also renders the first event irreversible. The reversibility is not restored upon changing the scan rate, suggesting that this is a EC event, whereby the electron transfer is followed by a rapid chemical step, which is attributed to the breaking and subsequent loss of the bridging peroxo. The E_{red2} values for this second redox event negatively correlate to the O–O bond lengths reported in Chapter 2. This shows that the complexes which bind O_2 most strongly, represented by a longer O–O bond, require more energy (more negative potentials) to be reduced. This reduction might result in breakage of the O–O bond (despite the longer O–O bond length). The position of the E_{red2} values have important implications for the potential reactivity of the complexes, since they indicate the "reducibility" of the O_2-adduct.

Electrochemical studies under acidic conditions resulted in a shift of the first E_{red1}, value to less negative potentials, accompanied by the loss of electrochemical reversibility. The redox potential changed by different amounts, with $\mathbf{Co5_{O_2}}$ and $\mathbf{Co6_{O_2}}$ showing the most pronounced shifts in electrochemical potential of 0.16 and 0.19 V, respectively, whilst $\mathbf{Co3_{O_2}}$ and $\mathbf{Co4_{O_2}}$ shifted by only 0.1 and 0.07 V, respectively.

The first, reversible, reduction (E_{mid1}) showed a clear correlation with the Hammett parameters of the pyrazole substituents (Figure 3.15). In comparison, the irreversible E_{red2} reduction did not correlate to the electronic properties of the substituents. This can be explained by the thermodynamic nature of the E_{mid1} values, whilst E_{red2} is a kinetic property.

Oxygen reduction reaction (ORR) studies show a significant range in the rates of reaction between the different complexes. $\mathbf{Co1_{O_2}}$ shows the fastest rates, whilst $\mathbf{Co2_{O_2}}$ and $\mathbf{Co6_{O_2}}$ are both exceptionally slow. VTNA studies show that $\mathbf{Co1_{O_2}}$ is first order, confirming the literature report,[113]. However, it also revealed catalyst deactivation which had not been previously reported. Unfortunately, the reaction profiles for the other 5 complexes did not produce overlays that were good enough to draw conclusions about the order of reaction. However, the VTNA did reveal that all complexes suffered from

catalyst deactivation. Studies of the complexes with TFA and Me_8Fc independently supported the assignment of PCET as the initial step in the catalytic cycle, but did not confirm that PCET was rate determining for all complexes. These studies also revealed that $\mathbf{Co6_{O_2}}$ reacted with Me_8Fc, suggesting electron transfer from Me_8Fc to $\mathbf{Co6_{O_2}}$. However, this did not correlate to high levels of activity for this complex in the ORR, suggesting that the position of the first reduction potential for these complexes is not significant in their reactivity in the ORR.

There is a correlation between the ORR results and the oxidation studies of the μ-Cl complexes, Figure 3.34. This further supports the suggestion that the ability of the complex to bind O_2, and its reoxidation to the Co_2^{III} state could be rate determining for some complexes in the ORR. This was further confirmed by a lack of correlation between the E_{red1}, potentials and the rates for the ORR. Previous studies of $\mathbf{Co1_{O_2}}$ found that the reaction was independent of O_2 concentration, and O_2 did not appear in the rate law. However, these results suggest that the mode of reactivity towards O_2 is not the same between the complexes, meaning functionalisation on the Hbpp backbone not only changes the rates of reactivity, but also the mechanism of reactivity towards O_2.

$\mathbf{Co1_{O_2}}$ and $\mathbf{Co5_{O_2}}$ showed promising oxygen atom transfer activity in preliminary studies with benzaldehyde, suggesting that the peroxo of the complex behaves in a nucleophilic manner towards the substrate. The product of the reaction is proposed to be a benzoate adduct, although further studies are necessary to confirm this.

The reactivity of $\mathbf{Co1_{O_2}}$ and $\mathbf{Co5_{O_2}}$ in the OAT can be explained on the basis of their electrochemical properties. Both complexes have E_{red2} values that are less negative than the other complexes, suggesting that the O_2-adduct is more easily reduced. This is in direct comparison to the ORR results, which do not show any correlation to the electrochemical results. These results, and the correlation between the ORR and oxidation studies of the μ-Cl complexes suggest that whilst the electrochemical properties of the complex is significant for oxygen atom transfer activity, reactivity in the ORR is better predicted by the ability of the complex to bind O_2.

3.8 Future work

3.8.1 Investigation of Catalyst Deactivation and Reaction Mechanism

It was not possible to definitively identify the RDS or identify whether functionalisation of the bpp^- ligand changed the mechanism of reaction from the oxygen reduction reactions discussed in Section 3.5. The results suggest that there might be a change in mechanism for some complexes, notably that reaction with O_2 might become rate limiting. However, there are a number of ways this could be investigated further, and there are a number of further studies that can be conducted to help determine the mechanism of ORR, and determine how catalyst deactivation is occurring.

The synthesis of the $Co^{II}{}_2$-bis aqua species for all six complexes, and comparing rates of catalysis using the bis-aqua species would give insight into the mechanism. Catalyst deactivation is observed for all six complexes in the ORR, although to varying extents. One of the simplest methods would simply be to add further Me_8Fc to the reaction mixture and observe the rate of reaction. A slower rate suggests permanent catalyst deactivation in the course of the reaction. Alternatively, if the problem is product inhibition, spiking the reactions with H_2O, the product of the reaction, should also result in a reduction in rate.

The studies of the complexes with TFA and Me_8Fc independently suggest that the electron transfer from the Me_8Fc to the complex is proton coupled, since with the exception of $\mathbf{Co6_{O_2}}$ no electron transfer was observed. However, in order to confirm whether the PCET is rate determining, it would be necessary to study the rate of electron transfer from Me_8Fc to the cobalt complex, in the presence of TFA, but without catalytic turnover. Such studies were carried out with $\mathbf{Co1_{O_2}}$, proving that PCET was indeed the RDS.[113] However, the pronounced differences in the order of catalyst suggest that the complexes might perform ORR *via* different mechanisms, such experiments would also help illuminate whether PCET is the RDS for the other complexes. These studies could be complimented by studying the kinetic isotope effect (KIE) by using deuterated trifluoroacetic acid. This would confirm whether proton transfer occurred in the rate determining step. If the binding of O_2 was rate determining, the use of labelled O_2 would help determine this mechanism.

Some kinetic studies suggested that the order in catalyst during the ORR was might

be half order for a number of the complexes, which can possibly be explained by dimerisation. Detection of intermediates can be challenging, but analysis of the resultant solution after the reaction, by NMR spectroscopy or crystallography might help identify whether the catalyst has undergone dimerisation over the course of the reaction. This might also help identify a deactivation pathway. The use of DOSY NMR spectroscopy could possibly help identify the presence of a dimer, since it would be expected to diffuse at a considerably slower rate than the original complexes. There are even examples of using DOSY in flow, meaning it could be used to monitor the reaction in real-time.[251]

Another method of determining the mechanism of reaction is monitoring the catalyst during the course of the reaction, rather than studying the production of products, or loss of reactants. This could be done using NMR spectroscopy, since the profile of the catalysts are well characterised, and the formation of any paramagnetic species would also give insight into the oxidation state on the metal centres throughout. However, NMR spectroscopy is limited by the relatively long timescales necessary, meaning any short lived species might be missed. It is a possibility that the liberation of H_2O in order to allow the binding of O_2, resulting in catalytic turnover, is rate determining. Synthesis of the corresponding bis-aqua complexes to $\mathbf{Co1_{O_2}}$ – $\mathbf{Co6_{O_2}}$ and using these for catalysis might also help in determining the rate determining step.

Finally, H_2O_2, the product of a two electron reduction of O_2, is sometimes a byproduct during the 4 electron reduction of O_2 to H_2O. A common way of testing whether the reaction is performing the full $4\,e^-$ reduction, rather than the $2\,e^-$ reduction to H_2O_2 is iodometric titrations.[94,95] This was previously studied for $\mathbf{Co1_{O_2}}$ and it was confirmed that there was no $2\,e^-$ reduction to H_2O_2.[113] However, the low reactivity of some of the other complexes, coupled with potential mechanistic changes, might indicate that the reaction wasn't going to completion, and was instead forming H_2O_2. This could also be complimented with studies of oxygen uptake during the course of the reaction, either through manometry, which would identify oxygen uptake from the headspace, or by using a Clarke Electode, which would determine uptake of dissolved oxygen in the solution. Previous studies by Llobet and coworkers found that oxygen pressure did not change the rate of reaction,[113] but determining uptake of dissolved oxygen might provide more insight into the reactivity. Alternatively, a rotating ring disk electrode can be used, which can be used to detect for formation of H_2O_2 or H_2O in situ.[229]

Over the past 10 years, cobalt oxide has also seen wide application in both oxygen

reduction[252–256] and water oxidation catalysis[257,258] as both CoO_x nanoparticles or as mixed metal catalysts. Since cobalt oxide nanoparticles are active for ORR catalysis,[253] the formation of nanoparticles during the course of the reaction cannot be ruled out. Llobet and coworkers reported in their water oxidation and ORR studies that the catalyst ($\mathbf{Co1_{O_2}}$) must be homogeneous because they modulate the ligands, by changing the terpyridine ligands to $(Me)_2$bimpy, resulting in a change of reaction rate,[113,166] However, there is evidence that it is possible to get ligand modulation on the surface of active nanoparticles,[133,259] meaning the formation of nanoparticles cannot be ruled out. The determination of nanoparticle formation under catalytic conditions is disucssed further in Chapter 5, using a different set of iridium-based catalysts.

3.8.2 Further OAT studies

The preliminary OAT studies were promising, suggesting that $\mathbf{Co1_{O_2}}$ and $\mathbf{Co5_{O_2}}$ are active towards benzaldehyde, suggesting nucelophilic behaviour by the peroxo of the complex. However, the reaction was very slow ($\approx$ 1 week), and the product was not confirmed for either complex. Identification of the paramagnetic species, through further experiments such as a wide-spectral width COSY would help, coupled with mass spectrometry. Crystallography would also give insight into the products formed, and help confirm the tentative NMR assignments. Additionally, if the product is a benzoate adduct, the liberation of benzoic acid upon addition of acid would help confirm this.

Due to the pronounced difference in reactivity of the complexes towards the ORR, it would be necessary to test all six complexes with all of the substrates, since it might be possible that the peroxo reacts differently with different functionalisation on the ligand backbone. The use of para-substitutued benzaldehydes would allow a Hammett study to be conducted, which would also give further insight into the mode of reactivity.[126,127]

3.9 Experimental

3.9.1 General

All cobalt complexes were synthesised as described in Chapter 2. All other reagents were used as received unless otherwise stated. High-purity Mulli-Q water was used in all electrochemical measurements. NMR and mass spectrometry data was collected as detailed in Section 2.7.1, DOSY NMR spectra were processed using Dynamics Centre software.

3.9.2 Electrochemical Analysis

All electrochemical experiments were performed using a standard, three-electrode cell and measurements were carried out on an Ivium Technologies CompactStat. All electrodes were purchased from Bioanalytical Systems, Inc. In all cases the reference electrode used was $Ag/AgNO_3$ (0.01 M $AgNO_3$ in 0.1 M TBAF (tetrabutylammonium hexafluorophosphate))

The CVs were referenced to the Standard Hydrogen Electrode (NHE) according to the following equation:[260]

$$E_{(\mathrm{NHE})} = E_{(\mathrm{Ag/AgNO_3})} + 0.197 \tag{3.4}$$

CVs were collected at range of scan rates (50, 100, 250, 500, 1000 mVs^{-1}, 5 scans of each) with a glassy carbon working electrode (0.3 cm diameter, 0.07 cm^2 surface area) and a 1 mm diameter platinum wire counter electrode. The glassy carbon electrode was polished before use with alumina paste (1.0 μm then 0.3 μm), sonicated briefly (10 s), rinsed with Milli-Q water and dried under a stream of argon.

Solutions were prepared using pre-dried and degassed MeCN from an Acros-sealed bottle stored over molecular sieves and further degassed by bubbling a stream of argon through the solution for 15 minutes immediately prior to data collection. Data collection was carried out under an argon atmosphere, [Co] = 1 mM, 0.1 M TBAF.

Blank CVs of the electrolyte (0.1 M TBAF) were collected prior to and post data collection. Narrow scan range: -0.8 to 1.7 V vs NHE, wide scan range: -1.3 to 1.7 V vs NHE.

In order to collect CVs in the presence of acid, a 1M solution of trifluoroacetic acid (TFA) in MeCN was made, and 10 µl added to a solution of [Co], before further degassing, [Co] = 1 mM, TFA = 2 mM, TBAF = 0.1 M.

3.9.3 Interconversion between µ-Cl and µ-OO

A standard quartz cuvette with a small magnetic stirrer bar (rpm = 100) and a subaseal were used to record the initial spectrum of the µ-Cl complexes (1.5 mL, 50 µM). Continuous data collection was started before the subaseal was removed and a solution of $NaPF_6$ in MeCN (1.5 mL, 50 µM) was added. Data collection was continued for 60 minutes.

Subsequent UV-vis time points were collected after 24 hr. The final conversion was calculated using ^{1}H NMR spectroscopy to determine the ratio between the paramagnetic and diamagnetic peaks, corresponding to remaining μ-Cl starting material and oxidised μ-OO species, respectively.

3.9.4 Oxygen Reduction Reaction

Stop-flow experiments were carried out using a 3-syringe stop-flow UV-vis pump supplied by TgK Scientific. The set-up is shown in Figure 3.27. Solutions of Me_8Fc (3 mM), TFA (150 mM) and [Co] (0.15 mM, 0.075 mM, 0.0375 mM) were made up in aerated MeCN (bubbling air through a stirred solution for 20 minutes prior to use) and loaded into the syringe pump. The apparatus was flushed through 10 times before continuous UV-vis data collection was started. 5 repeats were collected for each set of conditions, and a representative reaction profile was used.

3.9.5 Testing the Stability of the Complexes

Using stock solutions of [Co] (0.075 mM), TFA (150 mM) and Me_8Fc (3 mM), 1 mL of [Co] was diluted by 1 mL MeCN, before addition of TFA (1 mL) or Me_8Fc (1 mL), yielding concentrations of [Co] = 0.025 mM, TFA = 50 mM, Me_8Fc = 1 mM. An initial UV-vis spectrum was collected and the solution stored in air, before a second reading after 15 minutes.

3.9.6 Oxygen Atom Transfer

Benzaldehyde and 1,4-cyclohexadiene were distilled immediately prior to use. A solution of 100 mM [Co] in MeCN (0.1 mL) was added to an air-free NMR tube, before addition of 50 mM [substrate] in MeCN (0.4 mL) and the NMR tube sealed. An initial (15 minute) time point was taken, after which the NMR tube was heated at 50 °C using an aluminium heating block before subsequent time points were recorded. In all cases a blank reaction was also recorded with the substrate in MeCN and heated at 50 °C. The reaction produced a number of products, and some impurities and unreacted starting material that was not separated. A benzoate adduct was confirmed by mass spectrometry and some tentative NMR assignments have been made (labelling system below as in Figure 3.40 and further details in Appendix, A.2.6).

^{1}H NMR (500 MHz, MeCN), δ (ppm): 9.07 (*f*, 2H, t, $^3J_{f,e}$ = 8.03 Hz), 8.98 (*e*, 4H, d, $^3J_{e,f}$ = 8.03 Hz), 8.56 (*a*, 4H, d, $^3J_{a,b}$ = 7.90 Hz), 8.21 (*b*, 4H, t, $^3J_{b,a}$ = 7.57 Hz), 7.96 – 7.99 (*p, bpp*, 2H, m), 7.52 – 7.57 (*bpp*, 2H, m), 7.41 (*c*, 4H, t, $^3J_{c,d}$ = 7.03 Hz), 7.21

(textitd, 4H, d, $^{3}J_{d,c}$ = 7.03 Hz), 7.09 (*m*, 2H, t, $^{3}J_{m,o}$ = $^{3}J_{m,p}$= 9.06 Hz), 6.96 (*bpp*, 2H, d, $^{3}J_{bpp,bpp}$ = 7.11 Hz), 5.40 (*o*, 2H, d, $^{3}J_{o,m}$ = 8.55 Hz). $^{13}C\{^{1}H\}$NMR (125 MHz, MeCN), δ (ppm): 156.8 (*h*), 156.5 (*g*), 153.8 (*l*), 152.9 (*d*), 149.9 (*k*), 146.5 (*f*), 143.6 (*b, m*), 143.0, 134.8, 134.5, 131.5 (*c*), 131.2 (*w*), 128.4 (*e*), 127.90 (*a*), 126.2 (*p*), 123.9 (*o*). MS (FTMS + pNSI), Calculated m/z $[M]^{+++}$ = 308.7223, Found m/z $[M]^{+++}$ = 308.7204

3.9.7 Reagents for Stop-Flow studies

Octamethyl ferrocene

Tetramethylcyclopendadione (Me_4Cp, 0.85 g, 695 mmol) was dissolved in THF (20 mL), and the solution cooled to 0 °C. ^{n}BuLi (4.8 mL, 765 mmol) was added dropwise over 30 minutes, and then stirred for a further 30 minutes. $FeBr_2$ (1 g, 464 mmol) was added and the solution warmed to room temperature, before stirring for 1 hr. The reaction was quenched by careful addition of H_2O before extraction with hexane (3 x 10 mL). The organic layers were combined, dried over $MgSO_4$ and the solvent removed to yield orange crystals. (0.80 g, 269 mmol, 58%) Prepared as described previously.[261]

Chapter 4

Further Synthesis of Bimetallic Complexes

The synthesis of a series of first row transition metal complexes was attempted, focusing primarily on copper. Although the intended product of the reaction was a 2:1 copper:ligand ratio, the complex obtained was a bimetallic copper dimer with two Hbpp ligands. Various attempts to prevent the formation of the dimer through the use of alternate co-ligands proved unsuccessful. The use of the *ortho*-substituted Hbpp ligand (HL2) resulted in the formation of a tetramer.

Zinc chemistry revealed similar limitations, with a cluster forming preferentially over the synthesis of a complex with an active site for catalysis. Preliminary investigations into the use of palladium appeared promising, although confirmation of the structure is still required.

In an effort to address the dimerisation, the synthesis of further functionalised Hbpp ligands was investigated. According to hard and soft acids and bases theory (HSAB), two different substitution patterns representing hard and soft were attempted.[65] The addition of a 'soft' phosphine was briefly investigated, before attention was turned to alkoxides. A number of different approaches were taken to introduce an alkoxide in the *ortho*-position of the Hbpp ligand, using sophisticated bases in an attempt to facilitate the substitution, although none were successful.

Finally, some preliminary studies into broadening the library of Hbpp pyrazole substitution is presented. Both phenyl and trifluoromethyl substituents are investigated. Although there were some initially promising results, it was not possible to isolate and characterise the products of the reaction.

4.1 Introduction

Copper is widely used in oxidation chemistry, particularly aerobic oxidations, and there is a wealth of literature detailing its use.[62,63] Indeed, copper is preferred over iron in some examples of haem-oxidases.[262] Of these catalysts, a number report a bimetallic mechanism, suggesting a copper-based bimetallic system would be active for oxidation chemistry. In addition, many of the existing copper complexes that show reactivity with dioxygen are based around ligand systems with chelating nitrogen donors, due to their similarity to the histidine residues found in natural systems.[36]

However, most of the examples of copper complexes use simple copper salts with high numbers of additives or high catalyst loadings. A review by Gulzar *et al.* included some examples with catalyst loadings of $CuCl_2$ of up to 20 mol%, coupled with the use of additives, such as TEMPO, in loadings of up to 50 mol%.[70]

An in depth study by Serrano-Plana *et al.* examined a number of subtly different bimetallic copper complexes, investigating the impact of different ligand systems by systematically changing the framework around the copper centre. They found that both the Cu — Cu distance, and the first coordination sphere of the copper ions, must be flexible enough to account for the "Cu_2O_2 unit".[33] They also state that in order to bind O_2, the copper must be Cu(I).

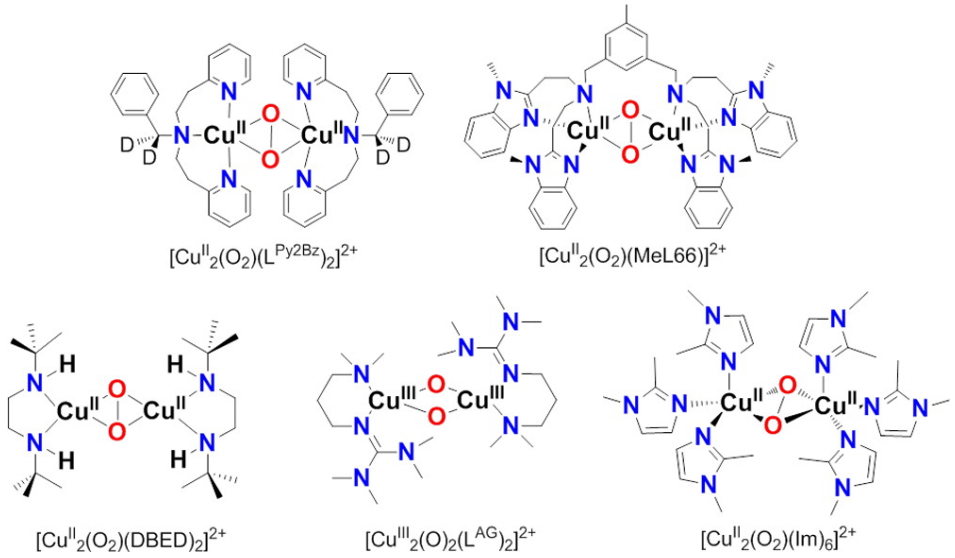

Figure 4.1: The different bimetallic copper species reported by Serrano-Plana *et al.* Reprinted with permission from *Acc. Chem. Res.* 2015, **48**, 2397–2406. Copyright (2015) American Chemical Society.

The oxidation of alcohols by copper/TEMPO systems has seen widespread application, and the proposed mechanism for such reactions is similar to the mechanism proposed for that of galactose oxidase, which proceeds via a radical mechanism.[18] A mechanistic study by Stahl *et al.* on a Cu/TEMPO catalyst system is shown in Figure 4.2. The study revealed a two part process: the oxidation of the catalyst and TEMPO-H by dioxygen, followed by oxidation of the substrate, and subsequent reduction of the copper centre.[71] In addition to the elucidation of the two-part process, they postulate that the oxidation of the substrate, and reduction of O_2, is a bimetallic process. They propose that O_2 is bound by the Cu(I) complex to form a superoxo species, before the superoxo species is subsequently reduced further to form a bridging peroxy species, before reacting with TEMPO-H in Step 3.

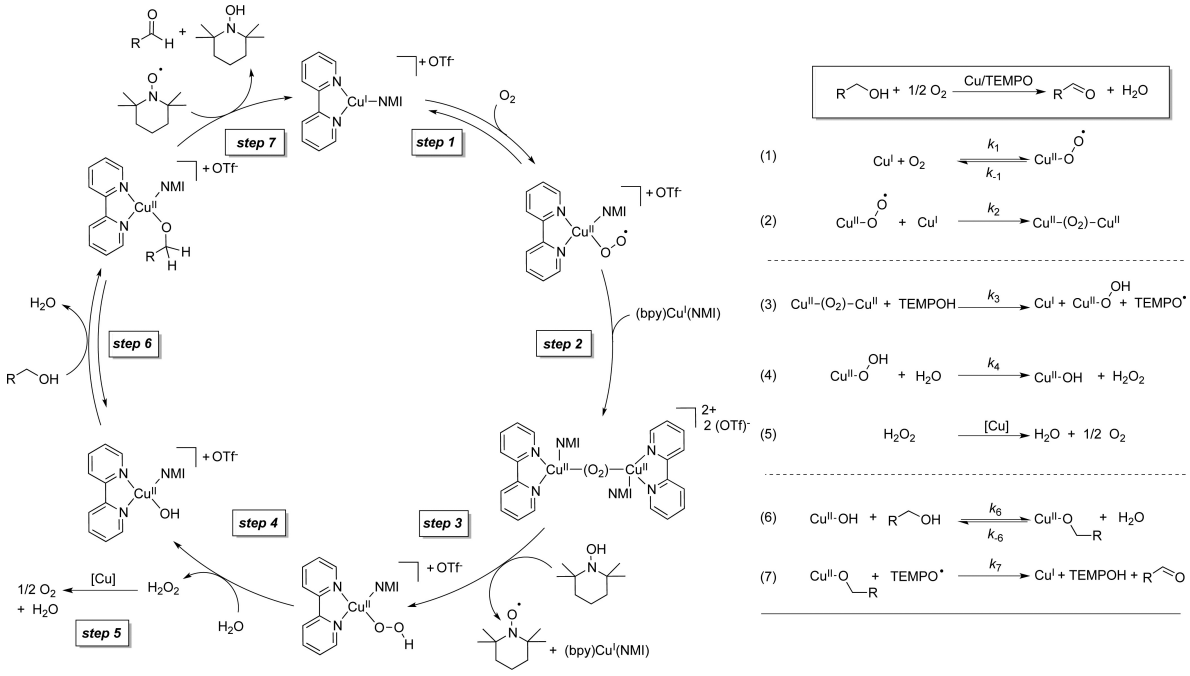

Figure 4.2: Proposed catalytic cycle for the aerobic oxidation of primary alcohols by a copper bipyridine complex. Of particular interest is the bimetallic species formed in Step 2. Reprinted with permission from *J. Am. Chem. Soc.* 2013, **135**, 2357–2367. Copyright (2013) American Chemical Society

The bimetallic mechanism, and identification of the oxidation state of the metal centre offer useful pointers for the development of bimetallic catalyst systems. They also identified that the rate limiting step differed depending on the substrate, in some cases it corresponded to step 1, the oxidation of the catalyst by O_2, in others, multiple steps contribute. They also commented on the impact of ligand choice and solvent, suggesting

that the use of acetonitrile and bipyridine both stabilise copper(I), possibly disfavouring the reaction with O_2. This study also highlights the use of stable radicals (TEMPO) as a means of catalysing and promoting the reaction. The use of stable radicals in aerobic oxidation catalysis is the focus of a review by Muldoon *et al.* from 2014.[72]

The high activity of palladium, and its use in Wacker oxidations, means it has been the focus of many studies into aerobic oxidation catalysis. Many of the early examples used simple palladium salts such as $PdCl_2$ or $Pd(OAc)_2$, but the loss of catalytic activity due to the degradation of the catalyst to Pd(0) led to the development of more elaborate ligand systems.[9]

4.1.1 Further Complexes using the Hbpp Ligand

Another class of widely reported complexes based on the Hbpp ligand are a series of multinuclear clusters. One of the earliest reported clusters was a tetranuclear copper cluster based on an unsymmetrically substituted Hbpp ligand, Figure 4.3. The authors used $Cu(NO_3)_2 \cdot 3\,H_2O$ as their copper precursor, resulting in a product with formula $[Cu_4L_4(NO_3)_3](NO_3)$ (where L = bpp^-). The copper is in the Cu^{II} oxidation state.

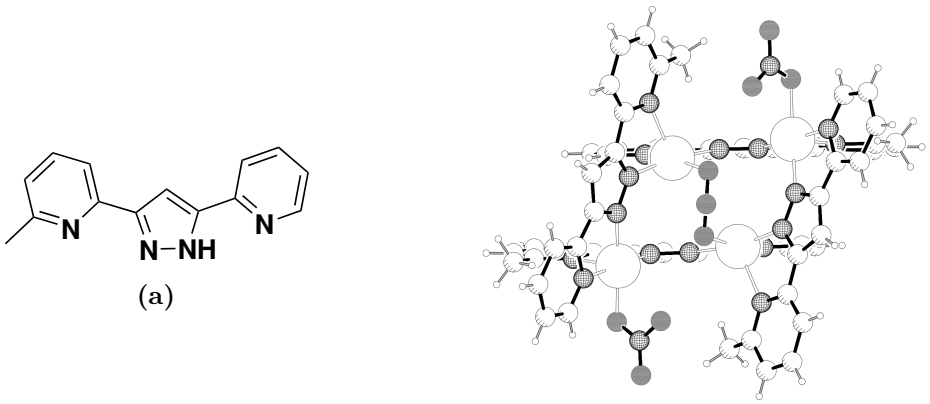

Figure 4.3: The ligand and resultant tetranuclear copper complex. Reprinted with permission from *Inorg. Chem. Comm.*, 2003, **6**, 833-836. Copyright (2003) Elsevier.[263])

More commonly reported than tetranuclear complexes are a series of pentanuclear helicates, with the general formula $M_5(bpp)_6(\mu\text{-O})$. Ishikawa *et al.* reported a copper cluster of this type in 2010, Figure 4.4.[264] Their studies focused predominantly on the magnetic properties of the complex, rather than any catalytic properties.

Early studies focused on the magnetic or redox properties of the complexes, which were

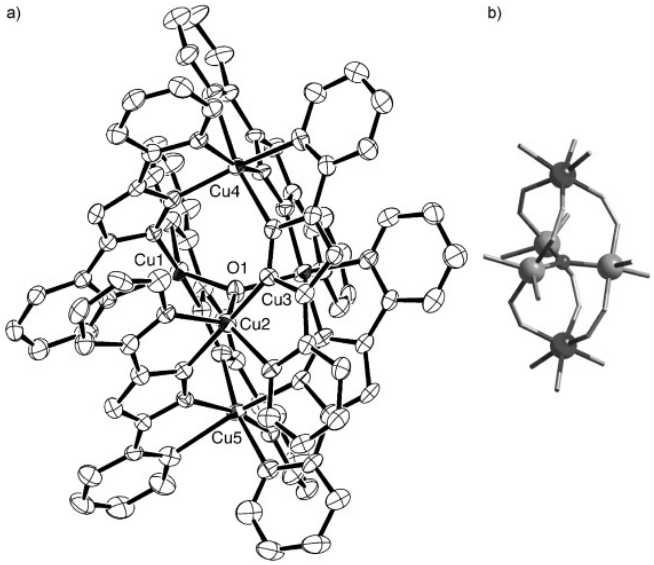

Figure 4.4: The pentanuclear copper complex reported by Ishikawa *et al.* showing the centrally bound oxygen. Reprinted with permission from *Chem. Eur. J.* 2010, **16**, 11139-11144. Copyright 2010 WILEY-VCH Verlag GmbH & Co. KGaA, Weinheim.[264]

of interest due to the mixed oxidation states of the metals in the helicates. Examples of manganese,[160,265] iron,[266,267] and copper[268] were all reported from the early 2000s.

However, the helicates have seen a renewed interest since a 2016 publication reporting that the iron cluster is active for water oxidation catalysis.[169] This work was further expanded upon in 2019 with further mechanistic studies and some investigation into ligand effects using a methyl and bromo pyrazole substituted Hbpp, Figure 4.5.[171] Interestingly, despite the difference in electron donating (Me) or withdrawing (Br) ability of the substituents, it was found that both functionalisations resulted in lower TON and TOF values when compared to the unsubstituted system, although the methyl substituted helicate was more active for water oxidation than the bromo equivalent.

In the absence of substrate (H_2O) both complexes exhibited redox potentials as expected, with the methyl values shifted to more negative potentials in comparison to the unsubstituted complex, and the bromo complex the opposite. However, both exhibited onset potentials lower than the that of the unsubstituted complex, and the bromo substituted complex was shifted significantly enough to suggest a change in mechanism from the methyl and unsubstituted complexes. This was further investigated and confirmed through the use of UV-vis spectroscopy and electrochemical methods.[171] In these complexes, there are two metal environments, the $Fe_3(\mu_3\text{-O})$ core and the two apical Fe

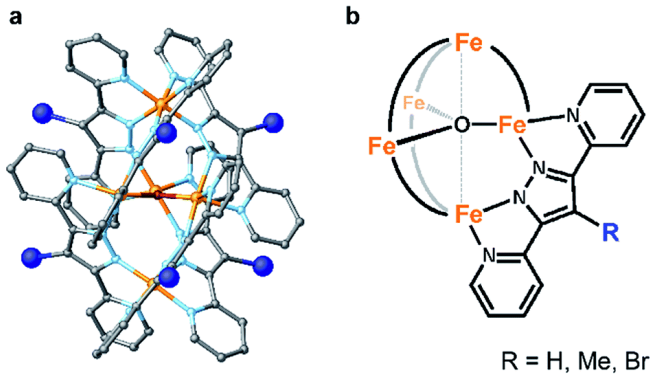

Figure 4.5: The iron WOC first synthesised by Okamura *et al.*, with the ligand functionalisation developed by Praneeth *et al.* shown. Figure reproduced with permission from *Chem. Sci.* (2019), **10**, 4628-4639. Copyright (2019) The Royal Society of Chemistry.[171]

ions. The introduction of a bromo-substituent on the backbone changes which metal centres undergo oxidation, and results in a concerted binding of water coupled with a further oxidation, whereas these processes are step-wise in the methyl and unsubstituted complexes.[171]

In 2020, an analogous cobalt cluster was reported, with the formula $[Co^{II}_5OH(bpp)_6]^{3+}$. Unlike the iron complex, the authors claim the central anion is OH^-, rather than O_2^-. The slightly longer Co–O bond length is used as evidence for this, although this is not supported with any further evicence, and is somewhat contradicted due to the symmetrical nature of the cluster. Preliminary studies suggest that the cluster performs photocatalytic CO_2 reduction.[269] Subsequent work has furthered the electrochemical characterisation, showing that the complex undergoes five successive reductions to the Co^{I}_5 species.[270]

Given that the Hbpp ligand has a known propensity to form helicate structures with 1st row transition metals, it is important to design synthetic strategies that avoid the formation of such structures. The transition metal precursors tend to be non-chloride based, with softer counter-ions such as $FeSO_4 \cdot 7\,H_2O$, $Co(Ac)_2 \cdot 4\,H_2O$, $Cu(BF_4)_2 \cdot 6\,H_2O$ or $Mn(NO_3)_2 \cdot 6\,H_2O$. This is not universal, with some examples of metal chloride salts being used in the synthesis of clusters, which may help avoid the formation of unwanted side products.

Having studied the cobalt-Hbpp-terpyridine systems described in Chapter 2 in some detail, the use of other transition metals will be investigated. In particular, drawing on the body of literature which uses copper for aerobic oxidations, and Wacker chemistry,

which uses a mixed copper/palladium system, synthesis of copper and palladium complexes will be carried out. The library of ligands will also be expanded by introducing substituents in a number of different places on the Hbpp ligand. Introduction of new backbone functionalisation will be studied, and the addition of an extra binding site through functionalisation in the *ortho*-position will also be investigated.

4.2 Preliminary Results to Expand the Library of Metal Complexes

4.2.1 Copper Complexes using the Hbpp Ligand

A copper-bpp complex was reported in the early 90s by Pons *et al.* with the structure suggested as a bridging chloride (μ-Cl) between the two copper centres and just one bpp^- ligand.[180,271] However, although the product was characterised by IR and UV spectroscopy, magnetic measurements and CHN analysis, structural assignment proved challenging. Since the initial publication, the crystal structure has been reported a number of times, and has shown a dimer configuration, as shown in Figure 4.6, rather than the proposed μ-Cl species.[159,272–274]

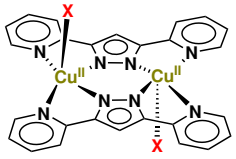

Figure 4.6: The reported copper(II) dimer, with two chelating bpp^- ligands, $[Cu_2(bpp)_2X_2]$. The nature of X depends on the method of synthesis, with examples of hexafluorophosphate ions,[274] sulphates[273] and water molecules.[272]

The possible d-orbital configurations of Cu^{II} are shown in Figure 4.7. The $Cu_2(bpp)_2X_2$ complex, Figure 4.6, adopts a geometry close to square-based pyramidal, with one unpaired electron per metal centre.

Using the Hbpp ligand, the aim was to make a bimetallic copper complex with a binding site available between the metal centres with which to bind substrates, either O_2 or organic substrates on which to perform aerobic oxidations. As a starting point, the initial procedure reported by Pons *et al.* was followed. The ligand was deprotonated using sodium ethoxide (NaOEt) and added to a solution of copper chloride in methanol. Almost immediately a solid formed which was stirred at room temperature for 12 hours,

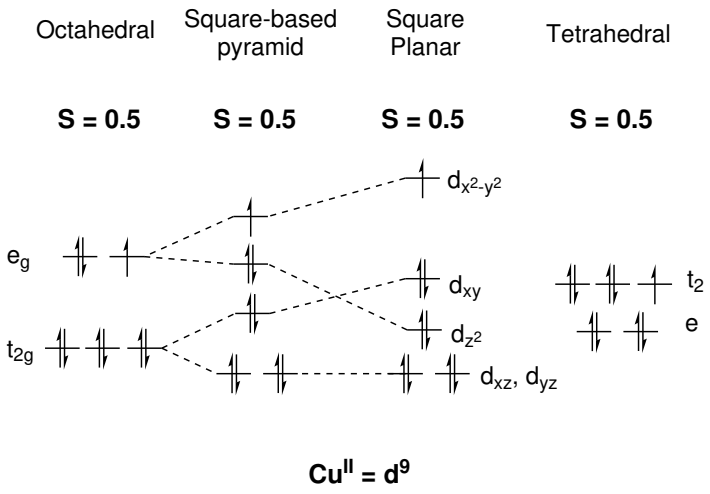

Figure 4.7: The possible d-orbital configurations for a Cu^{II} d^9 complex.

before filtering and drying in air. The green solid was insoluble in most solvents, including: acetonitrile, methanol, water, dichloromethane, acetone and toluene.

In an attempt to solvate the product an anion exchange was attempted using silver tetrafluoroborate ($AgBF_4$). To a suspension of the solid in MeCN an excess of $AgBF_4$ was added and the resulting mixture stirred in the dark for 30 minutes. This yielded a pale blue solution and white silver chloride solids, which were removed by filtration. After removal of the solvent, the blue solid was characterised by ^{1}H NMR and mass spectrometry. The ^{1}H NMR was obtained using a wide spectral width and a pulse delay, and showed a number of paramagnetic peaks at 11.3 ppm, 21.3 ppm and 23.1 ppm. Without the use of computational techniques it was not possible to assign the spectra.

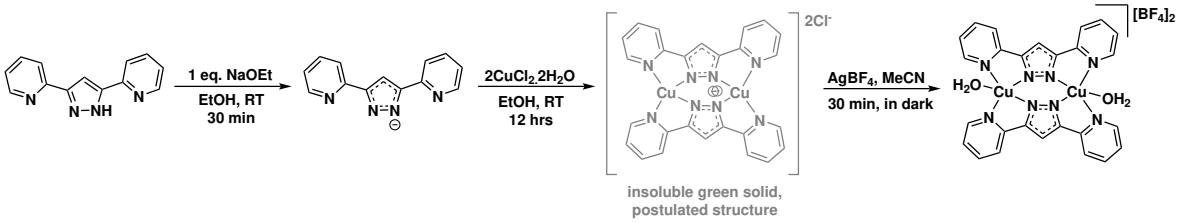

Scheme 4.1: Synthetic route to the copper dimer, addition of $AgBF_4$ required to yield the soluble $[Cu_2(bpp)_2(OH_2)_2][BF_4]_2$. Final conversion was performed on a small scale but was assumed to be quantitative.

X-ray standard crystals were grown from acetonitrile using the layering method with diethyl ether as the antisolvent, and the structure obtained is show in Figure 4.8. The

X-ray crystal structure shows that in the solid state, the reaction yielded the dimer shown in Figure 4.6, despite the 2:1 metal:ligand ratio in the reaction mixture. Some bond angles and distances are shown in Table 4.1. It is important to note that the crystallography results only give insight into the structure in the solid state. However, mass spectrometry data also confirms the presence of a dimer, suggesting that the complex retains its structure in solution.

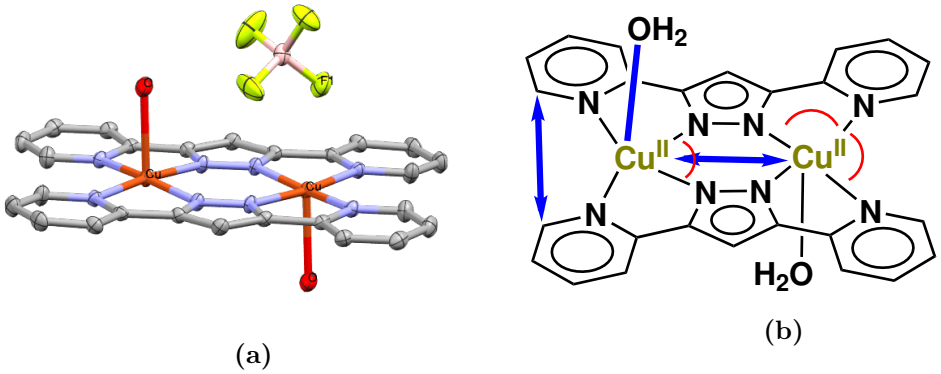

(a) **(b)**

Figure 4.8: **(a)** X-ray crystal structure of $[Cu_2(bpp)_2(OH_2)_2][BF_4]_2$, showing coordinated water molecules and one BF_4 counter ion. Hydrogen atoms and other BF_4 counter-ion omitted for clarity, rendered with 50% ellipsoids. **(b)** The bond angles and lengths reported in Table 4.1.

Table 4.1: Selected bond angles and lengths from the crystal structure shown in Figure 4.8.

Bond Angles / °		Distances / Å	
N_{py}–Cu–N_{py}	107.91(6)	Cu–Cu	4.0449(6)
N_{pz} – Cu – N_{pz}	91.63(6)	C – C	3.575(3)
N_{py} – Cu – N_{pz}	80.09(6)	Cu – O (H_2O)	2.085(3)
-	-	Cu – F (BF_4)	2.266(2)

Particularly important to note is the Cu — Cu distance of 4.045 Å. Looking at natural copper systems, it can be seen that the 4.045 Å distance between the copper centres sits between the Cu(II)-Cu(II) state (3.3 Å) and Cu(I)-Cu(I) state (4.4 Å) in catechol oxidase.[34] This suggests that the Hbpp ligand provides a good framework to mimic the distance in a naturally occurring system that performs O_2 reduction and concurrent oxidation of a substrate.

The distance between the copper centre and the closest fluorine on the BF_4 counter ion is 2.266 Å which is short enough to assume that there is some sort of interaction

between them and makes the environment around the copper centres closer to elongated octahedral, rather than the trigonal bipyramidal it appears initially.

The copper dimer has been reported a number of times in the literature, and investigated for applications in metal coordination polymers.[271,275,276] However, the preference of the copper centres to form the square planar dimer with two bpp ligands, despite the 1:2 ratio in the synthesis, means there is no possibility for a bridging O–O peroxo unit across the two metal centres, suggesting that the dimer will not be reactive for catalysis.

Synthesis of a Copper Complex with HL2

As discussed in Section 4.1.1, there is precedent for the formation of copper clusters. However, the aim was to make a dicopper complex supported by one bpp^- ligand, with sites available for catalysis. The short distance between the two bpp ligands in the copper dimer synthesised above (C – C distance, Table 4.1) suggests that the introduction of a steric constraint in the *ortho* position of the Hbpp ligand might prevent dimer formation, leaving an active site available for catalysis. Using the same conditions as Scheme 4.1, synthesis with HL2 was attempted. Initially, an orange solid was obtained which was also insoluble in all common laboratory solvents. After addition of $AgBF_4$, black solids were obtained after filtering the solution to remove AgCl and removing the solvent in vacuo. The significant difference in colour between the solid obtained originally, and the crystals grown after the halide extraction suggests that the copper is in a different electronic environment to the $Cu_2(bpp)_2$ species reported above.

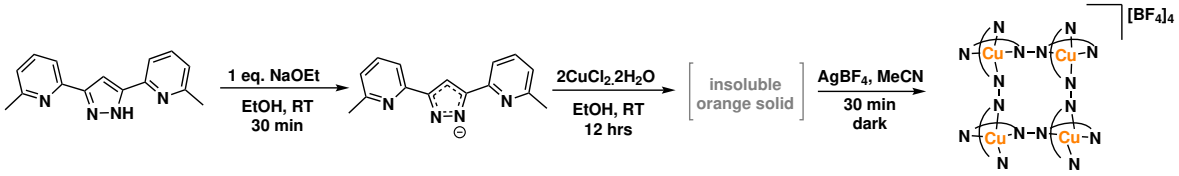

Scheme 4.2: Synthetic route to the copper tetramer.

^{1}H NMR showed the presence of a paramagnetic species, although once again it was not possible to assign the peaks. X-ray standard crystals were grown by the layering method using acetonitrile and diethyl ether as cosolvent. Upon analysis, these were found to have the structure shown in Figure 4.9. The parallel ligands are off-set, in order to maximise $\pi \rightarrow \pi^*$ stacking between the bpp ligands. The two sets of parallel ligands are not perpendicular to each other, the average angle between the planes is

57.40(12)° suggesting a deviation from perpendicular of around 33°.

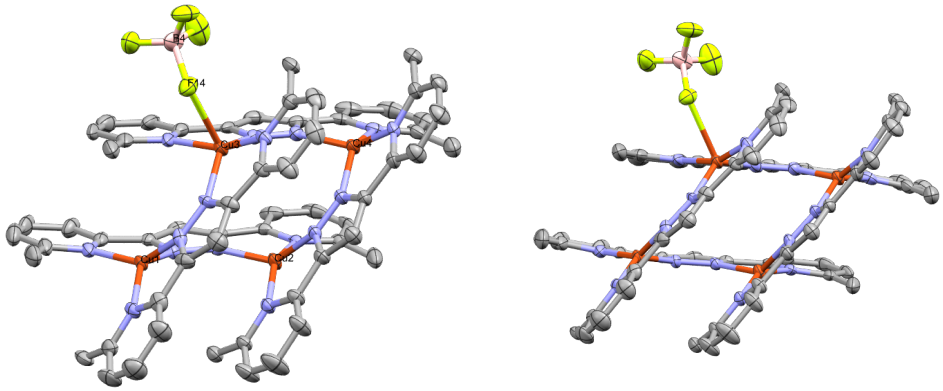

(a) (b)

Figure 4.9: X-ray crystal structure of $[Cu_4(bpp)_4][BF_4]_4$ from two different perspectives. Solvent molecules, hydrogen atoms and some counter ions omitted for clarity, ellipsoids rendered at 50% probability.

Table 4.2: Selected bond angles and lengths from the crystal structure shown in Figure 4.9.

Bond Angles / °		Distances / Å	
N_{py} – Cu – N_{pz}	81.76(11)	Cu–Cu	4.1902(6), 4.175(3), 4.339(14), 4.232(13)
bpp distortion	5.25(15)		
plane offset	57.40(12)		

The complexes Figure 4.8 and Figure 4.9 both contain Cu^{II} centres. However, there is a pronounced difference in the colour of the complexes. This is explained by the difference in binding environment between the two complexes. In the copper-bpp dimer, the metal is in a square-planar conformation, whilst in the tetramer, the copper centres are in an intermediate confirmation between square planar and tetrahedral. The energy gap between the HOMO and LUMO depends on the configuration around the metal centre, as shown in Figure 4.7, explaining the difference in colour.

Although the environment around the copper centres suggests that this complex will exhibit limited catalytic activity due to the lack of available binding sites for a target substrate, there are reports of similar tetranuclear copper complexes based on a variation of the Hbpp ligand system performing water oxidation.[167] However, in this example the complex has hydroxy groups in the *ortho* position, rather than methyl groups, which acted as a proton shuffle in order to enable the catalysis.

The aim was to make a bimetallic copper complex with a ligand:metal ratio of 1:2, leaving sites on the copper centres available for further reactivity, ideally with monodentate ligands. However, the reaction with the Hbpp (HL1) and Mebpp (HL2) ligands showed that the chelate effect of the ligands is too strong, driving the formation of dimers or clusters. It was thought, therefore, that using a copper precursor with an existing chelating ligand might prevent the formation of such complexes, similar to the role of terpyridine in the cobalt chemistry of Chapters 2 and 3.

Attempted Synthesis of a Copper Bipyridine Complex

In an attempt to prevent dimer formation, the use of a common chelate ligand was employed, bipyridine (bipy). The intended structure is shown in Scheme 4.3, yielding tetrahedral copper centres, with a binding site available between them.

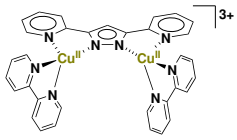

Scheme 4.3: Intended product of the reaction shown in Scheme 4.4. The Cu^{II} centres would be in a distorted tetrahedral geometry.

The copper chloride was dissolved in methanol and a solution of bipy was added, Scheme 4.4. Pale blue solids started to form almost immediately, which were assumed to be $Cu(bipy)Cl_2$. After stirring for 10 minutes, the deprotonated bpp^- ligand was added, upon which the solution turned darker green, and pale green solids formed. The solution was heated at 40 °C for one hour, before stirring at room temperature overnight. The pale green solid formed showed poor solubility in common laboratory solvents, so $AgBF_4$ was used to perform a halide extraction and improve the solubility.

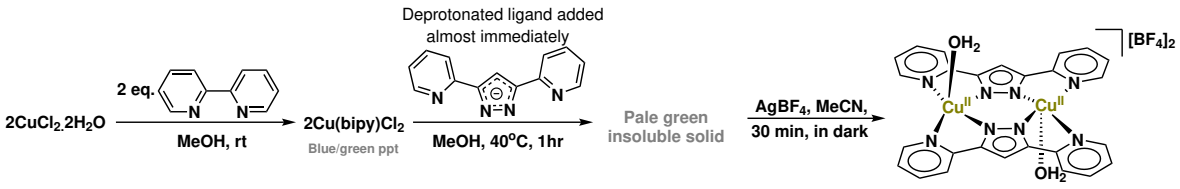

Scheme 4.4: Attempted synthetic route to $Cu_2(bipy)_2(bpp)$ (Scheme 4.3). Instead of the intended product, the result of the reaction was the copper/aqua dimer, Figure 4.8.

Unfortunately, the solid that was obtained was the known Cu-bpp dimer, shown in Figure 4.8, and confirmed by X-ray spectroscopy. This suggests that although $Cu(bipy)Cl_2$

forms initially indicated by the pale blue solids forming in methanol, upon addition of bpp^- exchange occurs. This suggests that although bipy is a good chelating ligand, the chelate effect and charge on the bpp^- ligand results in displacment of the bipy ligand to preferentially form the dimer. Potentially, the use of a less polar solvent might have mitigated this effect, making the ligand exchange less facile. However, this needs to be balanced with the poor solubility of the complexes.

Attempted Synthesis of a Copper Acetate Complex

The formation of the dimer, despite the presence of a chelating ligand like bipyridine, suggested that the use of a charged chelate ligand might prevent displacement by the bpp ligand. Copper acetate is a common copper(II) precursor and acetate is charged and weakly chelating. The intended product of the reaction is shown in Scheme 4.5.

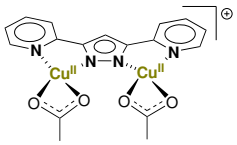

Scheme 4.5: Intended product of the reaction of $Cu(OAc)_2$ with the Hbpp ligand.

Following the synthetic procedure shown in Scheme 4.6, the synthesis of $Cu_2(bpp)(OAc)_2$ was attempted, using $Cu(OAc)_2$ as the precursor, rather than $CuCl_2$.

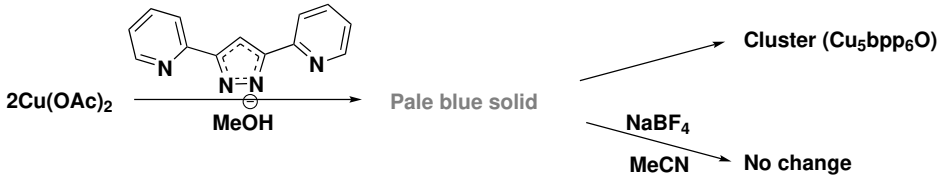

Scheme 4.6: Attempted synthetic route to the complex shown in Scheme 4.5. The Hbpp ligand was deprotonated prior to addition by NaOMe.

The reaction yielded a light blue solid, which was sparingly soluble in a mixture of methanol, diethyl ether and toluene. An attempt at a counter-ion exchange using sodium tetrafluoroborate did not result in any change to the solubility or colour of the solution. Slow growth of X-ray standard crystals yielded the cluster shown in Figure 4.10, $Cu_5(bpp)_6\mu_3$-O.

The cluster is analogous to those discussed in Chapter 2, Section 4.1.1, with the general formula $M_5(bpp)_6\mu_3$-O. A copper cluster has been previously reported by Ishikawa *et al.*, which is reported to have an overall charge of 3+ and consist of five Cu^{II} centres,

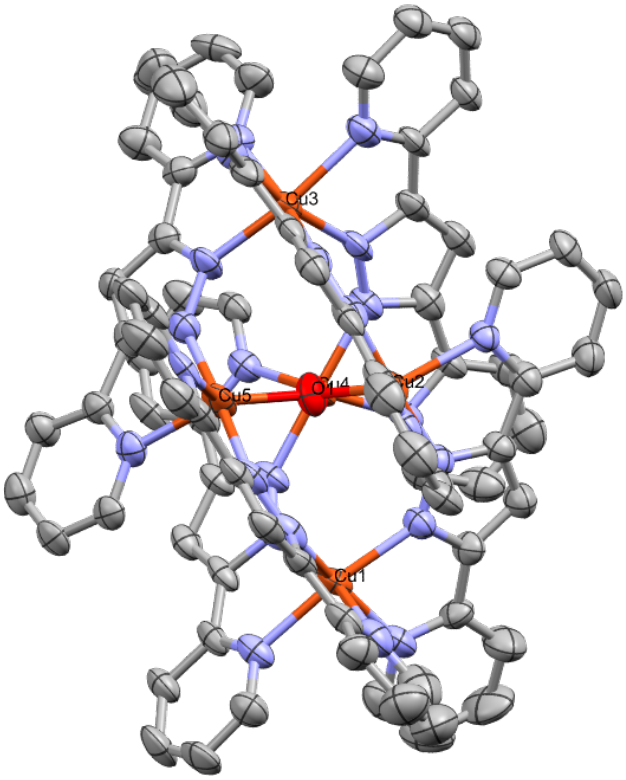

Figure 4.10: $Cu_5(bpp)_6\mu_3$-O, the product of the reaction shown in Scheme 4.6.

with the formula $[(Cu^{II}(\mu\text{-bpp})_3)_2Cu^{II}_3(\mu_3\text{-OH})]^{3+}$.[264] This complex was also synthesised from a $Cu(OAc)_2$ precursor, suggesting that the acetate perhaps promotes the formation of the cluster. However, the complex shown in Figure 4.10 crystallised with a large number of solvent molecules present in the lattice, and due to high levels of disorder it was not possible to confidently assign any of the apparent solvent molecules as acetate. Therefore, identifying the overall charge on the complex in the crystal structure was not possible. Additionally, due to the poor solubility of the complex, it was not possible to obtain NMR spectroscopy or mass spectrometry characterisation of the complex.

As discussed previously, both the iron and cobalt analogues of the cluster are active for catalysis.[169,171,269] Future work would fully characterise the copper cluster before testing it for catalytic activity.

Attempted Synthesis of a Copper Acetylacetone Complex

Although acetate is negatively charged, it has a relatively weak chelate effect, conversely, bipyridine has a stronger chelate effect than acetate but is uncharged. Acetylacetone

(acac) is both charged and has a relatively strong chelate effect, suggesting that it should not be displaced by bpp^- to form the dimer. The synthesis was attempted by the addition of the Hbpp ligand to Cu(II)$(acac)_2$ in MeOH.

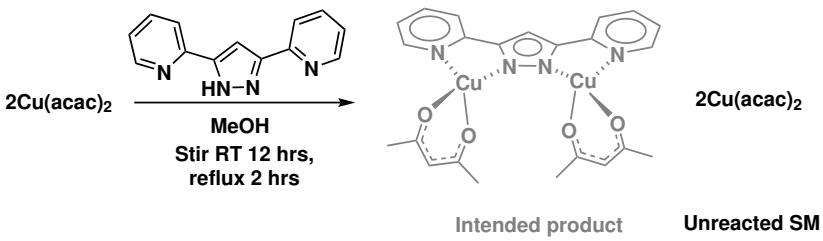

Scheme 4.7: Attempted synthetic route to $Cu_2(bpp)(acac)_2$. The results of the reaction showed that the main product of the reaction was unreacted starting material.

However, although a subtle colour change was observed upon addition, the colour did not change further, even after a number of hours at elevated temperatures. The solvent was removed under vacuum until solids appeared, after which the green supernatant was removed by decantation, yielding dark blue solids. X-ray crystals were grown by slow evaporation of the solvent, but were found to be unreacted $Cu^{II}(acac)_2$.

The pKa is Hbpp is not reported, but the pKa of diphenylpyrazole is 12.9,[277] which will be close to that of Hbpp. The pKa of acetylacetone is 8.9[278] which suggests that the higher pKa of the Hbpp ligand prevented the ligand exchange.

It was clear from the results of the reaction shown in Scheme 4.7 that the addition of the protonated Hbpp ligand and elevated temperatures was not enough to drive the ligand exchange. Additionally, the charges on the proposed Cu^{II} product are not balanced without the addition of a counter-ion. Therefore, in order to facilitate the reaction, $Cu(acac)_2$ was stirred in the presence of two equivalents of HBF_4 (as an etherate species). A colour change occurred immediately from the dark blue of the starting material to a light blue/turquoise. After stirring for 10 minutes, bpp^- was added in MeOH, upon which the solution immediately turned darker blue. Hbpp was deprotonated using NaH, since hydride bases result in irreversible deprotonation due to the loss of H_2. The product of the reaction was again found to be $Cu(acac)_2$, Scheme 4.8.

It is likely that the addition of HBF_4 liberated acac from the copper complex, forming acacH and a $Cu(acac)(BF_4)$ species. However, upon addition of the deprotonated bpp^-, proton exchange occurred again, resulting in the formation of Hbpp, and the reformation of $Cu(acac)_2$. A potential solution to this problem would be the complete removal of

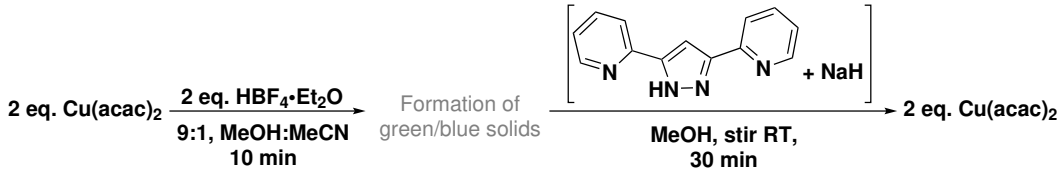

Scheme 4.8: An alternative route to $Cu_2(bpp)(acac)_2$. The results of the reaction again showed that the main product of the reaction was unreacted starting material.

the solvent and acacH after the addition of HBF_4 to the $Cu(acac)_2$ starting material. Addition of the deprotonated bpp^- ligand at this stage should result in the formation of the desired complex.

Use of Phosphines

Although phosphines are often avoided in aerobic oxidation catalysis due to their susceptibility to oxidative degradation *via* the formation of phosphine oxides, recent studies have suggested that in some cases such concerns are unwarranted.[279]

Having used a range of hard ligands in the attempt to prevent dimerisation of the copper complex, the use of a soft phosphine (PPh_3) was attempted. The intended product is shown in Scheme 4.9. Unfortunately, it was found that the product of the reaction was again the dimer, suggesting that the soft nature of the phosphines did not prevent dimer formation.

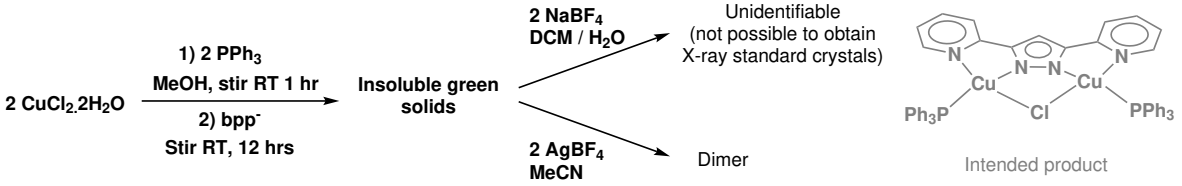

Scheme 4.9: Attempted synthetic routes to $Cu_2(bpp)(PPh_3)_2(\mu\text{-}Cl)$. Centrifugation was used to separate the insoluble green solids from the solvent.

4.2.2 Zinc Complexes using the Hbpp Ligand

Due to its d^{10} configuration, it was thought that synthesis of the corresponding zinc complexes might make characterisation of the products simpler, since they would be diamagnetic, and NMR spectroscopy could be more easily used to identify the products of reaction.

The synthesis of a mono-zinc complex was attempted, using the conditions shown in Scheme 4.10. After deprotonation of the Hbpp ligand using NaOMe, one equivalent of

$ZnCl_2$ was added and the reaction stirred for 12 hours. The reaction yielded a yellow solid that was insoluble in all common laboratory solvents. Following a similar method to the copper complexes, a halide exchange was performed using $AgBF_4$, yielding an off-white solid.

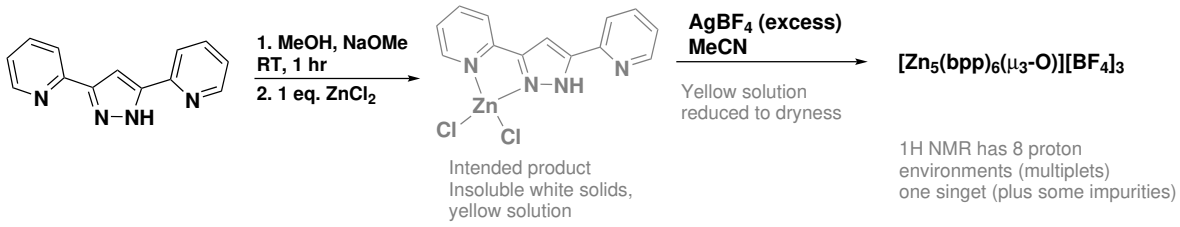

Scheme 4.10: Attempted synthesis of a mono-zinc complex. The product is the cluster shown in Figure 4.11.

The ^{1}H NMR of the resultant solid has 9 proton environments, 8 multiplets, and one singlet, which is assigned to the pyrazole proton. All peaks integrate to 1, suggesting that all nine protons on the Hbpp ligand are in distinct environments to each other.

X-ray crystallography revealed that the product was another cluster with the general formula $M_5(bpp)_6(\mu_3\text{-O})$, drawing a similarity to the copper cluster synthesised previously, Figure 4.10. The complex has an overall charge of 3^+, suggesting five Zn^{II} centres.

Further work would involve more thorough NMR spectroscopic characterisation of the complex, in conjunction with mass spectrometry studies. Additonally, potential reactivity of the complex could be studied alongside the reactivity of the copper complex.

4.2.3 Palladium Complexes using the Hbpp Ligand

Due to its prevalence in Wacker chemistry and other aerobic oxidations, the synthesis of a di-palladium complex was attempted. It was hoped that a bimetallic copper/palladium complex could be synthesised, mimicking the Wacker system in one complex. Commonly known for its Pd(0) and Pd(II) oxidation states, more recently a wider range of oxidation states have been observed in palladium chemistry.[280] This includes direct reaction O_2 with a Pd(II) precursor in an oxygen-insertion mechanism into a Pd–Me bond to produce a methylperoxide complex *via* a Pd(III) oxidation state.[281]

Initially, a simple palladium chloride precursor was added in a 1:1 ratio of a solution of Hbpp in methanol and stirred at room temperature for 12 hours, Scheme 4.11. After this time the solution was filtered, yielding red solids and a yellow filtrate. The red

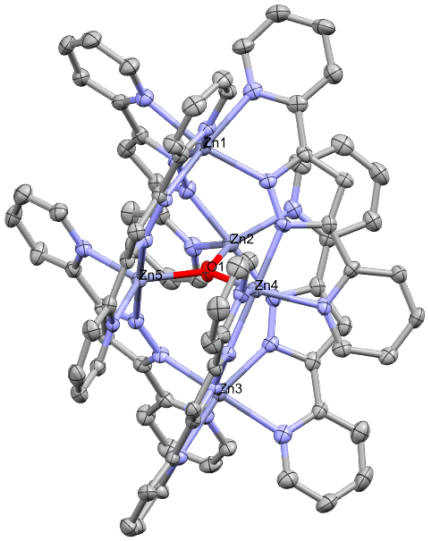

Figure 4.11: X-ray crystal structure of the zinc cluster formed by the reaction shown in Scheme 4.10. BF_4 counter-ions, hydrogen atoms and solvent molecules omitted for clarity, shown with 50% probability ellipsoids.

solids were stable in air, showing no visible changes over time. However, they were not soluble in any common laboratory solvents, with the exception of DMSO. Upon dissolving in DMSO, the solution turned yellow, suggesting a change in the state of the palladium complex.

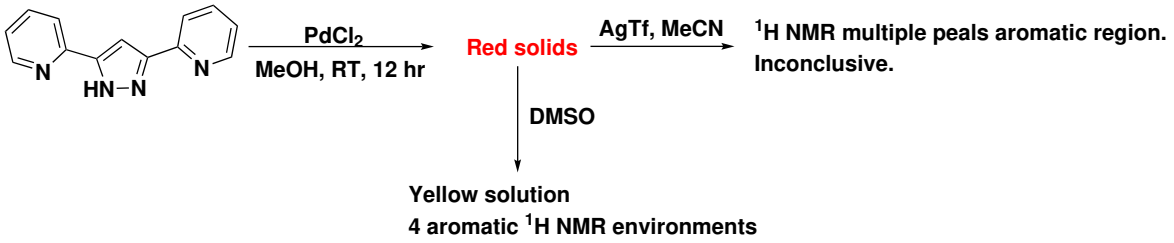

Scheme 4.11: Attempted synthesis of a mono-metallated palladium complex. The reaction yielded a red solid and yellow filtrate. The products have not been identified.

The ^{1}H NMR of the yellow solution in DMSO showed 4 broad peaks between 7.5 - 8.5 ppm, Figure 4.12. Integration of the peaks suggests that the singlet corresponding to the pyrazole proton sits underneath one of the peaks. The broadness of the peaks means there is no splitting patterns. The NMR also suggests that the complex is symmetrical, since it would be expected that the protons around the bpp$^-$ ligand would be unsymmetrical, corresponding to 9 distinct proton environments, in a monometallated species.

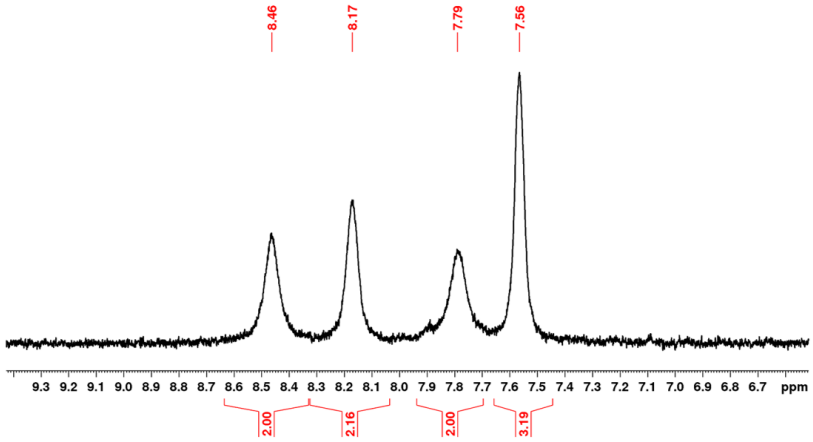

Figure 4.12: ^{1}H NMR of the palladium complex in DMSO. The peaks were too broad to show any splitting, but the integration pattern suggests that the pyrazole proton sits directly over another proton environment at 7.56 ppm.

It was not possible to obtain ^{13}C NMR data for the complex, since increasing the concentration resulted in poor solubility. Additionally, it was not possible to obtain mass spectrometry data for the complex. It is worth noting that the complex was observed to be stable in DMSO over a number of weeks, without any sign of palladium black formation. Reaction of the red solids with silver triflate (AgOTf) yielded multiple undetermined species, suggesting an unwanted side-reaction occurred.

4.2.4 Conclusion to Further Metal Complex Synthesis

Synthesis of a bimetallic copper complex with a potential binding site for catalysis were unsuccessful. Despite varying the auxiliary ligands, the formation of a $Cu_2(bpp)_2$ dimer was the favoured outcome in most cases. The *ortho*-methyl HL2 ligand was used to try and prevent dimerisation, but this resulted in the formation of a tetramer. Bipyridine was employed to try and prevent dimerisation occurring, but was unsuccessful. The use of phosphines as ligands again resulted in the formation of the $Cu_2(bpp)_2$ dimer.

The use of a $Cu(OAc)_2$ precursor resulted in the formation of a pentanuclear copper cluster, with a centrally bound μ-O atom. A similar cluster was also formed when using $ZnCl_2$. The ^{1}H NMR of the zinc complex suggested that the six bpp^{-} ligands are equivalent to each other, as might be expected from the symmetry that is present in the crystal structure.

Some preliminary studies using palladium suggest that a bimetallic complex is formed,

although further characterisation is needed to identify the product of this reaction. The product is formed as a red solid, but is soluble in DMSO, where it changes colour to produce a yellow solution, suggesting a change in coordination environment around the palladium centres.

4.3 A brief discussion of an *ortho*-Bromo Ligand

Synthesis of an *ortho*-bromo ligand, analogous to HL2, was attempted. It was thought this would offer a valuable comparison to the *ortho*-methyl HL2 ligand since in comparison to methyl substituents, the bromine substituents have a larger negative inductive effect.[183] Additionally, the group offers the possibility of further functionalisation through lithiation of the bromopyridine and subsequent reactions with appropriate electrophiles. Finally, both the bromo-functionalised starting materials (2-bromo-6-acetylpyrdine and 2-bromo-picolinic acid) were commercially available. Both starting materials were used for synthesis as received.

Conducting the esterification of the starting material in the microwave reactor resulted in a larger number of impurities, lowering the yield of the product to 40% by spectroscopic determination. To avoid the harsh microwave conditions the esterification was carried out at reflux over 12 hours, yielding the product in higher yields, with lower quantities of impurities. The Claisen condensation and Paal-Knorr synthesis to form the pyrazole proceeded as reported for all other ligands reported in Chapter 2, to yield the *ortho*-bromo ligand HL7, Figure 4.13.

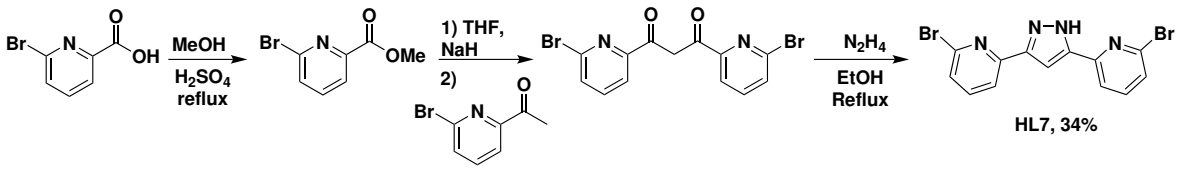

Figure 4.13: Synthesis of the *ortho*-bromo ligand (HL7).

Although NMR spectroscopy yielded a clean product, mass spectrometry suggested the presence of chlorine in the product. Further investigations revealed a statistical mixture of chloro and bromo substituents on the resultant ligand. This contamination likely originated in the starting materials.

4.4 Further Ligand Functionalisation

The issues encountered with the synthesis of copper complexes suggest that the rigid structure of the Hbpp ligand is not conducive to the synthesis of a bimetallic copper complex with an open binding site for catalysis. Many reported copper complexes are based on chelate ligands with nitrogen donors and flexible ligand backbones.[36] The problems with dimerisation could be due to the lack of flexibility of the Hbpp ligand coupled with its strong chelate effect.

In an attempt to address this, further functionalisation of the ligand was investigated. The functionalisation of the Hbpp ligand can be broadly broken down into three categories: addition of steric bulk in the ortho-position on the pyridine rings (S), electronic substitution on the pyrazole backbone (E) and addition of a binding site (X) to make an NNX tridentate ligand, Figure 4.14. It would be expected that each functionalisation will have an impact on reactivity and that the substituent chosen will also result in varied activity.

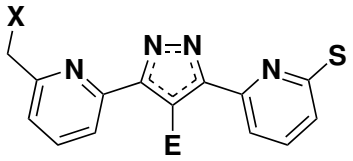

Figure 4.14: Functionalisation of Hbpp

The impact of substitution in the *ortho-* (S) and pyrazole position (E) is discussed in Chapters 2 and 3. Preliminary results into the addition of a binding site, and further pyrazole substitutions can be found below.

4.4.1 Addition of a Binding Site: NNX Functionalisation

Functionalisation of position X (Figure 4.14) offers further scope for both electronic and steric functionalisation. These systems will be less directly comparable to the other substitution patterns, but might change the binding environment around the metal centre in such a manner as to prevent dimerisation occurring.

PNN functionalisation

The addition of phosphines is often used to tune both the electronic and steric characteristics of a ligand in catalysis, indeed, they are even used to impart stereochemistry in certain systems.[282] As a consequence, the ability to add or change a phosphine on

the ligand backbone offers a vast degree of control over the system.

Functionalisation of the **HL2** ligand with one or two phosphine substituents changes the binding pocket from an NN system to an NNP binding moiety, significantly changing the binding environment. Such pincer-type ligands have seen a growing interest since 1970 and have seen application in a vast array of fields.[282–285]

Previous work in the Hintermair group successfully phosphorylated lutidiene (2,6-dimethylpyridine) using BuLi and tetramethylethylenediamene (TMEDA) which acts to stabilise BuLi. It was found that varying conditions could have a pronounced impact on the success of the functionalisation. Using a range of conditions previously tried in the group, the installation of the phosphine on HL2 was attempted (Scheme 4.12). The conditions tried can be found in Table 4.3.

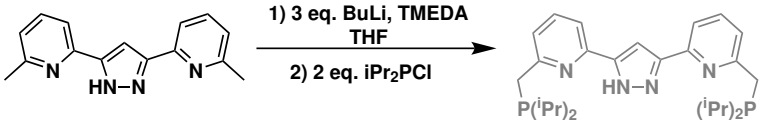

Scheme 4.12: Attepted synthetic route to the NNP functionalised ligand $^{i}(Pr_2P)$bpp via deprotonation of HL2, before addition of the chlorophosphine.

Unfortunately, although some new product was observed by ^{31}P NMR, the small scale of the reaction meant it was not possible to isolate and characterise the product, despite a number of attempts, outlined in Table 4.3.

A report by Meyer and coworkers suggests that a two step synthesis, via the mono-functionalised ligand, to achieve the diphosphorylated Hbpp ligand, is more successful.[185] The group used the phosphine functionalised ligand to synthesise iron[185] and rhodium complexes.[286]

Despite the promising results reported by Meyer and coworkers, this synthetic route was not pursued further. The introduction of a CH_2 group, in addition to the presence of a phosphine, makes the ligand susceptible to oxidation,[279] which limits its reactivity for oxygen reduction or aerobic oxidation reactions.

NNO Chelating Ligands - Alkoxide Functionalisation

As an alternative to the oxidatively fragile phosphine substitution, the introduction of alkoxide functionalisation was investigated. The alkoxide functionality is oxidatively robust, and the synthetic route discussed below means the product does not have a CH_2

Table 4.3: The different conditions tried in the attempted installation of a phosphine on HL2, Scheme 4.12

Base	Solvent	Temp [°C]	Time	Electophile	Comments
BuLi/TMEDA (3 eq.)	Hexane	-20	4 hrs	I_2	Solubility issues. No product observed
BuLi/TMEDA (3 eq.)	Diethyl ether	-20	4 hrs	I_2	Solubility issues. No product observed
BuLi/TMEDA (3 eq.)	THF	0	4 hrs	I_2	No change by ^{31}P NMR
BuLi/TMEDA (3 eq.)	THF	0	6 hrs	$^{i}Pr_2PCl$	Mixture of SM, some functionalised product, other side products
1) KO^tBu (1.1 eq.) BuLi/TMEDA (2 eq.)	THF	-10	4 hrs	$^{i}Pr_2PCl$	No product observed

group which is also vulnerable to oxidation. A 2015 report of a copper water oxidation catalyst with a tridentate NNO alkoxide ligand lends support to the use of the hard alkoxide functionalisation for copper complexes.[149]

Previous work in the Hintermair group expanded a family of pyridine-alkoxide ligands for iridium water oxidation catalysis (WOC) to seven different systems, which had a pronounced effect on the water oxidation activity of the catalysts.[118,287] The synthesis of the pyridine alkoxide ligands proceeded through the lithiation of bromopyridine, followed by reaction with symmetrical ketones to give the alcohol product, with yields ranging from 17% to 72%, Scheme 4.13.[287]

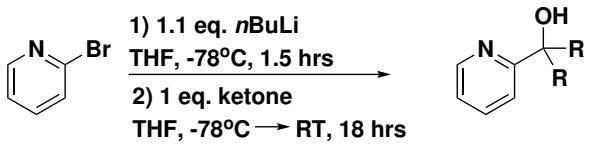

Scheme 4.13: Synthetic route to pyridine alkoxide ligands from bromopyridine used previously in the Hintermair group. Symmetrical ketones were used, the simplest of which being acetone.

In an effort to mimic the lithiation of bromo-pyridine, the di-*ortho*-bromo substituted Hbpp ligand discussed in Section 4.3 was used. The ligand was first deprotonated,

before lithiation in the 2-position and addition of the ketone, Scheme 4.14.

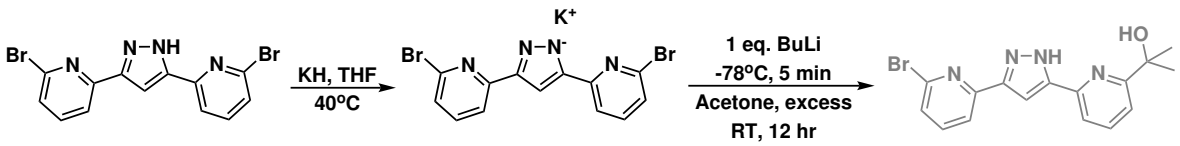

Scheme 4.14: Synthetic conditions for the attempted synthesis of alkoxide functionalised HL7. Unfortunately the product(s) of the reaction were not identifiable.

Unfortunately, repeated attempts to carry out the lithiation in this manner were unsuccessful, yielding to an intractable mixture of products. See Table 4.4 for a full list of conditions attempted. This could be due to unwanted reactivity at the 4-postion of the pyrazole competing with reactivity in the ortho-position of the pyridine rings. *n*BuLi is also a very strong base (pKa = 50) which could lead to ring opening occurring, resulting in a mixture of products.

Additionally, as discussed previously (Section 4.3), further investigation into this ligand by mass spectrometry and X-ray crystallography showed the ligand is contaminated with some chloro-substitution, rather than bromine. This impurity likely arises from the bromo-substituted starting materials. The stronger C – Cl bond means the lithium/chloro exchange is less successful, helping to explain the lack of success with this synthetic route.

In order to circumvent the problems associated with ^{n}BuLi, more sophisticated bases were investigated for substitution directly on the Hbpp ligand, taking advantage of the pyridine heteroatom to direct the substitution.[288] Rather than using harsh alkyllithium reagents, which lack selectivity and suffer from nucleophilic activity, attention was turned to alkali-metal secondary amides. Such bases have been shown to demonstrate high regioselectivity in the substitution of aromatic substrates.[289]

Research conducted in the late 90s and early 2000s investigated the use of zinc-based reagents, so called "zincates" as bases for chemoselective, and in some cases, chiral, deprotonation of arenes.[288–291] They have been shown to have high functional group tolerance, and required milder conditions than alkyl lithium bases.[292] Bulky secondary amines such as hexamethyldisilazide, diisopropylamide, or tetramethylpiperidide are most commonly used in the synthesis of zincate reactions, as shown in Scheme 4.15.[288,289]

Kondo *et al.* showed that the use of TMP-zincate for the alpha-metalation of pyridine proceeded smoothly, yielding 2-iodopyridine after quenching with iodine with yields of

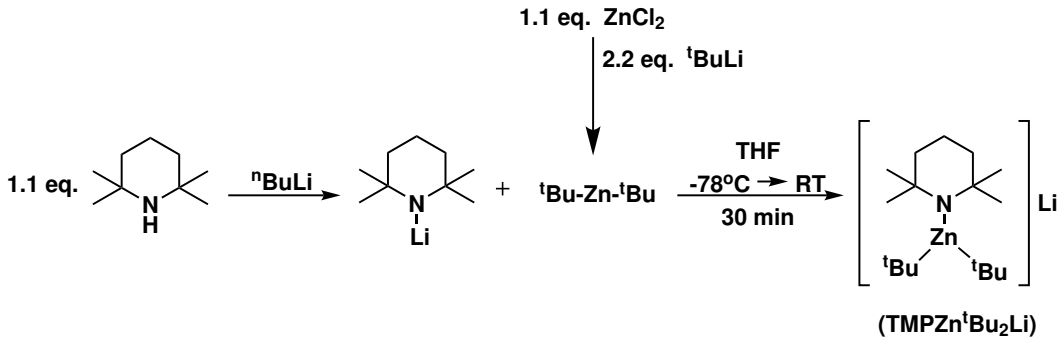

Scheme 4.15: Synthesis of the TMP zincate reagent.[288] The LiTMP is made from the reaction of *n*BuLi with 1.1 equivalents of TMP at −78 °C before stirring at 0 °C for 30 minutes. Di-*tert*butyl zinc was prepared from the addition of *t*BuLi to zinc chloride at −78 °C in THF.

up to 76%, Scheme 4.16.[288] Since 1999, there have been a number of examples of the use of alkali-metal zincate bases for reaction with pyridine.[293]

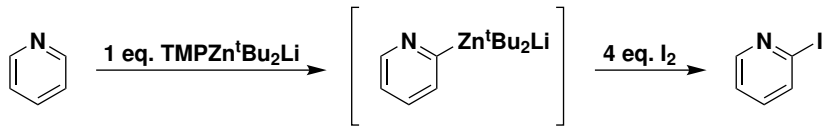

Scheme 4.16: Example of functionalisation by TMP zincate by Kondo *et al.* producing the functionalised product in 76% yield.[288]

The ligand is first deprotonated using potassium hydride (KH) as a non reversible base, since the H_2 produced will bubble off. After the synthesis of the zincate, Scheme 4.15, the deprotonated ligand is slowly added to the base and stirred for 3 hours at room temperature. This addition was accompanied by a colour change from yellow to red, which slowly turned orange/yellow after quenching with acetone and stirring for 12 hours. Upon quenching the reaction with water the solution went yellow, Scheme 4.17.

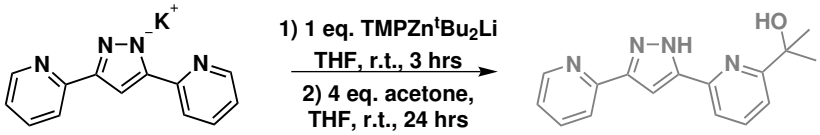

Scheme 4.17: Synthetic conditions for the attempted functionalisation of the deprotonated Hbpp ligand with TMP zincate. The product was not observed.

The crude ^{1}H NMR suggested at least two species were present, and no starting material remained. However, the distinctive peaks associated with the CH_3 groups were not identifable, and the large number of peaks in the aromatic region made attempts at

assignment challenging. Mass spectrometry results suggested that the product might be present, although in low concentrations. Upon recrystalisation of the product the ^{1}H NMR appeared to show just one species with 9 distinct proton environments in the aromatic region, and no CH_3 peaks.

A 2009 study on the use of potassium zincates for the metalation of 4-substituted pyridines found that the nature of the substitution greatly impacted the outcome of the reaction.[294] They found that substituents such as H, Et or *i*Pr resulted in mixtures of products, whereas amines, aryls or *t*Bu groups resulted in clean metalation in the alpha position. It is therefore possible that the presence of the pyrazole ring resulted in substitution in multiple positions around both pyridine rings on the substrate.

To avoid the potential reactivity caused by the pyrazole, the reaction was attempted with ethylpicolinate as the substrate, since there is literature precendent for the use of zincate bases in the presence of ester functionality.[288] However, the outcome of this reaction proved to be an intractable mixture of products, potentially including the products of ring-opening, Scheme 4.18.

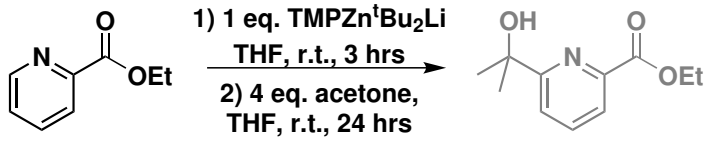

Scheme 4.18: Synthetic conditions for the attempted functionalisation of ethyl picolinate with TMP zincate. The product was not observed.

It is notable that the reaction with the ethylpicolinate resulted in a "messier" reaction than the reaction with the deprotonated ligand (Kbpp). Despite reports of zincates tolerating ester functionality, it is possible that the combination of an ester on a pyridine ring resulted in unforseen reactivity, resulting in the formation of multiple products.

In all cases, the intended product was not determined to be present in the result of the reaction, either through the use of NMR spectroscopy, or using thin layer chromatography (TLC) as an initial test. The large numbers of products suggest that the zincates are resulting in unwanted reactivity with the Hbpp and picolinate substrates used.

An alternative to the zincates and group 1 amides are Hauser bases and their turbo-charged variants. Developed in 2006 by Knochel and coworkers, the Hauser bases are

magnesium amide systems synthesised from the reaction between a Grignard reagent and an amine.[295,296] The addition of lithium chloride (LiCl), to form a "turbo-Hauser" base, increases their solubility resulting in higher kinetic activity. However, despite the addition of LiCl, the turbo-Hauser bases are less reactive than the group 1 amides, meaning higher levels of chemoselectivity can be achieved. They have been shown to be effective at magnesiation of functionalised heteroaromatic substrates, including tolerance of esters.[295,296]

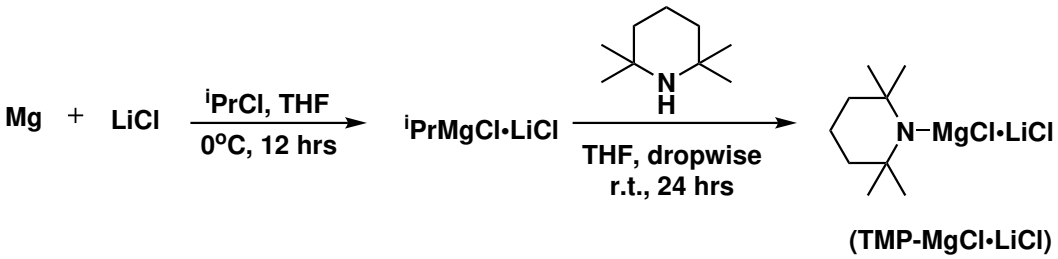

Scheme 4.19: Synthesis of the turbo-Hauser base. Addition of LiCl results in increased solubility and stability of the resultant base.

The reactivity of the turbo-Hauser bases was tested towards ethyl picolinate, Scheme 4.20, and Hbpp, Scheme 4.21. The reaction with ethyl picolinate yielded predominantly starting material, although ^{1}H NMR spectroscopy showed some minor peaks of around 10% intensity. It was not possible to characterise these fully due to overlap with the ethyl picolinate starting material and the low concentrations. Reaction with Hbpp yielded just the starting material with no apparant reaction. Unfortunately, the results suggest that the milder Hauser bases were not strong enough to activate the C–H bond of the pyrdine.

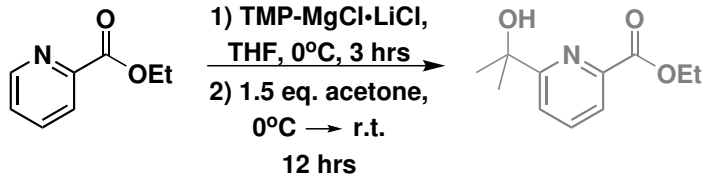

Scheme 4.20: Attempted synthesis of an alkoxide functionalised ethyl picoliate, using a Hauser base. The outcome of the reaction was undetermined.

In a similar manner to Grignard reagents, Hauser bases have complex Schlenk equilibria, whereby a number of different magnesium species exist in solution.[296] The position of the equilibrium is dependent on the concentration, solvent, temperature and both

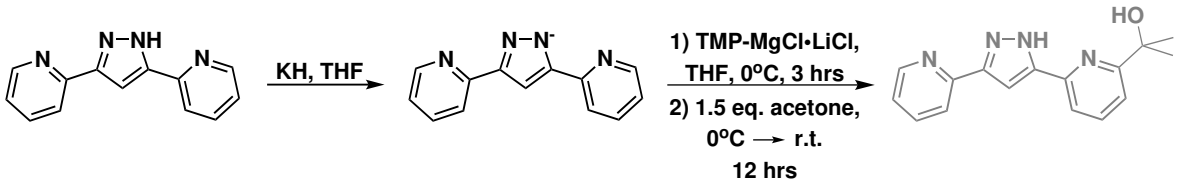

Scheme 4.21: Attempted synthesis of an alkoxide functionalised Hbpp ligand, using a Hauser base. The outcome of the reaction was undetermined.

the organic substituents and the halide.[296] It is therefore plausible that although the conditions reported in Table 4.4 were not successful in producing the functionalised Hbpp or ethyl picolinate, tweaking of the reaction conditions could prove successful.

Table 4.4: A summary of the different conditions tried to functionalise the Hbpp ligand or ethyl picolinate synthon.

Substrate	Base	Electrophile	Conditions	Results	Ref.
ortho-Br_2 (HL7)	2.2 eq. ^{n}BuLi	1.2 eq. acetone	Ligand in THF. ^{n}BuLi added at −78 °C, stir 1.5 hrs −78 °C, acetone added −78 °C, stir 18 hrs, RT.	Inconclusive, many unidentifiable species present by TLC.	
ortho-Br_2 (KL7)	1 eq. ^{n}BuLi	acetone (excess)	Ligand deprotonated with KH in THF. ^{n}BuLi added at −78 °C, stir 5 min −78 °C, acetone added −78 °C, stir 18 hrs, RT.	Inconclusive. Multiple species present by ^{1}H NMR, no identifable CH_3 peaks.	[288]
Kbpp	TMP$Zn^{t}Bu_2Li$ (zincate)	4 eq. acetone	Ligand deprotonated with KH in THF. TMP in THF (−78 °C), addition of ^{n}BuLi, stir 30 min. ^{t}BuLi added to $ZnCl_2$ at −78 °C. Di-*t*-butylzinc added to TMP/BuLI (−78 °C), warm to RT, stir 30 min. Add Kbpp in THF (R.T.), stir 3 hrs, add acetone, stir 18 hrs, RT.	Inconclusive. ^{1}H NMR suggests at least two species present. Mass spectrometry suggests product might be present.	
Ethyl picolinate	TMP$Zn^{t}Bu_2Li$ (zincate)	4 eq. acetone	As above	Inconclusive. Many unidentifable peaks via ^{1}H NMR. Possible ring opening?	
Ethyl picolinate	TMP MgCl.LiCl (Hauser)	1.5 eq. acetone	Mg, LiCl and *i*PrCl in THF. Stir rapidly 12 hours. Add TMP-H to *i*PrMgCl.LiCl at r.t. Stir 24 hrs. Dissolve substrate in THF. Add TMPMgCl.LiCl at 0 °C. Stir r.t. 3 - 6 hrs. Add acetone at 0 °C. Stir r.t. 18 hrs.	No reaction	[295, 297]
Ethyl picolinate	TMP MgCl.LiCl (Hauser)	1.5 eq. acetone	As above, but activate Mg with I_2 prior to use.	No reaction, some minor peaks by ^{1}H NMR	
Kbpp	TMP MgCl.LiCl (Hauser)	1.5 eq. acetone	As above, but activate Mg with I_2 prior to use.	No reaction	

4.4.2 Substitution on the Ligand Backbone

The impact of ligand substitution on the pyrazole backbone had a pronounced effect on the activity of the resultant cobalt complexes. In particular, $\mathbf{Co6_{O_2}}$, the NO_2 substituted species, showed markedly different behaviour to $\mathbf{Co5_{O_2}}$ (Br-substituent), with its behaviour more closely mirroring that of $\mathbf{Co2_{O_2}}$, the *ortho*-methyl substituted complex. However, the electrochemical results presented in Chapter 3 suggest that complexes with electron withdrawing substituents should be more accessible for reductive activity, such as the ORR. In order to investigate whether the deviation from the trend is due to purely an electron withdrawing effect of the NO_2 group, or whether this substitution pattern changes the reactivity of the complex *via* another method, the introduction of two different substituents were investigated.

Towards the Addition of a Phenyl ring and CF_3

Trifluoromethyl (CF_3) and a phenyl (Ph) group were chosen to further investigate the reactivity of the cobalt complexes. CF_3 is electron withdrawing, but less so than an NO_2 substituent, and more than a bromo group, Table 4.5. Since there is a pronounced difference in the reactivity of $\mathbf{Co5_{O_2}}$ and $\mathbf{Co6_{O_2}}$ towards the ORR and in the oxygen atom transfer studies, this would allow the impact of ligand substitution to be further studied.

Table 4.5: Hammett constants for the substituents shown. Values are the σ(para) constants reported by Taft and coworkers.[183] Positive is electron-withdrawing, negative is electron-donating.

Ligand	Substituent	Hammett Parameter
HL1	H	0
HL2, HL3	Me	-0.17
HL4	NH_2	-0.66
HL5, HL7	Br	0.23
HL6	NO_2	0.78
HL8	Ph	-0.01
HL9	CF_3	0.54

The phenyl group has a very minor electron donating effect, although according to Table 4.5 can be effectively viewed as neutral, like the unsubstituted HL1. Synthesis of a cobalt complex based on HL8 would mean the potential steric effect of a substituent on the pyrazole backbone could be studied, since the electronic effect of the phenyl

group would be minor, and is therefore comparable to HL1.

Addition of a trifluoromethane group and a phenyl ring were investigated via Route 1 (as discussed in Chapter 2, Section 2.2), which required the synthesis of the substituted ketone starting materials, before diketone synthesis followed by formation of the pyrazole.

The synthesis of the phenyl substituted ketone proceeded via the reaction of ethylpicolinate with benzyl magnesium bromide, yielding the ketone product in 89% yield, Scheme 4.22.[298] There are a number of examples of synthetic routes to this complex, including the use of pyridine epoxides,[299] or cyanopyridine.[300]

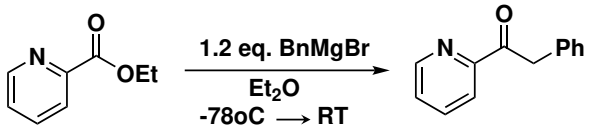

Scheme 4.22: Addition of a phenyl group to acetylpyridine through reaction with benzyl magnesium bromide.

The phenyl functionalised ketone was deprotonated using NaH and reacted with ethyl picolinate. Since isolation of the diketone product proved challenging previously, the product was not isolated and used directly for the synthesis of the pyrazole product, Scheme 4.23. Preliminary results on a small scale were promising for the formation of HL8 by ^{1}H NMR spectroscopy. However, scaling up the synthesis of the phenyl substituted ketone was unsuccessful. The outcome appeared to be a product that had undergone multiple nucleophilic additions of the benzyl group to the starting material. This is possibly due to the small scale reaction being carried out with low concentrations, which, upon scaling up, were not sufficiently accounted for due to the high volumes of solvent required.

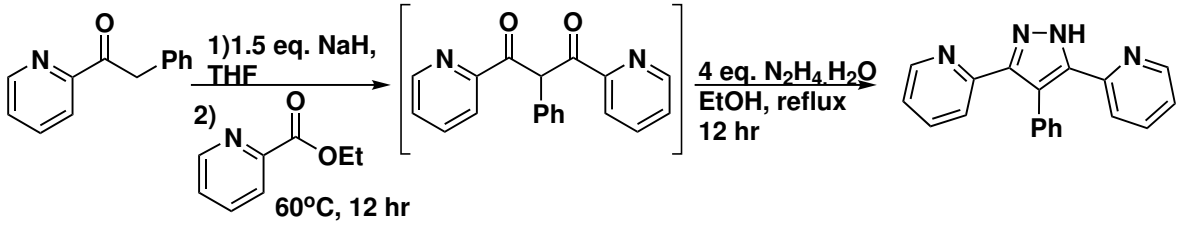

Scheme 4.23: Synthesis of the phenyl substituted variant of the Hbpp ligand, HL8.

Further work would perform a parallel synthesis of the phenyl substituted ketone on a

smaller scale, before combining the products to carry out the subsequent steps of the synthesis to yield a workable quantity of HL8. HL8 could be used for synthesis of a cobalt complex with a phenyl substituent on the pyrazole backbone to offer comparison to $\mathbf{Co1_{O_2}}$ – $\mathbf{Co6_{O_2}}$.

Following a procedure reported by Li and coworkers, the CF_3 functionalised pyridine was synthesised in 33% yield, Scheme 4.24.[301] The synthesis proceeds *via* synthesis of an enol triflate, before rearrangement in the presence of catalytic amounts of silver ($AgNO_3$) and an oxidant ($(NH_4)_2S_2O_8$). The mechanism is a radical process, and the authors tentatively propose that the reaction is initiated by the formation of a sulfate radical through reaction of the silver(I) with the persulfate.[301]

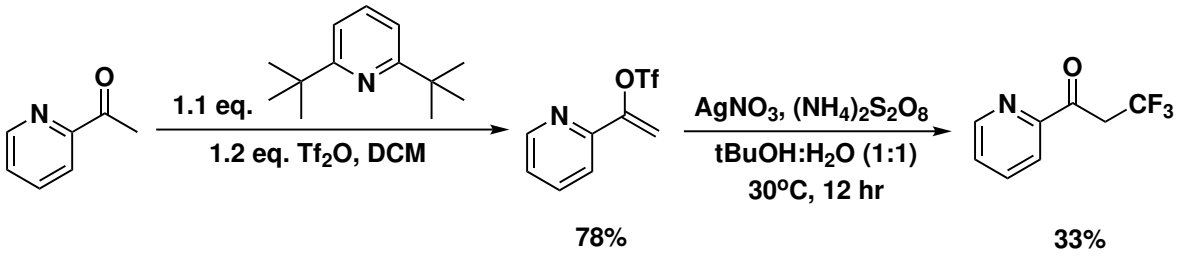

Scheme 4.24: Synthetic route to the CF_3 substituted acetylpyridine with yields shown.[301]

Unfortunately, the subsequent synthetic steps proved challenging. A small-scale reaction to form the diketone intermediate formed an oily substance that proved challenging to purify. Crude ^{1}H NMR after heating the reaction at 60 °C for 12 hours revealed at least 10% unreacted starting material remained. The use of ^{19}F NMR revealed the presence of only one fluorine containing species, that corresponded to the CF_3-ketone shown in Scheme 4.24 suggesting that the formation of the diketone had not occurred. Further synthesis was not attempted.

In Chapter 2 ligand synthesis routes 2 and 3 proved more successful for the functionalisation of the pyrazole backbone, where the functionality was installed on the diketone or pyrazole, rather than the ketone starting materials. It is likely that the reactivity of the CF_3 group resulted in unwanted side reactions during the formation of the pyrazole. Therefore, successful addition of a trifluoromethyl group to the pyrazole backbone might be more successfully incorporated into the Hbpp ligand after the Paal-Knorr synthesis of the pyrazole.

Although work by Francas *et al* installed a benzyl group on the backbone of the diketone

using a benzyl grignard,[165], the introduction of a CH_2 group makes the ligand more susceptible to oxidative degradation under catalytic conditions.

These findings are supported by results from Meyer *et al.*, who report that in a related ligand system their functionalised ketone degrades over time, resulting in low yields from route 1. This lead them to develop an alternative synthetic route, more similar to route 2.[186] The combination of increased reactivity of the functionalised ketone starting material with potential degradation might explain why the phenyl and trifluoromethane substitution reactions were unsuccessful. Future work would investigate the installation of the trifluoromethyl group to the diketone intermediate, rather than the ketone starting material, which should avoid the problems with the synthesis of the diketone.

4.5 Conclusions and Future Work

Multiple attempts were made to synthesise a bimetallic copper complex with a 2:1 metal:ligand ratio, leaving a binding site available for catalysis. However, despite the use of multiple different auxiliary ligands, the synthesis was not successful. When attempting the synthesis using a copper acetate precursor a copper cluster was formed, with five copper centres and six bpp^- ligands. This cluster was also the product of a reaction with $ZnCl_2$. Both structures mirror those reported in iron and cobalt systems, both of which show catalytic activity. Future work would fully characterise the clusters, including electrochemically, and investigate their reactivity towards aerobic oxidations.

Preliminary studies into the synthesis of a palladium Hbpp complex suggested the formation of a bimetallic species. However, it was not possible to characterise this complex further, and future work would focus on isolating and characterising the complex. However, the lack of formation of palladium black, even over extended periods of time, was promising.

Future work might use different copper precursors, including $CuBr_2$ or Cu^I precursors, to investigate whether the formation of the dimer is also favoured. Unlike Cu^{II}, which tends to form square planar or pyramidal (trigonal and square-based) geometries, Cu^I preferentially forms linear or tetrahedral geometries, which might lend itself more readily to forming complexes with vacant binding sites.[302,303] Cu^I will also more readily react with O_2 than Cu^{II} making it a more appropriate precursor for synthesis of an oxygen activation catalyst.

However, many examples of copper complexes for aerobic oxidations use nitrogen-based

ligands with more flexible backbones, meaning the copper can adopt a distorted tetrahedral or trigonal bipyramidal arrangement.[36,38,53,112] These more flexible binding modes leave a vacant site for binding of a substrate. The rigid Hbpp ligand constrains the possible binding modes, meaning it might not be a suitable ligand for copper catalysis.

Further synthesis of the ligand focused on addition of a binding site or functionalisation of the pyrazole backbone. The addition of a binding site investigated the addition of an alkoxide binding site through the use of sophisticated bases to activate the *ortho*-position of the Hbpp ligand, before the use of acetone as an electrophile. Although the use of zincate bases had some potentially promising results, identification and isolation of the desired product was never achieved. There are examples of substitution directly onto the pyridine, using BuLi and LiDMAE and a LiCl additive.[304] However, the presence of the pyrazole might cause issues, and is susceptible to ring opening.

Attempts at introducing new functionality onto the pyrazole backbone focused on the introduction of phenyl and a trifluoromethyl groups. Neither route was successful, but a small scale reaction of the phenyl group had some promising results by ^{1}H NMR spectroscopy. It was thought that the reactivity of the CF_3 group might be interfering with the diketone formation and subsequent pyrazole formation. Therefore, further work might investigate ways to introduce such reactivity directly onto the Hbpp ligand, in a method similar to the introduction of the bromo and nitro groups described in Chapter 2

4.5.1 Towards the Synthesis of Heterobimetallics

In order to synthesise heterobimetallic complexes, it is necessary to first obtain monometallated systems. There are a number of potential approaches to this, including "blocking" a binding site, either by the addition of a protecting group, or more simply by not deprotonating the ligand, therefore blocking the second binding pocket. Alternatively, the use of unsymmetrical ligands would facilitate this process, as the binding pockets could be tuned to the target metal.

There are limited examples of heterobimetallic systems based on the Hbpp ligand, including a ruthenium/zinc complex with the formula $[RuCl(trpy)]_2(\mu\text{-}[Zn(bpp)_2])^{2+}$.[192] This synthesis has also been repeated with cobalt and manganese in the place of zinc.[305] There is also an example of a nickel/iron cluster with cyanide bridges,[306] and a chromium/lanthanide series of examples with acetylacetone as auxiliary ligands.[191] A more recent example reports a series of three iridium Cp* complexes with cobalt, nickel and

copper as the second metal, which performs H_2 evolution.[307] In all cases, a monometalled complex is synthesised first, before introduction of the second metal.

4.6 Experimental

4.6.1 Analytical Techniques

All reactions and workups were carried out in air unless specified otherwise. Reactions under argon were performed using standard Schlenk techniques or an MBraun Unilab Plus glovebox.

NMR spectra were recorded using a Bruker Avance III NMR spectrometer operating either at 500.13 MHz or 400.04 MHz for ^{1}H experiments or a 500 MHz Agilent ProPulse. Unless otherwise specified organic samples were analysed in $CDCl_3$ and metal complexes analysed in MeCN - at 25 °C using standard Bruker pulse sequences (Topspin 2.1). Chemical shifts (δ) are reported in ppm. Typically ^{1}H spectra were acquired with a spectral width (SW) of 20 ppm, and 16 transients. $^{13}C\{^1H\}$ spectra were obtained with a SW of 220 ppm and with 1024 transients. Spectra were referenced using the residual solvent signal, at 7.26 or 1.95 ppm for ^{1}H (in $CDCl_3$ or MeCN respectively) and 77.0 or 1.32 ppm for ^{13}C (in $CDCl_3$ or CD_3CN respectively). Where diamagnetic samples were prepared in protonated solvents ^{1}H spectra were acquired with (pre-saturation) solvent suppression pulse sequences. Unless stated otherwise, paramagnetic samples were acquired using a wide spectral width (SW = 200 ppm) with the spectrum origin = 50 ppm, acquisition times were set to 0.5 s, and relaxation delay reduced to 1 s. Note that the paramagnetic spectra did not show any splitting, so only the ppm values and integrals are reported.

Mass Spectrometry of ligands were conducted on an Agilent Electrospray Quadrupole Time-of-Flight (QTOF) mass spectrometer. Mass spectrometry of $\mathbf{Co1_{O_2}}$ and $\mathbf{Co2_{Cl}}$ were performed at the EPSRC National Mass Spectrometry Facility in Swansea. Analysis of all other cobalt complexes were conducted using a MaXis HD quadrupole electrospray time-of-flight (ESI-QTOF) mass spectrometer (Bruker Daltonik GmbH, Bremen, Germany), using a glass syringe (Hamilton) and syringe pump (KD Scientific, Model 781100) for infusions at a flow rate of 3 µl/min. Analyses were performed in ESI positive mode with the capillary voltage was set to 4500 V, nebulizing gas at 1 bar, drying gas at 6 L/min at 180 °C in each case. The TOF scan range was from 50 - 1000 mass-to-charge ratio (m/z). The MS instrument was calibrated using an infusion

of sodium formate calibrant solution. The calibrant solution consisted of 3 parts of 1 M NaOH to 97 parts of 50:50 water:isopropanol with 2% formic acid. Data processing was performed using the Compass Data Analysis software version 4.3 (Bruker Daltonik GmbH, Bremen, Germany).

Single crystal X-ray diffraction analysis was carried out by Dr Gabriele Kociok-Köhn at the University of Bath using a RIGAKU SuperNova Dual. Crystallography images were rendered using Mercury 4.3.1 software. Angles between atoms, bond distances and angles between planes were calculated using Olex2 software.[203]

Commercially available materials were obtained from Sigma Aldrich, Fisher or Acros and used as received unless otherwise stated. Methanol was dried by distillation from magnesium. Toluene was dried by distillation from sodium. THF, Et_2O and hexane were dried by distillation from potassium. Acetonitrile was dried by distillation from calcium hydride and stored over 4 Å molecular sieves.

4.6.2 Metal Complexes

$[Cu_2(bpp)_2(OH)_2][BF_4]_2$

To a solution of Hbpp (32.6 mg, 0.15 mmol) in 15 mL ethanol (dry), add sodium ethoxide (7.9 mg, 0.15 mmol) in ethanol. Stir at room temperature for 1 hour. Add copper (II) chloride dihydrate (50 mg, 0.29 mmol), stir at room temperature for 24 hours. Separate by centrifugation. Resultant solid is insoluble in all common laboratory solvents. A suspension of the insoluble copper product was made in acetonitrile (10 mg, 0.75 mmol), to which an excess of silver tetrafluoroborate ($AgBF_4$) was added and stirred in the dark for 2 hours. The resulting blue solution was filtered to remove silver chloride and the solvent removed. X-ray crystallography standard crystals were grown by layer diffusion using acetonitrile and diethyl ether. ^{1}H NMR (400 MHz, $CDCl_3$, δ (ppm): 23.1, 21.3, 11.3 MS (FTMS + pNSI), Calculated m/z $[M - 2\,BF_4 - 2\,H_2O]^{++}$ = 284.0118, 284.5132, 285.0111, Found m/z $[M - 2\,BF_4 - 2\,H_2O]^{++}$ = 284.0117, 284.5131, 285.0108

$[Cu_4(Mebpp)_4][BF_4]_4$

To a solution of MeHbpp (36.7 mg, 0.15 mmol) in 15 mL ethanol (dry), add sodium ethoxide (7.9 mg, 0.15 mmol) in ethanol. Stir at room temperature for 1 hour. Add copper (II) chloride dihydrate (50 mg, 0.29 mmol), stir at room temperature for 24 hours. Separate by centrifugation. Resultant solid is insoluble in all common laboratory

solvents. 70 mg insoluble solid obtained.

A suspension of the insoluble copper product was made in acetonitrile (10 mg, 0.75 mmol), to which an excess of silver tetrafluoroborate ($AgBF_4$) was added and stirred in the dark for 2 hours. The resulting blue solution was filtered to remove silver chloride and the solvent removed. X-ray crystallography standard crystals were grown by layer diffusion using acetonitrile and diethyl ether. ^{1}H NMR (500 MHz, CD_3CN, δ (ppm): 56.13, 47.25, 45.14, 38.62, 26.76, 19.89, 12.38, -2.47

Copper Bipyridine Synthesis

$CuCl_2 \cdot 2\,H_2O$ (0.05 g, 0.2 mmol) was dissolved in methanol. In a separate vessel, bipyridine (0.046 g, 0.2 mmol) was dissolved in methanol and added to the copper solution. Hbpp (0.033 g, 0.1 mmol) and NaOMe (0.009g, 0.11 mmol) were stirred together in methanol and added to the copper solution. The mixture was heated at 40 °C for 2 hours before stirring at R.T. for 12 hours. The solids were separated by centrifugation and counter-ion exchange performed by stirring the solid in MeCN with $AgBF_4$ (10 mg, 0.05 mmol) in the dark for 15 minutes. After filtering the solution, the filtrate was left to stand allowing slow evaporation of the MeCN, yielding X-ray standard crystals. Upon analysis, they were found to be $Cu_2(bpp)_2(H_2O)_2$.

Copper Acetate Precursor Synthesis

The Hbpp ligand (30.5 mg, 0.14 mmol) was dissolved in EtOH. NaOEt (1.1 eq., 8.2 mg, 1.5 mmol) was added and the solution stirred at R.T. for 30 minutes. A solution of $Cu(OAc)_2$ (50 mg, 0.28 mmol) in EtOH was added and the resulting mixture stirred at room temperature for 24 hours. Almost immediately, pale blue solids formed, which were stirred in solution. The solids were separated from the supernatant by centrifugation. Growth of X-ray standard crystals by slow evaporation from a mixture of MeCN, MeOH and toluene yielded a crystal with formula $Cu_5(bpp)_6\mu$-O.

Copper Acetylacetone Precursor Synthesis

$Cu(acac)_2$ (0.05 g, 0.19 mmol) was dissolved in MeOH (dry). Hbpp (0.021 g, 0.09 mmol) was added and the solution heated at reflux for 2 hours before stirring at R.T. for 12 hours. The solvent was removed under vacuum until solids appeared, after which they were separated by centrifugation yielding dark blue solids. The solids were analysed by X-ray crystallography after growth of crystals by slow evaporation from a solution of MeCN, and were found to be unreacted $Cu(acac)_2$.

Cu phosphine synth

$CuCl_2$ (0.05 g, 0.29 mmol) and PPh_3 (0.077 g, 0.29 mmol) were dissolved in MeOH and stirred at R.T. for 1 hour. In a separate vessel, Hbpp (0.033 g, 0.15 mmol) was deprotonated by NaOMe (0.009 g, 0.16 mmol) in MeOH before combining both mixtures and stirring the resultant solution for 12 hours. The pale green solids were isolated by centrifugation. Halide exchange was performed with $AgBF_4$ in MeCN, and X-ray standard crystals were grown by slow evaporation of MeCN, yielding the dimer, $Cu_2(bpp)_2(H_2O)_2$.

Zinc Cluster

To a solution of Hbpp (81.5 mg, 0.37 mmol) dissolved in MeOH (15 mL), NaOMe (22 mg, 0.40 mmol) was added. The solution was stirred for 1 hour at room temperature, before $ZnCl_2$ (50 mg, 0.37 mmol) in MeOH (10 mL) was added. The solution was stirred at R.T. for 12 hours before filtration to remove white solids which were not soluble in any common laboratory solvents. The solvent was removed *in vacuo* from the yellow filtrate.

A small sample of the yellow solid was taken and added to MeCN (5 mL), before addition of $AgBF_4$ (20 mg, 0.10 mmol). The solution was stirred in the dark for 15 minutes before filtration to remove silver salts. The filtrate was concentrated before NMR spectroscopy was collected, and X-ray standard crystals were grown by slow evaporation of the solvent from the NMR tube post analysis, yielding the product $Zn_5(bpp)_6\mu$-O. ^{1}H NMR (500 MHz, CD_3CN, δ (ppm): 6.98 (1H, td, J = 7.67, 1.31 Hz), 6.77 (1H, td, J = 7.76, 1.12 Hz), 6.68 (1H, d, J = 7.95 Hz), 6.56 (1H, s (br)), 6.30 (1H, d, 7.10 Hz), 6.27 - 6.25 (1H, m), 5.75 - 5.72 (1H, m), 5.68 (1H, s (br)), 5.38 (1H, s) $^1\{H\}^{13}$C NMR (125 MHz, CD_3CN), δ (ppm): 149.9, 148.1, 147.5, 142.3, 141.5, 125.3, 124.0, 101.1

Palladium Complexes

$PdCl_2$ (50 mg, 2.2 mmol) was suspended in MeOH and Hbpp (63 mg, 2.2 mmol) was added in MeOH. The solution was stirred at room temperature for 12 hours. The red solid formed was separated through centrifugation and washed with methanol. A small sample of the red solid was stirred with silver triflate (AgOTf) for 1 hour before filtering. Analysis of the solids by ^{1}H NMR spectroscopy revealed a number of very broad peaks that were not possible to assign.

Dissolving an NMR scale sample of the red solid in DMSO-d6 yielded a yellow solution. ^{1}H NMR (500 MHz, DMSO$-d_6$), δ (ppm): 8.46 (2H, s (br)), 8.17 (2H, s (br)), 7.79 (2H, s (br)), 7.56 (3H, s (br)). $^{1}\{H\}^{13}$C NMR (125 MHz, DMSO$-d_6$), δ (ppm): 126.5, 140.6 *Note that due to solubility issues it was not possible to obtain full ^{13}C NMR data of the complex*

4.6.3 Further Ligand Synthesis: *ortho*-Bromo Substitution

Ethyl 6-bromopicolinate

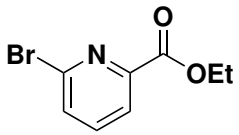

[230.064 g mol^{-1}]

6-bromopicolinic acid (1 g, 5.0 mmol) was dissolved in EtOH (20 mL) and three drops of HCl (37%) were added. The solution was refluxed for 12 hours in air, before cooling to room temperature. The solution was quenched by careful addition of Na_2CO_3 before extraction with DCM (3 x 10 mL). (0.65 g, 2.8 mmol, 57%) ^{1}H NMR (400 MHz, $CDCl_3$, δ (ppm): 8.04 (1H, dd, J=0.90, 7.62 Hz), 7.79 (1H, t, J=7.80 Hz), 7.50 (1H, dd, J=0.90, 7.98 Hz), 4.47 (1H, q, J=7.13 Hz), 1.42 (1H, t, J=7.12 Hz) $^{1}\{H\}^{13}$C NMR (100 MHz, $CDCl_3$, δ (ppm): 164.0, 151.6, 148.6, 139.5, 127.9, 123.6, 62.3, 14.3 *In agreement with reported literature values.*[219]

2-pyridyl-2-(6-bromo)pyridyl-1,3-propanedione

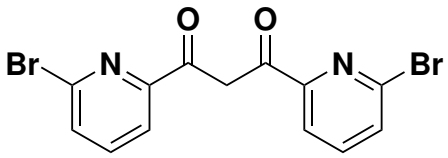

[384.03]

Ethyl-6-bromopicolinate (0.65 g, 2.8 mmol) was dissolved in tetrahydrofuran (THF). Sodium hydride (60% dispersion in paraffin oil) (0.17 g, 5.6 mmol) was added and the solution stirred for 30 minutes before adding 2-acetyl-6-bromopyridine (0.57 g, 2.8 mmol). THF was added as the mixture thickened (total 100 mL). The solution was stirred at 60 °C for 12 hours. The solvent was removed under vacuum, before carefully adding water (50 mL) whilst stirring vigorously. Upon addition of acetic acid (5 – 10 mL) a yellow/white solid formed which was separated by filtration and washed with ice-cold water. Although a crude ^{1}H NMR spectrum was collected, the crude product was not thoroughly dried and purified, and was used directly in the synthesis of the ligand, HL7. (0.84 g, 2.2 mmol, 78%) ^{1}H NMR (400 MHz, $CDCl_3$, δ (ppm): 8.17 (2H,

dd, J = 7.52, 0.98 Hz), 7.92 (2H, t, J = 7.87 Hz), 7.61 (2H, dd, J = 8.04, 1.02 Hz)

HL7: 2,2'-(1H-Pyrazole-3,5-diyl)bis(6-bromopyridine) (BrHbpp)

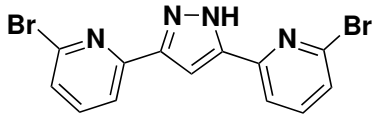

[380.04]

Crude 2-pyridyl-2-(6-bromo)pyridyl-1,3-propanedione (0.84 g, 2.2 mmol) was dissolved in EtOH (50 mL) and an excess of hydrazine hydrate ($N_2H_4 \cdot H_2O$) (0.5 mL, 11 mmol) was added. The reaction was heated at reflux for 12 hours, before cooling to room temperature. After cooling the total volume was reduced until solids formed, which were separated by filtration and washed with ice-cold ethanol. The solids were purified by recrystallization from boiling ethanol and diethyl ether. (0.28 g, 0.75 mmol, 34%) ^{1}H NMR (400 MHz, $CDCl_3$, δ (ppm): 11.13 (1H, br), 7.71 (2H, t, J = 7.76 Hz), 7.60 (2H, t, J = 7.78 Hz), 7.42 (1H, s), 7.26 (2H, d, J = 7.80 Hz) $^1\{H\}^{13}$C NMR (100 MHz, $CDCl_3$, δ (ppm): 102.7, 123.5, 127.2, 139.1, 139.5 MS (ESI+), Calculated m/z [M+H]+ = 378.9188, 380.9168, 382.9148 Found [M+H]+ = 378.9189, 380.9168, 382.9147

4.6.4 Further Ligand Synthesis: Addition of a Binding Site

PNN Functionalisation

Conditions were varied according to Table 4.3. In all cases, HL2 (0.02 g, 0.08 mmol) was dissolved in the appropriate solvent and TMEDA (0.04 mL, 0.24 mmol) was added. The solution was cooled to the temperature shown in the table and *n*-BuLi (1.4 M in hexane, 0.2 mL, 0.24 mmol) added and stirred at temperature shown for the time shown. The electrophile (I_2: one pellet, ↑iPr2PCl: 0.025 mL, 0.16 mmol) was added and the resultant solution stirred for 12 hours, before quenching the solution with careful addition of water, and extraction with DCM. Analysis was performed with ^{1}H and ^{31}P NMR spectroscopy, showing a lack of product formation.

Methylation of Br_2Hbpp with BuLi

Hbpp (62 mg, 0.28 mmol) was dissolved in THF and cooled to 0 °C. Butyl lithium in hexane (0.4 ml, 0.56mmol) was added dropwise and the solution stirred at 0 °C for 30 minutes. Methyl iodide was added and the resulting solution stirred at 0 °C for 2 hours. After stirring at room temperature for 12 hours, the solution was quenched by careful addition of water. The solution was extracted with DCM (3 x 10 mL). The resultant NMR showed a range of products and was not purified further.

Methylation of Br_2Kbpp with BuLi

Br_2Hbpp (50 mg, 0.13 mmol) was dissolved in THF (10 mL) and added to a solution of KH (5.3 mg, 0.13 mmol) in THF and stirred at 40 °C for 5 hours. The solution was cooled to 78 °C and *n*-BuLi (0.08 mL, 0.13 mmol) was added dropwise. After 10 minutes acetone (1 mL, 17 mmol) was added dropwise and the solution allowed to warm to room temperature and stirred for 12 hours. The solution was quenched by careful addition of water before extraction with DCM (3 x 10 mL). The resultant NMR showed a range of products and was not purified further.

Synthesis of Zincates

2,2,6,6-tetramethylpiperidine (0.19 mL, 1.1 mmol) was dissolved in THF (15 mL) and cooled to −78 °C. *n*-BuLi (0.63 mL, 1.0 mmol) was added dropwise and the mixture stirred at0 °C for 30 minutes. In a separate vessel, $ZnCl_2$ (0.16 g, 1.2 mmol) was dissolved in THF (15 mL) and *t*-BuLi (1.4 mL, 1.2 mmol) was added at −78 °C. The di-*t*-butylzinc was added to the TMP/BuLi mixture at −78 °C and the mixture warmed to room temperature and stirred for 30 minutes. The substrate (Kbpp: 0.26 g, 1.0 mmol or ethylpicolinate: 0.14 mL, 1 mmol) was dissolved in THF and added to the TMPZntBu$_2$Li solution and stirred at room temperature for 3 hours, after which acetone (4.0 mmol) dissolved in THF was added and the resultant mixture stirred at room temperature for 24 hours. The reaction was quenched by addition of H_2O and the aqueous phase extracted with$CHCl_3$. The organic layers were combined and dried over $MgSO_4$ and the solvent removed *in vacuo* to yield a yellow solid. Many species identified by ^{1}H NMR spectroscopy, and product was not purified further.

Synthesis of Hauser Bases

Magnesium (2.5 g, 0.1 mol) was preactivated by addition of I_2 with vigorous stirring and sonication immediately prior to use. LiCl (0.51 g, 12 mmol) was dissolved in THF (10 mL) and added to the Mg/I_2. ^{i}PrCl (1.1 mL, 12 mmol) in THF was added dropwise at 0 °C and the resultant solution stirred for 12 hours. TMP-H (2.12 mL, 12.5 mmol) was dissoved in THF and added to the ^{i}PrMgCl · LiCl at room temperature and the solution stirred for 24 hours. The substrate (ethylpicolinate: 0.68 mL, 5 mmol or Kbpp: 0.8 g, 5 mmol) was dissolved in THF and cooled to 0 °C. The TMPMgCl.LiCl was added dropwise at 0 °C and the solution stirred at 0 °C for 5 hours, after which acetone (0.15 mL, 2 mmol) in THF was added and the solution allowed to heat from 0 °C to room temperature and stirred for a further 12 hours. The reaction was quenched by addition

of sodium bisulphate ($NaHSO_4$, excess), causing solids to precipitate which were filtered off. The solvent was removed *in vacuo* yielded orange/yellow solids in both cases. ^{1H} NMR spectroscopy revealed the starting materials in both cases, suggesting no reaction had occurred.

4.6.5 Further Ligand Synthesis: Substitution on the Pyrazole Backbone

2-phenyl-1-(pyridine-2-yl)ethanone

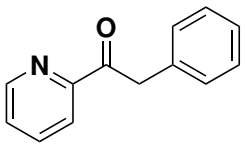

[197.24 g mol^{-1}]

Ethyl picolinate (0.2 mL, 1.5 mmol) was dissolved in THF and the solution cooled to −78 °C. Benzyl magnesium chloride (1.3 mL, 1.8 mmol) was added dropwise at −78 °C. The solution was warmed slowly to room temperature and stirred for 12 hours. The solution was quenched by addition of aqueous ammonium chloride solution, and the aqueous phase extracted by diethyl ether (3 x 10 mL). The organic fractions were combined and dried over $MgSO_4$, before removal of the solvent in vacuo. (0.26 g, 1.32 mmol, 89%) ^{1}H NMR (400 MHz, $CDCl_3$, δ (ppm): 8.72 (1H, m), 8.05 (1H, m), 7.82 (1H, td, J = 7.75, 1.69 Hz),7.47 (1H, ddd, J = 7.75, 4.72, 1.26 Hz), 7.30 - 7.27 (4H, m), 7.25 - 7.20 (1H, m), 4.46 (2H, s) $^1\{H\}^{13}$C NMR (100 MHz, $CDCl_3$), δ (ppm): 199.3, 153.4, 149.1, 137.0, 135.0, 130.1, 128.6, 127.3, 126.8, 122.5, 44.1 *In agreement with reported literature values.*[299]

2-phenyl-1,3-di(pyridin-2-yl)propane-1,3-dione

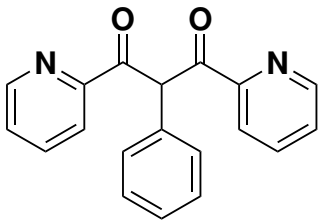

[302.33]

The picolinate derivative (0.33 g, 1.7 mmol) was dissolved in tetrahydrofuran (THF) (50 mL). Sodium hydride (60% dispersion in paraffin oil) (0.1 g, 2.5 mmol) was added and the solution stirred for 30 minutes before adding ethylpicolinate (0.23 mL, 1.7 mmol). THF was added as the mixture thickened (total 30 mL). The solution was stirred at 60 °C for 12 hours. The solvent was removed under vacuum, before carefully adding water (10 mL) whilst stirring vigorously. Upon addition of acetic acid (5 – 10 mL) a

viscous brown oil formed. Purification or isolation of the oil proved challenging, so the crude substance was used directly for the synthesis of HL8.

HL8: 2,2'-(4-phenyl-1H-pyrazole-3,5-diyl)dipyridine

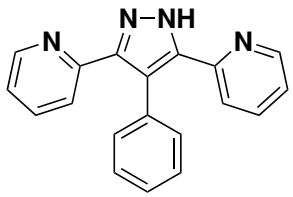

[298.35]

Crude 2-phenyl-1,3-di(pyridin-2-yl)propane-1,3-dione (*since isolation of the diketone was challenging, full conversion was assumed.* 1.7 mmol) was dissolved in EtOH (50 mL) and an excess of hydrazine hydrate ($N_2H_4 \cdot H_2O$) (0.33 mL, 6.8 mmol) was added. The reaction was heated at reflux for 12 hours, before cooling to room temperature. After cooling the total volume was reduced. A small amount of brown oil formed, and the solvent was removed by decantation. Et_2O was added, stirred and removed by decantation. Due to the small quantity produced, the oil was not purified further. ^{1}H NMR (400 MHz, $CDCl_3$, δ (ppm): 8.56 (2H, d, J = 4.91 Hz), 8.01 (2H, dt, J = 8.15, 1.03 Hz), 7.66 (2H, td, J = 7.82, 1.82), 7.21 - 7.26 (2H, m), 7.21 - 7.17 (5H, m) $^1\{H\}^{13}$C NMR (100 MHz, $CDCl_3$, δ (ppm): 161.6, 154.8, 148.7, 137.4, 136.2, 129.5, 129.3, 128.2, 125.8, 124.1, 122.1.

1-(pyridine-2-yl)vinyl trifluoromethanesulfonate

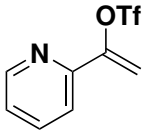

[253.195 g mol^{-1}]

Acetyl pyridine (0.5 mL, 5.0 mmol) was dissolved in dichloromethane and the solution cooled to 0 °C. 2,6-di-*tert*-butyl-4-methylpyridine (1.12 g, 5.4 mmol) and trifluoromethane sulfonic anydride (1 mL, 5.9 mmol) were added. The solution was allowed to warm to room temperature and stirred for 12 hours. The solvent was removed yielding yellow solids. Petroleum ether was added and the pyridinium triflate filtered off and further washed with petrol. ether. The petrol. ether fractions were washed with cold hydrochloric acid (1M) and saturated brine solution, before drying over $MgSO_4$ and removal of the solvent in vacuo, yielding a pale yellow oil (0.98 g, 3.9 mmol, 78%) ^{1}H NMR (500 MHz, $CDCl_3$, δ (ppm): 8.60 - 8.58 (m, 1H), 7.78 (1H, td, J = 7.83, 1.76 Hz), 7.56 (1H, td, J = 8.00, 0.92 Hz), 7.32 (1H, ddd, J = 7.73, 4.75, 1.03 Hz), 6.30 (1H, d, J = 3.36 Hz), 5.55 (1H, d, J = 3.40 Hz) $^1\{H\}^{13}$C NMR (125 MHz, $CDCl_3$), δ (ppm): 152.1, 149.8, 149.3, 137.0, 124.3, 119.2, 117.0, 106.7 *In agreement with reported literature values.*[301]

3,3,3-trifluoro-1-(pyrdine-2yl)propan-1-one

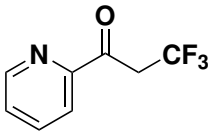

[189.14 g mol^{-1}]

Ammonium persulfate ($(NH_4)_2S_2O_8$) (0.18 g, 0.8 mmmol) and silver nitrate ($AgNO_3$) (0.007 mg, 0.04 mmol) were added to a vessel, followed by addition of 1-(pyridine-2-yl)vinyl trifluoromethanesulfonate (0.98 g, 3.9 mmol). A 1:1 mixture of H_2O and tBuOH (degassed) were added and the solution stirred vigorously at 30 °C for 12 hours. The solution was diluted with Et_2O and the aqueous layer washed with further Et_2O (3 x 10 mL). The combined organic layers were dried over $MgSO_4$ and the solvent removed *in vacuo* yielding a brown / black solid (0.24 g, 1.3 mmol, 33 %).

^{1}H NMR (500 MHz, $CDCl_3$), δ (ppm): 8.66 (1H, m), 8.05 (1H, dt, J = 7.75, 1.06 Hz), 7.86 (1H, td, J = 7.72, 1.74 Hz), 7.52 (1H, ddd, J = 7.59, 4.73, 1.24 Hz), 4.12 (1H, q, J = 10.40 Hz) ^{1}\{H\}^{13}C NMR (125 MHz, $CDCl_3$), δ (ppm): 191.68 (q, J = 2.2 Hz), 160.0 (q, J = 1.58 Hz), 149.04, 137.10, 127.93, 124.36 (q, J = 276.63 Hz), 122.0, 40.67 (q, J = 28.22 Hz) ^{19}F NMR (470 MHz, $CDCl_3$), δ (ppm): -62.3 *In agreement with reported literature values.*[301]

2-trifluoromethyl-1,3-di(pyridin-2-yl)propane-1,3-dione

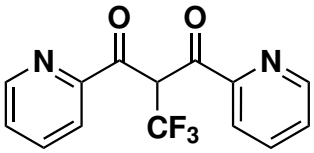

[294.233]

The 3,3,3-trifluoro-1-(pyrdine-2yl)propan-1-one (0.24 g, 1.3 mmol) was dissolved in tetrahydrofuran (THF) (15 mL). Sodium hydride (60% dispersion in paraffin oil) (0.1 g, 2.3 mmol) was added and the solution stirred for 30 minutes before adding ethylpicolinate (0.23 mL, 1.7 mmol). THF was added as the mixture thickened (total 40 mL). The solution was stirred at 60 °C for 12 hours. The solvent was removed under vacuum, before carefully adding water (10 mL) whilst stirring vigorously. Upon addition of acetic acid (5 – 10 mL) dark brown viscous solids formed. Recrystallisation from EtOH/Et_2O yielded an oily solid. NMR data suggested there were unreacted starting materials present and a number of other species, suggesting some decomposition of the CF_3-functionalised pyridine.

Chapter 5

In-situ Monitoring of Nanoparticle Formation during Iridium-catalysed Oxygen Evolution by real-time Small Angle X-ray Scattering

The work presented in this chapter has been published in the journal *ChemCatChem*, 11, **21**, 5313 – 5321. As an open access article it is reproduced here under a Creative Commons CC BY license.

Page, reference and figure numbers altered for consistency. Some figures originally published in Electronic Supplementary Information have been included in the main text.

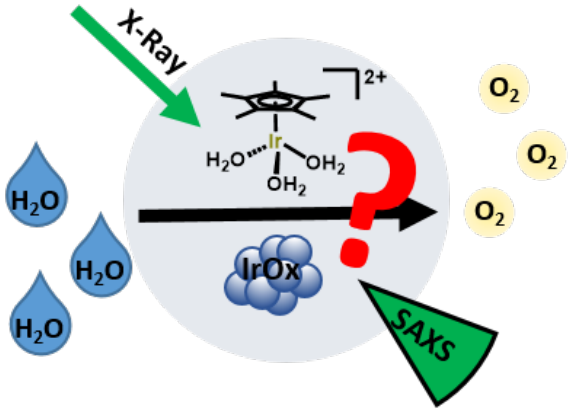

5.1 Introduction to Published Work

As touched on in Chapter 1, a specific concern for electrocatalysts is their stability under the extreme redox potentials required to drive catalysis.[145] This can also be a problem with chemically driven catalysts, and as cobalt oxide is a known catalyst for oxygen reduction[252,253,308] and water oxidation,[258,309] it is important to consider the possibility of catalyst deactivation. As discussed in 3.8.1, the speciation of the cobalt complexes during catalysis has not been studied, but they appear to undergo deactivation under the conditions employed for ORR, 3.5. Therefore further investigation of the deactivation pathways and products is required.

There are a number of commonly used methods of testing the homogeneity of molecular catalysts, the most common of which is the mercury drop test.[310] The test works through the introduction of mercury to the reaction after precatalyst activation. If the reaction is truly homogeneous, rates of reaction should be unaffected. However, if the active catalyst is heterogeneous, the mercury binds to the active sites, significantly reducing or entirely preventing activity.[138] Unfortunately, the mercury drop test is not an effective test for metal oxides.

Scattering methods have seen increased use as a method of determining the active catalytic species. Dynamic light scattering (DLS) is commonly used, allowing the determination of the presence of nanoparticles during catalysis.[140,147,311] However, one of the significant limitations of DLS is that as a diffusional technique, solutions must be static, meaning it is not possible to collect data in-*situ* under reaction conditions.

As a consequence there has been an increased interest in the use of spectroscopy and scattering methods to study catalytic systems in-*situ* using flow techniques.[259,312,313] Despite an increase in the use of SAXS to study nanoparticle formation, there are limited examples of the investigation molecular catalysts under reaction conditions.

In order to carry out a benchmark study it is necessary that the systems used are well understood, and to identify a comparable catalyst precursor that is known to form nanoparticles. Therefore, a series of iridium water oxidation catalysts previously synthesised and investigated in the Hintermair group[118,287] were studied using SAXS at Diamond Light Source. The intention was to develop a protocol that could then be applied to a wider range of systems, including the cobalt complexes discussed in Chapters 2 and 3.

5.2 Small Angle X-ray Scattering (SAXS)

Small Angle X-ray Scattering (SAXS) can give detailed information about the nano-structural details of a sample.[150] As a sample deflects the rays of an incident X-ray, detailed information about the structure of the scatterer can be obtained. Although commonly used for biological materials and colloids[314], it is also used to extract valuable information about nanoparticle nucleation, growth and size,[259,312] along with polymers and nanocomposites.[315]

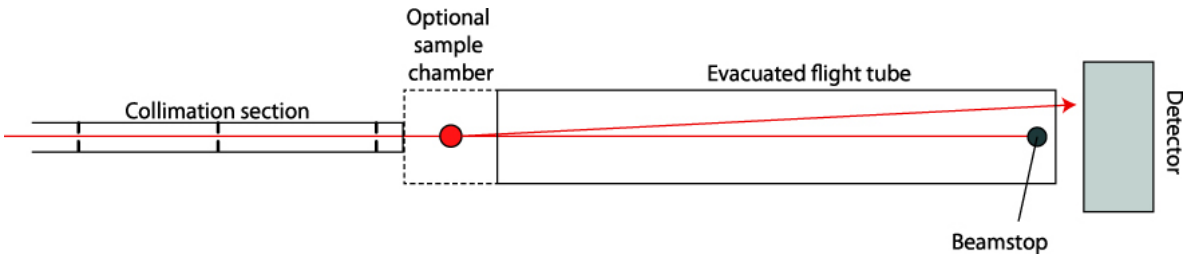

Figure 5.1: Reproduced with permission from *J. Phys. Condens. Matter*, 2013, **25** 383201 under a Creative Commons Attribution 3.0 licence (2013).[150]

As shown in Figure 5.1, the sample is irradiated with X-rays, which are scattered and detected at small angles. Particles in the sample scatter the X-rays forming a scattering pattern, which is detected and used to determine structural information about the sample.[315] There are a number of different types of scattering, including Compton scattering, where the scattered radiation has a different wavelength than the incident radiation (a change in energy) whereas Rayleigh or Thomson scattering do not occur with a loss of energy. Thomson scattering is used in SAXS.

Scattering patterns are usually reported as a function of the scattering vector, q, 5.1:

$$\mathrm{q} = \frac{4\pi}{\lambda} \cdot \sin(\theta) \tag{5.1}$$

Where λ = wavelength of X-rays and θ = scattering angle.[259] Since q is described as 1/length, the scattering pattern is often referred to as the "structure in reciprocal space".[315] The form factor describes the oscillations of the intensity of scattering vector, and is used to extract information about the shape of the particle.

One of the advantages of using SAXS to extract information about a chemical system is that it can be used under reaction conditions. There are a number of examples of the

use of SAXS in flow,[259,314] or the use of stopped-flow apparatus for rapid nanoparticle formation.[312,316]

5.3 Statement of Authorship

This declaration concerns the article entitled:			
In-situ Monitoring of Nanoparticle Formation during Iridium-catalysed Oxygen Evolution by real-time Small Angle X-ray Scattering			
Publication status: **Draft manuscript** ☐ **Submitted** ☐ **In review** ☐ **Accepted** ☐ **Published** ☑			
Publication details (reference):	M. Singer Hobbs, E. V. Sackville, A. J. Smith, K. J. Edler and U. Hintermair, *ChemCatChem*, 2019, **11**, 5313–5321.		
Copyright status: I hold the copyright for this material ☐ Copyright is retained by the publisher, but I have been given permission to replicate the material here ☑			
Candidate's contribution to the paper (provide details, and also indicate as a percentage)	**The candidate contributed to / considerably contributed to / predominantly executed the…** **Formulation of ideas: 10%** The project was conceived by UH with some input from MSH. **Design of methodology: 20%** The methodology was developed by UH, AJS and KJE with input from MSH. **Experimental work: 80%** SAXS experimental work carried out by MSH and UH with support from AJS. Synthesis and O_2 evolution measurements were carried out by EVS and MSH. **Presentation of data in journal format: 70%** Data analysis was carried out by MSH with support from AJS, KJE and UH. Figures and an initial draft manuscript were prepared by MSH, with data interpretation and editing led by UH.		
Statement from Candidate	This paper reports on original research I conducted during the period of my Higher Degree by Research candidature.		
Signed	[redacted]	**Date**	07/02/21

5.4 In-situ Monitoring of Nanoparticle Formation during Iridium-catalysed Oxygen Evolution by real-time Small Angle X-ray Scattering

Maya Singer Hobbs,[a], Emma V. Sackville,[a] Andrew J. Smith,[b] Karen J. Edler,[c] Ulrich Hintermair*[a]

[a] Centre for Sustainble Chemical Technologies, University of Bath, Claverton Down, Bath, BA2 7AY, United Kingdom.

[b] Diamond Light Source, Diamond House, Harwell Science and Innovation Campus, Harwell, Didcot, Oxfordshire, OX11 0DE, United Kingdom.

[c] Department of Chemistry, University of Bath, Claverton Down, Bath BA2 7AY, United Kingdom.

Real-time Small Angle X-ray Scattering (SAXS) has been used to investigate the homogeneity of a series of half-sandwich iridium(III) complexes during water oxidation catalysis in aqueous $NaIO_4$ solution through a continuous flow cell. The results obtained for the unstable $[Cp^*Ir(OH_2)_3]^{2+}$ precursor forming amorphous IrO_x NPs in-situ validate and complement previous Dynamic Light Scattering (DLS) studies by providing enhanced sensitivity for small particle sizes and increased temporal resolution under more realistic reaction conditions. Correlating particle formation profiles with O_2 evolution traces allowed homogeneous catalysis to be clearly distinguished from heterogeneous catalysis. A series of seven pyridine-alkoxide Cp*Ir complexes are shown to be fully homogeneous by SAXS, validating previous studies and confirming their catalysis to be molecular in nature throughout the reaction.

5.4.1 Introduction

Chemical energy conversion by means of water splitting is widely recognised as a key strategy for mitigating the problem of intermittency of many renewable energy sources.[317–321] Efficient water oxidation catalysts (WOCs) are required for minimising energy losses during electrolysis,[173,318,322–324] and improving their stability under the demanding operational conditions is a persistent challenge.[257,322,325,326] The fate of molecular precursors is particularly difficult to elucidate,[139,311,327] as even the seemingly

simple question of whether the catalysis is homogeneous or heterogeneous in nature can be hard to address with certainty.[133,145,328–330] This is particularly true for precursors of metals which may form conductive oxide clusters, nanoparticles or thin films that are also active in water oxidation such as ruthenium and iridium.[331–333] Efficient iridium precursors have to strike a particularly fine balance between a sacrificial placeholder ligand to be degraded during activation (e.g. Cp*)[139–144] and a robust chelate ligand that remains bound to the metal to modulate its activity and prevent degradation into IrO_x nanoparticles (e.g. pyridine-alkoxides).[56,334]

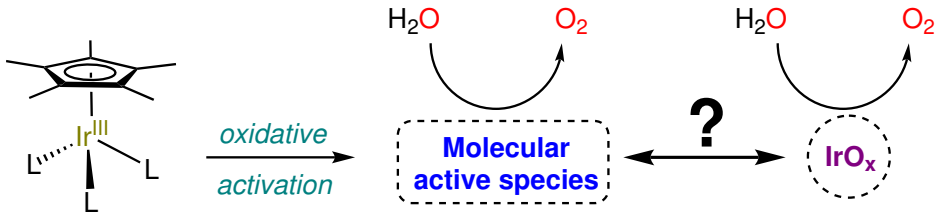

Figure 5.2: While precursor activation and global O_2 evolution activity may easily be measured experimentally, ascertaining the origin of the catalysis and understanding the potential interconversion of molecular and particulate catalyst species remain challenging.

Previous investigations into the speciation of half-sandwich Cp*Ir(III) precatalysts under oxygen evolution conditions in aqueous solution (Figure 5.2) have been carried out using dynamic light scattering (DLS) as a probe for in-situ nanoparticle formation.[334] $IrCl_3$, $[Cp^*IrCl_2]_2$ and $[(Cp^*Ir)_2(OH)_3]^+ \leftrightarrow [Cp^*Ir(OH_2)_3]^{2+}$ (**IrA**, Figure 5.3) were all found to form large, amorphous IrO_x particles of several hundred nm in size after a lag phase of 2 – 20 minutes, and their growth profile was strongly influenced by [Ir] concentration, oxidant loading, solvent and pH. The initial formation of very small (primary) NPs remained beyond the detection range and sensitivity of DLS, however. Other Cp*Ir precursors bearing various chelate ligands (including **Ir1**, Figure 5.3) showed no signs of IrO_x formation during and after O_2 evolution, suggesting these systems to be fully homogeneous within the accuracy of the DLS analysis.[334]

Investigating ligand effects in the privileged family of pyridine-alkoxide ligands for Ir-based WOCs, we recently reported a series of derivatives of **Ir1** with high activity for both water and C-H oxidation (**Ir2-7**, Figure 5.3).[118,287] While we have previously delineated precursor activation from catalysis, and observed pronounced ligand effects on turnover across the different substitution patterns, the homogeneity of complexes **Ir2-7** under O_2 evolution conditions has not been investigated yet.

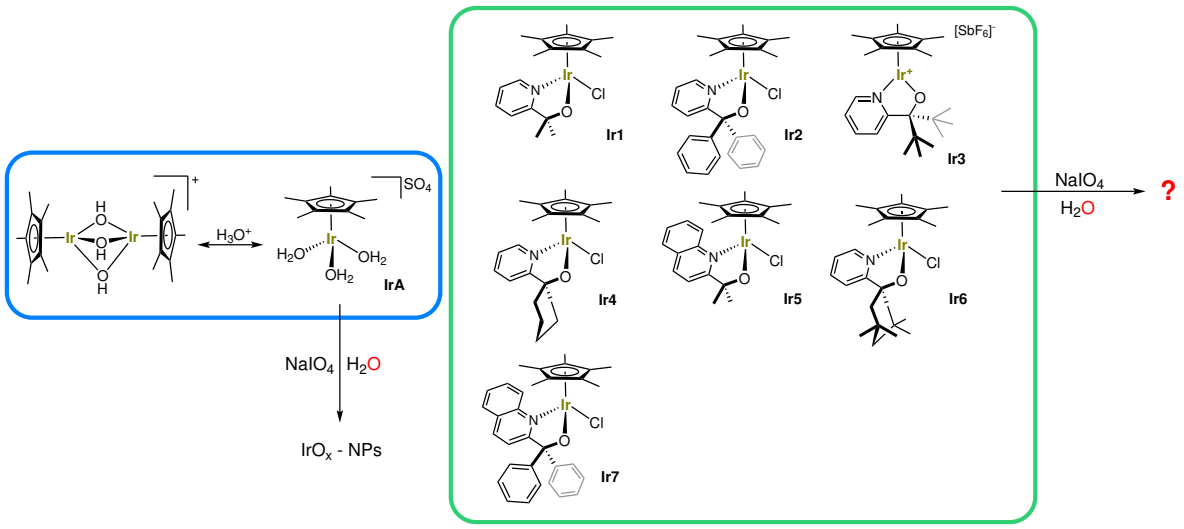

Figure 5.3: Iridium precatalysts investigated for homogeneity during O_2 evolution from aqueous $NaIO_4$ by SAXS. Complex **IrA** has previously been shown to form nanoparticles by DLS,[334] while complex **Ir1** is presumed to be homogeneous. The homogeneity of **Ir2-7** are unknown.

Non-crystalline diffraction based on Small Angle X-ray scattering (SAXS) has seen extensive use in the characterisation of heterogeneous catalysts in low ordered environments.[335–338] Due to X-rays being scattered by electron density differences, SAXS is especially sensitive for aggregates of heavy elements (such as iridium) in light matrices (e.g. aqueous solution) down to 0.1 nm length scales.[150] Additionally, it is not restricted to diffusional conditions as light scattering techniques are, meaning that more realistic reaction conditions with active mixing may be investigated.[339] SAXS has been used to determine the speciation of metal-oxo clusters[340] and the growth of metal nanoparticles in solution, both using static measurements[312] and in flow.[259,341] Polyoxometalate (POMs) based catalysts, which are often plagued from similar homogeneity ambiguities as molecular precursors,[329,342] have been investigated for in-situ agglomeration using SAXS.[343] However, the use of X-ray scattering to monitor the homogeneity of molecular catalysis has only recently seen development.[313] Here we apply SAXS to investigate the speciation of iridium precursor complexes **IrA-7** under typical water oxidation reaction conditions from aqueous $NaIO_4$ at room temperature. Independent O_2 evolution experiments serve to correlate the formation of IrO_x NPs with the reaction progress to kinetically elucidate the potential involvement of any IrO_x NPs in water oxidation catalysis.

5.4.2 Results and Discussion

Using a quartz capillary flow cell connected to a magnetically stirred batch reactor via a peristaltic pump (Figure 5.4, Section 5.4.9), background SAXS data could be collected on a steady flow of freshly prepared oxidant solution before a concentrated catalyst solution was injected into the reactor via a remote-controlled syringe pump to start the reaction. We chose to investigate literature conditions of 2.5 – 5 mM [Ir] with 250 – 500 mM [$NaIO_4$] in neat water at room temperature to allow direct comparison with previous reports, particularly Crabtree and Elimelech's DLS investigation.[334]

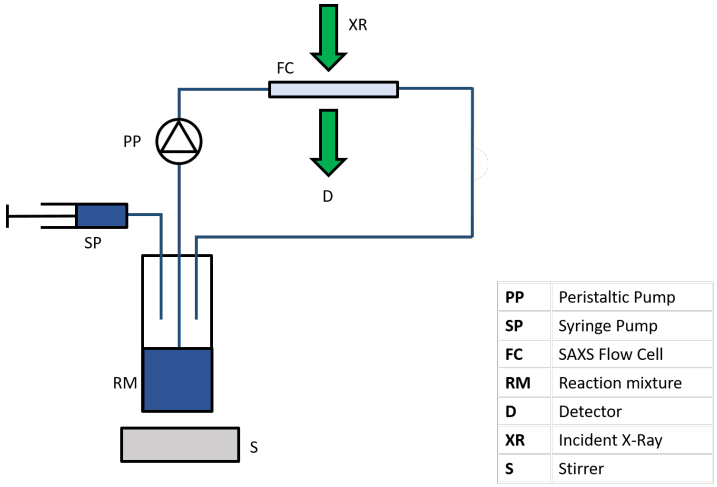

Figure 5.4: The oxidant solution was flowed from a stirred vessel into the SAXS cell. The reaction was initiated by injection of concentrated catalyst solution from the syringe pump (SP) into the stirred vessel, and the resultant reaction mixture (RM) was flowed continuously through the SAXS flow cell (FC) throughout the experiment.

The background-subtracted scattering profiles collected during O_2 evolution catalysis with complex **IrA** showed the reaction solution to be a genuinely homogeneous phase with no scattering objects present over the first 22 minutes of the reaction (Figure 5.5). Thereafter some minor scattering features appeared in the SAXS profiles, which slowly grew in intensity over the following 6 – 8 minutes before noticeable X-ray scattering was detected from 30 minutes after initiating the catalysis.

5.6a depicts the total scattering intensity (across all q values) from the data shown in Figure 5.5 over time, in comparison with previously published DLS data collected under identical conditions (5.6b).[334] As it can be seen, the major NP formation event around t = 30 min was detected by both techniques. However, while no meaningful results could be derived from the correlation function of the DLS data prior to the onset of

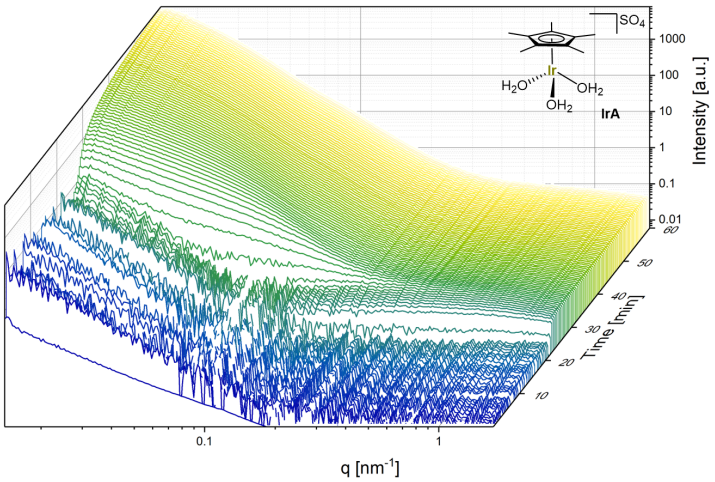

Figure 5.5: SAXS data for **IrA** (2.5 mM) at room temperature injected into 250 mM $NaIO_4$ (100 equiv) in H_2O at t = 0 (30 s intervals, data baseline subtracted).

large NP formation (blue shaded region in 5.6b), SAXS was able to detect significant scattering intensity during the nucleation phase (blue shaded region in 5.6a; for details see data fitting below, 5.4.3).

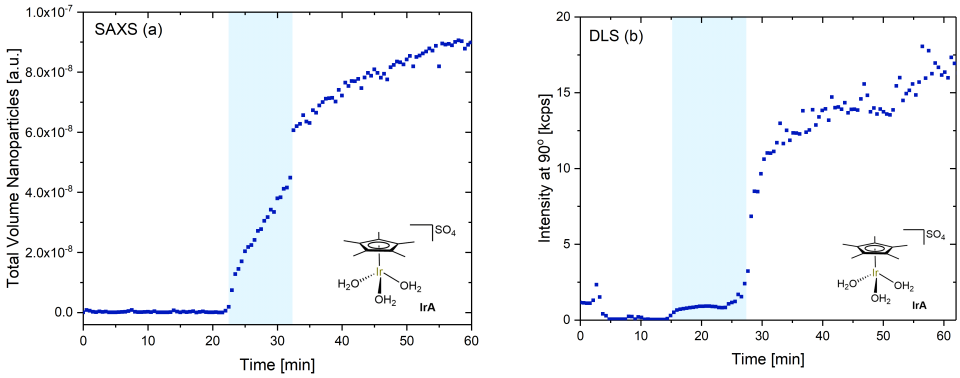

Figure 5.6: (a). SAXS intensity over time for **IrA** (2.5 mM) injected into 250 mM $NaIO_4$ at t = 0 (room temperature). (b) Complementary DLS data for **IrA** under identical conditions (from[334]). Nucleation stages highlighted in blue.

As nanoparticle growth kinetics are strongly affected by concentration[344] we also investigated a reaction at double precursor and oxidant loading (Figure 5.7). In this case the time it took for NPs to develop from **IrA** was almost halved (t = 14.5 min), and overall scattering intensity increased by close to an order of magnitude due to a larger number of NPs being formed. The Porod oscillations in q observed at early stages of NP formation (t ≈ 16 min) are fingerprints of narrow initial size distributions that

quickly grew out into polydispersity over time (as shown by smooth q curves from t > 18 mins, Figure 5.7).[345]

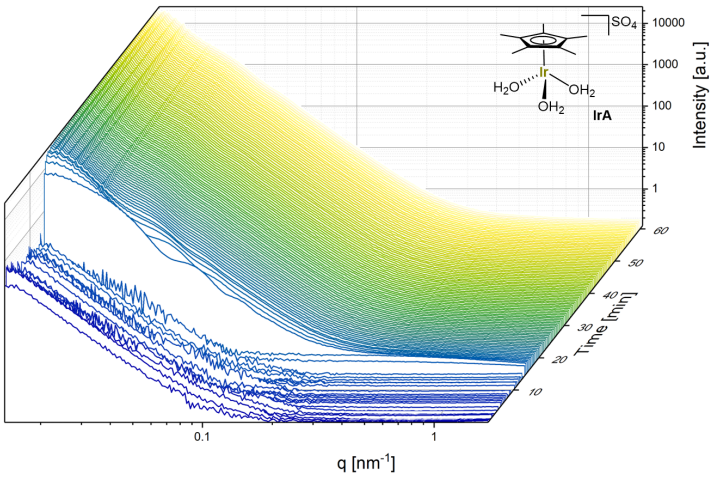

Figure 5.7: SAXS data for **IrA** (5 mM) at room temperature injected into 500 mM $NaIO_4$ (100 equiv) in H_2O at t = 0 (30 s intervals, data baseline subtracted).

5.4.3 Data Fitting

In order to derive particle size distributions, the SAXS data were fitted using a spherical body model. Checking scattering profiles from different stages of the reaction showed a good fit between the experimental data and the model (Figure 5.8). While there was some slight deviation in the pre-nucleation stage (partly due to very low signal intensities), during nanoparticle nucleation and growth, the spherical fit matched the experimental data well with chi^2 values of <2.

The size plot shown in 5.9a illustrates the monodisperse onset of small NP formation from t = 20 – 28 mins at [**IrA**] = 2.5 mM. At [**IrA**] = 5 mM, where NP formation occurred almost twice as rapidly, the lifetime of the small, monodisperse NPs formed initially was lower, and larger, polydisperse aggregates formed more quickly from them (5.9b).

A close-up of the first few minutes of NP formation clearly showed the emergence of primary particles of <4 nm from a homogeneous solution, which then transformed into larger agglomerates that initially were fairly monodisperse (5.10a). This narrow initial size distribution was lost within 2 – 3 minutes after their formation, broadening out to a distribution of larger particle sizes up to 200 nm. While the latter observation is similar to previous DLS results (5.6b),[334] the additional detection of small NPs prior

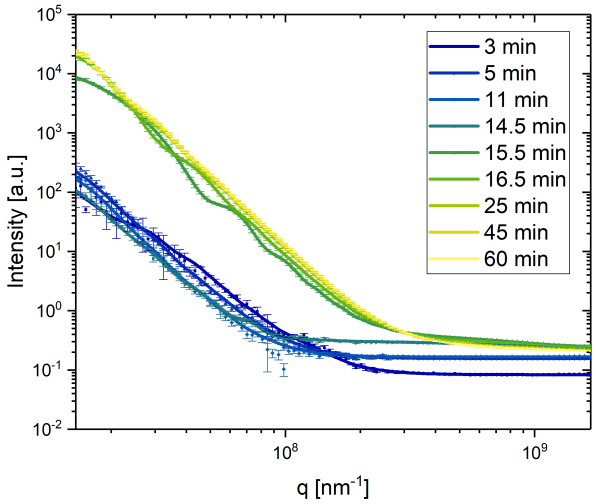

Figure 5.8: SAXS data (points with error bars) versus spherical model fit (solid lines) during pre-nucleation (3, 5, 11 minutes), nucleation (14.5, 15.5, 16.5 min) and post-nucleation (25, 45, 60 min) phases of IrO_x NP formation from **IrA** at room temperature (5 mM + 500 mM $NaIO_4$).

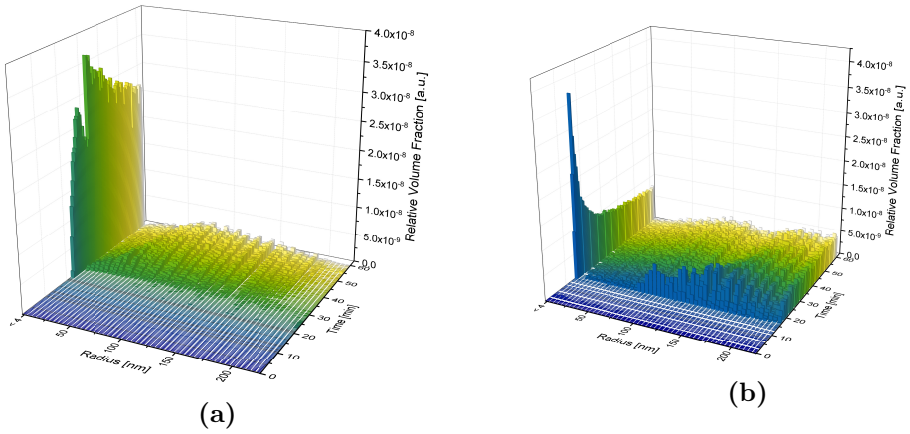

Figure 5.9: Relative volume fractions of IrO_x nanoparticles formed from **IrA** (a: 2.5 mM, b: 5 mM) with 100 equiv. $NaIO_4$ in H_2O at room temperature over time.

to the appearance of larger agglomerates by SAXS is valuable information for their mechanism of formation, and allows deeper insight into the origin of the catalysis.

The rapid increase in size of the small NPs fitted a mono-exponential growth function (Figure 5.11) consistent with a classical La Mer mechanism[344,346,347] consisting of an initial nucleation burst followed by growth within a constant particle volume (5.10b).[348–350] Total scattering intensities derived from DLS decreased over time as sedimentation set in, an effect which was not apparent in the actively mixed flow system investigated

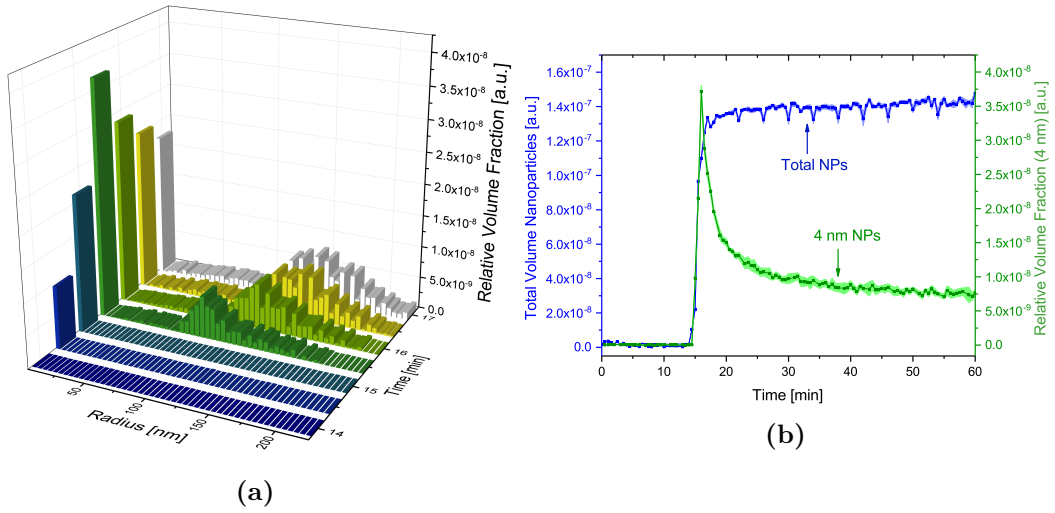

(a) (b)

Figure 5.10: (a) IrO_x NP formation from **IrA** (5 mM) with 100 equiv. $NaIO_4$ in H_2O at room temperature. (b) Volume fraction of initial NPs with r < 4 nm (green) and their relative volume fraction in solution (blue) over the course of the reaction.

by SAXS. Particle growth must be aggregative rather than proceeding via Ostwald ripening, as indicated by the continued presence of small NPs throughout the duration of the experiment (note two particle size distributions at t = 60 min in 5.9b).[350] The pronounced dependence of time, rate and amount of NP formation on [Ir] concentration (see Figure 5.5 and Figure 5.7) is consistent with super-saturation of the solution being the driver for the initial nucleation burst.[348]

5.4.4 Cp*Ir(pyalk) precursor complexes

Having established the utility of SAXS as a highly sensitive technique to detect small IrO_x NPs during O_2 evolution catalysis with molecular precursors, the more active pyalk-ligated Cp*Ir complexes **Ir1-7** were investigated for homogeneity. The setup and conditions were identical as for the **IrA** complex, with the reaction initiated by addition of the precatalyst to the flowing $NaIO_4$ solution (100 equiv). The baseline subtracted data for **Ir1** depicted in Figure 5.12a shows a distinct lack of any scattering objects over the entire duration of the experiment. Similar to previous DLS results, no features characteristic of NPs could be found in any of the 120 measurements collected over 1 hour, even with the much more sensitive SAXS measurement. The detection limit under the conditions applied was estimated to be around 1.4 ppm of IrO_x clusters of 4 nm in an aqueous solution containing 483 ppm of homogeneously dissolved [Ir]. Thus, these results unambiguously confirm the previous conclusion of **Ir1** forming a molecular

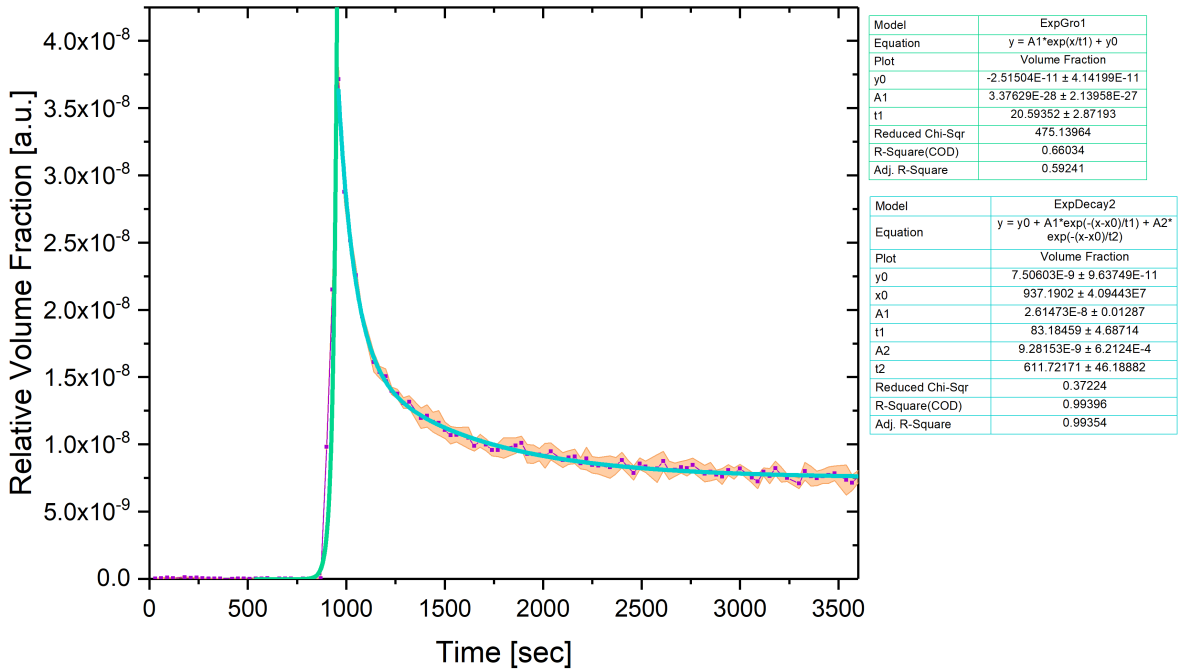

Figure 5.11: Modelling of the growth and decay of 4 nm nanoparticles formed from IrA (5 mM injected into 500 mM $NaIO_4$) with data collection every 30 s. A 1st order growth curve ($y = A1e^{(x/t1)} + y0$) and 2nd order decay curve ($y = y0 + A1e^{(-(x-x0)/t1)} + A2e^{(-(x-x0)/t2)}$) were fit to the data using the default fitting routines in the Origin2017 software package).

catalyst species that is stable towards IrO_x formation.[334,351]

Moving to other substitution patterns not previously investigated for homogeneity, complexes **Ir2-7** also showed no scattering features under identical conditions. In-situ SAXS showed a consistent lack of any signs for nanoparticle formation over the course of the reaction in all cases (Figure 5.12b, Figure A.33), so we can confidently conclude that the entire class of **Ir1-7** are operationally homogeneous oxidation catalysts that do not form IrO_x NPs.[118]

5.4.5 Correlation with Catalytic O_2 Evolution

It was previously reported that the amorphous IrO_x NPs recovered at the end of the reaction with labile WOC precursors were also active in O_2 evolution catalysis themselves.[328,334,352] In order to further elucidate the role of any NPs in catalysis starting from molecular precursors, we correlated the in-situ SAXS profiles with O_2 evolution traces. Figure 5.13a shows the activities of precatalysts **Ir1-7** under SAXS conditions as derived from headspace manometry, which mirror their relative initial rates measured electrochemically in solution.[118] Overlaying O_2 evolution activity with X-ray scattering

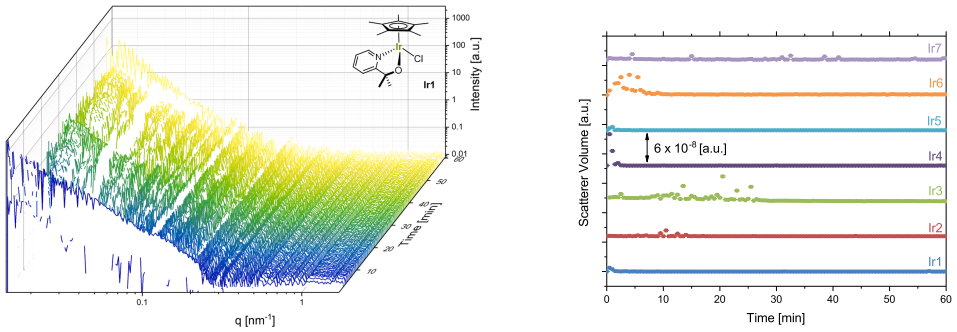

(a) **(b)**

Figure 5.12: (a) SAXS data for **Ir1** (2.5 mM) with 250 mM $NaIO_4$ (30 s intervals, data baseline subtracted). (b) Relative scatter volumes for **Ir1 Ir7** (all 2.5 mM Ir, injected into 250 mM $NaIO_4$ in H_2O at room temperature) obtained from data fitting. Occasional scattering events are due to bubble formation or undissolved catalyst precursor.

intensity for **Ir1** as an example (5.13b) clearly shows that the solution remained homogeneous during and after the reaction, and that the catalyst must be a stable molecular entity.

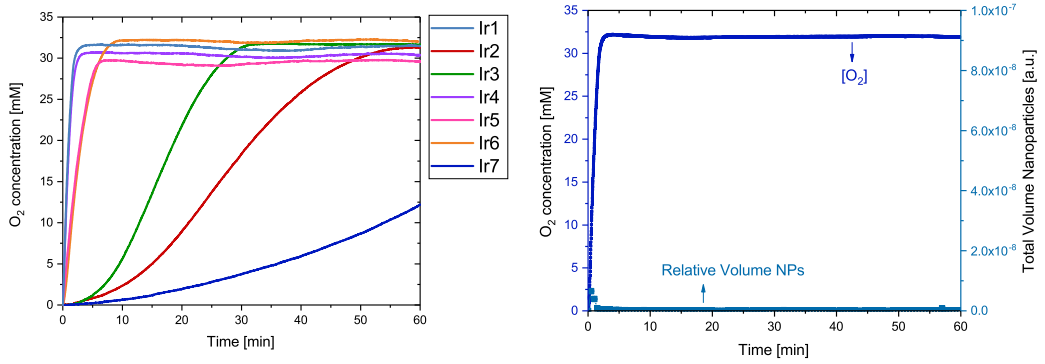

(a) **(b)**

Figure 5.13: (a) Manometrically measured O_2 evolution traces for **Ir1-7** and (b) Total volume of NPs detected for **Ir1** against O_2 evolution (all [Ir] = 2.5 mM, [$NaIO_4$] = 250 mM, neat H_2O, room temperature).

By contrasting SAXS intensity with O_2 evolution activity for the unstable complex **IrA** (Figure 5.14), we could show that NP formation only set in after the reaction had come to completion (t = 22 minutes). Thus, any catalytic activity observed must have originated from molecular species even in case of the unstable aqua complex. IrO_x formation appeared to be a post-catalytic decomposition pathway, and any NPs observed at the end of the reaction were thus not the active species.[328,352]

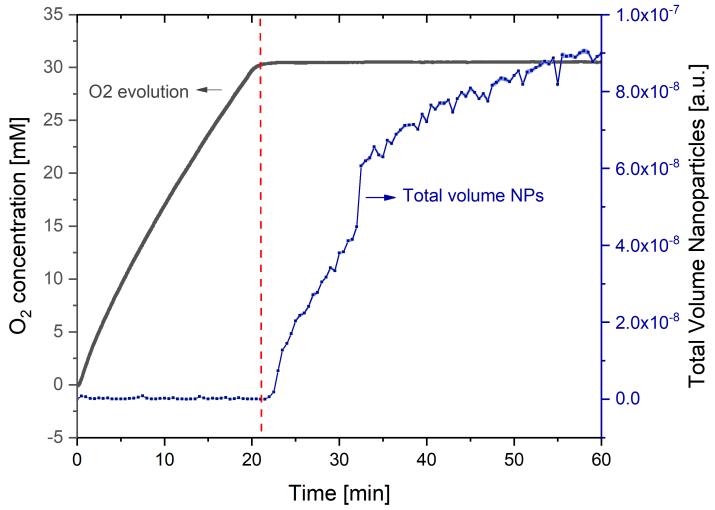

Figure 5.14: O_2 evolution for **IrA** (2.5 mM + 250 mM $NaIO_4$ in H_2O at room temperature) plotted against total volume of NPs from in-situ SAXS (5.6a).

In order to compare the homogeneous and heterogeneous forms of **IrA** in catalysis, additional portions of $NaIO_4$ were added to the solution after completion of IrO_x NP formation after 1 hour (5.15a). As it can be seen from the profiles of O_2 evolution and the corresponding catalytic rates summarised in Table 5.1, the IrO_x NPs formed after the first cycle were 4 times more active than the initial homogeneous catalyst form of **IrA**, despite their large size of >200 nm and correspondingly low surface fraction of Ir atoms. The pyalk-ligated catalyst **Ir1** on the other hand showed over 10 times higher activity than **IrA** with higher TONs, consistent rates and no NP formation over at least three cycles (5.15b), confirming the notion of a well-defined and stable molecular catalyst entity.

Table 5.1: Observed turnover numbers (TON) and turnover frequencies (TOF) of O_2 evolution upon sequential additions of oxidant to **IrA** and **Ir1** in H_2O at room temperature (2.5 mM [Ir] + 100 equiv. $NaIO_4$ each time).

Catalyst	Oxidant Addition	TON[a]	TOF[b]/ min^{-1}	NPs
IrA	1	24	1.2	×
	2	28	5.0	✓
	3	28	4.7	✓
Ir1	1	38	17.4	×
	2	39	14.3	×
	3	38	17.7	×

[a] $n(O_2)$ / n(Ir) [b] TON / time (initial slope 0.6 – 1.5 min)

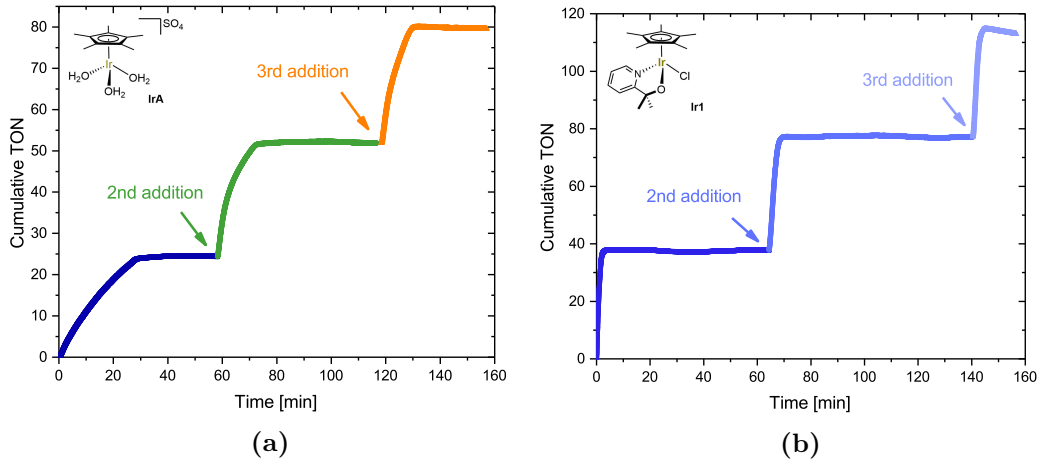

Figure 5.15: Repeat additions of $NaIO_4$ (1.25 mmol) to **IrA** (a) and **Ir1** (b) (both 2.5 mM in H_2O at room temperature).

5.4.6 Conclusion

Using a simple recirculating flow setup with remote-controlled sample addition, we have shown the utility of real-time SAXS as a non-invasive tool for investigating nanoparticle formation during operationally homogeneous catalysis with molecular precursors in solution. With synchrotron X-ray sources and CCD detectors highly sensitive measurements could be acquired at good temporal resolution of <1 min. SAXS profiles contain a wealth of particle shape and dispersity information extractable by modelling, and additional X-ray absorption and diffraction patterns may be collected to obtain further insight into the composition and morphology of the NPs if required. In case of the eight molecular WOC precursors **IrA-7** investigated during catalytic O_2 evolution from aqueous $NaIO_4$, SAXS has been able to detect small IrO_x clusters of <4 nm formed from $[Cp^*Ir(OH_2)_3]SO_4]$ that had escaped previous DLS analyses. Correlation with O_2 evolution profiles showed NP formation to be a post-catalytic decomposition event, forming a heterogeneous catalyst that is more active than the initial molecular species. On the other hand, a family of seven pyridine-alkoxide ligated Cp*Ir complexes have been shown to be >99.7% homogeneous throughout the reaction by SAXS. These solutions may be reactivated by repeat addition of fresh oxidant with identical rates, firmly establishing the molecular origin of the catalysis and lending weight to previous mechanistic deductions about their mode of operation. We hope that these findings will help to assist the development of improved catalysts for water splitting and other applications where the important question of catalyst homogeneity has remained difficult

to address.[133,145,328–330]

5.4.7 Acknowledgements

This work was supported by the Royal Society (UF160458; University Research Fellowship to UH), the EPSRC Centre for Doctoral Training in Sustainable Chemical Technologies (EP/L016354/1; PhD studentships to MSH and EVS), and the UK Catalysis Hub (EP/K014714/1). We thank Diamond for the award of beamtime under experiment number SM17245, and Dr. Julien Schmitt (LSFC Cavaillon, France) for helpful discussions and guidance.

5.4.8 Conflict of Interest

US Patent No. 9,790,605 by UH et al. contains intellectual property described in this article. The other authors declare no competing financial interest.

5.4.9 Experimental

All chemicals were purchased from major commercial suppliers and used as received. Ultrapure DI water (18.2 mohm) was supplied from an Elga deionisation unit (Diamond Light Source, Harwell). [(η5-pentamethylcyclopentadienyl)Ir(OH_2)$_3$]SO_4 was prepared following an adapted literature procedure,[353] iridium complexes **Ir1**–**7** were prepared according to literature procedures,[287] and all analytical data were in agreement with reported values. Syntheses were performed under argon using standard Schlenk techniques.

Analysis – Experimental set-up. In a typical experiment, the desired amount of oxidant (535 mg, 2.5 mmol or 1070 mg, 5.0 mmol) was dissolved in 9 mL water in air. The resulting clear solution was passed through a 0.2 μm PTFE syringe filter into a 30 mL glass vial magnetically stirred at 400 RPM and flowed through a 1.35 mm I.D. quartz capillary at a rate of 26 mL min-1 via a peristaltic pump with silicone tubing. 1 mL of aqueous catalyst solution (containing 0.025 mmol Ir) were added via a remote-controlled syringe pump to start the reaction after having collected a background measurement. SAXS data were continuously collected in 30s intervals for 1 hour at room temperature. In between each catalytic run the flow setup was flushed with at least 50 mL DI water. The scattering pattern of the empty capillary checked after runs 5, 10 and 14 showed no deposition of any nanoparticles.

Analysis – Small Angle X-ray Scattering (SAXS). Time-resolved SAXS meas-

urements were carried out at the I22 beamline at the Diamond Light Source (Harwell, UK) using a beam energy of 12.4 keV. The sample to detector distance was calibrated to 9.763 m using a silicon nitride diffraction grating with a period of 100 nm (Silson, UK). Data were collected on a Pilatus3 2M photon counting hybrid pixel detector (Dectris AG, Switzerland). The usable q-range for this experiment geometry was $0.0015 < q < 0.167$ Å-1 , giving access to scattering from objects in the size range of 37 – 4180 Å. Data were placed onto an absolute intensity scale by comparing scattering from a piece of calibrated glassy carbon (NIST SRM3600), collected during the experiment, with the reference dataset.[354] Data were corrected and reduced using the DAWN package[355,356] and standard pipelines developed at Diamond.[357]

Models for SAXS. The Scattering Length Density (SLD) contrasts were calculated using the assumption of $IrO_2(OH)_2$ particles with a density of 11.66 g cm^{-3} to give a SLD contrast of 6.96 e-5 / angstrom^2 calculated for a 250 mM solution of $NaIO_4$ as the matrix (composition of 0.25 Na, 0.25 I, 55.52 O, and 111.05 H) with an overall density of 1.053 g cm^{-3}. A total of 120 SAXS patterns were measured per kinetic run and fitted with a spherical model using the McSAS software.[358] For most data points chi_2 was <2, except for around 10 patterns per kinetic run where the minimum chi^2 had a lower tolerance of up to 5 due to occasional bubble formation from the O_2 evolution reaction.

Analysis – Gas evolution. Reactions were carried out using a MotM X103 manometric gas evolution kit in a 20 mL round bottom glass flask. Experiments were carried out at room temperature on a 5 mL reaction volume stirred at 400 RPM. Oxidant ($NaIO_4$, 267 mg, 1.25 mmol) was dissolved in deionized water (4 mL) and the vessel sealed. Data collection was started before the reaction was initiated by the injection of 1 mL of aqueous catalyst solution (containing 0.0125 mmol Ir) through the septum cap of the flask. During repeat addition experiments the vessel was depressurised before addition of additional $NaIO_4$ (267 mg, 1.25 mmol). Catalyst turnover numbers (TONs) were calculated by the conversion of differential pressure readings (mbar) into moles of O_2 assuming ideal gas behaviour in the 15 mL headspace at T = 296 K, divided by the number of moles of iridium in solution. Turnover frequencies (TOFs) were determined from linear regression of the initial slope of the TON/time curves.

5.5 Commentary and Conclusions

The use of SAXS to determine the speciation of the active catalysts during water oxidation proved successful, definitively confirming the homogeneous nature of **Ir1** − **7**. The use of SAXS offered insight into the mechanism of NP growth for **IrA**, and in conjunction with gas evolution studies confirmed that NP formation occurs after the completion of catalytic turnover.

The modelling of the rates of formation and decrease of the small nanoparticles, Figure 5.11, gave slightly more insight into nanoparticle growth. The decrease followed a bi-exponential decay model, suggesting the growth of larger nanoparticles follows two mechanisms. The first, and more significant contribution is a fast component consisting of the association of two small nanoparticles (or nuclei). The second is a slower component consisting of the association of a small and a large nanoparticles.[359] Subsequent particle growth is aggregative, rather than proceeding via Ostwald ripening, indicated by the continued presence of small nanoparticles throughout the duration of the experiment. This is supported by the presence of two particle size distributions at t = 60 min present in 5.9b.[350]

The evidence that **IrA** catalyst deactivation occurs after catalytic turnover offers further insight into catalyst stability, and the lack of nanoparticle formation with **Ir1** − **7** shows the significance of careful ligand tuning.

Having successfully proved the viability of SAXS to study catalytic systems under reaction conditions, the technique can then be applied to a wider library of catalysts and systems. The determination the speciation of some well-characterised iridium water oxidation catalysts and the mechanisms of NP formation offered further insight into a well understood system.

As discussed in Chapter 3, cobalt oxide, like iridium oxide, is an active catalyst for both water oxidation and oxygen reduction. Given the evidence discussed in CHapter 3 for catalyst deactivation, the use of in-*situ* SAXS would help determine whether the deactivation pathway is the formation of NPs.

Chapter 6

Conclusions and Future Work

A series of six cobalt complexes were synthesised and investigated for their reactivity towards oxygen. The ability of the complexes to bind O_2 was found to be a predictor of their ORR activity, whilst electrochemical properties were found to be predictors of the activity of the complexes towards oxygen atom transfer.

A series of six ligands, HL1 – HL6, were synthesised using modified literature procedures. The synthesis of HL4 was improved by reducing the need for multiple synthetic steps, and improving the overall atom economy of the synthesis. The ligands were chosen to represent a range of steric and electronic variations, with substitutions in two different positions. They were used to synthesise a series of bimetallic cobalt complexes, based on a system described originally by Llobet and coworkers.[113] Using two different synthetic routes allowed the complex to be obtained as Co_2^{III} μ-peroxo complex, $\mathbf{Co1_{O_2}}$ – $\mathbf{Co6_{O_2}}$, or as Co_2^{II} μ-chloro species, $\mathbf{Co1_{Cl}}$ – $\mathbf{Co6_{Cl}}$, Figure 6.1.

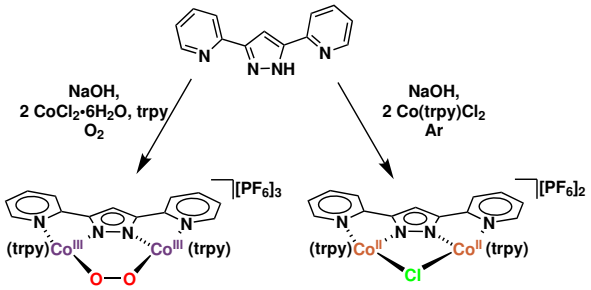

Figure 6.1: The two classes of cobalt complexes obtained and the synthetic conditions required. **HL1** used as an example.

Analysis of the complexes using a range of techniques revealed the structural impact of changing substituents on the Hbpp ligand backbone. The use of NMR spectroscopy, in conjunction with X-ray crystallography, gave insight into the symmetry of the complexes. The Co^{III} μ-OO complexes were found to be less symmetrical than their Co^{II} μ-Cl equivalents. Substituents on the pyrazole backbone were found to have a minor effect on the distortion of the Hbpp ligand, and the complexes with electron-donating

substituents ($\mathbf{Co3_{O_2}}$ and $\mathbf{Co4_{O_2}}$, with Me and NH_2 substituents, respectively) had slightly longer O–O bond lengths than the other complexes, normally an indication of a weaker O–O bond.

Electrochemical studies on $\mathbf{Co1_{O_2}}$ – $\mathbf{Co6_{O_2}}$ revealed that the complexes underwent two irreversible reduction events when scanning to negative potentials. By stopping the sweep before the onset of the second reduction event, reversibility was restored. The first reduction was studied in more detail using Randles-Sevcik analysis to determine the number of electrons in the redox event. It was shown that the redox event was a 1 electron reduction to the $Co^{III/II}$ state, meaning electrochemical reduction of the cobalt centres take places sequentially. The second, irreversible, reduction peak (E_{red2}) is likely an EC mechanism, where the redox event is followed immediately by an irreversible chemical process, which is ascribed to the breaking of the O–O bond. This was found to negatively correlate to the O–O bond lengths determined previously. Counter to expectations, the complexes that had the shortest O–O distance, i.e. the strongest O–O bonds, had the least negative E_{red2} values, meaning it required less energy to break the bond. $\mathbf{Co1_{O_2}}$ had the shortest O–O bond length, followed by $\mathbf{Co5_{O_2}}$, suggesting that these O_2-adducts are most likely to be capable of performing oxidation on a substrate.

The reactivity of the Co^{II} μ-Cl complexes towards O_2 was studied, revealing that $\mathbf{Co1_{O_2}}$ showed the fastest rates, followed by the two complexes with electron donating substituents; $\mathbf{Co4_{O_2}}$ and $\mathbf{Co3_{O_2}}$. Both $\mathbf{Co2_{O_2}}$ and $\mathbf{Co6_{O_2}}$ showed very slow rates, suggesting limited oxidation occurred under these conditions. These results were compared to electrochemical studies of the oxidation of these complexes. There was a lack of correlation observed between the rates of oxidation and the electrochemistry, possibly due to the kinetic nature of the oxidation versus the thermodynamic nature of the E_{mid} values. However, the lack of correlation might also suggest that the dissociation of the bridging chloro or binding of O_2 is more significant to the rate of oxidation than the electrochemical properties of the complexes.

The Co^{III} μ-OO complexes were studied for their reactivity towards the oxygen reduction reaction (ORR). $\mathbf{Co1_{O_2}}$ showed the fastest rates, followed by $\mathbf{Co4_{O_2}}$. Analysis of the ORR reactivity was attempted using Variable Time Normalised Analysis (VTNA). The VTNA showed that there was clear catalyst deactivation for all six complexes and revealed an order in catalyst of 1 for $\mathbf{Co1_{O_2}}$, which which is in agreement with previous studies.[113] However, as a consequence of the catalyst deactivation, it was not possible

to use the VTNA to determine order in catalyst for the other complexes, due to poor overlaps of the kinetic profiles.

Although studies on $\mathbf{Co1_{O_2}}$ by others suggested that the binding of O_2 was not rate determining,[113] it is plausible that changing the substituents on the pyrazole backbone resulted in a change in the mechanism of reaction. It is therefore possible that the binding of O_2 and concurrent reoxidation of the cobalt centres to the Co_2^{III} state to form the μ-OO species is rate determining for some of the other complexes, particularly $\mathbf{Co6_{O_2}}$. The correlation between the rates of the ORR and the μ-Cl oxidation studies supports the proposal that O_2-binding becomes rate limiting for some of the complexes in the ORR.

In order to study the sequence of reactivity, and help establish whether PCET is a key step in the reactivity of the complexes, the interaction between the complexes with trifluoracetic acid or octomethyl ferrocene was studied. All complexes were observed to be stable in the presence of both TFA and Me_8Fc, except $\mathbf{Co6_{O_2}}$, which showed signs of reduction in the presence of Me_8Fc. This confirms that the first step in the ORR is likely PCET, although it does not clarify whether this is the rate determining step. The unusual behaviour of $\mathbf{Co6_{O_2}}$ is explained by an E_{mid} value of -0.29 V vs NHE, the least negative value of the six complexes, suggesting that Me_8Fc is reducing $\mathbf{Co6_{O_2}}$, albeit at a slower rate than during ORR. Interestingly, despite the potential oxidation of $\mathbf{Co6_{O_2}}$ by Me_8Fc, the reactivity of $\mathbf{Co6_{O_2}}$ was notably slow for the ORR. This suggests that the presence of the strongly electron-withdrawing NO_2 substituent hindered the reactivity of the complex towards oxygen reduction.

The results of ORR show no correlation with the E_{red} values of the complexes, suggesting that the rate of reactivity is not dependent on the electrochemical properties of the complexes. This is further supported by the fact that the reduction of $\mathbf{Co6_{O_2}}$ by Me_8Fc did not result in higher rates of activity in the ORR further highlights that the reactivity of the complexes inthe ORR is not dependent on their electrochemical behaviour.

Introduction of *ortho*-methyl groups on $\mathbf{Co2_{O_2}}$ and $\mathbf{Co2_{Cl}}$ had a pronounced effect on the reactivity, effectively preventing any oxidation activity of the μ-Cl species towards O_2 or the μ-OO species towards oxygen reduction. The electrochemical properties of these two complexes was also notably different to the other five complexes, with a considerably higher oxidation potential of the $\mathbf{Co2_{Cl}}$ species to the $Co^{III/II}$ oxidation

state, and also the first reduction of the $\mathbf{Co2_{O_2}}$ complex. The electrochemical results for $\mathbf{Co2_{O_2}}$ suggested that there was both an electronic and steric effect of substitution in the *ortho*-position, since the redox potentials were so shifted relative to the other five complexes. These results, in conjunction with the fact that the μ-OO form proved challenging to isolate, suggests that introduction of substituents in the *ortho*-position hinders the activity of the complex towards O_2, likely as a result of steric hinderance.

The trends observed for the six complexes towards the ORR do not suggest that the binding of O_2 is accelerated by a higher electron density on the metal centres. Fitting the kinetic profile of $\mathbf{Co2_{O_2}}$ and $\mathbf{Co6_{O_2}}$ revealed biexponential behaviour, suggesting multiple reaction mechanisms at play. It is possible that the second, slow, mechanism is also present in the other four complexes, but the effect is not observable due to the higher activity of the fast mechanism. Since $\mathbf{Co1_{O_2}}$ displays the fastest rates for ORR and binding of O_2, these results suggest that future attempts to optimise complexes of this type should not target the pyrazole backbone or the *ortho* position.

Initial studies were carried out into the activity of $\mathbf{Co1_{O_2}}$ – $\mathbf{Co6_{O_2}}$ for oxygen atom transfer reactivity. Studies have shown that metal peroxo complexes can demonstrate amphoteric reactivity, so a series of substrates were chosen to investigate a range of possible reactivities. Using $\mathbf{Co1_{O_2}}$ as a test complex, six substrates were tested, although reactivity was only observed with the substrates where the peroxo species acts as a nucleophile. $\mathbf{Co1_{O_2}}$ showed minor activity towards 1,4-cyclohexadiene, but the most promising reactivity was with benzaldehyde. Although full characterisation of the products were not possible, the use of NMR spectroscopy (including wide spectral width ^{1}H NMR spectroscopy) and mass spectrometry suggests that the reaction yields two main products: a diamagnetic Co_2^{III} complex with a bridging benzoate adduct, and an unidentified paramagnetic species. Assignment of both species proved challenging, although through the use of multiple 2D techniques, tentative assignment of the diamagnetic adduct was carried out. Due to the similarity in position of some of the peaks corresponding to the terpyridine ligands on the $\mathbf{Co1_{Cl}}$ complex, the paramagnetic product is assigned as a Co_2^{II} species, rather than a mixed $Co^{III/II}$ species.

A screening of the reactivity of other five complexes towards benzaldehyde showed that only $\mathbf{Co5_{O_2}}$ displayed any reactivity. This was a somewhat surprising finding, since metal-oxygen complexes are well documented as reacting in a nucleophilic manner towards benzaldehyde, and the mild electron-withdrawing effect of the bromo-substituent

of $\mathbf{Co5_{O_2}}$ would render it less electron-rich than both $\mathbf{Co3_{O_2}}$ and $\mathbf{Co4_{O_2}}$. However, the reduction potential of the more electron-rich $\mathbf{Co3_{O_2}}$ and $\mathbf{Co4_{O_2}}$ is 0.1 V more negative than $\mathbf{Co1_{O_2}}$ and $\mathbf{Co5_{O_2}}$. The lower E_{red2} values of $\mathbf{Co1_{O_2}}$ and $\mathbf{Co5_{O_2}}$ is used to explain the reactivity of these complexes. This reduction potential is a measure of the activation of the O–O bond, and lower reduction potentials suggest the bond is more likely to oxidise substrates. The reaction of benzaldehyde with $\mathbf{Co5_{O_2}}$ was considerably slower than the rate observed with $\mathbf{Co1_{O_2}}$, and it was not possible to assign any products from the reaction. This slower in reactivity might be explained by the difference in reduction potentials, $\mathbf{Co1_{O_2}}$ = -0.80 V vs NHE, whilst $\mathbf{Co5_{O_2}}$ = -0.84 V vs NHE.

The results of the oxidation studies on the μ-Cl complexes, and the ORR and OAT on the μ-OO complexes suggest that functionalisation on the Hbpp ligand on the pyrazole backbone or the *ortho*-positions has no discernible advantage to the reactivity of the complexes, and in all cases reduced the activity. Substitution in the *ortho*-position had the most pronounced effect, effectively stopping all reactivity of the complex towards O_2. The addition of a nitro group on the pyrazole backbone also significantly reduced the reactivity of the complex. The other pyrazole substituents tested, methyl, amine and bromo, also had a negative impact on the rate of reaction of the complex compared to the unsubstituted $\mathbf{Co1_{O_2}}$. Identification of some of the rate determining features in the reactivity of the complex towards the ORR or OAT, as discussed in Section 3.8, can help inform further synthesis or studies into these complexes.

The finding that electrochemical properties did not predict the reactivity of the complexes towards the ORR or O_2-binding ability is important when thinking about further synthesis of ORR catalysts. However, the activity of OAT was found to be directly related to the 'reducibility' of the the peroxo complex. Since the optimisation of the catalyst required for the ORR is different to that required for OAT, this suggests that efforts should be focused on each activity independently, rather than optimising for both in the same set of complexes.

It is also worth noting that there is a tension between the stability of μ-OO complexes and their oxidative reactvity. Complexes that react readily with O_2 to form stable peroxo species are unlikely to be highly reactive towards organic substrates. Design of a complex that can bind and activate oxygen, but not form a metal-oxygen species that is too stable to react further is necessary to design effective aerobic oxidation catalysts.

****** reference design criteria here *******

A number of attempts were made to synthesis a bimetallic copper complex for aerobic oxidations. Unfortunately, despite employing a number of copper precursors and other ligands, a copper-bpp dimer ($[Cu_2(bpp)_2]^{2+}$) preferentially formed each time, blocking any potential active sites for catalysis. The use of the more sterically congested HL2 ligand was used, in the hope that this would block the formation of the dimer. However, this resulted in the formation of a tetramer, rather than the desired product. Using a copper acetate precursor a copper cluster was formed. An analogous cluster was also formed when using a $ZnCl_2$ precursor. The recent reports of catalytic activity by pentanuclear clusters based on the Hbpp ligand, particularly of water oxidation by an iron cluster, suggests investigations of these complexes for O_2-activation might be fruitful.

Further ligand synthesis focussed on two main outputs: diversifying the backbone substituents and the addition of another binding site on the Hbpp ligand. A number of bases were used to try to activate the *ortho* C–H of the pyridine to allow the addition of another binding side, namely an alkoxide group, making the binding pocket an NNO chelate. Unfortunately, all bases tried resulted in an intractable mixture of products. This was possibly due to the reactivity of the pyrazole ring, so further work in this area might investigate the use of protecting groups or methods of introducing the functionality at an earlier stage in the synthesis. Addition of further substituents on the pyrazole backbone also proved to be unsuccessful, despite successful synthesis of the relevant precursors.

Small Angle X-ray Scattering (SAXS) was shown to be an effective method of studying the homogeneity of a catalyst under reaction conditions. The use of well characterised iridium water oxidation catalysts, with a benchmark system that is known to form nanoparticles under reaction conditions, allowed the sensitivity of the technique to be investigated. Subsequent gas evolution studies allowed the correlation between nanoparticle formation and catalyst turnover to be investigated, revealing that nanoparticle formation occurs after catalyst turnover. Having established the capabilities of the technique, SAXS could be used to study $\mathbf{Co1_{O_2}}$ – $\mathbf{Co6_{O_2}}$ under ORR conditions to determine whether the catalyst deactivation that is observed is due to nanoparticle formation.

$\mathbf{Co1_{O_2}}$ has been previously studied for water oxidation,[166] but the impact of changing

substituents on the bridging ligand backbone have not been studied. A first step would be carrying out aqueous electrochemical analysis of all six μ-OO complexes, which would give an indication of any water oxidation activity. The impact of ligand substitution had a negative impact on the rates of ORR, compared to $\mathbf{Co1_{O_2}}$. It would therefore be interesting to study whether the same trends are observed in water oxidation catalysis.

6.1 Future Work

6.1.1 Raman Spectroscopy

Due to the symmetrical nature of the O-O stretch, it is infrared (IR) silent. Therefore, Raman spectroscopy is commonly used to characterise complexes with an O-O bond.[53,126,223] Additionally, the use of resonance Raman (RR) allows the investigation of specific bonds, or species in low concentration. There are a number of examples that use resonance raman as a means of identifying the specific binding mode of the bound O_2.[58] Although the O–O bond length can give a rough idea of the strength of the bond, Raman spectroscopy would give a more accurate representation of the strength of the bond. This might help with predicting future reactivity, or with tuning ligand functionalisation to help promote high activity by the complex.

Some preliminary data was collected on a solid sample of $\mathbf{Co1_{O_2}}$ using an excitation wavelength of 532 nm to test the viability of the technique for these complexes, Figure 6.2. Using previously assigned cobalt complexes, the peaks were assigned as the Co-O stretch at around 530 cm^{-1} and the stretch at around 900 cm^{-1} is the O-O bond.[360,361]

6.1.2 EPR Spectroscopy

Electron paramagnetic resonance (EPR) spectroscopy is also an invaluable tool in the sturctural characterisation of paramagnetic complexes.[362–364] The information obtained from EPR spectroscopy can give insight into the location of the unpaired electron, its interaction with various nuclei, and the distribution of electron density in the complex.[364] Additionally, unlike NMR spectroscopy, EPR spectroscopy operates on much shorter timescales, in the range of 0.1 ns, meaning it is possible to study short-lived intermediates. This means that EPR offers the possibility of monitoring the reactions of the complexes *in-situ*, as it would allow the detection of paramagnetic intermediates in the reaction cycle.

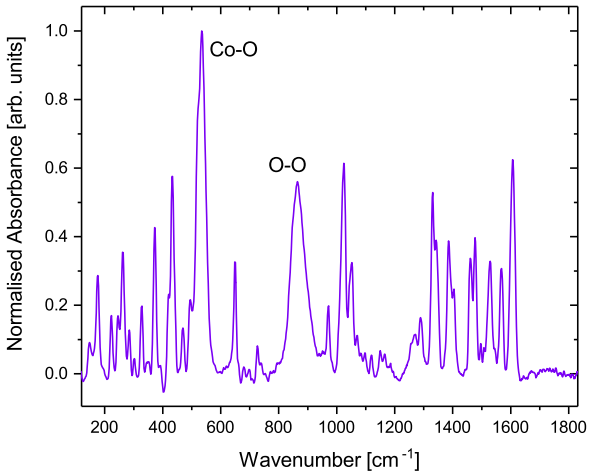

Figure 6.2: Raman data for $\mathbf{Co1_{O_2}}$ with the key stretches labelled. Data collected on a Renishaw InVia Confocal Raman Microscope

Bibliography

(1) J. Priestly, *Experiments and Observations on Different Kinds of Air, Volume 1*, London, 1974.

(2) N. W. Best, *Foundations of Chemistry*, 2015, **17**, 137–151.

(3) B. Srinivasan, *The FEBS Journal*, 2021, **288**, 2068–2083.

(4) M. W. Rossiter, in *The Cambridge History of Science*, Cambridge University Press, 2001, pp. 54–71.

(5) J.-E. Backvall, *Modern Oxidation Methods*, ed. J.-E. Backvall, Wiley-VCH Verlag, Second Edi, 2011.

(6) K. Omura and D. Swern, *Tetrahedron*, 1978, **34**, 1651–1660.

(7) J. S. Carey, D. Laffan, C. Thomson and M. T. Williams, *Organic & Biomolecular Chemistry*, 2006, **4**, 2337.

(8) S. Caron, R. W. Dugger, S. G. Ruggeri, J. A. Ragan and D. H. Brown Ripin, *Chemical Reviews*, 2006, **106**, 2943–2989.

(9) S. S. Stahl, *Angewandte Chemie*, 2004, **43**, 3400–3420.

(10) Z. Shi, C. Zhang, C. Tang and N. Jiao, *Chemical Society Reviews*, 2012, **41**, 3381–3430.

(11) O. N. Temkin, *Kinetics and Catalysis*, 2020, **61**, 663–720.

(12) X. Ye, M. D. Johnson, T. Diao, M. H. Yates and S. S. Stahl, *Green Chemistry*, 2010, **12**, 1180.

(13) M. L. Pegis, C. F. Wise, D. J. Martin and J. M. Mayer, *Chemical Reviews*, 2018, **118**, 2340–2391.

(14) S. Dey, B. Mondal, S. Chatterjee, A. Rana, S. Amanullah and A. Dey, *Nature Reviews Chemistry*, 2017, **1**, 0098.

(15) A. L. Ward, L. Elbaz, J. B. Kerr and J. Arnold, *Inorganic Chemistry*, 2012, **51**, 4694–4706.

(16) P. W. van Leeuwen, *Applied Catalysis A: General*, 2001, **212**, 61–81.

(17) P. M. Kroneck and M. E. Sosa Torres, *Sustaining Life on Planet Earth: Metalloenzymes Mastering Dioxygen and Other Chewy Gases*, ed. P. M. H. Kroneck and M. E. Sosa Torres, Springer International Publishing, Cham, 2015, vol. 15, pp. vii–ix.

(18) L. Que and W. B. Tolman, *Nature*, 2008, **455**, 333–340.

(19) W. T. Borden, R. Hoffmann, T. Stuyver and B. Chen, *Journal of the American Chemical Society*, 2017, **139**, 9010–9018.

(20) K. P. Kepp and P. Dasmeh, *The Journal of Physical Chemistry B*, 2013, **117**, 3755–3770.

(21) X. Huang and J. T. Groves, *Chemical Reviews*, 2018, **118**, 2491–2553.

(22) B. Battistella and K. Ray, *Coordination Chemistry Reviews*, 2020, **408**, 213176.

(23) C. N. Cornell and M. S. Sigman, *Inorganic Chemistry*, 2007, **46**, 1903–1909.

(24) A. Gavriilidis, A. Constantinou, K. Hellgardt, K. K. Hii, G. J. Hutchings, G. L. Brett, S. Kuhn and S. P. Marsden, *Reaction Chemistry & Engineering*, 2016, **1**, 595–612.

(25) P. M. Osterberg, J. K. Niemeier, C. J. Welch, J. M. Hawkins, J. R. Martinelli, T. E. Johnson, T. W. Root and S. S. Stahl, *Organic Process Research & Development*, 2014, 141223071236001.

(26) P. M. Osterberg, J. K. Niemeier, C. J. Welch, J. M. Hawkins, J. R. Martinelli, T. E. Johnson, T. W. Root and S. S. Stahl, *Organic Process Research & Development*, 2015, **19**, 1537–1543.

(27) B.-Z. Zhan and A. Thompson, *Tetrahedron*, 2004, **60**, 2917–2935.

(28) D. J. C. Constable, P. J. Dunn, J. D. Hayler, G. R. Humphrey, J. L. Leazer, Jr., R. J. Linderman, K. Lorenz, J. Manley, B. A. Pearlman, A. Wells, A. Zaks and T. Y. Zhang, *Green Chemistry*, 2007, **9**, 411–420.

(29) K. Alfonsi, J. Colberg, P. J. Dunn, T. Fevig, S. Jennings, T. A. Johnson, H. P. Kleine, C. Knight, M. A. Nagy, D. A. Perry and M. Stefaniak, *Green Chemistry*, 2008, **10**, 31–36.

(30) D. Munz and T. Strassner, *Inorganic Chemistry*, 2015, **54**, 5043–5052.

(31) A. Dale, C. Lythall, J. Aucott and C. Sayer, *Thermochimica Acta*, 2002, **382**, 47–54.

(32) M. S. Ghiorso, *Contributions to Mineralogy and Petrology*, 1990, **104**, 645–667.

(33) J. Serrano-Plana, I. Garcia-Bosch, A. Company and M. Costas, *Accounts of Chemical Research*, 2015, **48**, 2397–2406.

(34) C. Gerdemann, C. Eicken and B. Krebs, *Accounts of Chemical Research*, 2002, **35**, 183–191.

(35) A. C. Rosenzweig and M. H. Sazinsky, *Current Opinion in Structural Biology*, 2006, **16**, 729–735.

(36) C. E. Elwell, N. L. Gagnon, B. D. Neisen, D. Dhar, A. D. Spaeth, G. M. Yee and W. B. Tolman, *Chemical Reviews*, 2017, **117**, 2059–2107.

(37) C. Citek, S. Herres-Pawlis and T. D. P. Stack, *Accounts of Chemical Research*, 2015, **48**, 2424–2433.

(38) S. M. Adam, G. B. Wijeratne, P. J. Rogler, D. E. Diaz, D. A. Quist, J. J. Liu and K. D. Karlin, *Chemical Reviews*, 2018, **118**, 10840–11022.

(39) Y. Le Mest, C. Inisan, A. Laouénan, M. L'Her, J. Talarmin, M. El Khalifa and J.-Y. Saillard, *Journal of the American Chemical Society*, 1997, **119**, 6095–6106.

(40) E. I. Solomon, P. Chen, M. Metz, S.-K. Lee and A. E. Palmer, *Angewandte Chemie International Edition*, 2001, **40**, 4570–4590.

(41) M. J. Behlen, Y.-Y. Zhou, T. J. Steiman, S. Pal, D. R. Hartline, M. Zeller and C. Uyeda, *Dalton Trans.*, 2017, **46**, 5493–5497.

(42) A. L. Gavrilova, C. J. Qin, R. D. Sommer, A. L. Rheingold and B. Bosnich, *Journal of the American Chemical Society*, 2002, **124**, 1714–1722.

(43) X.-J. Su, C. Zheng, Q.-Q. Hu, H.-Y. Du, R.-Z. Liao and M.-T. Zhang, *Dalton Transactions*, 2018, **47**, 8670–8675.

(44) M. F. Pinto, M. Olivares, Á. Vivancos, G. Guisado-Barrios, M. Albrecht and B. Royo, *Catalysis Science & Technology*, 2019, DOI: 10.1039/C9CY00685K.

(45) J. I. van der Vlugt, *European Journal of Inorganic Chemistry*, 2012, **2012**, 363–375.

(46) C. J. Cramer, W. B. Tolman, K. H. Theopold and A. L. Rheingold, *Proceedings of the National Academy of Sciences*, 2003, **100**, 3635–3640.

(47) A. B. P. Lever and H. B. Gray, *Accounts of Chemical Research*, 1978, **11**, 348–355.

(48) Y. Liu, G. Zhou, Z. Zhang, H. Lei, Z. Yao, J. Li, J. Lin and R. Cao, *Chemical Science*, 2020, **11**, 87–96.

(49) G. Givaja, M. Volpe, M. A. Edwards, A. J. Blake, C. Wilson, M. Schröder and J. B. Love, *Angewandte Chemie International Edition*, 2007, **46**, 584–586.

(50) M. Volpe, H. Hartnett, J. W. Leeland, K. Wills, M. Ogunshun, B. J. Duncombe, C. Wilson, A. J. Blake, J. McMaster and J. B. Love, *Inorganic Chemistry*, 2009, **48**, 5195–5207.

(51) T. Nishiura, Y. Chiba, J. Nakazawa and S. Hikichi, *Inorganic Chemistry*, 2018, **57**, 14218–14229.

(52) G. Y. Park, M. F. Qayyum, J. Woertink, K. O. Hodgson, B. Hedman, A. A. Narducci Sarjeant, E. I. Solomon and K. D. Karlin, *Journal of the American Chemical Society*, 2012, **134**, 8513–8524.

(53) M. T. Kieber-Emmons, J. W. Ginsbach, P. K. Wick, H. R. Lucas, M. E. Helton, B. Lucchese, M. Suzuki, A. D. Zuberbühler, K. D. Karlin and E. I. Solomon, *Angewandte Chemie International Edition*, 2014, **53**, 4935–4939.

(54) T. J. Collins, *Accounts of Chemical Research*, 1994, **27**, 279–285.

(55) M. J. Bartos, S. W. Gordon-Wylie, B. G. Fox, L. James Wright, S. T. Weintraub, K. E. Kauffmann, E. Münck, K. L. Kostka, E. S. Uffelman, C. E. Rickard, K. R. Noon and T. J. Collins, *Coordination Chemistry Reviews*, 1998, **174**, 361–390.

(56) T. K. Michaelos, D. Y. Shopov, S. B. Sinha, L. S. Sharninghausen, K. J. Fisher, H. M. C. Lant, R. H. Crabtree and G. W. Brudvig, *Accounts of Chemical Research*, 2017, **50**, 952–959.

(57) G. McLendon and A. E. Martell, *Journal of the Chemical Society, Chemical Communications*, 1975, 223.

(58) I. Garcia-Bosch, R. E. Cowley, D. E. Díaz, R. L. Peterson, E. I. Solomon and K. D. Karlin, *Journal of the American Chemical Society*, 2017, **139**, 3186–3195.

(59) J. J. Berzelius, *Annalen der Physik und Chemie*, 1828, **89**, 435–488.

(60) R. J. Sheehan, in *Ullmann's Encyclopedia of Industrial Chemistry*, Wiley-VCH Verlag GmbH & Co. KGaA, Weinheim, Germany, 2011.

(61) R. A. F. Tomás, J. C. M. Bordado and J. F. P. Gomes, *Chemical Reviews*, 2013, **113**, 7421–7469.

(62) A. E. Wendlandt, A. M. Suess and S. S. Stahl, *Angewandte Chemie International Edition*, 2011, **50**, 11062–11087.

(63) S. D. McCann and S. S. Stahl, *Accounts of Chemical Research*, 2015, **48**, 1756–1766.

(64) A. N. Campbell and S. S. Stahl, *Accounts of Chemical Research*, 2012, **45**, 851–863.

(65) J. Hagen, *Industrial Catalysis: A Practical Approach*, WILEY-VCH Verlag GmbH, 2nd Editio, 2006, vol. 53.

(66) Y. Liang, J. Wei, X. Qiu and N. Jiao, *Chemical Reviews*, 2018, **118**, 4912–4945.

(67) M. M. Pereira, L. D. Dias and M. J. F. Calvete, *ACS Catalysis*, 2018, **8**, 10784–10808.

(68) E. A. Lewis and W. B. Tolman, *Chemical Reviews*, 2004, **104**, 1047–1076.

(69) R. J. H. Clark and T. J. Dines, *Angewandte Chemie International Edition in English*, 1986, **25**, 131–158.

(70) N. Gulzar, B. Schweitzer-Chaput and M. Klussmann, *Catalysis Science & Technology*, 2014, **4**, 2778–2796.

(71) J. M. Hoover, B. L. Ryland and S. S. Stahl, *Journal of the American Chemical Society*, 2013, **135**, 2357–2367.

(72) Q. Cao, L. M. Dornan, L. Rogan, N. L. Hughes and M. J. Muldoon, *Chemical Communications*, 2014, **50**, 4524–4543.

(73) C. W. Anson, S. Ghosh, S. Hammes-Schiffer and S. S. Stahl, *Journal of the American Chemical Society*, 2016, **138**, 4186–4193.

(74) A. I. Nguyen, R. G. Hadt, E. I. Solomon and T. D. Tilley, *Chem. Sci.*, 2014, **5**, 2874–2878.

(75) N. A. Milas, *Chemical Reviews*, 1932, **10**, 295–364.

(76) R. A. Fernandes, A. K. Jha and P. Kumar, *Catalysis Science & Technology*, 2020, **10**, 7448–7470.

(77) W. Xu, Z. Huang, X. Ji and J.-P. Lumb, *ACS Catalysis*, 2019, **9**, 3800–3810.

(78) L. Boisvert and K. I. Goldberg, *Accounts of Chemical Research*, 2012, **45**, 899–910.

(79) D. Pun, T. Diao and S. S. Stahl, *Journal of the American Chemical Society*, 2013, **135**, 8213–8221.

(80) S.-S. Meng, L.-R. Lin, X. Luo, H.-J. Lv, J.-L. Zhao and A. S. C. Chan, *Green Chemistry*, 2019, **21**, 6187–6193.

(81) D. Wang, A. B. Weinstein, P. B. White and S. S. Stahl, *Chemical Reviews*, 2018, **118**, 2636–2679.

(82) S. S. Stahl, *Angewandte Chemie International Edition*, 2004, **43**, 3400–3420.

(83) Y.-F. Liang and N. Jiao, *Accounts of Chemical Research*, 2017, **50**, 1640–1653.

(84) K. P. Bryliakov, *Chemical Reviews*, 2017, **117**, 11406–11459.

(85) M. Rueping, C. Vila, A. Szadkowska, R. M. Koenigs and J. Fronert, *ACS Catalysis*, 2012, **2**, 2810–2815.

(86) C.-K. Wu, T.-J. Liou, H.-Y. Wei, P.-S. Tsai and D.-Y. Yang, *Tetrahedron*, 2014, **70**, 8219–8225.

(87) X. Zhang, K. P. Rakesh, L. Ravindar and H.-l. Qin, *Green Chemistry*, 2018, **20**, 4790–4833.

(88) C. Tao, B. Wang, L. Sun, Z. Liu, Y. Zhai, X. Zhang and J. Wang, *Organic & Biomolecular Chemistry*, 2017, **15**, 328–332.

(89) D. C. Fabry and M. Rueping, *Accounts of Chemical Research*, 2016, **49**, 1969–1979.

(90) P. J. Dyson and P. G. Jessop, *Catalysis Science & Technology*, 2016, **6**, 3302–3316.

(91) M. Hirotsu, N. Kuwamura, I. Kinoshita, M. Kojima, Y. Yoshikawa and K. Ueno, *Dalton Transactions*, 2009, 7678.

(92) A. A. Gewirth and M. S. Thorum, *Inorganic Chemistry*, 2010, **49**, 3557–3566.

(93) E. S. Rountree, B. D. McCarthy, T. T. Eisenhart and J. L. Dempsey, *Inorganic Chemistry*, 2014, **53**, 9983–10002.

(94) K. Mase, K. Ohkubo, Z. Xue, H. Yamada and S. Fukuzumi, *Chemical Science*, 2015, **6**, 6496–6504.

(95) Y.-H. Wang, M. L. Pegis, J. M. Mayer and S. S. Stahl, *Journal of the American Chemical Society*, 2017, **139**, 16458–16461.

(96) C. Sandford, M. A. Edwards, K. J. Klunder, D. P. Hickey, M. Li, K. Barman, M. S. Sigman, H. S. White and S. D. Minteer, *Chemical Science*, 2019, **10**, 6404–6422.

(97) M. L. Pegis, J. A. S. Roberts, D. J. Wasylenko, E. A. Mader, A. M. Appel and J. M. Mayer, *Inorganic Chemistry*, 2015, **54**, 11883–11888.

(98) M. Wikström, K. Krab and V. Sharma, *Chemical Reviews*, 2018, acs.chemrev.7b00664.

(99) T. Tsukihara, H. Aoyama, E. Yamashita, T. Tomizaki, H. Yamaguchi, K. Shinzawa-Itoh, R. Nakashima, R. Yaono and S. Yoshikawa, *Science*, 1995, **269**, 1069–1074.

(100) E. Kim, M. E. Helton, I. M. Wasser, K. D. Karlin, S. Lu, H.-w. Huang, P. Moenne-Loccoz, C. D. Incarvito, A. L. Rheingold, M. Honecker, S. Kaderli and A. D. Zuberbuhler, *Proceedings of the National Academy of Sciences*, 2003, **100**, 3623–3628.

(101) I. Katsounaros, S. Cherevko, A. R. Zeradjanin and K. J. J. Mayrhofer, *Angewandte Chemie International Edition*, 2014, **53**, 102–121.

(102) J. Rosenthal and D. G. Nocera, *Accounts of Chemical Research*, 2007, **40**, 543–553.

(103) W. Zhang, W. Lai and R. Cao, *Chemical Reviews*, 2017, **117**, 3717–3797.

(104) J. P. Collman, P. Denisevich, Y. Konai, M. Marrocco, C. Koval and F. C. Anson, *Journal of the American Chemical Society*, 1980, **102**, 6027–6036.

(105) C. K. Chang, H. Y. Liu and I. Abdalmuhdi, *Journal of the American Chemical Society*, 1984, **106**, 2725–2726.

(106) J. P. Collman, P. S. Wagenknecht and J. E. Hutchison, *Angewandte Chemie International Edition in English*, 1994, **33**, 1537–1554.

(107) C. J. Chang, Z.-H. Loh, C. Shi, F. C. Anson and D. G. Nocera, *Journal of the American Chemical Society*, 2004, **126**, 10013–10020.

(108) R. Zhang and J. J. Warren, *Journal of the American Chemical Society*, 2020, **142**, 13426–13434.

(109) K. Mittra, S. Chatterjee, S. Samanta and A. Dey, *Inorganic Chemistry*, 2013, **52**, 14317–14325.

(110) M. H. V. Huynh and T. J. Meyer, *Chemical Reviews*, 2007, **107**, 5004–5064.

(111) J. J. Warren, T. A. Tronic and J. M. Mayer, *Chemical Reviews*, 2010, **110**, 6961–7001.

(112) L. Tahsini, H. Kotani, Y.-M. Lee, J. Cho, W. Nam, K. D. Karlin and S. Fukuzumi, *Chemistry - A European Journal*, 2012, **18**, 1084–1093.

(113) S. Fukuzumi, S. Mandal, K. Mase, K. Ohkubo, H. Park, J. Benet-Buchholz, W. Nam and A. Llobet, *Journal of the American Chemical Society*, 2012, **134**, 9906–9909.

(114) S. Fukuzumi, S. Mochizuki and T. Tanaka, *Inorganic Chemistry*, 1989, **28**, 2459–2465.

(115) N. Elgrishi, K. J. Rountree, B. D. McCarthy, E. S. Rountree, T. T. Eisenhart and J. L. Dempsey, *Journal of Chemical Education*, 2018, **95**, 197–206.

(116) G. Passard, A. M. Ullman, C. N. Brodsky and D. G. Nocera, *Journal of the American Chemical Society*, 2016, **138**, 2925–2928.

(117) A. J. Ingram, A. B. Wolk, C. Flender, J. Zhang, C. J. Johnson, U. Hintermair, R. H. Crabtree, M. A. Johnson and R. N. Zare, *Inorganic chemistry*, 2014, **53**, 423–433.

(118) E. V. Sackville, F. Marken and U. Hintermair, *ChemCatChem*, 2018, **10**, 4280–4291.

(119) X. Han, K. Wang, G. Zhang, W. Gao and J. Chen, *Advanced Synthesis & Catalysis*, 2019, **361**, 2804–2824.

(120) M. Sankaralingam, Y.-M. Lee, W. Nam and S. Fukuzumi, *Coordination Chemistry Reviews*, 2018, **365**, 41–59.

(121) J. Cho, S. Jeon, S. A. Wilson, L. V. Liu, E. A. Kang, J. J. Braymer, M. H. Lim, B. Hedman, K. O. Hodgson, J. S. Valentine, E. I. Solomon and W. Nam, *Nature*, 2011, **478**, 502–505.

(122) M. Liu and C.-J. Li, *Angewandte Chemie International Edition*, 2016, **55**, 10806–10810.

(123) B. Wang, Y.-M. Lee, W.-Y. Tcho, S. Tussupbayev, S.-T. Kim, Y. Kim, M. S. Seo, K.-B. Cho, Y. Dede, B. C. Keegan, T. Ogura, S. H. Kim, T. Ohta, M.-H. Baik, K. Ray, J. Shearer and W. Nam, *Nature Communications*, 2017, **8**, 14839.

(124) B. Shin, K. D. Sutherlin, T. Ohta, T. Ogura, E. I. Solomon and J. Cho, *Inorganic Chemistry*, 2016, **55**, 12391–12399.

(125) M. Sankaralingam, Y.-M. Lee, S. H. Jeon, M. S. Seo, K.-B. Cho and W. Nam, *Chemical Communications*, 2018, **54**, 1209–1212.

(126) J. Cho, R. Sarangi, H. Y. Kang, J. Y. Lee, M. Kubo, T. Ogura, E. I. Solomon and W. Nam, *Journal of the American Chemical Society*, 2010, **132**, 16977–16986.

(127) J. Cho, R. Sarangi and W. Nam, *Accounts of Chemical Research*, 2012, **45**, 1321–1330.

(128) M. T. Kieber-Emmons, J. Annaraj, M. S. Seo, K. M. Van Heuvelen, T. Tosha, T. Kitagawa, T. C. Brunold, W. Nam and C. G. Riordan, *Journal of the American Chemical Society*, 2006, **128**, 14230–14231.

(129) J. Annaraj, J. Cho, Y.-M. Lee, S. Y. Kim, R. Latifi, S. P. de Visser and W. Nam, *Angewandte Chemie International Edition*, 2009, **48**, 4150–4153.

(130) S. Murahashi, T. Naota and N. Hirai, *The Journal of Organic Chemistry*, 1993, **58**, 7318–7319.

(131) P. Mastrorilli, C. F. Nobile, G. P. Suranna and L. Lopez, *Tetrahedron*, 1995, **51**, 7943–7950.

(132) O. Wilhelm, *Nature*, 1902, **65**, 522–526.

(133) R. H. Crabtree, *Chemical Reviews*, 2012, **112**, 1536–1554.

(134) D. B. Eremin and V. P. Ananikov, *Coordination Chemistry Reviews*, 2017, **346**, 2–19.

(135) N. D. Schley, J. D. Blakemore, N. K. Subbaiyan, C. D. Incarvito, F. D'Souza, R. H. Crabtree and G. W. Brudvig, *Journal of the American Chemical Society*, 2011, **133**, 10473–10481.

(136) R. K. Arvela, N. E. Leadbeater, M. S. Sangi, V. A. Williams, P. Granados and R. D. Singer, *The Journal of Organic Chemistry*, 2005, **70**, 161–168.

(137) S. L. Buchwald and C. Bolm, *Angewandte Chemie International Edition*, 2009, **48**, 5586–5587.

(138) R. H. Crabtree, *Chemical Reviews*, 2015, **115**, 127–150.

(139) J. M. Thomsen, S. W. Sheehan, S. M. Hashmi, J. Campos, U. Hintermair, R. H. Crabtree and G. W. Brudvig, *Journal of the American Chemical Society*, 2014, **136**, 13826–13834.

(140) D. Hong, J. Jung, J. Park, Y. Yamada, T. Suenobu, Y.-M. Lee, W. Nam and S. Fukuzumi, *Energy & Environmental Science*, 2012, **5**, 7606.

(141) S. W. Sheehan, J. M. Thomsen, U. Hintermair, R. H. Crabtree, G. W. Brudvig and C. A. Schmuttenmaer, *Nature Communications*, 2015, **6**, 6469.

(142) U. Hintermair, S. W. Sheehan, A. R. Parent, D. H. Ess, D. T. Richens, P. H. Vaccaro, G. W. Brudvig and R. H. Crabtree, *Journal of the American Chemical Society*, 2013, **135**, 10837–10851.

(143) J. M. Thomsen, D. L. Huang, R. H. Crabtree and G. W. Brudvig, *Dalton Transactions*, 2015, **44**, 12452–12472.

(144) R. H. Crabtree, *Journal of Organometallic Chemistry*, 2014, **751**, 174–180.

(145) V. Artero and M. Fontecave, *Chem. Soc. Rev.*, 2013, **42**, 2338–2356.

(146) K. J. Lee, B. D. McCarthy and J. L. Dempsey, *Chemical Society Reviews*, 2019, **48**, 2927–2945.

(147) M. M. Najafpour, F. Ebrahimi, M. Amini, M. Rahimi, A. El-Sawy and S. L. Suib, *Dalton Transactions*, 2015, **44**, 15121–15125.

(148) M. M. Najafpour, F. Ebrahimi, R. Safdari, M. Z. Ghobadi, M. Tavahodi and P. Rafighi, *Dalton Transactions*, 2015, **44**, 15435–15440.

(149) W.-B. Yu, Q.-Y. He, X.-f. Ma, H.-t. Shi and X. Wei, *Dalton Transactions*, 2015, **44**, 351–358.

(150) B. R. Pauw, *Journal of Physics: Condensed Matter*, 2013, **25**, 383201.

(151) A. T. Fiedler and A. A. Fischer, *JBIC Journal of Biological Inorganic Chemistry*, 2017, **22**, 407–424.

(152) A. J. Jasniewski and L. Que, *Chemical Reviews*, 2018, **118**, 2554–2592.

(153) P. W. Ball and A. B. Blake, *Journal of the Chemical Society A: Inorganic, Physical, Theoretical*, 1969, **2**, 1415.

(154) J. Casabó, J. Pons, K. S. Siddiqi, F. Teixidor, E. Molins and C. Miravitlles, *J. Chem. Soc., Dalton Trans.*, 1989, **6**, 1401–1403.

(155) C. Sens, I. Romero, M. Rodríguez, A. Llobet, T. Parella and J. Benet-Buchholz, *Journal of the American Chemical Society*, 2004, **126**, 7798–7799.

(156) K. Nakano, S. Kawata, K. Yoneda, A. Fuyuhiro, T. Yagi, S. Nasu, S. Morimoto and S. Kaizaki, *Chem. Commun.*, 2004, **2**, 2892–2893.

(157) F. Bozoglian, S. Romain, M. Z. Ertem, T. K. Todorova, C. Sens, J. Mola, M. Rodríguez, I. Romero, J. Benet-Buchholz, X. Fontrodona, C. J. Cramer, L. Gagliardi and A. Llobet, *Journal of the American Chemical Society*, 2009, **131**, 15176–15187.

(158) J. Klingele, S. Dechert and F. Meyer, *Coordination Chemistry Reviews*, 2009, **253**, 2698–2741.

(159) M. Du, S.-T. Chen, Y.-M. Guo, X.-H. Bu and J. Ribas, *Journal of Molecular Structure*, 2005, **737**, 17–21.

(160) S. Romain, J. Rich, C. Sens, T. Stoll, J. Benet-Buchholz, A. Llobet, M. Rodriguez, I. Romero, R. Clérac, C. Mathonière, C. Duboc, A. Deronzier and M.-N. Collomb, *Inorganic Chemistry*, 2011, **50**, 8427–8436.

(161) K. Nakano, N. Suemura, S. Kawata, A. Fuyuhiro, T. Yagi, S. Nasu, S. Morimoto and S. Kaizaki, *Dalton Trans.*, 2004, **2**, 982–988.

(162) C. Dowling, D. R. Dinsdale and M. T. Lemaire, *Canadian Journal of Chemistry*, 2015, **93**, 769–774.

(163) C. J. Schneider, J. D. Cashion, B. Moubaraki, S. M. Neville, S. R. Batten, D. R. Turner and K. S. Murray, *Polyhedron*, 2007, **26**, 1764–1772.

(164) R. Ishikawa, S. Ueno, S. Nifuku, Y. Horii, H. Iguchi, Y. Miyazaki, M. Nakano, S. Hayami, S. Kumagai, K. Katoh, Z. Li, M. Yamashita and S. Kawata, *Chemistry – A European Journal*, 2020, **26**, 1278–1285.

(165) L. Francàs, X. Sala, E. Escudero-Adán, J. Benet-Buchholz, L. Escriche and A. Llobet, *Inorganic Chemistry*, 2011, **50**, 2771–2781.

(166) M. L. Rigsby, S. Mandal, W. Nam, L. C. Spencer, A. Llobet and S. S. Stahl, *Chemical Science*, 2012, **3**, 3058.

(167) V. K. K. Praneeth, M. Kondo, P. M. Woi, M. Okamura and S. Masaoka, *ChemPlusChem*, 2016, **81**, 1123–1128.

(168) G. Li, D. Zhu, X. Wang, Z. Su and M. R. Bryce, *Chemical Society Reviews*, 2020, **49**, 765–838.

(169) M. Okamura, M. Kondo, R. Kuga, Y. Kurashige, T. Yanai, S. Hayami, V. K. K. Praneeth, M. Yoshida, K. Yoneda, S. Kawata and S. Masaoka, *Nature*, 2016, **530**, 465–468.

(170) J. I. van der Vlugt, S. Demeshko, S. Dechert and F. Meyer, *Inorganic Chemistry*, 2008, **47**, 1576–1585.

(171) V. K. K. Praneeth, M. Kondo, M. Okamura, T. Akai, H. Izu and S. Masaoka, *Chemical Science*, 2019, **10**, 4628–4639.

(172) N. Planas, G. Christian, S. Roeser, E. Mas-Marzá, M.-R. Kollipara, J. Benet-Buchholz, F. Maseras and A. Llobet, *Inorganic Chemistry*, 2012, **51**, 1889–1901.

(173) X. Sala, S. Maji, R. Bofill, J. García-Antón, L. Escriche and A. Llobet, *Accounts of Chemical Research*, 2014, **47**, 504–516.

(174) R. Matheu, M. Z. Ertem, J. Benet-Buchholz, E. Coronado, V. S. Batista, X. Sala and A. Llobet, *Journal of the American Chemical Society*, 2015, **137**, 10786–10795.

(175) S. Roeser, M. Z. Ertem, C. Cady, R. Lomoth, J. Benet-Buchholz, L. Hammarström, B. Sarkar, W. Kaim, C. J. Cramer and A. Llobet, *Inorganic Chemistry*, 2012, **51**, 320–327.

(176) S. Maji, L. Vigara, F. Cottone, F. Bozoglian, J. Benet-Buchholz and A. Llobet, *Angewandte Chemie International Edition*, 2012, **51**, 5967–5970.

(177) A. C. Sander, S. Maji, L. Francàs, T. Böhnisch, S. Dechert, A. Llobet and F. Meyer, *ChemSusChem*, 2015, **8**, 1697–1702.

(178) S. Roeser, F. Bozoglian, C. J. Richmond, A. B. League, M. Z. Ertem, L. Francàs, P. Miró, J. Benet-Buchholz, C. J. Cramer and A. Llobet, *Catalysis Science & Technology*, 2016, **6**, 5088–5101.

(179) S. Mandal, S. Shikano, Y. Yamada, Y.-M. Lee, W. Nam, A. Llobet and S. Fukuzumi, *Journal of the American Chemical Society*, 2013, **135**, 15294–15297.

(180) J. Pons, X. López, E. Benet, J. Casabó, F. Teixidor and F. Sánchez, *Polyhedron*, 1990, **9**, 2839–2845.

(181) H. Stöckmann, A. A. Neves, S. Stairs, K. M. Brindle and F. J. Leeper, *Organic & Biomolecular Chemistry*, 2011, **9**, 7303.

(182) W. Zhang, J. Liu, K. Jin and L. Sun, *Journal of Heterocyclic Chemistry*, 2006, **43**, 1669–1672.

(183) C. Hansch, A. Leo and R. W. Taft, *Chemical Reviews*, 1991, **91**, 165–195.

(184) J. Pons Picart, F. J. Sanchez, J. Casabó, J. Rius, A. Alvarez-Larena and J. Ros, *Inorganic Chemistry Communications*, 2002, **5**, 130–133.

(185) S. Samanta, S. Demesko, S. Dechert and F. Meyer, *Angewandte Chemie International Edition*, 2015, **54**, 583–587.

(186) B. Schneider, S. Demeshko, S. Neudeck, S. Dechert and F. Meyer, *Inorganic Chemistry*, 2013, **52**, 13230–13237.

(187) J. Tu, M. Xu, S. Parvez, R. T. Peterson and R. M. Franzini, *Journal of the American Chemical Society*, 2018, **140**, 8410–8414.

(188) L.-H. Zou, Y.-C. Li, P.-G. Li, J. Zhou and Z. Wu, *European Journal of Organic Chemistry*, 2018, **2018**, 5639–5643.

(189) L. Terborg, S. Nowak, S. Passerini, M. Winter, U. Karst, P. R. Haddad and P. N. Nesterenko, *Analytica Chimica Acta*, 2012, **714**, 121–126.

(190) C. Sens, M. Rodríguez, I. Romero, A. Llobet, T. Parella and J. Benet-Buchholz, *Inorganic Chemistry*, 2003, **42**, 8385–8394.

(191) R. Kawahata, T. Tsukuda, T. Yagi, A. Fuyuhiro and S. Kaizaki, *Journal of Alloys and Compounds*, 2006, **408-412**, 976–980.

(192) L. Mognon, J. Benet-Buchholz, S. M. W. Rahaman, C. Bo and A. Llobet, *Inorganic Chemistry*, 2014, **53**, 12407–12415.

(193) F. H. Köhler, in *Encyclopedia of Magnetic Resonance*, John Wiley & Sons, Ltd, Chichester, UK, 2011.

(194) A. J. Pell, G. Pintacuda and C. P. Grey, *Progress in Nuclear Magnetic Resonance Spectroscopy*, 2019, **111**, 1–271.

(195) J. Carlos Cobas, M. A. Bernstein, M. Martín-Pastor and P. G. Tahoces, *Journal of Magnetic Resonance*, 2006, **183**, 145–151.

(196) T. D. Claridge, *High-Resolution NMR Techniques in Organic Chemistry*, Elsevier Ltd, 2009, pp. 1–383.

(197) K. Długopolska, T. Ruman, M. Danilczuk and D. Pogocki, *Applied Magnetic Resonance*, 2009, **35**, 271–283.

(198) S. A. Rouf, J. Mareš and J. Vaara, *Journal of Chemical Theory and Computation*, 2015, **11**, 1683–1691.

(199) H. S. Chow, E. C. Constable, C. E. Housecroft, K. J. Kulicke and Y. Tao, *Dalton Trans.*, 2005, **0**, 236–237.

(200) M. Kruck, D. C. Sauer, M. Enders, H. Wadepohl and L. H. Gade, *Dalton Transactions*, 2011, **40**, 10406.

(201) S. Aroua, T. K. Todorova, P. Hommes, L.-M. Chamoreau, H.-U. Reissig, V. Mougel and M. Fontecave, *Inorganic Chemistry*, 2017, **56**, 5930–5940.

(202) M. Green, *Journal of Organometallic Chemistry*, 1995, **500**, 127–148.

(203) O. V. Dolomanov, L. J. Bourhis, R. J. Gildea, J. A. K. Howard and H. Puschmann, *Journal of Applied Crystallography*, 2009, **42**, 339–341.

(204) R. W. Taft, *Journal of the American Chemical Society*, 1952, **74**, 2729–2732.

(205) C. A. Tolman, *Chemical Reviews*, 1977, **77**, 313–348.

(206) N. L. Allinger and E. L. Eliel, *Topics in Stereochemistry*, ed. N. L. Allinger and E. L. Eliel, John Wiley & Sons, Inc., Hoboken, NJ, USA, 1967, vol. 1, pp. 1–254.

(207) K. Angermund, W. Baumann, E. Dinjus, R. Fornika, H. Görls, M. Kessler, C. Krüger, W. Leitner and F. Lutz, *Chemistry - A European Journal*, 1997, **3**, 755–764.

(208) S. C. Abrahams, R. L. Collin and W. N. Lipscomb, *Acta Crystallographica*, 1951, **4**, 15–20.

(209) I. Mayer, *Chemical Physics Letters*, 1983, **97**, 270–274.

(210) M. B. Robin and P. Day, in *Advances in Inorganic Chemistry and Radiochemistry*, 1968, vol. 10, pp. 247–422.

(211) J. W. Egan, B. S. Haggerty, A. L. Rheingold, S. C. Sendlinger and K. H. Theopold, *Journal of the American Chemical Society*, 1990, **112**, 2445–2446.

(212) D. Ramprasad, A. G. Gilicinski, T. J. Markley and G. P. Pez, *Inorganic Chemistry*, 1994, **33**, 2841–2847.

(213) L. Vaska, *Accounts of Chemical Research*, 1976, **9**, 175–183.

(214) V. Talrose, A. Yermakov, A. Usov, A. Goncharova, A. Leskin, N. Messineva, N. Trusova and M. Efimkina, in *NIST Chemistry WebBook, NIST Standard Reference Database Number 69*, ed. P. Linstrom and W. Mallard.

(215) E. I. Solomon and A. B. P. Lever, *Inorganic Electronic Structre and Spectroscopy: Volume I, Methodology*, Wiley, New York, 1999.

(216) E. I. Solomon and A. B. P. Lever, *Inorganic Electronic Structure and Spectroscopy: Volume II, Applications and Case Studies*, Wiley, New York, 1999.

(217) P. Atkins and J. De Paula, *Atkins' Physical Chemistry*, Oxford University Press, Oxford, 9th Editio, 2010.

(218) N. I. o. A. I. S. and Technology, *National Institute of Advanced Industrial Science and Technology: Spectral Database for Organic Compounds (SDBSWeb).*

(219) M. Mizuno, H. Hayashi, S. Fujinami, H. Furutachi, S. Nagatomo, S. Otake, K. Uozumi, M. Suzuki and T. Kitagawa, *Inorganic Chemistry*, 2003, **42**, 8534–8544.

(220) X. Yang, D. Su, L. Song, X. Wang, Q. Xiao, Q. Feng and S. Ding, *Separation and Purification Technology*, 2020, **232**, 115969.

(221) N. I. o. A. I. S. and Technology, *National Institute of Advanced Industrial Science and Technology: Spectral Database for Organic Compounds (SDBSWeb).*

(222) Z.-H. Zhou, C.-K. Li, S.-F. Zhou, A. Shoberu and J.-P. Zou, *Tetrahedron*, 2017, **73**, 2740–2746.

(223) C. Gimbert-Suriñach, D. Moonshiram, L. Francàs, N. Planas, V. Bernales, F. Bozoglian, A. Guda, L. Mognon, I. López, M. A. Hoque, L. Gagliardi, C. J. Cramer and A. Llobet, *Journal of the American Chemical Society*, 2016, **138**, 15291–15294.

(224) T. A. Stich, J. G. McAlpin, R. M. Wall, M. L. Rigsby and R. D. Britt, *Inorganic Chemistry*, 2016, **55**, 12728–12736.
(225) V. J. Catalano and T. J. Craig, *Inorganic Chemistry*, 2003, **42**, 321–334.
(226) J. Clayden, N. Greeves, S. Warren and P. Wothers, *Organic Chemistry*, Oxford University Press, 1st Editio, 2001.
(227) K. J. Lee, N. Elgrishi, B. Kandemir and J. L. Dempsey, *Nature Reviews Chemistry*, 2017, **1**, 0039.
(228) D. J. Graham, *Standard Operating Procedures for Cyclic Voltammetry*.
(229) J.-m. Savéant, *Chemical Reviews*, 2008, **108**, 2348–2378.
(230) C. Costentin and J.-M. Savéant, *Nature Reviews Chemistry*, 2017, **1**, 0087.
(231) D. G. Blackmond, *Angewandte Chemie International Edition*, 2005, **44**, 4302–4320.
(232) D. G. Blackmond, *Journal of the American Chemical Society*, 2015, **137**, 10852–10866.
(233) J. Burés, *Angewandte Chemie - International Edition*, 2016, 2028–2031.
(234) J. Burés, *Angewandte Chemie International Edition*, 2016, **55**, 16084–16087.
(235) J. Burés, *Topics in Catalysis*, 2017, **60**, 631–633.
(236) A. M. R. Hall, P. Dong, A. Codina, J. P. Lowe and U. Hintermair, *ACS Catalysis*, 2019, **9**, 2079–2090.
(237) K. Muzyka, J. Sun, T. H. Fereja, Y. Lan, W. Zhang and G. Xu, *Analytical Methods*, 2019, **11**, 397–414.
(238) D. T. Sawyer, G. Chiericato, C. T. Angelis, E. J. Nanni and T. Tsuchiya, *Analytical Chemistry*, 1982, **54**, 1720–1724.
(239) C. Franco and J. Olmsted III, *Talanta*, 1990, **37**, 905–909.
(240) W. R. Browne, *Electrochemistry*, Oxford University Press, 2018.
(241) N. G. Tsierkezos, *Journal of Solution Chemistry*, 2007, **36**, 289–302.
(242) C. R. Wilke and P. Chang, *AIChE Journal*, 1955, **1**, 264–270.
(243) D. E. Richardson and H. Taube, *Inorganic Chemistry*, 1981, **20**, 1278–1285.
(244) B. D. McCarthy, D. J. Martin, E. S. Rountree, A. C. Ullman and J. L. Dempsey, *Inorganic Chemistry*, 2014, **53**, 8350–8361.
(245) S. J. Cobb, Z. J. Ayres and J. V. Macpherson, *Annual Review of Analytical Chemistry*, 2018, **11**, 463–484.
(246) C. R. Bagshaw, in *Encyclopedia of Biophysics*, Springer Berlin Heidelberg, Berlin, Heidelberg, 2013, pp. 2460–2466.
(247) J. M. Achord and C. L. Hussey, *Analytical Chemistry*, 1980, **52**, 601–602.

(248) A. Martínez-Carrión, M. G. Howlett, C. Alamillo-Ferrer, A. D. Clayton, R. A. Bourne, A. Codina, A. Vidal-Ferran, R. W. Adams and J. Burés, *Angewandte Chemie International Edition*, 2019, **58**, 10189–10193.

(249) D. G. Hendry and D. Schuetzle, *Journal of the American Chemical Society*, 1975, **97**, 7123–7127.

(250) A. Banerjee and S. Chattopadhyay, *Polyhedron*, 2020, **177**, 114290.

(251) J. H. Vrijsen, I. A. Thomlinson, M. E. Levere, C. L. Lyall, M. G. Davidson, U. Hintermair and T. Junkers, *Polymer Chemistry*, 2020, **11**, 3546–3550.

(252) Y. Liang, H. Wang, J. Zhou, Y. Li, J. Wang, T. Regier and H. Dai, *Journal of the American Chemical Society*, 2012, **134**, 3517–3523.

(253) Y. Liang, H. Wang, P. Diao, W. Chang, G. Hong, Y. Li, M. Gong, L. Xie, J. Zhou, J. Wang, T. Z. Regier, F. Wei and H. Dai, *Journal of the American Chemical Society*, 2012, **134**, 15849–15857.

(254) Y. Jiao, Y. Zheng, M. Jaroniec and S. Z. Qiao, *Chemical Society Reviews*, 2015, **44**, 2060–2086.

(255) F. Cheng, J. Shen, B. Peng, Y. Pan, Z. Tao and J. Chen, *Nature Chemistry*, 2011, **3**, 79–84.

(256) S. Wang, X. Wu, C. Tang, Y. Cheng, X. Min and S. P. Jiang, *Chemistry – A European Journal*, 2020, **26**, chem.201905346.

(257) A. Singh and L. Spiccia, *Coordination Chemistry Reviews*, 2013, **257**, 2607–2622.

(258) X. Deng and H. Tüysüz, *ACS Catalysis*, 2014, **4**, 3701–3714.

(259) L. C. McKenzie, P. M. Haben, S. D. Kevan and J. E. Hutchison, *The Journal of Physical Chemistry C*, 2010, **114**, 22055–22063.

(260) B. Kratochvil, E. Lorah and C. Garber, *Analytical Chemistry*, 1969, **41**, 1793–1796.

(261) M. Roemer, B. W. Skelton, M. J. Piggott and G. A. Koutsantonis, *Dalton Transactions*, 2016, **45**, 18817–18821.

(262) A. Bhagi-Damodaran, M. A. Michael, Q. Zhu, J. Reed, B. A. Sandoval, E. N. Mirts, S. Chakraborty, P. Moënne-Loccoz, Y. Zhang and Y. Lu, *Nature Chemistry*, 2017, **9**, 257–263.

(263) J. Pons, F. J. Sanchez, J. Casabó, A. Alvarez-Larena, J. F. Piniella and J. Ros, *Inorganic Chemistry Communications*, 2003, **6**, 833–836.

(264) R. Ishikawa, M. Nakano, A. Fuyuhiro, T. Takeuchi, S. Kimura, T. Kashiwagi, M. Hagiwara, K. Kindo, S. Kaizaki and S. Kawata, *Chemistry - A European Journal*, 2010, **16**, 11139–11144.

(265) H. Sato, M. Yamaguchi, T. Onuki, M. Noguchi, G. N. Newton, T. Shiga and H. Oshio, *European Journal of Inorganic Chemistry*, 2015, **2015**, 2193–2198.

(266) K. Yoneda, K. Adachi, K. Nishio, M. Yamasaki, A. Fuyuhiro, M. Katada, S. Kaizaki and S. Kawata, *Angewandte Chemie International Edition*, 2006, **45**, 5459–5461.

(267) E. Gouré, B. Gerey, M. Clémancey, J. Pécaut, F. Molton, J.-M. Latour, G. Blondin and M.-N. Collomb, *Inorganic Chemistry*, 2016, **55**, 9178–9186.

(268) S.-Z. Zhan, M. Li, J.-Z. Hou, J. Ni, D. Li and X.-C. Huang, *Chemistry - A European Journal*, 2008, **14**, 8916–8921.

(269) T. Akai, M. Kondo, S. K. Lee, H. Izu, T. Enomoto, M. Okamura, Y. Saga and S. Masaoka, *Dalton Transactions*, 2020, **49**, 1384–1387.

(270) E. Gouré, B. Gerey, F. Molton, J. Pécaut, R. Clérac, F. Thomas, J. Fortage and M.-N. Collomb, *Inorganic Chemistry*, 2020, acs.inorgchem.0c01102.

(271) J. Pons, F. Sánchez, A. Labarta, J. Casabó, F. Teixidor and A. Caubet, *Inorganica Chimica Acta*, 1993, **208**, 167–171.

(272) M. Munakata, L. P. Wu, M. Yamamoto, T. Kuroda-Sowa, M. Maekawa, S. Kawata and S. Kitagawa, *Journal of the Chemical Society, Dalton Transactions*, 1995, 4099.

(273) A. Mishima, A. Fuyuhiro, H. Kumagai and S. Kawata, *Acta Crystallographica Section E Structure Reports Online*, 2011, **67**, m1523–m1524.

(274) A. Mishima, N. Katsuta, M. Furusyou, A. Fuyuhiro and S. Kawata, *Acta Crystallographica Section E Structure Reports Online*, 2013, **69**, m455–m456.

(275) J. Pons, X. López, J. Casabó, F. Teixidor, A. Caubet, J. Rius and C. Miravitlles, *Inorganica Chimica Acta*, 1992, **195**, 61–66.

(276) R. Ishikawa, S. Ueno, Y. Hamatake, Y. Horii, Y. Miyazaki, M. Nakano, T. Noda, M. Uematsu and S. Kawata, *CrystEngComm*, 2019, **21**, 1886–1894.

(277) M. Swaminathan and S. Dogra, *Journal of Photochemistry*, 1983, **21**, 245–250.

(278) M. L. Eidinoff, *Journal of the American Chemical Society*, 1945, **67**, 2072–2073.

(279) S. J. Tereniak, C. R. Landis and S. S. Stahl, *ACS Catalysis*, 2018, **8**, 3708–3714.

(280) R. Jagadeesan, G. Sabapathi, J. Madhavan and P. Venuvanalingam, *Inorganic Chemistry*, 2018, **57**, 6833–6846.

(281) L. Boisvert, M. C. Denney, S. K. Hanson and K. I. Goldberg, *Journal of the American Chemical Society*, 2009, **131**, 15802–15814.

(282) M. E. van der Boom and D. Milstein, *Chemical reviews*, 2003, **103**, 1759–92.

(283) S. Musa, I. Shaposhnikov, S. Cohen and D. Gelman, *Angewandte Chemie*, 2011, **50**, 3533–3537.

(284) A. V. Polezhaev, C.-H. Chen, Y. Losovyj and K. G. Caulton, *Chemistry - A European Journal*, 2017, **23**, 8039–8050.

(285) M. A. Lawrence, K.-A. Green, P. N. Nelson and S. C. Lorraine, *Polyhedron*, 2017, 1–17.

(286) A. Gers-Barlag, P. Goursot, M. Li, S. Dechert and F. Meyer, *European Journal of Inorganic Chemistry*, 2019, **2019**, 3329–3334.

(287) E. V. Sackville, G. Kociok-Köhn and U. Hintermair, *Organometallics*, 2017, **36**, 3578–3588.

(288) Y. Kondo, M. Shilai, M. Uchiyama and T. Sakamoto, *Journal of the American Chemical Society*, 1999, **121**, 3539–3540.

(289) R. E. Mulvey and S. D. Robertson, *Angewandte Chemie International Edition*, 2013, **52**, 11470–11487.

(290) M. Uchiyama, Y. Matsumoto, D. Nobuto, T. Furuyama, K. Yamaguchi and K. Morokuma, *Journal of the American Chemical Society*, 2006, **128**, 8748–8750.

(291) D. R. Armstrong, W. Clegg, S. H. Dale, J. García-Álvarez, R. W. Harrington, E. Hevia, G. W. Honeyman, A. R. Kennedy, R. E. Mulvey and C. T. O'Hara, *Chem. Commun.*, 2008, 187–189.

(292) B. Haag, M. Mosrin, H. Ila, V. Malakhov and P. Knochel, *Angewandte Chemie - International Edition*, 2011, **50**, 9794–9824.

(293) B. Conway, D. V. Graham, E. Hevia, A. R. Kennedy, J. Klett and R. E. Mulvey, *Chemical Communications*, 2008, 2638.

(294) W. Clegg, B. Conway, D. V. Graham, E. Hevia, A. R. Kennedy, R. E. Mulvey, L. Russo and D. S. Wright, *Chemistry - A European Journal*, 2009, **15**, 7074–7082.

(295) A. Krasovskiy, V. Krasovskaya and P. Knochel, *Angewandte Chemie International Edition*, 2006, **45**, 2958–2961.

(296) R. Neufeld, T. L. Teuteberg, R. Herbst-Irmer, R. A. Mata and D. Stalke, *Journal of the American Chemical Society*, 2016, **138**, 4796–4806.

(297) W. Lin, O. Baron and P. Knochel, *Organic Letters*, 2006, **8**, 5673–5676.

(298) L. S. Harikrishnan, H. J. Finlay, J. X. Qiao, M. G. Kamau, J. Jiang, T. C. Wang, J. Li, C. B. Cooper, M. A. Poss, L. P. Adam, D. S. Taylor, A. Y. A. Chen, X. Yin, P. G. Sleph, R. Z. Yang, D. F. Sitkoff, M. A. Galella, D. S. Nirschl, K. Van Kirk, A. V. Miller, C. S. Huang, M. Chang, X.-Q. Chen, M. E. Salvati, R. R. Wexler and R. M. Lawrence, *Journal of Medicinal Chemistry*, 2012, **55**, 6162–6175.

(299) P. Saisaha, C. Nerungsi, S. Iamsaard and T. Thongpanchang, *Tetrahedron Letters*, 2009, **50**, 4217–4220.

(300) J. Easmon, G. Pürstinger, K.-S. Thies, G. Heinisch and J. Hofmann, *Journal of Medicinal Chemistry*, 2006, **49**, 6343–6350.

(301) X. Su, H. Huang, Y. Yuan and Y. Li, *Angewandte Chemie International Edition*, 2017, **56**, 1338–1341.

(302) R. R. Conry, in *Encyclopedia of Inorganic Chemistry*, John Wiley & Sons, Ltd, Chichester, UK, 2006.

(303) C. E. Housecroft and A. G. Sharpe, *Inorganic Chemistry*, Pearson Education Limited, 3rd Editio, 2008.

(304) P. Gros, Y. Fort and P. Caubère, *Journal of the Chemical Society, Perkin Transactions 1*, 1997, 3597–3600.

(305) L. Mognon, S. Mandal, C. E. Castillo, J. Fortage, F. Molton, G. Aromí, J. Benet-Buchhlolz, M.-N. Collomb and A. Llobet, *Chemical Science*, 2016, **7**, 3304–3312.

(306) C. Krüger, H. Sato, T. Matsumoto, T. Shiga, G. N. Newton, F. Renz and H. Oshio, *Dalton Transactions*, 2012, **41**, 11270.

(307) D. Hong, Y. Shimoyama, Y. Ohgomori, R. Kanega, H. Kotani, T. Ishizuka, Y. Kon, Y. Himeda and T. Kojima, *Inorganic Chemistry*, 2020, acs.inorgchem.0c00812.

(308) A. A. Gewirth, J. A. Varnell and A. M. DiAscro, *Chemical Reviews*, 2018, **118**, 2313–2339.

(309) S. A. Bonke, A. M. Bond, L. Spiccia and A. N. Simonov, *Journal of the American Chemical Society*, 2016, **138**, 16095–16104.

(310) G. M. Whitesides, M. Hackett, R. L. Brainard, J. P. P. M. Lavalleye, A. F. Sowinski, A. N. Izumi, S. S. Moore, D. W. Brown and E. M. Staudt, *Organometallics*, 1985, **4**, 1819–1830.

(311) X. Wu, F. Li, B. Zhang and L. Sun, *Journal of Photochemistry and Photobiology C: Photochemistry Reviews*, 2015, **25**, 71–89.

(312) B. Abécassis, F. Testard, O. Spalla and P. Barboux, *Nano Letters*, 2007, **7**, 1723–1727.

(313) A. I. Frenkel, J. A. Rodriguez and J. G. Chen, *ACS Catalysis*, 2012, **2**, 2269–2280.

(314) A. G. Kikhney and D. I. Svergun, *FEBS Letters*, 2015, **589**, 2570–2577.

(315) H. Schnablegger and Y. Singh, *The SAXS Guide: Getting acquainted with the principles*, Anton Paar GmbH, Austria, 4th Editio, 2017.

(316) I. Grillo, *Current Opinion in Colloid & Interface Science*, 2009, **14**, 402–408.

(317) W. Rüttinger and G. C. Dismukes, *Chemical Reviews*, 1997, **97**, 1–24.

(318) S. Berardi, S. Drouet, L. Francàs, C. Gimbert-Suriñach, M. Guttentag, C. Richmond, T. Stoll and A. Llobet, *Chem. Soc. Rev.*, 2014, **43**, 7501–7519.

(319) K. S. Joya, Y. F. Joya, K. Ocakoglu and R. van de Krol, *Angewandte Chemie International Edition*, 2013, **52**, 10426–10437.

(320) M. D. Kärkäs, E. V. Johnston, O. Verho and B. Åkermark, *Accounts of Chemical Research*, 2014, **47**, 100–111.

(321) T. J. Meyer, *Accounts of Chemical Research*, 1989, **22**, 163–170.

(322) J. D. Blakemore, R. H. Crabtree and G. W. Brudvig, *Chemical Reviews*, 2015, **115**, 12974–13005.

(323) P. Garrido-Barros, C. Gimbert-Suriñach, R. Matheu, X. Sala and A. Llobet, *Chemical Society Reviews*, 2017, **46**, 6088–6098.

(324) A. Harriman, *European Journal of Inorganic Chemistry*, 2014, **2014**, 573–580.

(325) R. Frydendal, E. A. Paoli, B. P. Knudsen, B. Wickman, P. Malacrida, I. E. L. Stephens and I. Chorkendorff, *ChemElectroChem*, 2014, **1**, 2075–2081.

(326) B. Limburg, E. Bouwman and S. Bonnet, *Coordination Chemistry Reviews*, 2012, **256**, 1451–1467.

(327) D. L. Huang, R. Beltrán-Suito, J. M. Thomsen, S. M. Hashmi, K. L. Materna, S. W. Sheehan, B. Q. Mercado, G. W. Brudvig and R. H. Crabtree, *Inorganic Chemistry*, 2016, **55**, 2427–2435.

(328) H. Junge, N. Marquet, A. Kammer, S. Denurra, M. Bauer, S. Wohlrab, F. Gärtner, M.-M. Pohl, A. Spannenberg, S. Gladiali and M. Beller, *Chemistry - A European Journal*, 2012, **18**, 12749–12758.

(329) J. J. Stracke and R. G. Finke, *ACS Catalysis*, 2014, **4**, 909–933.

(330) S. Fukuzumi and D. Hong, *European Journal of Inorganic Chemistry*, 2014, **2014**, 645–659.

(331) A. Harriman, I. J. Pickering, J. M. Thomas and P. A. Christensen, *Journal of the Chemical Society, Faraday Transactions 1: Physical Chemistry in Condensed Phases*, 1988, **84**, 2795.

(332) A. Mills and T. Russell, *Journal of the Chemical Society, Faraday Transactions*, 1991, **87**, 1245.

(333) S. Stucki and A. Menth, *Berichte der Bunsengesellschaft für physikalische Chemie*, 1980, **84**, 1008–1013.

(334) U. Hintermair, S. M. Hashmi, M. Elimelech and R. H. Crabtree, *Journal of the American Chemical Society*, 2012, **134**, 9785–9795.

(335) M. A. Newton and W. van Beek, *Chemical Society Reviews*, 2010, **39**, 4845.

(336) M. Povia, J. Herranz, T. Binninger, M. Nachtegaal, A. Diaz, J. Kohlbrecher, D. F. Abbott, B.-J. Kim and T. J. Schmidt, *ACS Catalysis*, 2018, **8**, 7000–7015.

(337) U. Bentrup, J. Radnik, U. Armbruster, A. Martin, J. Leiterer, F. Emmerling and A. Brückner, *Topics in Catalysis*, 2009, **52**, 1350–1359.

(338) F. Meirer and B. M. Weckhuysen, *Nature Reviews Materials*, 2018, **3**, 324–340.

(339) R. Chung and J. E. Hein, *Topics in Catalysis*, 2017, **60**, 594–608.

(340) M. Nyman, *Coordination Chemistry Reviews*, 2017, **352**, 461–472.

(341) M. Harada, N. Tamura and M. Takenaka, *The Journal of Physical Chemistry C*, 2011, **115**, 14081–14092.

(342) Y. V. Geletii, Q. Yin, Y. Hou, Z. Huang, H. Ma, J. Song, C. Besson, Z. Luo, R. Cao, K. P. O'Halloran, G. Zhu, C. Zhao, J. W. Vickers, Y. Ding, S. Mohebbi, A. E. Kuznetsov, D. G. Musaev, T. Lian and C. L. Hill, *Israel Journal of Chemistry*, 2011, **51**, 238–246.

(343) S. Goberna-Ferrón, J. Soriano-López, J. R. Galán-Mascarós and M. Nyman, *European Journal of Inorganic Chemistry*, 2015, **2015**, 2833–2840.

(344) J. Polte, *CrystEngComm*, 2015, **17**, 6809–6830.

(345) T. Rieker, A. Hanprasopwattana, A. Datye and P. Hubbard, *Langmuir*, 1999, **15**, 638–641.

(346) V. K. LaMer and R. H. Dinegar, *Journal of the American Chemical Society*, 1950, **72**, 4847–4854.

(347) V. K. L. Mer, *Industrial & Engineering Chemistry*, 1952, **44**, 1270–1277.

(348) N. T. K. Thanh, N. Maclean and S. Mahiddine, *Chemical Reviews*, 2014, **114**, 7610–7630.

(349) D. B. K. Chu, J. S. Owen and B. Peters, *The Journal of Physical Chemistry A*, 2017, **121**, 7511–7517.

(350) F. Wang, V. N. Richards, S. P. Shields and W. E. Buhro, *Chemistry of Materials*, 2014, **26**, 5–21.

(351) S. A. Bartlett, E. V. Sackville, E. K. Gibson, V. Celorrio, P. P. Wells, M. Nachtegaal, S. W. Sheehan and U. Hintermair, *Chemical Communications*, 2019, **55**, 7832–7835.

(352) D. B. Grotjahn, D. B. Brown, J. K. Martin, D. C. Marelius, M.-C. Abadjian, H. N. Tran, G. Kalyuzhny, K. S. Vecchio, Z. G. Specht, S. A. Cortes-Llamas, V. Miranda-Soto, C. van Niekerk, C. E. Moore and A. L. Rheingold, *Journal of the American Chemical Society*, 2011, **133**, 19024–19027.

(353) S. Ogo, N. Makihara and Y. Watanabe, *Organometallics*, 1999, **18**, 5470–5474.

(354) A. J. Allen, F. Zhang, R. J. Kline, W. F. Guthrie and J. Ilavsky, *Journal of Applied Crystallography*, 2017, **50**, 462–474.

(355) M. Basham, J. Filik, M. T. Wharmby, P. C. Y. Chang, B. El Kassaby, M. Gerring, J. Aishima, K. Levik, B. C. A. Pulford, I. Sikharulidze, D. Sneddon, M. Webber, S. S. Dhesi, F. Maccherozzi, O. Svensson, S. Brockhauser, G. Náray and A. W. Ashton, *Journal of Synchrotron Radiation*, 2015, **22**, 853–858.

(356) J. Filik, A. W. Ashton, P. C. Y. Chang, P. A. Chater, S. J. Day, M. Drakopoulos, M. W. Gerring, M. L. Hart, O. V. Magdysyuk, S. Michalik, A. Smith, C. C. Tang, N. J. Terrill, M. T. Wharmby and H. Wilhelm, *Journal of Applied Crystallography*, 2017, **50**, 959–966.

(357) B. R. Pauw, A. J. Smith, T. Snow, N. J. Terrill and A. F. Thünemann, *Journal of Applied Crystallography*, 2017, **50**, 1800–1811.

(358) I. Bressler, B. R. Pauw and A. F. Thünemann, *Journal of Applied Crystallography*, 2015, **48**, 962–969.

(359) J. Y. Rempel, M. G. Bawendi and K. F. Jensen, *Journal of the American Chemical Society*, 2009, **131**, 4479–4489.

(360) K. Nakamoto, M. Suzuki, T. Ishiguro, M. Kozuka, Y. Nishida and S. Kida, *Inorganic Chemistry*, 1980, **19**, 2822–2824.

(361) K. Nakamoto, Y. Nonaka, Ishiguro, M. W. Urban, M. Suzuki, M. Kozuka, Y. Nishida and S. Kida, *Journal of the American Chemical Society*, 1982, **104**, 3386–3391.

(362) M. M. Roessler and E. Salvadori, *Chemical Society Reviews*, 2018, **47**, 2534–2553.

(363) M. Goswami, A. Chirila, C. Rebreyend and B. de Bruin, *Topics in Catalysis*, 2015, **58**, 719–750.

(364) V. Checkik, E. Carter and D. Murphy, *Electron Paramagnetic Resonance*, Oxford University Press, 2016.

(365) J. Keeler, *Understanding NMR Spectroscopy*, Wiley, Second Edi, 2010.

(366) I. Bertini and C. Luchinat, *Coordination Chemistry Reviews*, 1996, **150**, 185–220.

(367) I. Bertini and C. Luchinat, *Coordination Chemistry Reviews*, 1996, **150**, 243–264.

(368) I. Bertini, C. Luchinat and G. Parigi, *Solution NMR of Paramagnetic Molecules: Applications to Metallobiomolcules and Models*, Elsevier, London, 2001.

(369) J. A. Iggo, *NMR Spectroscopy in Inorganic Chemistry*, Oxford University Press, 1999.

(370) N. E. Jacobsen, in *NMR Spectroscopy Explained*, John Wiley & Sons, Inc., Hoboken, NJ, USA, 2007, pp. 289–352.

(371) B. Jacobson, G. Andersson, G. Sundkvist and G. Sundkvist, *Acta Chemica Scandinavica*, 1955, **9**, 997–1006.

(372) A. Burrows, J. Holman, A. Parsons, G. Pilling and G. Price, *Chemistry3*, Oxford University Press, 2nd Editio, 2013.

Appendix A

A.1 Appendix to Chapter 2

A.1.1 An Introduction to Paramagnetic NMR Spectroscopy

This section is not intended to be a comprehensive introduction to paramagnetic NMR spectroscopy, rather to introduce a number of key concepts that are necessary to explain some of the phenomena observed. An interested reader is referred to both Claridge - *"High-Resolution NMR Techniques in Organic Chemistry"*[196] and Keeler - *"Understanding NMR Spectroscopy"*[365] for an explanation of some of the key terms and concepts in NMR more broadly. For comprehensive introductions to the theory, use and application of paramagnetic NMR, the reader is referred to Köhler - *"Paramagnetic Complexes in Solution; The NMR Approach"*[193] and Pell - *"Paramagnetic NMR in Solution and the Solid State"*[194]. For more information on the use of 2D experiments with paramagnetic complexes, including details of appropriate pulse sequences, the reader is referred to the 1996 reviews by Bertini *et al.*[366,367]

The presence of one or more unpaired electrons can result in a number of stark changes to the collected NMR spectra, including significant line broadening of the peaks in the spectrum, resulting in a lack of splitting. They can also lead to incredibly wide spectral widths, with some peaks shifted by over 100 ppm. The impact of the unpaired electron(s) and the processes leading to these differences are briefly described below.

Perhaps the most notable property of paramagnetic species in NMR spectroscopy is the paramagnetic relaxation enhancement (PRE), which refers to the very short relaxation times associated with paramagnetic complexes. In NMR spectroscopy there are two key relaxation processes, which are described by the T_1 and T_2 values, which are relaxation time constants. The T_1 value, sometimes referred to as "spin-lattice" or "longitudinal" relaxation, describes a time constant for the relaxation of the spin back to the equilibrium state, after the initial magnetic pulse. T_1 values for diamagnetic protons usually

fall between 0.5 – 5 s, whilst those of paramagnetic complexes fall well under 1 s.[196] Low-spin cobalt (II) complexes are recorded as having T_1 and T_2 values in the range of $10^{-9} - 10^{-10}$ s.[194] Due to the short timescales, these values are recorded using EPR in conjunction with NMR spectroscopy.[368] For comparison, some carbon nuclei can have T_1 values of over 10 s.

There are four key mechanisms of relaxation of the nuclear spins; dipole-dipole relaxation, chemical shift anisotropy relaxation, spin-rotation relaxation and quadrupolar relaxation. A detailed description of these mechanisms can be found in Claridge.[196] Of these, the dipole-dipole relaxation mechanism is important in the context of paramagnetic NMR spectroscopy. This is due to the large magnetic moment of an unpaired electron when compared to a proton, making this relaxation mechanism very efficient in paramagnetic complexes. This phenomenon can be exploited when collecting data on a paramagnetic sample by reducing the delay time between scans, reducing the time taken to collect a full data set. It is worth noting that these rapid relaxation rates do not have an impact on the accuracy of the integrals. Indeed, unlike in diamagnetic species, where very long relaxation times are required to ensure quantitative integrals, the short relaxation times means that accurate paramagnetic integrals can be collected with shorter delay times.

The T_2 value, also called "spin-spin" or "transverse" relaxation is also affected by the paramagnetic relaxation enhancement. T_2 describes the effect caused by spins in a sample precessing at slightly different rates due to inhomogeneity of the magnetic field experienced by the sample. The shorter the T_2 value, the larger differences in the frequencies of the precessing spins, which results in broadening of the peaks in the spectrum.

For most nuclei with spin $\frac{1}{2}$, $T_1 \approx T_2$. However, in a highly inhomogeneous magnetic field, for example, due to the presence of an unpaired electron, T_2 can become short. As the peak widths are inversely proportional to the T_2 value, in species with very short T_2 values the peaks can be much broader than in a correspondingly similar diamagnetic complex.

In order to explain the broad range of chemical shifts in paramagnetic complexes, it is first necessary to explain how chemical shifts arise in diamagnetic NMR. After a pulse is applied, there is a net alignment with the magnetic field, where the spins become "bunched" along the axis of excitation. Spins in different environments will align along

the axis upon application of the pulse, however, they will then precess at different frequencies, resulting in different chemical shifts.[196,369]

The isotropic shift describes the difference between an observed paramagnetic peak and the peak from an analogous diamagnetic species, and is the reason behind the large spectral widths observed with paramagnetic complexes. There are two key mechanisms that underly the isotropic shift, contact and pseudo-contact shifts. Both describe the interaction of the unpaired electron with the nucleus, the contact shift arises due to the through-bond transfer of the spin polarisation from the unpaired electron onto the nucleus, whilst the pseudo contact shift describes the through-space coupling between the unpaired electron(s) and the nucleus.[194]

One would expect the NMR signals to be split as a result of the nuclear spins coupling with the unpaired electron. However, due to the timescales of the technique this splitting is not observable using NMR spectroscopy. Instead, a weighted average (determined by the population of the nuclear spin states) is observed. However, the coupling effect results in considerably different rates of precession upon application of the magnetic pulse - resulting in the varied shifts observed in paramagnetic spectra. This phenomenon also explains why there is no splitting observed in paramagnetic NMR spectra, the peaks observed are already an average, so any fine detail such as splitting patterns will be lost. This splitting can be observed using EPR spectroscopy.

Pseudo contact shifts are an effect caused by the magnetic field emanating from the unpaired electron. However, the effect is strongly distance dependent, scaling with $\frac{1}{r^3}$, where r is distance from the unpaired electron. It results in smaller isotopic shifts, often within the 20 ppm range of diamagnetic complexes, and mostly affects those nuclei in closest proximity to the unpaired electron.

Finally, there are a number of complications associated with acquiring data over a large spectral width. Many commonly used NMR probes can struggle with the excitation of the wide spectral width needed to collect paramagnetic data.[194] The radio frequency pulse used in NMR spectroscopy has a Gaussian excitation profile and results in an excitation bandwidth that is inversely proportional to the length of the pulse, so a short pulse is able to excite a wide frequency window and vice versa, Figure A.1.[370] The Gaussian excitation profile means that peaks at the edge of the spectrum will not receive as much power as those in the middle. This is not usually a problem over the spectral window of ^{1}H NMR spectroscopy as the use of a narrow excitation pulse

(Figure A.1, centre) has only minimal "droop" at the edges of the spectrum.[370] For a standard 90° pulse with a duration of 10 µs, the width of the excitation profile is 1/10 µs = 100,000 / 1 s = 100 kHz. For a spectral width of 12 ppm on a 300 mHz spectrometer, the results in a 12 x 300 = 3600 Hz, meaning the excitation bandwidth is almost 30 times wider than the spectral window (1000,000 / 3600).[370] However, for nuclei with wide frequency distributions, such as ^{13}C or paramagnetic ^{1}H, this can lead to inaccurate integrals at the edges of the spectrum or distortions in the phasing.[196,370]

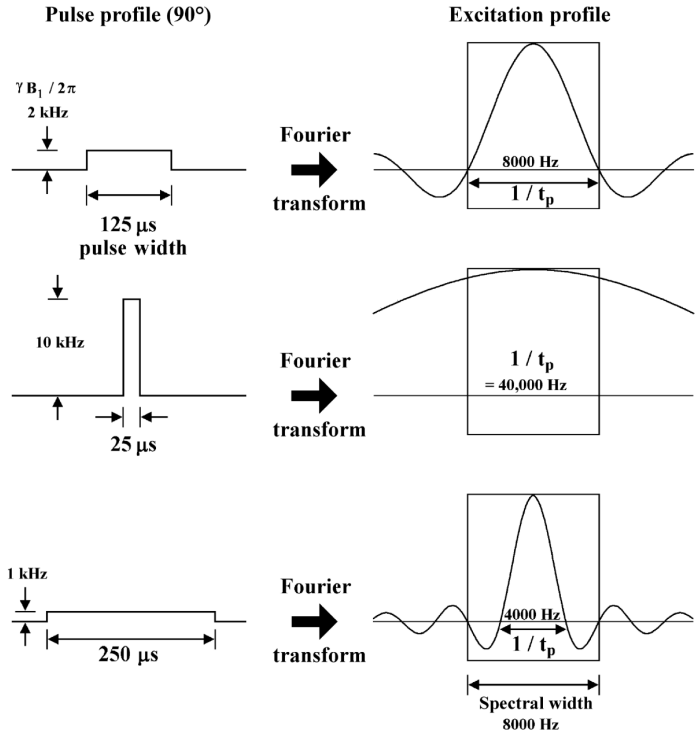

Figure A.1: Example of different rectangular pulses (different pulse widths and power), showing the impact on the excitation profile. Reproduced permission from NMR Spectroscopy Explained, 2007, 289-352. Copyright (2007) John Wiley & Sons, Inc.[370]

This effect, coupled with the short relaxation times, can result in a loss of resolution and low sensitivity. This is further complicated by the Nyquist condition, which states that to characterise a frequency of F Hz, the data must be sampled at a frequency of at least 2F Hz. The ramifications of this can be understood through the spectral acquisition time (AQ), which dictates the resolution of the spectrum. The AQ is determined by Equation A.1,[196] where DW = dwell time, and refers to the interval between samples points, TD = number of data points, SW = spectral width (Hz), which determines the

highest accurately represented frequency.

$$\mathrm{AQ} = \mathrm{DW} \cdot \mathrm{TD} = \frac{\mathrm{TD}}{2\ \mathrm{SW}} \tag{A.1}$$

As the resolution is determined by acquisition time, in order to collect a high resolution wide spectral width spectrum, the number of data points also has to increase significantly, leading to very large datasets. This can lead to problems because not only are very large datasets unwieldy to analyse, in some cases, the acquisition time is limited by available computer hardware which cannot handle datasets over a certain size. The result can be truncation of the FID, which means the FID is cut off before the signal has fully decayed to zero, due to the short acquisition time necessary to collect such a wide spectral width.[365] This can result in artefacts in the spectrum, such as 'sinc wiggles', broad distortions, and poor resolution.

A.1.2 Paramagnetic NMR Assignments

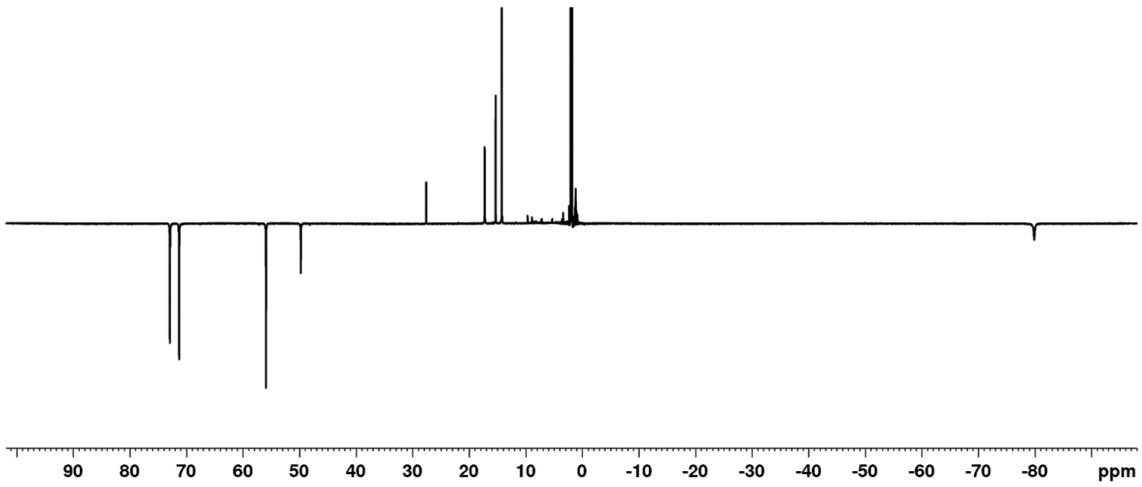

Figure A.2: ^{1}H NMR of $\mathbf{Co2_{Cl}}$ showing the inversion of peaks when the spectrum is run with a solvent suppression programme.

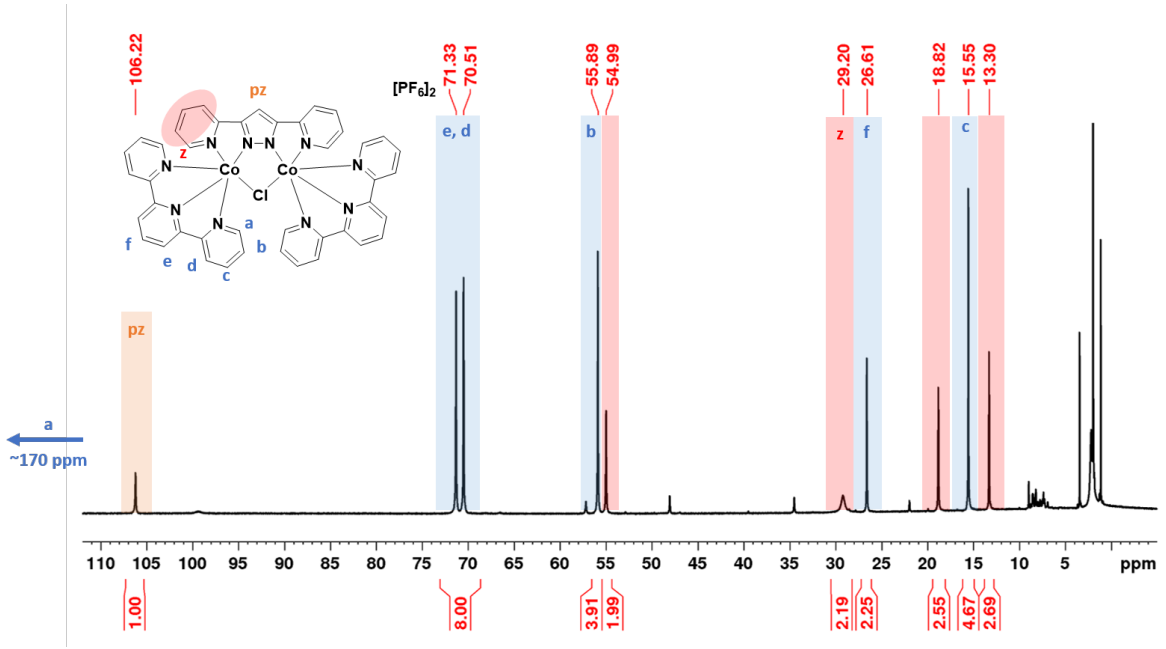

Figure A.3: $\mathbf{Co1_{Cl}}$ ^{1}H NMR in MeCN, non-solvent suppressed. Tentative assignment. Peaks between 5 and 10 ppm are diamagnetic peaks, formed through air contamination during the handling of the sample. Non-labelled peaks are unreacted $Co(trpy)Cl_2$ which proved challenging to remove.

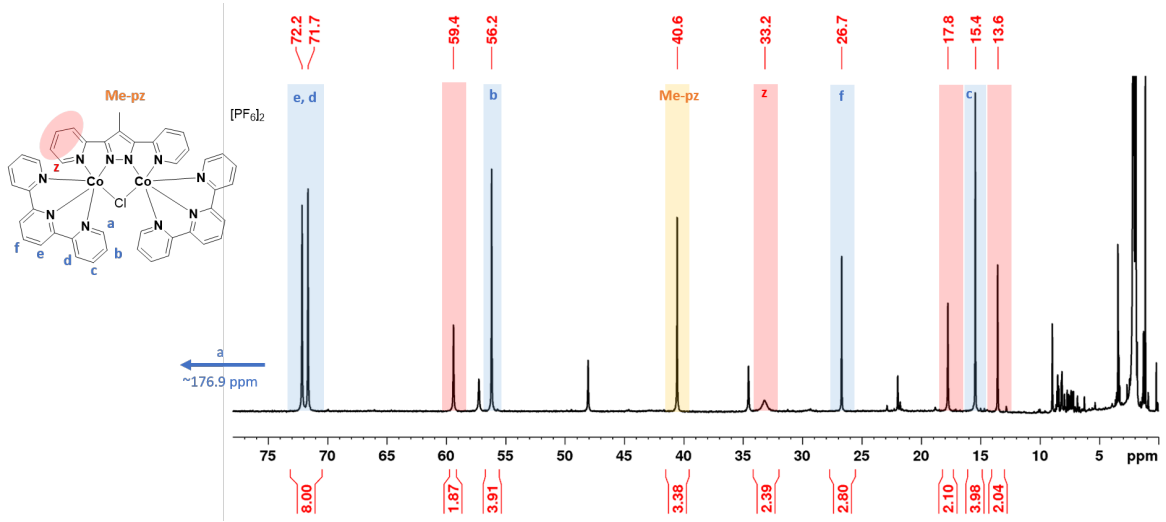

Figure A.4: $\mathbf{Co3_{Cl}}$ ^{1}H NMR in MeCN, non-solvent suppressed. Tentative assignment. Peaks between 5 and 10 ppm are diamagnetic peaks, formed through air contamination during the handling of the sample. Non-labelled peaks are unreacted $Co(trpy)Cl_2$ which proved challenging to remove.

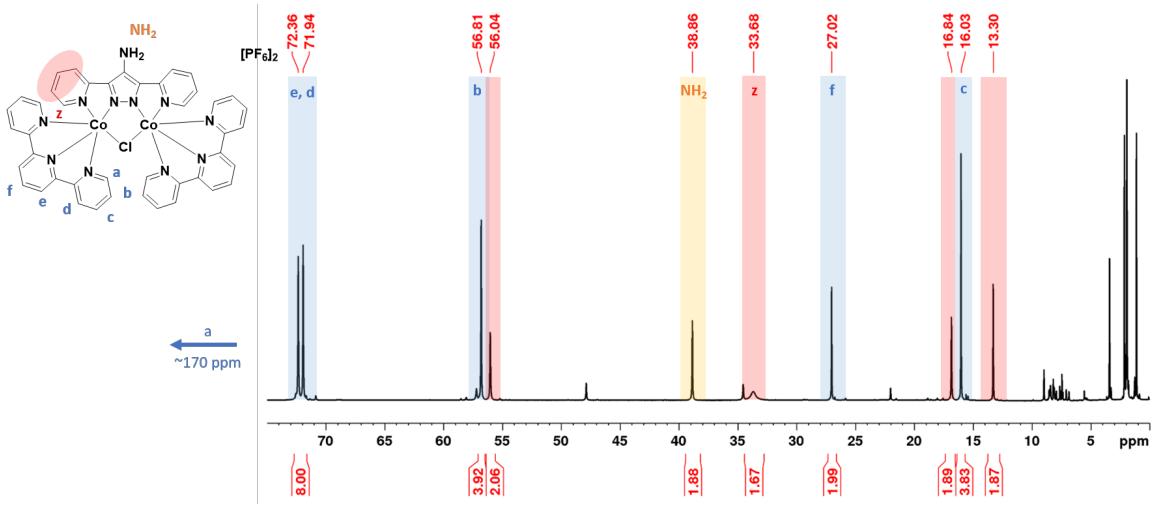

Figure A.5: $\mathbf{Co4_{Cl}}$ ^{1}H NMR in MeCN, non-solvent suppressed. Tentative assignment. Peaks between 5 and 10 ppm are diamagnetic peaks, formed through air contamination during handling of the sample. Non-labelled peaks are unreacted Co(trpy)Cl_2 which proved challenging to remove.

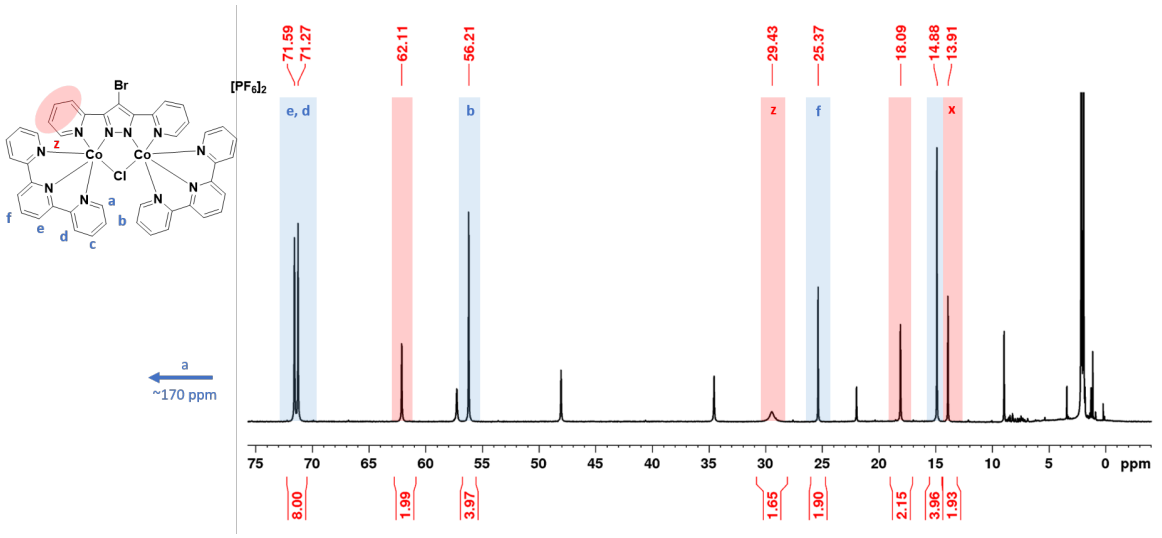

Figure A.6: $\mathbf{Co5_{Cl}}$ ^{1}H NMR in MeCN, non-solvent suppressed. Tentative assignment. Peaks between 5 and 10 ppm are diamagnetic peaks, formed through air contamination during handling of the sample. Non-labelled peaks are unreacted Co(trpy)Cl_2 which proved challenging to remove.

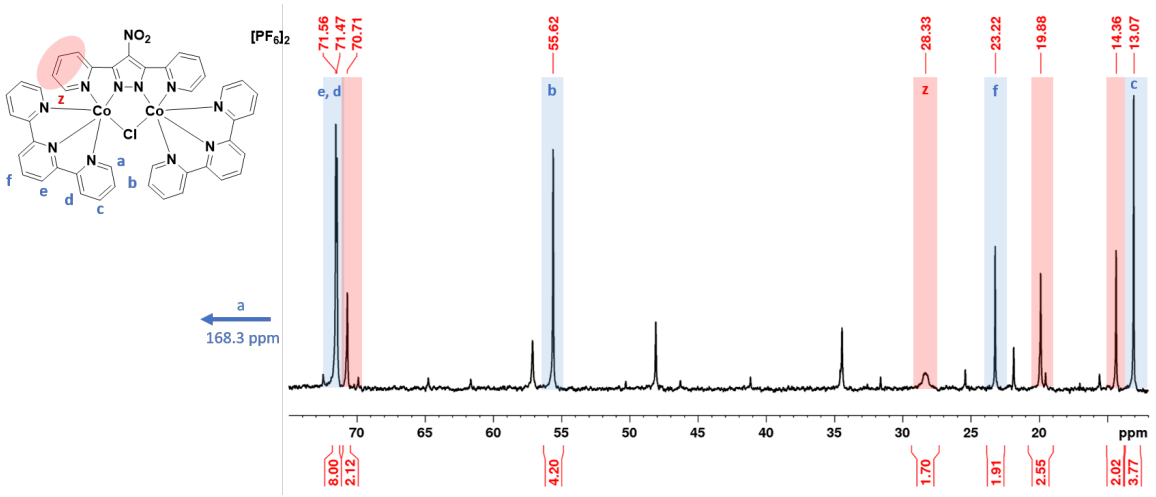

Figure A.7: $Co6_{Cl}$ ^{1}H NMR in MeCN, non-solvent suppressed. Tentative assignment. Non-labelled peaks are unreacted $Co(trpy)Cl_2$ which proved challenging to remove.

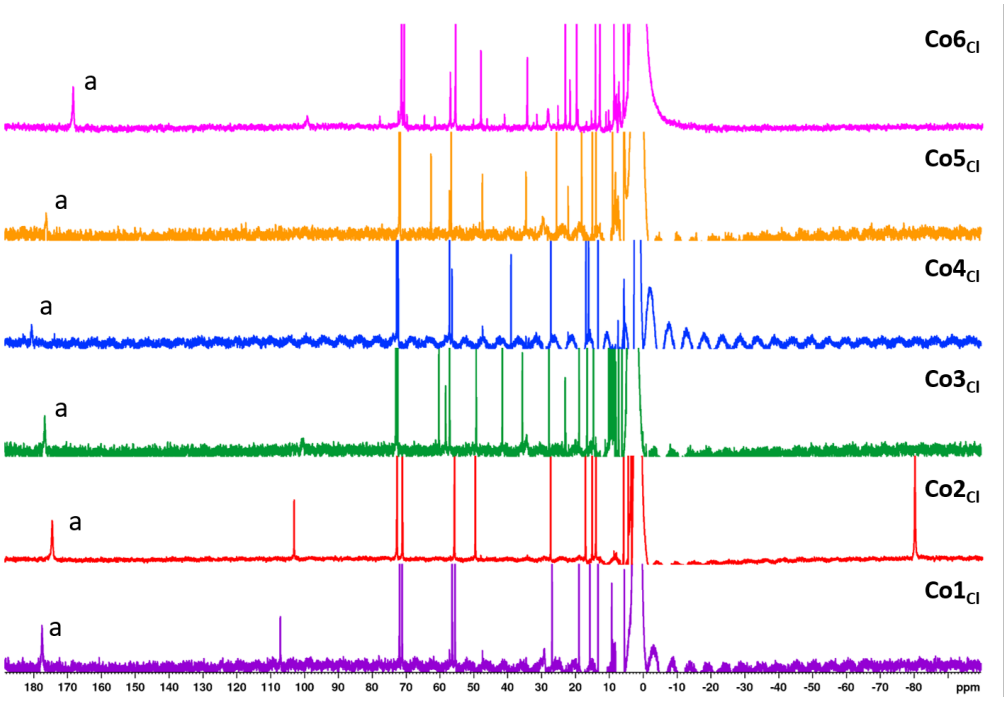

Figure A.8: $Co1_{Cl}$ – $Co6_{Cl}$ wide spectral width ^{1}H NMR in MeCN, non-solvent suppressed. The peak **a** can be clearly seen for all six complexes between 170 and 180 ppm. The distortion of the baseline due to sinc wiggles can be clearly seen.

A.2 Appendix to Chapter 3

A.2.1 Oxidation Studies Initial Rates

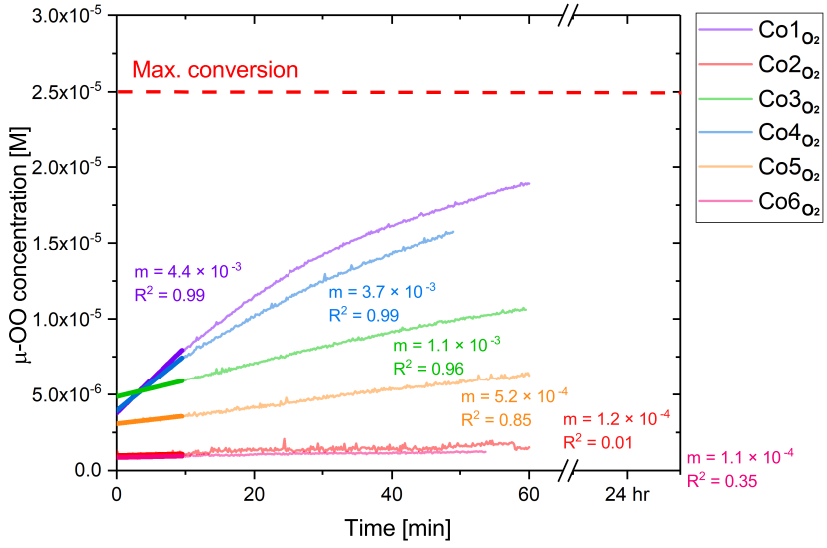

Figure A.9: Linear fits overlaid on Figure 3.9 to determine the initial rates shown with value for k and the R^2 value shown for the oxidation of μ-Cl complexes to their μ-OO variants.

A.2.2 Electrochemistry Details

Peak Current Ratio at Different Scan Rates for $\mathbf{Co1_{O_2}}$ – $\mathbf{Co6_{O_2}}$

Table A.1: The ratio between the maximum oxidation and reduction currents (i_{ox} / i_{red}) at different scan rates for $\mathbf{Co1_{O_2}}$ – $\mathbf{Co6_{O_2}}$, from the CVs reported in Figure 3.12.

Complex	50 mVs^{-1}	100 mVs^{-1}	250 mVs^{-1}	500 mVs^{-1}	1000 mVs^{-1}
$\mathbf{Co1_{O_2}}$	0.57	0.56	0.53	0.57	0.66
$\mathbf{Co2_{O_2}}$	0.83	0.96	0.91	0.95	1.2
$\mathbf{Co3_{O_2}}$	1.00	0.92	0.79	0.79	0.70
$\mathbf{Co4_{O_2}}$	0.58	0.87	0.86	0.55	0.52
$\mathbf{Co5_{O_2}}$	0.66	0.64	0.67	0.72	0.69
$\mathbf{Co6_{O_2}}$	0.69	0.61	0.66	0.65	0.65

Table A.2: ΔE values at different scan rates, for the reversible peak shown in Figure 3.12.

Complex	50 mVs^{-1}	100 mVs^{-1}	250 mVs^{-1}	500 mVs^{-1}	1000 mVs^{-1}
$\mathbf{Co1_{O_2}}$	0.11	0.13	0.15	0.15	0.20
$\mathbf{Co2_{O_2}}$	0.08	0.08	0.13	0.15	0.20
$\mathbf{Co3_{O_2}}$	0.08	0.08	0.10	0.15	0.10
$\mathbf{Co4_{O_2}}$	0.08	0.095	0.013	0.17	0.24
$\mathbf{Co5_{O_2}}$	0.09	0.10	0.13	0.10	0.10
$\mathbf{Co6_{O_2}}$	0.13	0.10	0.13	0.15	0.20

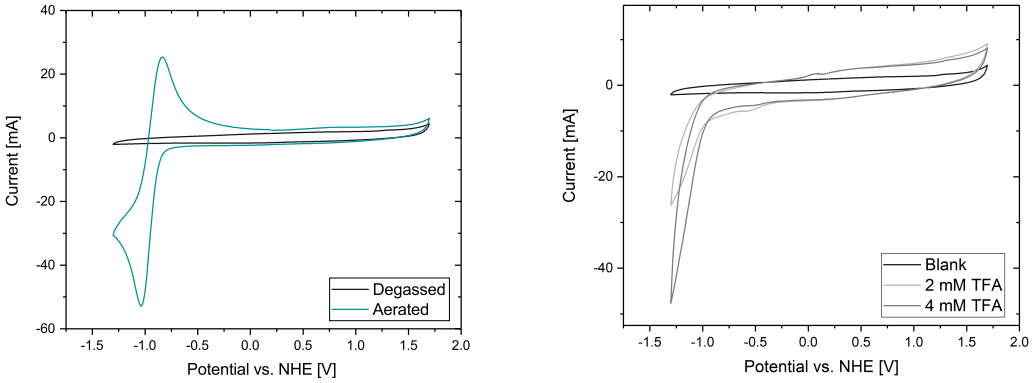

(a) Aerated blank electrolyte

(b) Addition of TFA to blank electrolyte

Figure A.10: (a) Cyclic voltammetry of blank electrolyte (TBAF = 0.1 M) (degassed) and an aerated solution, clearly showing the reversible reduction of O_2 by the electrode at around -1 V vs NHE, (b) with the addition of trifluoracetic acid (2 mM and 4mM). Conditions for all: WE: GC, CE: Pt wire, RE: $Ag/AgNO_3$, SR: 100 mV/s

ΔE values at Different Scan Rates for $\mathbf{Co1_{o_2}}$ – $\mathbf{Co6_{o_2}}$

Randles-Sevcik analysis

In order to calculate the number of electrons, the Randles-Sevcik equation is rearranged as follows:

$$n^{-3/2} = 0.446F^{-3/2}AC^0(\nu D_o)^{1/2}(RT)^{-1/2}i_p^{-1} \tag{A.2}$$

Where n = number of transferred electrons, F = Faraday constant, A = surface area of electrode, ν = scan rate, D_o = diffusion coefficient, C^0 = concentration of bulk analyte, R = 8.315 $JK^{-1}mol^{-1}$, T = temperature (K).

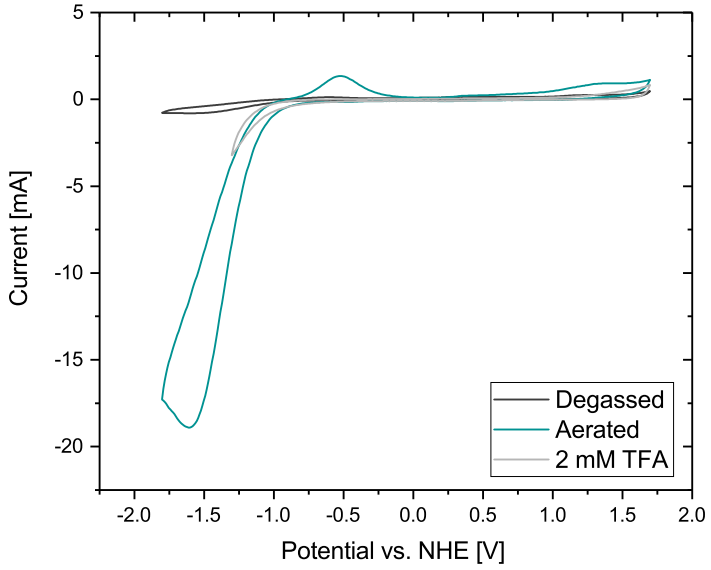

Figure A.11: Cyclic voltammetry of blank electrolyte (TBAF = 0.1 M) (degassed) and an aerated solution, clearly showing the irreversible reduction of O_2 by the electrode at around -1.5 V vs NHE. The trace with the addition of trifluoracetic acid (2 mM) is shown at a narrower scan window. Conditions for all: WE: BDD, CE: Pt wire, RE: $Ag/AgNO_3$, SR: 100 mV/s

Calculation of the Diffusion Coefficient

The diffusion coefficient is calculated using Equation A.3 as reported by Wilke and Chang;[242]

$$D = 7.4 \times 10^{-8} \frac{(xM)^{1/2} T}{\eta V^{0.6}} \tag{A.3}$$

where: D = diffusion coefficient (see Table A.4), x = association parameter (1.5)[i], M = molecular weight of solvent (41 $gmol^{-1}$), T = temperature (293 K), η = viscosity of solution (centipoise) (0.34 mPa s) V = molal volume of the solute at normal boiling point, (cc/g) ($\mathbf{Co1_{O_2}}$ = 844.4, $\mathbf{Co2_{O_2}}$ = 885.8, $\mathbf{Co3_{O_2}}$ = 866.6, $\mathbf{Co4_{O_2}}$ = 858.6, $\mathbf{Co5_{O_2}}$ = 867.7, $\mathbf{Co6_{O_2}}$ = 874.7. Wilke and Chang give a series of atomic and molecular volumes, in conjunction with a series of rules with which to calculate the molal volume

[i]Wilke and Chang define x as a value "introduced to define the effective molecular weight of the solvent with respect to the diffusion process." Water is given an x value of 2.6, nonassociated solvents are given a value of 1, with MeOH and EtOH given values of 1.9 and 1.5 respectively. Unfortunately, MeCN is not given a value, and there is no clear method for calculating one. A comparison is drawn with "Jacobsen association numbers", which, although includes a larger range of solvents, does also not report a value for MeCN.[371] Calculating the diffusion coefficient and subsequent number of electrons for the process shows that the change is within 0.1 and does not significantly change the outcome of the calculation, Table A.3. Therefore a value of 1.5 is chosen and used throughout.

of the solute.)[ii]

Table A.3: The diffusion coefficient and number of electrons caluclated using different values for the association parameter for $\mathbf{Co1_{O_2}}$ at 100 mVs^{-1}.

Association Parameter x	Diffusion Coefficient / cm^2s^{-1}	Number of electrons (Ox. peak)
1	7.16×10^{-6}	0.82
1.5	8.77×10^{-6}	0.77
2	1.01×10^{-5}	0.735
2.6	1.16×10^{-5}	0.70

Table A.4: Diffusion coefficients for $\mathbf{Co1_{O_2}}$ - $\mathbf{Co6_{O_2}}$, calculated using Equation A.3

Complex	Diffusion Coefficient / cm^2s^{-1}
$\mathbf{Co1_{O_2}}$	8.77×10^{-6}
$\mathbf{Co2_{O_2}}$	8.52×10^{-6}
$\mathbf{Co3_{O_2}}$	8.64×10^{-6}
$\mathbf{Co4_{O_2}}$	8.69×10^{-6}
$\mathbf{Co5_{O_2}}$	8.63×10^{-6}
$\mathbf{Co6_{O_2}}$	8.59×10^{-6}

[ii]The atomic/molecular volumes and rules used to calculate the molal volumes of $\mathbf{Co1_{O_2}}$- $\mathbf{Co6_{O_2}}$ are as follows: C = 14.8, H = 3.7, N (double-bonded) = 15.6, N (primary amine) = 10.5, N (nitro) = 12.0, Br = 27.0, O = 7.4, O (nitro) = 11.0, pyridine = -15, pyrazole = 11.5. There is not a method for the calculation of metals, but using the reported values for Cl (24.6), Br (27.0) and I (37.0) it is clear the value increases down a series, therefore Co is estimated to have the same value as Br. There is some ambiguity for some atoms, particularly for the nitro and μ-OO. However, It is worth noting that due to the form of Equation A.3, changes in the molal volume are raised to the power of 0.6, so have a minimal influence on the value for the diffusion coefficient. Therefore, the value is taken as a rough estimation for the calculation.

A.2.3 Conversion between μ-Cl and μ-OO species

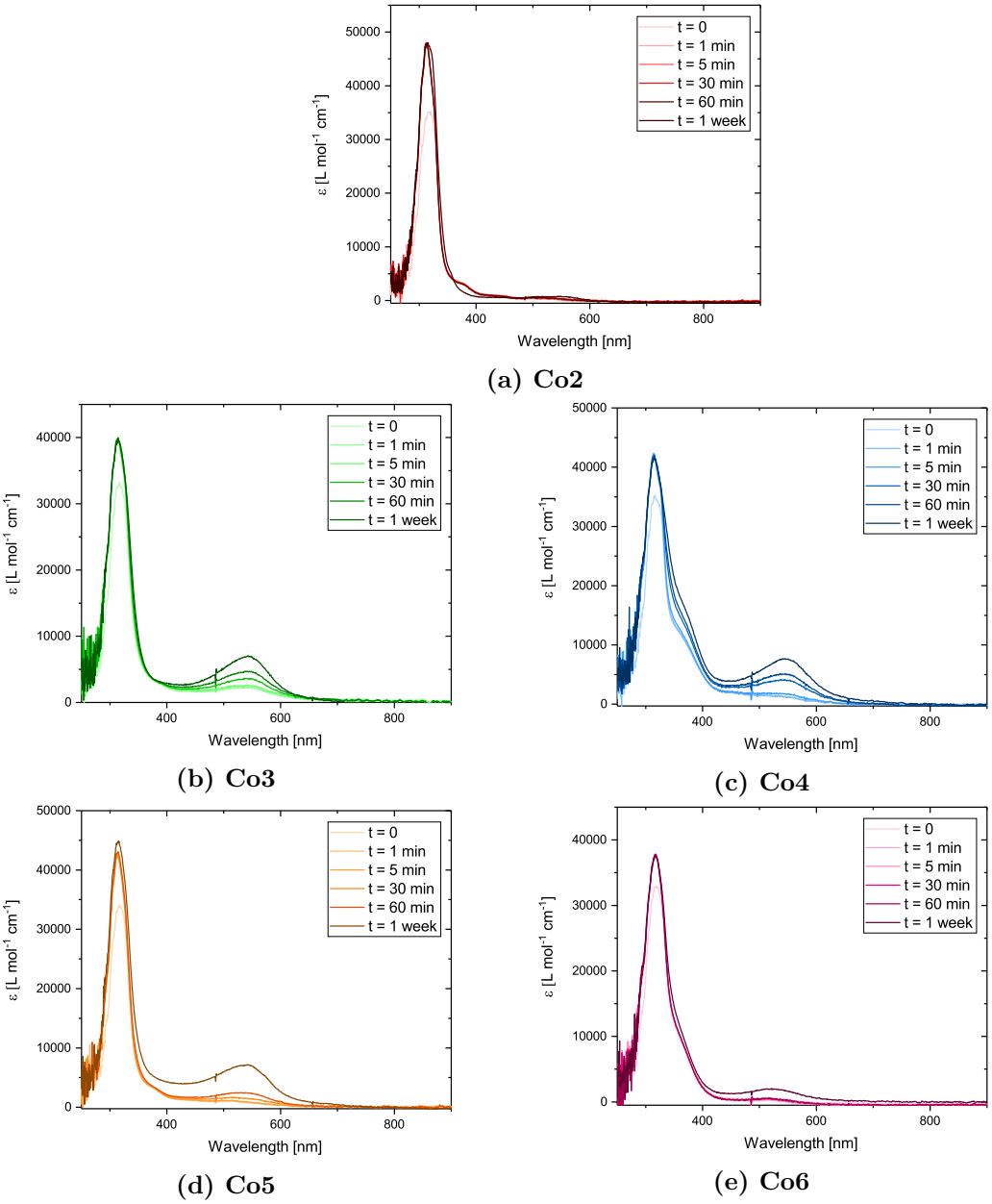

(a) Co2

(b) Co3

(c) Co4

(d) Co5

(e) Co6

Figure A.12: Overlaid spectra of $\mathbf{Co2_{Cl}}$ - $\mathbf{Co6_{Cl}}$ after the addition of $NaPF_6$ and exposure to air showing the increase of the peak around 550 nm corresponding to the formation of $\mathbf{Co2_{O_2}}$-$\mathbf{Co6_{O_2}}$. [Co] = 25 μM, [$NaPF_6$] = 25 μM, solvent = MeCN, temperature = r.t. (*NOTE: the spectra for* $\boldsymbol{Co1_{Cl}}$ *can be found in Chapter 3, Figure 3.8.*)

A.2.4 Oxygen Reduction Reaction

Initial Rates

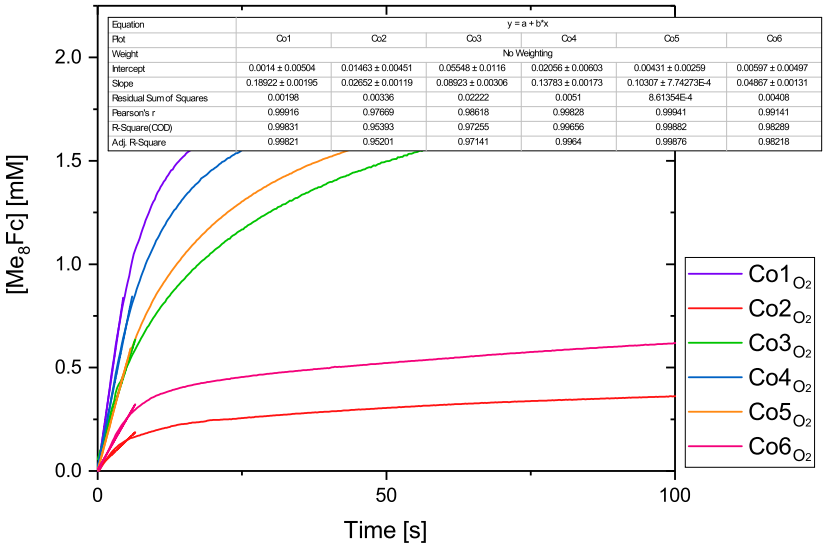

Figure A.13: Calculation of initial rates using a reproduction of Figure 3.29 and the linear fit tool in the Origin2017 software package. Parameters are shown in table.

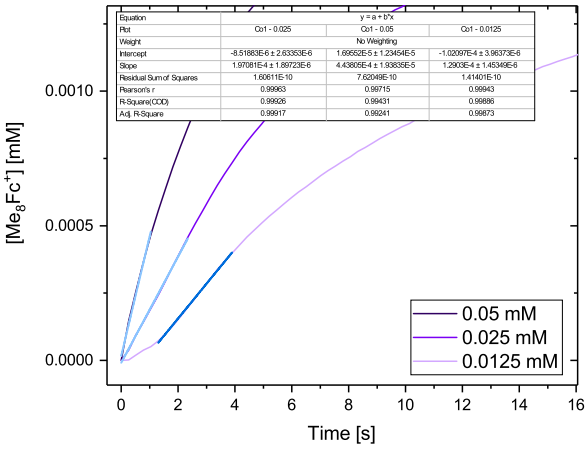

Figure A.14: Fitting of initial rates on various concentrations of $\mathbf{Co1_{O_2}}$ using the linear fit tool in the Origin2017 software package. *NOTE: The lowest concentration shows a dip at the beginning due to resistance in the system, so the linear fit is started from 1s.*

Initial Rates Analysis and Log/Log plots

Initial rates for each catalyst were determined by plotting linear fits to the initial gradient, example shown in Figure A.14. Plots of initial rate against concentration of catalyst raised to the power of 1 or 0.5 according to order in catalyst were plotted, the goodness of fit (R^2) is included. Log/log plots are included to, Figure A.15.[372]

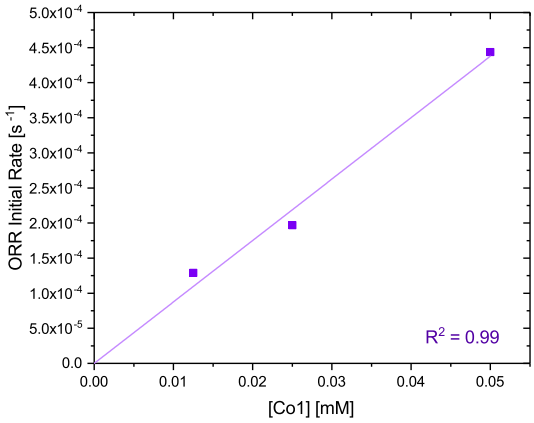

(a) $\mathbf{Co1_{O_2}}$ initial rates plot

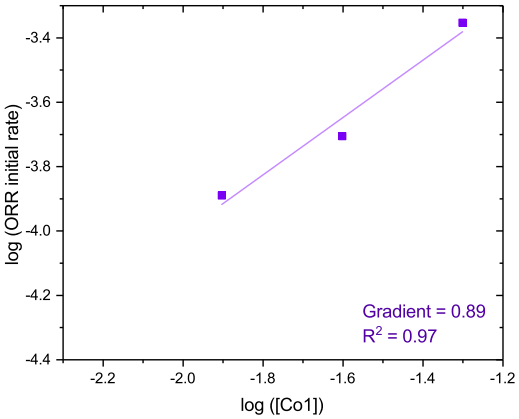

(b) $\mathbf{Co1_{O_2}}$ log/log plot

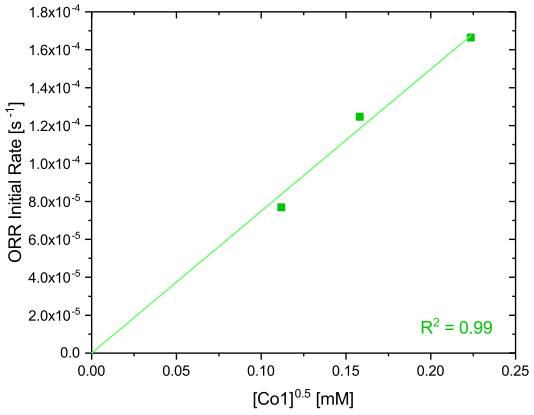

(c) $\mathbf{Co3_{O_2}}$ initial rates plot

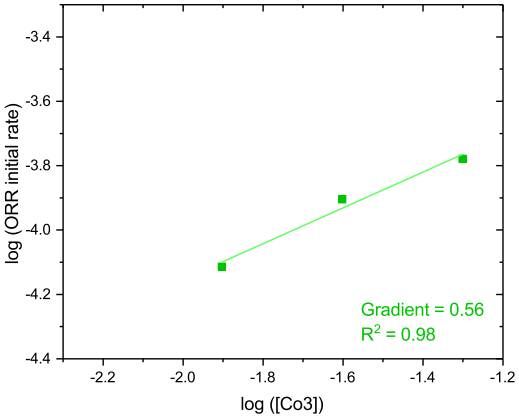

(d) $\mathbf{Co3_{O_2}}$ log/log plot

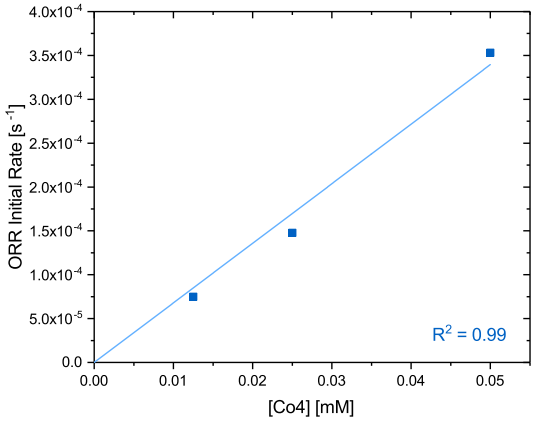

(e) $\mathbf{Co4_{O_2}}$ initial rates plot

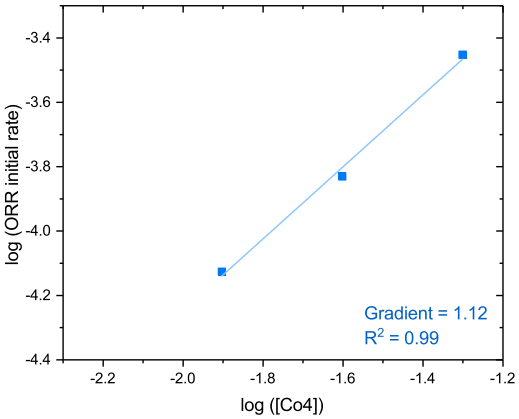

(f) $\mathbf{Co4_{O_2}}$ log/log plot

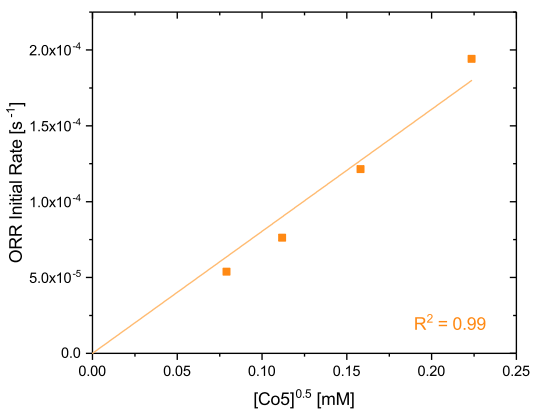

(g) $\mathbf{Co5_{O_2}}$ initial rates plot

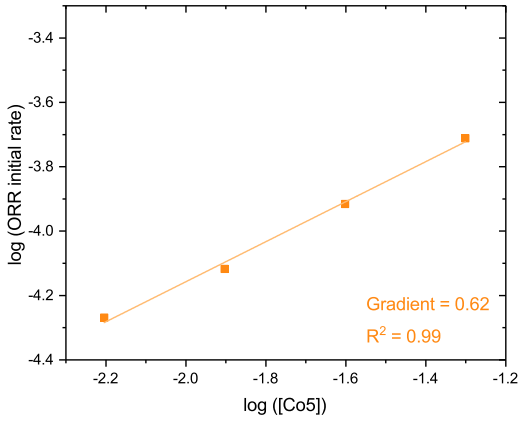

(h) $\mathbf{Co5_{O_2}}$ log/log plot

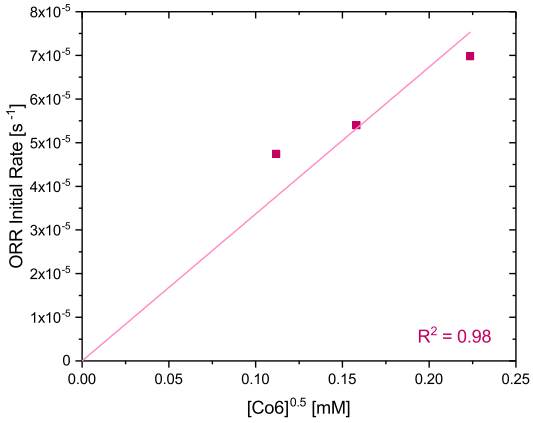

(i) $\mathbf{Co6_{O_2}}$ initial rates plot

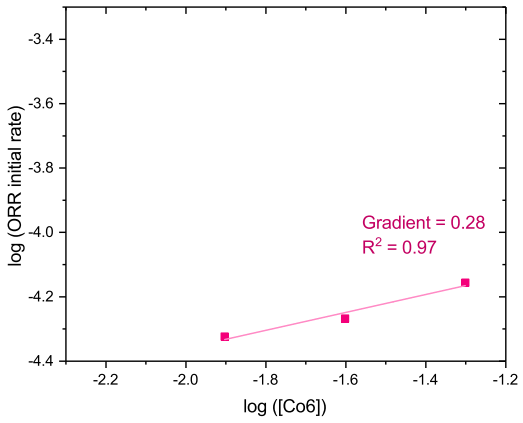

(j) $\mathbf{Co6_{O_2}}$ log/log plot

Figure A.15: Initial rates analysis and log/log plots for $\mathbf{Co1_{O_2}}$ and $\mathbf{Co3_{O_2}}$ – $\mathbf{Co6_{O_2}}$ (excluding $\mathbf{Co2_{O_2}}$ where conversion was so low it was not deemed useful information could be extracted). The gradient of the log/log plots is shown with the R^2 value for the linear fit on all graphs.

A.2.5 Degradation Studies

Me_8Fc Studies

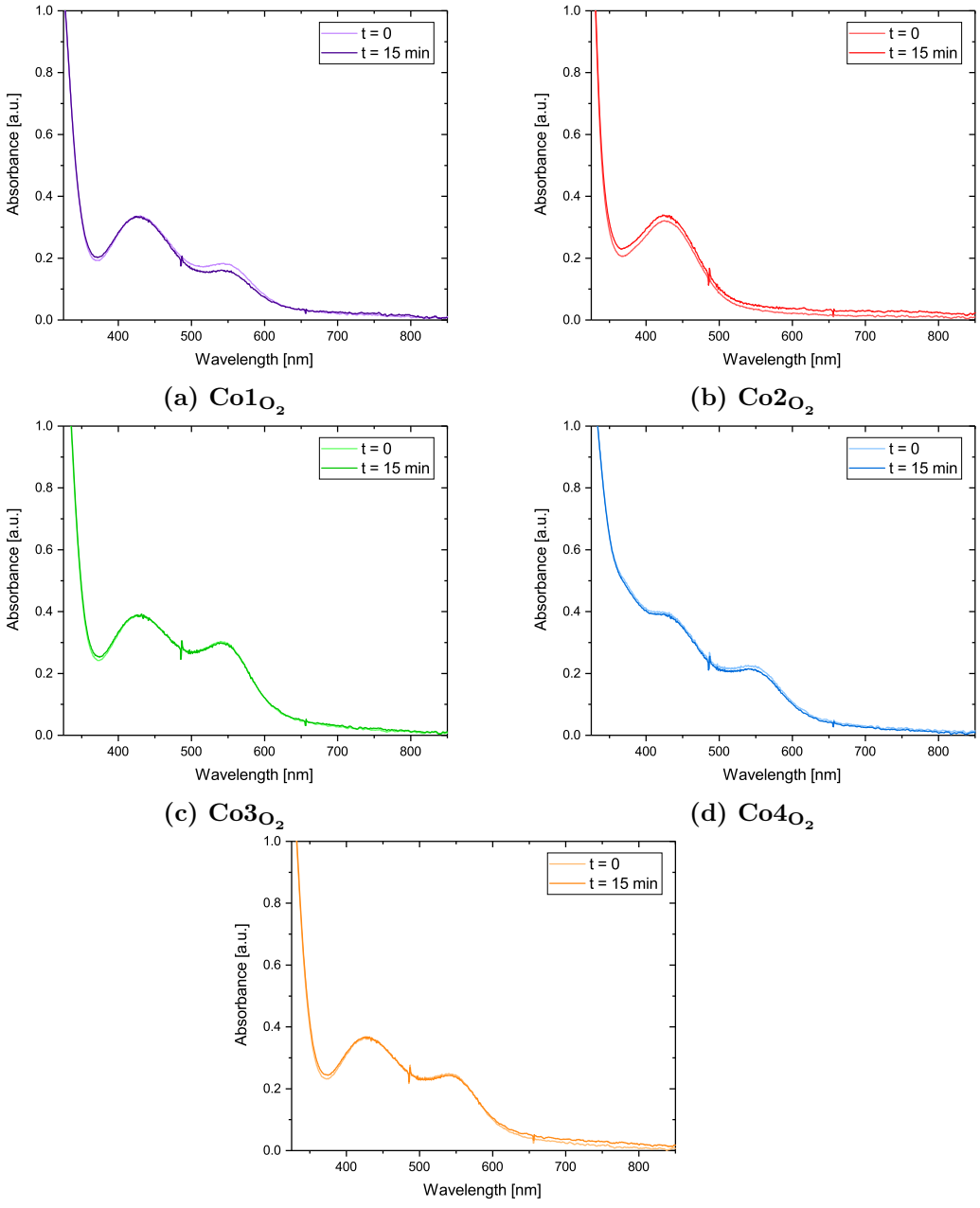

(a) $\mathbf{Co1_{O_2}}$ (b) $\mathbf{Co2_{O_2}}$

(c) $\mathbf{Co3_{O_2}}$ (d) $\mathbf{Co4_{O_2}}$

(e) $\mathbf{Co5_{O_2}}$

Figure A.16: Overlaid spectra of $\mathbf{Co1_{O_2}}$ - $\mathbf{Co5_{O_2}}$ after the addition of Me_8Fc. [Co] = 25 µM, [Me_8Fc] = 2 mM

TFA Studies

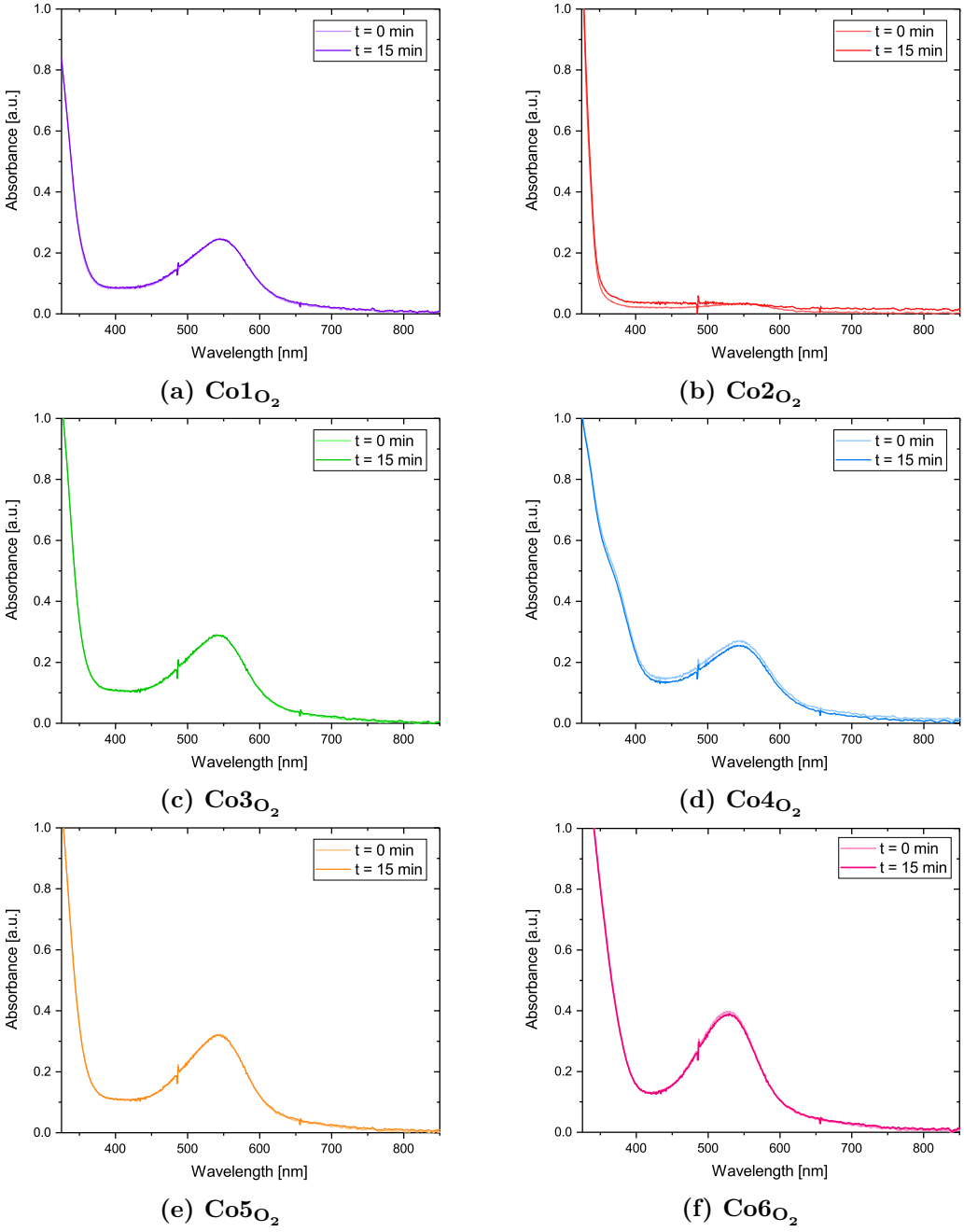

(a) $\mathbf{Co1_{O_2}}$ (b) $\mathbf{Co2_{O_2}}$

(c) $\mathbf{Co3_{O_2}}$ (d) $\mathbf{Co4_{O_2}}$

(e) $\mathbf{Co5_{O_2}}$ (f) $\mathbf{Co6_{O_2}}$

Figure A.17: Overlaid spectra of $\mathbf{Co1_{O_2}}$ - $\mathbf{Co6_{O_2}}$ after the addition of TFA. [Co] = 25 µM, [TFA] = 50 mM

ORR Comparison

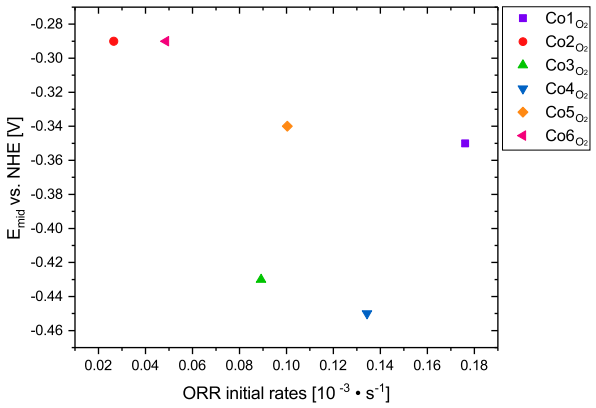

Figure A.18: Comparison of ORR initial rates with the E_{mid} values for $\mathbf{Co1_{O_2}}$ – $\mathbf{Co6_{O_2}}$, showing a lack of correlation between them.

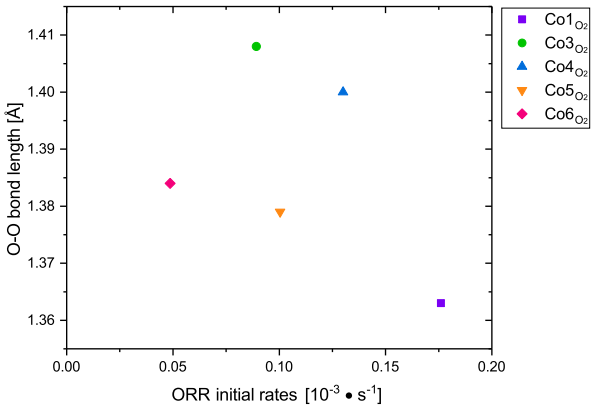

Figure A.19: Comparison of ORR initial rates with O–O bond length in $\mathbf{Co1_{O_2}}$ and $\mathbf{Co3_{O_2}}$ – $\mathbf{Co6_{O_2}}$. *NOTE:* $\boldsymbol{Co2_{O_2}}$ *is not included as the O–O bond length is unknown due to the lack of X-ray crystal structure for this complex.*

A.2.6 Oxygen Atom Transfer

Supporting Spectra for $\mathbf{Co1_{O_2}}$

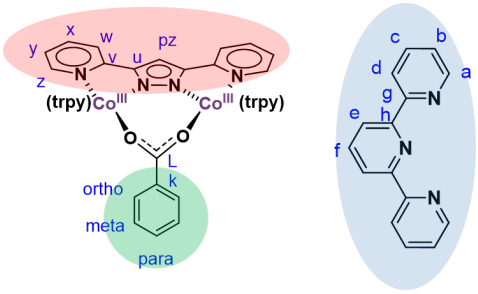

Figure A.20: Proposed product of the reaction of $\mathbf{Co1_{O_2}}$ with benzaldehyde, with labels used for NMR assignments.

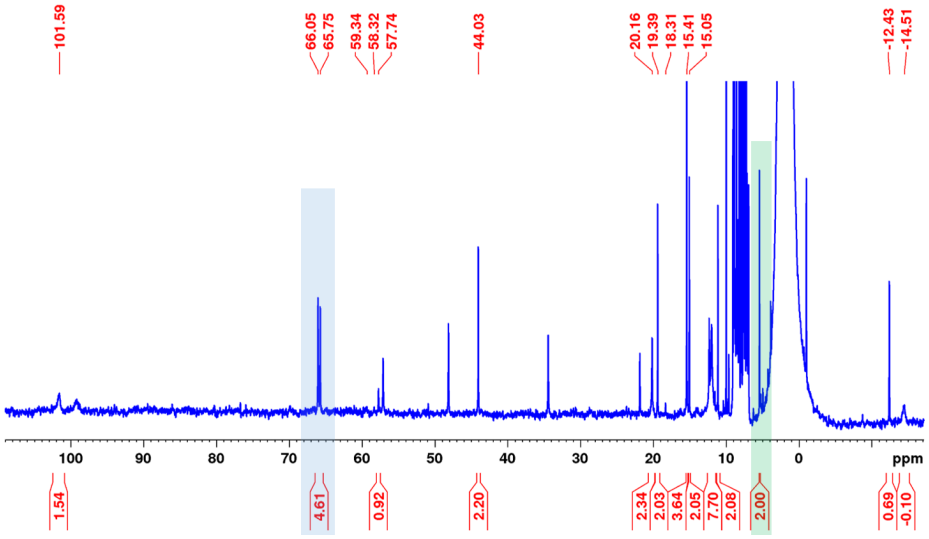

Figure A.21: ^{1}H NMR spectra used to determine the ratio between the dia- and paramagnetic species after the reaction of $\mathbf{Co1_{O_2}}$ with benzaldehyde. The peaks corresponding to the paramagnetic species are highlighted in blue with an integral of ≈ 4. The characteristic peak at ≈ 5.5 ppm of the diamagnetic species is calibrated to 2. *Note that unlabelled peaks are unreacted Co(trpy)Cl$_2$ present in the batch of catalyst.*

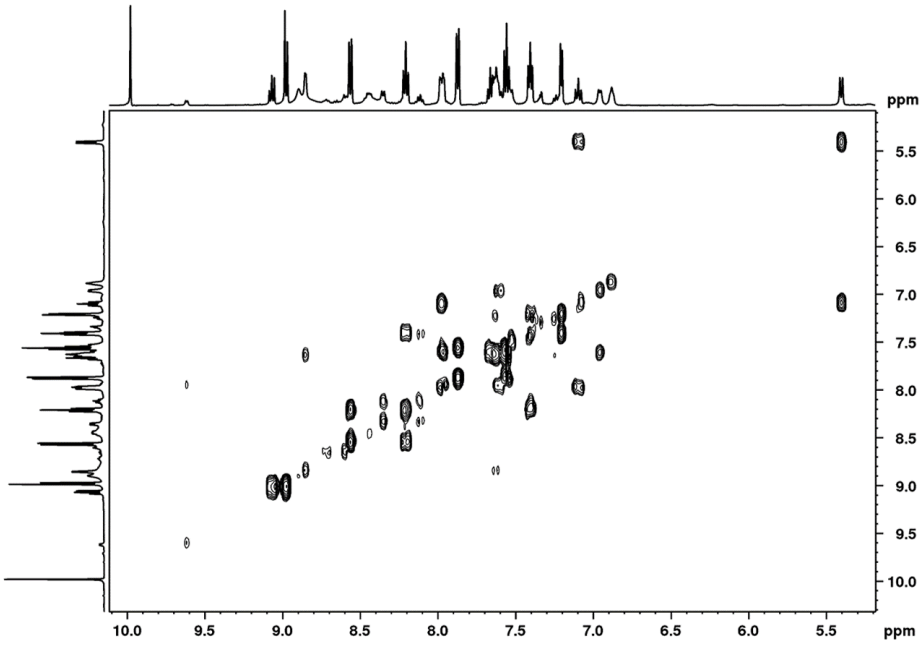

Figure A.22: COSY spectrum of the product from the reaction between $\mathbf{Co1_{O_2}}$ and 2 equivalents of benzaldehyde after 120 hr. (Conditions: [$\mathbf{Co1_{O_2}}$] = 20 mM, [benzaldehyde] = 40 mM, T = 50 °C), solvent = MeCN (0.5 mL)

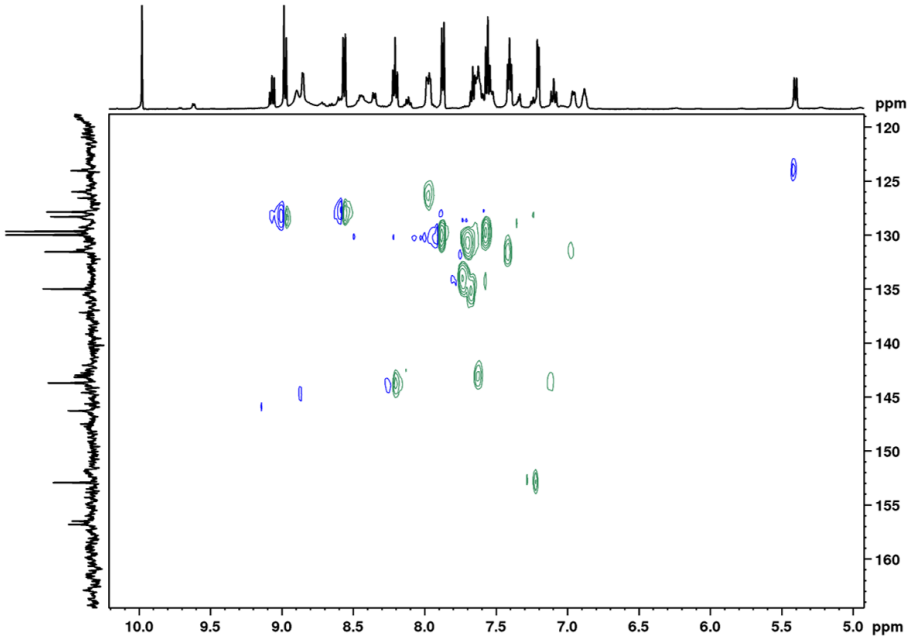

Figure A.23: HSQC spectrum of the product from the reaction between $\mathbf{Co1_{O_2}}$ and 2 equivalents of benzaldehyde after 120 hr. (Conditions: [$\mathbf{Co1_{O_2}}$] = 20 mM, [benzaldehyde] = 40 mM, T = 50 °C), solvent = MeCN (0.5 mL)

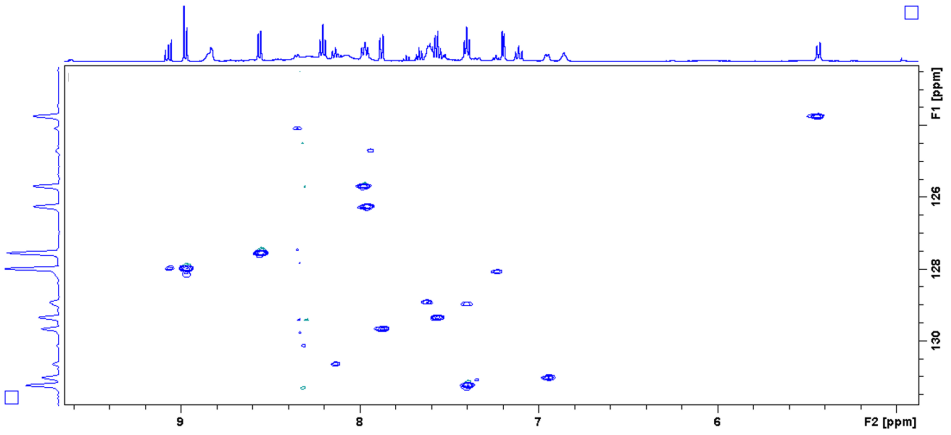

Figure A.24: Region selective HSQC spectrum of the product from the reaction between $\mathbf{Co1_{O_2}}$ and 2 equivalents of benzaldehyde after 120 hr. (Conditions: $[\mathbf{Co1_{O_2}}] = 20\,\text{mM}$, [benzaldehyde] = 40 mM, T = 50 °C), solvent = MeCN (0.5 mL)

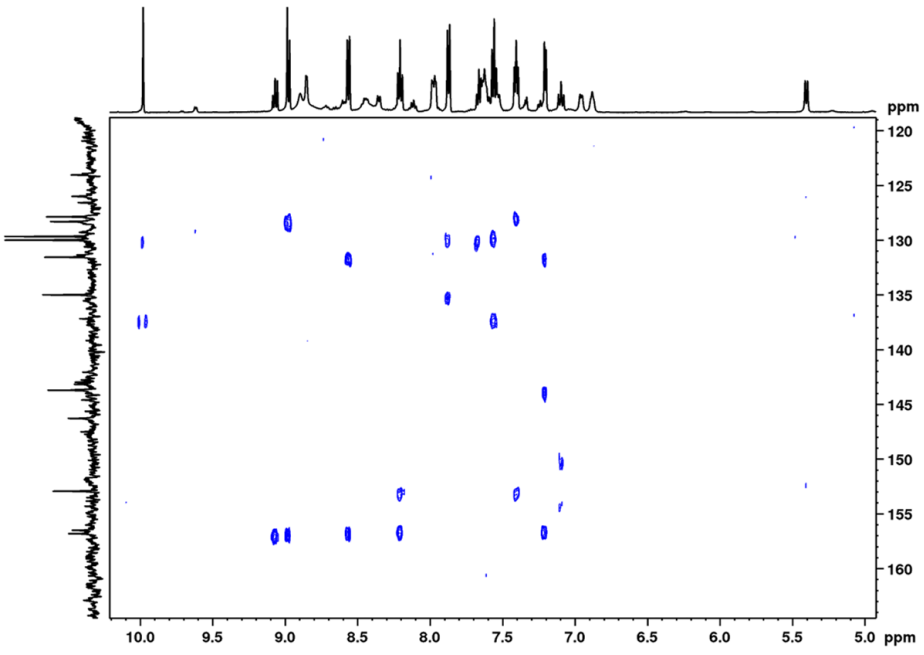

Figure A.25: HMBC spectrum of the product from the reaction between $\mathbf{Co1_{O_2}}$ and 2 equivalents of benzaldehyde after 120 hr. (Conditions: $[\mathbf{Co1_{O_2}}] = 20\,\text{mM}$, [benzaldehyde] = 40 mM, T = 50 °C), solvent = MeCN (0.5 mL)

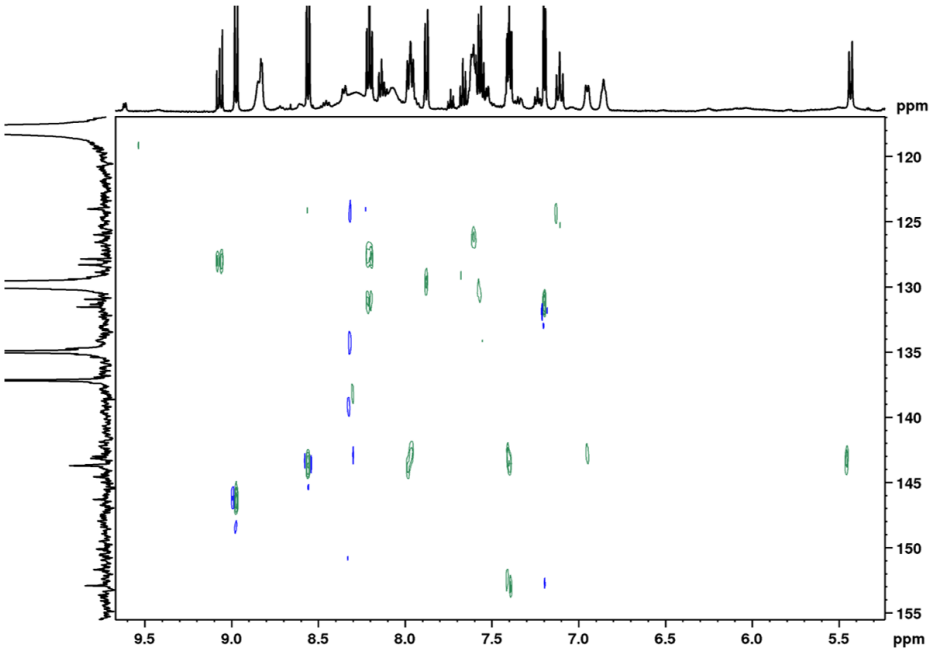

Figure A.26: H2BC spectrum of the product from the reaction between $\mathbf{Co1_{O_2}}$ and 2 equivalents of benzaldehyde after 120 hr. (Conditions: $[\mathbf{Co1_{O_2}}] = 20\,\text{mM}$, [benzaldehyde] = 40 mM, T = 50 °C), solvent = MeCN (0.5 mL)

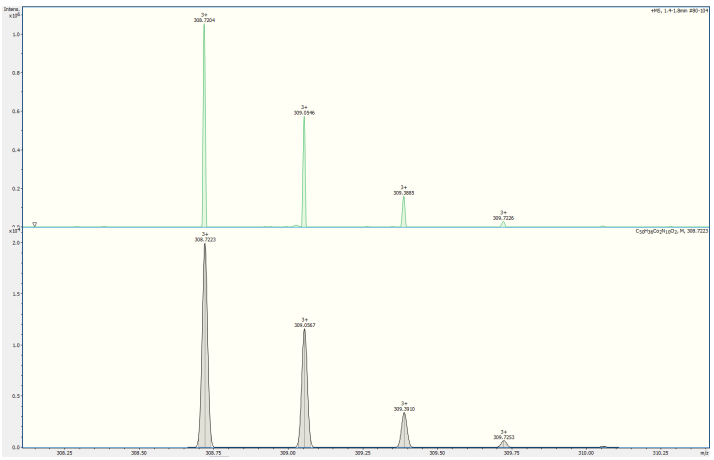

Figure A.27: Mass spectrometry showing the agreement between the predicted isotope pattern for the cobalt-benzoate adduct (bottom), and the recorded isotope pattern (top).

Table A.5: NMR spectroscopy assignments for the reaction between $\mathbf{Co1_{O_2}}$ and 2 equilvalents of benzaldehyde, labelled structure shown in Figure A.20.

Proton	^{1}H Assignment	Carbon	^{13}C Assignment (HSQC correlation)	HMBC correlations	H2BC correlations
pz-H	-	pz-H	-	-	-
W	6.96 (2H, d, J = 7.11 Hz)	w	131.2, 163.0	-	-
X, Y	7.52 – 7.57 (2H, m) (overlap with excess benzaldehyde)	X, Y	134.8	124.7, 132.6, 134.9	
X, Y	7.59 – 7.65 (2H, m)	X, Y	143.0	129.8 (benzaldehyde), 124.8, (133, 137, 157, - tentative)	
Z (overlap with *para*)	7.96 – 7.99 (2H, m)	Z	-	123.9, 157.3, 130, 131.1, 153.6 (L)	-
U	-	U	-	-	-
V	-	V	-	-	-
A	8.56 (4H, d, J = 7.90 Hz)	A	127.9	131.6 (c), 156.5 (g)	143.6 (B)
B	8.21 (4H, t, J = 7.57 Hz)	B	143.6	152.7 (d), 156.5 (g)	127.9 (A), 131.5 (C)
C	7.41 (4H, t, J = 7.03 Hz)	C	131.5	127.9 (a), 152.7 (d)	143.6 (B), 152.9 (D)
D	7.21 (4H, d, J = 7.03 Hz)	D	152.9	131.6 (c), 143.9 (b), 156.8 (g)	131.5 (C)
E	8.98 (4H, d, J = 8.03 Hz)	E	128.4	156.8 (h)	146.5 (F)
F	9.07 (2H, t, J = 8.03 Hz)	F	146.5	156.8 (h)	128.4 (E)
G	-	G	156.5	-	-
H	-	H	156.8	-	-
ortho	5.40 (2H, d, J = 8.55 Hz)	*ortho*	123.9	125.9 (*para*), 149.9 (K?)	-
meta	7.09 (2H, t, J = 9.06 Hz)	*meta*	143.6	150.2, 153.8 (L?)	-
para (overlap with w/z)	7.96 – 7.99 (1H, m)	*para*	126.2	123.9 (*ortho*), 153.6 (L?), 157.3, 130, 131.1	-
K	-	K	149.9	-	-
L	-	L	153.8	-	-

Supporting Spectra for $\mathbf{Co5_{O_2}}$

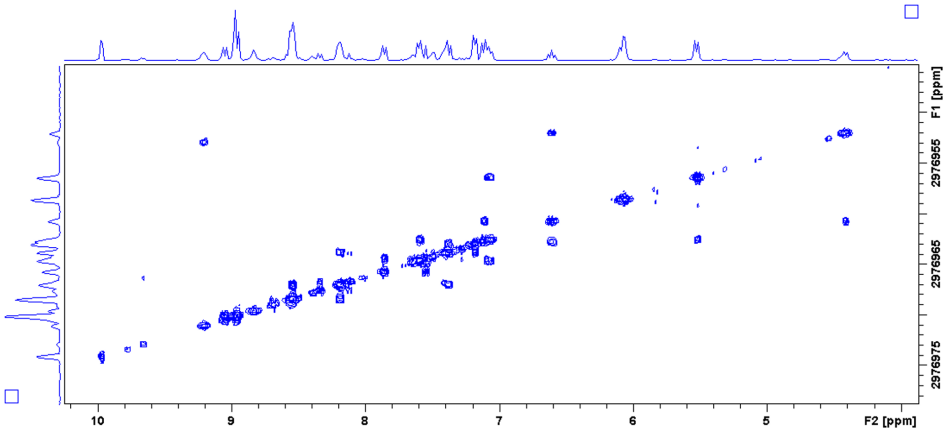

Figure A.28: COSY spectrum of the product from the reaction between $\mathbf{Co5_{O_2}}$ and 2 equivalents of benzaldehyde after 120 hr. (Conditions: [$\mathbf{Co5_{O_2}}$] = 20 mM, [benzaldehyde] = 40 mM, T = 50 °C), solvent = MeCN (0.5 mL)

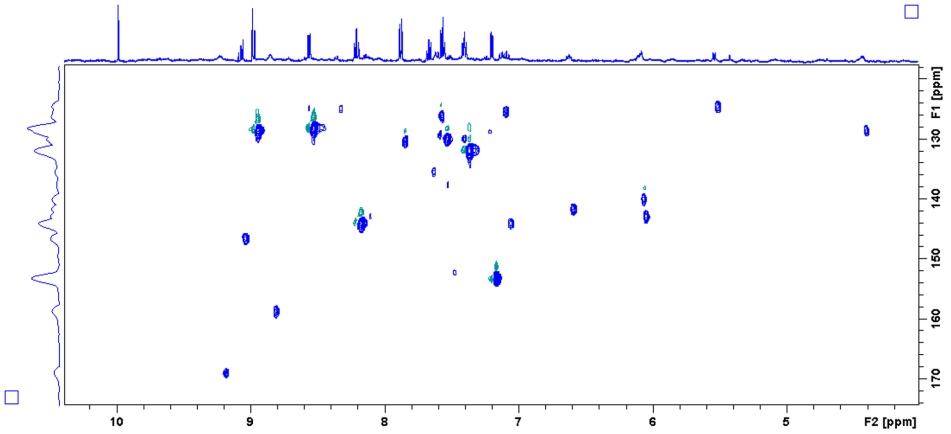

Figure A.29: HSQC spectrum of the product from the reaction between $\mathbf{Co5_{O_2}}$ and 2 equivalents of benzaldehyde after 120 hr. (Conditions: [$\mathbf{Co5_{O_2}}$] = 20 mM, [benzaldehyde] = 40 mM, T = 50 °C), solvent = MeCN (0.5 mL)

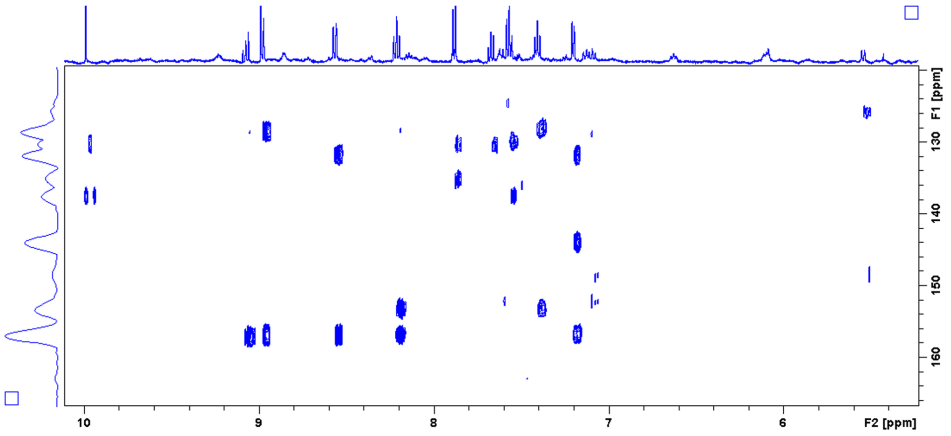

Figure A.30: HMBC spectrum of the product from the reaction between $\mathbf{Co5_{O_2}}$ and 2 equivalents of benzaldehyde after 120 hr. (Conditions: $[\mathbf{Co5_{O_2}}] = 20\,\text{mM}$, [benzaldehyde] = 40 mM, T = 50 °C), solvent = MeCN (0.5 mL)

A.3 Appendix to Chapter 5

A.3.1 SAXS Apparatus

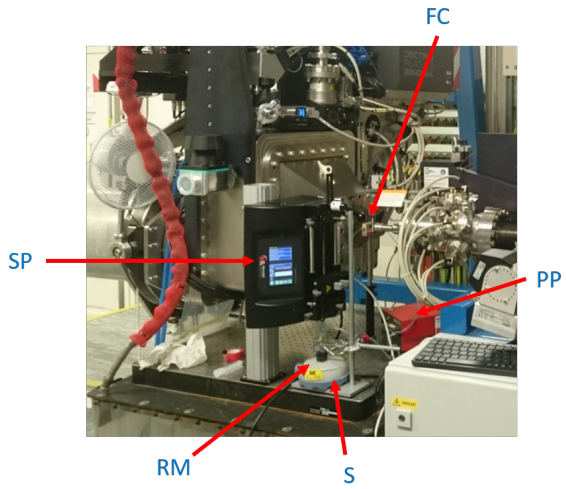

Figure A.31: Flow SAXS apparatus at beamline I22, with key pieces labelled according to Figure 5.4. (PP = peristaltic pump, SP = syringe pump, FC = SAXS flow cell, S = stirrer, RM = reaction mixture)

A.3.2 Particle Size Distribution for IrA

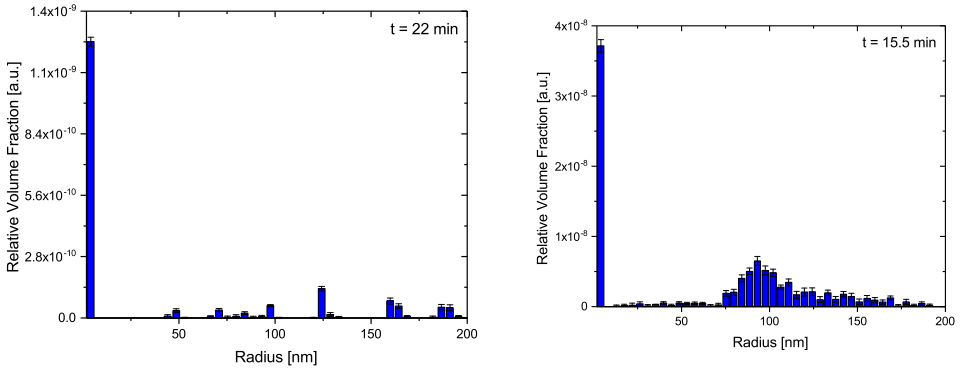

(a) **(b)**

Figure A.32: (a) Particle-size distribution for IrA (2.5 mM injected into 250 mM $NaIO_4$) immediately after initial nucleation. (b) Particle-size distribution for IrA (5 mM injected into 500 mM $NaIO_4$) at 1 minute after initial nucleation.

A.3.3 SAXS data for complexes Ir2 - Ir7

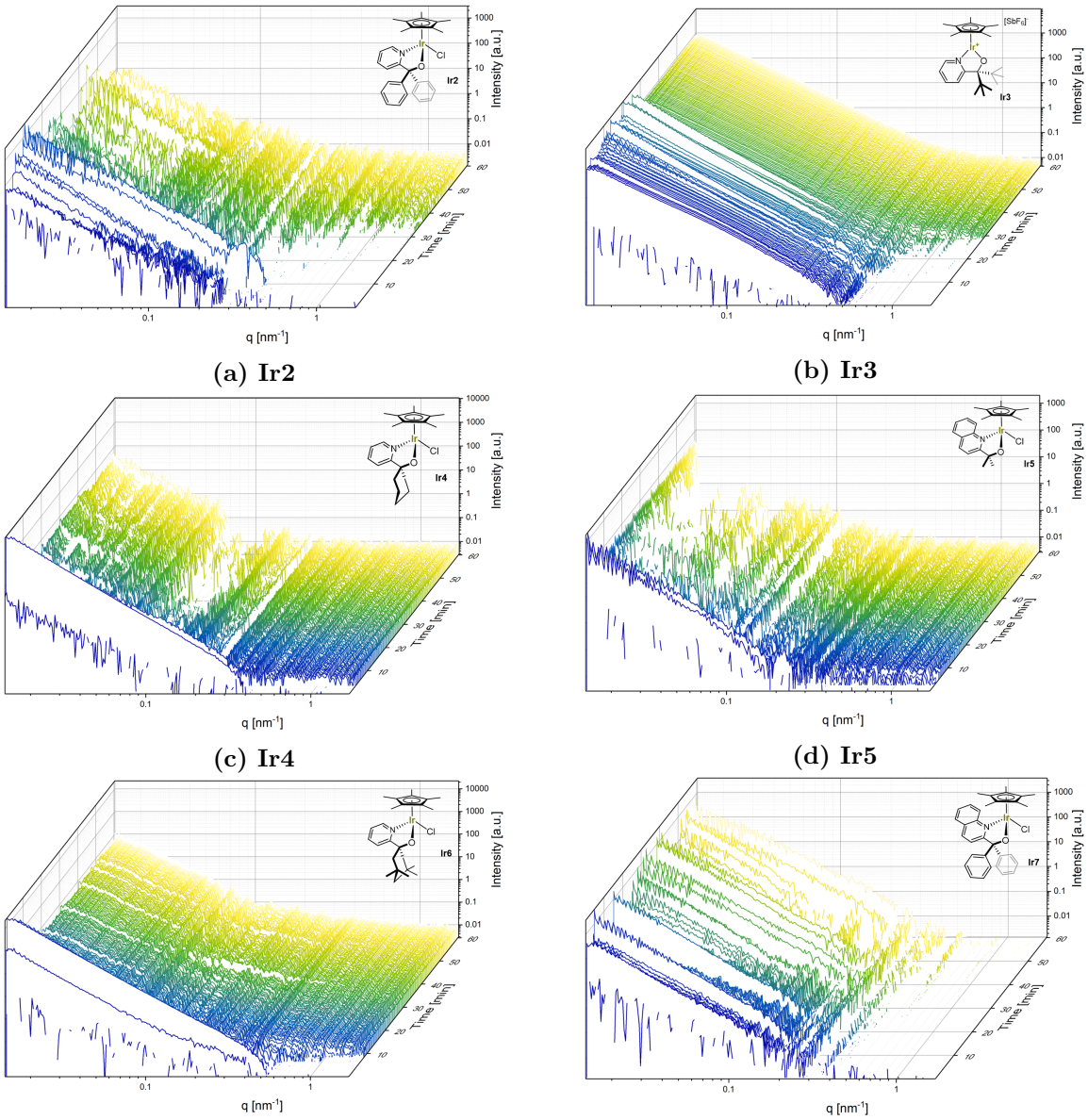

(a) **Ir2** (b) **Ir3**

(c) **Ir4** (d) **Ir5**

(e) **Ir6** (f) **Ir7**

Figure A.33: Baseline subtracted SAXS data for complexes **Ir2** – **Ir7** (2.5 mM Ir injected into 250 mM $NaIO_4$ in neat H_2O). Data collected every 30 seconds over 1 hour. Minor irregularities are due to bubble formation or undissolved catalyst precursor.

A.3.4 O_2 evolution overlaid with NP formation, [IrA] = 5 mM

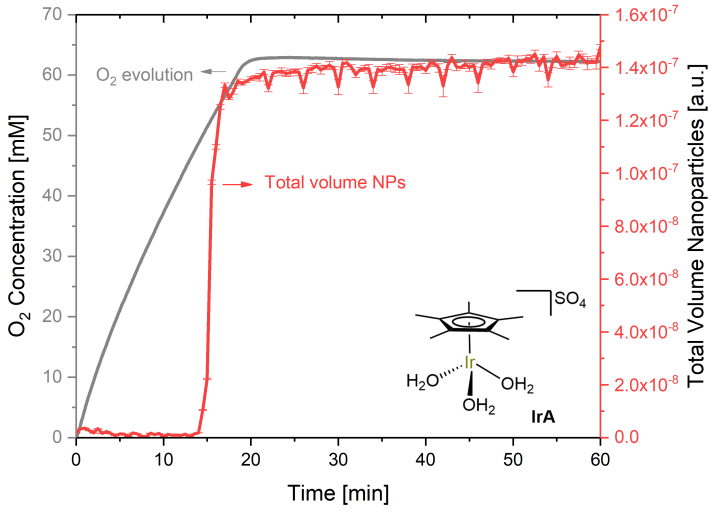

Figure A.34: Total nanoparticle volume against with O_2 evolution for **IrA** (5 mM + 500 mM $NaIO_4$ in neat H_2O at room temperature).

A.4 Crystallography Data

A.4.1 $Co2_{Cl}$

Table 1. Crystal data and structure refinement for **Co2Cl**.

Identification code	e17uh1	
Empirical formula	C45 H35 Cl Co2 F12 N10 P2	
Formula weight	1159.08	
Temperature	150.00(10) K	
Wavelength	0.71073 Å	
Crystal system	Monoclinic	
Space group	I2/a	
Unit cell dimensions	a = 12.5478(3) Å	α= 90°.
	b = 18.7040(4) Å	β= 102.481(2)°.
	c = 20.1077(5) Å	γ = 90°.
Volume	4607.63(19) $Å^3$	
Z	4	
Density (calculated)	1.671 Mg/m^3	
Absorption coefficient	0.944 mm^{-1}	
F(000)	2336	
Crystal size	0.350 x 0.200 x 0.150 mm^3	
Theta range for data collection	3.429 to 29.385°.	
Index ranges	-16<=h<=17, -23<=k<=25, -27<=l<=26	
Reflections collected	29906	
Independent reflections	5755 [R(int) = 0.0305]	
Completeness to theta = 1.000°	100.0 %	
Absorption correction	Semi-empirical from equivalents	
Max. and min. transmission	1.00000 and 0.92649	
Refinement method	Full-matrix least-squares on F^2	
Data / restraints / parameters	5755 / 0 / 327	
Goodness-of-fit on F^2	1.038	
Final R indices [I>2sigma(I)]	R1 = 0.0353, wR2 = 0.0855	
R indices (all data)	R1 = 0.0459, wR2 = 0.0909	
Extinction coefficient	n/a	
Largest diff. peak and hole	0.561 and -0.465 $e.Å^{-3}$	

A.4.2 $Co3_{O2}$

Table 1. Crystal data and structure refinement for **Co3O2**.

Identification code	s18uh5	
Empirical formula	C44 H33 Co2 F15 N10 O2 P2.50	
Formula weight	1214.09	
Temperature	150(2) K	
Wavelength	1.54184 Å	
Crystal system	Triclinic	
Space group	P-1	
Unit cell dimensions	a = 13.5860(7) Å	α= 61.382(9)°.
	b = 21.9379(15) Å	β= 81.717(6)°.
	c = 22.006(2) Å	γ = 75.366(5)°.
Volume	5568.7(9) $Å^3$	
Z	4	
Density (calculated)	1.448 Mg/m^3	
Absorption coefficient	6.198 mm^{-1}	
F(000)	2438	
Crystal size	0.100 x 0.100 x 0.030 mm^3	
Theta range for data collection	3.653 to 69.136°.	
Index ranges	-16<=h<=16, -26<=k<=24, -26<=l<=17	
Reflections collected	36655	
Independent reflections	19930 [R(int) = 0.0674]	
Completeness to theta = 67.684°	98.8 %	
Refinement method	Full-matrix least-squares on F^2	
Data / restraints / parameters	19930 / 0 / 1362	
Goodness-of-fit on F^2	1.103	
Final R indices [I>2sigma(I)]	R1 = 0.1290, wR2 = 0.3440	
R indices (all data)	R1 = 0.1806, wR2 = 0.3762	
Extinction coefficient	n/a	
Largest diff. peak and hole	1.790 and -0.771 $e.Å^{-3}$	

A.4.3 $Co4_{O2}$

Table 1. Crystal data and structure refinement for **Co4O2**.

Identification code	s19uh10	
Empirical formula	C108 H99 Co4 F36 N32 O6 P6	
Formula weight	3046.73	
Temperature	150.01(10) K	
Wavelength	1.54184 Å	
Crystal system	Triclinic	
Space group	P-1	
Unit cell dimensions	a = 15.1017(6) Å	α= 66.364(3)°.
	b = 16.2658(6) Å	β= 64.796(4)°.
	c = 16.6128(6) Å	γ = 66.272(4)°.
Volume	3247.8(3) $Å^3$	
Z	1	
Density (calculated)	1.558 Mg/m^3	
Absorption coefficient	5.664 mm^{-1}	
F(000)	1541	
Crystal size	0.390 x 0.185 x 0.148 mm^3	
Theta range for data collection	3.060 to 74.141°.	
Index ranges	-14<=h<=18, -20<=k<=20, -20<=l<=20	
Reflections collected	66645	
Independent reflections	12916 [R(int) = 0.0673]	
Completeness to theta = 67.684°	100.0 %	
Absorption correction	Gaussian	
Max. and min. transmission	1.000 and 0.348	
Refinement method	Full-matrix least-squares on F^2	
Data / restraints / parameters	12916 / 163 / 1024	
Goodness-of-fit on F^2	1.024	
Final R indices [I>2sigma(I)]	R1 = 0.0573, wR2 = 0.1314	
R indices (all data)	R1 = 0.0815, wR2 = 0.1435	
Extinction coefficient	n/a	
Largest diff. peak and hole	0.576 and -0.538 $e.Å^{-3}$	

A.4.4 Co5$_{O2}$

Table 1. Crystal data and structure refinement for **Co5O2**.

Identification code	s19uh15	
Empirical formula	C49 H43 Br Co2 F18 N11 O3 P3	
Formula weight	1466.62	
Temperature	150.00(10) K	
Wavelength	1.54184 Å	
Crystal system	Triclinic	
Space group	P-1	
Unit cell dimensions	a = 12.4073(4) Å	α= 82.490(2)°.
	b = 12.7428(3) Å	β= 74.616(3)°.
	c = 19.7998(6) Å	γ = 68.521(3)°.
Volume	2806.68(16) Å^3	
Z	2	
Density (calculated)	1.735 Mg/m^3	
Absorption coefficient	7.301 mm^{-1}	
F(000)	1468	
Crystal size	0.321 x 0.309 x 0.119 mm^3	
Theta range for data collection	3.730 to 73.084°.	
Index ranges	-15<=h<=15, -11<=k<=15, -19<=l<=24	
Reflections collected	26908	
Independent reflections	11139 [R(int) = 0.0307]	
Completeness to theta = 67.684°	100.0 %	
Absorption correction	Gaussian	
Max. and min. transmission	0.766 and 0.172	
Refinement method	Full-matrix least-squares on F^2	
Data / restraints / parameters	11139 / 4 / 818	
Goodness-of-fit on F^2	1.018	
Final R indices [I>2sigma(I)]	R1 = 0.0454, wR2 = 0.1211	
R indices (all data)	R1 = 0.0472, wR2 = 0.1230	
Extinction coefficient	n/a	
Largest diff. peak and hole	0.941 and -0.572 e.Å^{-3}	

A.4.5 Co6$_{O2}$

Table 1. Crystal data and structure refinement for **Co6O2**.

Identification code	s20uh3	
Empirical formula	C96 H81.50 Co4 F36 N24.50 O10 P6	
Formula weight	2843.89	
Temperature	150.00(10) K	
Wavelength	0.71073 Å	
Crystal system	Triclinic	
Space group	P-1	
Unit cell dimensions	a = 12.3996(2) Å	α= 82.7631(15)°.
	b = 13.0253(2) Å	β= 73.0906(17)°.
	c = 19.5910(3) Å	γ = 66.6610(19)°.
Volume	2779.40(9) Å^3	
Z	1	
Density (calculated)	1.699 Mg/m^3	
Absorption coefficient	0.803 mm^{-1}	
F(000)	1431	
Crystal size	0.248 x 0.217 x 0.130 mm^3	
Theta range for data collection	2.745 to 27.484°.	
Index ranges	-16<=h<=16, -16<=k<=12, -23<=l<=25	
Reflections collected	25175	
Independent reflections	12726 [R(int) = 0.0237]	
Completeness to theta = 25.242°	99.9 %	
Absorption correction	Semi-empirical from equivalents	
Max. and min. transmission	1.00000 and 0.69306	
Refinement method	Full-matrix least-squares on F^2	
Data / restraints / parameters	12726 / 144 / 976	
Goodness-of-fit on F^2	1.024	
Final R indices [I>2sigma(I)]	R1 = 0.0439, wR2 = 0.1173	
R indices (all data)	R1 = 0.0529, wR2 = 0.1251	
Extinction coefficient	n/a	
Largest diff. peak and hole	0.760 and -0.497 e.Å^{-3}	

A.4.6 Mononuclear Co6

Table 1. Crystal data and structure refinement for **mono-NO2**.

Identification code	s19uh16	
Empirical formula	C30 H22 Cl Co F6 N9 O2 P	
Formula weight	779.91	
Temperature	150.00(10) K	
Wavelength	1.54184 Å	
Crystal system	Monoclinic	
Space group	$P2_1/c$	
Unit cell dimensions	a = 14.8449(2) Å	α= 90°.
	b = 8.26670(10) Å	β= 92.0850(10)°.
	c = 25.0374(3) Å	γ = 90°.
Volume	3070.51(7) Å^3	
Z	4	
Density (calculated)	1.687 Mg/m^3	
Absorption coefficient	6.433 mm^{-1}	
F(000)	1576	
Crystal size	0.228 x 0.185 x 0.141 mm^3	
Theta range for data collection	2.979 to 73.115°.	
Index ranges	-18<=h<=16, -10<=k<=10, -31<=l<=31	
Reflections collected	70471	
Independent reflections	6121 [R(int) = 0.0543]	
Completeness to theta = 67.684°	100.0 %	
Absorption correction	Gaussian	
Max. and min. transmission	0.733 and 0.408	
Refinement method	Full-matrix least-squares on F^2	
Data / restraints / parameters	6121 / 0 / 516	
Goodness-of-fit on F^2	1.047	
Final R indices [I>2sigma(I)]	R1 = 0.0360, wR2 = 0.0936	
R indices (all data)	R1 = 0.0391, wR2 = 0.0959	
Extinction coefficient	n/a	
Largest diff. peak and hole	0.471 and -0.483 e.Å^{-3}	

A.4.7 Copper Dimer

Table 1. Crystal data and structure refinement for e17uh2.

Identification code	e17uh2	
Empirical formula	C26 H22 B2 Cu2 F8 N8 O2	
Formula weight	779.21	
Temperature	150.00(13) K	
Wavelength	0.71073 Å	
Crystal system	Monoclinic	
Space group	$P2_1/n$	
Unit cell dimensions	a = 7.9509(3) Å	α= 90°.
	b = 13.5071(4) Å	β= 106.786(4)°.
	c = 13.6711(6) Å	γ = 90°.
Volume	1405.63(10) $Å^3$	
Z	2	
Density (calculated)	1.841 Mg/m^3	
Absorption coefficient	1.611 mm^{-1}	
F(000)	780	
Crystal size	0.270 x 0.240 x 0.130 mm^3	
Theta range for data collection	3.395 to 30.237°.	
Index ranges	-11<=h<=11, -19<=k<=18, -19<=l<=17	
Reflections collected	27113	
Independent reflections	3904 [R(int) = 0.0334]	
Completeness to theta = 25.242°	99.8 %	
Absorption correction	Semi-empirical from equivalents	
Max. and min. transmission	1.00000 and 0.84105	
Refinement method	Full-matrix least-squares on F^2	
Data / restraints / parameters	3904 / 0 / 225	
Goodness-of-fit on F^2	1.023	
Final R indices [I>2sigma(I)]	R1 = 0.0314, wR2 = 0.0727	
R indices (all data)	R1 = 0.0389, wR2 = 0.0758	
Extinction coefficient	n/a	
Largest diff. peak and hole	0.616 and -0.658 $e.Å^{-3}$	

A.4.8 Copper Tetramer

Table 1. Crystal data and structure refinement for e17uh3.

Identification code	e17uh3	
Empirical formula	C70 H67 B4 Cu4 F16 N21	
Formula weight	1803.84	
Temperature	150.0(3) K	
Wavelength	0.71073 Å	
Crystal system	Triclinic	
Space group	P-1	
Unit cell dimensions	a = 13.0843(4) Å	α= 70.299(3)°.
	b = 17.5387(5) Å	β= 70.200(3)°.
	c = 18.5752(7) Å	γ = 88.362(2)°.
Volume	3758.2(2) $Å^3$	
Z	2	
Density (calculated)	1.594 Mg/m^3	
Absorption coefficient	1.215 mm^{-1}	
F(000)	1828	
Crystal size	0.400 x 0.150 x 0.100 mm^3	
Theta range for data collection	3.291 to 27.532°.	
Index ranges	-16<=h<=16, -22<=k<=17, -23<=l<=23	
Reflections collected	46744	
Independent reflections	16618 [R(int) = 0.0382]	
Completeness to theta = 25.242°	99.8 %	
Absorption correction	Semi-empirical from equivalents	
Max. and min. transmission	1.00000 and 0.86782	
Refinement method	Full-matrix least-squares on F^2	
Data / restraints / parameters	16618 / 192 / 1349	
Goodness-of-fit on F^2	1.015	
Final R indices [I>2sigma(I)]	R1 = 0.0520, wR2 = 0.1153	
R indices (all data)	R1 = 0.0890, wR2 = 0.1335	
Extinction coefficient	n/a	
Largest diff. peak and hole	0.674 and -0.520 $e.Å^{-3}$	

A.4.9 Copper Cluster

Table 1. Crystal data and structure refinement for e18uh1.

Identification code	e18uh1	
Empirical formula	C44.50 H46.50 Cu2.50 N12 O5.50	
Formula weight	996.28	
Temperature	150(2) K	
Wavelength	0.71073 Å	
Crystal system	Triclinic	
Space group	P-1	
Unit cell dimensions	a = 17.0371(10) Å	a= 65.064(6)°.
	b = 17.9462(10) Å	b= 89.248(5)°.
	c = 19.5498(12) Å	g = 72.810(5)°.
Volume	5135.0(6) $Å^3$	
Z	4	
Density (calculated)	1.289 Mg/m^3	
Absorption coefficient	1.083 mm^{-1}	
F(000)	2056	
Crystal size	0.300 x 0.200 x 0.080 mm^3	
Theta range for data collection	3.322 to 25.388°.	
Index ranges	-20<=h<=20, -17<=k<=21, -23<=l<=22	
Reflections collected	40866	
Independent reflections	17912 [R(int) = 0.0737]	
Completeness to theta = 25.242°	95.2 %	
Refinement method	Full-matrix least-squares on F^2	
Data / restraints / parameters	17912 / 220 / 1413	
Goodness-of-fit on F^2	1.033	
Final R indices [I>2sigma(I)]	R1 = 0.0922, wR2 = 0.2535	
R indices (all data)	R1 = 0.1843, wR2 = 0.3159	
Extinction coefficient	n/a	
Largest diff. peak and hole	0.810 and -0.663 e.$Å^{-3}$	

A.4.10 Zinc Cluster

Table 1. Crystal data and structure refinement for s18uh4.

Identification code	s18uh4	
Empirical formula	C168 H128 B6 F24 N54 O3 Zn10	
Formula weight	4125.80	
Temperature	150.0(3) K	
Wavelength	1.54184 Å	
Crystal system	Monoclinic	
Space group	$P2_1/n$	
Unit cell dimensions	a = 17.0379(4) Å	α= 90°.
	b = 24.969(6) Å	β= 106.371(2)°.
	c = 20.9326(4) Å	γ = 90°.
Volume	8544(2) Å^3	
Z	2	
Density (calculated)	1.604 Mg/m^3	
Absorption coefficient	2.353 mm^{-1}	
F(000)	4168	
Crystal size	0.200 x 0.040 x 0.020 mm^3	
Theta range for data collection	2.824 to 68.517°.	
Index ranges	-19<=h<=20, -30<=k<=26, -19<=l<=25	
Reflections collected	56168	
Independent reflections	15691 [R(int) = 0.0853]	
Completeness to theta = 67.684°	100.0 %	
Absorption correction	Semi-empirical from equivalents	
Max. and min. transmission	1.00000 and 0.67603	
Refinement method	Full-matrix least-squares on F^2	
Data / restraints / parameters	15691 / 3 / 1243	
Goodness-of-fit on F^2	1.029	
Final R indices [I>2sigma(I)]	R1 = 0.0665, wR2 = 0.1644	
R indices (all data)	R1 = 0.1086, wR2 = 0.1933	
Extinction coefficient	n/a	
Largest diff. peak and hole	1.000 and -0.842 e.Å^{-3}	